USE OF CHLORINATED CARBON MATERIALS TO MAKE NITROGEN DOPED AND UN-DOPED CARBON NANOMATERIALS AND THEIR USE IN WATER TREATMENT

by

Winny Kgabo Maboya

Student No: 0310549A

A thesis submitted to the Faculty of Science at the University of the Witwatersrand, Johannesburg, in fulfilment of the requirements for the degree of

Doctor of Philosophy in Chemistry

Johannesburg, 2018

DECLARATION

I declare that this thesis is my own work under the supervision of Prof. Sabelo D. Mhlanga and Prof. Neil J. Coville. It is submitted for the degree of Doctor of Philosophy in the University of the Witwatersrand, Johannesburg. It has not been submitted before for any degree or examination in any other University.

(*Signed*) Winny Kgabo Maboya

On this _____ day of _____2018

ABSTRACT

Carbon nanomaterials (CNMs) and nitrogen doped CNMs (NCNMs) with different morphologies were obtained by decomposition of various chlorinated organic solvents using a chemical vapor deposition (CVD) bubbling and injection methods over a Fe-Co/$CaCO_3$ catalyst. CNFs, CNTs with secondary CNT or CNF growth, bamboo-compartmented and hollow CNTs were obtained. Increasing the growth time to 90 min resulted in growth of ~ 90 % of secondary CNFs on the surface of the main CNTs, using dichlorobenzene (DCB) as source of chlorine. The secondary CNFs grew at defects sites of the CNT wall. Secondary CNFs were not observed at other studied temperatures, 600, 650. 750 and 800 °C.

Using an injection CVD method, horn-, straw- and pencil-shaped closed and open-ended CNTs/CNFs were obtained from CH_3CN/DCB solutions of various volume ratios. CNT growth was enhanced after addition of chlorine. Highly graphitic carbon materials were produced from feed solutions containing low and high DCB concentrations. CNTs with defects were obtained from solutions containing 66.7 vol.% DCB. Post-doping of the N-CNTs with chlorine and of the chlorinated CNTs with nitrogen resulted in production of highly graphitic materials. Using a bubbling CVD method, mixtures of CNMs namely, hollow and bamboo-compartmented CNTs with and without intratubular junctions and carbon nano-onions filled with metal nanoparticles were obtained from feed solutions containing TTCE.

MWCNT/PVP composite nanofibers were successfully synthesized using an electrospinning technique. Adsorption capacities of 15–20 g/g were obtained in pure oil or in oil-water mixtures. The adsorption capability of the MWCNT/PVP composite depended on the type of oil and its viscosity.

DEDICATION

I would like to dedicate this thesis to the following people:

1. My husband (Hosea) and children (Kagiso, Reshoketswe and Phetogo) for bearing with me throughout this journey.
2. My siblings (Judy, Stephina, Regina, Diana and Happy) for always putting me in their prayers.
3. My late parents in law (Mr. Kgabo and Mrs. Johanna Maboya). It has always been my father in law's wish that I become a doctor one day, this is for him.
4. My parents for bringing me into this world and raising me to be a God fearing woman.

ACKNOWLEDGEMENTS

Firstly, I would like to thank God, for giving me strength throughout this journey.

Above all I would like to thank my co-supervisor Professor Neil J. Coville for his outstanding contribution to this work. His knowledge and expertise enhanced my research and thinking skills. He gave me a reason to complete this work.

My sincere gratitude to my supervisor Professor Sabelo D. Mhlanga (University of South Africa, UNISA) for giving me an opportunity to study for my doctoral degree. His valuable contribution to this work is highly appreciated.

Thank you to the University of the Witwatersrand for providing the facilities to conduct my research. My sincere gratitude to the microscopy (MMU) unit at the University of the Witwatersrand for providing instrumental facilities to characterize the materials produced in this research. Special thanks to Professor Alexander Ziegler, Dr. Reddy, Mr. Geber, Dr. Tetana, Dr. Maubane and Ms. Duduzile at the MMU unit for their invaluable training on the instruments.

I am grateful to the Vaal University of Technology for proving financial support throughout the study. Special thanks to Professor Justice Moloto, for always being there especially when it was tough. His words of encouragement, always trying to secure research money for me, I am humbled by his kindness. Greatest appreciation to my boss and HOD, Professor Bobby Naidoo, for always giving me time off when I needed it. Thanks to Dr. Postlet Shumbula from Mintek.

I would also like to extent my appreciation to all CATOMAT group members, past and present. Special mention to Dr. Isaac Nogwe, Dr. William Dlamini, Ms. Boitumelo Matsoso, Ms. Alice Magubane, and Mr. Thomas Mongwe.

Thank you to Ms. Dikeledi More for helping me get started on the electrospinning experiments.

Thank you to Mr. Lebea Nthunyane (UNISA), for selflessly helping me with the electrospinning experiments at UNISA.

PUBLICATIONS AND PRESENTATIONS

Publications:

1. Winny K. Maboya, Neil J. Coville and Sabelo D. Mhlanga, "The Synthesis of Carbon Nanomaterials using Chlorinated Hydrocarbons over a Fe-Co/$CaCO_3$ Catalyst", *South African Journal of Chemistry*, 2016, **69**, 15–26.
2. Winny K. Maboya, Neil J. Coville and Sabelo D. Mhlanga, "One step synthesis of CNTs with secondary nanofiber growth: the role of chlorine", **To be published.**
3. Winny K. Maboya, Neil J. Coville and Sabelo D. Mhlanga, "Synthesis of chlorinated nitrogen-doped MWCNTs by injection CVD method", **To be published.**
4. Winny K. Maboya, Neil J. Coville and Sabelo D. Mhlanga, "Heteroatom of chlorine and nitrogen doped carbon nanomaterials using acetonitrile with aromatic and aliphatic chlorinated solvents: Post-doping treatments", **To be published.**
5. Winny K. Maboya, Neil J. Coville and Sabelo D. Mhlanga, "Fabrication of MWCNT/PVP composite fibers with enhanced interaction formed by chlorinating the MWCNT and their use as adsorbents for oil", **To be published.**

Presentations:

1. W.K. Maboya, "Role of chlorine on the morphology of carbon nanotubes synthesized over Fe-Co/$CaCO_3$ catalyst", Poster presentation, Walter Sizulu University, South African Chemical Institite (SACI) 2013 Conference,
2. W.K. Maboya, "The effect of chlorine in the synthesis of carbon nanomaterials using Fe-Co/$CaCO_3$ catalysts", Oral presentation, Nano Africa International 2014 Conference,

3. W.K. Maboya, “The synthesis of carbon nanomaterials using chlorinated hydrocarbons over a Fe-Co/$CaCO_3$ catalyst”, Poster presentation, 27th Annual CATSA Conference 2016, 6 – 9 November 2016.
4. W.K Maboya, “One-step synthesis of CNTs with secondary growth: The role of chlorine”, Poster presentation, DST/NRF CoE in strong materials research showcase, University of the Witwatersrand, April 2017.

TABLE OF CONTENTS

LIST OF FIGURES

Chapter 4

Chapter 5

Chapter 6

Appendix A: Supplementary Data

LIST OF TABLES

Chapter 5

Chapter 7

ABBREVIATIONS

a.u.	**Arbitrary units**
BET	**Brunauer-Emmet-Teller**
CB	**Chlorobenzene**
Cl-MWCNTs	**Chlorinated multi walled carbon nanotubes**
CNFs	**Carbon nanofiber(s)**
CNM(s)	**Carbon nanomaterial(s)**
CNSs	**Carbon nanospheres**
CNT(s)	**Carbon nanotube(s)**
CVD	**Chemical vapor deposition**
D	**Disorder-induced band**
DCB	**Dichlorobenzene**
DCE	**Dichloroethane**
EDX	**Energy dispersive X-ray**
FTIR	**Fourier transform infrared**
G	**Graphitic band**
I_D/I_G ratio	**Intensity ratio of D to G bands**
min	**minutes**
mL/min	**Milliliter per minute**
MWCNTs	**Multi walled carbon nanotubes**
N-CNMs	**Nitrogen-doped carbon nanomaterials**

N-CNTs	**Nitrogen-doped carbon nanotubes**
N-MWCNTs	**Nitrogen-doped multi walled carbon nanotubes**
PECVD	**Plasma-enhanced chemical vapor deposition**
PVP	**Polyvinylpyrrolidone**
s	**seconds**
SEM	**Scanning electron microscopy**
SWCNTs	**Single walled carbon nanotube**
r.t.	**Room temperature**
TCB	**Trichlorobenzene**
TCE	**Trichloroethane**
TEM	**Transmission electron microscopy**
TGA	**Thermogravimetric analysis**
TTCE	**Trichloroethane**
XRD	**X-ray diffraction**
XPS	**X-ray photoelectron spectroscopy**

CHAPTER 1

Introduction

1.1 Background and motivation

Most materials fit into the following general categories, namely metals, ceramics, ceramics, organic/inorganic polymers, composites, semi-conductors, biomaterials, and advanced materials, with carbon nanomaterials being a type of an advanced material. Materials play a major role in many technological fields and in human lives. Materials are the basis for improving human production and their living standards[1]. Whenever there is a new material of great importance, a huge development in productivity will be received and human society will leap forward[1]. There is a need to create a new generation of materials in order to better our lives. In order to create the new generation of materials, it is necessary to understand the relationship between the existing materials and their structure. Combination of appropriate materials can result in production of materials with desirable properties[2]. Nanoscience has paved the way to tailor the properties and performance of materials to a new level, as researchers create new materials by working at the atomic or molecular level.

The need for lightweight, high strength materials has been recognized since the invention of the airplane. As the strength and stiffness of a material increases, the dimensions, and consequently, the mass, of the material required for a certain load bearing application is reduced. This leads to several advantages in the case of aircraft and automobiles such as increase in payload and improvement of fuel efficiency[3].

Since reported by Ijima[4], carbon nanotubes (CNTs) proved to be excellent materials because of their higher strength and low weight. CNTs have become the material of choice for many applications due to their excellent thermal, mechanical and electronic properties. CNTs are useful for any application where robustness and flexibility are desired, due to their stability under extreme chemical environments, high temperatures and moisture[5]. The unique properties of CNTs have aroused interest in their possible applications namely, as sensors[6], in field emission

devices[7], as flat panel displays[8], for energy storage[9], in biomedicine[10], as adsorbent materials[11], and in composites[12], to name a few.

Application of CNTs in materials and devices is hindered by the difficulty to process and manipulate them and their inability to be dispersed in most solvents (both water and organic solvents). Functionalization of CNTs by attaching appropriate chemical groups was found to enhance their solubility.

In this study CNTs and nitrogen-doped CNTs (NCNTs) were functionalized with chlorine, and the effect of chlorine on their morphology was studied. Due to the purification properties that chlorine has, it is expected that the materials produced after chlorination will be more graphitic and have less amorphous carbon. It has been shown that incorporation of Cl in the CNMs results in surface functionalisation,[13] ease of purification,[14] increased yields[15] and surface restructuring.[16]

The synthesized CNTs in this study will then be used as fillers in polymer matrices. The combination of polymer matrix and CNT as nanofillers offer opportunities for future materials that can be applied in various fields, namely, in aerospace technology[17], drug delivery[18], filtration[19], and as sensors[20]. CNTs have previously been used as fillers for polymer matrix. However, use of chlorine functionalized CNTs with secondary carbon nanofiber growth as fillers in polymer matrices has not been reported. The presence of secondary nanofibers on the surface of the primary CNTs is expected to enhance the surface area of the nanomaterials and in turn increase the interfacial bonding between the CNTs and the polymer matrix for mechanical applications. It has been difficult to translate the mechanical properties of CNTs into useful materials due to interfacial sliding, matrix/fiber dispersion, and the introduction of defects. Even though these carbon nanotubes have exceptional strength and modulus the difficulty in dispersing the unmodified nanotubes into polymers, as well as aligning them linearly, makes the progress on their integration into fiber slow. This problem has been combated through the use of CNT surface modification by oxidation, functionalization and by physical coating. Fixation of oxygen is usually carried out by oxidation in a liquid or gas phase but this process is not selective as it results in functionalization of CNTs with several types of oxygen containing groups, i.e. COOH, C=O, OH.[21] Functionalization of CNT surfaces with oxygen groups often result in destruction of the CNT structure, mainly decapping at the end of the tubes and cutting and

breaking of the tube length. Destruction of the CNT structure may cause changes in their mechanical properties.

The CNT/polymer composite materials will then be applied as adsorbents for oil in oil-spill cleanups. Water scarcity has emerged as one of the most serious global challenges which threatens over one-third of the world's population[22]. Recovery and recycling of wastewater has been two promising ways to combat the water scarcity. Oil is one of the pollutants that can enter our water streams. Oil spills can affect wildlife, marine and coastal habitats, fisheries and recreational activities. The oil harms the wildlife through toxic contamination (inhalation and ingestion) or by physical contact. Use of adsorbents to clean oil-spill was found to be the most effective. Polymeric materials such as polypropylene and polyurethane foams are the most commonly used commercial sorbents in oil spill cleanup due to their oleophilic and hydrophobic characteristics[23,24]. The disadvantage of using these polymeric materials is that they degrade very slowly. Hence, in this study PVP was used as polymer since it is easily degradable. Since PVP is soluble in water we embedded CNTs inside it in order to improve its properties and render it useful in oil adsorption from oil-water emulsions.

The research questions posed were:

1. What effect does chlorine have on the morphology of the CNTs and NCNTs?
2. Can varying the concentration of chlorine in the feed have an impact on the morphology of the CNTs and N-CNTs?
3. Does using an injection or bubbling CVD method have an impact on the morphology of chlorine containing MWCNTs and N-MWCNTs?
4. Can use of chlorine functionalized MWCNTs improve their interaction with the polymer matrix?
5. Can the chlorine functionalized MWCNT/PVP composite membranes be used as adsorbents for oil in oil-spill cleanups.

1.2 Aims and objectives of the study

1. Investigation of the effect of chlorine on the morphology of carbon nanotubes (CNTs) using acetylene as carbon source, dichlorobenzene as chlorine source and a Fe-Co/$CaCO_3$ as catalyst by chemical vapor deposition (CVD) method.
2. Investigation of the effect of chlorine on the morphology of nitrogen-doped carbon nanotubes (N-MWCNTs) using acetylene as carbon source, dichlorobenzene as chlorine source, acetonitrile as carbon and nitrogen source and a Fe-Co/$CaCO_3$ as catalyst by injection chemical vapor deposition (CVD) method.
3. Investigation of the effect of chlorine on the morphology of N-MWCNTs using acetylene as carbon source, dichlorobenzene as chlorine source, acetonitrile as carbon and nitrogen source and a Fe-Co/$CaCO_3$ as catalyst by bubbling chemical vapor deposition (CVD) method.
4. Synthesis of chlorine functionalized CNTs/polyvinylpyrrolidone (PVP) composite nanomaterials using an electrospinning method.
5. Application of the CNTs/PVP composite nanofiber membranes as adsorbents of oil in oil-spill cleanups.

1.3 Outline of thesis

Chapter 1: Present the background and motivation as well as the aims and objectives of the study.

Chapter 2: Present a literature review of carbon nanotubes (CNTs), their structure, synthesis methods, growth mechanisms, their modification by functionalization and doping, and review of CNT/polymer composites, their synthesis methods and applications and finally a brief review of application of CNT/polymer composites as adsorbents in oil-spill cleanups.

Chapter 3: Presents the synthesis of chlorine functionalized MWCNTs, their method of synthesis and various morphologies obtained using various chlorinated organic reagents by bubbling CVD method.

Chapter 4: Present a one-step synthesis of CNTs with secondary nanofiber growth using dichlorobenzene as chlorine source by bubbling CVD method. The effect of reaction time and temperature on the morphology of the CNTs was investigated.

Chapter 5: Presents the study on the effect of chlorine on the morphology of N-doped MWCNTs, and their synthesis method using dichlorobenzene as chlorine source by injection CVD method

Chapter 6: Presents the study on the effect of chlorine on the morphology of N-doped MWCNTs and their synthesis method using dichlorobenzene and tetrachloroethane as chlorine sources by bubbling CVD method.

Chapter 7: Presents synthesis of chlorine functionalized MWCNTs/PVP composite nanofiber membranes by electrospinning method and their use as adsorbents of oil in oil-spill cleanups.

Chapter 8: General conclusions, summarizing the conclusions of all the results of this study and recommendations from the study.

References

1. R.-M. Wang, S.-R. Zheng and Y.-P. Zheng, *Polymer Matrix Composites and Technology*, 1st Edition, Science Press, Woodhead Publishing in Materials, 2011.
2. G. Mittal, V. Dhand, K.Y. Rhee, S,-J. Park and W.R. Lee, *J. Ind. Eng. Che.*, 2005, **21**, 11-25.
3. S.R. Bakshi, D. Lahiri and A. Agarwal, *Int. Mat. Rev.*, 2010, **55**, 41-64.
4. S. Ijima, *Nature*, 1991, **354**, 56-66.
5. S. Sasmal, B. Bhuvaneshwari and N.R. Iyer, *Progress in Nanotechnology and Nanomaterials*., 2013, **2**, 117-129.
6. P. Soundarrajan, A. Patil, and D. Liming, *Am. Vac. Soc.*, 2002, 1198 – 1201.
7. A.G. Rinzler, J.H. Hafner, P. Nikolaev, P. Nordlander, D.T. Colbert, R.E. Smalley, L. Lou, S.G. Kim, and D. Tomanek, *Science*, 1995, **269**, 1550 – 1553.
8. Q.H. Wang, A.A. Setlur, J.M. Lauerhaas, J.Y. Dai, E.W. Seelig, and R.H. Chang, *Appl. Phys. Lett*., 1998, **72**, 399 – 400.
9. M.S. Islam, Y. Deng, L. Tong, S.N. Faisal, A.K. Roy, A.I. Minett, and V.G. Gomes, *Carbon*, 2016, **96,** 701–710.
10. A. Abarrategi, M.C. Gutierrez, C. Moreno-Vicente, V. Ramos, J.L. Lopez-Lacomba, M.L. Ferrer, and F. del Monte, *Biomaterials*, 2008, **29**, 94 – 102.
11. H.M. Al-Saidi, M.A. Abdel-Fadeel, A.Z. El-Sonbati, and A.A. El-Bindary, *J. Mol. Liq.*, 2016, **216,** 693–698.
12. M. Irfan, H. Basri, M. Irfan and W.-J. Lau, *RSC Adv*., 2015, **5**, 95421 – 95432.
13. W.H. Lee, S.J. Kim, W.J. Lee, J.G. Lee, R.C. Haddon, and P.J. Reucroft, *Appl. Surf. Scie*., 2001, **181,** 121–127.
14. I. Pełech, U.Narkiewicz, D. Moszyński, and R. Pelech, *J. Mater. Res*., 2012, **27,** 2368–2374.
15. H. Qiu, Z. Shi, L. Guan, L. You, M. Gao, S. Zhang, J. Qiu, and Z. Gu, *Carbon*, 2006, **44,** 516–521.
16. M. A. Keane, G. Jacobs, and P. M. Patterson, *J. Colloid Interface Sci*., 2006, **302,** 576–588.
17. A.H. Esbati and S. Irani, *Aerosp. Sci. Technol.*, 2016, **55**, 120-130.
18. X. Zong, K.S. Kim, D. Fang, S. Ran, B.S. Hsiao and B. Chu, *Polymer*, 2002, **43**, 4403 – 4412.

19. Z. Tang, C. Qiu, J.R. McCutcheon, K. Yoon, H. Ma, D. Fang, E. Lee, C. Kopp, B.S. Hsiao and B. Chu, *J. Polym. Sci., Part B: Polym. Phys.*, 2009**, 47**, 2288 – 2300.

20. Q. Liu, Y. Li, and M. Yang, *Sensor Actuat. B Chem.*, 2012, **161**, 967.

21. F. Avile'S, J.V. Cauich-RodríGuez and L. Moo-Tah, *Carbon*, 2009, **47**, 2970-2975.

22. A.G. Volkov, *Liquid-Liguid Interfaces: Theory and Methods*, CRC Press, Florida, 1996.

23. The International Tanker Owner Pollution Federation Limited, Measures to Combat Oil Pollution (Graham & Trotman Limited, London, 1980.

24. P. Schatzberg and D.F. Jackson, U.S. Coast Guard Report No. 734209.9 (U.S. Coast Guard Headquarters, Washington, DC, 1972).

CHAPTER 2

Literature review

2.1 Carbon nanotubes

CNTs were first discovered in 1952 from the observation of the tubular nature of some nano-sized carbon filaments that had been made and studied using transmission electron microscope (TEM).[1] Discovery of multi-walled carbon nanotubes (MWCNTs) was later reported and their study popularised by Ijima in 1991.[2] These MWCNTs were found in the hard deposit growing at the cathode without a catalyst, during electric arc experiments to produce fullerenes. CNTs have become the material of choice in most applications due to their excellent thermal, mechanical and electronic properties. These properties have aroused interest in their possible applications namely, as sensors and probes[3,4], in field emission devices[5,6], as flat panel displays[7], in electrochemical devices[8,9], for energy storage[10], in biomedicine[11-13], as adsorbent materials[14], and in composites[15-17].

2.1.1 Structure of carbon nanotubes

Based on the electronic configuration of carbon, there is a small energy difference between the 2s and 2p orbital levels which allows the carbon atom to exist in several hybridization states in different materials namely, sp, sp^2 and sp^3 (Figure 2.1).

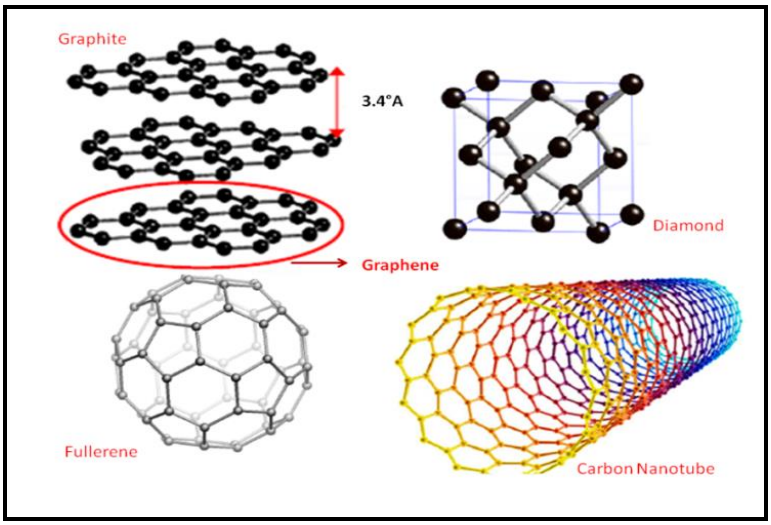

Figure 2.1 Schematic representation of carbon allotropes, (a) graphite, (b) diamond, (c) fullerene, and (d) single wall carbon nanotube (SWCNTs)[18].

The carbon atoms can arrange themselves in structures of different dimensions ranging from diamond (3D), graphite (2D), carbon nanotubes (1D) and fullerene (0D) due to their hybridization flexibility of the carbon orbitals (Figure 2.1).

In graphite, atoms of carbon form planar layers called graphene layers. Each layer is made up of rings containing six carbon atoms, linked to each other in a hexagonal structure. Graphite is a good conductor of electricity due to the presence of mobile electrons.

Diamond, is one of the hardest substances known to man and is a naturally occurring form of carbon. Each carbon atom is bonded tetrahedrally to four other carbon atoms in an sp^3 hybridized fashion. Its hardness arises from the fact that all the four valence electrons of carbon are all utilized, hence there are no free electrons available for bonding. Diamond is used in industrial cutting tools due to its hardness and it is also used for making jewelry.

Amorphous carbon (Ac) is another form of carbon containing varying proportions of sp^2 and sp^3 bonded carbons. Amorphous carbon is usually formed when a carbon material burns in limited amount of oxygen. Ac is given several names, such as a lampblack, gas black and channel black[19]. It is not considered an allotrope of carbon because its structure is not well defined.

Fullerenes are closed-cage carbon molecules with three-coordinate carbon atoms comprising of spherical or nearly-spherical surfaces. A well-known fullerene molecule is buckminsterfullerene, C_{60}, which has sixty carbon atoms forming a truncated-icosahedral structure with twelve pentagonal rings and twenty hexagonal rings[20]. While regular hexagons can tile a plane, pentagons can tile a sphere,[20]. Some sp^3 character is present in the essentially sp^2 carbons of fullerenes. It has a structure of a soccer ball.

A carbon nanotube (CNT) is a tubular structure made of carbon atoms, having a nanometer diameter and a large length/diameter ratio. Carbon nanotubes are a type of carbon fiber which comprises coaxial cylinders of graphitic sheets, which range from 2 to 50 sheets.

CNT samples are usually found in one of two forms: multi-wall carbon nanotubes (MWCNTs) consisting of an array of coaxial nanotubes and single-wall carbon nanotubes (SWCNTs) composed of a single graphene sheet. Diameters of the CNTs usually range between 2 and 25 nm and the distance between the sheets is about 0.34 nm[21].

Three types of SWCNTs exist, namely armchair, chiral and zigzag and each depends on how the graphene layer is "rolled up" during its creation process. The structure of a SWCNT is characterized by a pair of indices (*n, m*) that describe the chiral vector and is directly linked to the electrical properties of CNTs[22]. When $m = 0$ the nanotube is called zigzag, when n = m the nanotube is called armchair and all other configurations are called chiral[23].

MWCNTs can be formed in two structural models; the Russian Doll model and the Parchment model. When a CNT contains another tube inside it and the outer nanotube has a greater diameter than the thinner nanotube, it is called the Russian Doll model[22]. When a single graphene sheet is wrapped around itself many times, the same as a rolled up scroll of paper, it is called the Parchment model[22].

2.1.2 Synthesis of CNTs

High temperature preparation techniques such as laser ablation and arc discharge have been used earlier to produce CNTs. These methods have been replaced by low temperature chemical vapor deposition (CVD) techniques which allow temperatures <800 °C to be used. CVD allows control

of the alignment, purity, orientation, length, diameter and density of the CNTs[24]. CVD can be used with a wide range of hydrocarbons in any state (solid, liquid or gas. The method enables the use of various substrates and offers better control of the growth parameters[25]. The methods used to synthesis CNTs and other CNMs are discussed below.

(i) Arc discharge method

The electric arc discharge method was the first technique used to synthesize multi-walled and single-walled CNTs. In this method an electric arc discharge is generated between two graphite electrodes under an inert atmosphere of helium or argon. A very high temperature is obtained which allows the sublimation of carbon. The synthesis can be performed by the arc evaporation of pure graphite or co-evaporation of graphite and a metal[26]. For the CNTs to be obtained, purification by gasification with oxygen or carbon dioxide is needed[27]. The first authors to successfully produce MWCNTs at the gram level were Ebbesen and Ajayan in 1992[28]. Substantial amounts of SWCNTs grown over a metal catalyst as substrate, were first produced in 1993 by Bethune and coworkers[29]. The process parameters used were small gaps between electrodes (<1 mm), a high current (100 A), and generation of a plasma between the electrode at about 4000 K and a voltage range of 30–35 V, using controlled electrode dimensions[30]. However, the use of an arc discharge method is limited by its drawbacks: the synthesis process is non-continuous (CNT growth needs to be interrupted to remove the product from the chamber) and poor product purity.

(ii) Laser ablation method

The second very useful and powerful technique used to produce CNTs is the laser ablation method. In this process, a piece of graphite is vaporized by laser irradiation under an inert atmosphere. This results in soot containing nanotubes which are cooled at the walls of a quartz tube. Two kinds of products are possible: MWCNTs or SWCNTs[26]. In this process a purification step by gasification to eliminate carbonaceous material is also needed. The effectiveness of the gasification depends on the type of reactant used. Growth of high quality SWCNTs was first

achieved by Collins and coworkers[31]. Although the laser ablation method is known to produce CNTs with high quality and high purity single walls[32], it is more expensive to use than the arc discharge method.

(iii) Chemical vapor deposition (CVD) method

Carbon filaments and fibers have been produced by thermal decomposition of hydrocarbons in the presence of a catalyst since the 1960s[33,34]. In the CVD process, metal or bimetallic catalyst nanoparticles (usually Fe[35-37], Co[37], Ni[38], Fe-Co[37,39], or Fe-Ni[40]) are used as substrates. They are placed in a quartz boat which is placed in the furnace. The nanoparticles are then subjected to reduction by heating under an inert carrier gas such as nitrogen or argon until the desired reaction temperature is achieved. A hydrocarbon gas is then passed into the furnace to grow the nanotubes. Methane and acetylene are the most widely used carbon sources. Carbon monoxide can also be used as carbon source. In some cases, liquid carbon sources like toluene, benzene, methanol, ethanol, etc., are heated and then the inert gas is bubbled through the liquid to transport their vapors into the furnace. The diameters of the CNTs formed usually depend on the size of the metal catalyst. The CNT growth can be explained by various mechanisms based on the catalyst-metal interaction. In situ TEM studies have demonstrated that the nanotube growth in CVD is initiated by the formation of a carbon cap at the surface of the particle.[41] Kuznetsov et al. hypothesized that the carbon nucleus has the form of a flat saucer whose edges are bent in order to bond to the metal surface.[42] They found that the change in Gibbs free energy for the formation of the nucleus includes four contributions: the free energy of precipitation of the carbon atoms from the particle, the free energy associated with the nucleus edges and the strain energy arising from bending the graphene layer. The model predicts that the critical radius of nucleus formation decreases with increasing temperature, increasing saturation of the metal-carbon solution and decreasing specific edge free energy. A good agreement was observed between the diameter and the average diameter of CNTs formed by different methods as a function of the catalyst nature and synthesis temperature.[42]

When the interaction is weak, CNT precipitates out across the metal bottom, pushing the whole metal particle off the substrate. This is called a “tip-growth model” (Figure 2.2a). When the

interaction between the substrate and the metal catalyst is strong, CNT precipitation emerges out from the metal's apex, which leads to CNT growing up with the catalyst particle rooted on its base in a mechanism called "base-growth model" (Figure 2.2b). A stronger metal-support distribution will improve dispersion, give a narrow size distribution and reduce sintering and agglomeration of active metal sites. It will also hinder the reduction of the oxide precursors on the active catalytic species[41].

Plasma-enhanced chemical vapor deposition (PECVD) is another CVD method used to produce CNTs. The PECVD method generates a glow discharge in a chamber or a reaction furnace by means of a high frequency voltage applied to both electrodes. A substrate is placed on the grounded electrode. The reaction gas is supplied from the opposite plate in order to form a uniform film. Catalytic metals such as Co, Fe and Ni are used. They are placed on a Si, SiO_2 or glass substrate using thermal CVD or sputtering. The advantage of using PECVD over the arc discharge and laser ablation methods is that the synthesis in PECVD uses feedstock gases such as CH_4 and CO, so there is no need for a solid graphite source. The argon-assisted plasma is used to break down the feedstock gases into C_2, CH and other reactive carbon species (C_xH_y) to facilitate growth at low temperature and pressure[43].

(iv) **The hydrothermal methods**

The sonochemical/hydrothermal technique is another method used to prepare different carbon nanostructures such as carbon nano-onions, nanowires, nanorods, nanobelts and MWCNTs. Horn-shaped CNTs were produced by hydrothermal processing where a mixture of pentachloropyridine and metallic sodium are placed into a 25 mL stainless steel autoclave[44]. The autoclave was sealed, heated to 350 °C and maintained at this temperature for 10 h, and cooled to room temperature in the furnace. The product was washed sequentially with ethanol, concentrated salt acid aqueous solution and distilled water to remove impurities. The final product was then dried at 100 °C in air for 4 h[44]. The hydrothermal process has advantages when compared to other methods namely, (i) the starting materials are easy to obtain and are stable in

ambient temperature, (ii) it is a low temperature process (about 150 – 180 °C), and (iii) there is no hydrocarbon or carrier gas required for operation.

2.1.3 Properties of CNTs

CNTs are nanostructured materials which exhibit unique thermal, mechanical, magnetic and electronic properties. CNT has the same hardness as diamond, but its thermal capacity is twice that of pure diamond. Its current-carrying capacity is 1000 times higher than that of copper and they are thermally stable up to 4000 K. CNTs can be metallic or semiconducting, depending on their diameter and chirality.

(i) Mechanical properties

The mechanical properties of a solid must ultimately depend on the strength of its interatomic bonds[45]. CNTs are predicted to have high stiffness and axial strength as a result of the carbon-carbon sp^2 bonding[46]. A perfect CNT exhibits an elastic modulus of the order 270–950 GPa and has a reported tensile strength of 11–63 GPa[47], which is 10–100 times higher than the strongest steel and with less weight[48]. CNTs have the highest Young's modulus when compared with composite tubes such as CN, C_3N_4, BN, BC_3, BC_2N, etc., These properties, coupled with the lightness of CNTs, makes them excellent candidates to use in the production of composite materials for various applications.

(ii) Electrical properties

CNTs can be either metallic or semiconducting depending on their structural parameters, i.e. chirality and diameter[49-52]. Carbon nanotubes conduct electricity better than metals. When electrons travel through the metal there is some resistance to their movement. This resistance happens when electrons bump into metal atoms. When an electron travels through a carbon nanotube, it travels under the rules of quantum mechanics, and so it behaves like a wave

traveling down a smooth channel with no atoms to bump into. This quantum movement of an electron within nanotubes is called ballistic transport.

(iii) Thermal properties

As diamond and graphite display the highest known thermal conductivity of all materials at moderate temperatures, it is likely that nanotubes should be outstanding in this regard[53]. The thermal properties of CNTs are related to their unique structure and small size. CNTs have thermal conductivity values of up to 6600 $Wm^{-1}K^{-1}$ at low temperatures[54].

(iv) Magnetic properties

The presence of encapsulated catalyst nanoparticles inside the CNTs can render them magnetic. Catalytic nanoparticles can form inside the CNTs via three routes: (1) in situ during CNT growth (e.g. from a metal especially an iron containing catalyst during CVD synthesis of MWCNTs), (2) from added metallic catalyst particles e.g. from Fe, Co or Ni metal filled electrodes during MWCNT or SWCNT synthesis via the arc discharge method, and (3) by filling the synthesized open-ended CNTs with nonmagnetic liquid metals[56]. Studies suggested that the presence of iron catalyst inside CNTs may be helpful in their magnetic manipulation, for example alignment of CNTs in polymer composites[57,58] or for targeted drug delivery[59]. Tethering of magnetic nanoparticles onto the surface of the CNTs have been another way of enhancing their magnetic properties[60,61].

2.2 Modification of carbon nanomaterials

2.2.1 Functionalization of carbon nanomaterials

Translation of CNTs into useful materials is often hindered by their limited solubility in water and most organic solvents. Scientists came up with ways to modify the surface of the CNTs in order to combat this problem. The surface of the CNTs can be modified by oxidation, functionalization or by physical coating. Oxidation involves use of oxidizing acids to add oxygen onto the sidewalls of the CNTs. Fixation of oxygen is usually carried out by oxidation in a liquid

or gas phase but this process is not selective as it results in functionalization of CNTs with several types of oxygen containing groups, i.e. COOH, C=O, OH,[62] etc. These types of C–O functionalities can be determined by X-ray photoelectron spectroscopy (XPS) and an example is shown in Figure 2.2[63]. Here O–C–O and C–O functionalities are detected in the O1s XPS spectra. Functionalization of CNT surfaces with oxygen groups often results in destruction of the CNT structure, mainly decapping at the end of the tubes and cutting and breaking of the tube length. Destruction of the CNT structure may cause changes in their mechanical properties. It is desirable to functionalize CNTs with heteroatoms that will result in only one type of chemical group. Functionalization can also involve addition of heteroatoms such as halogens, nitrogen, sulphur, etc. onto the sidewall of the CNTs. Halogens are a good alternative to attach to CNTs, as shown in many studies that they can render only one type of chemical group for every halogen (Figure 2.3)[64].

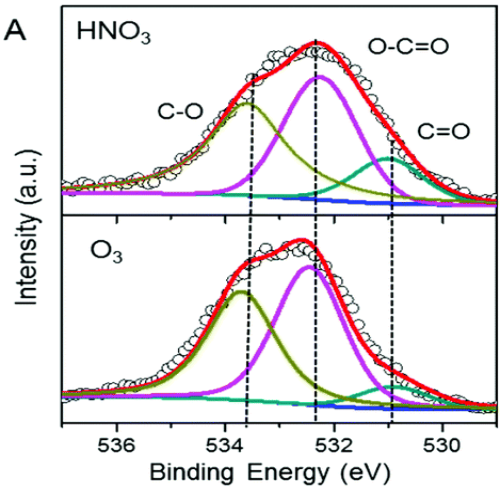

Figure 2.2 XPS spectra of the O1s region after treatment of CNTs with nitric acid (HNO_3) acid and ozone (O_3)[63].

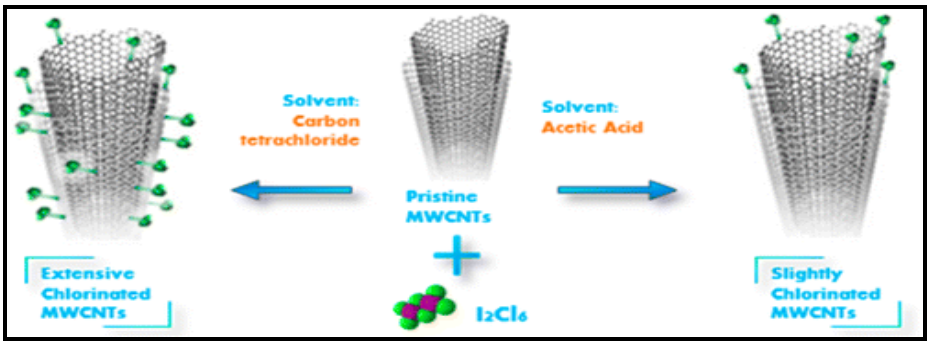

Figure 2.3 Chlorination of MWCNTs by mixing I_2Cl_6 solution with acetic acid or with carbon tetrachloride[64].

Modification of the carbon surface and electronic properties with chlorine has been explored but the effect of chlorine (Cl) on the morphology of carbon nanomaterials is still not well established. Incorporation of Cl in the CNMs resulted in their surface functionalization,[65] ease of purification,[66-68] increased yields[69] and surface restructuring.[70] The presence of chlorine atoms also produced CNTs with increased inner diameters, which resulted in filling of CNTs with metal particles.[71]

2.2.2 Doping of carbon nanomaterials

Introduction of heteroatoms into the walls of the CNTs by replacing one of the carbon atoms in a CNT, was found to enhance their application. Incorporation of nitrogen atom into the structure of the CNT results in the formation of an n-type material due to the presence of one extra valence electron in the electronic structure of nitrogen.[72,73] N-doped CNTs are more chemically active but less stable than the un-doped CNTs. The nitrogen doped CNTs has found applications in various fields for example in, electronic devices,[74] fuel cells,[75] and biomedicine.[76]

Theoretical calculations[77] and experimental measurements[78] have demonstrated that the field-emission performance of CNTs depends sensitively on their tip structure. An open-ended CNT is superior to a close-ended one. Enhanced field emission properties of the CNTs were demonstrated by Lv et al. by using a chlorine-containing benzene (trichlorobenzene) as carbon

precursor which resulted in the production of open-ended, thin-walled CNTs filled with long continuous ferromagnetic metal nanowires.[79]

Doping of CNTs with nitrogen was also found to improve the field emission property of the CNTs.[80] Thin-walled, open-ended and well-aligned N-doped CNTs synthesized using acetonitrile as carbon and nitrogen source were found to have enhanced field emission properties.[81] An increase in the amount of nitrogen incorporated into the CNTs was observed when halogenated catalyst sources were used.[82]

2.2.3 Synthesis of Cl functionalized CNTs and chlorinated N-doped CNTs

Generally, chlorine functionalization of undoped and nitrogen-doped carbon structures can be achieved using the same synthesis methods used to produce carbon nanomaterials. In the usual approach the synthesis process involves pyrolysis of hydrocarbons, or other carbon feedstock with the addition of a nitrogen source (e.g. nitrogen, ammonia, amines, nitriles) diluted in a stream of an inert gas in the furnace system over the surface of the metal catalyst particles. Detailed methods used in this study will be given in Chapters 3 – 6. In general, undoped and nitrogen-doped carbon structures can be synthesized using two methods:[73] (i) "in situ" doping, where gases of liquids containing ad-atoms either mixed or individually are bubbled through to the reactor containing a catalyst material using appropriate gases during the synthesis of carbon nanomaterials, and (ii) post-doping, where the pre-synthesized carbon nanomaterials are post-treated with a nitrogen precursor (either in liquid or gaseous form).

2.3 Carbon nanotube polymer composites

A composite is a multiphase material formed from a combination of materials which differ in composition or form. Composites retain their own chemical and physical properties and maintain an interface between components which act in concert to provide improved specific or synergistic characteristics not obtainable by any of the original components acting alone.[83,84] A composite is usually made of two components of materials, namely, the reinforcement and the matrix. The reinforcement provides useful properties such as mechanical, electrical, thermal,

optical, etc. needed to enhance the properties of the matrix. The unique mechanical and electrical properties of carbon nanotubes make them ideal reinforcing agents in many applications. It is because of their outstanding mechanical properties such as high Young's modulus, high tensile strength, high flexibility and high bulk modulus,[85] that CNTs promise to be the ultimate fiber reinforcements in strong, lightweight polymer composite materials. Use of CNTs as fillers in polymer nanocomposites has been a subject of many studies. Challenges exist in the utilization of CNTs as fillers in polymer composites, namely CNTs (i) are normally found as mixtures of various chiralities, diameters and length, (ii) often contain impurities, (iii) occur as aggregates and bundles which leads to non-uniform dispersion and (iv) have poor interfacial bonding with the polymer matrix. There have been various reports focusing on increasing the strength and modulus of the polymer matrices through the incorporation of CNTs. Improvement in tensile modulus and break stress to about 36-42 and 25 % were achieved when 1 wt.% of MWCNTs was added to a polystyrene matrix using a solution-evaporation method.[86] The modulus and hardness of the composite was increased by 1.8 and 1.6 times, when 1 wt.% of MWCNTs was added to polyvinyl alcohol (PVA).[87] An increase in the storage modulus was observed when the MWCNTs loading increased due to a stiffening effect of the nanotubes, during preparation of poly(methyl methacrylate) (PMMA)/MWCNTs composites by a melt processing method.[88] The indentation elastic modulus and micro-hardness characteristics increased when 1 wt.% of functionalized and non-functionalized MWCNTs were added to the PMMA matrix.[89] Addition of 1 wt.% of MWCNTs to a polycarbonate (PC) matrix resulted in enhancement of the tensile strength and modulus by up to 23 and 75 % and reduction of their electrical resistivity significantly from being an insulator to a semi-conductor, indicating a percolation threshold.[90] An enhanced electrical conductivity was observed for nanofiber composites consisting of PVA, MWCNTs and manganese dioxide synthesized by an electrospinning process.[91] Alignment of the MWCNTs into a polyvinylpyrrolidone (PVP) matrix was achieved and resulted in a composite with improved electromagnetic interference shielding performance.[92]

2.3.1 Nanocomposite synthesis methods

Several synthesis methods have been developed to incorporate CNTs into polymer matrices. The challenge of producing such nanocomposites is presented by the tendency of CNTs to occur in bundles or aggregates which are difficult to break up and to disperse in solution which leads to non-uniform distributions within the polymer matrix. In this section we will briefly describe the most important processing techniques for synthesis of CNT/polymer nanocomposites.

(i) Solution processing

The most common and simplest technique to form CNT/polymer nanocomposites is solution processing. The method involves intensive agitation (e.g. magnetic stirring, vigorous shaking, refluxing, homogenization or even bath/probe sonication) which results in thorough mixing of the CNTs with a polymer in a solvent, in order to facilitate nanotube de-bundling and their dispersion inside a host polymer matrix.[58,93,94] This processing technique is however limited to polymers that are soluble in solvents. The process involves dispersion of nanotubes in a suitable solvent and mixing with the polymer solution, followed by film casting and solvent evaporation leaving behind a nanocomposite sheet. The solvent for the CNTs and a polymer may be the same or different, but should be of good miscibility to realize intimate mixing between phases. In some cases, CNTs are added directly to the polymer solution followed by intensive mixing before film casting. Use of high power ultrasonication or shear mixing for long periods can lead to shortening of tube lengths, leading to deterioration of composite properties.

(ii) Melt processing

Due to the fact that thermoplastic semicrystalline polymers soften when heated above their melting point, melt processing has been a very valuable technique for the fabrication of CNT-based composites. The method is suitable for polymers that cannot be processed with solution techniques due to their insolubility in common solvents. In general, melt processing involves the blending of a polymer melt with the CNT material by application of intense shear forces. The melt mixing can be carried out in a batch or continuous operation using a high shear mixer (e.g.

Sigma mixer) and extruder, respectively. A sigma mixer is often used to prepare highly concentrated nanocomposites called masterbatches, which may be used to synthesize desired CNT-loading composites by mixing with appropriate amounts of neat matrix polymer using an extruder. The polymer granules are caught by the rotating screws and pushed forward; they then melt inside a heated melting zone due to the externally provided heat and shearing of the material between screw and barrel. The CNTs are loaded into the extruder via a separate hopper, such that melt-phase mixing takes place due to the combination of shearing and kneading action, and when the molten-mixture reaches the homogenization zone, it has already achieved a significant degree of mixing. Finally, the mixture passes to the die before coming out as semisolid strands, which may be cooled (via air drying or passing through a water bath) and chopped into granules for further use. In the melt mixing technique high shear forces and elevated temperatures need to be properly addressed in order to avoid the deterioration of the nanocomposites.

(iii) In situ polymerization

In situ polymerization remains the only viable option for the preparation of composites based on insoluble and thermally unstable matrix polymers, which cannot be processed by solution or melt processing routes. The main advantage of this method is that it produces polymer-grafted tubes, mixed with free polymer chains. Moreover, due to the small size of the molecules, the homogeneity of the resulting composite adduct is much higher when compared to mixing CNTs and polymer chains in solution. The method allows the preparation of composites with high CNT weight percent. The synthesis involves dispersion of CNTs in a monomer, followed by in situ polymerization leading to the formation of CNT/polymer nanocomposites. Exploitation of functionalized CNTs or use of monomer-grafted CNTs are known to improve the initial dispersion of the nanotubes in the monomer and consequently in the formed nanocomposites.

(iv) Electrospinning

Electrospinning is a versatile method used to produce continuous nanofibers mainly from polymer solutions. Electrospinning involves pumping a polymer solution at a constant rate

through a needle tip that is placed a set distance away from a grounded or oppositely charged collector. When a voltage is applied at the needle tip, an electrostatic field introduces charges in the solution and when the mutual repulsions between charges reach a threshold value, a fluid jet forms a conical droplet at the tip of a capillary tube, resulting in the formation of a Taylor cone.[95] The jet travels in a straight path, called the jet's length, and experiences bending instabilities to form spiral motions. The polymer fiber is collected on a screen, which is either grounded or connected to a DC supply of opposite polarity.

2.4 Treatment of oil-water emulsions by adsorption onto CNT/polymer composites

Water scarcity is becoming a huge problem all over the world due to contamination of water, rapid growth of population, development of an economy and lack of rain. Recently, in Gauteng and Cape Town, water restrictions were put into place due to alarming low water levels in the water collection and distribution dams. Clean water is essential for both human life and the ecosystem. A higher demand for fresh water has forced researchers to look for alternative sources to treat wastewater.

Oil spillage in water bodies can have negative environmental and socio-economical impacts. Oil spill pollution can be due to petroleum hydrocarbon discharged into the environment (marine or land). This can be caused by accidental spillage or operational spillage whenever oil is produced or transported.[96] Oil spills can affect wildlife species, marine and coastal habitats, fisheries and recreational arears. The oil harms the wildlife through toxic contamination (inhalation and ingestion) or by physical contact. The adverse impacts to ecosystems and the long-term effects of environmental pollution by these and other releases call for a need to develop a wide range of materials for cleaning up oil from oil impacted areas. The effectiveness of oil treatment varies with time, the type of oil and spill, the location and the weather conditions.[97] Among all of the oil spill cleanup methods that show good results in removal of oil from the water surface, the sorbent cleaning-up is considered to be one of the most efficient method to remove oil.[98] The contact of oil with a highly adsorbent material can be a way to collect the oil that is present in water.[96] Stokes' Law indicates that, given time and enough surface area, oil and water will eventually separate, forming two layers. Oil will float on top of the water forming a thin layer

called a slick since it has a lower density than water. A wide range of adsorbents materials have been used for oil remediation such as mineral products (zeolites, silica, perlite, graphite, vermiculites, sorbent clay, diatomite),[99,100] vegetable products (corn cob, straw, kenaf, cotton fiber, wood fiber, peat moss, etc.,),[100,101] organic synthetic products (propylene, polyurethane, etc.,),[102,103] activated carbon,[104] and CNT sponges.[105] Polymeric materials such as polypropylene and polyurethane foams are the most commonly used commercial sorbents in oil spill cleanup because of their oleophilic and hydrophobic characteristics.[106,107] A major disadvantage of using polymer materials is that they degrade very slowly in comparison with the mineral or vegetable products and are not as naturally occurring as mineral products.[101,106, 108,109]

Effective dispersion of MWCNTs in PVP during creation of composite materials has been reported, and PVP was found to reduce the aggregation effect of CNTs. However, application of a nanocomposite of PVP with functionalized MWCNTs in water treatment has rarely been reported. This is because PVP is a highly polar, non-ionic, amphiphilic, and water-soluble polymer, that can swell in aqueous media.[110-112] PVP has been used as a hydrophilizing additive in a variety of CNT/polymer composites, since it increases the number and size of pores in the composites.[113,114] Chang et al. fabricated a graphene oxide/PVP based PVDF membrane via hydrogen bonding and van der Waals forces.[115] They observed that without graphene oxide, an increasing amount of PVP tended to create larger pores in the PVDF/PVP membranes, and most of the PVP was washed away during membrane fabrication.[115] However, addition of graphene oxide to the membrane resulted in its interaction with PVP, reducing PVP leaching and enhancing the anti-fouling properties of the membranes.[115]

A few studies have been done on oil adsorption using CNT/PVP composite membranes. Nan et al. fabricated CNT/PVP composite nanofibers by electrospinning for oil adsorption.[116] CNTs were found to be stuck and tightly embedded on the surface of PVP fibers, making it easy to utilize CNTs in the adsorption of the oil. The composites showed a high oil adsorption capacity of ~ 1 g/cm^3, which is higher than that of a carbon sponge (~ 0.7 to 0.8 g/cm^3).[105] Castro et al. fabricated silica-supported PVP filtration membranes via a graft polymerization process for use in the treatment of oil-in-water emulsions. They found that incorporation of PVP improved selectivity and reduced the fouling tendency of the membranes due to an increased hydrophilicity of the membrane.[117]

2.4.1 Adsorption studies

The sorption capacity of the adsorbent is usually expressed in grams of pollutant (e.g. oil) absorbed by an adsorbent per gram of the adsorbent used (i.e. $g.g^{-1}$):

$$Q_t = \frac{m_t - m_0}{m_0} \quad (1)$$

where Q_t ($g.g^{-1}$) is the adsorption capacity of the adsorbent at a certain time t(s), m_t (g) is the weight of the adsorbent after adsorption and m_0 (g) is the initial weight of the adsorbent. The sorption capacity will reach a saturated value Q_m ($g.g^{-1}$) when Q_t does not change with t.

The sorption kinetics process has been used for CNT sponges[105] and was described using a second-order adsorption model.[118,119]

$$\frac{1}{Q_m - Q_t} = \frac{1}{Q_m} + kt \quad (2)$$

where Q_t is the sorption capacity at time t, Q_m is the saturated sorption capacity, t is the sorption time, and k is the sorption constant, which is related to the viscosity, surface tension of the oil and the pore structure of the CNT sponge. The slope of a t/q_t vs t curve gives the saturated sorption capacity, Q_m and the intercept can be used to calculate the sorption constant, k.

In this study the role of chlorine on the morphology of un-doped and nitrogen-doped carbon nanomaterials will be explored. The effect of using chlorine functionalized CNTs to facilitate interaction between CNTs and polymer matrix in formation of CNT/polymer matrix will also be investigated. The composite materials will then be applied as adsorbents for oil in oil spill cleanups. To date, production of chlorine functionalized CNT/polymer matrices has never been reported. Studies on use of chlorinated materials during synthesis of nitrogen-doped carbon nanomaterials surfaced recently. The study involved use of chlorine containing catalysts rather than chlorinated organic solvents as it is in our case. Hence this will also present some novelty.

References

1. L.V. Radushkevich, and V.M. Lukyanovich, *Zurn Fisic Chim*, 1952, **26**, 88–89.
2. S. Ijima, *Nature*, 1991, **354**, 56–66.
3. P. Soundarrajan, A. Patil, and D. Liming, *Am. Vac. Soc*., 2002, 1198–1201.
4. P. Kim, and C.M. Lieber, *Science*, 1999, **286**, 2148.
5. A.G. Rinzler, J.H. Hafner, P. Nikolaev, P. Nordlander, D.T. Colbert, R.E. Smalley, L. Lou, S.G. Kim, and D. Tomanek, *Science*, 1995, **269**, 1550 – 1553.
6. W.A. de Heer, A. Châtelain and D. Ugarte, *Science*, 1995, **270**, 1179 – 1180.
7. Q.H. Wang, A.A. Setlur, J.M. Lauerhaas, J.Y. Dai, E.W. Seelig, and R.H. Chang, *Appl. Phys. Lett*., 1998, **72**, 399 – 400.
8. J. Wu, W.-W. Liu, Y.-X. Wu, T.-C. Wei, D. Geng, J. Mei, H. Liu, W.-M. Lau and L.-M. Liu, *Electrochim. Acta*, 2016, **203**, 21 – 29.
9. V. Thirumal, A. Pandurangan, R. Jayavel, S.R. Krishnamoorthi and R. Ilangovan, *Curr. Appl. Phys.*, 2016, **16**, 816 – 825.
10. M.S. Islam, Y. Deng, L. Tong, S.N. Faisal, A.K. Roy, A.I. Minett, V.G. Gomes, *Carbon*, 2016, **96**, 701–710.
11. A. Abarrategi, M.C. Gutierrez, C. Moreno-Vicente, V. Ramos, J.L. Lopez-Lacomba, M.L. Ferrer, and F. del Monte, *Biomaterials*, 2008, **29**, 94 – 102.
12. N.W.S. Kam, M. O'Connell, J.A. Wisdom and H. Dai, *Proc. Natl. Acad. Sci. USA*, 2005, **102**, 11600 – 11605.
13. M.I. Sajid, U. Jamshaid, T. Jamshaid, N. Zafar, H. Fessi, and A. Elaissari, *Int. J. Pharm*., 2016, **501**, 278–299.
14. H.M. Al-Saidi, M.A. Abdel-Fadeel, A.Z. El-Sonbati, A.A. El-Bindary, *J. Mol. Liq.*, 2016, **216**, 693–698.
15. M. Irfan, H. Basri, M. Irfan and W.-J. Lau, *RSC Adv*., 2015, **5**, 95421 – 95432.
16. Z. Rahimi, A.A.L. Zinatizadeh and S. Zinadini, *J. Ind. Eng. Chem.*, 2015, **29**, 366 – 374.
17. H. Yu, T. Huang, M. Lu, M. Mao, Q. Zhang and H. Wang, *Nanotechnology*, 2013, **24**, 405401 (1 – 9), doi:10.1088/0657-4484/24/40/405401.
18. K. Singh, A. Ohlan and S.K. Dhawan, *Nanocomposites – New Trends and Developments*, Intech Open Science, dx.doi.org/10.5772/50408, 2012.

19. H.O. Pierson, *Handbook of Carbon, Graphite, Diamond and Fullerenes*, William Andrew Publishing, Norwich, 1993.

20. C.N.R. Rao, R. Seshadri, A. Govindaraj and R. Sen, *Mat. Sci. Eng. R,* 1997, **15**, 209–262.

21. P.M. Ajayan, *Chem. Rev*., 1999, **99**, 1787.

22. A. Eatemadi, H. Daraee, H. Karimkhanloo, M. Kouhi, N. Zarghami, A. Akbarzadeh, M. Abasi, Y. Hanifepour and S.W. Joo, *Nanoscale Res. Lett.*, 2014, **9**, 393 (1–13).

23. N. Salfuddin, A.Z. Raziah and A.R. Junizah, *J. Chem.*, 2013, 676815 (1–18), dx.doi.org/10.1155/2013/676815.

24. Z.B. He, J.L. Maurice, C.S. Lee, C.S. Cojocaru and D. Pribat, *Arabian J. Sci. Eng. Sect. B*, 2010, **35**, 19-28.

25. M. Kumar and Y. Ando, *J. Nanosci. Nanotech.*, 2010, **10**, 3739-3758.

26. C. Journet and P. Bemier, *Appl. Phys.* A, 1998, 1-9.

27. K. Morishita and T. Takarada, *J. Mater. Sci.*, 1999, **34**, 1169-1174.

28. T.W. Ebbesen and P.M. Ajayan, *Nature*, 1992, **358**, 220-222.

29. D.S. Bethune, C.H. Kiang, M. de Vries, G. Gorman, R. Savoy, J. Vazquez, and R. Beyers, *Nature*, 1993, **363**, 605-607.

30. M. Paradise and T. Goswami, *Mater. Des.*, 2007, **28**, 1477-1489.

31. P.G. Collins, A. Zettl, H. Bando, A. Thess and R.E. Smalley, *Science*, 1997, **278**, 100 – 103.

32. M. Chiang, K. Liu, T. Lai, C. Tsai, H. Cheng and I. Lin, *J. Vac. Sci. Technol. B*, 2001, **19**, 1034-1039.

33. R.T.K. Baker, *Carbon*, 1989, **27**, 315.

34. G.G. Tibbetts, *Carbon*, 1989, **27**, 745.

35. M.C. Bahome, L.L. Jewell, D. Heidebrandt, D. Glasser and N.J. Coville, *Appl. Catal., A,* 2005, **287**, 60-67.

36. S. Maghsoodi, A. Khodadadi and Y. Mortazavi, *Appl. Surf. Sci.*, 2010, **256**, 2769-2774.

37. E. Couteau, K. Hernadi, J.W. Seo, L. Thiên-Nga, Cs. Mikó, R. Gaál and F. Forró, *Chem. Phys. Lett.*, 2003, **378**, 9-17.

38. C. Branca, F. Frusteri, V. Magazú and A. Mangione, *J. Phys. Chem.*, B, 2004, **108**, 3469-3473.
39. T.C. Schmitt, A.S. Biris, D.W. Miller, A.R. Biris, D. Lupu, S. Trigwell and Z.U. Rahman, *Carbon*, 2006, **44**, 2032-2038.
40. T. Tsoufis, P. Xidas, L. Jankovic, D. Gournis, A. Saranti, T. Bakas and M.A. Karakassides, *Diamond Relat. Mater*., 2007, **16**, 155-160.
41. V. Jourdain, and C. Bichara, *Carbon*, 2013, **58**, 2 – 39.
42. V.L. Kuznetsov, A.N. Usoltseva, A.L. Chuvilin, E.D. Obraztsova, and J.M. Bonard, *Phys. Rev. B*, 2001, **64**, 235 – 401.
43. K. Varshney, *Int. J. Eng. Res. Gen. Sci.*, 2014, **2**, 660-677.
44. X. Wu, Y. Tao, C. Mao, L. Wen and J. Zhu, *Carbon*, 2007, **45**, 2253 – 2259.
45. V.K. Thakur, M.K. Thakur and M.R. Kessler, *Handbook of Composites from Renewable Materials, Nanocomposite: Science and Fundamentals*, Volume 7, John Wiley & Sons, 2017.
46. S.J. Tans, R.M. Verschueren and C. Dekker, *Nature*, 1998, **393**, 49 – 52.
47. M. Yu, *Science*, 2000, **287**, 637-640.
48. E. Thoteson, Z. Ren and T. Chou, *Compos. Sci. Technol.*, 2001, **61**, 1899-1912.
49. H. Dai, E.W. Wong and C.M. Lieber, *Science*, 1996, **272**, 523-526.
50. T.W. Odom, J.L. Huang, P. Kim and C.M. Lieber, *Nature*, 1998, **391**, 62-64.
51. N. Hamada, S. Sawada and A. Oshiyama, *Phys. Rev. Lett.*, 1992, **68**, 1579.
52. R. Saito, M. Fujita, G. Dresselhaus and M.S. Dresselhaus, *Phys. Rev. B*, 1992, **45**, 6234.
53. J. Hone, M.C. Llaguno, M.J. Biercuk, A.T. Johnson, B. Batlogg, Z. Benes and J.E. Ficher, *Appl. Phys. A*, 2002, **74**, 339-343.
54. S. Berber, Y.K. Kwon and D. Tomanek, *Phys. Rev, Lett*. 2000, **84**, 4613.
55. P. M. Ajayan, T. W. Ebbesen, T. Ichihashi, S. Iijima, K. Tanigaki, and H. Hiura, *Nature (London)*, 1993, **362**, 522–525.
56. P. M. Ajayan, and S. Ijima, *Nature (London),*1993, **361**, 333–334.
57. D.A. Walters et al., *Chem. Phys. Lett*., 2001, **338**, 14 – 20.
58. E. Thostenson, C. Li and T. Chou, *Compos. Sci. Technol.*, 2005, **65**, 491 – 516.
59. V. Gupta and R.K. Kotnala, *Angew. Chem. Int. Ed*., 2012, **51**, 2916 – 2919.
60. S.T. Hussain, S.R. Gilani, S.D. Ali and H.S. Bhatti, *J. Alloys Compd.*, 2012, **544**, 99 – 104.
61. S.D. Ali, S.T. Hussain and S.R. Gilani, *Appl. Surf. Sci.*, 2013, **271**, 118 – 124.

62. F. Avile'S, J.V. Cauich-RodríGuez and L. Moo-Tah, *Carbon*, 2009, **47**, 2970-2975.

63. J. Luo, Y. Liu, H. Wei, B. Wang, K.-H. Wu, B. Zhanga and D.S. Su, *Green Chem.*, 2017, **19**, 1052 – 1062.

64. V.K. Abdelkader, M. Domingo-García, M.D. Gutiérrez-Valero, R. López-Garzón, M. Melguizo, C. García-Gallarín, F.J. López-Garzón, and M.J. Pérez-Mendoza, *J. Phys. Chem., C*, 2014, **118**, 2641 – 2649.

65. W.H. Lee, S.J. Kim, W.J. Lee, J.G. Lee, R.C. Haddon, and P.J. Reucroft, *Appl. Surf. Sci*., 2001, **181,** 121–127.

66. J-M. Yuan, X-H. Chen, X-H Chen, Z-F Fan, X- Yang, and Z-H.Chen, *Carbo*n, 2008, **46,** 1266–1269.

67. I. Pełech, U.Narkiewicz, D. Moszyński, and R. Pelech, *J. Mater. Res*., 2012, **27,** 2368–2374.

68. J. Barkauskas, I. Stankevičiene, and A. Selskis, *Sep. Pur. Tech*., 2010, **71**, 331–336.

69. H. Qiu, Z. Shi, L. Guan, L. You, M. Gao, S. Zhang, J. Qiu, and Z. Gu, *Carbon*, 2006, **44,** 516–521.

70. A.N. Márquez, J. L. Valverde, and M.A. Keane, *Appl. Catal. A: Gen*., 2007, **332,** 237–246.

71. R. Lv, F. Kang, W. Wang, J. Wei, J. Gu, K. Wang, and D. Wu, *Carbon*, 2007, **45,** 1433–1438.

72. S.H. Lim, H.I. Elim, X.Y. Gao, A.T.S. Wee, W. Ji, J. Y. Lee and J. Lin, *Phys. Rev., B*, 2006, **73**, 045402.

73. C.P. Ewels and M. Glerup, *J. Nanosci. Nanotechnol.*, 2005. **5**, 1345-1363.

74. P. Avouris, and J. Chen, *Mater. Today*., 2006, **9**, 46 – 54.

75. S. Ratso, I. Kruusenberg, A. Sarapuu, P. Rauwel, R. Saar, U. Joost, J. Aruväli, P. Kanninen, T. Kallio, and K.Tammeveski, *J. Power Sources*, 2016, **332**, 129 – 138.

76. Y. Zhao, Y. Tang, Y. Chen, and A. Star, *ACS. Nano*, 2012, **6**, 6912–6921.

77. G. Zhou, W.H. Duan and B.L. Gu, *Phys. Rev. Lett.*, 2001, 8709(9):095504-1–4.

78. M.S. Wang, L.M. Peng, Y.J. Wang, C.H. Jin and Q. Chen, *J. Phys. Chem. B*, 2006, **110**, 9349-9402.

79. R. Lv, F. Kang, D. Zhu, Y. Zhu, X. Gui, J. Wei, J. Gu, D. Li, K. Wang and D. Wu, *Carbon*, 2009, **47**, 2709-2715.

80. Y.H. Lai, H.B. Lian and K.Y. Lee, *Diamond Relat. Mater*., 2009, **18**, 544 – 547.
81. T. Cui, R. Lv, F. Kang, Q. Hu, J. Gu, K. Wang and D. Wu, *Nanoscale Res. Lett*., 2010, **5**, 941-948.
82. L.M. Ombaka, P.G. Ndungu, B. Omondi, J.D. McGettrick, M.L. Davies, and V.O. Nyamori, *J. Solid State Chem.*, 2016, **235**, 202–211.
83. I.M. Daniel, *Engineering mechanics of composite materials*, Oxford University Press, 2006.
84. P. Saini, *Fundamentals of Conjugated Polymer Blends, Copolymers and Composites*, John Wiley & sons, Inc., 1-118, http://doi.wiley.com/10.1002/9781119137160.ch1, 2015.
85. M.M.J. Treacy, T.W. Ebbesen, and J.M. Gibson, *Nature*, 1996, **381**, 678-680.
86. D. Qian, E.C. Dickey, R. Andrews and T. Rantell, *Appl. Phys. Lett*., 2000, **76**, 2868 – 2870.
87. M. Cadek, J.N. Coleman, V. Barron, K. Hedicke and W.J. Blau, *Appl. Phys. Lett*., 2002, **81**, 5123 – 5125.
88. Z. Jin, K.P. Pramoda, G. Xu and S.H. Goh, *Chem. Phys. Lett*., 2001, **337**, 43-47.
89. G. Zamfirova, V. Gaydarov, F. Faraguna, E. Vidović and A. Jukić, *Colloids Surf., A: Physicochem. Eng. Aspects*, 2016, **510**, 169-175.
90. W. Thaithae, C. Antonio and P. Wattanachai, *Asia-Pac. J. Chem. Eng*., 2016, **11**, 34-50.
91. M.F.M.A. Zamri, S.H.S. Zein, A.Z. Abdullah and N. I. Basir, *Int. J. Eng. Technol. IJET-IJENS.*, 2011, **11**, 15-21.
92. K. Nasouri, A. Mousavi, and M.R.M. Mojtahedi, *Polym. Compos.*, 2016, 23774, doi 10.1002/pc.23774.
93. P.-C. Ma, N.A. Siddiqui, G. Marom and J.-K. Kim, Compos. *Part Appl. Sci. Manuf*., 2010, **41**, 1345-1367.
94. L. Jin, C. Bower and O. Zhou, *Appl. Phys. Lett*., 1998, **73**, 1197-1199.
95. P.R. Kumar, N. Khan, S. Vivekanandhan, N. Satyanarayana, A.K. Mohanty and M. Misra, *J. Nanosci. Nanotechnol.*, 2012, **12,** 1 – 25.
96. R.V. Maulion, S.A. Abacan, G.G. Allorde and Ma. C.S. Umali, *Asia Pacific Journal of Multidisciplinary Research*, 2015, **3**, 146 – 151.
97. M. Fingas, *Chem. Ind.*, 1996, **24**, 1005 – 1008.
98. Artemiev A.V., Pinkin A.V. *Sorption Techniques to Clean Up Water from Oil Pollutions. Water: Chemistry and Ecology*. 2008; **1**, 19-25.

99. R.W. Melvold, S.C. Gibson, and R. Scarberry, *Sorbents for liquid Hazardous Substance Cleanup and Control*, Noyes Data Corp., Park Ridge, NJ, 1988.

100. P. Scharzberg, *U.S. Coast Guard Report* No.724110.1/2/1, U.S. Coast Guard Headquarters, Washington, DC, 1971.

101. H.M. Choi and R.M. Cloud, *Environ. Sci. Technol*., 1992, **26**, 772 – 776.

102. H.T.T. Duong, and R.P. Burford, *J. Appl. Polym. Sci.*, 2006, **99**, 360 – 367.

103. D. Ceylan, S. Dogu, B. Karacik, S.D. Yakan, O.S. Okay and O. Okay, *Environ. Sci. Technol*., 2009, **43**, 3846 – 3852.

104. K. Okiel, M. El-Sayed and M.Y. El-Kady, *Egypt. J. Petroleum*, 2011, **20**, 9 – 15.

105. X. Gui, H. Li, K. Wang, J. Wei, Y. Jia, Z. Li, L. Fan, A. Cao, H. Zhu and D. Wu, *Acta Mater*., 2011, **59**, 4798 – 4804.

106. The International Tanker Owner Pollution Federation Limited, Measures to Combat Oil Pollution: The improvement of oil spill response within the European Community, Graham & Trotman Limited, London, 1980.

107. P. Schatzberg and D.F. Jackson, *U.S. Coast Guard Report* No. 734209.9, U.S. Coast Guard Headquarters, Washington, DC, 1972.

108. M. Toyoda, J. Aizawa, and M. Inagaki, *Desalination*, 1998, **115**, 199 – 201.

109. C. Teas, S. Kalligeros, F. Zanikos, S. Stournas, E. Lois, and G. Anastopoulos, *Desalination*, 2001, **140**, 259 – 264.

110. Q. Yang, T.-S. Chung and M. Weber, *J. Membr. Sci*., 2009, **326**, 322 – 331.

111. M. Sun, Y. Su, C. Mu and Z. Jiang, *Ind. Eng. Chem. Res*., 2009, **49**, 790 – 796.

112. J. Barzin, S. Madaeni, H. Mirzadeh, and M. Mehrabzadeh, *J. Appl. Polym. Sci.*, 2004, **92**, 3804 – 3813.

113. M. Irfan, H. Basri, M. Irfan and W.-J. Lau, *RSC Adv*., 2015, **5**, 95421 – 95432.

114. K. Zhu, G. Wang, S. Zhang, Y. Du, Y. Lu, R. Na, Y. Mu and Y. Zhang, *RSC Adv*., 2017, **7**, 30564 – 30572.

115. X. Chang, Z. Wang, S. Quan, Y. Xu, Z. Jiang and L. Shao, *Appl. Surf. Sci*., 2014, **316**, 537 – 548.

116. D. Nan, J. Wei, F. Guo, G. Fan, F. Xu, L. Li, H. Zhu, K. Wang and D. Wu, *J. Nanosci. Nanotechnol.*, 2014, **14**, 6461 – 6465.

117. R.F. Castro, Y. Cohen, and H.G. Monbouquette, *J. Membr. Sci.*, 1996, **115**, 179 – 190.

118. D. Bastani, A.A. Safekordi, A. Alihosseini, and V. Taghikhani, *Sep. Purif. Technol*., 2006, **52**, 295 – 300.

119. Z. Yaneva, and B.J. Koumanova, *J. Colloid Interf. Sci*., 2006, **293**, 303 – 311.

CHAPTER 3

The synthesis of carbon nanomaterials using chlorinated hydrocarbons over a Fe-Co/$CaCO_3$ catalyst

---

3.1 Introduction

Nanotechnology is a topic that is attracting the interest of scientists in academia, research institutions and industry as well as government officials and journalists. Carbon nanotubes (CNTs) and carbon nanomaterials (CNMs) in general are key components in the progress of nanotechnology. Polyhedral carbon clusters (fullerenes) were discovered in 1985[1] and this eventually led to the seminal studies on carbon nanotubes (CNTs) by Ijima in 1991.[2] CNTs offer opportunities for the development of novel material systems because they possess unique electronic properties,[3] exhibit high thermal conductivity,[4] and mechanical properties[5] such as stiffness, strength and resilience. SWCNTs were observed to exhibit an electrical current density of ~ 4×10^9 A cm^{-2} and single-layer graphene sheet was found to possess thermal conductivities in the range ~ 4.84×10^3 to 5.30×10^3 W/mk.[3,4] An effective increase in the strength to ~17 GPa for of double-walled CNTs bundles[5] and ~60 GPa for multi-walled carbon nanotubes (CNTs)[6] was achieved by applying high-energy electron irradiation, which crosslinks inner shells and tubes. These unique properties render CNTs suitable for application in various fields for example, their use in environmental monitoring,[7] in water purification,[8] as tips for atomic force microscope probes,[9] as catalyst supports[10], in field emission devices[11], as chemical sensors[12], and in fuel cells.[13] Methods for making CNTs such as arc discharge, laser ablation, and catalytic chemical vapor deposition (CCVD) have been developed.[14] To date the production of CNTs by the CCVD method remains the preferred route for their large scale production.

A limitation related to the use of CNTs in many applications has always been the difficulty in dispersing them in solvents. Scientists have thus functionalized the outer walls of CNTs with various groups like halogens and carboxylic groups to improve their solubility. Chemical modification of CNTs surface to fine tune their properties has thus led to the creation of new materials.[16] Doping of the carbonaceous materials with non-carbon atoms, such as nitrogen,[12-19]

boron,[20-24] sulphur,[25-29] oxygen[30-36] and halogens[11,37-55] has been explored over the past two decades. Modification of the carbon surface and electronic properties has also been explored but the effect of chlorine (Cl) on the morphology of carbon nanomaterials is not well established.

It has been shown that incorporation of Cl in the CNMs results in surface functionalisation,[41-44] ease of purification,[40,43,45,46] increased yields[47-49] and surface restructuring.[49,50] The presence of chlorine atoms thus produces materials with increased inner diameters, which results in filling of CNTs with metal particles[51-53] and provides a chemically modified pathway to an ordered carbon product.[48,49,54] Liquid chlorination of multi-walled CNTs (MWCNTs) gave a Cl loading of about 0.23 at.%[40] based on EDS. XPS analysis of single-walled carbon nanotubes produced from dichlorocarbene gave Cl substituted CNTs at a concentration of 1.6 at.%.[41] A small number of Cl anions were also observed on the surface of the CNTs generated from dichloromethane by XPS analysis.[11] Chlorine-functionalized CNTs were also produced in the gas phase using a ball-milling method.[42] Purification of CNTs with Cl in both the liquid phase (using CCl_4) and the gas phase to remove metal particles showed that the gas phase was more effective, but a high concentration of Cl on the surface was loaded in the liquid phase.[43] Purification and growth of vertically aligned MWCNTs in the presence of Cl was also reported, which resulted in the synthesis of CNT arrays with 3.5 mm height.[44]

The yield of MWCNTs increased from 10% to over 50% using an arc discharge method and KCl as a promoter.[47] CNMs produced from chlorobenzene were more ordered and their yield increased as compared to those obtained from benzene.[48] The beneficial role of halogens to form charge transfer with Ni particles has been shown by other authors.[48,49] An interaction between Cl and Ni leading to metal site restructuring was observed when carbon nanofibers (CNFs) were grown from Ni/SiO_2 and chlorobenzene.[50] When the CNMs were grown over Ni/SiO_2 carbon yields were also shown to increase in the presence of Cl, in the order $C_2H_6 < C_2H_4 < C_2H_4Cl_2 < C_2H_3Cl_3 < C_2H_2Cl_2 \leq C_2HCl_3$. The fibre diameter increased with increased Cl substitution in the feed.[49] Structural changes to give carbons with different structure (CNFs to carbon spheres) were observed when CCl_2=CHCl was used as a chlorine feed.[49] CNFs with tripod-like morphology were also synthesized over a NiO xerogel catalyst using trichloroethylene as Cl feed and carbon source.[54] Synthesis of CNTs over a Fe-Ni catalyst was achieved using chlorinated benzenes and

it was observed that the hollow degree of the CNTs increased with an increase in Cl content in the feed, which resulted in the CNTs being filled with a Fe-Ni alloy.[51] Previous work in our group has also shown that the use of chlorobenzene can facilitate growth of CNTs with a large inner cavity.[53] The participation of Cl was found to play an important role in the synthesis of turbostratic CNFs by pyrolysis of a 1,2-dichloroethane/ethanol mixture in the presence of a nickel catalyst.[55] Ni-Cl bonding on the surface of the catalyst created a poor crystalline layer, leading to a coarse surface which caused the disordered precipitation of carbon species and thus the formation of turbostratic CNFs.[55] Most of the studies of the role of chlorine on the morphology of the CNMs have been investigated using a nickel or iron-nickel catalyst.

In previous studies by our group it was found that a Fe-Co/$CaCO_3$ catalyst can be used to make good quality CNTs[56,57] and nitrogen doped CNTs.[58] To further explore the role of this catalyst we have investigated the role of chlorine on the morphology of CNTs produced by pyrolysis of various chlorine-substituted benzene and ethane feeds using a CCVD method. The results of the study are shown below.

3.2 Experimental

$Fe(NO_3)_3 \cdot 9H_2O$ (Sigma Aldrich) ≥ 98 %, $Co(NO_3)_2 \cdot 6H_2O$ (Sigma Aldrich) ≥ 98 %, $CaCO_3$ (Sigma Aldrich) ≥ 99 %, HNO_3 (Sigma Aldrich) ≥ 98 % ACS, chlorobenzene (CB) (Merck), > 99 % GC, 1,2-dichlorobenzene (DCB) (Sigma Aldrich) 99 % Reagent plus, 1,2,4-trichlorobenzene (TCB) (Sigma Aldrich) 99 % GC, 1,2-dichloroethane (DCE) (BDH reagent) AnalaR grade, 1,1,2-trichloroethane (TCE) (Fluka Chemika) > 98 % GC, 1,1,2,2-tetrachloroethane (TTCE) (UniLAB SAARChem) 98 % GLC and toluene (UniLab SAARChem, Merck) ACS reagent grade, were used. All the reagents were commercially available and used without further purification.

3.2.1 Preparation of catalyst by the wet impregnation method[56,57]

$Fe(NO_3)_3.9H_2O$ and $Co(NO_3)_2.6H_2O$ were used to prepare the catalyst. Calculated amounts of the Fe and Co nitrates were weighed and mixed in a beaker. The salts were then dissolved using

30 mL of distilled water to make a 0.3 mol/L Fe and 0.3 mol/L Co precursor solution. The metal solution was then transferred to a burette and added dropwise while stirring to a 10 g $CaCO_3$ support that was placed in a beaker. The mixture was stirred for 30 min. The beaker containing the metal-support mixture was then dried paced in an oven for drying at 120 °C for 12 h. The metal-support solid was then cooled to room temperature, transferred to a mortar and ground with a pestle, followed by screening through a 150 µm molecular sieve. The catalyst powder was then calcined at 400 °C for 16 h in a static air oven. This catalyst was completely characterized as reported in an earlier article.[56]

3.2.2 Carbon nanotube synthesis

The catalyst (1.0 g) was spread in a quartz boat (120 mm × 15 mm) and the boat was placed in the center of a quartz tube. The furnace was then heated to 700 °C at a rate of 10 °C/min under flowing N_2 (50 mL/min). Once the temperature reached 700 °C, the N_2 flow rate was set to 240 mL/min and C_2H_2 was set at 90 mL/min for chlorinated benzenes; for chlorinated ethanes flow rates were set at 280 mL/min N_2 and 50 mL/min C_2H_2, respectively. Both gases were bubbled through a chlorinated organic solvent, before introduction into a quartz tube. After 60 min of reaction time, the C_2H_2 flow and bubbling was stopped and the system was left to cool down to room temperature under a continuous flow of N_2 (50 mL/min). The reaction setup is shown in Fig. 1. The quartz boat was then removed from the reactor and the carbon deposit (Cl-MWCNTs) that formed was weighed.

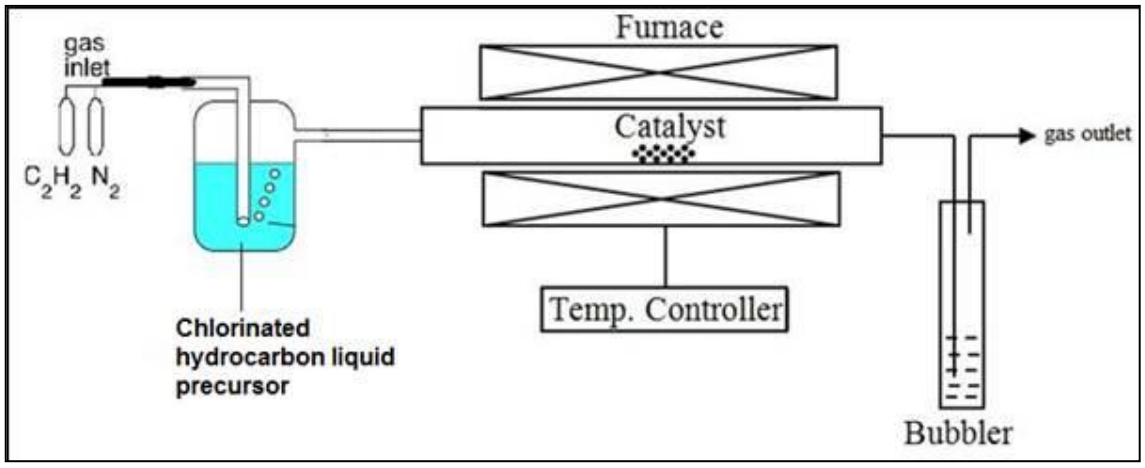

Figure 3.1 Schematic diagram of apparatus used for CNTs synthesis

3.2.3 Purification of the CNTs

Purification of the CNT materials was adapted from Mhlanga et al.[56] The carbon materials produced were added into a beaker, followed by addition of 30% HNO_3. The material mixture was stirred in acid at room temperature for at least 30 minutes. The acid-treated carbon materials were then filtered over a Whatman No.1 filter paper and the deposits on the filter paper were washed with distilled water until the filtrates were neutral (~ pH 7). A pH meter was used to measure the final pH of the filtrates. The carbon materials obtained were then dried in an oven at 120 °C for 12h, weighed and stored in a glass vial.

3.2.4 Characterization of the CNTs

The morphology and size distribution of the CNTs before and after HNO_3 acid treatment were analyzed by transmission electron microscopy (TEM) using a FEI TECNAI G^2 SPIRIT. The samples for TEM analysis were prepared by sonication in ethanol and thereafter deposited on a holey carbon-coated TEM Cu grid. The percentage yield of the carbon deposit (% C) was determined as described elsewhere.[59] The CNTs were also characterized by Raman spectroscopy using a Jobin-Yvon T6400 micro-Raman spectrometer. Excitation was provided by the 532 nm green laser with spectral resolution of 3-5 cm^{-1}. The impurity content of the CNTs was monitored by thermogravimetric analysis (TGA) using a Perkin Elmer TGA 7. The sample was loaded onto a platinum pan and heated to 900 °C at a heating rate of 5 °C/min, in a flowing air and nitrogen stream both at 20 mL/min. The phase composition of the samples was determined by powder X-ray diffraction (PXRD) using a D2 Bruker PXRD with a continuous scan mode using CoKα radiation. The scan range was 10–90 2θ degree. The presence of chlorine species in the CNT samples was determined by energy dispersive X-ray spectroscopy (EDX) incorporated into the SEM. XPS analysis was performed using a PHI 5000 Versaprobe – Scanning ESCA Microprobe operating with a 100 µm 25 W 15 kV Al monochromatic X-ray beam. The samples were sputtered with 2 kV 2 µA 1 ×1 mm raster – Ar ion gun at a sputter rate of about 18 nm/min for 60 seconds.

3.3 Results and discussion

The results from the studies of Mhlanga *et al.*[56] and Tetana *et al.*[58] showed that good quality MWCNTs and nitrogen doped MWCNTs can be produced from a Fe-Co/$CaCO_3$ catalyst. This led us to assume that other hydrocarbons, such as chlorinated hydrocarbons, could be used to make CNTs over this catalyst. All products made in this study were black in color; those obtained with CB, DCB, DCE, and TCE as chlorine sources appeared soft and spongy, while those obtained with TCB, TTCE and toluene were hard.

3.3.1 Structural analysis of the Cl-MWCNTs

TEM analysis of the carbon deposits after acid treatment showed that the morphologies of CNMs varied with the type of feed used. A range of carbons were produced in varying amounts, i.e. amorphous material, CNFs and CNTs (open and bamboo), but CNTs were the predominant products formed in most cases.

Purified CNTs produced from CB, DCB and TCB all appeared entangled with a wavy (cooked spaghetti-like) morphology (Figs. 3.2, 3.3 and 3.4). It appears that all the aromatic chlorine containing reactants gave similar carbon yields (*ca.* 63-70 %). Purified MWCNTs produced using TCB were more entangled and their inner and outer diameters appeared uniform over the entire length of the tube (Fig. 3.4). The diameters of the purified CNTs produced from the three reactants are given in Table 3.1. Both the inner and outer diameters increased with the reactant's chlorine content.

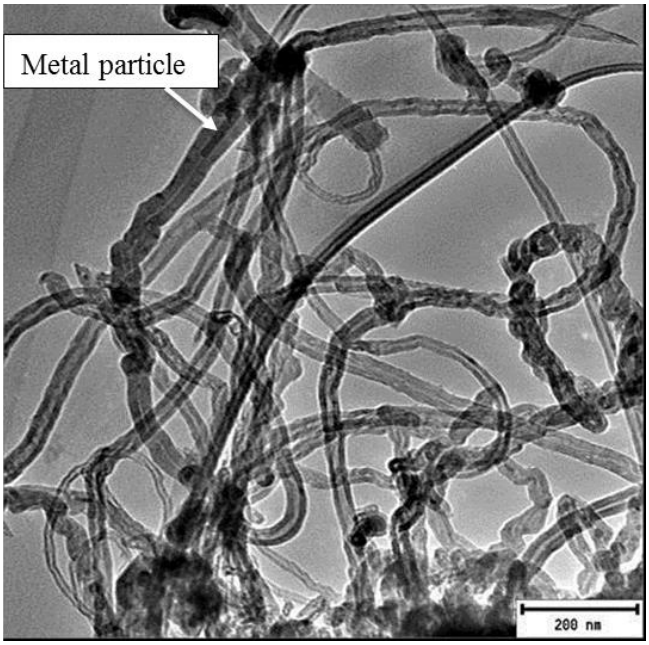

Figure 3.2 TEM image of the purified carbonaceous materials generated using chlorobenzene as chlorine source.

TEM analysis also showed the presence of rod shaped catalyst particles embedded inside the nanotubes (Figs. 3.2 and 3.4) and some at the tips of the CNFs (Fig.3.3 insert), which were formed as a result of un-reacted catalyst particles. This shows that CNTs obtained from the aromatic compounds were difficult to purify and this was attributed to the coiled structures as well as their narrow inner diameters (Table 3.1).

Further analysis of TEM images of purified carbon materials produced from DCB revealed the presence of small open ended fibrous particles attached to the outside of the CNTs (Fig. 3.3 and Supplementary Fig. S4). The secondary nanofibres were initially broad and then became narrower as they grew from the primary CNTs. Close inspection of the numerous CNFs produced revealed that they all have an inverted cap-like morphology suggesting a loss of metal catalyst particles at the tip. The secondary growth was thought to originate from unreacted catalyst particles that were left on the surface of the CNTs grown *via* a tip-growth mechanism. The catalyst responsible for the secondary growth was presumably trapped on the surface of the

growing CNTs and provided a growth site for secondary CNTs. Similar behavior was reported in the literature where some particles were found attached to the ends of CNTs.[60]

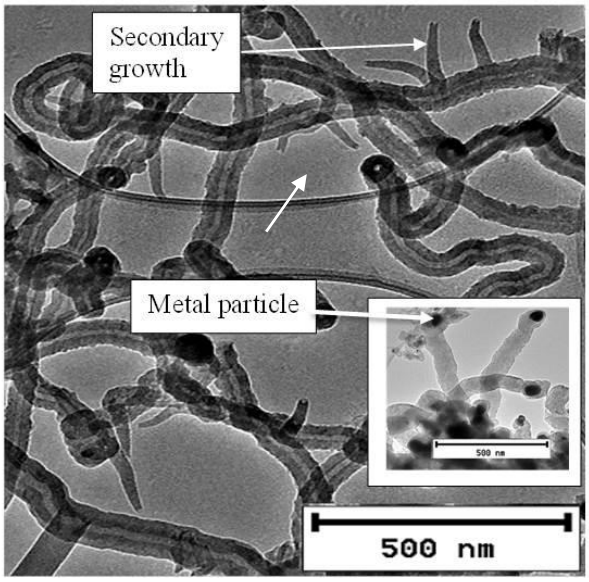

Figure 3.3 TEM image of the purified carbonaceous materials generated using dichlorobenzene as chlorine source. Growth of small carbon materials on the surface of the CNTs. Insert shows metal particles at tips of CNFs.

A small carbon deposit was obtained when TCB was used as chlorine source (Fig. 3.4). The large amount of chlorine in the TCB feed was responsible for the few CNTs measured, which was attributed to Cl/Fe-Co interactions leading to metal site restructuring that impacted on carbon diffusion/precipitation.[50] The various morphologies that resulted from the different chlorinated feeds were possibly associated with the interaction of gaseous chlorine with the catalyst particles. As more chlorine was introduced into the reactor the rate of CNT formation decreased, due to catalyst poisoning.

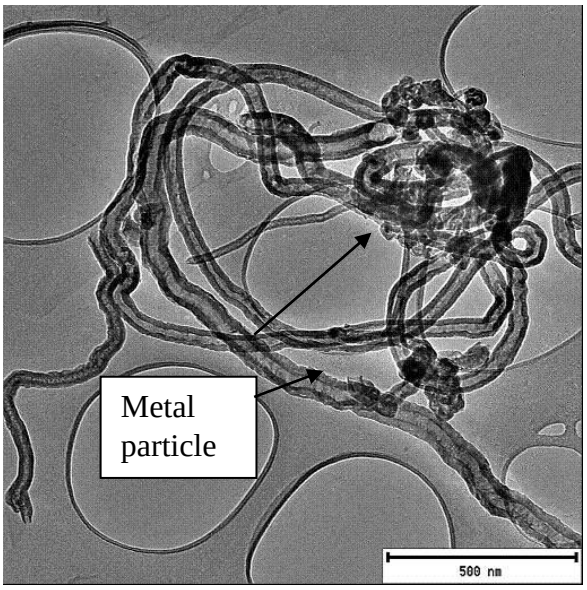

Figure 3.4 TEM images of the purified carbonaceous materials generated using trichlorobenzene.

Toluene as a representative of a Cl free aromatic hydrocarbon was also tested in this study (Fig. 3.5). Toluene produced irregular CNTs of similar inner (3 nm) and variable outer diameters (7–79 nm). MWCNTs of variable inner (7–14 nm) and outer (22–64 nm) diameters were produced from a mixture of toluene and ferrocene; iron oxide particles were also seen embedded inside some on the outer walls of the CNTs.[61] In another study mixed quality carbon structures (irregular tubes of different diameters, rods, spirals, fibers, etc.) were found by electron microscopy when toluene was used as a hydrocarbon source over an Fe/silica substrate.[62] Metal particles can also be seen embedded inside the some of the CNTs produced in this study (Fig. 3.5). Comparison of the CNTs produced using chlorinated benzenes to those obtained using toluene shows that the presence of chlorine in the aromatic feed leads to more regular CNTs.

Table 3.1 Effect of the reactants on the structure, outer and inner diameters of the purified MWCNTs.

Chlorine source	Outer diameter /nm	Average Outer diameter /nm	Inner diameter /nm	Carbon structure(s)	% CNTs	Carbon yield /%	Volume of hydrocarbon source used after reaction /mL
CB	11–44	29	3–9	CNTs and a measurable quantity of "Bamboo-like" CNTs	90	70	0
DCB	22–41 (CNTs) 62–100 (CNFs)	33 77	6–11	CNTs	80	68	0
TCB	23–79	49	17–21	CNTs	70	63	0
Toluene	7–79	29	3	CNTs	90	72	5
DCE	52–166 (CNFs) 10–30 (CNTs)	108 15	4	CNTs, CNFs	20	92	5
TCE	16–23	20	5	CNTs and "Bamboo-like" CNTs	70	82	2
TTCE	29–66	50	12	CNTs and "Bamboo-like" CNTs	80	81	1

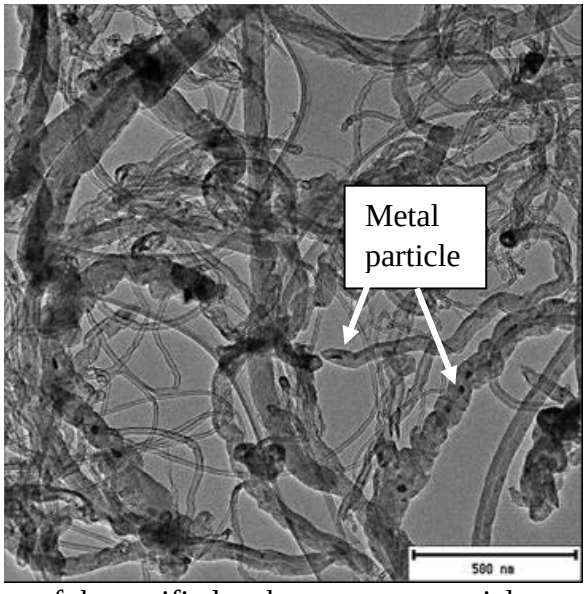

Figure 3.5 TEM images of the purified carbonaceous materials generated using toluene.

TEM images of the purified MWCNTs produced from the three chlorinated ethanes all appeared entangled with a coiled spaghetti-like shape (Fig. 3.6, 3.7 and 3.8). The purified CNMs produced from DCE contained a mixture of mainly CNFs (Fig. 3.6a and Supplementary Figure S5) and some CNTs (Fig. 3.6b). CNTs with little by-product formation were obtained from TCE and TTCE (Fig. 3.7 and 3.8). The formation of CNFs must relate to the amount of hydrogen present in the DCE ($C_2H_4Cl_2$) feed.[63]

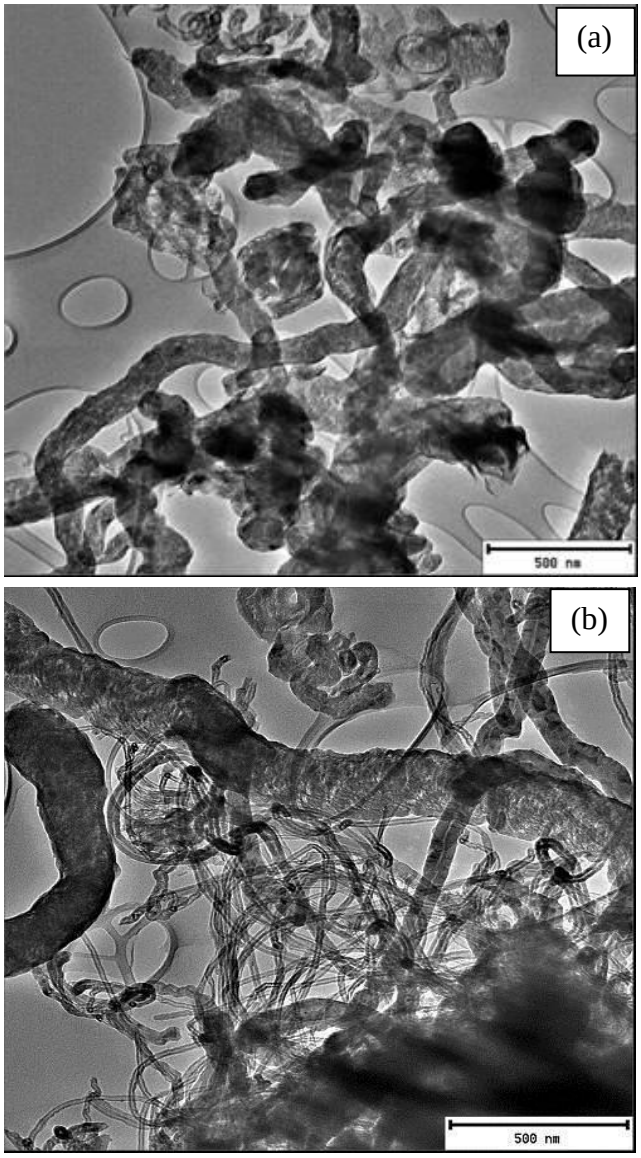

Figure 3.6 TEM image of the purified carbonaceous materials generated using dichloroethane as chlorine source.

The carbon yields obtained using chlorinated ethanes were 92, 82 and 81 % for DCE, TCE and TTCE, respectively. The carbon yields were not dependant on the amount of chlorine present in the feed.

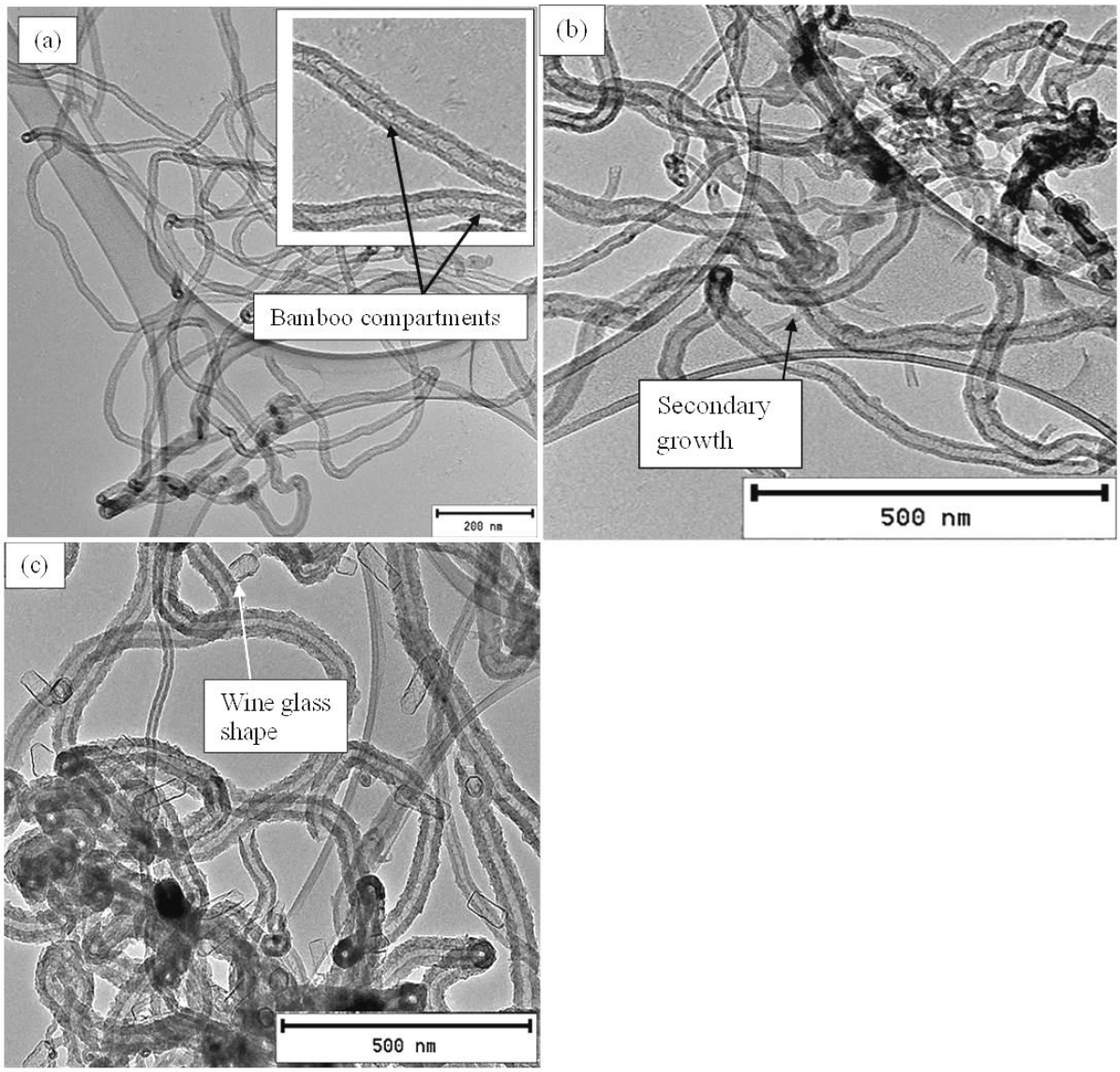

Figure 3.7 TEM images of the purified carbonaceous materials generated using (a) trichloroethane. Growth of small carbon materials of different shapes on the surface of the CNTs can be seen in (b) and (c).

The TEM images of carbon materials produced from TCE are shown in Fig. 3.7. The three figures reveal different features associated with the CNTs. Fig. 3.7a highlights the entangled CNTs and many of these CNTs appear to show bamboo compartment features. Fig. 3.7b shows secondary growth of short CNTs with hollow tips, which seem to originate from the main CNTs. These are similar to those seen above in Fig. 3.3 when DCB was used as a reactant, but here tubes do not taper and the hollow structures can be clearly seen. Finally, wine glass-like secondary structures were also seen in Fig. 3.7c. These secondary structures had very thin walls and did not show the presence of catalyst particles. The presence of un-reacted catalyst material on the surface of the CNTs could be responsible for the secondary growth *via* a tip-growth mechanism.

MWCNTs produced using TTCE also appeared entangled with different outer wall diameters (Fig. 3.8a, b). Numerous small particles can also be observed on the surface of the CNTs, but no secondary nanofibre growth was observed. This might also be attributed to the amount of chlorine in the feed, which if present in large amounts inhibits the growth of secondary fibrous particles. The inner diameters of the MWCNTs produced using chlorinated ethanes also increased with an increase in the amount of Cl contained in the organic reagent (Table 3.1), which suggests HCl-induced metal agglomeration, as has been demonstrated elsewhere.[48,50]

TEM images of carbon materials produced from TCE and TTCE (Fig. 3.7a and 3.8b respectively) also revealed some morphological differences. The carbon materials showed nanotubes with 'segmented' appearance i.e., a 'bamboo-like' structure. TEM images have been reported previously in the literature where 'bamboo-like' nanofibers were produced when DCE, dichloroethylene and TCE were used as sources of Cl over Ni/SiO_2 catalyst and were attributed to a seed metal reconstruction leading to unequal diffusion of carbon through the metal particle.[49] In our case the bamboo structures might arise from effects related to the interaction of chlorine with metal particles leading to catalysts restructuring. Bamboo structures were not seen for the CNTs obtained in this study when DCE was used which might be due to their limited production but the segmentation was observed from CNFs produced from DCE (Supplementary Fig. S2).

More segmented CNTs were observed for CNTs produced from TCE (Fig. 3.7a). The distances between compartments appeared similar for both reactants.

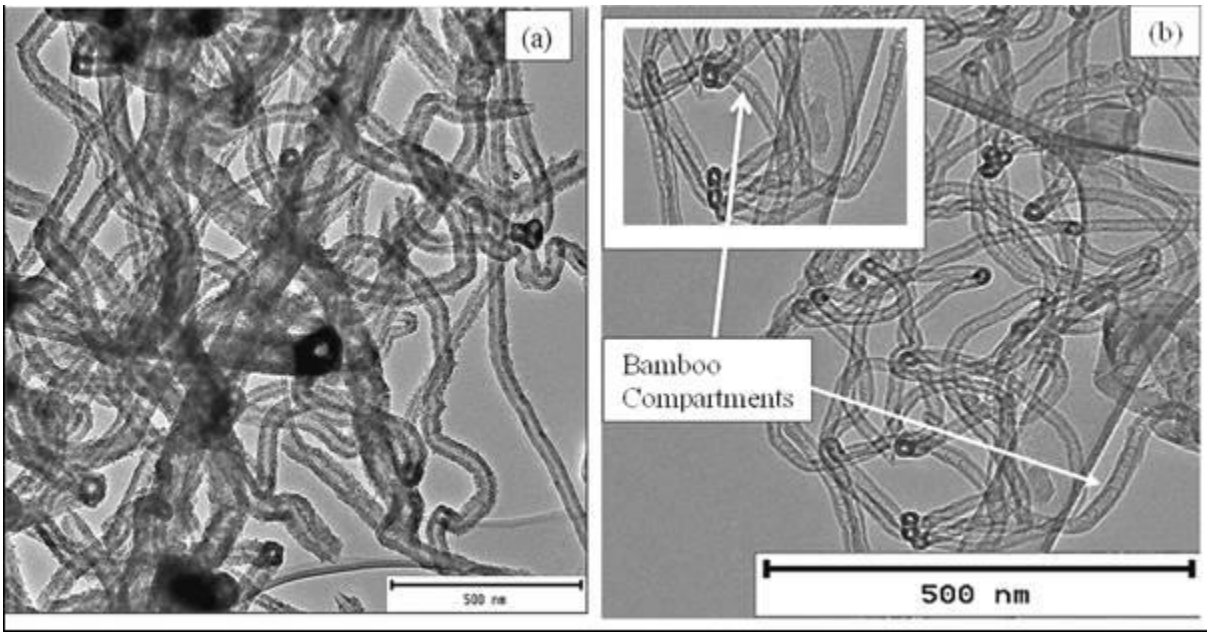

Figure 3.8 TEM images of the purified carbonaceous materials generated using (a) tetrachloroethane. Bamboo compartments can be seen in (b).

3.3.2 TGA and PXRD analysis

TGA and derivative TGA (DTGA) curves of the purified (Fig. 3.9) and un-purified (Supplementary Fig. S6). MWCNTs samples were recorded in an oxygen atmosphere to monitor the weight loss and thermal stability of the samples. CNTs synthesized in the presence of chlorine using CB, DCB and TCB as chlorine sources, revealed oxidation peaks at ~612 °C, 601 °C and 589 °C, respectively (Table 3.2). Previously, Mhlanga *et al.*[56] showed that CNTs synthesized using this catalyst with non-chlorinated reactants oxidized at ~ 550 °C.

From these thermographs and DTGA data (Table 3.2) it can be seen that the decomposition temperature of the purified CNTs made from the aromatic carbon feeds decreased with an increase in the amount of chlorine. The DTGA curves of the CNTs also show the appearance of peaks at ~ 690 °C. These peaks are well-defined for CNTs generated from CB, but appeared as

shoulder peaks for DCB and TCB CNTs. These peaks are assigned to the presence of small amounts of graphitic materials.[64,65]

Further evaluation of the thermographs obtained from chlorinated benzenes, revealed that the CNTs contained residues even after purification in 30 % HNO_3 for 30 min (~21 %, 6 % and 10 % for CB, DCB and TCB (Table 3.2)). An attempt was made to further purify the materials generated from CB by stirring the product in 30% HNO_3 for 2 h and 3 h (Supplementary Fig. S7). The residual mass had not changed (~18% and 20%) after the 2 h and 3 h acid treatments. A further harsher treatment was employed by refluxing the product in acid at 110 °C for 4 h which resulted in destruction of the CNTs structure but a residual non-carbon mass of 8 % still remained (Supplementary Fig. S7). This showed that catalyst particles remained intact and could not be removed from the CNTs despite the harsh acid treatment used. The results correlated with the TEM observations; where images showed the presence of many catalyst particles embedded inside the CNTs (Fig. 3.2) as well as at the tip of a few CNFs made from materials produced using DCB (Fig. 3.3 insert). This implied that the catalyst particles were embedded (i) inside bamboo structures, (ii) within the graphitic layers of the CNTs and (iii) inside the tips of some CNFs (Fig. 3.3 insert). Similar results were observed in the literature using FeNi catalyst when the residual metal contents of 31, 27 and 24 wt.% were observed from TGA curves generated from trichlorobenzene, dichlorobenzene and chlorobenzene as carbon sources; a 3 wt.% residue was observed under the same conditions using xylene as carbon precursor.[51]

TGA (Fig. 3.9c) and DTGA (Fig. 3.9d) curves generated from chlorinated ethanes all show similar oxidation peaks at ~ 619 °C (for DCE and TTCE) and ~ 621 °C for TCE. The chlorinated materials are more thermally stable than those produced from chlorinated benzenes. Catalyst particles were not embedded inside the CNTs (< 2 %) for the CNTs produced from chlorinated alkanes.

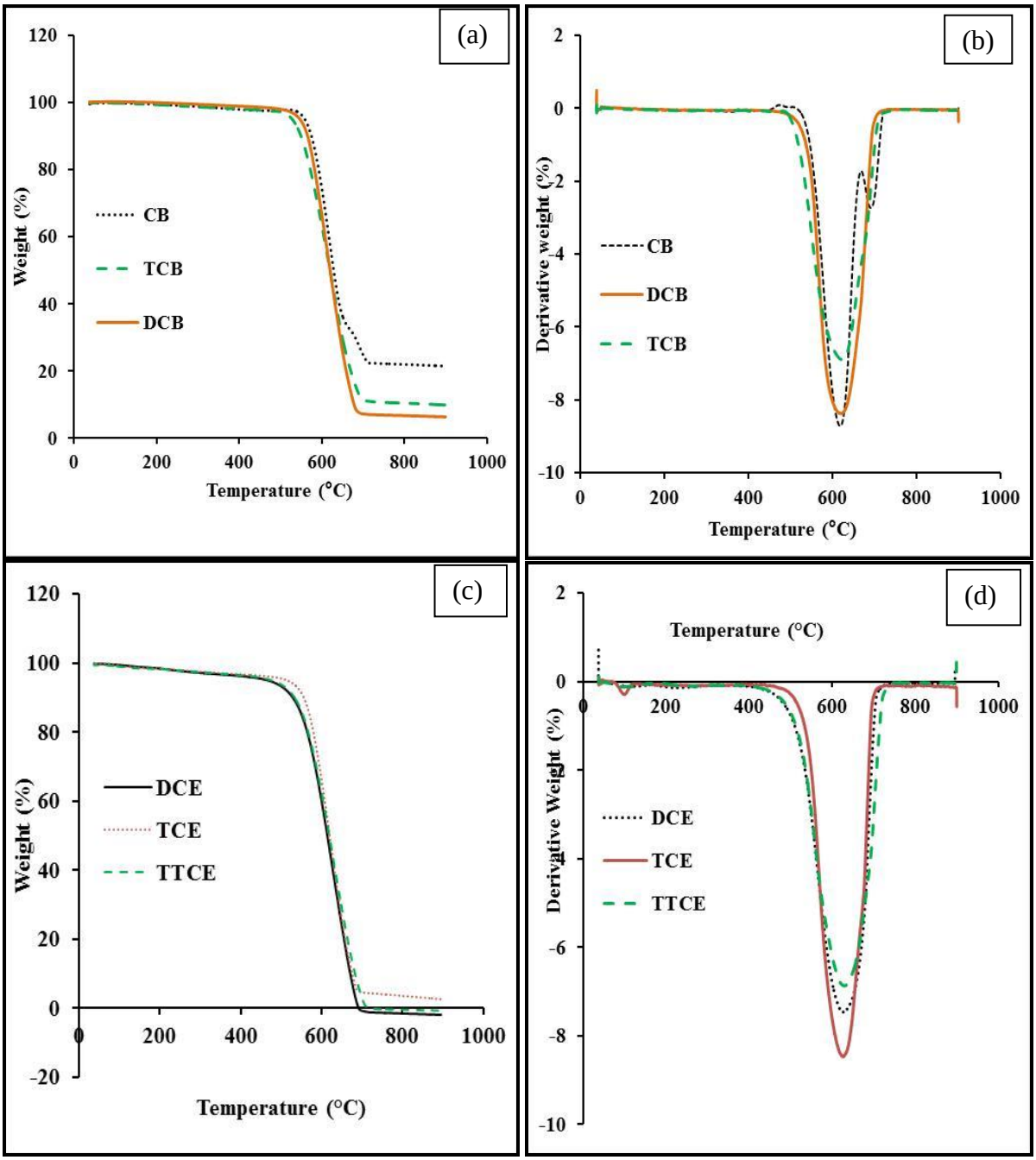

Figure 3.9 TGA and corresponding derivative profiles of the purified MWCNT samples produced using chlorinated benzenes (a and b) and ethanes (c and d) as Cl sources.

Table 3.2 Decomposition temperatures and residual masses (determined by TGA) of the un-purified and purified (P) chlorinated CNMs.

Chlorine source	Decomposition temperature / °C	Residual mass / %
CB	617	26.7
CB(P)	612	21.6
DCB	597	29.6
DCB(P)	601	6.6
TCB	600	29.8
TCB(P)	589	10.1
DCE	550	15.9
DCE(P)	619	0.0
TCE	594	13.6
TCE(P)	621	2.5
TTCE	615	13.5
TTCE(P)	619	0.0

XRD characterization was performed, to further analyze the purity of the CNTs. The XRD profiles of the purified MWCNTs generated from chlorinated hydrocarbons are presented in Fig. 3.10. All XRD patterns show the presence of graphitic carbon represented by a $C_{(002)}$ peak at 2θ = 30° and another peak at 2θ = 53 °. The peak at 2θ = 30 ° has been attributed to MWCNTs.[66] The $C_{(002)}$ peak for CNTs synthesized without chlorine was broader when compared to $C_{(002)}$ peaks of CNTs synthesized in the presence of chlorine. The full width at half maximum (FWHM) of the $C_{(002)}$ peak decreased after introduction of chlorine, and increased with an increase in the amount of chlorine in the feed (Table 3.3). The smaller broadening of the FWHM of the $C_{(002)}$ peak with an increase in the amount of chlorine was attributed to an increased crystallinity of the materials.[66,67]

For chlorinated ethanes, the FWHM of the $C_{(002)}$ peak decreased in the order DCE=TTCE>TCE (Table 3.3). CNTs synthesized using TCE were more crystalline than those generated from DCE and TTCE. These observations agree well with the TGA graphs where CNTs generated from TCE were oxidized at higher temperatures, meaning they were more thermally stable than those generated from other chlorinated-ethane feeds.

Another broad peak closer to the one at 53 ° was attributed to small amounts of carbides in the carbon material. PXRD analysis revealed peaks at 2θ ~ 38 °, 43 ° and 64 ° due to the presence of

cobalt ferrite nanoparticles[68] for CNTs generated from CB, DCB, TCB and TCE, confirming that some metal particles still remained after purification as confirmed by the TGA analysis.

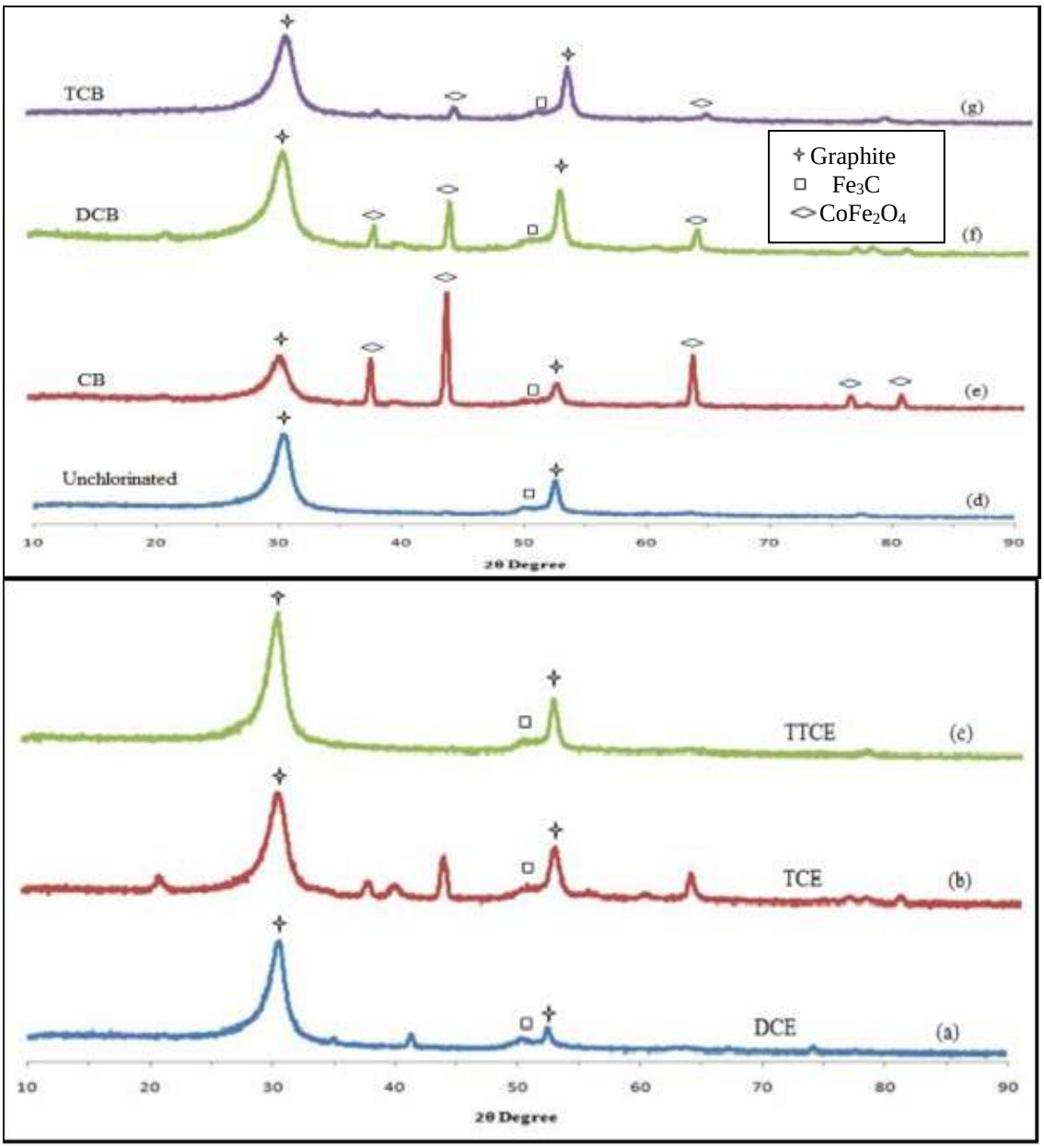

Figure 3.10 XRD spectra of the purified CNTs produced from (a) DCE, (b) TCE, (c) TTCE, (d) Fe-Co/$CaCO_3$ without chlorine[56] (e) CB, (f) DCB and (g) TCB.

Table 3.3 PXRD structural parameters of purified CNTs synthesized in the absence and presence of chlorine.

Chlorine Source	FWHM of $C_{(002)}$ peak (°)
None	3.2
CB	1.2
DCB	2.5
TCB	2.8
DCE	3.2
TCE	2.2
TTCE	3.2

3.3.3 Raman spectral analysis

The crystalline nature of the MWCNT structures was verified by Raman spectroscopy. Raman spectra for all chlorinated MWCNTs (Fig. 3.11 and 3.12) shows a D-band at around 1350 cm^{-1} which is attributed to defects in the curved graphene layers and tube ends and a G-band at around 1576 cm^{-1} which correspond to the movement in the opposite direction of two neighboring carbon atoms in a graphene sheet. The intensity ratio I_D/I_G is known to depend on the structural characteristics of the CNTs.[69] An increase in I_D/I_G corresponds to a higher proportion of sp^3 carbon that is usually attributed to the presence of more structural defects.[70] I_D/I_G ratios of 0.96, 0.96 and 0.76 were observed for CNTs produced from CB, DCB and TCB respectively (Table 4.4). These ratios increased slightly as compared to those shown by Mhlanga et.al[56] for unchlorinated CNTs (0.7). This shows that the CNTs remained graphitic after addition of chlorine, but functionalization of carbon with chlorine produced some defects which agrees with the TGA and XRD data.

The I_D/I_G peak ratio for CNTs produced from DCE (0.89) and TTCE (0.89) were similar, and agreed well with the TGA and the XRD data. Structural defects, shown by the highly intense D peak (Fig. 3.12), were obtained when TCE was used as a source of chlorine. These can be associated with to the formation of bamboo-like CNTs and the growth of open-ended carbon nanotubes onto the main CNTs as observed from TEM images. An overtone 2D peak was also observed at ~ 2680 cm^{-1} in the spectra of CNTs generated from DCE, TTCE, CB, TCB and toluene (Fig. 3.11 and 3.12). This suggests that the materials have a good percentage of graphitic carbon, which agrees with the lower I_D/I_G ratios produced for these materials.

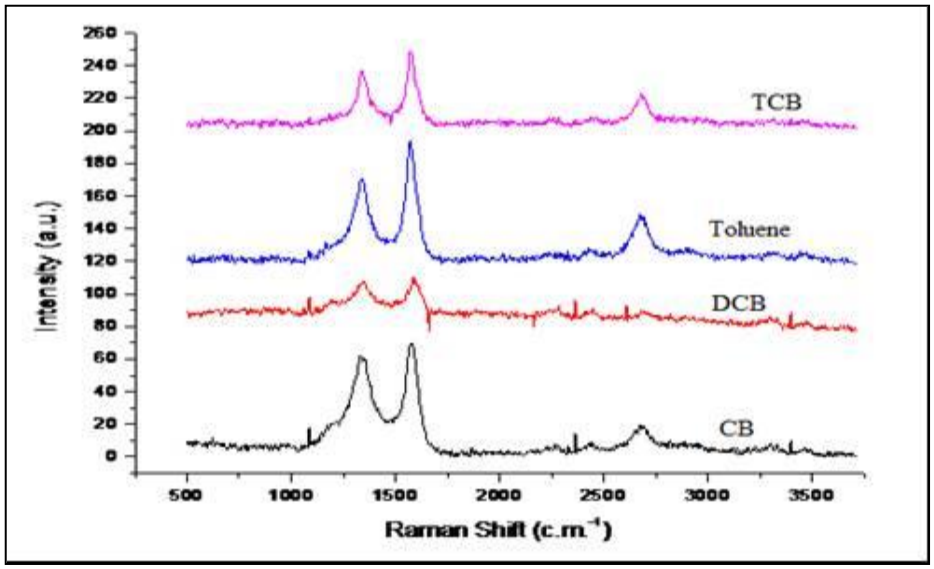

Figure 3.11 Raman spectra of the purified CNTs produced from CB, DCB, TCB and toluene.

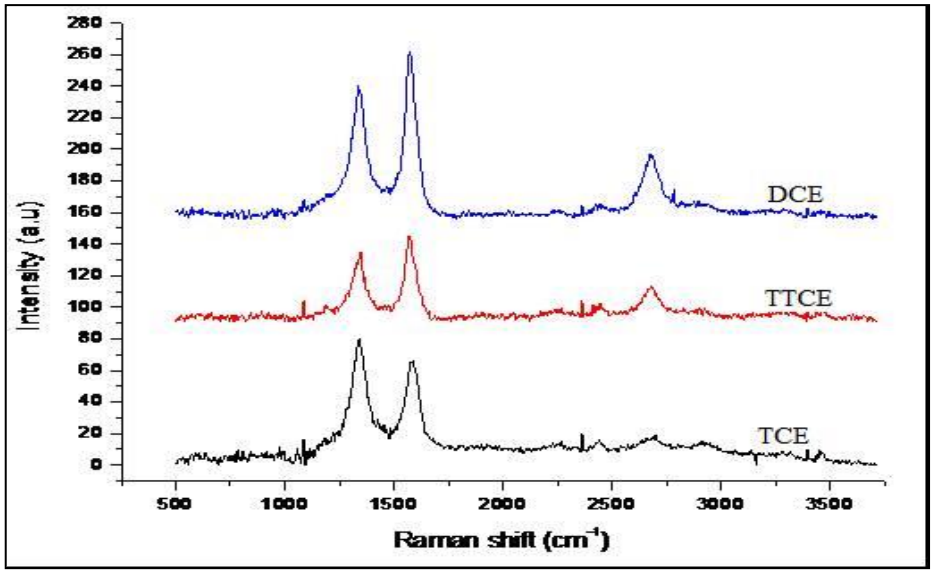

Figure 3.12 Raman spectra of the purified CNTs produced from DCE, TCE and TTCE.

Table 3.4 D-bands, G-bands, 2D-bands and I_D/I_G ratios of the purified chlorinated CNMs.

Chlorine source	D-band /cm^{-1}	G-band /cm^{-1}	2D-band /cm^{-1}	I_D/I_G ratio (peak height)	I_D/I_G ratio (peak area)
CB	1338	1576	2681	0.96	1.8
DCB	1338	1589	-	0.96	2.1
TCB	1341	1576	2680	0.76	1.5
Toluene	1338	1574	2678	0.71	1.3
DCE	1339	1575	2679	0.89	1.8
TCE	1341	1581	-	1.19	2.1
TTCE	1338	1574	2678	0.89	1.5

- No peak observed or the observed peak height is negligible.

3.3.4 Energy dispersive X-ray spectroscopy analysis

The EDX analysis (Table 3.5) revealed the presence of Cl species in all chlorinated samples. It was found that the amount of Cl on the MWCNTs (i) increased with an increase in the amount of Cl in the organic reagents and (ii) aromatic reactants gave less Cl substitution than aliphatic reactants (Table 3.5). This demonstrates that the use of highly chlorine substituted feeds, gives greater functionalization of CNTs with Cl. The data correlates with the TEM data where TCE and TTCE gave more segmented CNTs; hence incorporation of Cl into the carbon structure and secondary fibrous growth observed on the surface of the CNTs can be related to the amount of Cl present.

Table 3.5 EDX analysis of Chlorinated-CNMs grown using different chlorinated organic solvents.

Chlorine source	**Chlorine (Cl) Weight /%**
CB	0.07
DCB	0.12
TCB	0.26
DCE	0.27
TCE	0.75
TTCE	1.53

3.3.5 XPS Analysis

The surface characteristics of purified MWCNTs were analysed by XPS. Supplementary Figure S8 and S9 shows the deconvoluted XPS plots of C1s and Cl2p for all the studied chlorinated organics. The C1s curve for all MWCNTs was deconvoluted into five components with binding energies of ~284.0, 284.8, 285.4, 286.1 and 286.8 eV (Table 3.6). Four of these peaks are readily assigned to Csp^2, Csp^3, C–OH and C=O; it is possible to tentatively assign the fifth peak at 285.4 to C covalently attached to Cl.[71,72]

The Cl2p spectrum of CNTs generated from chlorinated organics (Supplementary Figs. S8 and S9) showed two signals at ~201 and 199 eV which are assigned to the $2p_{1/2}$ and $2p_{3/2}$ of a chloride ion (e.g. as found in metal chlorides).[72,73] Unfortunately the $2p_{1/2}$ peak associated with covalent C-Cl bonds overlaps with the $2p_{3/2}$ associated with the presence of the chloride ion peak. Furthermore, the low concentration of the Cl in the samples generates very small peaks for Cl and this makes it difficult to quantify the amount of covalent Cl in the CNTs. However, the $2p_{1/2}/2p_{3/2}$ ratios for the Cl peaks indicate values below ca.1.6, the value expected when *only ionic chloride* is present (Table 3.6). This suggests that indeed small amounts of C-Cl bonds have been made; the CNTs made from TTCE thus have the largest amount of C-Cl bonds. This chlorine would be attached to sp^2 carbons at the periphery of the aromatic structures, or at defect sites.[71] The low Cl content is not unexpected as C-Cl bonds are readily broken under the high temperature condition employed in the CNT synthesis.

Table 3.6 XPS analysis of purified chlorine functionalized CNTs grown using different chlorine sources

Binding energy /eV (and atomic concentration /%)		
Chlorine source	C	Cl
CB	284.0 (69.7 %) 284.8 (14.7 %) 285.3 (7.44 %) 286.0 (4.20 %) 287.0 (3.95 %)	199.4 (58.1 %) 201.0 (41.9 %)
DCB	284.0 (65.5 %) 284.8 (16.5 %) 285.4 (13.2 %) 286.2 (1.43 %) 287.0 (3.50 %)	199.0 (59.8 %) 200.1 (40.2 %)
TCB	284.0 (72.1 %) 284.9 (13.9 %) 285.5 (6.51 %) 286.0 (2.00 %) 287.0 (5.52 %)	199.2 (62.9 %) 200.8 (37.1 %)
DCE	283.9 (62.3 %) 284.5 (16.5 %) 285.1 (12.7 %) 285.7 (4.88 %) 286.7 (3.64 %)	199.0 (63.8 %) 200.6 (36.2 %)
TCE	284.0 (69.1 %) 284.7 (8.82 %) 285.2 (13.9 %) 286.0 (5.72 %) 286.7 (2.42 %)	199.0 (59.1 %) 200.9 (40.8 %)
TTCE	284.0 (69.2 %) 284.7 (22.1 %) 285.2 (10.7 %) 285.8 (3.52 %) 286.6 (0.685 %)	199.3 (54.5 %) 200.9 (45.6 %)

3.4 Conclusion

The role of chlorine on the morphology of MWCNTs synthesized by the catalytic pyrolysis of chlorinated organic reagents over a Fe-Co/$CaCO_3$ catalyst was studied. The structural morphology of CNTs produced depended on the amount of chlorine present in the feed and on the type of organic chlorine compound used. CNTs generated from TCE and TTCE showed the formation of bamboo-like structures, which were due to catalyst restructuring by chlorine.

Secondary nanofibre and nanotube growth onto the main CNTs was observed when DCB and TCE chlorine sources were used. Carbon nanofibers were found to be dominant when chlorine sources (i.e, DCE) that contained high concentration of hydrogen were used. Addition of chlorine favoured the growth of carbon materials of high purity. Alkanes gave cleaner CNMs with higher yields than those formed from the aromatic reactants. XPS studies revealed that most of the Cl found in the CNTs was ionic chlorine, most probably associated with the Fe and in the CNT tubes. Some surface functionalization of carbon with chlorine is suggested when TTCE was used as a reagent. The amount of chlorine functionalized on the surface of CNTs was less than 1% for all chlorinated organics studied, evidenced by XPS and EDS. The role of chlorine on the morphology of nitrogen-doped CNTs and the use of chlorinated MWCNTs as adsorbents for selected heavy metals in wastewater treatment is underway.

References

1. H.W. Kroto, J.R. Heath, S.C. O' Brien, R.F. Curl, and R.E. Smalley, *Nature*, 1985, **318**, 162–163.
2. S. Ijima, *Nature*, 1991, **354**, 56–66.
3. P.G. Collins, and P. Avouris, *Scientific American*, 2000, **283**, 62–69.
4. Q. Zeng, Z. Li, and Y. Zhou, *J. Nat. Gas Chem*., 2006, **15,** 235–246.
5. B.M. Endo, T. Hayashi, Y.A. Kim, M. Terrones, and M.S. Dresselhaus, *Phil. Trans. Roy. Soc. London. A.*, 2004, **362,** 2223–2238.
6. M. Terrones, A. Jorio, M. Endo, Y.A. Kim, T. Hayashi, H. Terrones, J.-C. Charlier, G. Dresselhaus, and M.S. Dresselhaus, *Mater. Today*, 2004, **7,** 30–45.
7. H. Zeng, L. Zhu, G. Hao, and R. Sheng, *Carbon*, 1998, **36,** 259–262.
8. A. Thess, R. Lee, P. Nikolaev, H. Dai, P. Petit, J. Robert, C. Xu, Y.H. Lee, S.G. Kim, A.G. Rinzler, D.T. Colbert, G.E. Scuseria, D. Tombnek, and J.E. Fischer, *Science*, 1996, **273,** 483–487.
9. D.C. Li, L. Dai, S. Huang, A.W.H. Mau, and Z.L. Wang, *Chem. Phys. Lett., 2000, **316,** 349–355.*
10. V. Ivanov, J.B. Nagy, P. Lambin, A. Lucas, X.B. Zhang, X.F. Zhang, D. Bernaerts, G. Van Tendeloo, S. Amelinckx, and J. Van Landuyt, *Chem. Phys. Lett*., 1994, **223**, 329–335.
11. S.Y. Brichka, G.P. Prikhod'ko, Y.I. Sementsov, A.V. Brichka, G.I. Dovbeshko, and O.P. Paschuk, *Carbon*, 2004, **42,** 2581–2587.
12. K. Chizari, A. Vena, L. Laurentius, and U. Sundararaj, *Carbon*, 2014, **68,** 369–379.
13. C. Wang, Z. Huang, L. Zhan, Y. Wang, W. Qiao, X. Liang, and L. Ling, *Diamond Relat. Mater*., 2011, **20,** 1353–1356.
14. T. Sharifi, F. Nitze, H. R. Barzegar, C-W. Tai, M. Mazurkiewicz, A. Malolepszy, L. Stobinski, and T. Wågberg, *Carbon*, 2012, **50,** 3535–3541.
15. G. Bepete, Z. N. Tetana, S. Lindner, M. H. Rummeli, Z. Chiguvare, and N. J. Coville, *Carbon*, 2013, **52,** 316–325.
16. H. Liu, Y. Zhang, R. Li, X. Sun, and H. Abou-Rachid, *J. Nanopart. Res*., 2012, **14**, 1016–1023.

17. L. Faba, Y.A. Criado, E. Gallegos-Suáres, M. Pérez-cadenas, E. Díaz, I. Rodríquez-Ramos, A. Guerrero-Ruiz, and S. Ordónez, *Appl. Cat. A: Gen*., 2013, **458,** 155–161.
18. R. Czerw, M. Terrones, J.-C. Charlier, X. Blasé, B. Foley, R. Kamalakaran, N. Grobert, H. Terrones, D. Tekleab, P.M. Ajayan, W. Blau, M. Rühle, and D.L. Carroll, *Nano. Lett*., 2001, **9**, 457–560.
19. S. Maldonado, S. Morin, and K. Stevenson, *Carbon*, 2006, **44,** 1429–1437.
20. P. L. Gai, O. Stephan, K. McGuire, A. M. Rao,M. S. Dresselhaus, G. Dresselhaus, and C. Colliex, *J. Mater. Chem*., 2004, **14,** 669-675.
21. R. Czerw, P.-W. Chiu, Y.-M. Choi, D.-S. Lee, D.L. Carroll, S. Roth, and Y.-W. Park, *Curr. Appl. Phys*., 2002, **2,** 473–477.
22. H. J. Ceragioli, A. C. Peterlevitz, J. C. R. Quispe, A. Larena, M. P. Pasquetto, M. A. Sampaio, and V. Baranauskas, *J. Phys.: Conf. Ser.*, 2008, **100,** 052029 doi:10.1088/1742-6596/100/5/052029.
23. K. McGuire, N. Gothard, P.L. Gai, M.S. Dresselhaus, G. Sumanasekera, and A.M. Rao, *Carbon*, 2005, **43**, 219–227.
24. F. H. Monteiro, D. G. Larrude, M. E. H. Maia da Costa, L. A. Terrazos, R. B. Capaz, and F. L. Freire Jr, *J. Phys. Chem. C*, 2012, **116**, 3281–3285.
25. T. Cui, R. Lv, Z.H. Huang, F. Kang, K. Wang, and D. Wu, *Nanoscale. Res. Lett*., 2011, **6,** 77–82.
26. F. Bottger-Hiller, A. Mehner, S. Anders, L. Kroll, G. Cox, F. Simon, and S. Spange, *Chem. Comm*., 2012, **48,** 10568–10570.
27. C. Shan, W. Zhao, X.L. Lu, D.J. O'Brien, Y. Li, Z. Cao, A.L. Elias, R. Cruz-Silva, M. Terrone, B. Wei, and J. Suhr, *Nano. Lett*., 2013, **13,** 5514–5520.
28. Q. Shi, F. Peng, S. Liao, H. Wang, H. Yu, Z. Liu, B. Zhang and D. Su, *J. Mater. Chem. A*., 2013, **1**, 14853–14857.
29. J. Li, L. Wang, Y.J. Su, P. Liu, and Y.F. Zhang, *Nano-Micro Lett*., 2009, **1,** 9–13.
30. X. Qu, P. J. J. Alvarez, and Q. Li, *Environ. Sci. Technol*., 2013, **47**, 14080−14088.
31. B. Zhong, H. Liu, X. Gu, and D. S. Su, *Chem. Cat. Chem*., 2014, **6,** 1553–1557.
32. D. Srivastava, T. Susi, M. Borghei, and L. Kari, *RSC Adv*., 2014, **4,** 15225-15235.
33. G. D. Nessim, A. Al-Obeidi, H. Grisaru, E. S. Polsen, C. R. Oliver, T. Zimrin, A. J. Hart, D. Aurbach, and C. V. Thompson, *Carbon*, 2012, **50,** 4002–4009.

34. P. C. P. Watts, N. Mureau, Z. Tang, Y. Miyajima, J. D. Carey, and S. R. P. Silva, *Nanotechnol*., 2007, **18**, 175701, doi:10.1088/0957-4484/18/17/175701.
35. J. Zhao, and R-H. Xie, *J. Nanosci. Nanotechnol*., 2003, **3,** 459–478.
36. S. Niyogi, M.A. Hamon, H. Hu, B. Zhao, P. Bhowmik, R. Sen, M.E. Itkis, and R.C. Haddon, *Acc. Chem. Res*., 2002, **35,** 1105–1113.
37. S.M. Kim, K.K. Kim, Y.W. Yo, M.H. Park, S.J. Chae, D.L. Duong, C.W. Yang, J. Kong, and Y.H. Lee, *ACS Nano*., 2011, **5**, 1236–1242.
38. J.K. Wassei, K.C. Cha, V.C. Tung, Y. Yang, and R.B. Kaner, *J. Mater. Chem*., 2011, **21,** 3391–3396.
39. D.L. Duong, I.H. Lee, K.K. Kim, J. Kong, S.M. Lee, and Y.H. Lee, *ACS Nano*., 2010, **4,** 5430–5436.
40. J-M. Yuan, X-H. Chen, X-H Chen, Z-F Fan, X- Yang, and Z-H.Chen, *Carbo*n, 2008, **46,** 1266–1269.
41. W.H. Lee, S.J. Kim, W.J. Lee, J.G. Lee, R.C. Haddon, and P.J. Reucroft, *Appl. Surf. Sci*., 2001, **181,** 121–127.
42. Z. Kónya, I. Vesselenyi, K. Niesz, A. Kukovecz, A. Demortier, A. Fonseca, J. Delhalle, Z. Mekhalif, J.B. Nagy, A.A. Koós, Z. Osváth, A. Kocsonya, L.P. Biró, and I. Kiricsi, *Chem. Phys. Lett*., 2002, **360**, 429–435.
43. I. Pełech, U.Narkiewicz, D. Moszyński, and R. Pelech, *J. Mater. Res*., 2012, **27,** 2368–2374.
44. C. Ghemes, A. Ghemes, M. Okada, H. Mimura, T. Nakano, and Y. Inoue, *Japanese J. Appl. Phys*., 2013, **52**, 035202.
45. J. Barkauskas, I. Stankevičiene, and A. Selskis, *Sep. Pur. Tech*., 2010, **71**, 331–336.
46. J.L. Zimmerman, R.K. Bradley, C.B. Huffman, R.H. Hauge, and J.L. Margrave, *Chem. Mater*., 2000, **12**, 1361–1366.
47. H. Qiu, Z. Shi, L. Guan, L. You, M. Gao, S. Zhang, J. Qiu, and Z. Gu, *Carbon*, 2006, **44,** 516–521.
48. L.D. Cherukuri, G. Yuan, and M.A. Keane, *Top. Catal*., 2004, **29,** 119–128.
49. A.N. Márquez, J. L. Valverde, and M.A. Keane, *Appl. Catal. A: Gen*., 2007, **332,** 237–246.
50. M. A. Keane, G. Jacobs, and P. M. Patterson, *J. Colloid Interface Sci*., 2006, **302,** 576–588.
51. R. Lv, F. Kang, W. Wang, J. Wei, J. Gu, K. Wang, and D. Wu, *Carbon*, 2007, **45,** 1433–1438.

52. X. Gui, K. Wang, J. Wei, X. Zhang, R. Lv, Y. Jia, Q. Shu, F. Kang and D. Wu, *Mater. Chem. Phys*., 2009, **113**, 634 – 637.
53. M. Kao, *Chemical Vapour Deposition Synthesis of Carbons From Halogen and Silicon Sources*, MSc. Dissertation, University of the Witwatersrand, Johannesburg, South Africa, 2010.
54. A. Shaikjee, and N.J. Coville, *Mater. Lett*., 2012, **68,** 273–276.
55. W.-H. Lin, T.-T. Lee, and Y.-Y. Li, *J. Taiwan Inst. Chem. Eng. E*, 2014, **45**, 1883–1891.
56. S.D. Mhlanga, K.C. Mondal, R. Carter, M.J. Witcomb, and N.J. Coville, *S. Afr. J. Chem*., 2009, **62**, 67–76.
57. S.D. Mhlanga, and N.J. Coville, *Diamond Relat. Mater*., 2008, **17**, 1489–1497.
58. Z.N. Tetana, S.D. Mhlanga, G. Bepete, R.W.M. Krause, and N.J. Coville, *S. Afr. J. Chem.*, 2012, **65**, 39–49.
59. H. Kathyayini, N. Nagaraju, A. Fonseca, and J.B. Nagy, *J. Mol. Catal. A: Chem*., 2004, **223**, 129–136.
60. A.A. Hosseini, S. Mehralitabar, A.A. Hosseini, M. Pashaee, and F. Taleshi, *Proceedings of the 4th International Conference on Nanostructures (ICNS4)*. 12 – 14 March, 2012. Kish Island. I.R. Iran. 1296–1298.
61. N. Das, A. Dalai, J. S. S. Mohammadzadeh, and J. Adjaye, *Carbon*, 2006, **44**, 2236–2245.
62. K. Hernadi, A. Fonseca, J. B. Nagya, A. Siska, and I. Kiricsi, *App. Cat. A: Gen.*, 2000, **199**, 245–255.
63. F. Ohashi, G. Y. Chen, V. Stolojan,S. and R. P. Silva, *Nanotechnol*., 2008, **19**, 445605.
64. C.H. See, and A.T. Harris, *Particle Tech. Fluidization*, 2008, **54**, 657–664.
65. S. Santangelo, M. Lanza, and C. Milone, *J. Phys. Chem*. C, 2013, **117**, 4815–4823.
66. I.D. Rosca, F. Watari, M. Uo, and T. Akasaka, *Carbon*, 2002, **43**, 3124–3131.
67. L.M. Ombaka, P.G. Ndungu, and V.O. Nyamori, *J. Mater. Sci.*, 2015, **50**, 1187 – 1200.
68. M. Sajjia, M. Oubaha, M. Hasanuzzaman, and A.G. Olabi, *Ceram. Int.*, 2014, **40,** 1147–1154.
69. L.G. Cancado, A. Jorio, E.H. Martins Ferreira, F. Stavale, C.A. Achete, R.B. Capaz, M.V.O. Moutinho, A. Lombardo, T.S. Kulmala and A.C. Ferrari, *Nano Letters*, 2011, **11**, 3190–3196.
70. L. Shao, G. Tobias, C.G. Salzmann, B. Ballesteros, S.Y. Hong, A. Crossley, B.G. Davis, and M. L. H. Green, *Chem. Commun*., 2007, 5090–5092.

71. E. Papirer, R. Lacroix, J.-B. Donnet, G. Nanse, and P. Fioux, *Carbon*, 1995, **33**, 63–72.
72. X. Zhang, A. Hsu, H. Wang, Y. Song, J. Kong, M.S. Dresselhaus and T. Palacios, *ASC Nano.*, 2013, **7**, 7262–270.
73. L. Fan, H. Zhang, P. Zhang and X. Sun, *Appl. Surf. Sci.*, 2015, **347**, 632–635.

CHAPTER 4

One step synthesis of carbon nanotubes with secondary growth: role of chlorine

---

4.1 Introduction

Since their discovery, the unique properties of carbon nanotubes (CNTs)[1] and of their less crystalline counterparts carbon nanofibers (CNFs)[2] have attracted the interest of many scientific communities. CNTs and CNFs possess excellent thermal properties,[3,4] as well as unique electronic[5,6] and mechanical properties[4,7] which exceed those of many currently applied materials. CNTs have a low density, high transparency, large surface area, and high aspect ratio.[8] This makes CNTs a good candidate for use as a nanoscale platform for sensors,[9] transparent electrodes,[10] a catalytic surface for fuel cells,[11] emitters for light sources based on field emission,[12,13] electron sources in transmission electron microscopes,[14] etc. Synthesis of CNTs with different shapes such as waved, coiled, crossed and branched has been a subject of many investigations and the synthesis strategy has the potential to open the way to various applications, such as in molecular electronics.[15] In order to enhance the use of CNTs as a nanoscale platform, a high density network structure of CNTs with chemically connected CNTs must be formed.[8] If the cross-links between the nanotubes establish a stable connection, then it should also be possible to create very strong polymer compound materials.[16] There are a few reports that have discussed the chemical connection between CNTs, between CNTs and CNFs and the synthesis of CNTs on graphite substrates. The limitations of any connections are due to various reasons, (i) the inert surface characteristics of CNTs allow only physically aggregated bundle structures without chemical connection between CNTs[8]; (ii) transition metals are easily diffused into the carbon substrates; and (iii) the different phases of carbon materials are able to form on the graphite substrate because the growth conditions are similar to the diamond or diamond-like carbon growth.[17,18] To overcome these issues it is proposed that covalent bonding between different carbon structures be used. The first report of CNT growth on carbon fibers was by Zhu, *et al*.[19] In their report CNTs were synthesized on graphite fibers by first coating the

fiber surface with iron nanoparticles to act as catalyst for CNT growth. CNTs could only be fabricated on the graphitic fiber surfaces at low temperatures with catalytic particles on the nanotube top ends.[19]

These structures in which carbon has secondary growth on top of CNTs or CNFs have found some applications. Enhancement of field emission properties of MWCNTs by secondary growth was reported by Klinke *et al*., after they coated primary CNTs with Ni, Au and ferritin before resubmission to CVD for secondary growth of nanotubes.[16] Electrochemical decoration of CNTs with Ni nanoparticles was also employed by Santini *et al*. for growing branched CNTs.[20] Attachment of colloidal FePt nanoparticles on primary CNTs by dispersion in solution was employed by Lee et al. in order to facilitate a uniform deposit of the catalyst on the CNTs for growth of secondary CNTs.[8] An electron beam welding technique was employed by Terrones *et al*. to locally melt and solidify CNTs at the junction of CNTs.[21]

In this study we explored the role of chlorine on the secondary growth of CNFs on the surface of CNTs by a one-step CVD method using dichlorobenzene (DCB). To our knowledge secondary growth of CNFs onto the primary CNTs by a one-step process has not previously been documented. The role of chlorine in the initiation of secondary nanofibers was discovered by serendipity in our earlier work.[22]

4.2. Experimental

4.2.1 Materials and Chemicals

$Fe(NO_3)_3 \cdot 9H_2O$ (Sigma Aldrich) ≥ 98 %, $Co(NO_3)_2 \cdot 6H_2O$ (Sigma Aldrich) ≥ 98 %, $CaCO_3$ (Sigma Aldrich) ≥ 99 %, HNO_3 (Sigma Aldrich) ≥ 98 % ACS, 1,2-dichlorobenzene (DCB) (Sigma Aldrich) 99 % Reagent plus, were used. All the reagents were commercially available and used without further purification.

4.2.2 One-step synthesis of CNTs with secondary growth

The Fe-Co/$CaCO_3$ catalyst (1.0 g) was spread in a quartz boat and the boat was placed in the center of a quartz tube. The furnace was then heated to 700 °C at a rate of 10 °C/min under

flowing N_2 (50 mL/min). Once the required temperature has been reached, the N_2 flow rate was increased to 240 mL/min and the C_2H_2 flow rate was set at 90 mL/min. Both gases were bubbled through dichlorobenzene, which was introduced into the quartz tube. After 60 min of reaction time, the C_2H_2 flow and bubbling was stopped and the system was left to cool down to room temperature under a continuous flow of N_2 (50 mL/min). The quartz boat was then removed from the reactor and the carbon deposit (chlorinated MWCNTs) that formed was weighed. The reaction time was varied from 60 to 120 minutes, in order to establish the effect of reaction time. The reaction temperature was also varied using the following temperatures, 600, 650, 700, 750, and 800 °C, respectively while maintaining the reaction time of 90 min.

4.2.3 Synthesis of secondary CNFs using CNTs as substrate

About 0.3 g of as-synthesized CNTs prepared using a method by Mhlanga *et al*.[23] In this method a Fe-Co/$CaCO_3$ catalyst, was spread in a quartz boat, which was placed in a quartz tube. The tube was inserted into a furnace, which was heated gradually to 700 °C at a rate of 10 °C/min under N_2 (50 mL/min) flow. Once the required temperature has been reached, the N_2 flow rate was increased to 240 mL/min and the C_2H_2 flow was set at 90 mL/min. The CNT substrate were then placed into the quartz boat, which was inserted into the quartz tube. The quartz tube was inserted into the furnace, which was gradually heated to 700 °C in the presence of an inert gas (N_2). At 700 °C, N_2 (240 mL/min) and C_2H_2 (90 mL/min) were bubbled through dichlorobenzene, and the gas stream was introduced into a quartz tube. After 120 min of reaction, the C_2H_2 flow and bubbling was stopped and the system was left to cool down to room temperature under a continuous flow of N_2 (50 mL/min). The quartz boat was then removed from the reactor and the carbon deposit that formed was weighed.

4.2.4 Synthesis of secondary CNFs onto primary CNTs using CNTs spread with catalyst

About 0.2 g of purified CNTs prepared over a Fe-Co/$CaCO_3$ catalyst using a method by Mhlanga et.al[23], was placed in a quartz boat and 0.2 g of Fe-Co/$CaCO_3$ catalyst was spread on top of the CNTs and submitted to a CVD process. A mixture of dichlorobenzene, N_2 (240 mL/min), and C_2H_2 (90 mL/min) was passed through the reactor for 60 min, while the CVD reactor was kept at 700 °C. The procedure employed was the same as the one used in 4.2.2.

4.2.5 Characterization of CNTs

The morphology and size distribution of the CNTs before and after HNO_3 treatment were analyzed by transmission electron microscopy (TEM) using a FEI TECNAI G^2 SPIRIT. The samples for TEM analysis were prepared by sonication in ethanol and thereafter deposited on a holey carbon-coated TEM Cu grid. The CNTs were also characterized by Raman spectroscopy using a Jobin-Yvon T6400 micro-Raman spectrometer. Excitation was provided by a 532 nm green laser with spectral resolution of 3-5 cm^{-1}. The impurity content of the CNTs was monitored by thermogravimetric analysis (TGA) using a Perkin Elmer TGA 7. The sample was loaded onto a platinum pan and heated to 900 °C at a heating rate of 5 °C/min, in a flowing air stream at 20 mL/min.

4.3 Results and discussion

4.3.1 Structural analysis of the chlorinated CNTs: Effect of reaction time and temperature

Figures 4.1 to 4.5 shows TEM images of CNTs generated from dichlorobenzene as a chlorine source at different reaction times, 60, 90 and 120 minutes, respectively. Multiple secondary CNFs with similar shapes and outer diameters were grown on various CNTs after 60 min of reaction (Figure 4.1). The secondary CNFs were initially broad and then became narrower as they grew. Close inspection of the numerous CNFs produced revealed that they all had an inverted cap-like morphology. The length of the secondary CNTs was short, ca. 21–179 nm (Figure 4.1). About 40 % of the primary CNTs had secondary CNFs after 60 min of reaction. Other carbon nanostructures, carbon nano-onion and carbon nanofibers with metal particles at their tips were observed at a 60 min reaction time. Increasing the reaction time to 90 min resulted in an increase in the number of secondary CNFs formed (Figure 4.2). The secondary CNFs were grown with consistency in terms of their size, length and shape compared to those obtained after 60 min of reaction (Figure 4.2). The secondary CNFs were also less graphitized and shorter in length than the primary CNTs. The quantity of the secondary CNFs increased at longer reaction times, with ~ 90 % observed after 90 min of reaction.

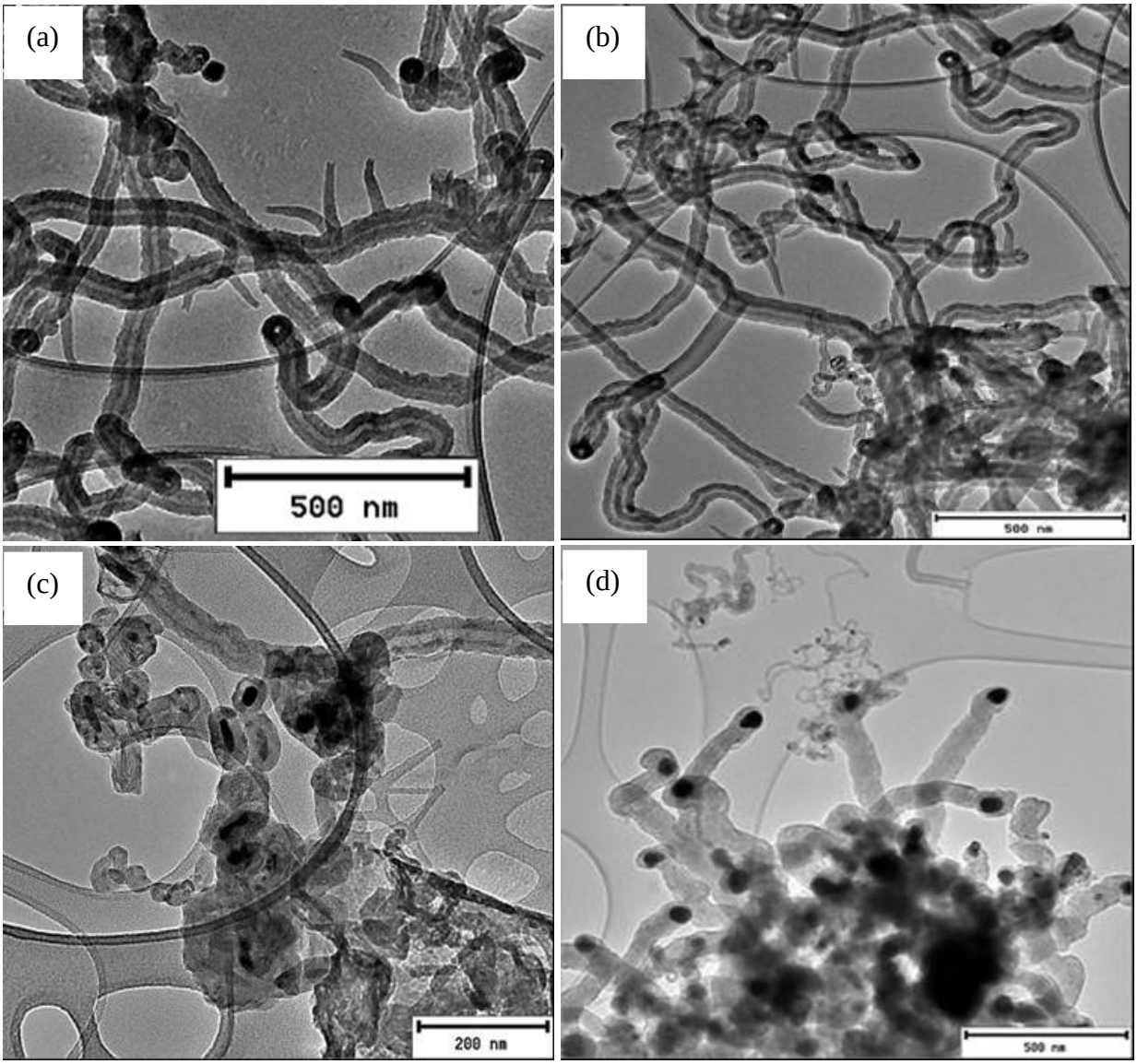

Figure 4.1 TEM image of purified CNTs showing secondary CNFs generated using dichlorobenzene as chlorine source at 60 min reaction time, using the following reaction conditions: 700 °C, 240 mL/min (N_2), 90 mL/min (C_2H_2)

Carbon platelets or some amorphous carbon materials were also observed from the images of the CNTs obtained from a 90 min reaction time (Figure 4.2d circled parts). A CNT with funnel-like open end was also observed from this TEM images (Figure 4.2d arrow).

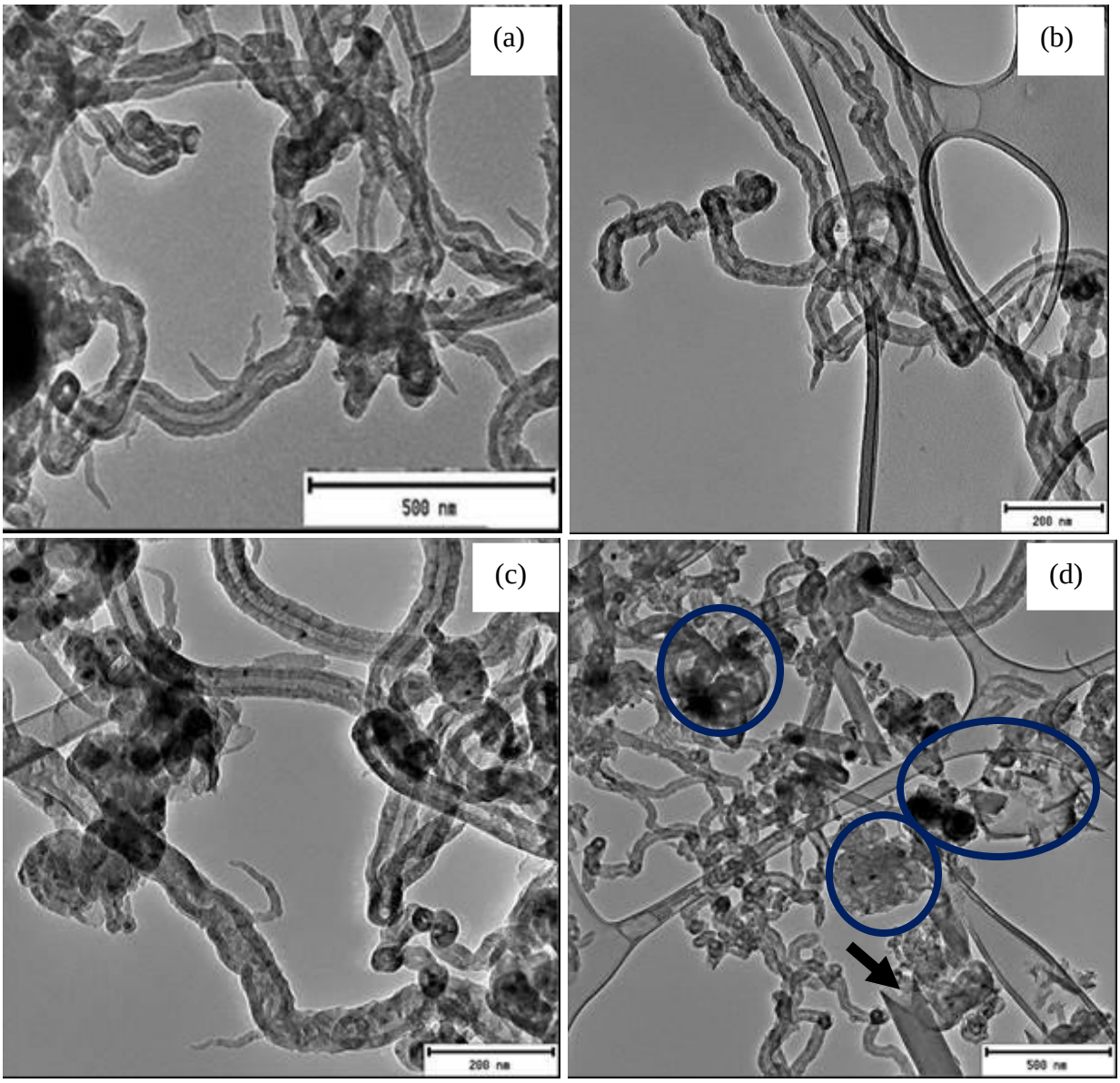

Figure 4.2 TEM images of purified CNTs showing secondary CNFs generated using dichlorobenzene as chlorine source at 90 min reaction time, using the following reaction conditions: 700 °C, 240 mL/min (N_2), 90 mL/min (C_2H_2).

High resolution TEM image revealed the absence of catalyst particles at the beginning of the secondary CNFs (Figure 4.3) which shows that the CNFs were grown from a catalyst free surface. Further analysis of the HRTEM images reveal that the secondary CNF appears as a continuous extension of the CNT sidewall and not simply attached to the outer wall of the CNTs.

This observation suggests that the secondary CNFs may have nucleated from defects or fractures in the CNT sidewall.

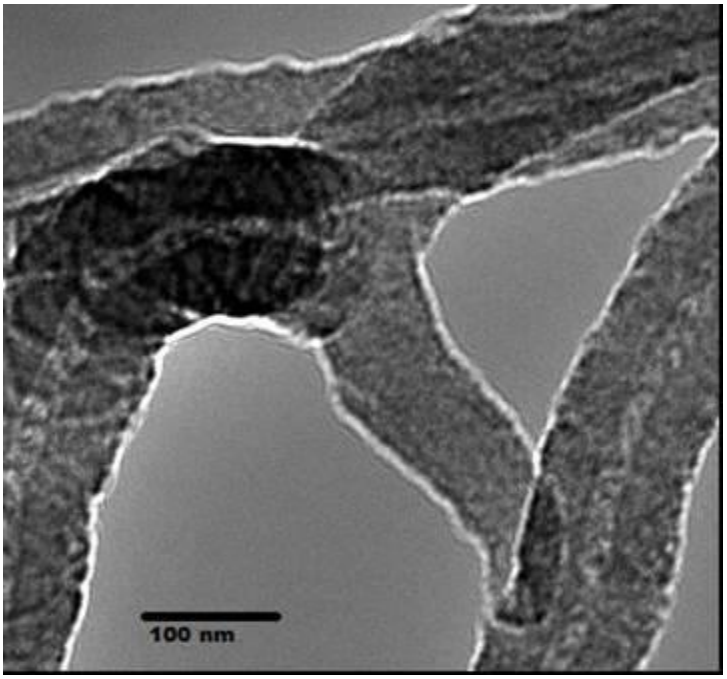

Figure 4.3 HRTEM image of purified CNTs showing the origin of the secondary CNFs growth synthesized at a 90 min reaction time and 700 °C temperature.

Few secondary CNFs were also observed growing at different positions of the CNT wall structure, for example CNFs were observed growing from the tip of a CNT that contained a metal particle embedded at its tip (Figure 4.4a and b shown by arrows). The secondary CNFs did not originate from the embedded catalyst it was a continuous extension of the CNT tip wall. A large aggregate of entangled CNTs covered with amorphous carbon materials or carbon platelets also showed a large aggregate of secondary structures (Figure 4.4c). Another secondary CNF was observed growing at the curved or bent part of the CNT (Figure 4.4d shown by arrow), which proves that the secondary CNFs were growing from defect sites of the main CNTs. Poncharal *et al*. observed from their in-situ TEM measurements that the greatest deformation occurs in the outer layers of a bent nanotube.[24] Another secondary CNF can also be observed lying on the wall of the main CNT (Figure 4.4d circled part). It appears that a large magnitude of

CNTs and CNFs can be grown from each other (i.e. using each other as templates) by simply fine tuning the reaction conditions. We suggest that the secondary structures grew via a catalyst free mechanism, and this was initiated by defects that were created by covalent bonding between carbon and chlorine. Since secondary structures were not observed from CNTs generated using the same reagents and reaction conditions in the absence of chlorine source.[23]

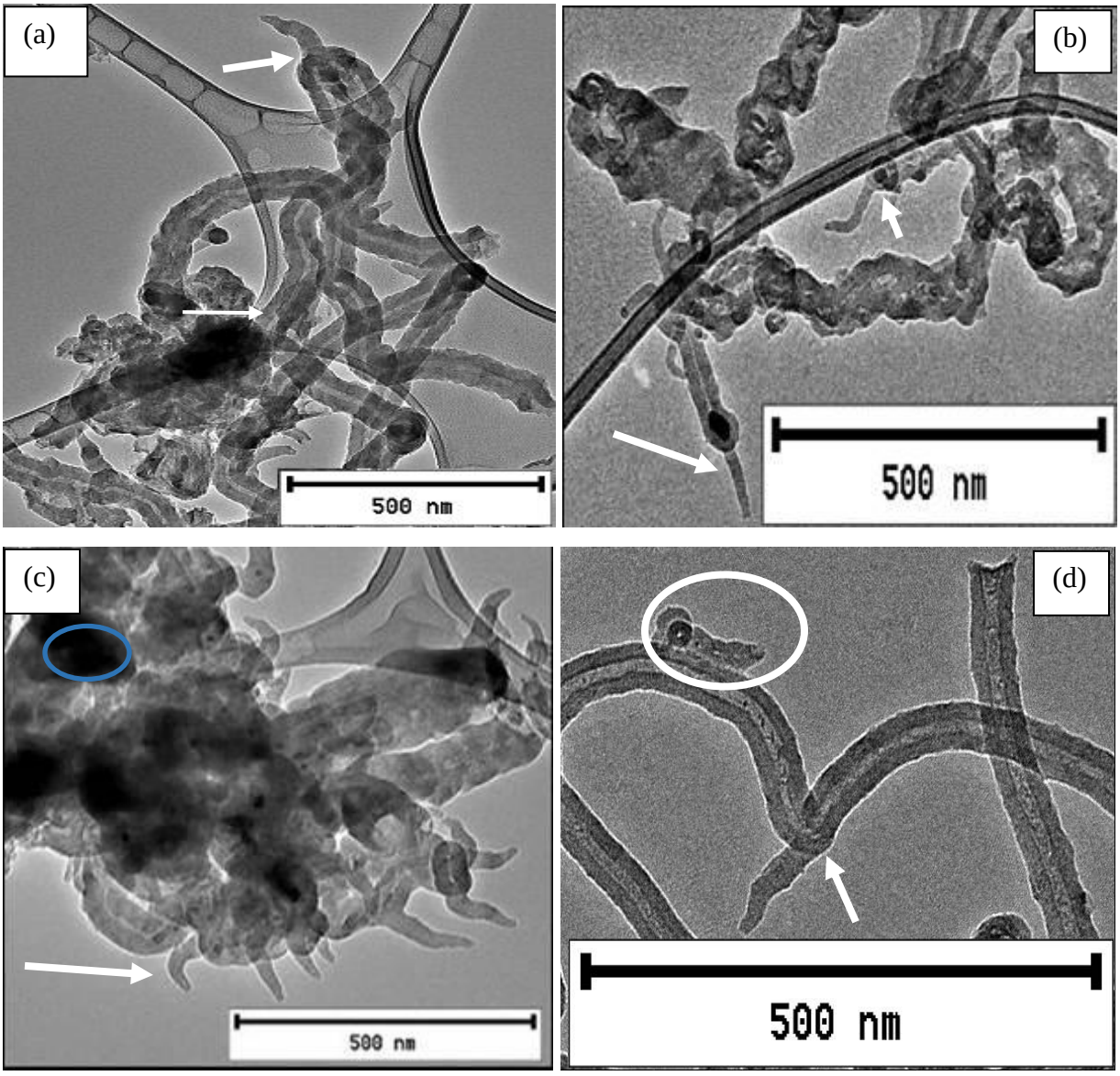

Figure 4.4 TEM images showing other interesting growth sites of the secondary CNFs from the main CNTs, synthesized at 90 min and 700 °C.

Increasing the reaction time to 120 min, resulted in a negligible growth of secondary CNFs and production of a measurable quantity of CNTs with rough surfaces (Figure 4.5). A single secondary CNF was observed growing on the sidewall of the CNT in the TEM image taken (Figure 4.5a, and b, see arrows). The secondary CNF in Figure 4.5c has grown from the tip of the CNT. The length of the secondary CNTs were longer than for those obtained from a 60 and 90 min reactions, about 166.7, 360 and 75 nm for Figure 4.5a, b and c, respectively. Limited growth of secondary CNFs at 120 min reaction time, shows that the secondary growth was time dependent. The negligible quantity of the secondary CNFs at high reaction times, could probably be as a result of lack or limited number of functionalized CNTs with chlorine which only resulted in the formation of metal chlorides. The metal chlorides at the surface of the CNTs were formed when the amount of chlorine that was purged into the system was too high. Metal chlorides blocked the active sites or the defect sites and induced a change in the structure of the CNT surface, hence inhibiting growth of the secondary CNFs.

Formation of amorphous carbon on the surface of the CNTs at longer reaction times was also reported.[25] We can also suggest that lack of secondary CNFs at longer reaction times was due to blockage of the main CNT surface by amorphous carbon. Raman spectra and TGA analysis will assist in making the final conclusion. The average outer diameters of the CNTs obtained using ~ 200 CNT samples were 33, 47 and 82 nm, after 60, 90 and 120 min growth time, respectively.

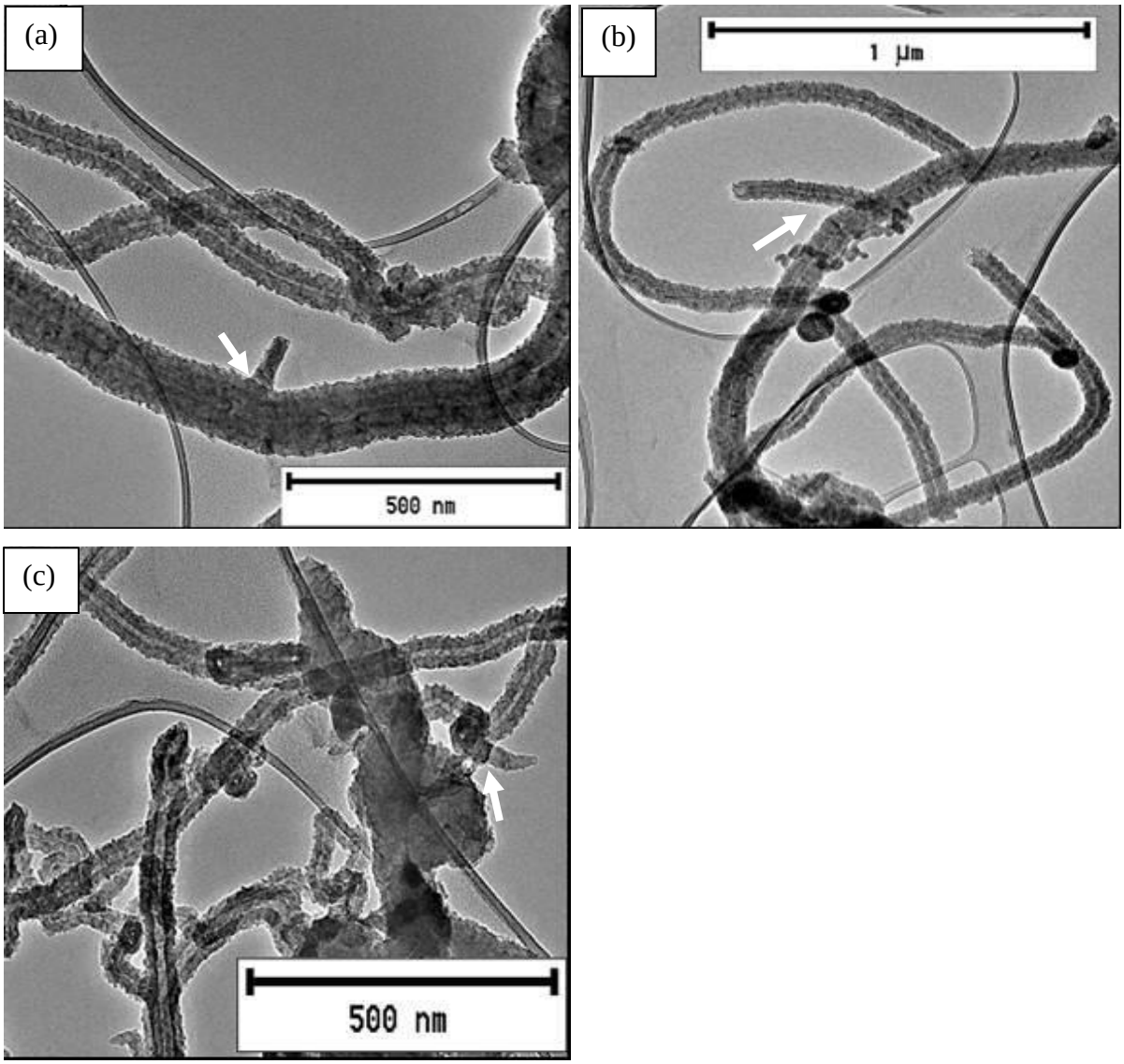

Figure 4.5 TEM images of (a) purified CNTs showing secondary CNFs generated using dichlorobenzene as chlorine source and (b) showing where the secondary growth originates, at following reaction conditions: 120 min, 700 °C, 240 mL/min (N_2), 90 mL/min (C_2H_2).

The effect of the synthesis temperature (600, 650, 700, 750, and 800 °C) on the growth of secondary CNFs on the surface of the primary CNTs was also investigated. TEM images revealed changes in the morphology of the carbon nanostructures with an increase in the synthesis temperature. At lower synthesis temperatures of about 600, 650 and 700 °C, the CNTs appeared hollow inside, and had smooth clean surfaces (Figure 4.6a and b, Figure 4.7a and b and

Figure 4.2). CNTs generated at 750 °C started to have curved rough surfaces, some appeared compartmented and others irregular (Figure 4.7c and d). Thin CNTs with hollow structures were also observed at 750 °C (Figure 4.7c and d). At 800 °C, thinner hollow structured CNTs were produced together with a few large compartmented CNTs with rough surfaces (Figure 4.8a). Carbon nanospheres were also obtained from the CNMs generated at high reaction temperature of 800 °C (Figure 4.8b). Secondary growth was not observed from CNTs generated at reaction temperatures 600, 650, 750 and 800 °C, as shown by their TEM images (Figure 4.6 a–d). At low temperatures < 650 °C, the reaction temperature was not sufficient for creation of defects needed for growth of secondary CNFs, possibly due to limited amount of chlorine atoms functionalized on the CNTs. At temperatures higher than 700 °C the synthesis temperature was too high and led to increased supply of chlorine atoms into the system, which interacted with catalyst metal particles. Interaction of chlorine with catalyst metal particles resulted in formation of metal chlorides which covered the substrate hence inhibiting CNT growth.

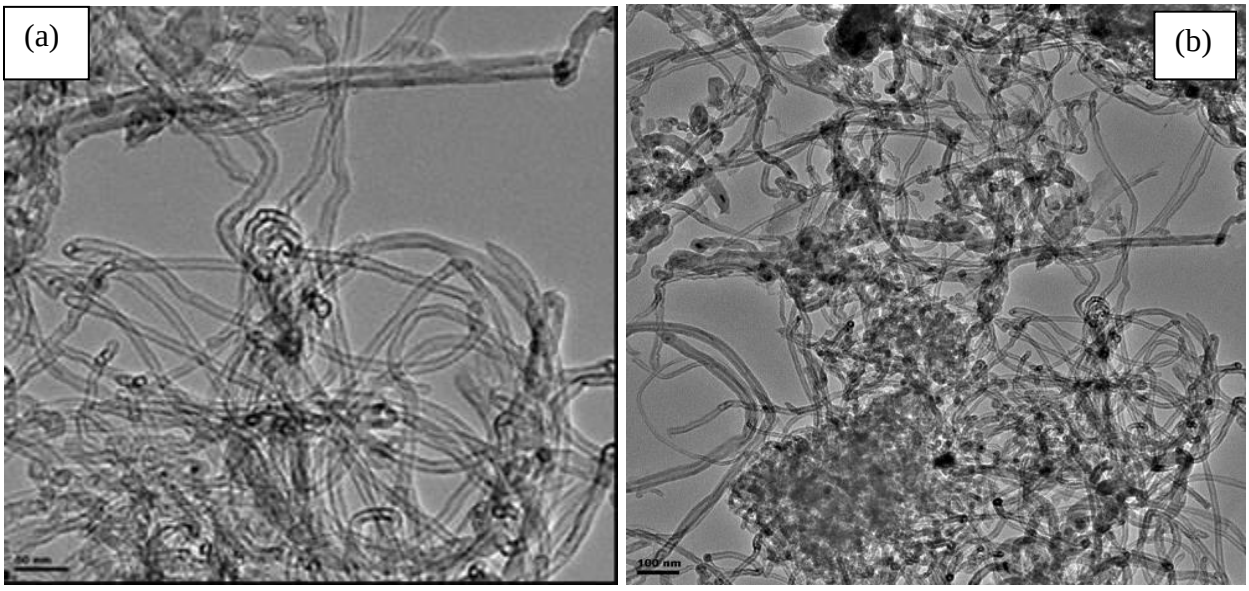

Figure 4.6 TEM images of purified CNTs generated using dichlorobenzene as chlorine source at a reaction time of 90 min and reaction temperature of 600 °C.

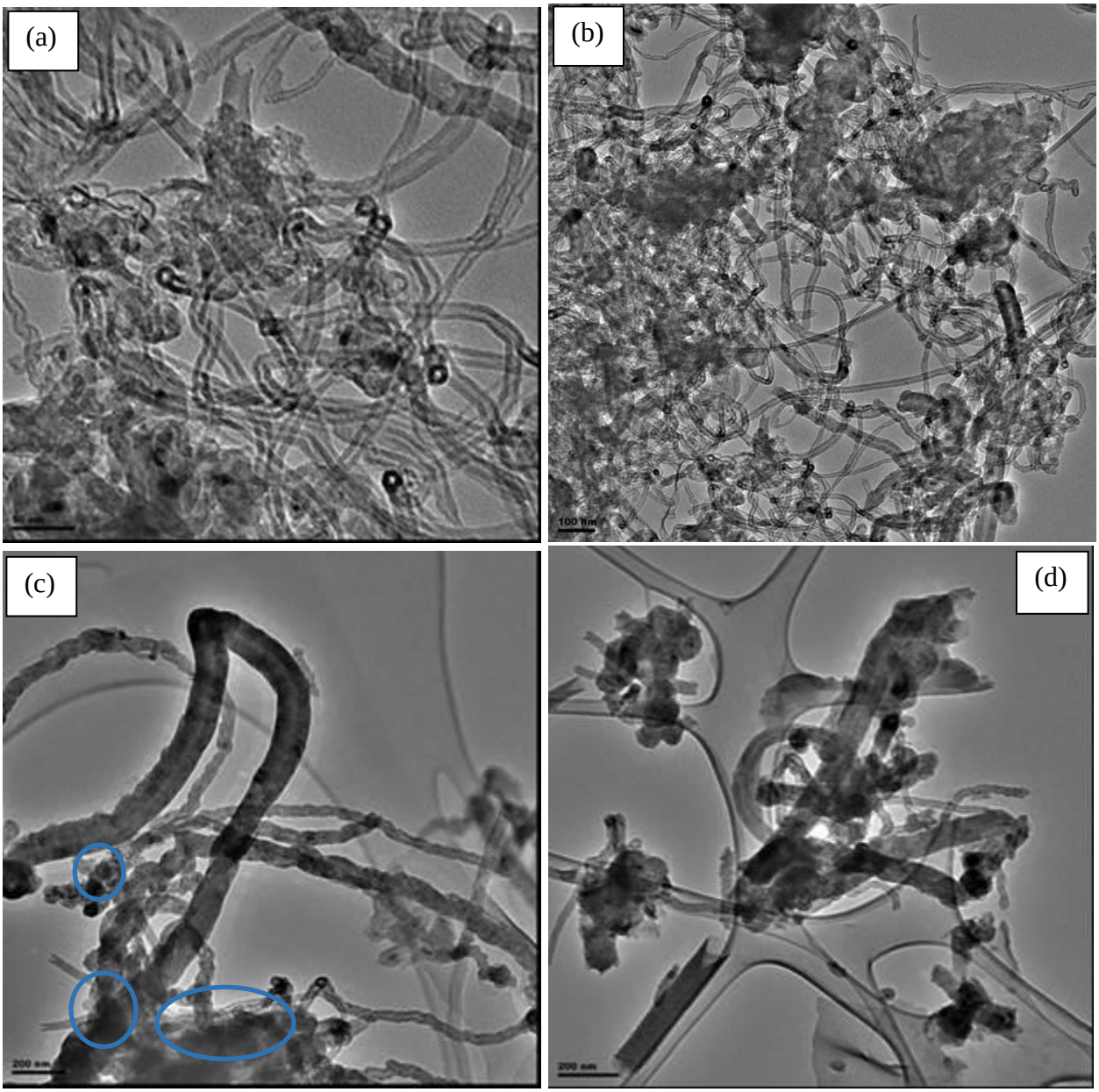

Figure 4.7 TEM images of purified CNTs generated using dichlorobenzene as chlorine source at a reaction time of 90 min and reaction temperature of 650 (a and b) and 750 (c and d) °C.

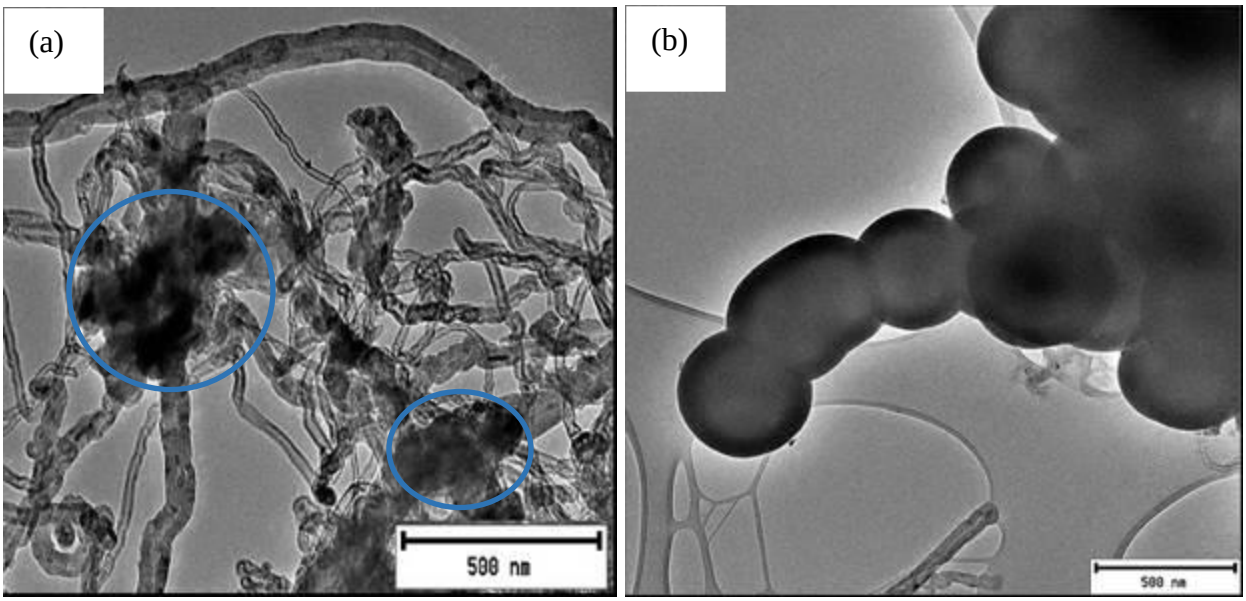

Figure 4.8 TEM images of purified CNTs generated using dichlorobenzene as chlorine source at a reaction time of 90 min and reaction temperature of 800 °C.

SEM images revealed smooth surfaced CNTs with nearly uniform outer diameters at 600 to 700 °C synthesis temperatures (Supplementary Figure S10). At 750 °C the amount of CNTs formed decreased, their length also decreased and they also had variable sizes and appeared open-ended (Supplementary Figure S10d). Clumps were observed from the SEM images where CNTs seemed to be originating and it was suggested that these clumps were metal chloride particles (Supplementary Figure S10). Metal chloride were formed from interaction of chlorine atoms with metal catalyst particles and blocked the surface of the substrate inhibiting carbon growth rates. The average outer diameters were found to increase with an increase in the reaction temperature up to 750 °C as follows, 23, 29, 47, and 72 nm at 600, 650, 700, and 750 °C respectively (Figure 4.9, Supplementary Figure S11 and Table 4.1). At low temperatures the catalyst particles had small sizes which favored growth of smaller diameter CNTs. Increasing the temperature resulted in an increase in an average diameter of the catalyst particles which in turn favored growth of large outer diameter CNTs. Hansen et al. observed an increase in particle size from 5 nm to 10 nm when the temperature was increased from 650 to 750 °C.[26] They explained the phenomena as due to a catalyst sintering process, they observed the particles under the electron beam of a TEM during temperature changes. They observed that particles at low

temperatures were stationary, with little noticeable random motion. With an increase in temperature migration occurred which was due to particles around 10 nm or larger. When these migrating particles encountered other particles on the support, they coalesced and became spheroidal within one image frame.[26] The average outer diameter decreased tremendously to 27 nm when the reaction temperature was increased to 800 °C (Supplementary Figure S11 and Table 4.1). At high temperatures other factors such as catalyst support sintering also takes effect.[26] Studies on various model catalyst supports (single crystals of sapphire, quartz, and yttria-stabilized zirconia) with similar loadings of Pd, which were subjected to long-term aging at 900 °C in N_2 were performed. They found that the final particle size was significantly different for each, with ZrO_2 yielding the smallest average particle size.[26]

The above findings suggest that at low temperatures > 750 °C, the chlorine supply was limited, resulting in exposure of the metal substrate surface to the carbon source favoring carbon growth. At 750 °C, chlorine supply was increased which resulted metal chlorides form at the surface of the substrate inhibiting carbon growth. At 800 °C, great increase in chlorine supply leading to formation of chlorine molecules which serve as a purification agent for the CNTs resulting in formation of clean amorphous free CNTs.

Table 4.1 Effect of temperature on the growth of secondary CNFs onto the primary CNTs

Synthesis temperature /°C	Average outer diameter /nm	Average inner diameter /nm	Mass of unpurified carbon product /g	Amount of secondary CNTs / %	Carbon structure
600	23 ± 75	5 ± 3.2	2.7715	0	CNTs
650	29 ± 67	5 ± 4.0	3.4915	0	CNTs
700	47 ± 39	11 ± 3.5	3.9218	90	CNTs
750	72 ± 43	11 ± 0.7	2.4726	0	CNTs
800	27 ± 77	11 ± 3.0	1.2929	0	CNTs

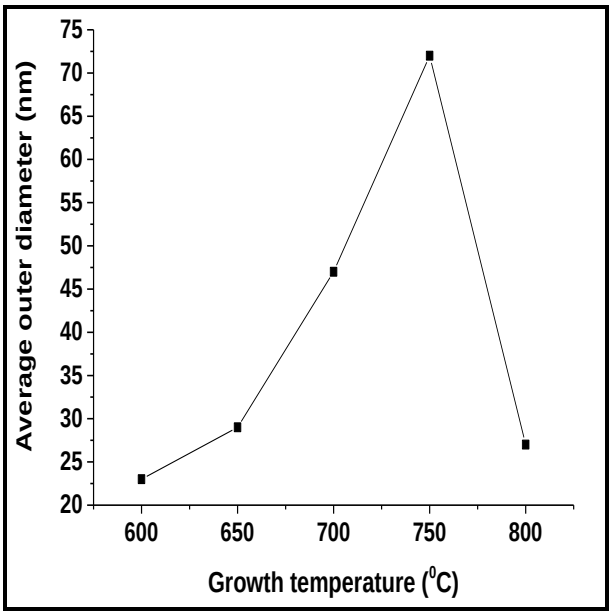

Figure 4.9 Plot of the relationship between the synthesis temperature and the average outer diameter of the CNTs produced at 90 min reaction time.

In another study the catalyst powder was spread over the synthesized CNTs and then resubmitted into the CVD reactor for further synthesis (Figure 4.10). Negligible secondary CNFs were grown using this method as shown by a few circled secondary CNFs in Figure 4.10a to c. Limited growth of the secondary CNFs was due to the weak interaction between the catalyst particles and the main CNTs. Strong interaction is required to produce secondary growth, which can be established either by depositing the catalyst particles onto the surface of the CNTs electrochemically,[20] by sputtering catalyst particles on the primary CNTs[16] or by dipping the primary CNTs into the catalyst solution then drying them in air.[16] It was noted in another study that the size and the number of the catalyst particles that are on the surface of the CNTs played a role on whether secondary growth will occur or not[12]. The metal particles may be too small or too big for nanotube growth. It was found that Ni particles with diameters in the order of 15 nm diffuse into the CNTs instead of nucleating secondary CNTs and the particles were not visible in the SEM after the second CVD step.[12] Ni particles with diameters larger than 30 nm also appeared to suffer from poisoning and did not nucleate secondary CNTs.[12] In our case the

inhibiting factor that contributed to lack of secondary growth was the lack of interaction between catalyst and CNTs.

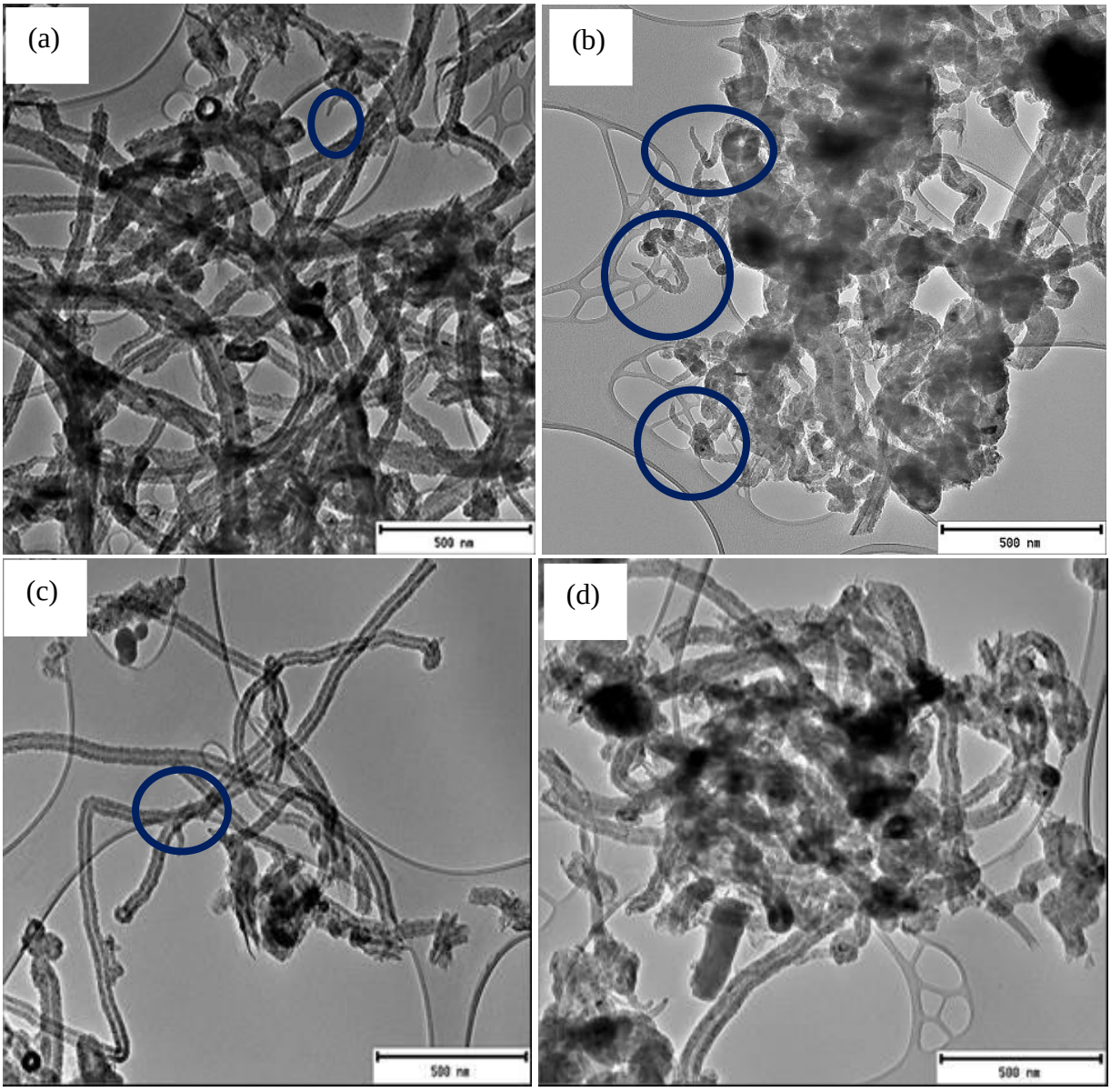

Figure 4.10 TEM image of purified CNTs spread with catalysts particles over their surface and bubbled with dichlorobenzene using the following reaction conditions: 60 min, 700 °C, 240 mL/min (N_2), 90 mL/min (C_2H_2).

Secondary growth of CNFs was also attempted by using the primary un-purified CNTs as substrate for secondary CNF growth. Dichlorobenzene was bubbled through the reactor using N_2 as carrier gas and C_2H_2 as carbon source. Again no visible growth of secondary CNTs was observed from the TEM images (Figure 4.11). The CNTs also appears to have shortened in length which might be due to increased reaction times (Figure 4.11b). Lack of secondary CNFs in this process shows that the growth only occurred in one-step, it required the catalyst as a substrate and also proves that the secondary CNFs grew from defects that were created on the main CNTs by chlorine. CNTs used in this method had no defects since they were prepared in the absence of chlorine and bubbling them with DCB was not enough to create defects.

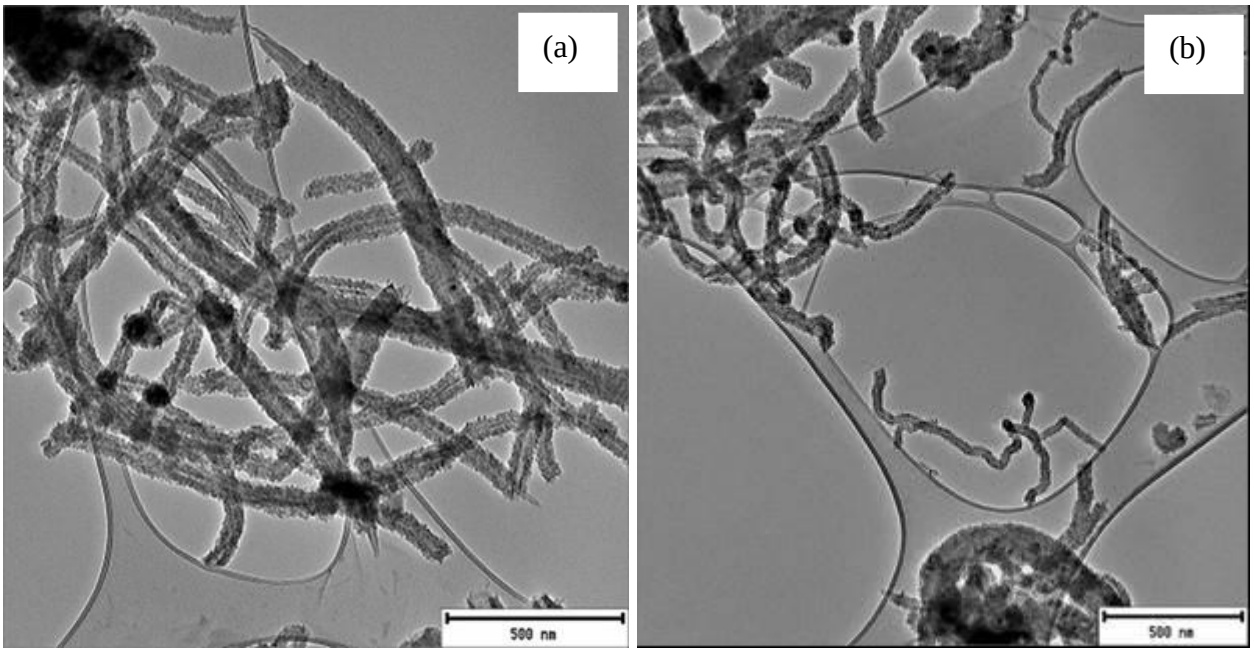

Figure 4.11 TEM image of un-purified CNTs post-doped with chlorine by bubbling dichlorobenzene through the reactor at the following reaction conditions: 60 min, 700 °C, 240 mL/min (N_2), 90 mL/min(C_2H_2).

4.3.2 Thermogravimetric analysis of the chlorinated CNTs: Effect of reaction time and temperature

The TGA and DTGA profiles of the three purified and un-purified CNTs generated at different reaction times are presented in Figure 4.12. Two regions of mass losses were observed from the TGA and DTGA curves generated from un-purified CNTs obtained at lower reaction times of 60 min (Figure 4.12a and b). The first mass loss at ~ 590 °C was assigned to oxidation of chlorine functionalized CNTs, while the mass loss at ~ 700 °C, was assigned to oxidation of other graphitic materials generated namely (carbon platelets or flakes). One mass loss was observed from purified CNTs generated at 60 min reaction time, at ~ 600 °C for oxidation of chlorine functionalized CNTs (Figure 4.12b). Two mass losses at ~ 570 and 660 °C and 600 °C and 630 °C were observed from un-purified and purified CNTs generated at 90 min reaction time (Figure 4.12c and d, and Table 4.2). The two mass losses were due to oxidation of chlorine functionalized CNTs and carbon platelets, respectively. The TGA curves of un-purified and purified samples appeared similar with little difference in the oxidation temperatures.

Only one region of mass loss was observed from TGA and DTGA curves generated at longer reaction time of 120 min (Figure 4.12e and f), which shifted to high temperatures ~ 641 °C as compared to those generated at lower synthesis temperatures. The thermal stability of the purified CNTs decreased in the order 120 < 90 < 60 min, which suggest that an increase in synthesis time result in formation of more thermally stable CNTs.

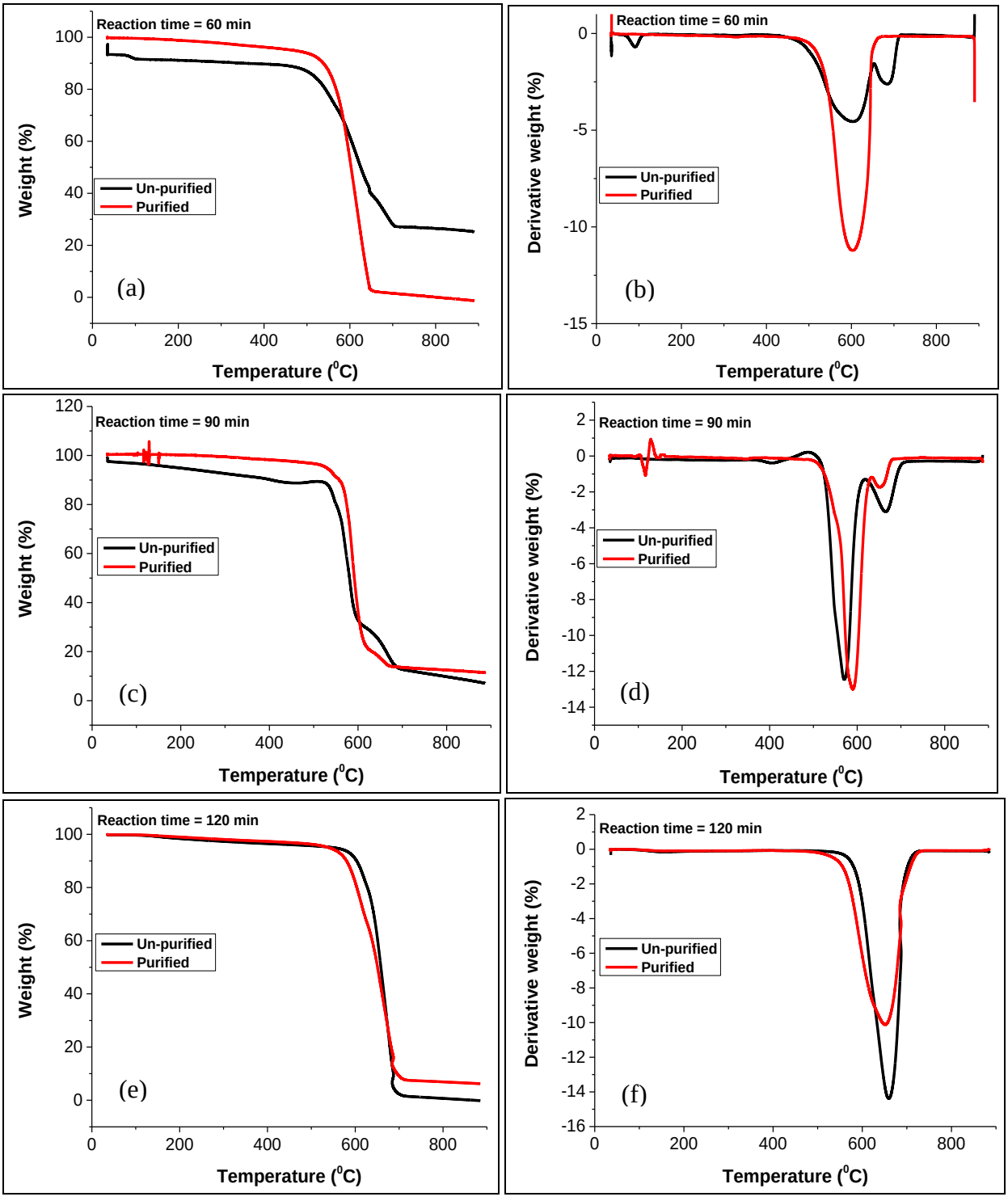

Figure 4.12 TGA and DTGA curves of un-purified and purified CNTs generated from DCB at different reaction times.

Analysis of the residues left after acid treatment revealed that ~ 6 % residues were left for CNTs generated using a 60 min reaction time, while the amount of residues remained the same for CNTs generated at 90 min reaction time (Table 4.2). The residues were completely removed by acid treatment from CNTs generated at 120 min reaction time (Table 4.2). Longer reaction times generated CNTs of high purity (100 %), with no secondary growth. This is due to the fact that CNTs generated at 120 min lack defects sites. The TGA results are in agreement with the TEM analysis where it was suggested that at higher reaction times chlorine (Cl_2) molecules form in the reactor and act as purifying agents leading to formation of cleaner, defect free CNTs. The absence of secondary CNFs from CNTs generated at longer reaction times is not due to the blockage of defects sites by amorphous carbon structures, since the oxidation peak of these structures was not observed from the TGA curve.

Table 4.2 Decomposition temperatures and residual masses (determined by TGA) of the un-purified and purified (P) chlorinated MWCNTs generated by varying the reaction time at a reaction temperature of 700 °C.

Reaction time /min	Decomposition temperature Peak 1 & Peak 2 /°C	Residual mass /%	Carbon (CNT) yield /%
60	590 & 700	29.2	
60(P)	590	6.3	93.7
90	570 & 660	12.2 (see Suppl. Fig.S4)	
90(P)	600 & 630	12.2	87.8
120	641	6.6	
120(P)	651	0	100

TGA profiles of the purified CNTs generated at various reaction temperatures at the reaction time of 90 min are also presented in Figure 4.13. Two weight losses were observed from the DTGA curves, for all studied carbon nanostructures, where the weight loss at lower temperatures corresponds to oxidation of CNTs and the second one at higher temperatures was due to oxidation of carbon platelets (Figure 4.13b). Decomposition of CNTs occurred at 630, 584, 600,

625, and 640 °C for CNTs generated at 600, 650, 700, 750 and 800 °C synthesis temperatures, respectively (Figure 4.13b and Table 4.3). Carbon yield decreased with an increase in the synthesis temperature up to 750 °C (Figure 4.14b and Table 4.3). There was another increase in carbon purity (as measured by TGA) at 800 °C (Figure 4.14b). This data is consistent with the structural analysis where thin, clean, hollow and smooth CNTs were produced at low temperatures (600 to 700 °C). At 750 °C the CNTs were rough, compartmented and had larger diameters, whilst at 800 °C a mixture of large compartmented and thin hollow CNTs were produced with the thin CNTs dominating. High temperature reactions were found to favor formation of single wall carbon nanotubes (SWCNTs).[27] As the average outer diameter of the CNTs increased the level of purity of the CNTs decreased, suggesting that large diameter CNTs encapsulated more metal particles. This is in agreement with the amount of residue obtained after acid treatment.

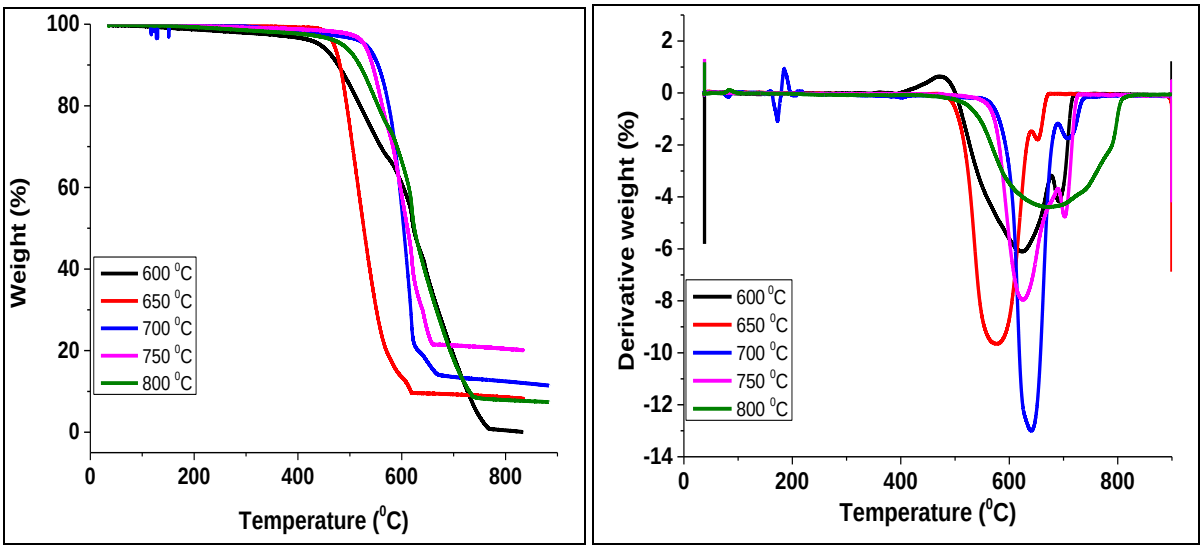

Figure 4.13 TGA and DTGA curves of purified CNTs generated from DCB at different reaction temperatures and a reaction time of 90 min.

The residual mass left after acid treatment of the CNTs increased with an increase in synthesis temperature as follows: 0, 8.3, 12.0 and 20.1 % for 600, 650, 700 and 750 °C, respectively (Table 4.3 and Figure 4.14a) but decreased as the synthesis temperature was increased to 800 °C

(~7.4 % residues). There is no correlation between the amount of catalyst residues and the inner diameter of the CNTs as various temperatures.

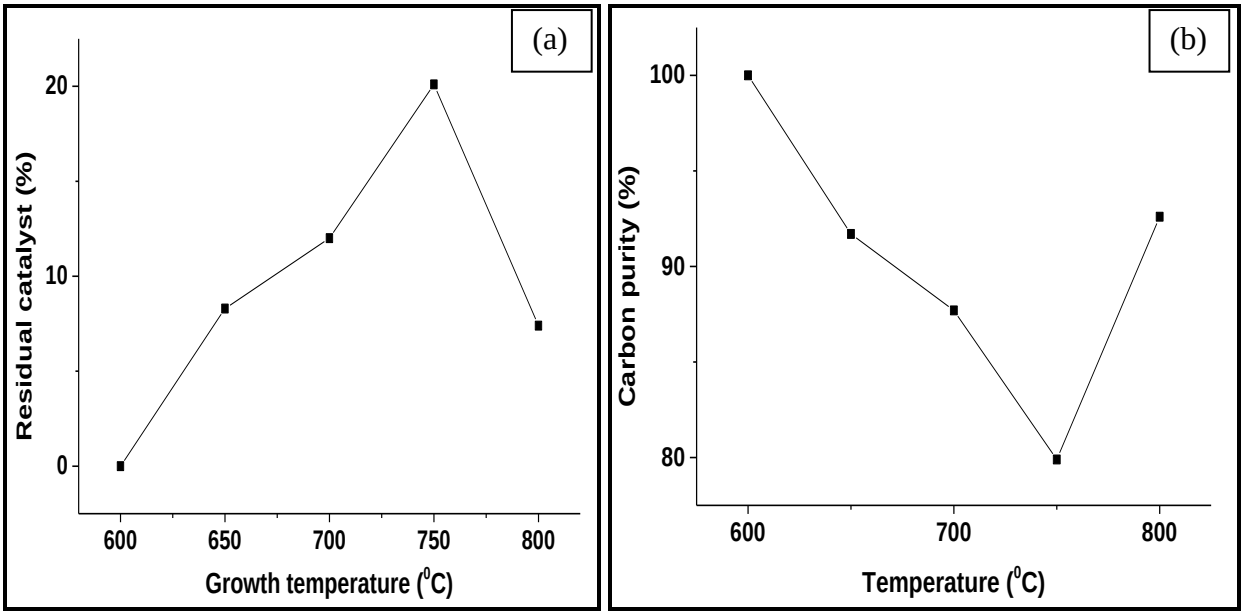

Figure 4.14 (a) Plot of the effect of the synthesis temperature on the amount of residual catalyst that was left after purification and (b) plot of the effect of the synthesis temperature on carbon purity, generated from DCB at 90 min and 700 °C.

Table 4.3 Decomposition temperatures and residual masses (determined by TGA) of purified (P) chlorine functionalized CNTs generated by varying the reaction temperature at a reaction time of 90 min.

Reaction temperature /°C	Decomposition temperature /°C	Residual mass /%	Carbon (CNT) yield /%
600(P)	630 & 700	0	100
650(P)	584 & 652	8.3	91.7
700(P)	600 & 630	12.2	87.7
750(P)	625 & 703	20.1	79.9
800(P)	640	7.4	92.6

4.3.3 Powder XRD analysis of the chlorinated CNTs: Effect of reaction temperature

XRD patterns of purified chlorine functionalized CNTs generated at various reaction temperatures and at a reaction time of 90 min, are presented in Figure 4.15. All XRD curves showed a strong intensity peak at 2θ ~ 26 ° (Figure 4.15a), which was assigned to the $C_{(002)}$ reflection of graphite associated with the interlayer spacing of graphene.[28] A decrease in the FWHM value and intensity of the C_{002} peak with increase in temperature was observed and was due to an increase in outer diameter of the CNTs (Table 4.4). The intensity and width of the C_{002} reflection of graphene can be associated with various microstructural parameters of N-CNTs, namely: the number of graphene layers, variations in the interlayer spacing, lattice distortions, tube outer diameter and crystallinity of the graphene layers.[29] This data is consistent with the TEM observations, where the outer diameters of the CNTs increased with an increase in synthesis temperature from 600 to 750 °C (Table 4.1). The FWHM and the intensity of the C_{002} peak increased when the temperature was increased to 800 °C (Table 4.4), which is consistent with TEM data where a decrease in outer diameter of the CNTs was observed (Table 4.1).

The peak appearing at 2θ ~ 45 ° which has a shoulder peak can be attributed to the C_{100} (shoulder) and C_{101} (main peak at 45 °) plane of CNTs and to some traces of iron carbide (Fe_3C) or iron metallic catalyst.[28] Three additional peaks were observed at 2θ ~ 32, 37 and 54 ° from the diffractogram of CNTs obtained from 650, 700 and 750 °C synthesis temperatures and were assigned to Fe_3C reflection. These peaks increased with an increase in synthesis temperature and were absent from diffractogram of CNT generated from 600 and 800 °C synthesis temperatures. The presence of an Fe_3C peak could imply that Fe_3C was the predominant catalytic phase during CNT growth.[30] An increase in the Fe_3C peak intensity with increase in reaction temperature can be due to increased amount of chlorine in the CVD reactor which interact with iron from the catalyst forming iron carbide. These data correlates with the TGA data, where the amount of residual metal present increased with an increase in the synthesis temperature from 650 to 750 °C (Table 4.3). The data also correlates with the TEM images, where poisoning was observed at high temperatures which resulted in reduced CNT growth up to 750 °C. For CNTs generated at 600 and 800 °C synthesis temperature, only one peak due to Fe_3C peak was observed at 2θ ~ 54 °. This peak was very small for CNTs generated from 600 °C, but increased in intensity for CNTs generated at 800 °C (Figure 4.15). This data also agrees with TGA data where a residual

mass of 0 and 7.4 % was obtained for CNTs generated at 600 and 800 °C synthesis temperature, respectively (Table 4.3).

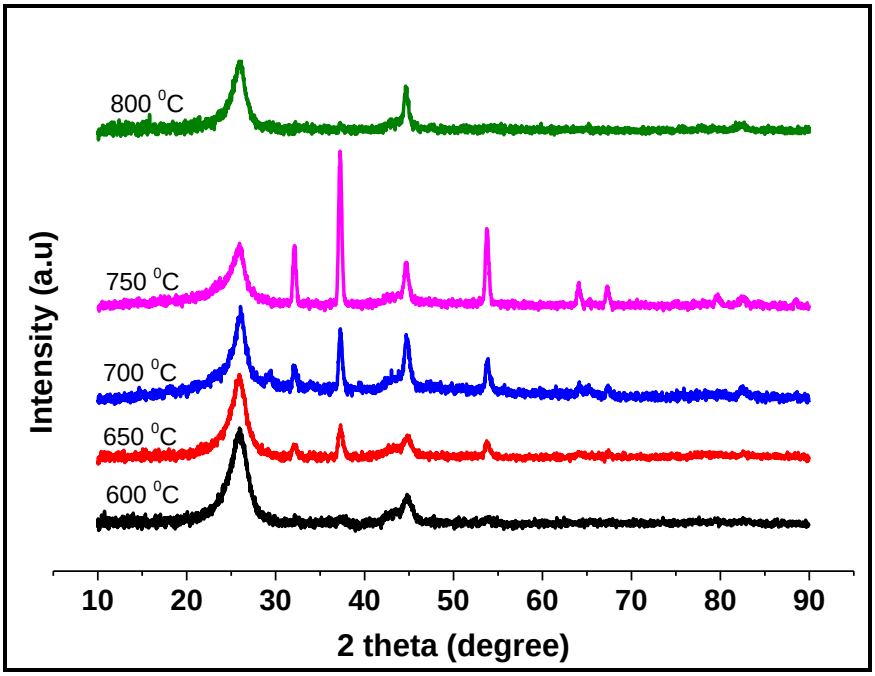

Figure 4.15 p-XRD curves of purified CNTs generated from DCB at a reaction time of 90 min and at different reaction temperatures.

Table 4.4 Powder X-ray structural parameters of chlorine functionalized CNTs generated at various reaction temperatures for 90 min.

Reaction temperature /°C	Position of $C_{(002)}$ peak	FWHM of $C_{(002)}$ peak / °	Intensity of $C_{(002)}$ peak	Intensity of Fe_3C peak at 32 °	Intensity of Fe_3C peak at 37 °
600	25.8	2.8	862.0	–	–
650	25.7	2.6	731.0	114.4	292.5
700	25.9	2.3	672.7	233.6	599.0
750	26.0	1.8	540.2	565.1	1338.8
800	25.8	2.2	620.0	–	–

4.3.4 Raman spectroscopy analysis of the chlorinated CNTs: Effect of synthesis time and temperature

The Raman spectra of the un-purified and purified chlorinated CNTs synthesized for 60 min is a characteristic of a disordered graphitic lattice, as it exhibits a broad highly intense D-band at ~ 1334 and 1330 cm^{-1} for un-purified and purified CNTs respectively, corresponding to a disordered graphite (Figure 4.16 and Table 4.5). Additional first-order bands were also observed a D2 and a G-band. The most intensive of them is a G-band appearing at 1595 and 1581 cm^{-1}, which corresponds to an ideal graphitic lattice. A D2 band at 1528 and 1496 cm^{-1} originates due to the presence of amorphous carbon structures on interstitial sites in the distorted carbon lattice of the CNTs.[31]

Table 4.5 Raman bands of the un-purified and purified chlorinated CNTs generated from pure DCB at 700 °C for 60 min

	Band name	**Band Position (cm^{-1})**	**Bond type**	**FWHM (cm^{-1})**	**Peak Area**	**Designation**
60 min un-purified	D	1334	sp^2	192	2868	Disordered graphite
	D2	1528	sp^3	79	433	Amorphous carbon structure
	G	1595	sp^2	63	1260	Graphitic like carbonyl group
60 min purified	D	1330	sp^2	166	8905	Disordered graphite
	D2	1496	sp^3	69	1091	Amorphous carbon structure
	G	1581	sp^2	73	4545	Graphitic like carbonyl group
	$2D_1$	2680		81	603	1^{st} overtone of D1 band
	$2D_2$ & D+G	2848		828	4802	1^{st} overtone of D1 and overtone of 2D

Second order bands were also observed from the Raman spectra of purified CNTs, a weak 2D band which assigned to the first overtone of D1 band occurring at 1290 cm^{-1}. A 2D band was

deconvoluted into $2D_1$ at 2680 cm^{-1} and a broad $2D_2$ at 2848 cm^{-1} which shifted upwards due to combination with a G + D band and shows increased disorders. The split of the 2D band has been described as a characteristic feature of undisturbed or highly ordered graphitic lattices.[32] A G + D band overlapping with the $2D_2$ band was assigned to characteristic for disturbed graphitic structures.[32]

A I_D/I_G peak ratio is used to characterize the degree of disorder in the disordered graphite, where large values are obtained from highly disordered materials. I_D/I_G values of 2.30 and 1.95 were obtained for un-purified and purified CNTs respectively, suggesting that both materials were highly disordered (Table 4.5). Large FWHM values also suggest that the materials contain some amorphous carbon structures (Figure 4.5).

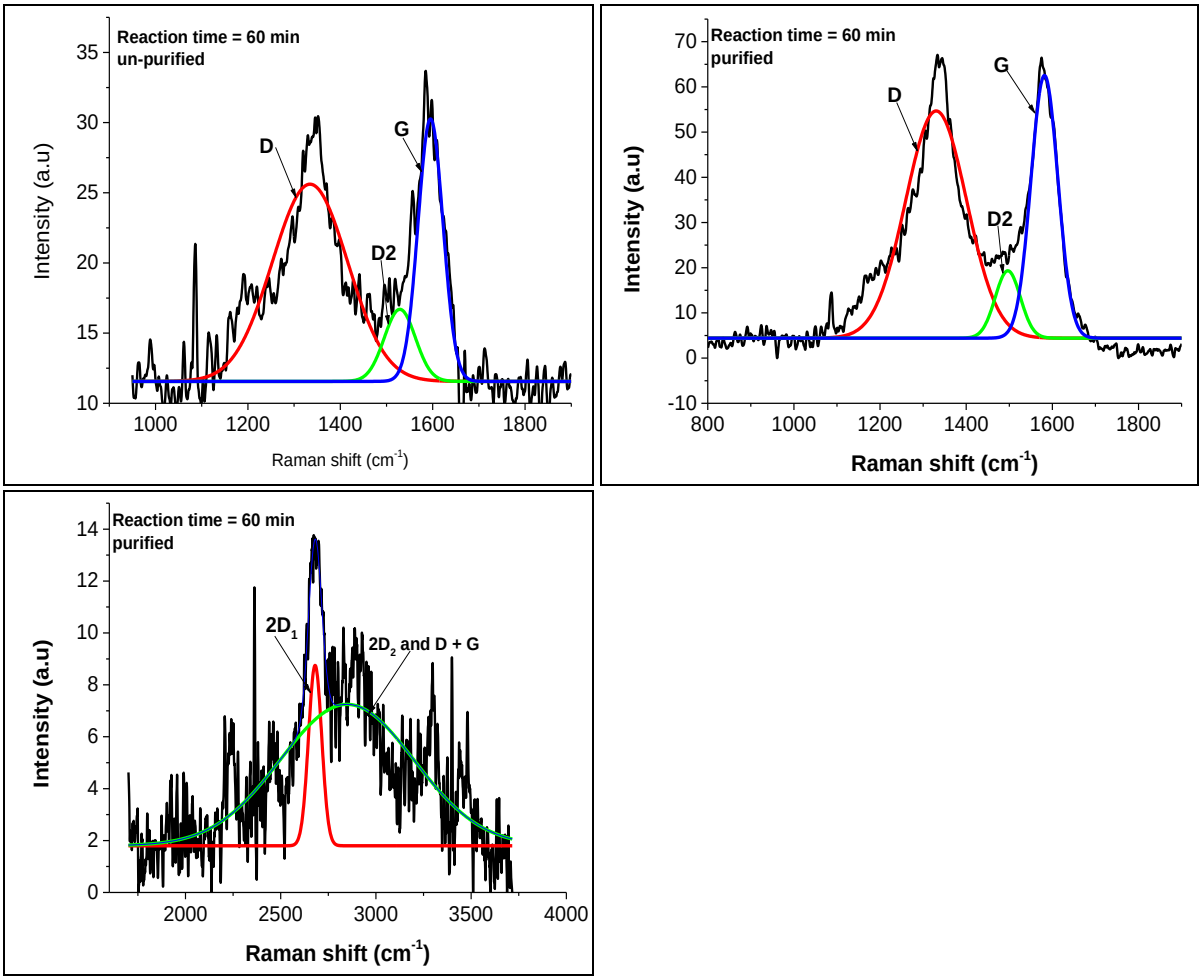

Figure 4.16 Raman spectra of un-purified and purified chlorinated CNTs synthesized at 700 °C for 60 min

Increasing the synthesis time to 90 min also resulted in formation of defected CNTs shown by the presence of a broad highly intense D-band at ~ 1336 cm^{-1} for un-purified samples (Figure 4.17 and Table 4.6). Additional first-order bands were also observed a G-band which deconvoluted into two bands a G and D' band. A D' band at ~ 1619 cm^{-1} accounts for structural disorders in the graphitic plane and is normally observed as a shoulder peak of the G band.[31] Second order bands were also observed from the Raman spectra of un-purified CNTs, a single 2D band at 2678 cm^{-1}, a G* band at 2444 cm^{-1} and a G + D band at 2923 cm^{-1} (Figure 4.17 and Table 4.6). A single 2D band is characteristic of disordered graphite. A G* band is the first overtone of a Raman-inactive graphitic lattice vibration (D4 band) occurring at 1220 cm^{-1}.[33] Raman spectra of purified CNTs exhibited additional bands, a D4 band at ~ 1226 cm^{-1} which appears a shoulder of a D-band was assigned to C=C stretching vibrations of a graphitic lattice.[31] Other authors attributed the presence of a D4 peak to existence of finite size of crystalline and defect induced carbon.[34] A D2 amorphous carbon band was also observed. Splitting of the 2D band occurred for purified materials, suggesting that the materials were more ordered. I_D/I_G values of 0.8 and 1.6 were obtained for un-purified and purified CNTs respectively, suggesting that more defects were created by acid treatment due to creation of more sp^3 bonding environments by addition of oxygen functional groups (Table 4.5). Increased FWHM values 74 and 116 cm^{-1} for D band generated from un-purified and purified CNTs, suggesting increased defects which favors formation of amorphous carbon structures. The ratio of $I_D/I_{D'}$ is used to provide information about the type of defects present in the material. If the ratio of $I_D/I_{D'}$ is 13, it indicates the presence of related sp^3 related defects, 10.5 corresponds to hoping defects, 7 for vacancy-like defects, 3.5 for boundary-like defects and 1.3 for on-site defects in graphene.[35,36] The large $I_D/I_{D'}$ value of 7.8 suggest that the type of defects is vacancy-like defects in addition to small hoping defects. Vacancy-like defects represent the single and double vacancy in the graphitic lattice (a property of a removed atom) and hoping defects represents any defects that distort the bonds between carbon atoms, retaining the general sp^2 configuration.[35,37] The creation of this defects resulted in formation of secondary carbon nanostructures. The results agree with the TEM observations.

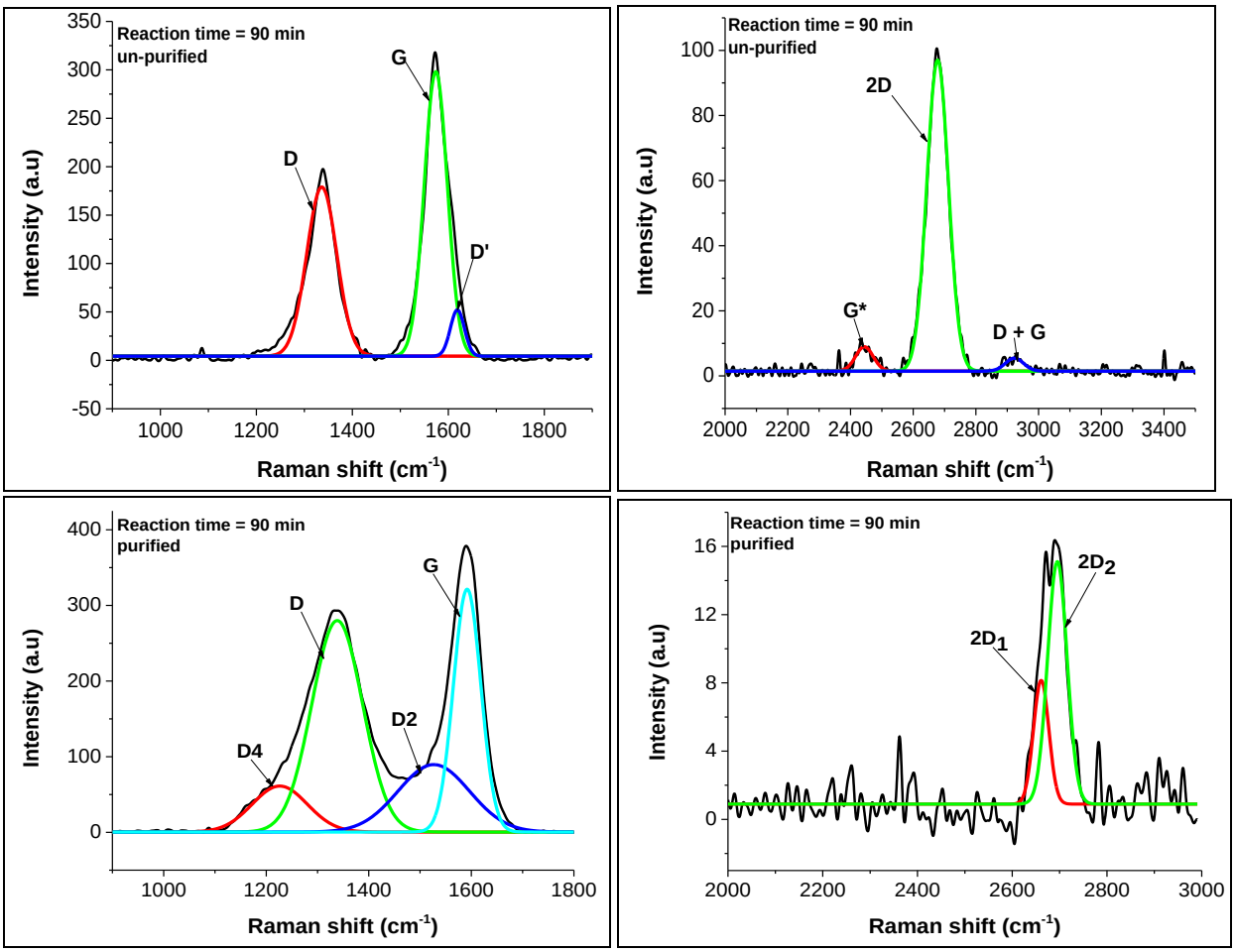

Figure 4.17 Raman spectra of un-purified and purified chlorinated CNTs synthesized at 700 °C for 90 min

Table 4.6 Raman bands of the un-purified and purified chlorinated CNTs generated from pure DCB at 700 °C for 90 min

	Band name	**Band Position (cm^{-1})**	**Bond type**	**FWHM (cm^{-1})**	**Peak Area**	**Designation**
90 min un-purified	D	1336	sp^2	74	13704	Disordered graphite
	G	1574	sp^2	57	17659	Graphitic like carbonyl group
	D’	1619	sp^2	34	1748	Defects in graphitic plane
	G^*	2444		66	526	1^{st} overtone of D4 band
	2D	2678		81	8264	1^{st} overtone of D1 band
	D + G	2923		68	290	2D overtone
90 min purified	D4	1226	$sp^2 – sp^3$	126	8120	
	D	1338	sp^2	116	34667	Disordered graphite
	D2	1526	sp^3	164	15588	Amorphous carbon structure
	G	1592	sp^2	63	21527	Graphitic like carbonyl group
	$2D_1$	2661		38	294	1^{st} overtone of D1 band
	$2D_2$	2695		48	731	1^{st} overtone of D1 band

Increasing the reaction time to 120 min resulted in increased defects in the carbon structure. A D4, D, D2 and G bands were observed from the Raman spectra of both un-purified and purified samples (Figure 4.18). For un-purified samples a weak 2D band was deconvoluted into two bands, suggesting that the materials were more ordered, but the weakness of the band suggest disordered materials. A D + G band which is a characteristic of disturbed graphitic structures was also observed from the Raman spectra of un-purified CNTs. Raman spectra of the purified samples were similar to those of the un-purified samples. The only difference was the absence of the 2D peak from the Raman spectra of the purified samples, indicating increased disorders in materials after purification. I_D/I_G values of 1.7 and 1.8, suggesting highly disordered materials (Table 4.7). The disorders increased in the order 90, 120 and 60 min. There is no correlation

between the creation of defects on the CNT surface with the formation of secondary structures or the synthesis time.

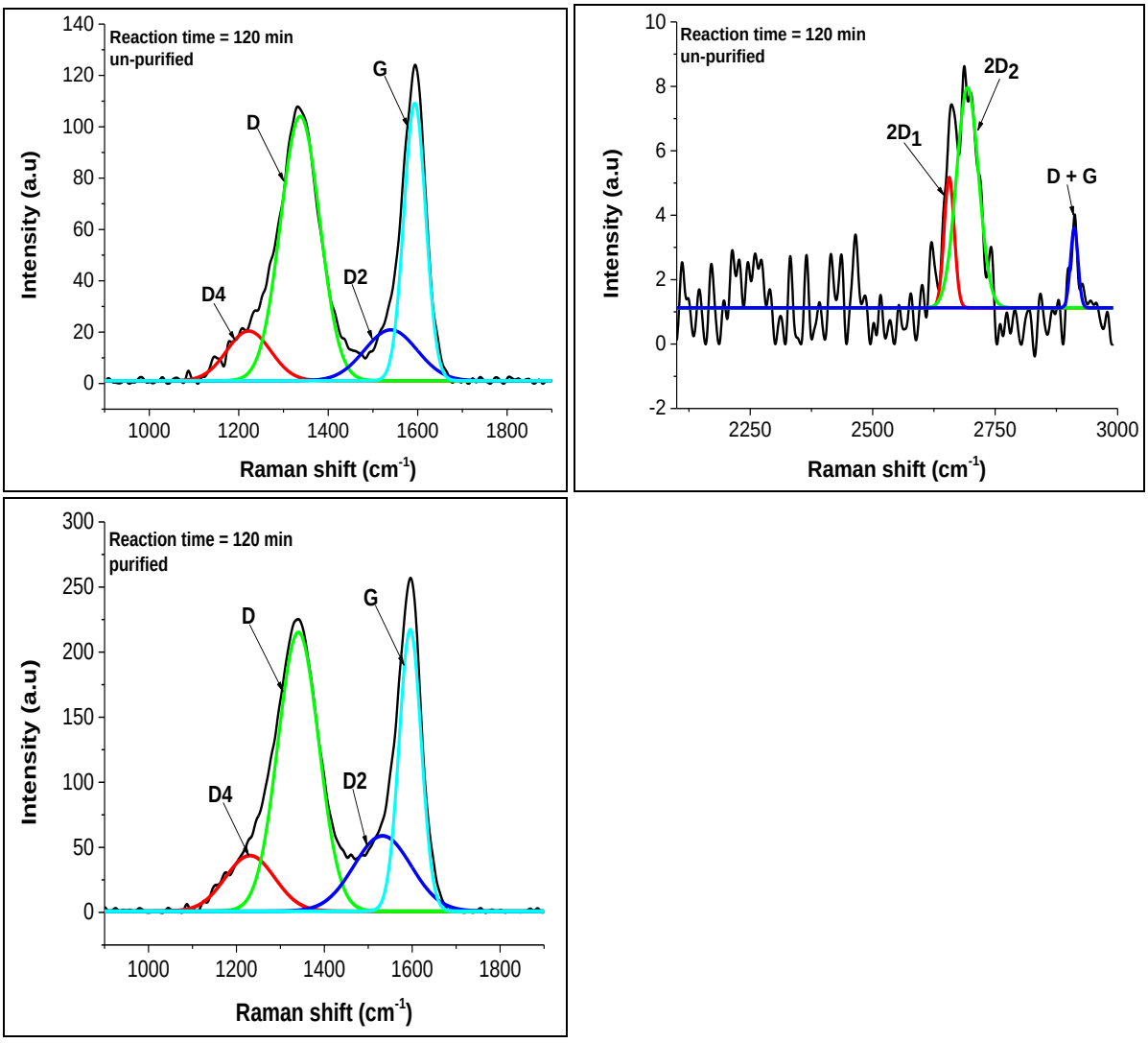

Figure 4.18 Raman spectra of un-purified and purified chlorinated CNTs synthesized at 700 °C for 120 min

Table 4.7 Raman bands of the un-purified and purified chlorinated CNTs generated from pure DCB at 700 °C for 60 min

	Band name	**Band Position (cm^{-1})**	**Bond type**	**FWHM (cm^{-1})**	**Peak Area**	**Designation**
120 min un-purified	D4	1222	sp^2 - sp^3	115	2376	C=C stretching vibrations
	D	1337	sp^2	103	11283	Disordered graphite
	D2	1540	sp^3	138	2910	Amorphous carbon structure
	G	1593	sp^2	57	6572	Graphitic like carbonyl group
	$2D_1$	2656		24	103	1^{st} overtone of D1 band
	$2D_2$	2693		53	386	1^{st} overtone of D1 band
	D + G	2911		18	47	2D overtone
120 min purified	D4	1231	sp^2 - sp^3	132	5999	
	D	1341	sp^2	109	24901	Disordered graphite
	D2	1532	sp^3	153	9427	Amorphous carbon structure
	G	1595	sp^2	59	13576	Graphitic like carbonyl group

The effect of temperature on the graphitic nature of the CNTs synthesized at a reaction time of 90 min, was also investigated using Raman spectroscopy. Raman spectra of the un-purified CNTs generated at a reaction temperature of 600 °C, revealed the presence of first order bands a D-, D2- and G-band at 1335, 1535 and 1588 cm^{-1} respectively, suggesting that the CNTs were disordered and contained amorphous carbon materials (Figure 4.19 and Table 4.8). Second order bands were also observed, a G^*, 2D and G + D bands at 2439, 2677 and 2921 cm^{-1}, suggesting defected graphitic structures. Raman spectra of purified CNTs showed removal of an amorphous D2 band by acid treatment and generation of a D' band at 1616 cm^{-1}, which is observed as a shoulder peak of the G band, due to generation of defects in the graphitic plane. Oxygenation and related changes in the interplanar process was found to results in an appearance of a D' band.[38] A

2D band was split into two bands after purification a $2D_1$ at 2656 cm^{-1} and a $2D_2$ at 2689 cm^{-1}, suggesting that acid purification decreased the amount of defects in the CNTs. I_D/I_G values of 1.5 and 1.1 were obtained for both un-purified and purified CNTs, suggesting that CNTs were disordered (Table 4.8). The large $I_D/I_{D'}$ value of 34 corresponds to the presence of sp^3 related defects, which arise due to covalent sp^3 bonded functional groups on the carbon atoms.[39]

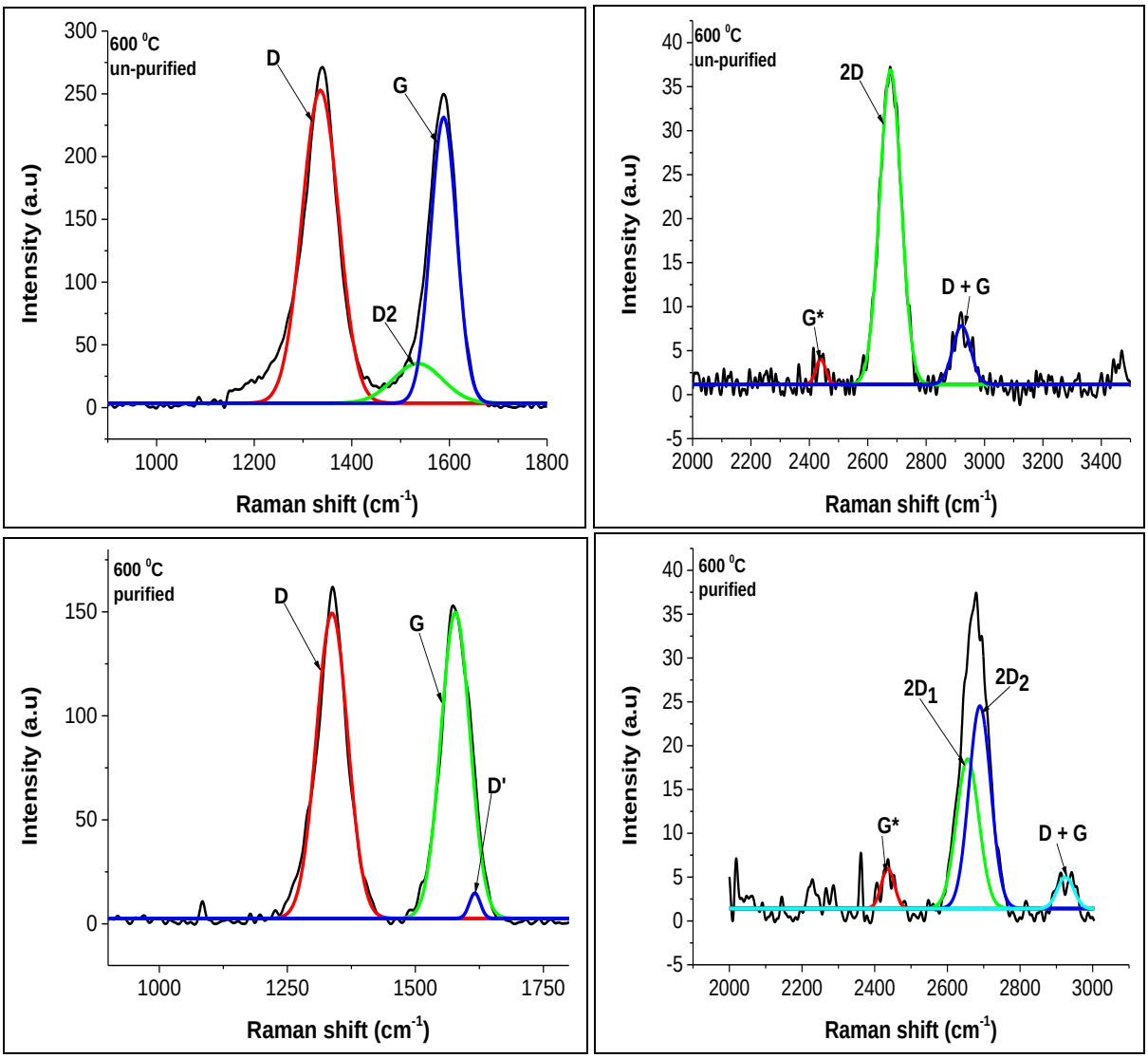

Figure 4.19 Raman spectra of un-purified and purified chlorinated CNTs synthesized at 600 °C for 90 min

Table 4.8 Raman bands of the un-purified and purified chlorinated CNTs generated from pure DCB at 600 °C for 90 min

	Band name	**Band Position (cm^{-1})**	**Bond type**	**FWHM (cm^{-1})**	**Peak Area**	**Designation**
600 °C un-purified	D	1335	sp^2	88	23368	Disordered graphite
	D2	1535	sp^3	119	4007	Amorphous carbon structure
	G	1588	sp^2	62	15122	Graphitic like carbonyl group
	G^*	2438		39	119	1^{st} overtone of D4 band
	$2D_1$	2677		86	3262	1^{st} overtone of D1 band
	D + G	2921		72	514	2D overtone
600 °C purified	D	1337	sp^2	72	11198	Disordered graphite
	G	1578	sp^2	66	10432	Graphitic like carbonyl group
	D’	1616	sp^2	25	328	Defects in graphitic plane
	G^*	2436		42	205	1^{st} overtone of D4 band
	$2D_1$	2656		73	1318	1^{st} overtone of D1 band
	$2D_2$	2689		70	1733	1^{st} overtone of D1 band
	D + G	2925		53	203	2D overtone

Raman spectra of the un-purified CNTs generated at a reaction temperature of 650 °C, revealed the presence of first order bands a D-, D2- and G-band at 1335, 1535 and 1588 cm^{-1} respectively, suggesting that the CNTs were disordered and contained amorphous carbon materials (Figure 4.20 and Table 4.9). Second order bands were also observed, a G^*, 2D and G + D bands at 2445, 2676 and 2913 cm^{-1}, suggesting defected graphitic structures. Raman spectra of purified CNTs showed removal of an amorphous D2 band by acid treatment. A 2D band was split into two bands after purification a $2D_1$ at 2656 cm^{-1} and a $2D_2$ at 2689 cm^{-1}, suggesting that acid purification decreased the amount of defects in the CNTs. I_D/I_G values of 1.3 were obtained for both un-purified and purified CNTs, suggesting that the CNTs were disordered (Table 4.9).

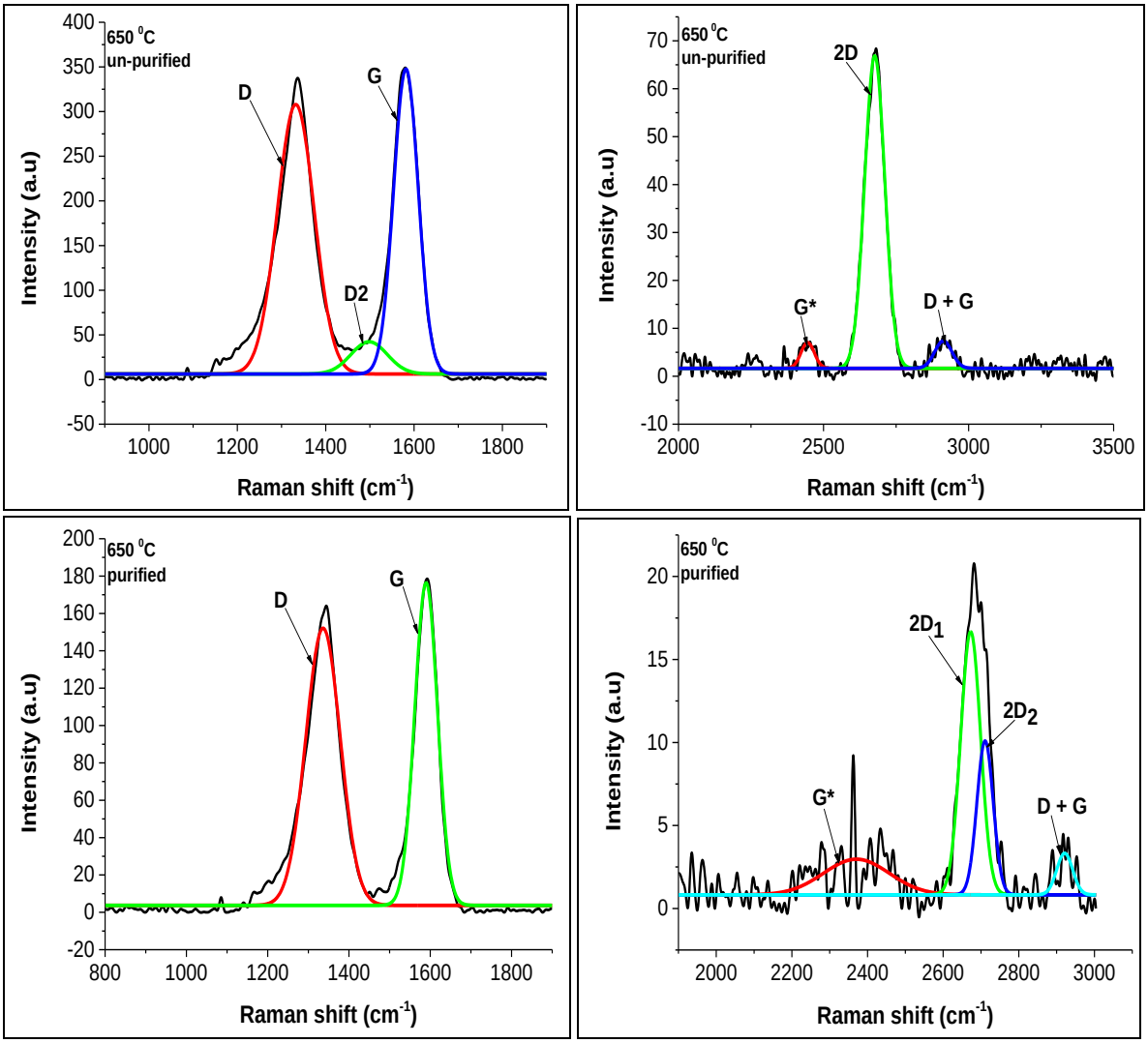

Figure 4.20 Raman spectra of un-purified and purified chlorinated CNTs synthesized at 650 °C for 90 min

Table 4.9 Raman bands of the un-purified and purified chlorinated CNTs generated from pure DCB at 650 °C for 90 min

	Band name	**Band Position (cm^{-1})**	**Bond type**	**FWHM (cm^{-1})**	**Peak Area**	**Designation**
650 °C un-purified	D	1332	sp^2	99	31703	Disordered graphite
	D2	1498	sp^3	97	3716	Amorphous carbon structure
	G	1581	sp^2	65	23845	Graphitic like carbonyl group
	G^*	2445		54	310	1^{st} overtone of D4 band
	$2D_1$	2676		81	5647	1^{st} overtone of D1 band
	D + G	2913		70	424	2D overtone
650 °C purified	D	1336	sp^2	100	15810	Disordered graphite
	G	1590	sp^2	66	12097	Graphitic like carbonyl group
	G^*	2370		205	468	1^{st} overtone of D4 band
	$2D_1$	2672		62	1044	1^{st} overtone of D1 band
	$2D_2$	2711		50	499	1^{st} overtone of D1 band
	D + G	2921		49	132	2D overtone

A D4, D, D2 and G bands were observed from the Raman spectra of both un-purified and purified samples generated at 750 °C (Figure 4.21). Second order Raman bands G*, and 2D were also observed from the spectra of the un-purified and purified CNTs. A D + G band which is a characteristic of disturbed graphitic structures appeared from the Raman spectra of purified CNTs, which suggest increased defects after purification. I_D/I_G values of 1.2 (un-purified CNTs) and 1.5 (purified CNTs), also suggest increased defects in the CNTs after purification (Table 4.10).

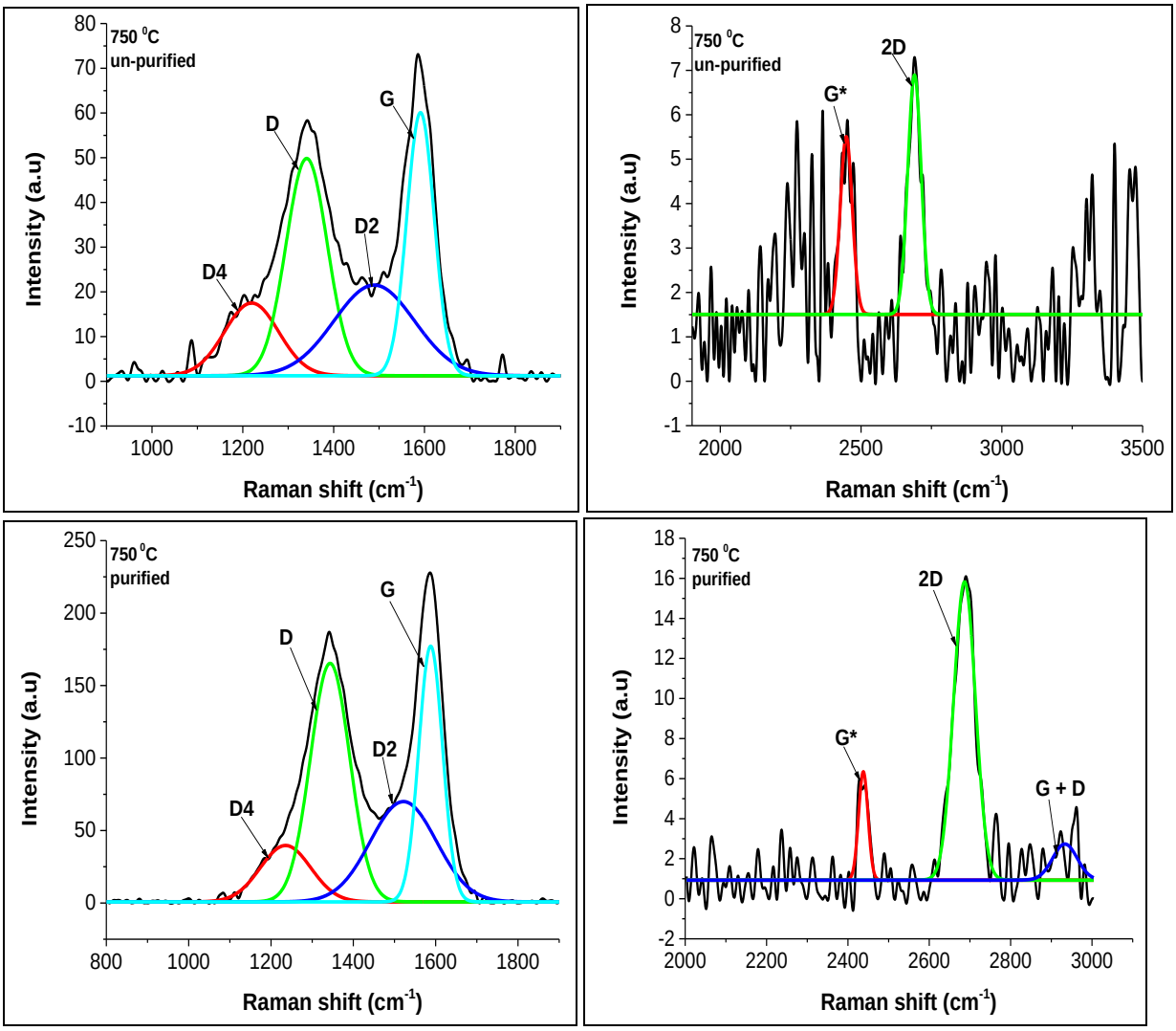

Figure 4.21 Raman spectra of un-purified and purified chlorinated CNTs synthesized at 750 °C for 90 min

Table 4.10 Raman bands of the un-purified and purified chlorinated CNTs generated from pure DCB at 750 °C for 90 min

	Band name	**Band Position (cm^{-1})**	**Bond type**	**FWHM (cm^{-1})**	**Peak Area**	**Designation**
750 °C un-purified	D4	1219	sp^2 - sp^3	140	2425	C=C stretching vibrations
	D	1341	sp^2	107	5535	Disordered graphite
	D2	1489	sp^3	208	4499	Amorphous carbon structure
	G	1591	sp^2	71	4437	Graphitic like carbonyl group
	G*	2447		50	214	1st overtone of D4 band
	2D	2690		56	320	1st overtone of D1 band
750 °C purified	D4	1235	sp^2 - sp^3	144	5970	C=C stretching vibrations
	D	1343	sp^2	112	19728	Disordered graphite
	D2	1521	sp^3	188	13891	
	G	1588	sp^2	68	12748	Graphitic like carbonyl group
	G*	2438		27	156	1st overtone of D4 band
	2D	2687		63	1002	1st overtone of D1 band
	D + G	2933		71	136	2D overtone

A D4, D, and G bands were observed from the Raman spectra of both un-purified samples generated at 800 °C (Figure 4.22). A single 2D band at 2679 cm^{-1} was also observed, suggesting the presence of few layered materials. Raman spectra of the purified CNTs showed the presence of a defect induced D' band at 1616 cm^{-1}. Other second order bands G* and G + D bands at 2427 and 2924 cm^{-1}, were also observed as additional peaks from purified samples. This suggest that purification resulted in formation of materials with increased disorders. I_D/I_G values of 1.3 and 0.8, suggest reduction in defects in the materials after purification (Table 4.11). The $I_D/I_{D'}$ value of 7 was obtained which corresponds to vacancy-like defects.

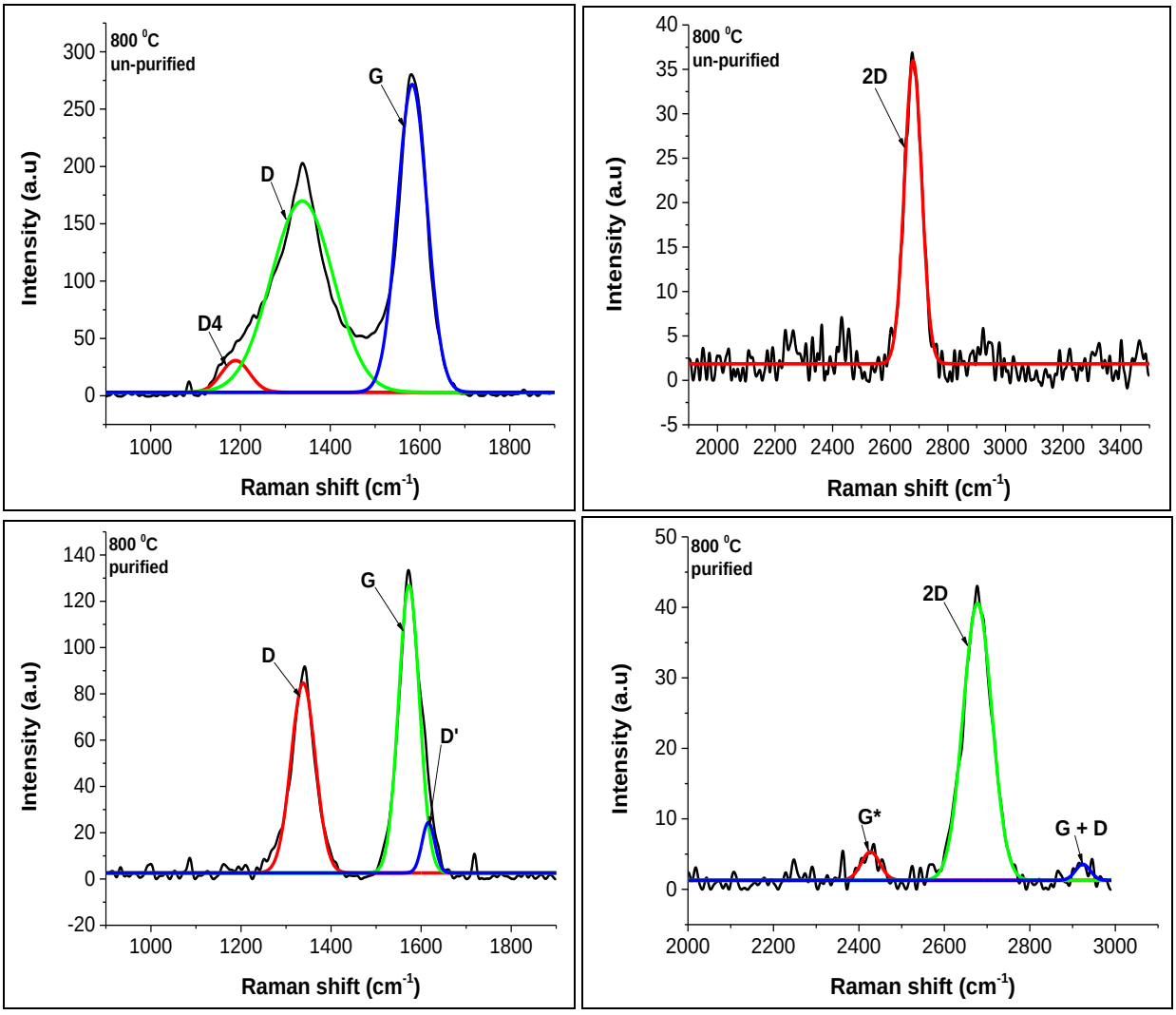

Figure 4.22 Raman spectra of un-purified and purified chlorinated CNTs synthesized at 800 °C for 90 min

Table 4.11 Raman bands of the un-purified and purified chlorinated CNTs generated from pure DCB at 800 °C for 90 min

	Band name	**Band Position (cm^{-1})**	**Bond type**	**FWHM (cm^{-1})**	**Peak Area**	**Designation**
800 °C un-purified	D4	1189	sp^2 - sp^3	74	2180	C=C stretching vibrations
	D	1337	sp^2	163	28909	Disordered graphite
	G	1582	sp^2	78	22248	Graphitic like carbonyl group
	2D	2679		70	2553	1st overtone of D1 band
800 °C purified	D	1338	sp^2	63	5557	Disordered graphite
	G	1573	sp^2	54	7184	Graphitic like carbonyl group
	D’	1616	sp^2	33	772	Defects in graphitic plane
	G*	2427		51	220	1st overtone of D4 band
	2D	2677		79	3320	1st overtone of D1 band
	D + G	2924		41	99	2D overtone

Structural information: Comparison of the Raman with other used techniques in this study

The following conclusions were deduced from the Raman spectra of the effect of synthesis time and temperature:

1. Purified CNTs generated at a reaction time of 120 min exhibited the lowest D and G band FWHM, which indicates that the highest degree of graphitization was achieved at this synthesis time. The data is consistent with the TGA analysis where materials generated at this synthesis temperature had increased thermal stability as compared to materials generated at low synthesis times. The thermal stability was observed to increase with an increase in the synthesis time as follows, 120 > 90 > 60 min.

2. Purified CNTs generated at 800 °C exhibited the lowest D and very low G band FWHM, which indicated that the highest degree of graphitization among all investigated temperatures

and is consistent with the TGA analysis and TEM results. The second reaction temperature that generated better graphitized materials was 600 °C. The number of defects (based on the FWHM value of the D band) increased as a function of reaction temperature as follows: 700 (116 cm^{-1}) < 750 (112 cm^{-1}) < 650 (100 cm^{-1}) < 600 (72 cm^{-1}) < 800 °C (63 cm^{-1}). There was no correlation between the FWHM value and the reaction temperature. The I_D/I_G value of purified CNTs generated at 800 °C is also the lowest, indicating that these materials were more graphitic.

4.4 Conclusion

The structure and yield of the CNTs was affected by the growth time and temperature. Formation of secondary CNFs on the surface of the main CNTs depended on the growth time and growth temperature. Longer synthesis times favored formation of high purity CNTs with no secondary growth and less defects. The largest number of secondary CNFs were observed at 90 min reaction time. Secondary CNFs were found to grow at defects sites of the CNTs as an extension of the CNT wall. For the first time, we have identified the type of defects for chlorinated CNTs. Vacancy-like defects in addition to small hoping defects due to removal of carbon atoms from the graphitic structure and distortion of bonds between carbon atoms as a result of carbon removal, were observed from chlorinated CNTs generated at 90 min reaction temperature. These type of defects seem to arise due to the presence of large magnitude of secondary CNFs observed from their TEM images. CNTs generated at very low (600 °C) and very high (800 °C) were the most graphitic, denoted by their low FWHM values of the D and G band and their high thermal stabilities. Reduction in the CNT growth was observed at high temperatures (~ 750 °C) due to poisoning of the CNT surface by iron carbides resulting from increased formation of chlorine in the reactor. CNTs generated at 600 °C contained sp^3 related defects, which arise due to covalent sp^3 bonded functional groups on the carbon atoms. This shows that greater functionalization of CNTs with chlorine was achieved at low synthesis temperatures. The large value of I_D/I_G of 1.1 suggest that functionalization of CNTs with chlorine increased defects in the graphitic structure. Vacancy like defects due to removal of some carbon atoms in the crystal lattice was obtained from CNTs generated at 800 °C. This suggest less involvement of chlorine in forming functional

groups with the carbon atoms. It was suggested in the TGA studies that at high synthesis temperature of 800 °C, a greater amount of chlorine atoms that are in close proximity are formed, which resulted in them interacting with each other to form Cl_2 molecules which escaped through the trap. Formation of these Cl_2 molecules resulted in them purifying the CNTs, leading to formation of highly graphitized CNTs.

The synthesized CNTs with secondary growth can be used as fillers for polymer matrix in production of polymer composites for water treatment. The presence of secondary CNFs is expected to ease the interaction between the CNTs and the polymer matrix. CNTs with secondary growth can also be used in electronics as their presence is expected to enhance the electrical conductivity of the matrix.

The effect of chlorine on the morphology of N-doped CNTs was then evaluated in the next chapter, because nitrogen-doped CNTs were also observed to enhance the electrical conductivity of the carbon materials.

References

1. S. Ijima, *Nature*, 1991, **354**, 56–66.
2. A. Oberlin and M. Endo, *Journal of Crystal Growth*, 1976, **32**, 335 – 349.
3. V. Popov, Mater. *Sci. Eng. R. Rep.,* 2004, **43**, 61 – 102.
4. R. Ruoff, and D. Lorents, *Carbon*, 1995, **33**, 925 – 930.
5. P.G. Collins, and P. Avouris, *Sci. Am.*, 2000, **283**, 62 – 69.
6. Y.K. Kwon, and D. Toma'nek, *Phys. Rev. B*, 1998, **58**, R16001.
7. J.P. Delmotte, and A. Rubio, *Carbon*, 2002, **40**, 1729 – 1734.
8. O.H. Lee, Q. Lu, Q. Hu, Y-J. Baek, Y-S. Lim and T-S. Yoon, *Curr. Appl. Phys.*, 2013, **13**, S84 – S87.
9. J. Kong, N.R. Franklin, C.W. Zhou, M.G. Chapline, S. Peng, K.J. Cho, and H.J. Dai, *Science*, 2000, **287**, 622.
10. W. Aloui, A. Ltaief, and A. Bouazizi, *Superlattices Microstruct.*, 2013, **64**, 581 – 589.
11. Z. Wen, Q. Wang and J. Li, *Adv. Funct. Mater.,* 2008, **18**, 959 – 964.
12. Y. Saito, S. Uemura, and K. Hamaguchi, *Jpn. J. Appl. Phys.,* 1998, **37**, 346.
13. J.M. Bonard, M. Croci, C. Klinke, R. Kurt, O. Noury and N. Weiss, *Carbon*, 2002, **40**, 1715.
14. N. de Jonge, Y. Lamy, K. Schoots, and T.H. Oosterkamp, *Nature*, 2002, **420**, 393 – 395.
15. M. Zhang, and J. Li, *Mater. Today*, 2009, **12**, 12 – 18.
16. C. Klinke, E. Delvigne, J.V. Barth and K. Kern. *J. Phys. Chem, B.* 2005, **109**, 21677–21680.
17. P.S. Weiser, S. Praoer, A. Hoffman, R.R. Manory, P.J.K. Puterson and S. Stuart, *J. Appl. Phys.*, 1992, **72**, 4643.
18. S. Zhu, F. Shahedipour and H.W. White, *J. Am. Ceram. Soc.*, 1998, **81**, 1041.
19. S. Zhu, C-H. Su, S.L. Lehoczky, I. Muntele and D. Ila, *Diamond Relat. Mater.*, 2003, **12**, 1825 – 1828.
20. C. A. Santini, P. M. Vereecken, C. Van Haesendonck, *Mater. Lett*., 2012, **88**, 33 – 35.
21. M. Terrones, F. Banhart, N. Grobert, J.-C. Charlier, H. Terrones and P.M. Ajayan, *Phys. Rev. Lett*., 2002, **89**, 075505-1 – 075505-4.
22. W.K. Maboya, N.J. Coville, and S.D. Mhlanga. *S. Afr. J. Chem*., 2016, **69**, 15 – 26.
23. S.D. Mhlanga, K.C. Mondal, R. Carter, M.J. Witcomb, and N.J. Coville, *S. Afr. J. Chem*., 2009, **62**, 67–76.

24. P. Poncharal,Z.L. Wang, D. Ugarte and W.A. de Heer, *Science*, 1999, **283**, 1513.
25. A.B. Suriani, M.S. Azmina, M. Salina, A.R. Dalila, A.N. Falina, J. Rostly and M. Rusop, IEEE *International Conference on Electronics Design, Systems and Applications* (ICEDSA), 978-1-4673-2163-1/12, 18 – 21, 2012.
26. T.W. Hansen, A.T. Delariva, S.R. Challa and A.K. Datye, *Acc. Chem. Res.*, 2013, **46**, 1720 – 1730.
27. M. Kumar and Y. Ando, *J. Nanosci. Nanotechnol*, 2010, **10**, 3739 – 3758.
28. A. Hachimi, B.Merzougui, A.Hakeem, T.Laoui, G.M.Swain, Q.Chang, M.Shao, M.A.Atieh, *J. Nanomater*., 2015, http://dx.doi.org/10.1155/2015/453725.
29. P. Lambin, A. Loiseau, C. Culot and L. Biro, *Carbon*, 2002, **40**, 1635 – 1684.
30. Chiang YC, Lin W-H, Chang Y-C, *Appl. Surf. Sci*., 2011, **257**, 2401 – 2410.
31. B. Manoj, *Int. J. Coal Sci. Technol*., 2016, **3**, 123 – 132.
32. A. Cuesta, P. Dhamelincourt, J. Laureyns, A. Martinez-Alonso and J.M.D. Tascon, *Carbon*, 1994, **32**, 1523 – 1532.
33. Y. Wang, D.C. Alsmeyer, and R.L. McCreery, *Chem Mater*., 1990, **2**, 557 – 563.
34. A.C. Ferrari and J. Robertson, *Phys. Rev. B*. 2004, 64:075414-1-075414-13.
35. A. Eckmann, A. Felten, A. Mishchenko, L. Britnell, R. Krupke, K.S. Novoselov and C. Casiraghi, *Nano Lett*, 2012, **12**, 3925 – 3930.
36. P. Venezuela, M. Lazzeri and F. Mauri, *Phys. Rev. B*. 2011, **84**, 035433.
37. K. Ganesan, S. Ghosh, N.G. Krishna, S. Ilango, M. Kamruddin and A.K. Tyagi, *Phys. Chem. Chem. Phys*., 2016, **18**, 22160 – 22167.
38. M. Mowry, D. Palaniuk, C.C. Luhrs and S. Osswald, *RSC Adv*, 2013, **3**, 21763 – 21775.
39. P. Venezuela, M. Lazzeri and F. Mauri, *Phys. Rev. B-Condens. Matter Matter. Phys*., 2011, **84**, 1 – 25.

CHAPTER 5

The synthesis of chlorinated nitrogen-doped multi-walled carbon nanotubes using a Fe-Co/$CaCO_3$ catalyst by use of an injection CVD method

---

5.1 Introduction

The difficulty in producing CNTs with controlled morphology, limits their application as this impact on the physicochemical properties of the CNTs. One way to overcome this limitation is to introduce foreign atoms into the structure of the CNTs. Addition of foreign atoms into CNTs can lead to either functionalization of the CNTs or introduction of a dopant into the walls of CNTs. Heteroatom doping of a material is defined as the intentional introduction of foreign atoms, known as dopants, into that material. Modification of the method of synthesis can also be used to produce CNTs of controlled morphology.

Doping carbon with nitrogen atoms was shown to enhance their application in various fields such as, in water purification, as fillers in composite materials, as supports in catalysis, for CO_2 adsorption, and in energy storage (lithium batteries and supercapacitors). Most work has appeared on use of N-doped carbon nanomaterials (N-CNMs) as an attractive electrode material in supercapacitors.[1-6] Use of N-doped CNMs as supercapacitors was encouraged by their high surface area, excellent electronic conductivity, high reversibility and eco-friendliness.[7] The beneficial effect of nitrogen is strongly related to the specific bonds it forms with carbon.[8] For instance, pyrrolic structure enriched nitrogen was found to be efficient for supercapacitor behavior.[9] Electron transfer was enhanced in materials where quartenary and pyridinic-N-oxides were dominating.[10,11] The pyridinic-N and pyridinic-N-oxide nitrogen groups were found to enhance the capacitance due to the positive charge.[12]

An increase in capacitance of about 4 times that of the pristine samples was produced from N doped graphene based electrodes[13], whilst capacitance of over 200 F/g which is about 2 times higher than that of pristine samples was achieved from using N doped mesoporous carbon.[14]

A limited amount of work has been reported on use of N doped CNTs in supercapacitors.[3,6, 15] A capacitance of about 60 F/g was achieved from using N doped CNTs, which was relatively low compared to other N doped carbon nanomaterials.[15] Enhancement of field emission properties and better electro-catalytic performance were observed from using open ended N-doped CNTs because of their large specific surface area, as compared to closed ended N-doped CNTs.[7,16] Enhanced electron conductivity was also observed when using open-ended N-doped CNTs because they are able to form more electron transport pathways in open tips.[17] A technique that is normally used for opening the CNT caps is acid treatment or oxidation. The disadvantage of opening CNT caps with acid oxidation is that it enhances the number of defects in CNTs and also increases both the nitrogen and oxygen functionalities.[18] The combined effect of N/O functionalities and open-ended tips is shown to improve the supercapacitor performance of the CNTs significantly. [19]

Chemical doping of reduced graphene oxide sheets with chlorine by introducing extra charge carriers was found to enhance their electrical conductivity.[20] Chlorinated reduced graphene oxide sheets were found to be very stable in solvents like N,N-dimethylformamide (DMF) possibly because of the enhanced repulsive forces between the graphene oxide sheets arising from absorbed Cl ions.[21] Yeon et al. found that etching a polymer derived SiCN with chlorine resulted in formation of carbon material that exhibited meso- and microporous and possessed a high specific surface area.[22] Zera et al. synthesized a nitrogen-doped carbide derived carbon aerogels with high capacitance by chlorine etching of a SiCN aerogel.[8]

In our previous work, we studied the effect of chlorine on the morphology of carbon nanomaterials prepared by catalytic pyrolysis of chlorinated organic hydrocarbons using C_2H_2 and N_2 gases over a Fe-Co/$CaCO_3$ catalyst.[23] We have shown that the type of chlorinated organic reagent used as a chlorine source influence the morphology of the CNMs.

The role of chlorine and chloride salts on the morphology of N-doped CNTs have been a subject of a few studies using various synthesis methods. 30 % of N-doped horn-like CNTs with dumbbell-shaped open-ends were prepared by reducing pentachloropyridine with metallic sodium in a stainless steel autoclave; the reaction also produced hollow carbon nanospheres. The horn-shaped CNTs were found to be initiated by the presence of sodium.[24] Various N-doped

carbon nanostructures including particles, whiskers, square frameworks, lamellar layers, hollow spheres and tubular structures have been synthesized by designed direct chemical reactions of small molecule carbon halides (such as CCl_4, C_2Cl_6) and nitridation reagents such as NaN_3 in the absence of any templates and catalysts in an autoclave at various temperatures.[25] The rupture of thick CNTs with arms or branches, which changed to a sharp nail structure with a further increase in the concentration of NaCl in the byproduct trap were observed when using a pyrolysis CVD method that was modified by adding NaCl into the water that was in the byproduct trap.[26] The nitrogen content was increased in N-doped CNTs synthesized using a halogenated ferrocenyl catalyst. A fluorine substituted ferrocene catalyst produced a highest nitrogen-doping level as compared to a chlorine substituted ferrocene catalyst, but the chlorine substituted catalyst also yielded iron-filled N-CNTs.[27]

In this study, we continue to study the effect of chlorine on the morphology of N-doped CNTs. The ultimate goal is to investigate if modification of N-doped CNTs with chlorine will improve their electronic conductivity, by identifying the dominant nitrogen species in the final material. To our knowledge, the role of chlorine on the morphology of N-CNTs using a Fe-Co supported on $CaCO_3$ as catalyst by an injection CVD method has not been studied. In this study the concentration of both chlorine and nitrogen was varied to explore the effect of chlorine on the morphology of the obtained CNTs. The effect of the injection flow rate of the liquid reagents mixture on the morphology of the chlorinated N-MWCNTs was also.

5.2 Experimental

5.2.1 Chemicals

$Fe(NO_3)_3 \cdot 9H_2O$ (Sigma Aldrich) ≥ 98 %, $Co(NO_3)_2 \cdot 6H_2O$ (Sigma Aldrich) ≥ 98 %, $CaCO_3$ (Sigma Aldrich) ≥ 99 %, HNO_3 (Sigma Aldrich) ≥ 98 % ACS, 1,2-dichlorobenzene (DCB) (Sigma Aldrich) 99 % Reagent plus, 1,1,2,2-tetrachloroethane (TTCE) (UniLAB SAARChem) 98 % GLC, acetonitrile (CH_3CN) ≥ 99.8 % (Sigma Aldrich) were used. All reagents were commercially available and used without further purification.

5.2.2 Catalyst preparation by wet impregnation method

$Fe(NO_3)_3.9H_2O$ and $Co(NO_3)_2.6H_2O$ were used to prepare the catalyst. Calculated amounts of the Fe and Co nitrates were weighed and mixed in a beaker. The salts were then dissolved using 30 mL of distilled water to make a 0.3 mol/L Fe and 0.3 mol/L Co precursor solution. The metal solution was then transferred to a burette and added dropwise while stirring to a 10 g $CaCO_3$ support that was placed in a beaker. The mixture was stirred for 30 min. The beaker containing the metal-support mixture was then dried paced in an oven for drying at 120 °C for 12 h. The metal-support solid was then cooled to room temperature, transferred to a mortar and ground with a pestle, followed by screening through a 150 µm molecular sieve. The catalyst powder was then calcined at 400 °C for 16 h in a static air oven. This catalyst was completely characterized as reported in an earlier article.[28]

5.2.3 Synthesis of chlorinated N-CNMs using an injection CVD method

Synthesis of chlorinated N-doped MWCNT was carried out at 800 °C under a nitrogen (N_2) and acetylene (C_2H_2) atmosphere. The flow rates were 240 and 90 ml/min for N_2 and C_2H_2 respectively. A 20 mL mixture of CH_3CN and DCB of various volume ratios were placed in a 20 mL syringe driven by a SAGE syringe pump. About 1 g of catalyst was placed in a quartz boat which was then pushed into the middle of the quartz tube. The quartz tube was then placed inside a furnace and ensured that a quartz boat is in the center of the furnace. After the temperature of the furnace has reached 800 °C, the solution mixture was injected at a rate of 0.24 mL/min into a quartz tube reactor (32 cm × 1 m) using a peristaltic pump over the flow of N_2 and C_2H_2. The reaction time was 1 h. At the end of the reaction the system was cooled down to room temperature under an N_2 atmosphere (40 mL/min). Carbon soot was removed from the tube, weighed and some of the product purified with 30 % HNO_3 by refluxing in acid at 110 °C for 4 h. The carbon product was then filtered and washed with distilled water until the pH of the filtrates reached ~ 7. The carbon product was then dried in an oven at 120 °C overnight. A schematic representation of the injection CVD setup is shown in Figure 5.1.

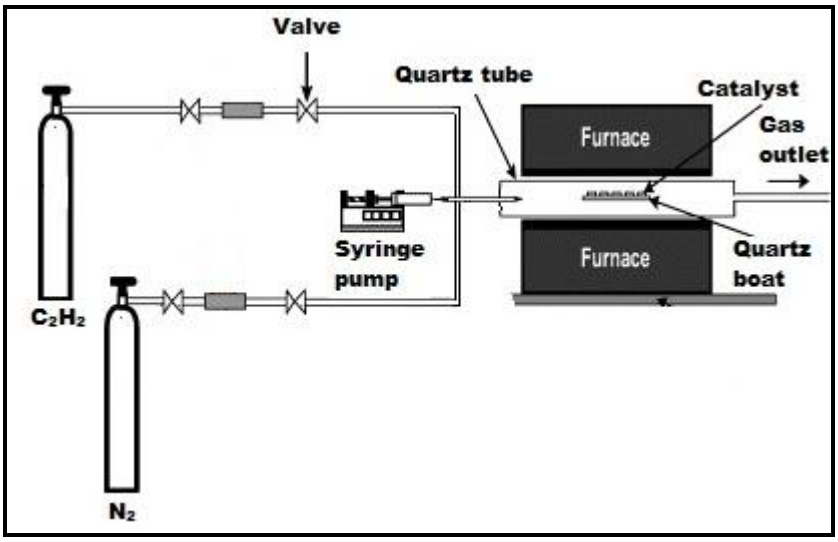

Figure 5.1 Schematic diagram of the assembled injection CVD setup used for the synthesis of CNMs.

5.2.4 Characterization of carbon nanomaterials

The morphology and size distribution of the produced MWCNTs before and after HNO_3 treatment were analyzed by transmission electron microscopy (TEM) using a T12 FEI TECNAI G^2 SPIRIT operating at 120 kV. The samples for TEM analysis were prepared by sonication in ethanol and thereafter deposited on a holey carbon-coated TEM Cu grid. The morphology and size distribution of the MWCNTs were also determined by scanning electron microscopy using FEI Nova Nanolab. The powdered samples were placed on top of a tape that was attached to a stub. The samples were coated with carbon and palladium to prevent them from charging. The impurity content of the MWCNTs was monitored by thermogravimetric analysis (TGA) using a Perkin Elmer TGA 7. The sample was loaded onto a platinum pan and heated to 900 °C at a heating rate of 5 °C/min, in a flowing air stream at flow rate of 20 mL/min. The CNTs were characterized by Raman spectroscopy using a Jobin-Yvon T6400 micro-Raman spectrometer. Excitation was provided by the 532 nm green laser with spectral resolution of 3-5 cm^{-1}. X-ray photoelectron spectroscopy (XPS) analysis was done using an AXIS Ultra DLD, with Al (monochromatic) anode equipped with a charge neutralizer, supplied by Kratos Analytical.

5.3 Results and discussion

In this section the morphology of the CNMs were evaluated using TEM and SEM. The effect of solvent mixture injection rate was optimized and the optimum flow rate used in the investigations that follows. The effect of chlorine concentration of the morphology of the CNMs was also evaluated. The TEM and SEM characterizations were confirmed by TGA, Raman spectroscopy and XPS.

Dichlorobenzene (DCB) was selected as a chlorine source to use for the investigation of its role on the morphology of the N doped CNMs. Our previous results showed that CNTs produced using DCB had more uniform diameters and were produced in large quantities.

5.3.1 Structural analysis of N doped CNMs: Effect of DCB concentration and injection flow rate

In order to study the role of chlorine on the morphology of the N-doped CNMs, we first had to study the morphology of the CNMs obtained from pure CH_3CN and pure DCB. To our knowledge CNMs obtained using pure CH_3CN as a nitrogen source and pure DCB as a chlorine source over a Fe-Co/$CaCO_3$ catalyst by using an injection CVD injection was never reported. The reaction conditions used in this study were as follows: N_2 flow rate = 240 mL/min, C_2H_2 flow rate = 90 mL/min, reaction temperature = 800 °C, reaction time = 1 h, injection rate = 0.24 mL/min.

The morphology of the CNMs using pure CH_3CN and DCB were studied by TEM. TEM images obtained from pure CH_3CN revealed the presence of a mixture of CNMs, hollow thin-walled CNTs (Figure 5.2a and b), bamboo compartmented CNTs (Figure 5.2c) and carbon nanospheres (CNS) (Figure 5.2d). A rod-shaped CNF with a measuring-cylinder like tip or base (Figure 5.2a shown by arrow) was also observed from a TEM image. Similar rod-shaped CNFs are presented in Supplementary Figure S1a and b circled parts.

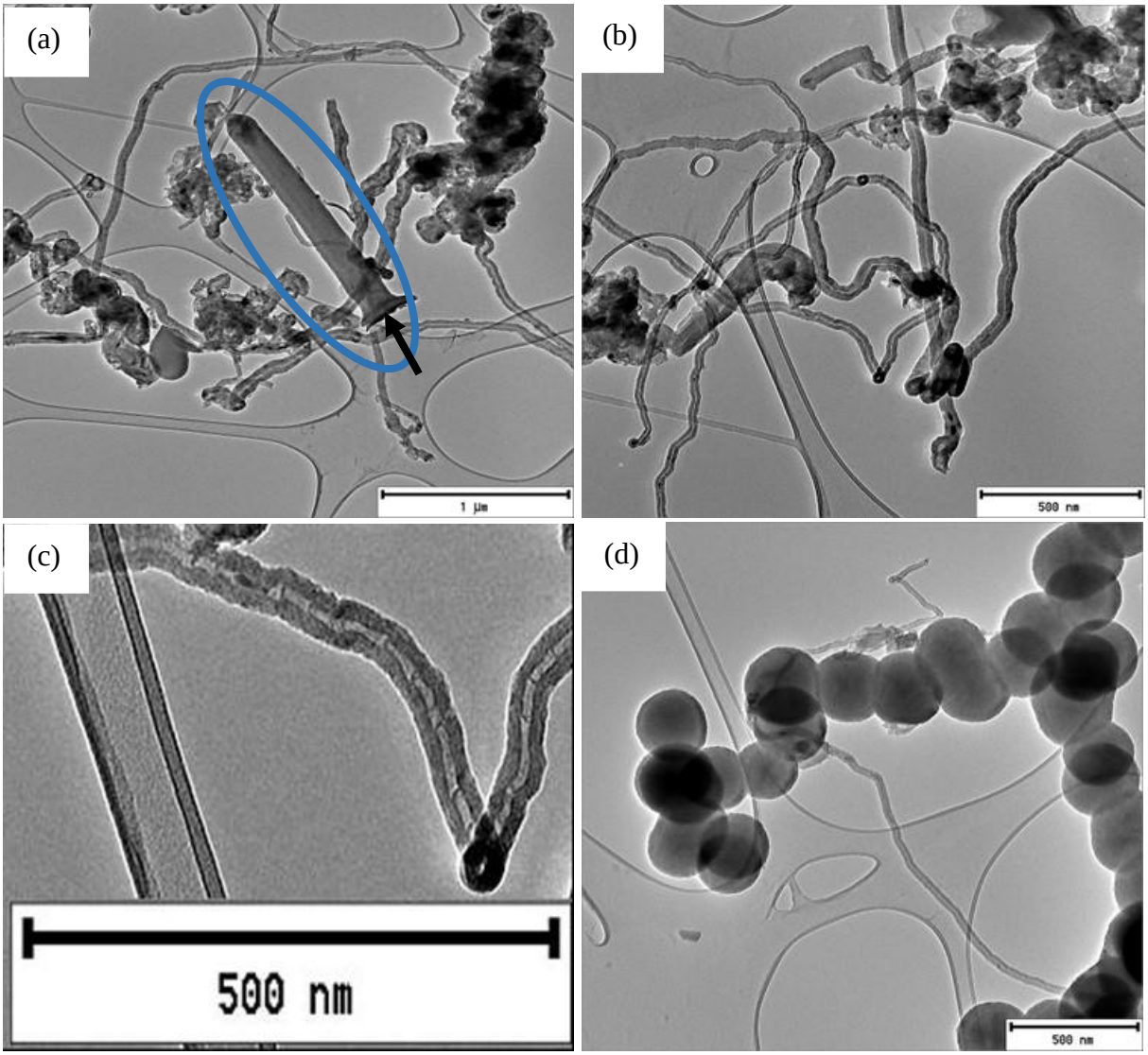

Figure 5.2 TEM images of purified MWCNTs generated from pure CH_3CN (20 mL) by a CVD injection method at the following reaction conditions: 0.24 mL/min, 800 °C, 1 h, 240 mL/min N_2, and 90 mL/min C_2H_2.

TEM images obtained from pure DCB also revealed mixtures of entangled thin- and thick-walled CNTs (Figure 5.3a and b). The tube tips and bases were not clearly observed from the TEM images due to entanglement and the greater length of the tubes. The quantity of the CNTs increased when DCB was used for the synthesis of the CNMs.

(b

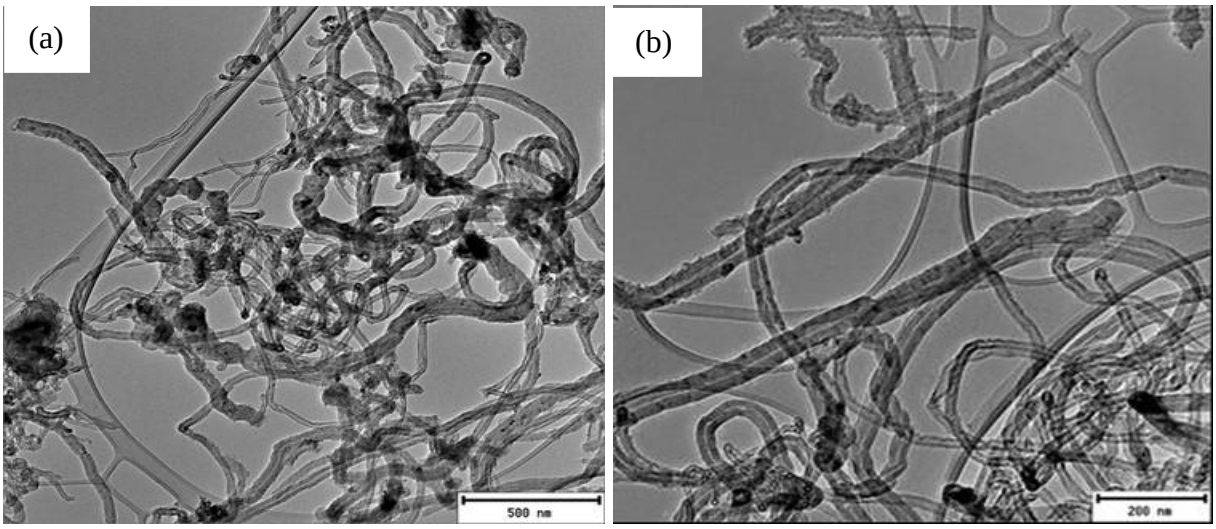

Figure 5.3 TEM images of purified MWCNTs generated from DCB (20 mL) by a CVD injection method at the following reaction conditions: 0.24 mL/min, 800 °C, 1 h, 240 mL/min N_2, and 90 mL/min C_2H_2.

To elucidate further on the morphology of the CNMs obtained from pure CH_3CN and pure DCB, SEM images were recorded. SEM images of the nanomaterials generated from CH_3CN revealed the presence of a large population of short-rod shaped CNMs (Figure 5.4a). A diameter distribution curve showed that the rod-shaped CNMs had average outer diameters of ~ 53 nm (Figure 5.4b and Table 5.1). High magnification SEM study showed that the rod-shaped CNMs are growing from or attached to some large agglomerated particles or carbon platelets (Figure 5.4b). The agglomerates were previously seen by other authors when they produced CNTs over pyrolysis of acetonitrile using Mg-Co-Al layered hydroxide as a catalyst material and were assigned to carbon plate-like particles.[29] The length of the rod-shaped CNMs ranged from ~ 60 to 160 nm. A number of spherical carbon nanomaterials (~15 %) and a few long CNTs (~15 %) were also observed from SEM images obtained from pure CH_3CN (Figure 5.4d).

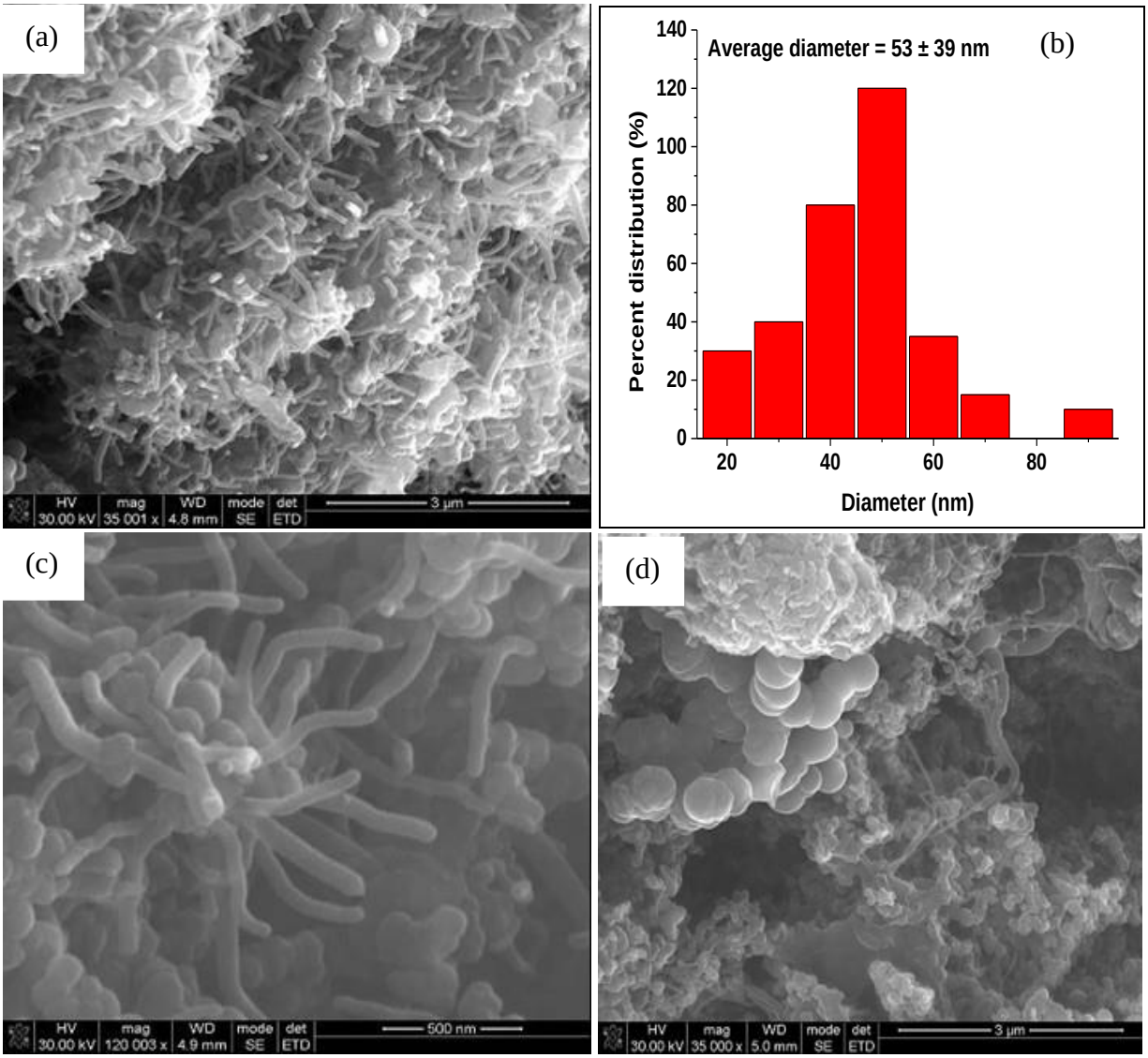

Figure 5.4 SEM images and the diameter distribution curves of purified MWCNTs generated from pure CH_3CN (20 mL) by a CVD injection method at the following reaction conditions: 0.24 mL/min, 800 °C, 1 h, 240 mL/min N_2, and 90 mL/min C_2H_2.

SEM images of the nanomaterials generated from pure DCB revealed the presence of a large population of entangled long CNTs (Figure 5.5a and b). A diameter distribution curve revealed that the CNTs had an average outer diameters of ~ 45 nm (Figure 5.5b and Table 5.1). Growth of a large quantity of highly entangled CNTs in the form of a CNT sponge were also reported in the literature, from spray pyrolysis of a mixture of ferrocene and DCB.[30]

Table 5.1 Diameters of purified CNMs generated from pure CH_3CN and pure DCB synthesized using an injection CVD method at a 0.24 mL/min injection rate

Hydrocarbon source	Average outer diameter /nm	Number of structures counted (number of samples analyzed)	Carbon structure
CH_3CN	53 (Carbon nanorods)	>200 (duplicates)	Carbon nanorods (70 %), CNTs and bamboo CNTs (15 %), CNSs (15 %)
DCB	45	>200 (duplicates)	CNTs

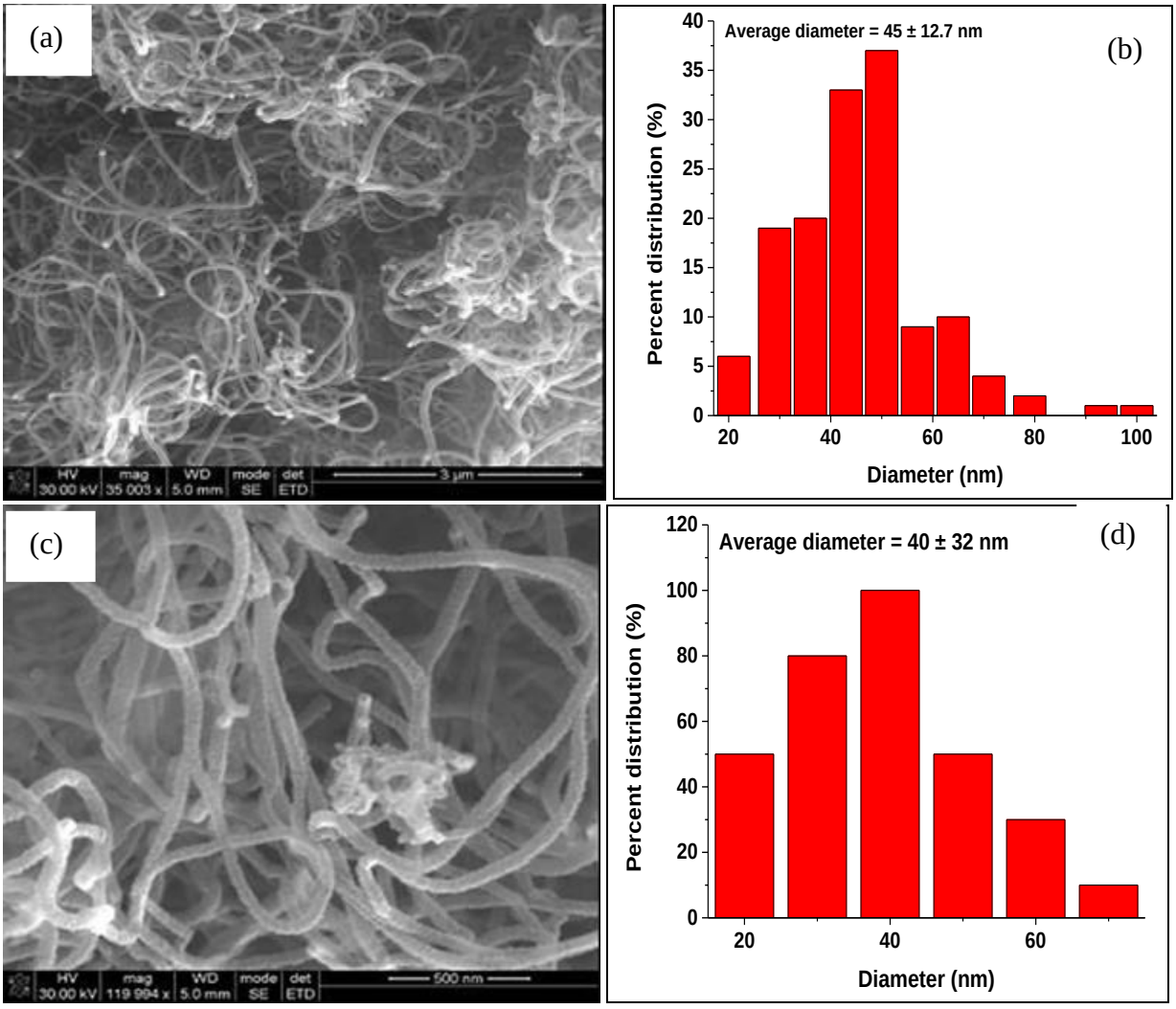

Figure 5.5 SEM images and the diameter distribution curves of purified MWCNTs generated from DCB (20 mL) by a CVD injection method at the following reaction conditions: 0.24 mL/min, 800 °C, 1 h, 240 mL/min N_2, and 90 mL/min C_2H_2.

The effect of a chlorine content on the morphology of N-doped CNMs was studied by TEM and SEM. The reaction conditions used in this study were as follows: N_2 flow rate = 240 mL/min, C_2H_2 flow rate = 90 mL/min, reaction temperature = 800 °C, reaction time = 1 h, injection rate = 0.24 mL/min. The studied concentrations, based on the volume percent of nitrogen and chlorine sources were as follows: CH_3CN:DCB (66.7:33.3); CH_3CN:DCB (33.3:66.7); CH_3CN:DCB (20:80).

TEM images of un-purified and purified CNMs obtained from mixtures containing various volume ratios of CH_3CN/DCB revealed the formation of nanomaterials with different morphologies (Figure 5.6, 5.7 and 5.8). TEM studies based on the solution containing 33.3 vol.% DCB showed that images obtained from un-purified and purified samples were similar (Figure 5.6a to d). CNTs with open-ends, some with closed-ends (rod-shaped) and large CNFs with "funnel-shaped" open-ends were obtained (Figure 5.6a to d). Studies have shown that acid treatment opens up the tube ends[31], but in our study the tube-ends were opened even before acid-treatment. This could be one of the roles of chlorine to act as a purifying agent leading to opening up of the tube ends.

TEM images obtained from an increase in DCB concentration in the feed to 66.7 vol.% showed formation of CNTs and CNFs of various sizes (Figure 5.7 a to d). A similarity was observed from CNMs generated from both un-purified and purified samples (Figure 5.7 a to d). Rod-shaped CNTs some with closed-ends and others with open-ends were obtained (Figure 5.7a and c). Large sized CNFs with pencil-shapes, some with open-ends and others with closed-ends were also obtained (Figure 5.7b, c and d circled parts). Some thinner CNFs which also appear to have "pencil-shapes" that are not well-developed can be seen from images obtained from solutions containing 33.3 vol.% and 66.7 vol.% DCB (Figure 5.6a and 5.7c shown by arrows).

TEM images of CNMs generated from un-purified samples containing 80 vol.% DCB showed rod-shaped CNMs with "funnel-like) open-ends, CNTs, carbon flakes and CNS (Figure 5.8a and b). Images obtained from purified samples showed a large quantity of entangled CNTs, CNSs, carbon flakes (Figure 5.8c and d) and rod-shaped CNMs (Supplementary Figure S2).

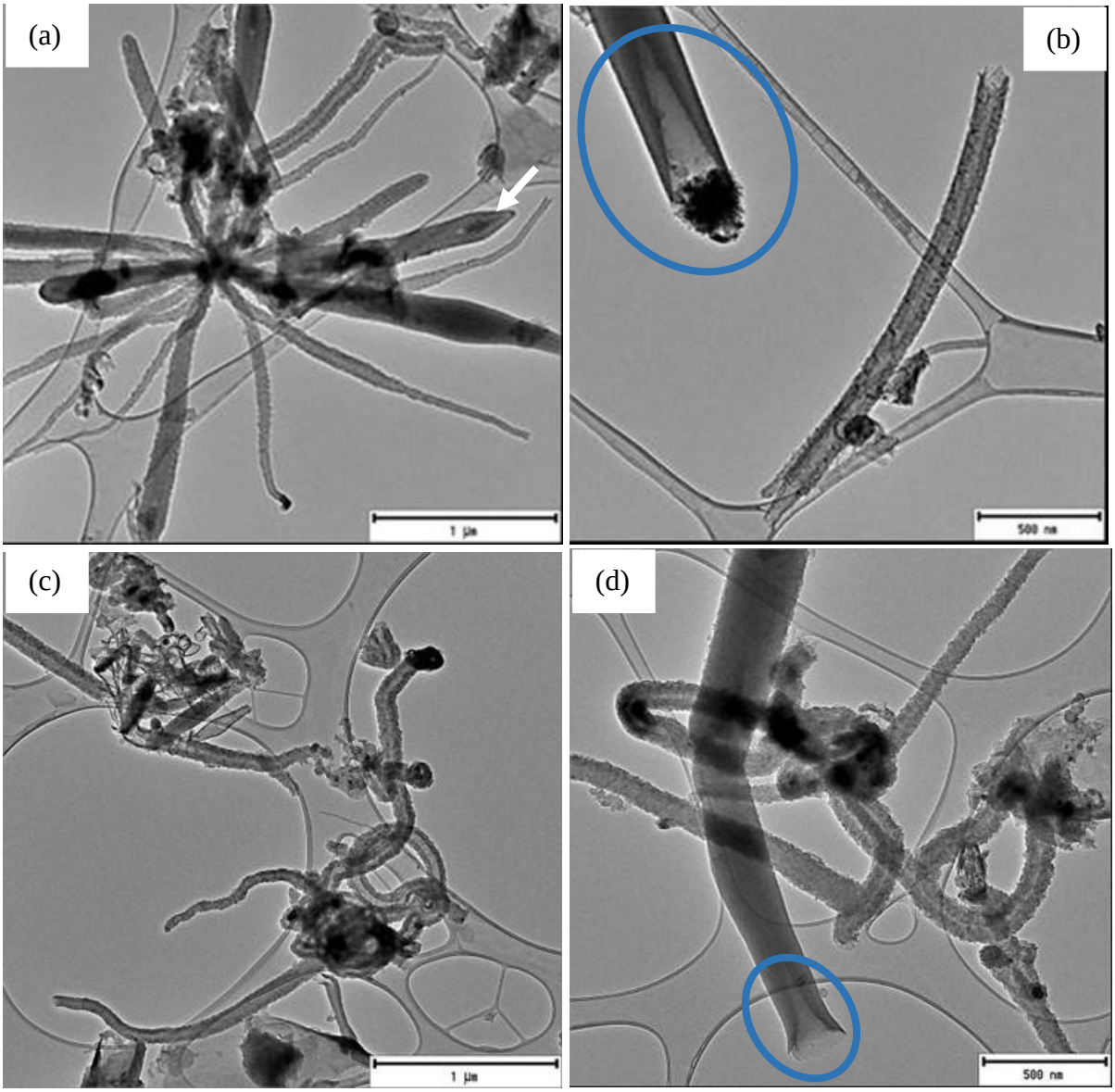

Figure 5.6 TEM images of un-purified (a and b) and purified (c and d) CNMs generated from a 66.7:33.3 vol.% CH_3CN:DCB reagent synthesized by a CVD injection at an injection rate of 0.24 mL/min.

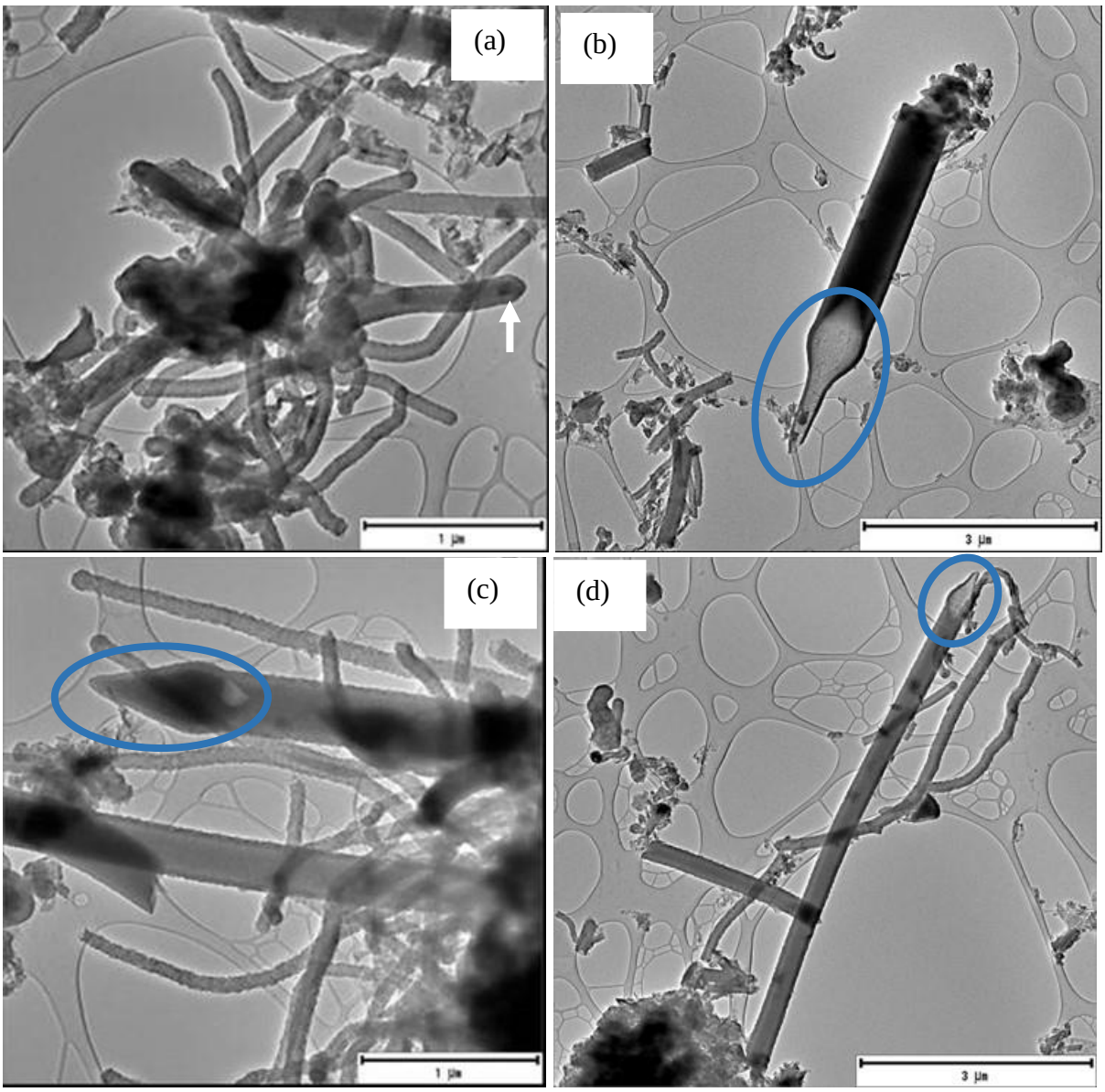

Figure 5.7 TEM images of un-purified (a and b) and purified (c and d) CNMs generated from a 33.3:66.7 vol.% CH_3CN:DCB reagent synthesized by a CVD injection at an injection rate of 0.24 mL/min.

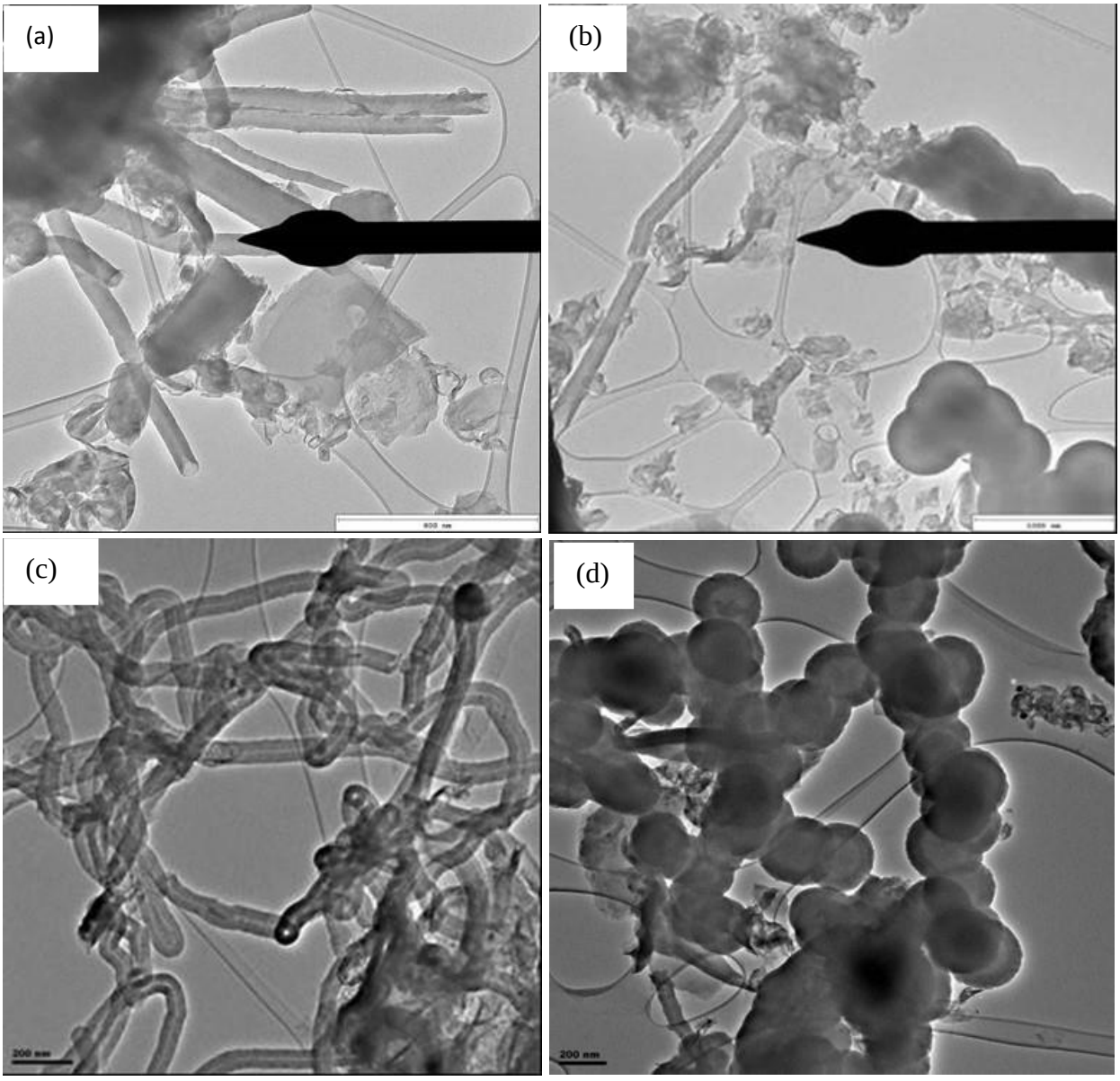

Figure 5.8 TEM images of un-purified (a and b) and purified (c and d) CNMs generated from a 20:80 vol.% CH_3CN:DCB reagent synthesized by a CVD injection at an injection rate of 0.24 mL/min..

SEM images were also recorded in order to obtain more information on the morphology and dominating carbon nanostructures. SEM images obtained from un-purified samples containing 33.3 vol.% DCB showed the presence of rod-shaped CNMs, covered by droplets of metal catalyst particles (Figure 5.9a and b). SEM images of the purified samples revealed that the majority of the CNMs in these feeds were "straw-shaped" CNTs with open-ends and of various

sizes (Figure 5.9c). The metal catalyst particle droplets were not observed after purification. Diameter distribution curves revealed that the open-ended CNTs had average outer diameters of ~ 107 nm (Figure 5.9b and Table 5.2). A measurable quantity of the rod-shaped CNMs were also observed from the SEM images obtained after purification (Figure 5.9c). Their diameter distribution curves revealed that they had an average outer diameter of ~ 78 nm (Figure 5.9d and Table 4.2). High magnification SEM images were also obtained to get a closer look at the obtained morphologies. Closer analysis of the open-ended CNTs showed that they were "horn-shaped" (Figure 5.10a). The rod-shaped CNMs seems to have increased in lengths in comparison to those obtained from pure CH_3CN, with the measured lengths of ~ 346 to 540 nm, which was about 3 times that obtained in pure CH_3CN (Figure 5.10b). This suggest that the presence of chlorine enhances the growth of CNMs. A measurable quantity of carbon nanospheres were also obtained from these solution (Figure 5.10c).

Table 5.2 Diameters analysis of CNMs generated from solutions containing various volume ratios of CH_3CN:DCB synthesized using an injection CVD method at an injection flow rate of 0.24 mL/min

Hydrocarbon source	**Molar ratio /vol.% (Mole ratio)**	**Average outer diameter /nm**	**Number of structures counted (number of samples analyzed)**	**Carbon structure**
CH_3CN: DCB	66.7:33.3 (1:0.25)	107 (open-ended CNTs) 78 (rod-shaped CNMs)	>200 (duplicates)	Horn- or straw-shaped CNTs (70 %), carbon nanorods (20 %), CNSs (10 %)
CH_3CN: DCB	33.3:66.7 (1:1)	157	>200 (duplicates)	Pencil-shaped CNFs, CNTs
CH_3CN: DCB	20:80 (1:2)	95	>200 (duplicates)	Straw-shaped CNTs, entangled CNTs, carbon nanorods, CNSs

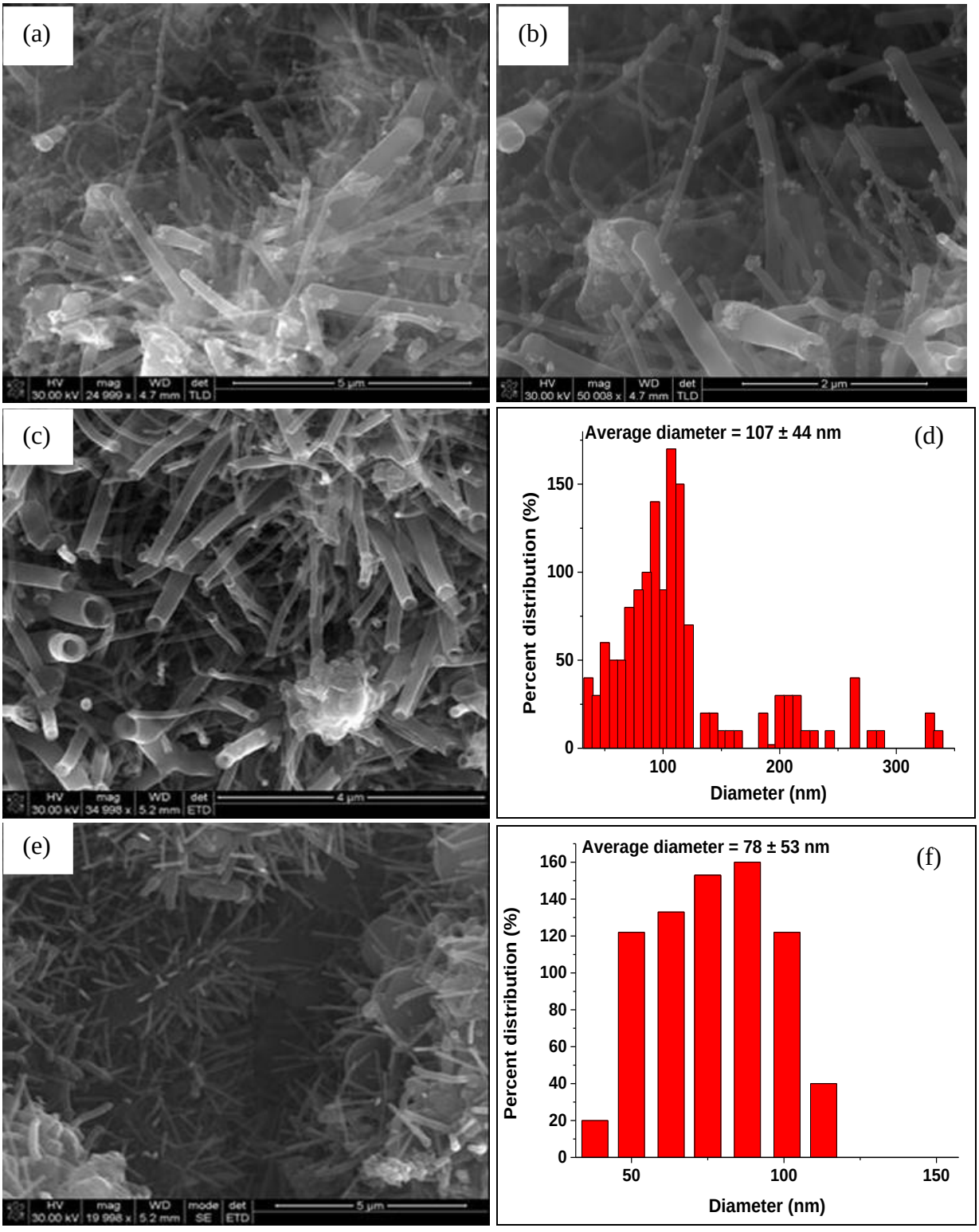

Figure 5.9 SEM images of un-purified (a and b) and purified (c,d,e and f) CNMs generated from a 66.7:33.3 vol.% CH_3CN:DCB reagent synthesized by a CVD injection at an injection rate of 0.24 mL/min.

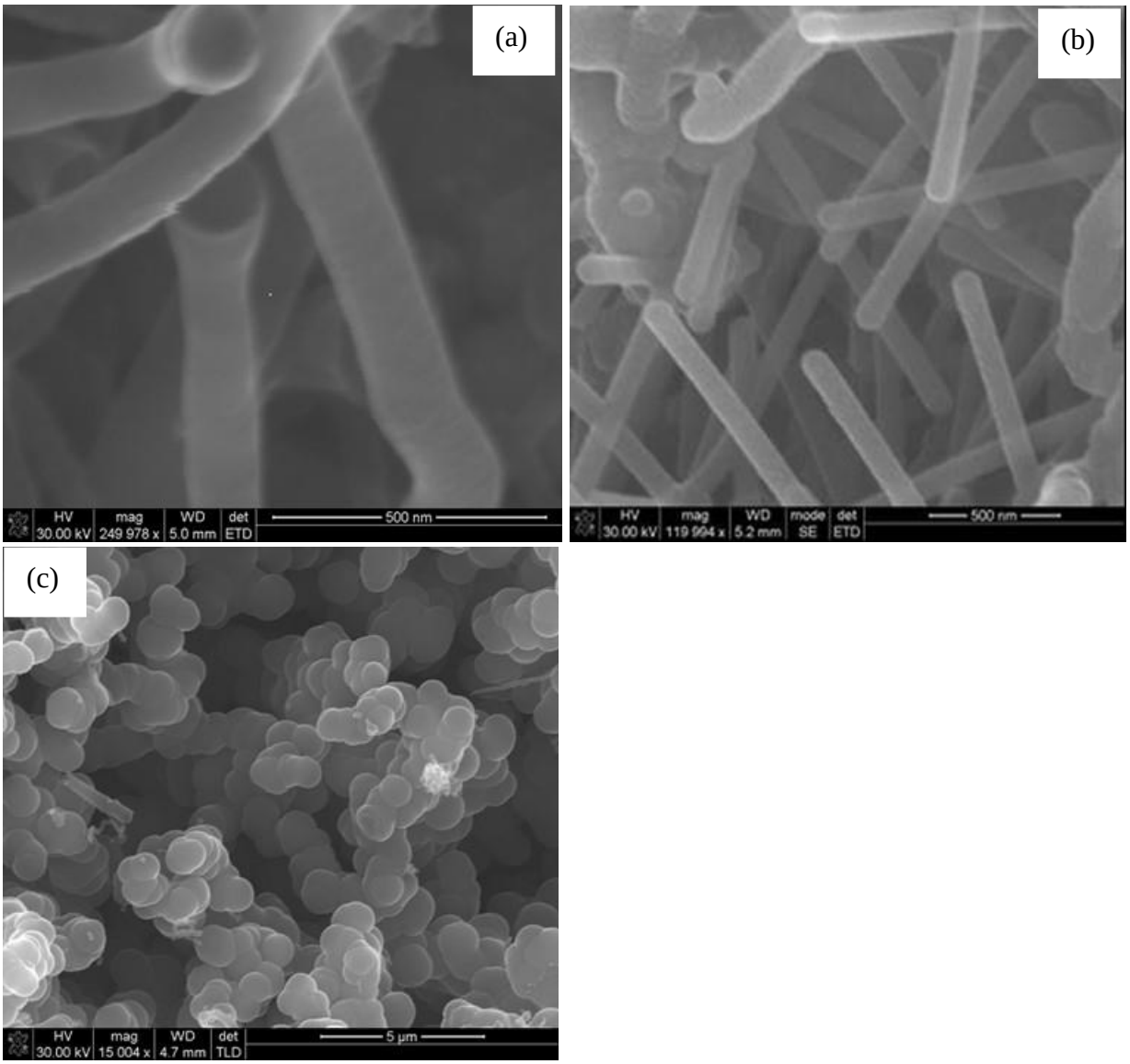

Figure 5.10 High magnification SEM images of purified (a, b) CNMs and (c) carbon nanospheres generated from a 66.7:33.3 vol.% CH_3CN:DCB reagent synthesized by a CVD injection at an injection rate of 0.24 mL/min.

SEM images obtained from un-purified and purified samples containing 66.7 vol.% DCB were similar (Figure 5.11a, b and c). A large quantity of rod-shaped CNMs of increased length were observed from this solution. A measurable quantity of large "pencil-shaped" CNFs, some with closed-ends and others with open-ends were also observed (Figure 5.11a, c, e and f and Supplementary Figure S12). A few of these "pencil-shaped" CNFs which were thinner and appeared undeveloped (shown by small pointed head) were observed from TEM images

generated from a solution containing 33.3 vol.% DCB. It appears that the presence of chlorine in the feed results in structural changes of the "rod-shaped" CNMs to "pencil-shaped" CNFs. This is shown by an increase in the thin ended part of the CNF resulting in a formation of a well-developed "pencil-like" CNF. The open-ended "pencil-shaped" CNFs appears as if their tips were broken, resulting in open-ends (Figure 5.11e). The reaction mechanism of this "pencil-shaped" CNTs still needs to be investigated, but it appears that chlorine is responsible for this. of covered by droplets of metal catalyst particles (Figure 5.9a and b). SEM images of the purified samples revealed that the majority of the CNMs in these feeds were "pencil-shaped" CNFs with most of them under developed shown by the small undefined tip-ends. The average outer diameter of all the observed CNMs was about 154 nm (Figure 5.11c and Table 5.3).

SEM images obtained from solutions containing 80 vol.% DCB concentration revealed also a mixture of CNMs. Un-purified samples showed rod-shaped CNMs covered by droplets of metal catalyst particles (Figure 5.12a). SEM images of the purified samples revealed mixtures of clean CNMs, CNSs, "straw-shaped" open-ended CNTs and entangled CNTs (Figure 5.12 b, c, and e and Figure 5.13). The "straw-shaped" CNTs were dominating in this solution and their average diameters were about 95 nm (Figure 5.12d and Table 5.3). The average outer diameter of the entangled CNTs was about 72 nm (Figure 5.12f and Table 5.3). It appears that in all concentrations studied, the tube length increased with an increase in amount of chlorine present in the feed.

"Sharp nail structures as claws were observed by other researchers when they modified the CVD method of producing N-doped CNTs by adding NaCl to the water that was in a by-product liquid trap, using benzylamine and ferrocene as nitrogen source and catalyst[28]. They claimed that as they increased the concentration of the salt in water changes in morphology of N-doped CNTs occurred. The changes in morphology were probably due to the evaporation of water but the authors claimed that it was due to the participation of Na and Cl atoms produced in the water as they move back into the hot zone. "How can the ions move back against a flow and take part in the reaction?" They also claimed that Na and Cl ions were participating in the catalysis, probably reducing the sizes of the nanoparticles".[26]

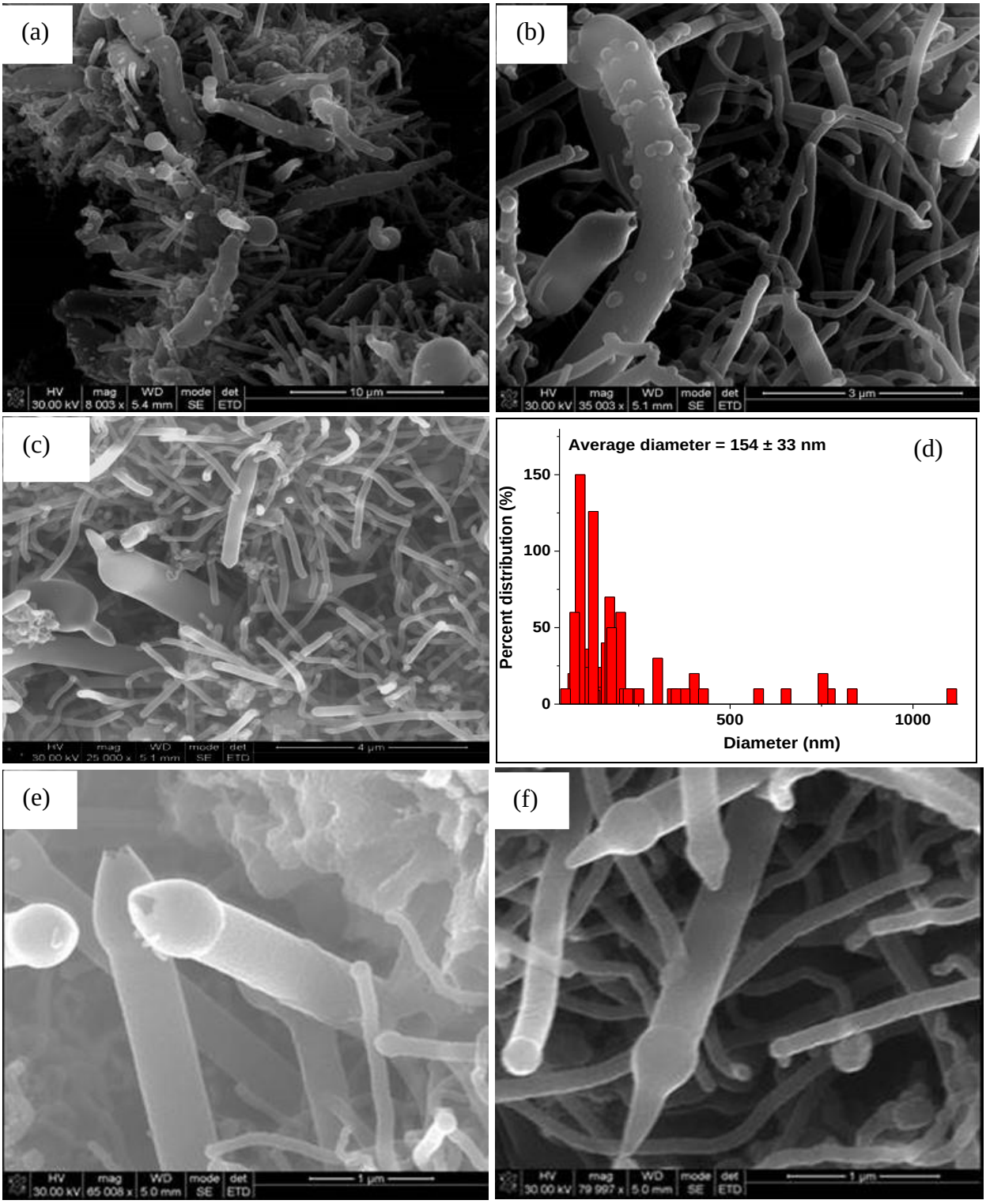

Figure 5.11 SEM images of un-purified (a and b) and purified (c (with its diameter distribution curve (d), e and f) CNMs generated from a 33.3:66.7 vol.% CH_3CN:DCB reagent synthesized by a CVD injection at an injection rate of 0.24 mL/min.

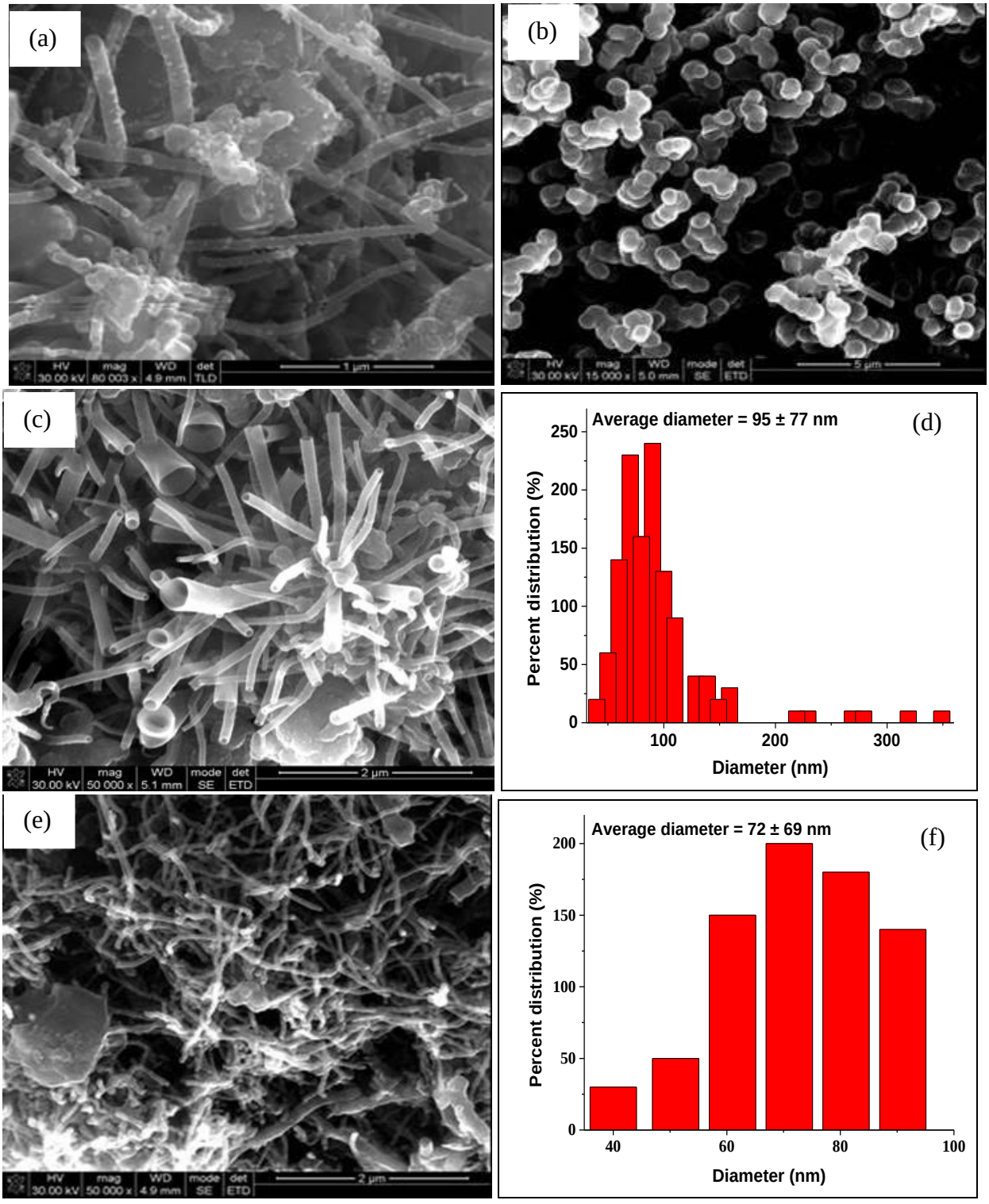

Figure 5.12 SEM images of un-purified (a and b) and purified (c (with its diameter distribution curve (d), e and f) CNMs generated from a 20:80 vol.% CH_3CN:DCB reagent synthesized by a CVD injection at an injection rate of 0.24 mL/min.

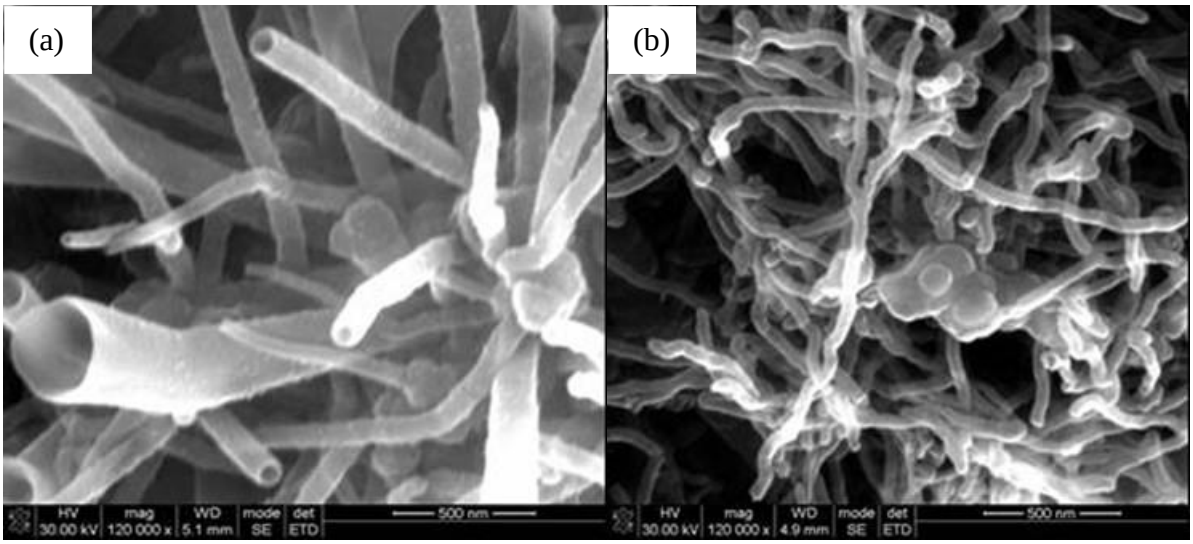

Figure 5.13 High magnification SEM images of purified (a, b) CNMs generated from a 20:80 vol.% CH_3CN:DCB reagent synthesized by a CVD injection at an injection rate of 0.24 mL/min.

TEM images of un-purified and purified CNMs synthesized at different injection flow rates, 0.1 and 0.16 mL/min are shown in Figure 5.14 and 5.15. TEM images for CNMs generated at all flow rates, revealed that un-purified and purified samples yielded similar CNMs. Images obtained from an injection flow rate of 0.24 mL/min were already discussed in the previous section. TEM images obtained from un-purified and purified samples generated at an injection flow rate of 0.16 mL/min revealed CNMs with "funnel-like" open ends (Figure 5.14a, c and d). Figure 5.14d shows that the inside of the CNMs are compartmented, "cup-shapes" can be seen inside the tube, especially at the tube-end. This shows that the CNMs are actually CNTs with thick walls and very thin inner diameters. Carbon flakes were also observed from the TEM images (Figure 5.14b, c and d). Decreasing an injection flow rate to 0.10 mL/min resulted in the formation of a large quantity of thin CNTs, together with large diameter CNTs with "funnel-like" open-ends (Figure 5.15a, b, c and d). Images of CNTs before purification and after purification appeared similar, all have open-ends and amorphous carbon particles can also be observed in both. We can conclude from the TEM images that varying the injection flow rate did not result in a great change on the morphology of the CNMs.

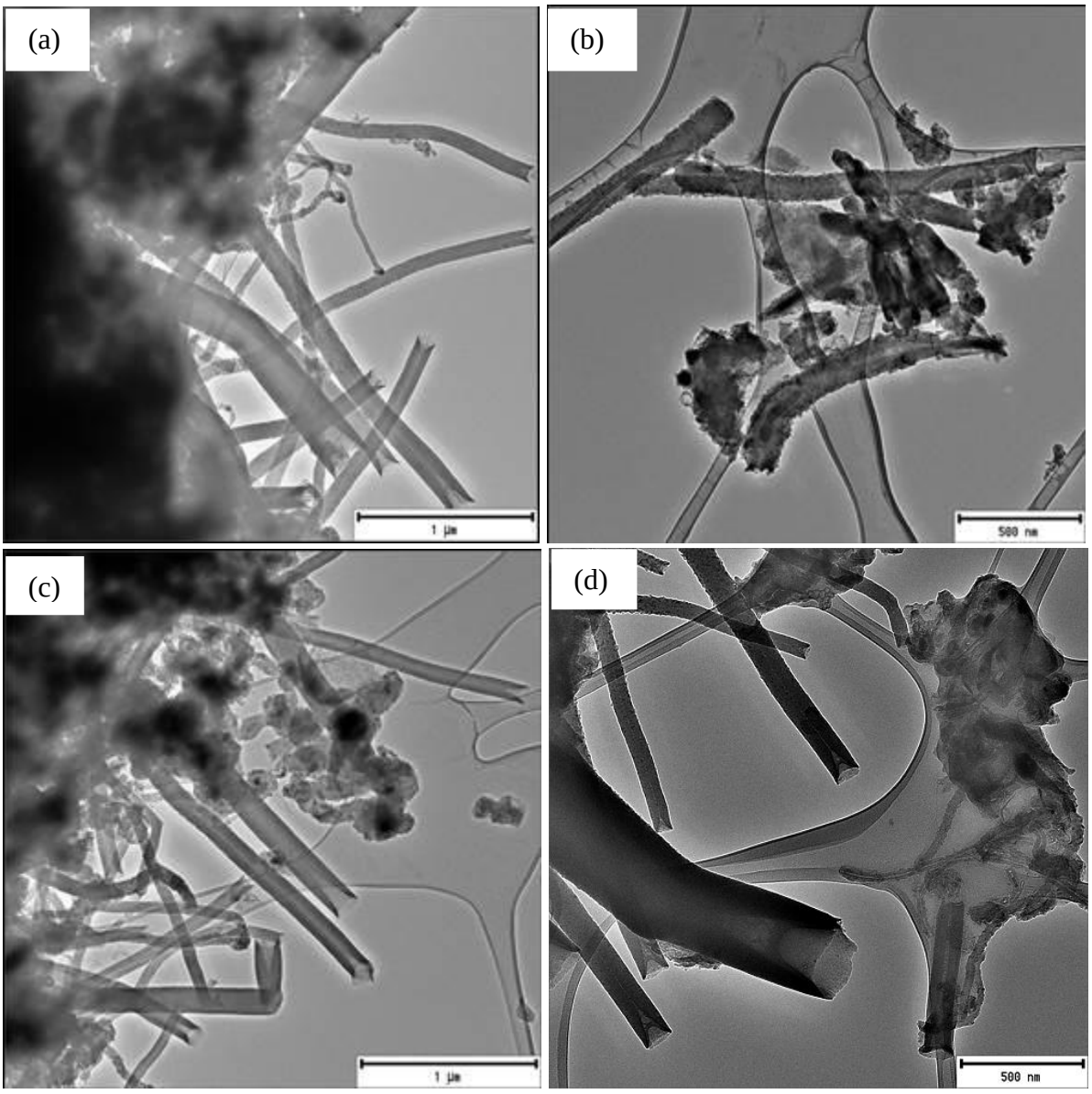

Figure 5.14 TEM images of un-purified (a and b) and purified (c and d) CNMs generated from a 66.7:33.3 vol.% CH_3CN:DCB reagent synthesized by a CVD injection at an injection rate of 0.16 mL/min.

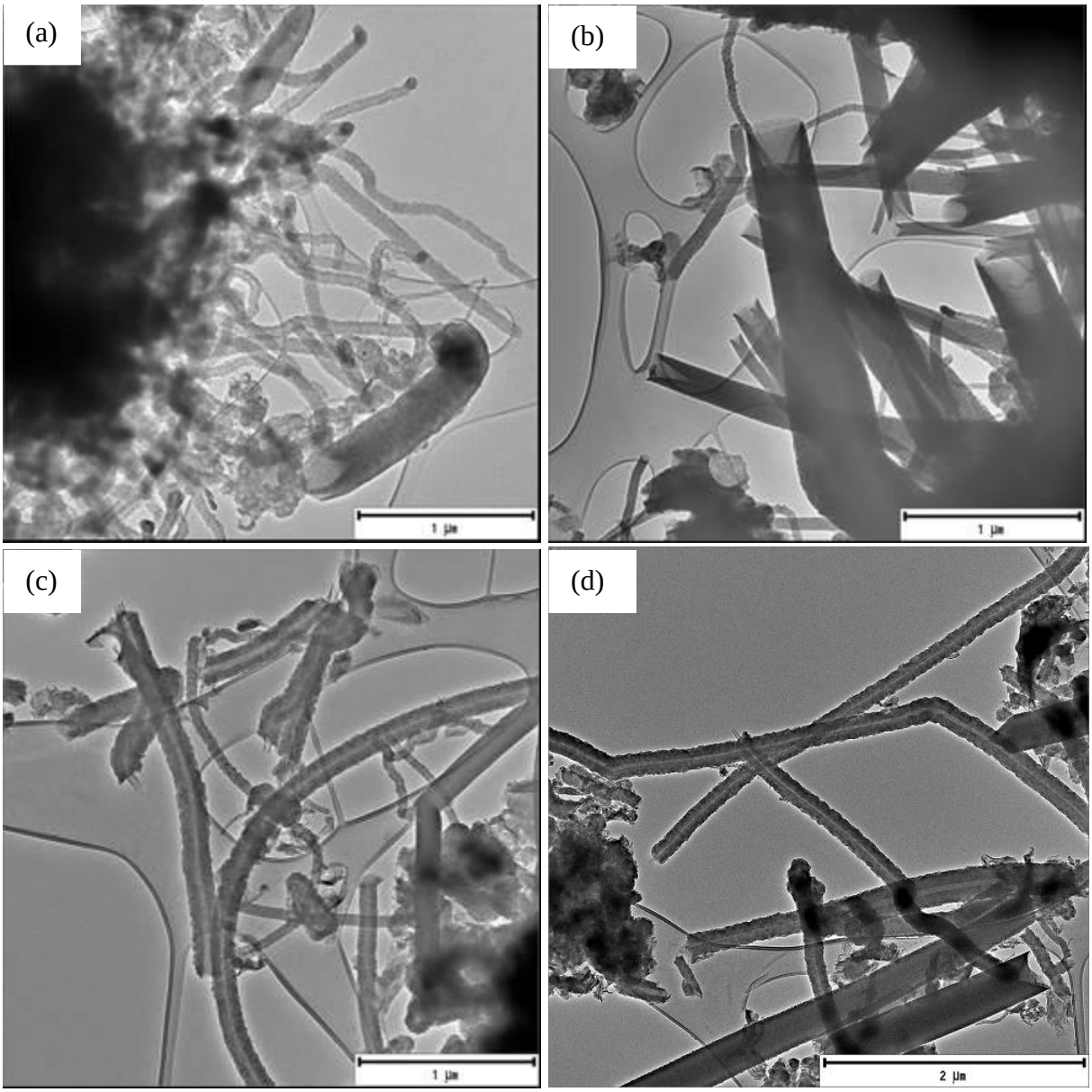

Figure 5.15 TEM images of un-purified (a and b) and purified (c and d) CNMs generated from a 66.7:33.3 vol.% CH_3CN:DCB reagent synthesized by a CVD injection at an injection rate of 0.10 mL/min.

SEM images were also recorded in order to obtain more information on the morphology and dominating carbon nanostructures. SEM images obtained from un-purified samples generated at an injection flow rate of 0.16 and 0.10 mL/min, showed the presence of rod-shaped CNMs, covered by droplets of metal catalyst particles (Figure 5.16a and b; Figure 5.17a and b). SEM images of the purified samples revealed that the majority of the CNMs in these feeds were "rod-shaped" CNTs with small outer diameters (Figure 5.16c, e and f; Figure 5.17c, e and f). The metal catalyst particle droplets were not observed after purification. Diameter distribution curves measured for all CNTs showed an average outer diameters of ~ 155 nm and 236 nm for CNMs generated from a 0.16 and 0.10 mL/min injection flow rate, respectively (Figure 5.16d and Figure 5.71d). A measurable quantity of the large open-ended CNTs were also observed from the SEM images obtained after purification (Figure 5.16c, and e and Figure 5.17 c and e). The mass of the product obtained at all studied injection flow rates were also similar, 1.3850, 1.1424 and 1.0433 g for 0.24, 0.16 and 0.10 mL/min injection flow rates respectively.

Increasing the flow rate to 0.57 mL/min resulted in no increase in the mass of the product obtained, instead the mass of the product obtained decreased which showed that the only thing that happened was the reduction of the catalyst material.

The average diameter of the CNMs increased with a decrease in an injection flow rate. Production of CNTs with open-ends decreased with an increase in an injection flow rate. CNMs generated from applying an injection flow rate of 0.16 and 0.10 mL/min possessed similar morphologies. We concluded that an injection flow rate of 0.24 mL/min was the best to use in these studies since even if it gave us mixtures of CNMs, it favored mostly formation of open-ended CNTs which are desirable in field emission devices and as supercapacitors.

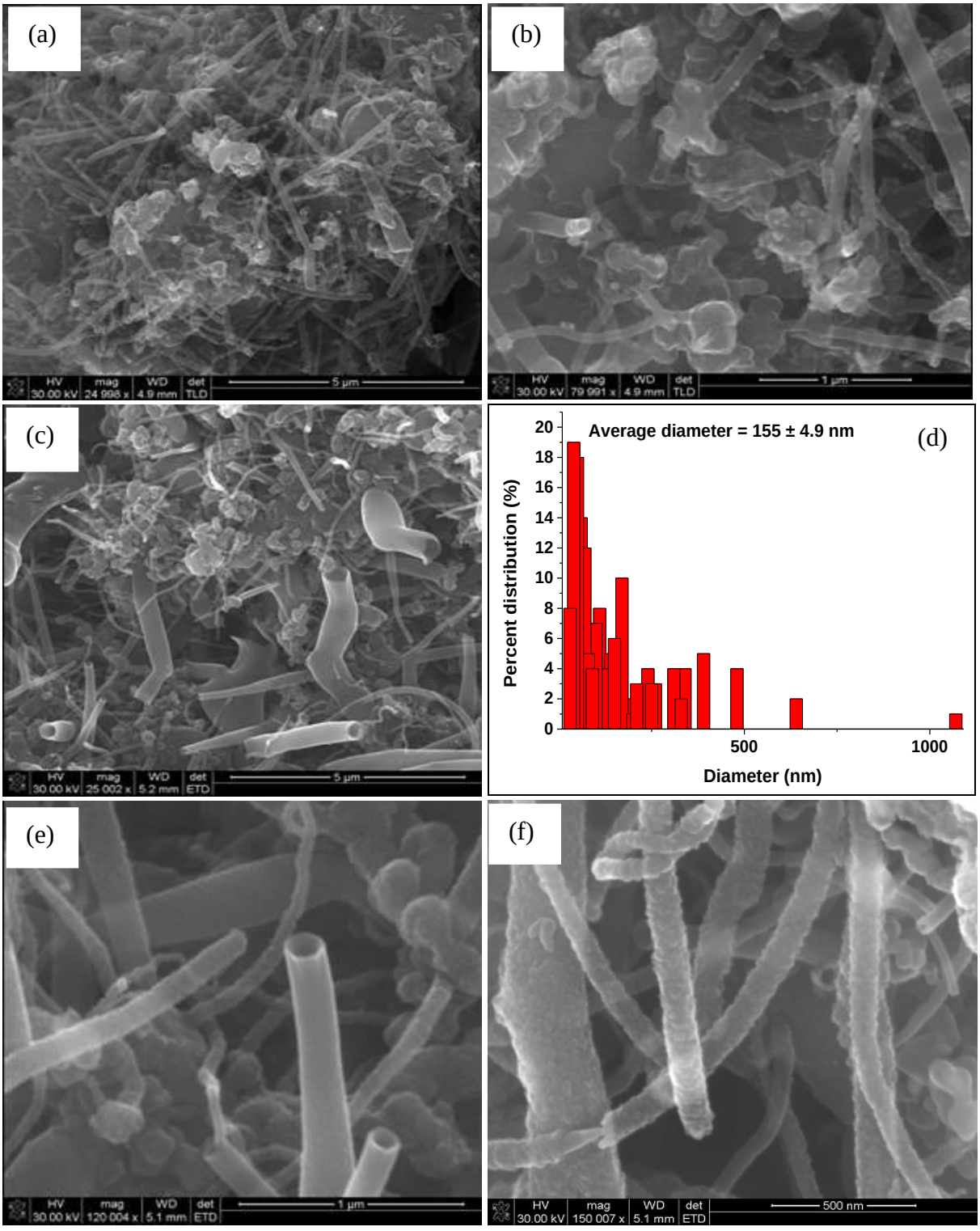

Figure 5.16 SEM images of un-purified (a and b), purified (c, and d) and high magnification SEM images of CNMs generated from a 66.7:33.3 vol.% CH_3CN:DCB reagent synthesized by a CVD injection at an injection rate of 0.16 mL/min.

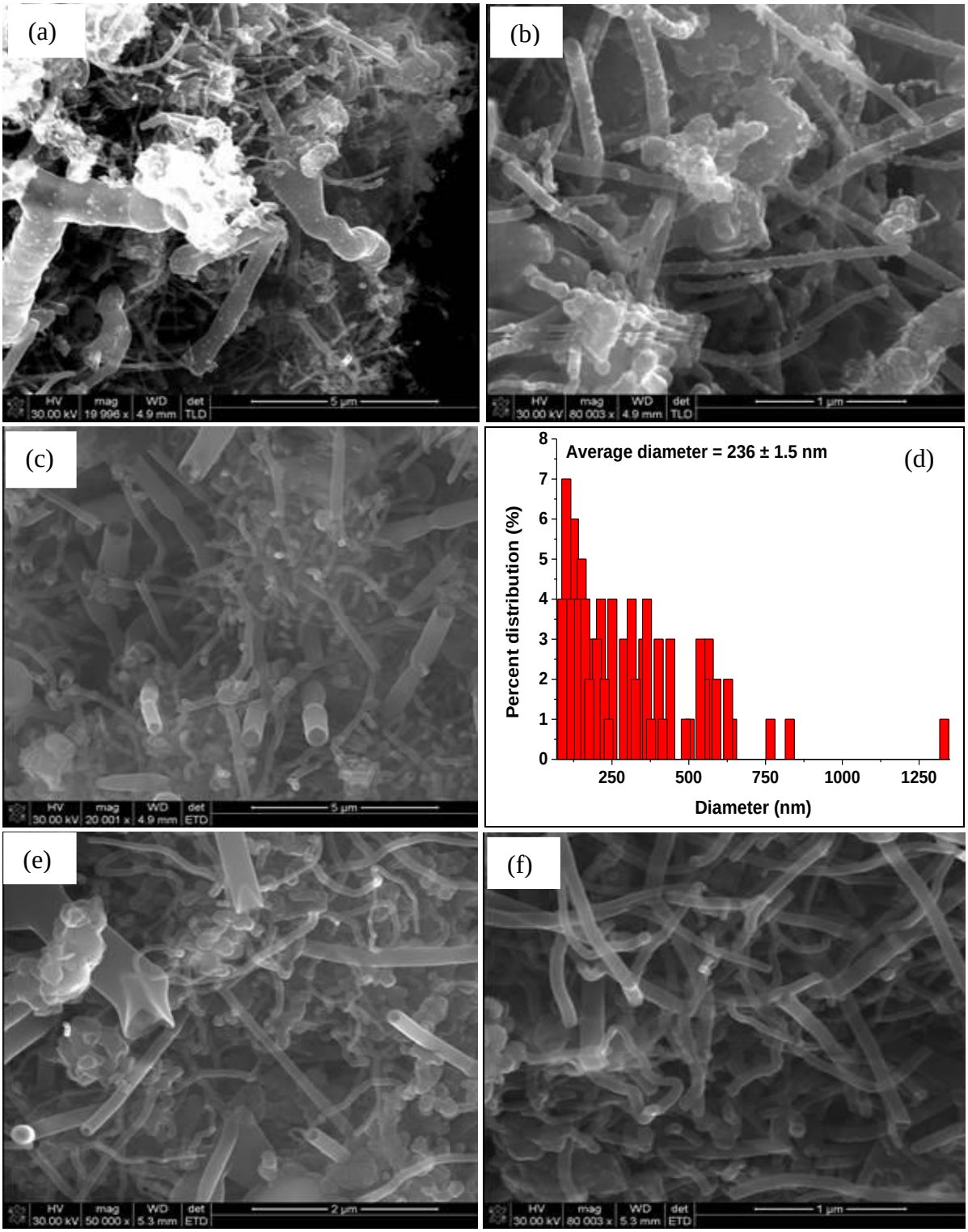

Figure 5.17 SEM images of un-purified (a and b), purified (c, and d) and high magnification SEM images of CNMs generated from a 66.7:33.3 vol.% CH_3CN:DCB reagent synthesized by a CVD injection at an injection rate of 0.10 mL/min.

5.3.2 Thermogravimetric analysis of N doped CNMs: Effect of DCB concentration and injection flow rate

The thermal stability and the reactivity of the obtained CNMs were analyzed by thermogravimetric analysis (TGA). Derivative TGA profiles of the un-purified samples generated from pure CH_3CN shows two initial minor weight losses at ~ 480 and 500 °C, due to oxidation of amorphous carbon and degradation of surface oxygen functionalities[32] (Figure 5.18b) (Figure 5.18 and Table 5.3). A third mass loss was observed at ~ 620 °C for the oxidation of N doped MWCNTs (rod-shaped, bamboo-compartmented and hollow CNTs) (Figure 5.18b). A fourth sharp mass loss at higher temperatures above 700 °C can be attributed to decomposition of other graphitic materials (CNSs, and carbon platelets observed from the TEM and SEM images). Similar mass losses were observed for CNMs generated from purified samples (Figure 5.18b). A shift to lower decomposition temperatures was observed from DTGA curves obtained from purified samples, suggesting that more defects were created by acid treatment. A fourth mass loss was greatly reduced in height after purification suggesting removal of other graphitic materials like carbon platelets and some catalyst metal particles.

DTGA curves of the un-purified CNTs generated from DCB alone showed a minor mass loss at ~ 100 °C due to evaporation of physisorbed water on CNT sheets. The water could have been adsorbed onto the CNTs during storage (the CNTs were stored in glass vials). Two more oxidation peaks were observed at higher temperatures ~ 600 and 700 °C. The mass loss at ~ 600 °C which appeared dominant was attributed to functionalized CNTs, while the mass loss at ~ 700 °C was attributed to impurities such as unreacted metal catalyst particles (Figure 5.18d and Table 5.3). A single major weight loss (~100 %) was observed from purified samples at ~ 600 °C and was attributed to chlorinated CNTs. Materials containing C–Cl bonds were shown to possess high thermal stabilities.[33]

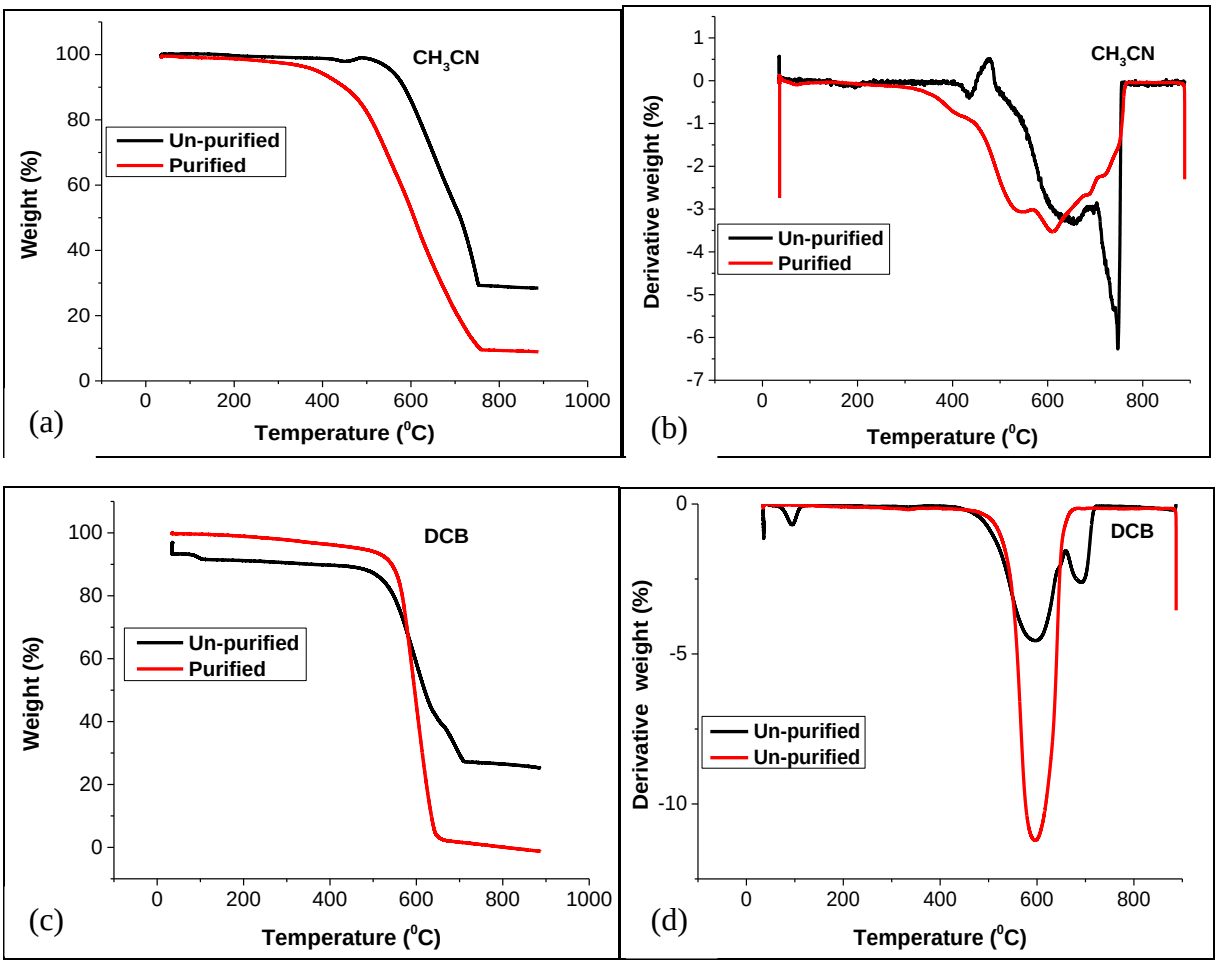

Figure 5.18 TGA and DTGA curves of un-purified and purified CNMs generated from pure CH_3CN (a & b) and pure DCB (c & d) synthesized by CVD injection at 0.24 mL/min.

Table 5.3 Decomposition temperatures and residual masses (determined by TGA) of the un-purified and purified (P) chlorinated N-MWCNTs generated by injecting different volume ratios of CH_3CN and DCB.

CH_3CN:DCB vol.%	**Peak 1 decomposition temperature, °C**	**Peak 2 decomposition temperature, °C**	**Residual mass, %**
100:0	643	744	28.5
100:0 (P)	540	621	8.9
0:100	601	695	25.7
0:100 (P)	607	–	0

Three mass losses were observed from DTGA curves generated from un-purified CNMs while two mass losses were observed from purified CNMs synthesized from solutions containing 33.3 vol.% DCB (Figure 5.19b). The first mass loss at ~ 100 °C, was due to physisorbed water on the CNT sheets. The second most intense weight losses at higher temperatures ~ 550, was attributed to oxidation of chlorinated N-doped CNTs (Figure 5.19 and Table 5.4). The third mass loss appeared at ~ 650 °C for purified CNMs and was at ~ 680 for un-purified CNMs. The third weight loss was assigned to oxidation of other graphitic materials (CNSs, and carbon platelets). These observations agree with the TEM observations were mixtures of CNMs were observed from un-purified and purified samples.

DTGA obtained from solutions containing 66.7 vol.% DCB were also analyzed. Two mass losses at lower temperatures were observed from un-purified samples at ~ 100 and 150 °C. The first mass loss at ~ 100 °C was assigned to physisorbed water and the mass loss at ~ 150 °C was assigned to decomposition of chemisorbed surface chloride groups[32]. A broad oxidation peak at higher temperatures from 600 to 750 °C which shows three mass losses, of which two are sharp at higher temperatures (Figure 5.19 and Table 5.4). The weight loss at ~ 600 °C can be attributed to stable C–Cl bonds from chlorinated N-doped CNTs. Two small sharp weight losses at ~ 680 and 750 °C can be attributed to the presence of other graphitic materials (like large "pencil-shaped" CNMs) respectively. Another broad oxidation peak at even higher temperatures ~ 800 °C (Figure 5.19d) was observed, which was assigned to the evolution of nitrogen which is known to be released from N-doped carbons.[33] Highest weight changes were observed for samples with highest chlorine content.[34] We can assume that the formation of large "pencil-shaped" CNTs some with open-ends and others with closed-ends were enhanced in feeds containing a large content of chlorine adatoms. The results agree with TEM images where large "pencil-shaped" CNTs were produced from solutions containing 66.7 vol.% DCB that is assumed to release large amounts of chlorine vapors into the feed. This situation prevails when formation of Cl_2 molecules which can escape through the trap is hindered by formation of Cl adatoms at opposite sides of the CNT tube.[35] Formation of Cl_2 molecules from two individual Cl atoms is energetically favorable when the two Cl atoms are at close proximity to each other.[35]

We then analyzed DTGA profiles obtained from solutions containing 80 vol.% DCB. Two mass losses at lower temperatures were observed from un-purified samples at ~ 100 and 150 °C

(Figure 5.19). The first mass loss at ~ 100 °C was assigned to physisorbed water and the mass loss at ~ 150 °C was assigned to decomposition of chemisorbed surface chloride groups[32]. Two broad mass losses were also observed further at high temperatures from the un-purified and purified samples at ~550 and 620 °C (Figure 5.19 and Table 5.4). The major weight loss at ~550 °C can be attributed to oxidation of chlorinated N-doped CNTs (entangled and straw shaped open ended CNTs) and the weight loss at higher temperature ~620 °C can be assigned to oxidation of other graphitic materials (CNSs, carbon platelets).

Table 5.4 Decomposition temperatures and residual masses (determined by TGA) of the un-purified and purified (P) chlorinated N-MWCNTs generated by injecting different volume ratios of CH_3CN and DCB.

CH_3CN:DCB vol.%	**Peak 1 decomposition temperature, °C**	**Peak 2 decomposition temperature, °C**	**Residual mass, %**
100:0	643	744	28.5
100:0 (P)	540	621	8.9
66.7:33.3	557	684	22.4
66.7:33.3 (P)	560	621	5.0
33.3:66.7	560	721	24.6
33.3:66.7 (P)	560	742	7.0
20:80	586	656	32
20:80 (P)	624	721	1.8
0:100	601	695	25.7
0:100 (P)	607	–	0

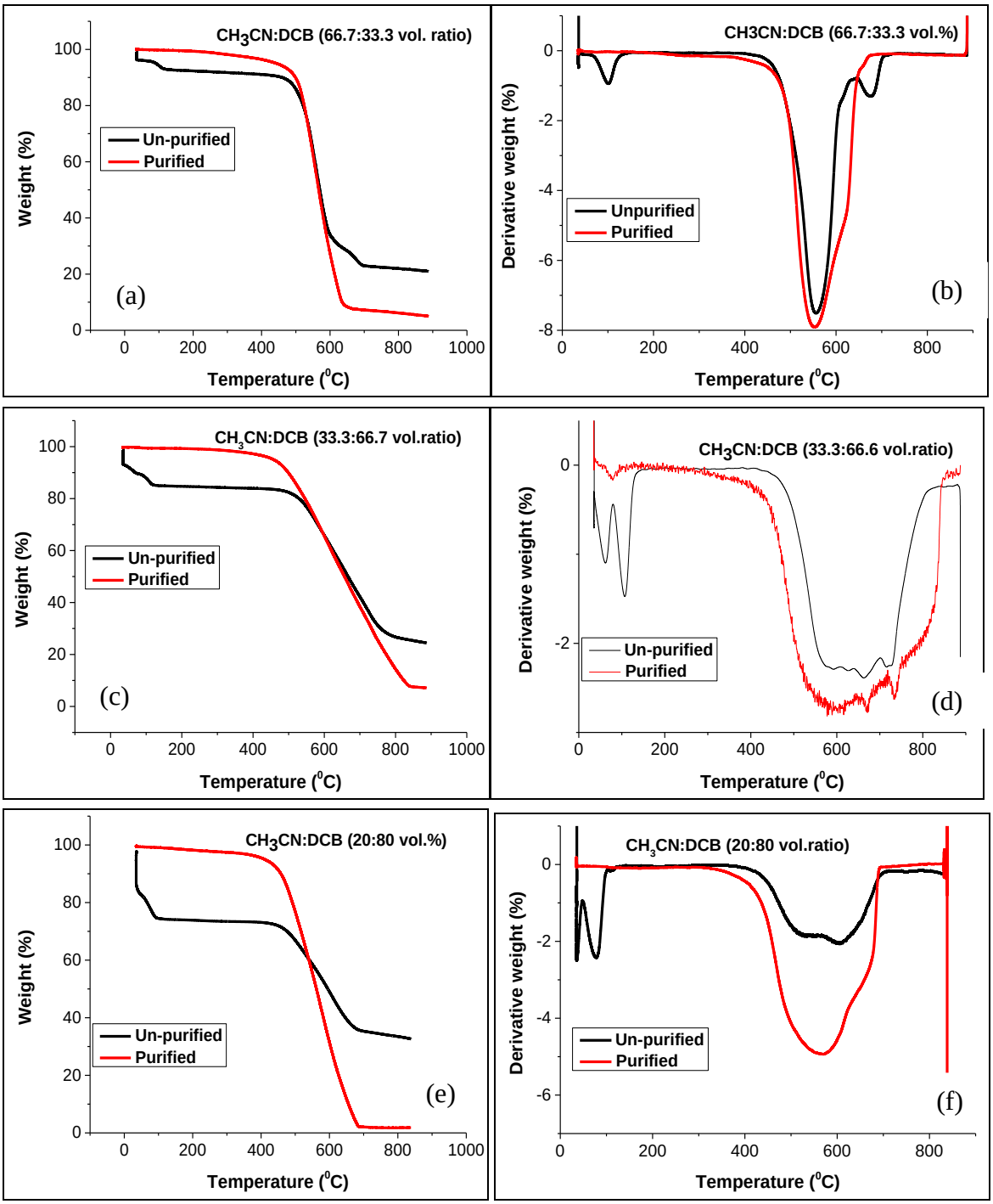

Figure 5.19 TGA and the corresponding derivative profiles of un-purified and purified CNMs generated by varying the volume ratio of CH_3CN:DCB synthesized by a CVD injection at an injection rate of 0.24 mL/min.

The thermal stability of the chlorinated N-MWCNTs produced at different injection rates was also studied using TGA. DTGA curves of the un-purified chlorinated CNMs generated from using a 0.16 mL/min injection flow rate displayed three oxidation peaks (Figure 5.20b). The mass loss at ~ 100 ° was due to physisorbed water onto the CNT walls, at ~ 564 °C was due to oxidation of chlorinated N-doped CNTs and the one at 670 °C was due to oxidation of other graphitic materials (CNSs, large CNTs with funnel-like open-ends and carbon nanoplatelets) (Figure 5.20b and d). The mass loss at 100 °C disappeared from the DTGA curves after purification, which showed removal of physisorbed water, whilst the other two mass losses at high temperature remained. The mass loss at ~ 670 °C remained the same after acid treatment for CNMs generated at 0.10 mL/min, but was greatly reduced for CNMs generated at 0.16 mL/min (Figure 5.20b and d). The residual mass observed from all the TGA curves (Table 5.5) corresponds to the metal oxide nanoparticles, which were probably embedded inside the MWCNTs and could not be removed by acid treatment. The residual mass content of the metal oxide obtained was different for each sample, and showed no apparent trend (Table 5.5).

Table 5.5 Decomposition temperatures and residual masses of the un-purified and purified (P) chlorinated N-MWCNTs generated by varying the injecting flow rate of a 66.7:33.3 vol.% CH_3CN/DCB solvent mixture.

Injection rate/mL.min^{-1}	**Decomposition temperature/°C**	**Residual mass/%**
0.10	560	21.8
0.10P	564	10.4
0.16	565	21.9
0.16P	552	3.5
0.24	567	21.1
0.24P	567	5.0

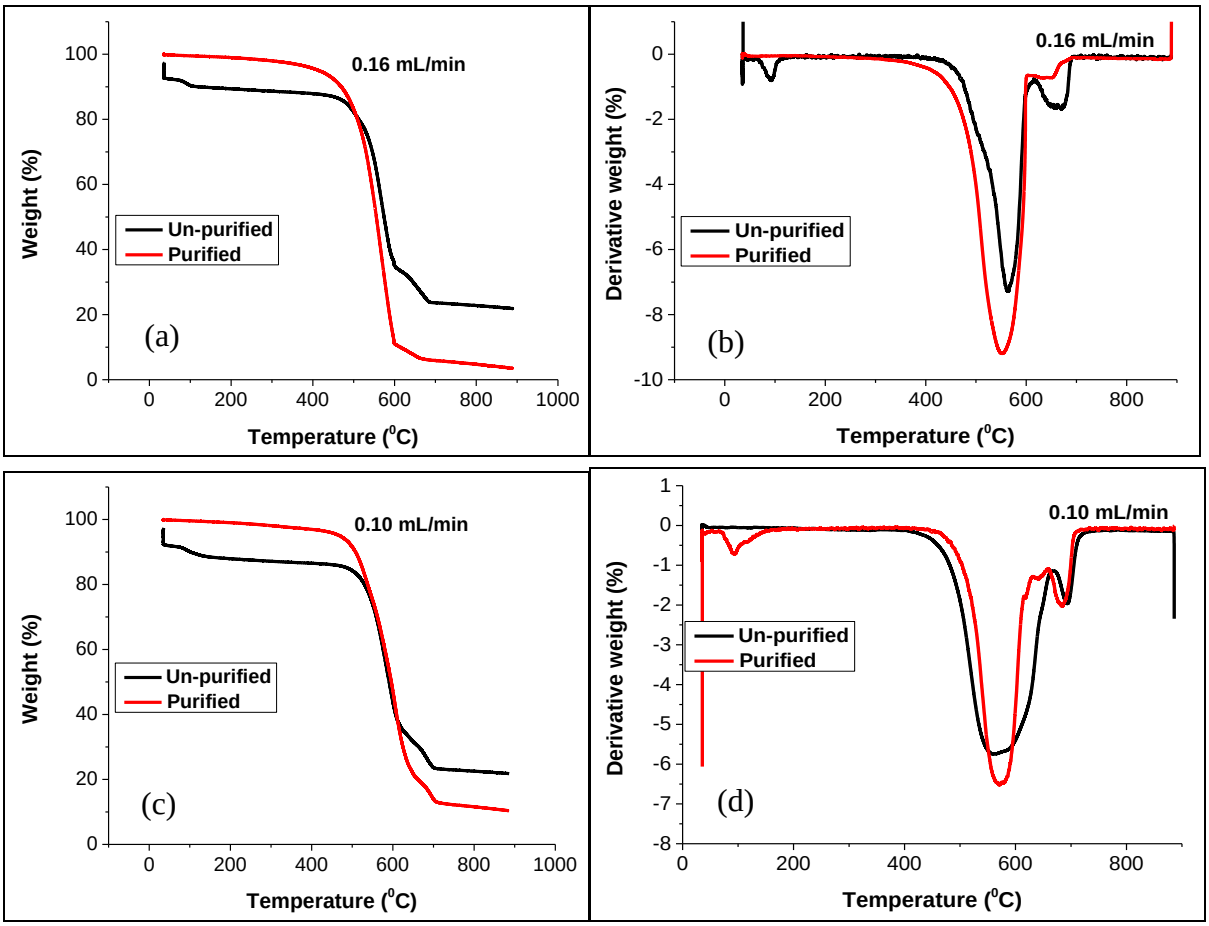

Figure 5.20 TGA and DTGA curves of the un-purified and purified chlorinated N-CNMs generated at 0.16 mL/min (a and b) and 0.10 mL/min (c and d) using a CH_3CN/DCB (66.7:33.3 vol.%) mixture.

5.3.3 Raman spectroscopy analysis of N doped CNMs: Effect of DCB concentration and injection flow rate

Raman spectra of the un-purified and purified CNMs generated from pure CH_3CN are presented in Figure 5.21 and Table 5.6. Raman spectra provides information about the graphitic nature and molecular structure of CNMs. Deconvoluted Raman spectra of the un-purified and purified CNMs showed two first-order bands, at ~ 1342 and 1576 cm^{-1}, attributed to defected graphite (D-band) and graphitic band (G-band), respectively. For un-purified CNMs, the D-band could only be deconvoluted into one band denoted as D3, the G-band was deconvoluted into two bands at 1576 cm^{-1} attributed to graphitic like carbonyl groups (denoted as D') and at 1621 cm^{-1} attributed to defected graphitic plane (Figure 5.21a). For purified CNMs, the D-band was deconvoluted into two peaks at 1272 cm^{-1} attributed to a hexagonal diamond carbon (denoted as D1) and a D3 band at 1344 cm^{-1}. The G-band was also deconvoluted into a D' at 1577 cm^{-1} and a defected graphitic plane as 1624 cm^{-1}. Second order bands were also observed in both Raman spectra. 2D band attributed to 1st overtone of a D1 band was observed at 2681 cm^{-1} for both spectra generated from pure CH_3CN. Another weak band a G* band which is a 1st overtone of a D4 band (which occurs at ~1200 cm^{-1}) appearing at 2435 cm^{-1} was observed from un-purified CNMs and is a defect activated peak. The order of crystallinity of the material can be estimated from the corresponding full-width half-maximum (FWHM). An amorphous structure leads to a FWHM of approximately 200 cm^{-1}.[36] FWHM values for all observed bands were low, suggesting that the materials generated from pure CH_3CN had no amorphous carbon. FWHM values of 60 and 63 cm^{-1} were observed for a D' band and 58 and 62 for a 2D band obtained from un-purified and purified CNMs, respectively (Table 5.6). Low I_D/I_G peak ratios of 0.56 for un-purified samples and 0.68 for purified CNMs were obtained suggesting formation of graphitic materials with less disorders (calculated from Table 5.6). There was not much difference between the un-purified and purified CNMs. These results agree with TEM observations, where mixtures of clean CNMs were obtained with no amorphous carbon materials observed, only lumps were observed which were attributed to carbon platelets materials. The ratio of $I_D/I_{D'}$ was used to provide information about the type of defects present in the material. If the ratio of $I_D/I_{D'}$ is 13, it indicates the presence of related sp^3 related defects, 10.5 corresponds to hoping defects, 7 for vacancy-like defects, 3.5 for boundary-like defects and 1.3 for on-site defects in graphene. [37,38]

The $I_D/I_{D'}$ value of 5.7 suggest that the type of defects is vacancy-like defects in addition to small boundary-like defects. Vacancy-like defects represent the single and double vacancy in the graphitic lattice (a property of a removed atom) and boundary-like arise from the scattering of phonons with defects from grain boundaries.[37,38]

Table 5.6 Raman bands of the un-purified and purified chlorinated CNTs generated from pure CH_3CN using injection CVD method at an injection rate of 0.24 mL/min

	Band name	**Band Position (cm^{-1})**	**Bond type**	**FWHM (cm^{-1})**	**Peak Area**	**Designation**
CH_3CN un-purified	D	1342	sp^2	82	3396	Disordered graphite
	G	1576	sp^2	60	5419	Graphitic like carbonyl group
	D’	1621	sp^2	35	620	Defect in graphitic plane
	G^*	2435		31	107	1^{st} overtone of D4 band
	$2D_1$	2669		51	696	1^{st} overtone of D1 band
	$2D_2$	2696		38	393	1^{st} overtone of D1 band
CH_3CN purified	D1	1272	$sp^2 – sp^3$	28	126	Hexagonal diamond carbon
	D	1344	sp^2	91	4554	Disordered graphite
	G	1577	sp^2	63	6323	Graphitic like carbonyl group
	D’	1624	sp^2	37	589	Defect in graphitic plane
	$2D_1$	2656		47	97	1^{st} overtone of D1 band
	$2D_2$	2683		59	1083	

The designation of the Raman bands was adopted from Manoj.[39]

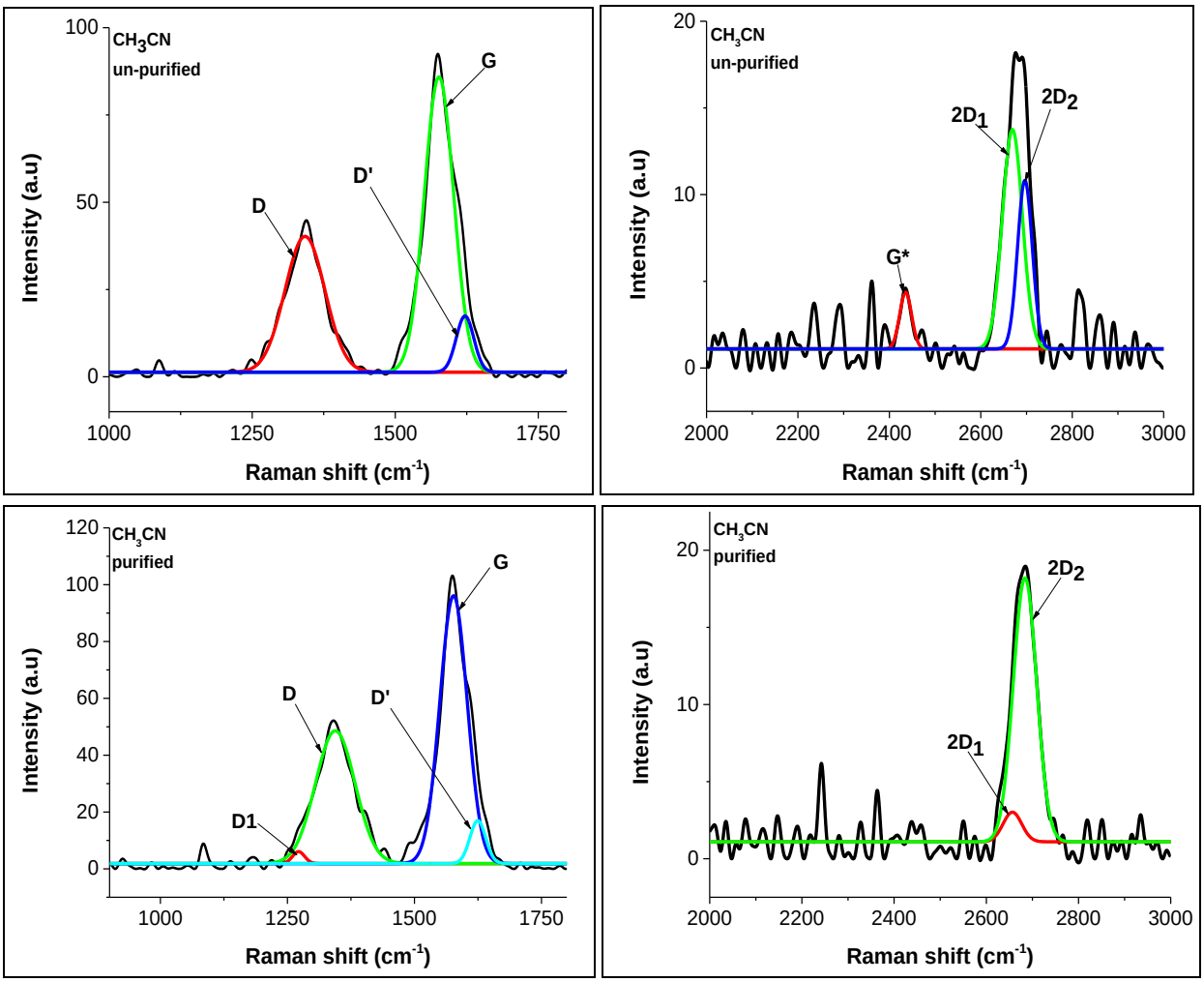

Figure 5.21 Deconvoluted Raman spectroscopy curves of purified CNMs generated from pure CH_3CN using an injection CVD method at an injection rate of 0.24 mL/min.

Raman spectra curves and data of the CNMs generated from pure DCB are presented in Figure 5.22 and Table 5.7. Deconvoluted Raman spectra of the un-purified and purified CNMs both showed three bands, attributed to a defect band (D-band) at 1337 cm^{-1}, a graphitic band (G-band) which was deconvoluted into two bands, an amorphous carbon structure induced band (D2) at 1491 and 1515 cm^{-1} and a graphitic like carbonyl group (G) at 1584 and 1587 cm^{-1}, respectively (Figure 5.23). Second-order bands were also observed in both un-purified and purified samples, a 1st overtone of D4 band (band at 1200 cm^{-1}) at 2444 and 2453 cm^{-1} (G^*), a 1st overtone of D1 band at 2683 cm^{-1} (2D) and a very weak overtone of D2 band at 2929 and 2926 cm^{-1} (D + G) (Figure 5.23). A 2D band was split into two bands for both un-purified and purified CNMs. This

split has been described as a characteristic feature of undisturbed or highly ordered graphitic lattices.[40] The spliting of the 2D band was also assigned to splitting's of the π and π* electronic states, owing to the interactions between the succesive layer planes.[41] The G* band has been classified as a defect activated peak.[42] The presence of a D + G band shows characteristics of disturbed graphitic structures, as a result of functionalization with chlorine.

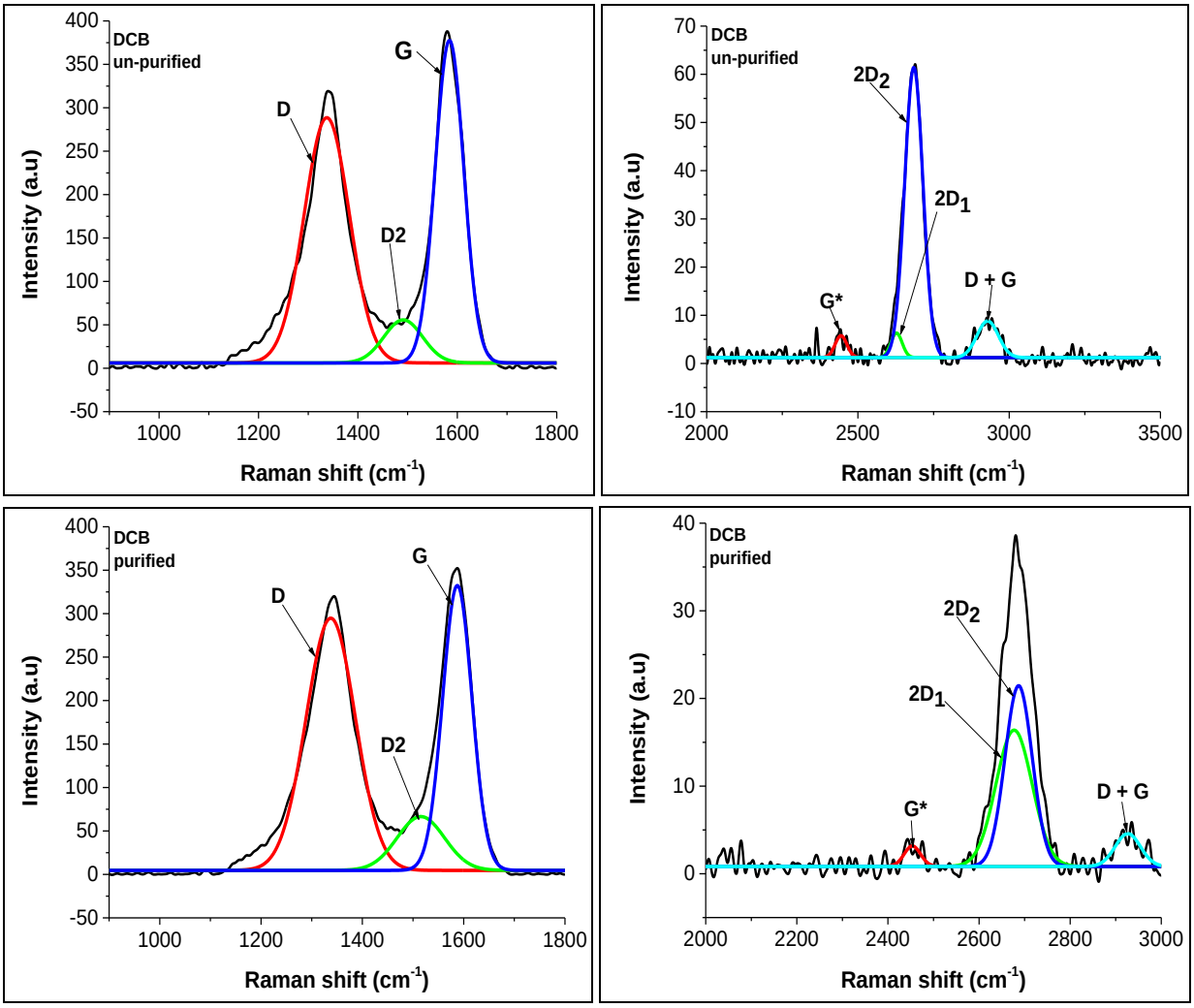

Figure 5.22 Raman spectroscopy curves of un-purified and purified CNTs generated from pure DCB using an injection CVD method at an injection rate of 0.24 mL/min

The I_D/I_G ratio of 1.2 and 1.5 for un-purified and purified CNMs also suggest that the materials are highly disordered (Table 5.7). FWHM values for all observed bands were high, suggesting

the presence of amorphous carbon structures. FWHM values of 68 and 72 cm^{-1} were observed for a G band and $2D_1$ band obtained from un-purified and purified CNMs (Table 5.7). Similar I_D/I_G peak ratio were obtained 1.0 for un-purified CNMs and 1.1 for purified CNMs. Peak ratios were high (~1) as compared to those generated from CH_3CN (~0.6) which shows that functionalization of CNMs with chlorine created more defects on the walls of the CNTs.

Table 5.7 Raman bands of the un-purified and purified chlorinated CNTs generated from pure DCB using injection CVD method at an injection rate of 0.24 mL/min

	Band name	**Band Position (cm^{-1})**	**Bond type**	**FWHM (cm^{-1})**	**Peak Area**	**Designation**
DCB un-purified	D	1337	sp^2	107	32236	Disordered graphite
	D2	1491	sp^3	92	4837	Amorphous carbon structure
	G	1584	sp^2	67	26732	Graphitic like carbonyl group
	G^*	2444		46	221	1^{st} overtone of D4 band
	$2D_1$	2627		44	239	1^{st} overtone of D1 band
	$2D_2$	2684		72	4548	1^{st} overtone of D1 band
	D + G	2929		83	671	2D overtone
DCB purified	D	1337	sp^2	114	35362	Disordered graphite
	D2	1515	sp^3	110	7251	Amorphous carbon structure
	G	1587	sp^2	68	23737	Graphitic like carbonyl group
	G^*	2453		42	105	1^{st} overtone of D4 band
	$2D_1$	2677		93	1544	1^{st} overtone of D1 band
	$2D_2$	2687		70	1544	
	D + G	2926		65	261	2D overtone

From the above observations it is clear that both chlorine and nitrogen play a certain role on the morphology and properties of the Cl/N doped carbon nanomaterials.

The role of chlorine on the graphitic nature of the N doped CNMs was also evaluated using Raman Spectroscopy. Raman curves of un-purified chlorinated N doped CNMs are presented in Figure 5.23. Un-purified CNMs generated from solutions containing 33.3 vol.% DCB and 66.7 vol.% CH_3CN, revealed the presence of D-band and G-band (Figure 5.23). For un-purified CNMs generated from a 33.3 vol.% DCB, a broad D-band was deconvoluted into two bands a weak band at 1182 attributed to C=C strecthing vibrations and and a broad dominating band at 1349 cm^{-1} due to disordered CNMs (Figure 5.23a). Both Cl and N created disorders in the graphitic lattice. A G-band was also deconvoluted into three bands at 1492, 1585 and 1601 cm^{-1} attributed to amorphous carbon structure, graphitic lattices and defects in the graphitic lattice. A deconvoluted spectra recorded from un-purified CNMs generated from solutions containing 66.7 vol.% DCB, showed a single D band and a G band that was deconvoluted into two bands at 1515 and 1593 cm^{-1} (Figure 5.23). A defected D' band was not observed from this CNMs, this could be attributed to the surface purification of the CNMs by chlorine resulting in formation of highly graphitic materials. A D band was still broad, this could be attributed to creation of defects due to functionalization of CNMs with chlorine. The presence of several CNMs of various morphologies observed from the TEM images could also contribute to the amount of defects created. A deconvoluted spectra recorded from un-purified CNMs generated from solutions containing 80 vol.% DCB, showed a broad D band that was deconvoluted into two bands at 1181 and 1346 cm^{-1} and a G band that was deconvoluted into two bands at 1508 and 1591 cm^{-1} (Figure 5.23). A defective graphitic lattice D' band was also not observed from these Raman curves. The large $I_D/I_{D'}$ value of 10 suggest that the type of defects is hopping defects in addition to small sp^3 related defects. Hoping defects represents any defects that distort the bonds between carbon atoms, retaining the general sp^2 configuration and sp^3 related defects arise due to covalent sp^3 bonded functional groups on the carbon atoms.[37,38]

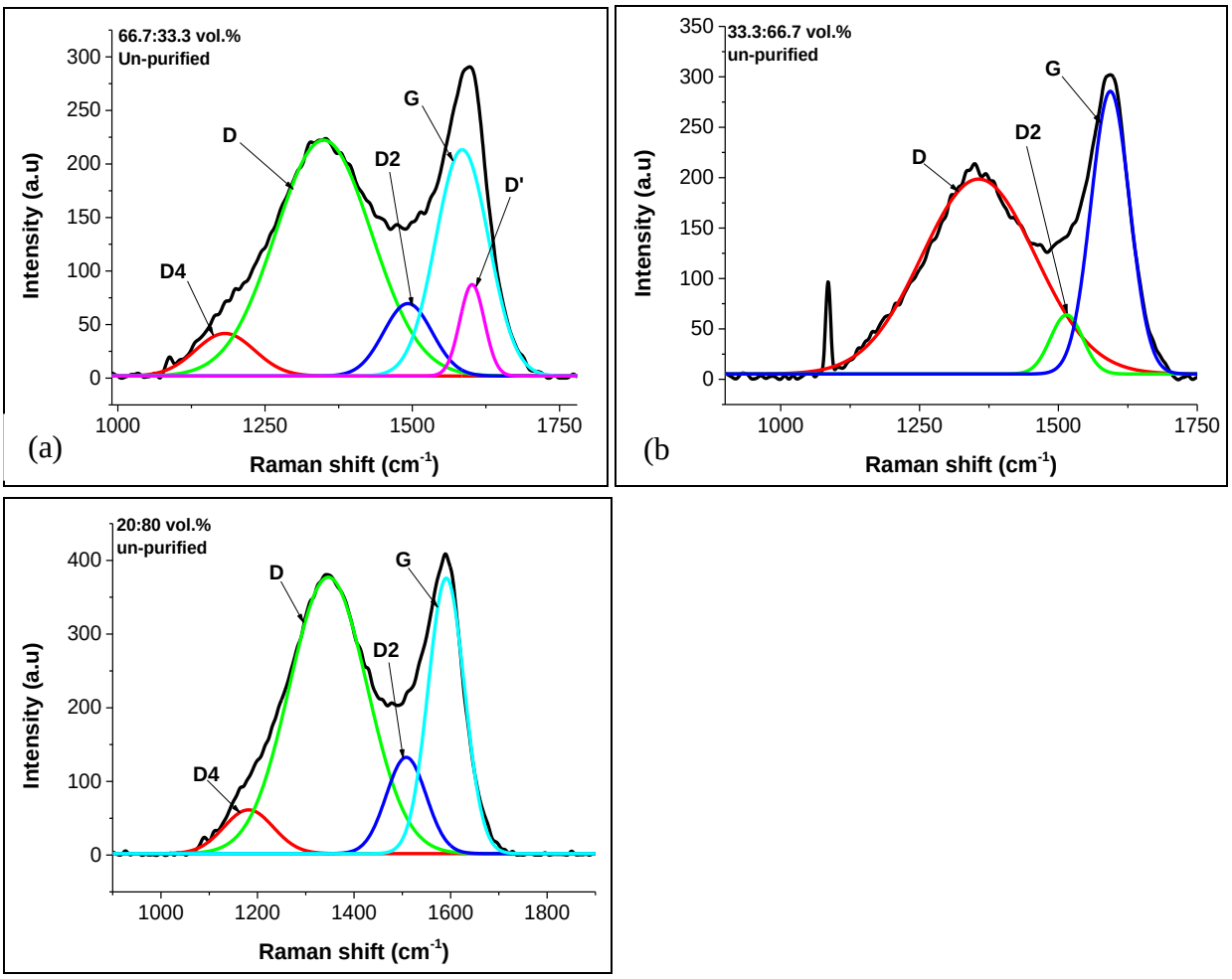

Figure 5.23 Deconvoluted Raman spectroscopy curves of un-purified CNMs generated from various vol.% of CH_3CN:DCB solution using an injection CVD method at an injection rate of 0.24 mL/min.

The I_D/I_G ratio of 1.4, 1.7 and 1.7 were obtained for un-purified CNMs generated from 33.3, 66.7 and 80 vol.% DCB solutions, which suggets highly defected materials (Table 5.8). Large FWHM values for all observed bands shows that the materials contained some amorphous carbon structures (Table 5.8).

Table 5.8 Raman bands of the un-purified CNMs generated from various volume ratios of a CH_3CN:DCB solution mixture using injection CVD method at an injection rate of 0.24 mL/min

CH_3CN:DCB Volume ratio (%)	**Band name**	**Band Position (cm^{-1})**	**Bond type**	**FWHM (cm^{-1})**	**Peak Area**	**Designation**
66.7:33.3	D4	1182	$sp^2 – sp^3$	118	4996	C=C stretching vibrations
	D	1349	sp^2	192	44968	Disordered graphite
	D2	1492	sp^3	97	6988	Amorphous carbon structure
	G	1585	sp^2	105	23770	Graphitic like carbonyl group
	D’	1601	sp^2	49	4465	Defect in graphitic plane
33.3:66.7	D	1356	sp^2	240	49532	Disordered graphite
	D2	1515	sp^3	68	4268	Amorphous carbon structure
	G	1593	sp^2	82	24424	Graphitic like carbonyl group
20:80	D4	1181	$sp^2 – sp^3$	120	7622	C=C stretching vibrations
	D	1346	sp^2	189	75621	Disordered graphite
	D2	1508	sp^3	97	13532	Amorphous carbon structure
	G	1591	sp^2	88	35092	Graphitic like carbonyl group

Defects in the graphitic structure were created after purification of the CNMs generated from all studied concentrations of DCB. Amorphous carbon structures were greatly reduced in the CNMs generated from solutions containing 33.3 and 66.7 vol.% DCB. Amorphous carbon structures

were compeletely removed by acid treatment from CNMs generated from solutions containing 80 vol.% DCB. CNMs generated from feeds solutions containing 66.7 vol.% DCB were highly defected, as shown by a large broad D peak. Second order bands were also observed from purified CNMs generated from solutions containing 33.3 and 80 vol.% DCB. A G^* band at ~2400 and a 2D band that was split into two bands (Figure 5.24 and Table 5.9). A defect induced G^* band was very weak for both, while a 2D band was weak for CNMs generated from feeds containing 33.3 vol.% DCB and very intense for CNMs generated from feeds containing 80 vol.% DCB CNMs, suggesting that the latter materials were highly graphitic. Another weak defect induced band (D + G band) at ~2900 cm^{-1} was observed from purified CNMs generated from solutions containing 80 vol.% DCB (Figure 5.24).

The I_D/I_G ratios of 0.72, 1.8 and 0.63 were obtained for purified CNMs generated from 33.3, 66.7 and 80 vol.% DCB (calculated from Table 5.9). I_D/I_G values showed that defects in the CNMs increased with an increase in the amount of chlorine in the feed, but then decreased with a further increase in the concentration of DCB to 80 vol.% in the feed. This results suggests that the highest functionalization of CNMs with chlorine was achieved from feeds that contained 66.7 vol.% DCB. The great involvement of chlorine in creation of defects in these feed was also observed from the changes in morphology of the CNMs from their TEM images, where "pencil-shaped" CNMs of various sizes, some with closed-ends and others with open-ends were observed. An $I_D/I_{D'}$ value of 16 which is due to the presence of sp^3 related defects, was obtained for purified CNTs generated from solutions containing 33.3 vol.% DCB. An I_D/I_G value of 9.3 due to vacancy-like defects and hoping defects was obtained from feeds containing 66.7 vol.% DCB. An $I_D/I_{D'}$ value of 3.7 which is due to boundary-like defects was obtained from solutions containing 80 vol.% DCB. FWHM values were 70, 116 and 39 for a G-band of CNMs generated from 33.3, 66.7 and 80 vol.%, respectively (Table 5.9), which are in correlation with the I_D/I_G values. We can also conclude that CNMs generated from feed solutions containing 66.7 vol.% DCB, contained huge amounts of defects. Materials generated from feeds containing 80 vol.% DCB were the most graphitic, based on the FWHM and I_D/I_G values. These data agree with the TGA observations where a broad oxidation peak with multiple oxidation peaks at ~ 450 to 800 °C was observed for CNMs generated from feed solutions containing 66.7 vol.% DCB, assigned to oxidation of various types of defected CNMs.

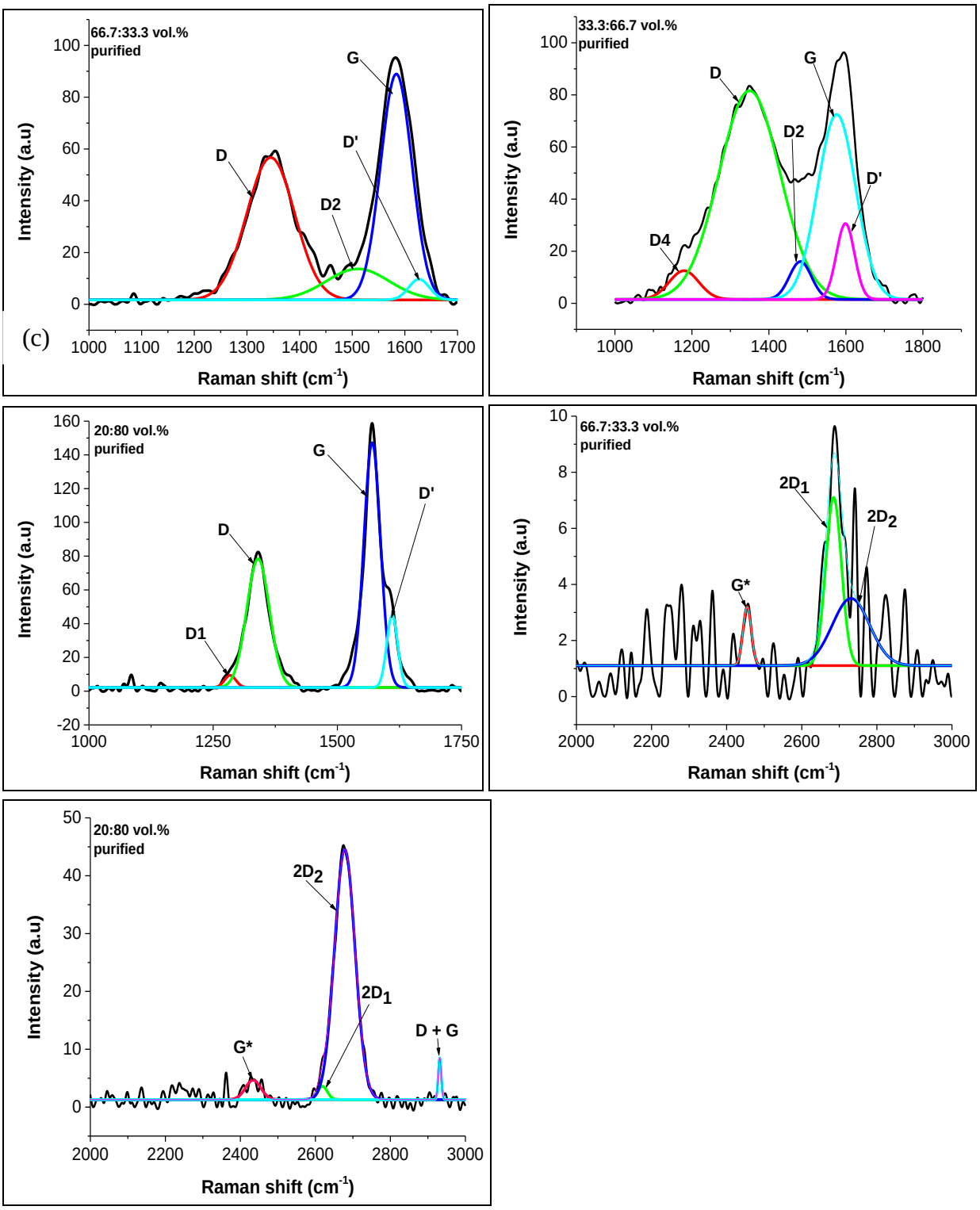

Figure 5.24 Deconvoluted Raman spectroscopy curves of purified CNMs generated from various vol.% of CH_3CN:DCB solution using an injection CVD method at an injection rate of 0.24 mL/min.

Table 5.9 Raman bands of the purified CNMs generated from various volume ratios of a CH_3CN:DCB solution mixture using injection CVD method at an injection rate of 0.24 mL/min

CH_3CN:DCB Volume ratio (%)	**Band name**	**Band Position (cm^{-1})**	**Bond type**	**FWHM (cm^{-1})**	**Peak Area**	**Designation**
66.7:33.3	D	1345	sp^2	107	6275	Disordered graphite
	D2	1510	sp^3	140	1786	Amorphous carbon structure
	G	1583	sp^2	70	6472	Graphitic like carbonyl group
	D’	1626	sp^2	46	393	Defect in graphitic plane
	G^*	2455		26	57	1^{st} overtone of D4
	$2D_1$	2684		49	314	1^{st} overtone of D1
	$2D_2$	2731		117	298	1^{st} overtone of D1
33.3:66.7	D4	1179	$sp^2 – sp^3$	91	1064	C=C stretching vibrations
	D	1349	sp^2	186	15915	Disordered graphite
	D2	1482	sp^3	67	1043	Amorphous carbon structure
	G	1576	sp^2	116	8785	Graphitic like carbonyl group
	D’	1599	sp^2	55	1705	Defect in graphitic plane
20:80	D1	1284	$sp^2 – sp^3$	27	205	Hexagonal diamond carbon
	D	1340	sp^2	54	4405	Disordered graphite
	G	1570	sp^2	39	6080	Graphitic like carbonyl group
	D’	1610	sp^2	25	1176	Defect in graphitic plane
	G^*	2434		48	172	1^{st} overtone of D4 band
	$2D_1$	2618		30	74	1^{st} overtone of D1 band
	$2D_2$	2678		64	2966	1^{st} overtone of D1 band
	D + G	2931		9	72	2D overtone

Raman spectra analysis was also performed for materials generated from varying the injection flow rate. Deconvoluted Raman spectroscopy curves of un-purified and purified CNMs generated from a 66.7 vol.% DCB solution at an injection rate of 0.16 mL/min are presented in Figure 5.25. A D, G, G^*, 2D, D+G and 2D' bands were observed from un-purified CNMs (Figure 5.25). A G-band was deconvoluted into two bands, an amorphous D2 band and a graphitic G band at 1493 and 1581 cm^{-1}, suggesting the presence of amorphous carbon in the CNMs. A 2D band was also deconvoluted to two bands a $2D_1$ and $2D_2$ bands at 2676 and 2720 cm^{-1}, suggesting the formation of highly graphitic CNMs of multiple layers. Raman spectroscopy of the purified CNMs revealed bands assigned to D, G, G^*, 2D and D+G (Figure 5.25). A D-band was deconvoluted into two bands at 1212 and 1344 cm^{-1} attributed to a D4 and D band. A G-band was deconvoluted into two bands at 1511 and 1585 cm^{-1} attributed to D2 and G band respectively. A G^* and a D2 (amorphous carbon) peaks were enhanced after purification, indicating increase in defects (Figure 5.25c and d). A 2D peak was greatly reduced after purification which suggest increase in the amount of disorders in the CNMs.

I_D/I_G values of 1.28 and 0.97 were obtained from un-purified and purified CNMs generated from a 0.16 mL/min injection rate (Table 5.10), showing that the two CNMs were not that different. Comparing with an I_D/I_G value of 0.72 obtained from CNMs generated from a 0.24 mL/min injection rate, we suggest that the materials generated at 0.24 mL/min were more graphitic. FWHM values of 73 and 70 were obtained for G bands of purified CNMs generated from 0.16 and 0.24 mL/min injection rates, respectively which again favored a 0.24 mL/min injection rate as the optimum with less amorphous carbon structures.

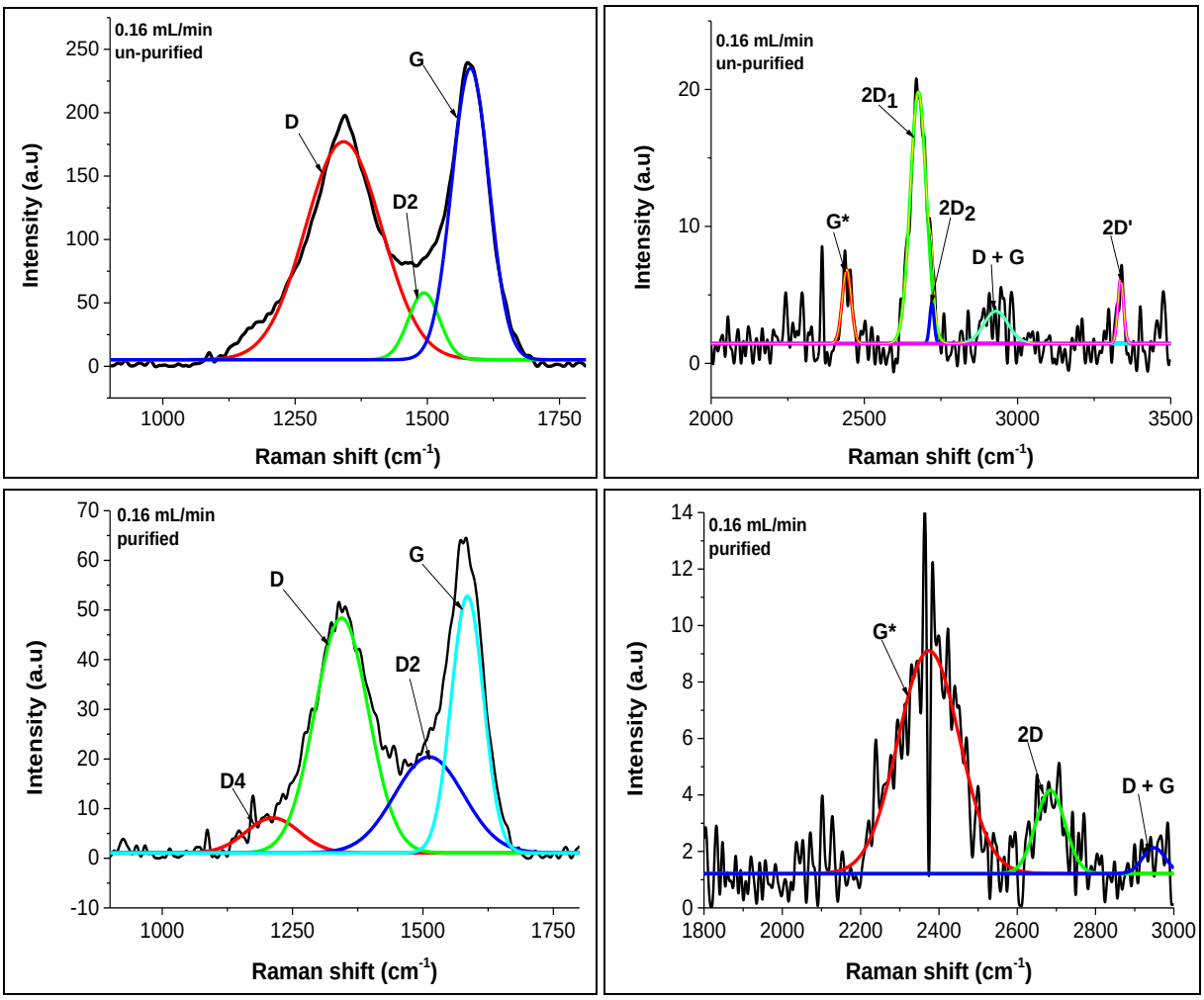

Figure 5.25 Deconvoluted Raman spectroscopy curves of un-purified and purified CNMs generated from a solutions containing 66.7:33.3 vol.% of CH_3CN:DCB using an injection CVD method at an injection rate of 0.16 mL/min

Table 5.10 Raman spectra analysis of the un-purified CNMs generated a 66.7:33.3 vol.% CH_3CN:DCB solution mixture using an injection CVD method at an injection rate of 0.16 mL/min

0.16 mL/min injection rate	Band name	Band Position (cm^{-1})	Bond type	FWHM (cm^{-1})	Peak Area	Designation
Un-purified	D	1341	sp^2	170	31071	Disordered graphite
	D2	1493	sp^3	69	3903	Amorphous carbon structure
	G	1581	sp^2	83	20352	Graphitic like carbonyl group
	G^*	2442		34	199	1^{st} overtone of D4
	$2D_1$	2676		61	1202	1^{st} overtone of D1
	$2D_2$	2720		17	52	1^{st} overtone of D1
Purified	D4	1212	$sp^2 – sp^3$	120	903	C=C stretching vibrations
	D	1344	sp^2	120	6086	Disordered graphite
	D2	1511	sp^3	156	3212	Amorphous carbon structure
	G	1585	sp^2	73	4008	Graphitic like carbonyl group
	G^*	2377		184	1544	1^{st} overtone of D4
	2D	2684		88	275	1^{st} overtone of D1
	D + G	2949		68	66	2D overtone

Deconvoluted Raman spectroscopy curves of un-purified and purified CNMs generated from a 66.7 vol.% DCB solution at an injection rate of 0.10 mL/min are presented in Figure 5.26. A D and G bands were observed from un-purified and purified CNMs. For both un-purified and purified CNMs, a D-band was deconvoluted into two peaks, a D4 band and a D band and a G-band was deconvoluted into two peaks, a D2 band and a G band.

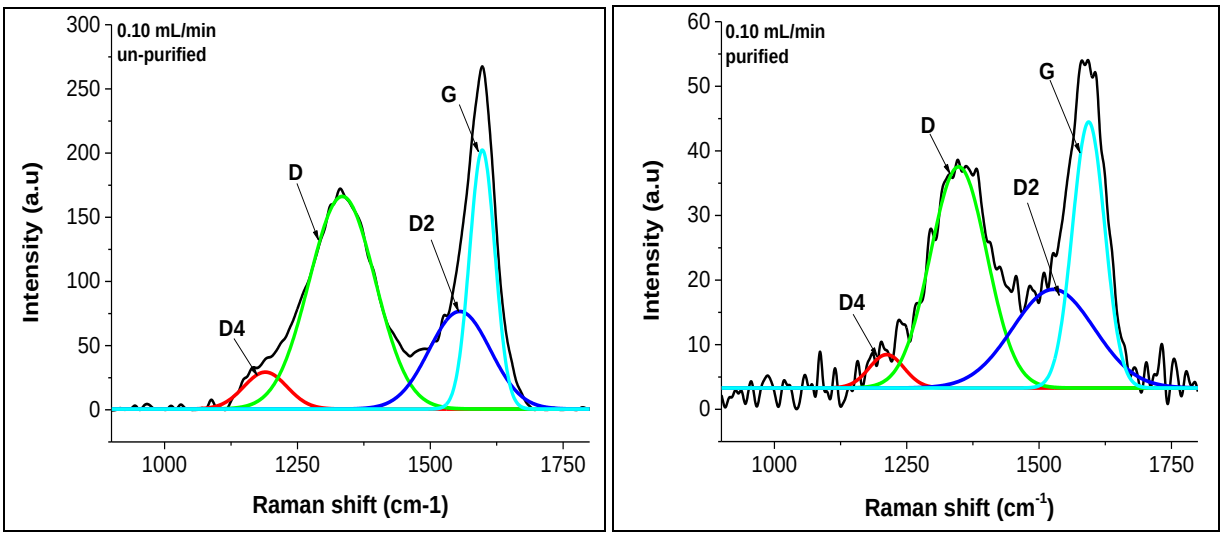

Figure 5.26 Deconvoluted Raman spectroscopy curves of un-purified and purified CNMs generated from a solutions containing 66.7:33.3 vol.% of CH_3CN:DCB using an injection CVD method at various injection rates.

I_D/I_G values of 1.4 and 0.82 were obtained from un-purified and purified CNMs generated from 0.10 mL/min injection rate (Table 5.11), showing that impurities or some materials were removed by purification. Comparison with an I_D/I_G value of 0.72 obtained from CNMs generated from a 0.24 mL/min injection rate, we conclude that the materials generated at 0.24 mL/min were more graphitic. FWHM value of 71 and 70 were obtained from G bands of purified CNMs generated from 0.10 and 0.24 mL/min injection rates, respectively which again favored both materials. We can conclude that 0.24 mL/min injection rate was a good choice since its Raman analysis showed that its materials were more graphitic, even though the difference is not that huge from other injection rates. The data is consistent with the TEM analysis were similar carbon nanostructures were obtained at all three injection rates.

Table 5.11 Raman spectra analysis of the un-purified CNMs generated a 66.7:33.3 vol.% CH_3CN:DCB solution mixture using an injection CVD method at an injection rate of 0.10 mL/min

0.10 mL/min injection rate	Band name	Band Position (cm^{-1})	Bond type	FWHM (cm^{-1})	Peak Area	Designation
Un-purified	D4	1189	$sp^2 – sp^3$	95	2924	C=C stretching vibrations
	D	1334	sp^2	146	29714	Disordered graphite
	D2	1555	sp^3	76	10978	Amorphous carbon structure
	G	1598	sp^2	56	12075	Graphitic like carbonyl group
Purified	D4	1212	$sp^2 – sp^3$	77	424	C=C stretching vibrations
	D	1348	sp^2	125	4572	Disordered graphite
	D2	1527	sp^3	181	2948	Amorphous carbon structure
	G	1593	sp^2	71	3139	Graphitic like carbonyl group

5.3.4 X-ray photoelectron analysis of N doped CNMs: Effect of DCB concentration

Three main peaks were observed from the wide scan XPS spectra of the N doped MWCNTs produced from pure acetonitrile at 284.2, 400 and 531 eV and were attributed to C 1s, N 1s and O 1s, respectively (Supplementary Figure S13). Three main peaks were also observed in the wide scan XPS spectra of chlorine functionalized MWCNTs produced from pure DCB. This peaks occured at 200, 284.2, and 531 eV and were attributed to Cl 2p, C 1s and O 1s, respectively (Supplementary Figure S13).

The deconvoluted C 1s peak for materials obtained from pure CH_3CN, was fitted into four components with binding energies 283.5, 284.8, 287.4 and 290.7 eV, the first two peaks were

attributed to graphite-like C–C sp^2 and sp^3 bonds, the next two to C–N and O–C=O bonds, respectively (Supplementary Figure S14). The relative broadness of the C–N peak was attributed to the lattice distortion introduced by nitrogen doping and that of the O–C=O was attributed to mixing of various CO-type bonds.[43,44] The deconvoluted C 1s peak for materials obtained from pure DCB, was fitted into four components with binding energies 283.4, 284.5, 287.7 and 290.1 eV, attributed to graphite-like C–C sp^2, C–C sp^3, C–Cl and O–C=O bonds, respectively (Supplementary Figure S14).

The deconvoluted C 1s peaks of all the studied N-doped materials that contained chlorine, were fitted into four components. The peaks were at the following binding energies 283.6–284.8, 287 and 287–290 eV and were attributed to C–C sp^2 and sp^3 carbon bonds, C–N or C–Cl groups and O–C=O carboxylic groups, respectively (Supplementary Figure S6). CNTs generated from a mixture of CH_3CN/DCB showed a broad peak at ~ 287 eV which was attributed to overlap between C–N and C–Cl groups. The intensity of this peak at ~287 eV increased after addition of DCB in the feed, which suggest formation of new C–Cl bonds which overlap with a C–N bond. Covalent bonding between carbon and chlorine was also suggested in the Raman data where the degree of disorder was found to increase with addition of chlorine due to formation of new sp^3 C–Cl bonds. The formation of sp^3 C – Cl bonds was evidenced by the presence of an additional peak an amorphous D2 peak, occuring from the Raman spectra of chlorinated CNMs (Figure 5.23 to 5.26).

The high resolution N 1s XPS spectra recorded for pure CH_3CN consisted of four peak components at 399.3, 401, 402.7 and 405.8 eV binding energies (Figure 5.27a). The peaks at 399.3 and 401.0 eV were attributed to pyrrolic ($N_{Pyr)}$ and quaternary nitrogen (N_Q). Quaternary nitrogen corresponds to substitution of carbon atoms located in the graphene sheet by nitrogen. The peak at 402.7 eV was attributed to oxidized nitrogen ($N_{Ox)}$ which was bonded to oxygen.[45] The peak at 405.8 eV was attributed to molecular nitrogen (N_{Mo}), since molecular nitrogen can be encapsulated inside the tubes[46] or can exist in an intercalated form between graphite layers during the formation of CN_x tubes.[47] Molecular nitrogen was the dominant peak in this case and pyridinic nitrogen was not observed. Other authors have attributed the N 1s peaks at 405.3 – 406.1 eV to the nitrogen atoms that form endohedral or exohedral complex with carbon-carbon

bond on the tube walls and called them sorbed nitrogen.[47] It has also been shown that these nitrogen atoms are covalently bound to the CNTs.[48] The peaks at ~407.8 – 408.9 eV were attributed to molecular nitrogen.[46]

Wide scan XPS spectra of chlorinated N-doped CNMs generated at various volume ratios of CH_3CN:DCB are presented in Supplementary Figure S15. Four peak components were observed from this spectra at ~ 200, 284, 400 and 531 eV, attributed to Cl2p, C1s, N1s and O1s, respectively.

The N1s peak for N-doped CNMs generated after addition of various concentrations of DCB are presented in Figure 5.27b to d. Addition of 33.3 and 66.7 vol.% of DCB to CH_3CN resulted in a solution with 1:0.25 and 1:1 molar ratios CH_3CN:DCB. The CNMs produced from these mixtures revealed an increase in the peak intensity ratio of the N_Q and the N_{Ox} species (Figure 5.27b,c and Figure 5.29a), while the peak intensities of the N_{Pyr} and the N_{Mo} were greatly reduced (Table 5.12). The pyridic nitrogen (N_P) peak was also present and appeared at 397.5 and 398.4 eV for CNMs generated from solutions containing 33.3 and a 66.7 vol.% DCB, respectively (Figure 5.27b and c and Table 5.12). The N_P peak increased in intensity with an increase in the amount of DCB in the feed up to 66.7 vol.%, but this peak was abscent in solutions containing no DCB (0 vol.%) and very large 80 vol.% DCB (Figure 5.27a,d and Figure 5.29a). Increasing the nitrogen concentration was shown to give rise to an increase in the peak intensity of the N_P peak.[49] Pyridine-like nitrogen atoms, contribute to the π system with a pair of π electrons and are bonded to two C atoms (C–N=C), which has been associated with generation of bamboo-like structures.[50] The intensity of the quaternary nitrogen peak increased with the introduction of chlorine in the system from pure CH_3CN to CH_3CN solutions containing 33.3 vol.% DCB, but decreased with a further increase in DCB concentration to 66.7 vol.% (Figure 5.29a). Increased functionalization of carbon atoms in CNMs with Cl appears to interfere with N doping, we suspect that N-substitution of carbon atoms in the CNM lattice will occur readily on non-functionalized carbon atoms. Highly disorderd CNMs were observed from Raman spectra of CNMS generated from a 66.7 vol.% DCB solution due to increased functionalization of the CNMs with chlorine. A great involvement of chlorine was also observed from the TEM images where a change in the morphology of the CNMs was evident from CNMs generated from solutions containing 66.7 vol.% DCB. A further increase in the DCB concentration in the

CH_3CN feed from 66.7 to 80 vol.%, resulted in an increase in the intensity of the N_Q peak, and the disappearance of a N_P peak (Figure 5.27d and Table 5.12). This was attributed to a less defected graphene sheet, due to reduced functionalization of CNMs with chlorine. This is consistent with the Raman data where a decrease in the I_D/I_G peak ratio to 0.63 was obtained at 80 vol.% DCB concentration.

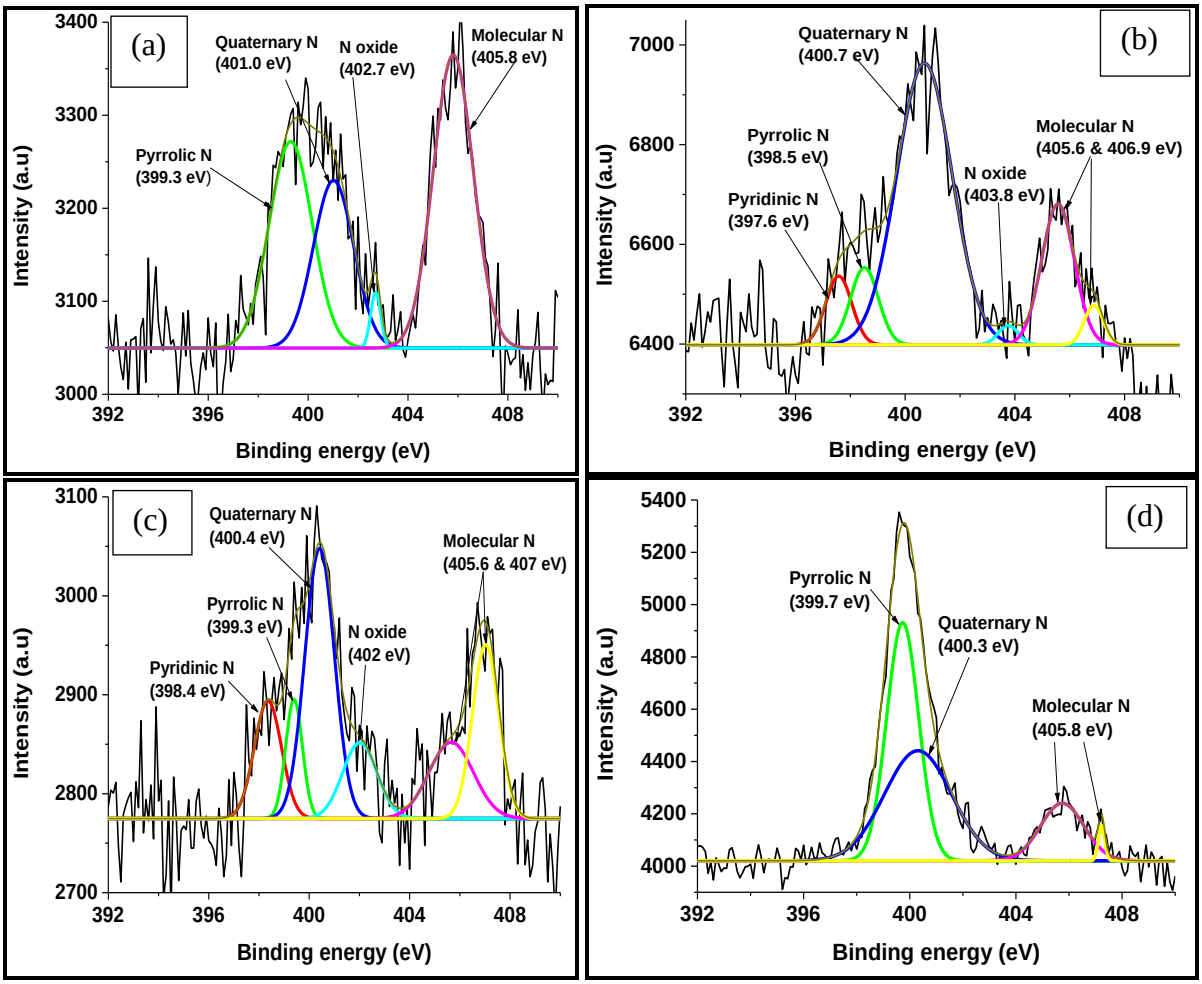

Figure 5.27 N 1s XPS spectra of purified CNTs generated from (a) pure CH_3CN, (b) 66.7:33.3 (c) 33.3:66.7 and (d) 20:80 vol.% of CH_3CN:DCB synthesized by an injection CVD at 0.24 mL/min.

Table 5.12 Nitrogen content and type of the N-species incorporated in the chlorinated N-MWCNTs grown at various volume ratios of CH_3CN:DCB solution.

CH_3CN:DCB volume ratio (mole ratio)	**Pyridinic N_P /(%)**	**Pyrrolic N_{Pyr}/(%)**	**Quaternary N_Q /(%)**	**Absorbed N or Nitrogen oxides N_{Ox}/(%)**	**Molecular N_{Mo} /(%)**
100:0 (1:0)	–	31.8	24.2	2.01	42.0
66.7:33.3 (1:0.25)	7.1	8.5	61.7	19.7	3.0
33.3:66.7 (1:1)	13.5	8.4	33.6	25.2	19.3
20:80 (1:2)	-	43	41.7	14.1	1.2

The deconvoluted Cl 2p XPS curves for CNTs generated from DCB and CH_3CN:DCB of various ratios were also recorded to determine the degree of chlorine functionalization at various DCB concentrations. Two or three distinct peaks at ~198, 200 and 202 eV, were observed from the deconvoluted Cl 2p spectra (Figure 5.28a,b, c, and d). For the CNTs generated from pure DCB, two peaks appearing at 200.1 and 201.7 eV were observed (Figure 5.28a). This peaks were attributed to C–Cl bonds, which indicate covalent bonding between chlorine and carbon atoms from the CNTs. CNTs generated from mixtures of CH_3CN:DCB of various volume ratios showed two peaks at binding energies ~ 198 and 200 eV (Figure 5.28a and b). Each of the Cl 2p peak was split into two peaks, where the first two peaks located at the lower binding energy ~ 198 eV were assigned to the ionic state of Cl and the two peaks located at higher binding energies ~ 200 eV were assigned to covalently bonded Cl. The two peaks appearing at ~200 and 201 eV were assigned to Cl–C=O and covalent C–Cl bonds, respectively. The two Cl 2p peaks appearing at ~ 198 eV were assigned to the presence of a chloride ion propably bonded to metal catalyst particles or ionically bonded to the CNT. From the TGA analysis it was shown that residual metal catalyst were still present after purification. The intensity of the Cl 2p peak at lower binding energies increased with an increase in the DCB concentration from 33.3 to 66.7 vol.%, but this peak was abscent from CNTs generated from 80 vol.% DCB and pure DCB solutions (Table 5.13). This data is consistent with TGA data where the residual mass remained after purification of CNMs generated from a 33.3 and 66.3 vol.% DCB solutions. No residual mass was observed from the CNMs generated from pure DCB and solutions containing 80 vol.% DCB, which agree with the absence of a chloride ion peak in the Cl 2p XPS spectra. The I_D/I_G

peak ratio slightly increased after addition of DCB as defects increased, from 0.68 (for pure CH_3CN) to 0.72 (for solutions containing 33.3 vol.% DCB). This was shown by an increase in the percentage of a Cl $2p_{1/2}$ peak at ~201 eV (Figure 5.29b) and was attributed to introduction of new sp^3 C–Cl bonds. A further increase in the DCB concentration to 66.7 vol.% resulted in a huge increase in the I_D/I_G value to 1.5, due to an increase in the number of C–Cl bonds. A further increase in the DCB concentration to 80 vol.% resulted in a huge decrease in the I_D/I_G peak ratio to 0.63 (Figure 5.29b). It was suggested that at high concentrations of DCB there was a release of Cl_2 gas to the trap, which resulted in production of fewer C–Cl covalent bonds.

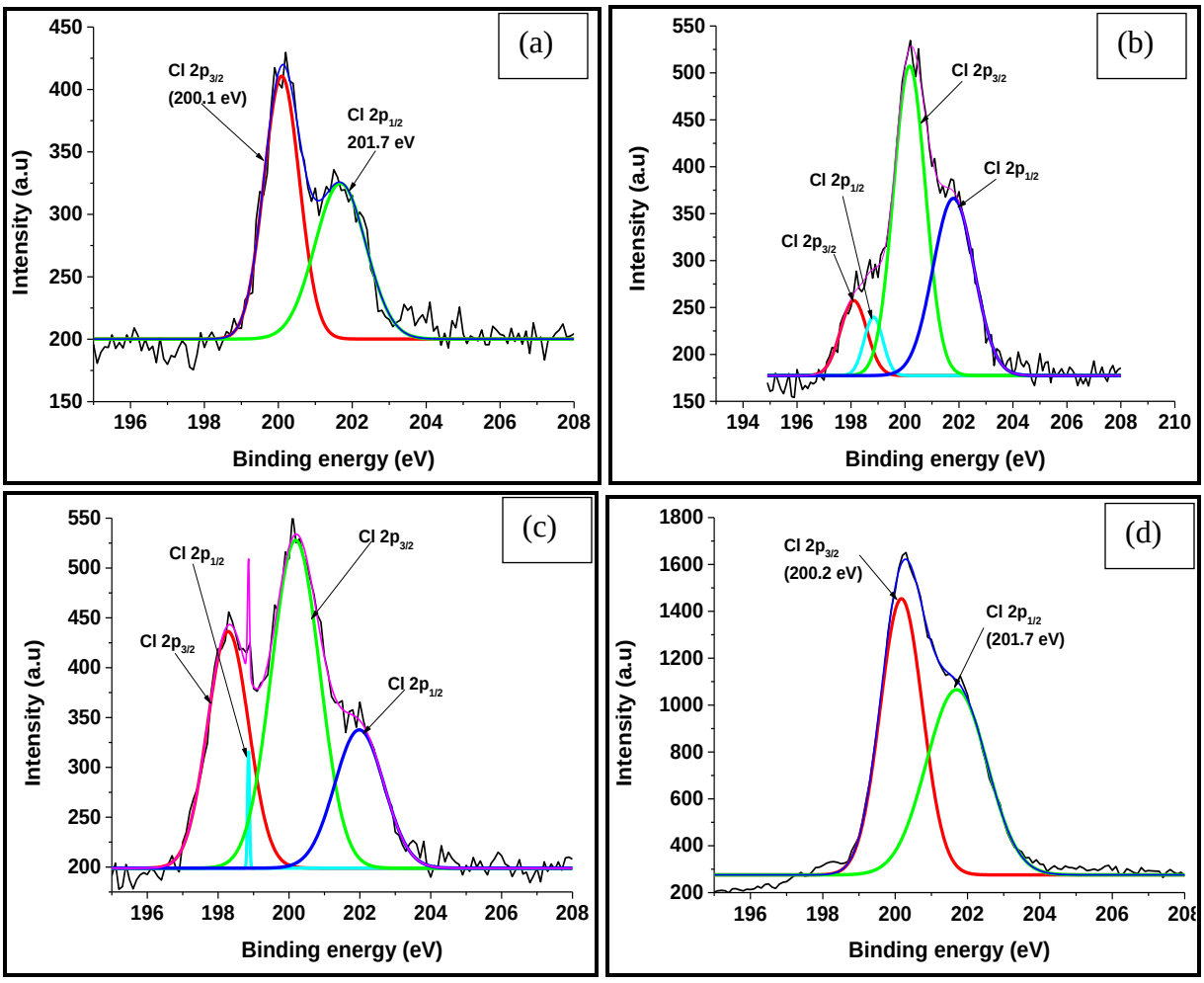

Figure 5.28 Cl 2p XPS spectra of purified CNTs generated from (a) pure DCB, (b) 66.7:33.3 (c) 33.3:66.7 and (d) 20:80 vol.% of CH_3CN:DCB synthesized by an injection CVD at 0.24 mL/min.

Table 5.13 Binding energy and atomic concentrations of chlorine in the chlorine functionalized N-MWCNTs grown at various volume ratios of CH_3CN:DCB solution.

CH_3CN:DCB volume ratio	**Binding energy (eV) and atomic concentration of $Cl\ 2p_{3/2}$/(%) for ionic Cl**	**Binding energy (eV) and atomic concentration of $Cl\ 2p_{1/2}$/(%) for ionic Cl**	**Binding energy (eV) and atomic concentration of $Cl\ 2p_{3/2}$/(%) for covalent Cl**	**Binding energy (eV) and atomic concentration of $Cl\ 2p_{1/2}$/(%) for Covalent Cl**
0:100	–		200.1 (54.1)	201.7 (45.9)
66.7:33.3	198.1 (9.8)	198.8 (5.4)	200.2 (48.7)	201.8 (36.0)
33.3:66.7	198.3 (29.9)	198.9 (0.72)	200.2 (48.5)	202.0 (20.9)
20:80	–		200.2 (51.0)	201.7 (49.0)

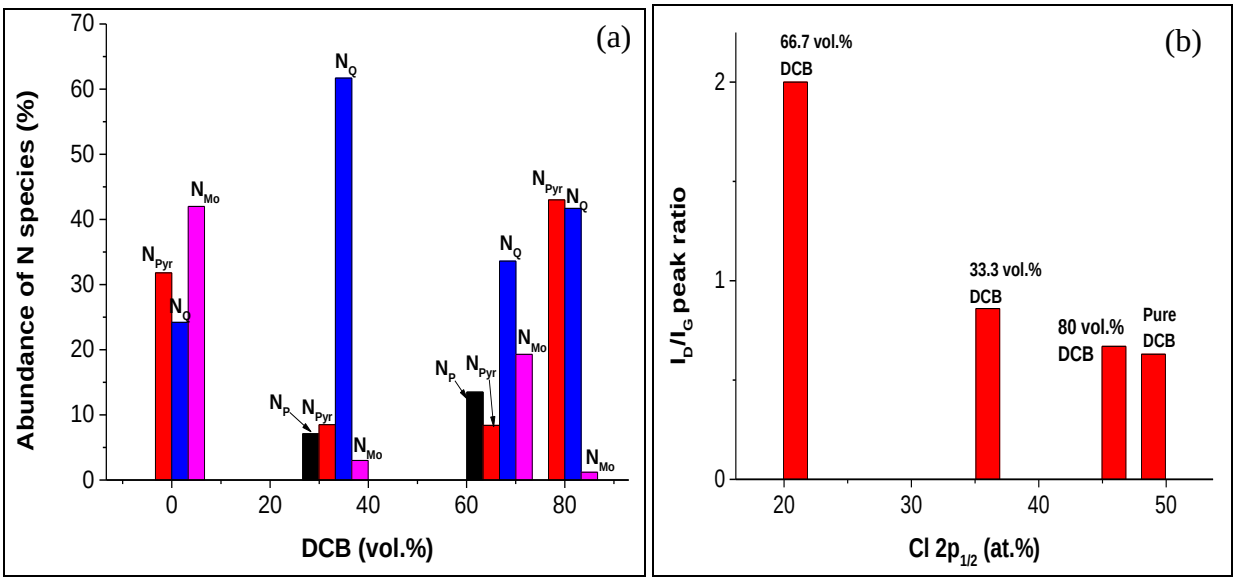

Figure 5.29 XPS data analysis of N-MWCNT and chlorinated N-MWCNTs (a) relative abundance behavior of different types of nitrogen as a function of chlorine content, bars are labelled with the type of nitrogen, (b) Raman peak ratio (I_D/I_G) versus Cl $2p_{1/2}$ (C–Cl covalent bonds) percent, squares on the graph are labelled with the DCB volume percent used.

5.4 Conclusion

Synthesis of chlorine-functionalized nitrogen-doped and un-doped CNMs using a CVD injection method over an Fe-Co/$CaCO_3$ catalyst was successful. DCB was found to be an excellent chlorine source that led to formation of a large quantity of CNTs. Chlorine influenced the morphology, length, and outer diameters of the N-doped CNMs, as well as enhanced their growth. Limited quantity of CNMs were obtained when pure CH_3CN was used as a feed solution. Horn-, straw- and pencil-shaped N-doped CNMs and CNFs were obtained from varying the amount of DCB in the feed. TGA, Raman and XPS analysis showed that an increase in the amount of DCB in the feed to 66.7 vol.% resulted in formation of highly defected CNMs, due to an increase in the number of chlorine atoms functionalized on the surface of the CNMs. Defects associated with sp^3 hybridization ($I_D/I_{D'}$ = 16), were observed from purified CNMs generated from a 33.3 vol.% mixture. We can conclude that addition of 33.3 vol.% DCB resulted in formation of defects due to functionalization of carbon atoms with chlorine and the type of covalent bonding that dominated. Vacancy-like and hopping defects ($I_D/I_{D'}$ = 9.3) were obtained from CNMs generated from feed streams containing 66.7 vol.% DCB, suggesting various bonding configurations between Cl and C, namely charge-transfer complexes, covalent bonding, and doping. Boundary like defects ($I_D/I_{D'}$ = 3.7) were observed from purified CNMs generated from 80 vol.% DCB solutions, suggesting non-bonding interactions between carbon and chlorine. This shows that Cl atoms that were produced at 80 vol.% DCB were in close proximity and hence they interated with each other to form Cl_2 molecules which acted as purifying agents for the CNMs resulting in production of CNMs with less defects and that were highly graphitic. A high FWHM value of 116 cm^{-1} for the G band of purified CNMs generated from a 66.7 vol.% DCB feed suggested that these materials were highly defected in comparison with the FWHM of 70 and 54 cm^{-1} found for CNMs generated from 33.3 vol.% and 80 vol.% DCB feeds. I_D/I_G value was also the highest at 1.8 for CNMs generated from feeds containing 66.7 vol.% DCB. The Raman data is thus consistent with the XPS analysis where all types of N-species were generated in appreciable amounts for CNMs generated from feeds containing 66.7 vol.% DCB, which is characteristic of highly defected materials. Graphitic nitrogen species dominated the XPS data of CNMs generated from feeds containing 80 vol.% DCB, which is also consistent with the Raman data. Raman data are also consistent with the TEM observations where various shaped and sized

CNMs were generated from feed solutions containing 66.7 vol.% DCB. Observation of the molecular nitrogen peak from the XPS spectra is also consistent with the broad peaks that were found when CNMs were oxidized at ~ 800 °C that led to nitrogen evolution, for CNMs generated from feeds containing pure CH_3CN and those containing 66.7 vol.% DCB. Effect of an injection flow rate did not have much effect on the morphology and graphitic nature of the CNTs.

In this work we have shown that it is possible to control the morphology of N-doped CNMs by adding chlorine, which can enhance their application in many fields. The open-ended CNTs generated from a mixture of CH_3CN and DCB can be applied in field emission devices, as supercapacitor electrodes for an electrochemical storage of energy, as magnets in water treatment by adding magnetic metals inside the open tubes and also as fillers in composite materials for production of membrane systems for water treatment.

In the chapter that follows we will evaluate post-doping treatments of synthesized heteroatoms of chlorine and nitrogen doped CNMs using acetonitrile with aromatic and non-aromatic chlorinated solvents.

References

1. L.-F. Chen, X.-. Zhang, H.-W. Liang, M. Kong, Q.-F. Guan, P. Chen, Z.-Y. Wu, and S.-H. Yu, *ACS Nano*, 2012, **6**, 7092 – 7102.
2. J. Hou, C. Cao, F. Idrees, and X. Ma, *ACS Nano*, 2015, 9, 2556 – 2564.
3. W.H. Shin, H.M. Jeong, B.G. Kim, J.K. Kang, and J.W. Choi, *Nano Lett*., 2012, **12**, 2283 – 2288.
4. B. Xu, S. Hou, G. Cao, F. Wu and Y. Yanga, *J. Mater. Chem*., 2012, **22**, 19088 – 19093.
5. Y. Zheng, J. Xu, Y. Zhang, X. Yang, Y. Zhang and Y. Shang, *New J. Chem*., 2018, **42**, 150 – 160.
6. D. Gueon and J. H. Moon, *ACS Appl. Mater. Interfaces*, 2015, **7**, 20083 – 20089.
7. M. Igagaki, H. Konno, and O. Tanaike, *J. Power Sources*, 2010, **195**, 7880 – 7903.
8. E. Zera, W. Nickel, G.P. Hao, L. Van Zetti, S. Kaskel and G.D. Sorarú, *J. Mater. Chem. A*, 2016, **4**, 4525 – 4533.
9. F.M. Hassan, V. Chabot, J. Li, B.K. Kim, L.R. Sandoval and A. Yu, *J. Mater. Chem. A*, 2013, **1**, 2904 – 2912.
10. D.H. Jurcakova, M. Seredych, G.Q. Lu, and T.J. Bandosz, *Adv. Funct. Mater*., 2009, **19**, 437 – 447.
11. M. Seredych, D.H. Jurcakova, G.Q. Lu and J.J. Bandosz, *Carbon*, 2008, **46**, 1475 – 1488.
12. J.-I. Kim, and S.-J. Park, *J. Solid State Chem*., 2011, **184**, 2184 – 2189.
13. H.M. Jeong, J.W. Lee, W.H. Shin, Y.J. Choi, H.J. Shin, J.K. Kang, and J.W. Choi, *Nano Lett*. 2011, **11** (6), 2472−2477.
14. M. Li, and J. Xue, *J. Phys. Chem*. C 2014, **118** (5), 2507−2517.
15. M. Sevilla, L. Yu, L. Zhao, C.O. Ania, and M.-M. Titiricic, *ACS Sustainable Chem. Eng*. 2014, **2** (4), 1049−1055.
16. T. Cui, R. Lv, F. Kang, Q. Hu, J. Gu, K. Wang, and D. Wu, *Nanoscale Res Lett*., 2010, **5**, 941 – 948.
17. S.C. Tsang, Y.K. Chen, P.J.F. Harris and M.I.H. Green, *Nature*, 1994, **372**, 159 – 162.
18. H. Liu, Y. Zhang, R. Li, X. Sun and H.A. Rachid, *J. Nanopart. Res*. 2012, **14**, 1016(1-8).
19. D.H. Jurcakova, M. Seredych, G.Q. Lu and T.J. Bandosz, *Adv. Funct. Mater*., 2009, **19**, 438 – 447.

20. D.H. Kim, J.K. Lae, J.H. Huh, Y.H. Kim, G.T. Kim, S. Roth, et al., *Phys Status Solidi B*, 2011, **248**, 2668 – 2671.
21. J.Y. Kim, W.H. Lee, J.W. Suk, J.R. Potts, H. Chou, I.N. Kholmanov, R.D. Piner, J. Lee, D. Akinwande and R.S. Ruoff, *Adv. Mater*., 2013, **25**, 2308 – 2313.
22. S.H. Yeon, P. Reddington, Y. Gogotsi, *Carbon*, 2010, **48**, 201 – 210.
23. W.K. Maboya, N.J. Coville, and S.D. Mhlanga. *S. Afr. J. Chem*., 2016, **69**, 15 – 26.
24. X. Wu, Y. Tao, C. Mao, L. Wen, and J. Zhu, *Carbon*, 2007, **45**, 2253-2259.
25. C. Wu, Q. G, P. Yin, T. Li, Q. Yang, and Y. Xie, *J. Phys. Chem. B*, 2005, **109**, 2597-2604.
26. M.L. García-Betancourt, Y.I. Vega-Cantu, S.M. Vega-Díaz, A. Morelos-Gómez, M. Terrones, and E. Muñoz-Sandoval, *J. Nanomater*., 2015, **587416**, 1-14.
27. L.M. Ombaka, P.G. Ngungu, B. Omondi, J.D. McGettrick, M.L.Davies, and V.O. Nyamori, *J. Solid State Chem.*, 2016, **235**, 202-211.
28. S.D. Mhlanga, K.C. Mondal, R. Carter, M.J. Witcomb, and N.J. Coville, *S. Afr. J. Chem*., 2009, **62**, 67–76.
29. A. Pacula, K. Uosaki, R. Socha, E. Bielańska, O. Pietrzyk, M. Zimowska, *Electrochim. Acta*, 2016, **212**, 47-58.
30. X. Gui, J. Wei, K. Wang, A. Cao, H. Zhu, Y. Jia, et al., *Adv. Mater*., 2010, **22**, 617 – 621.
31. X.R. Ye, L.H. Chen, C. Wang, J.F. Aubuchon, I.C. Chen, A.I. Gapin, J.B. Talbot and S. Jin, *J Phys. Chem. B.*, 2006, **26**, 12938 – 12942.
32. S.Y. Sawant, R.S. Somani, M.H. Cho and H.C. Bajaj, *RSC Adv*., 2015, **5**, 46589 – 46597.
33. S. Zhang, S. Tsuzuki, K. Ueno, K. Dokko and M. Watanabe, *Angew. Chem. Int. Ed.*, 2015, **54**, 1302 – 1306.
34. D. Bouša, J. Luxa, V. Mazánek, O. Jankovský, K. Klímová, M. Pumera and Z. Sofer, *RSC Adv*., 2016, **6**, 66884 – 66892.
35. H. Sahin and S. Ciraci, *J. Phys. Chem. C*, 2012, **116**, 24075 – 24083.
36. D. Beeman, J. Silverman, R. Lynds and M.R. Anderson, *Phys. Rev. B*. 1984, **30**, 870 – 875.

37. A. Eckmann, A. Felten, A. Mishchenko, L. Britnell, R. Krupke, K.S. Novoselov and C. Casiraghi, *Nano Lett*, 2012, **12**, 3925 – 3930.
38. K. Ganesan, S. Ghosh, N.G. Krishna, S. Ilango, M. Kamruddin and A.K. Tyagi, *Phys. Chem. Chem. Phys*., 2016, **18**, 22160 – 22167.
39. B. Manoj, *Int. J. Coal Sci. Technol*., 2016, **3**, 123 – 132.
40. A. Cuesta, P. Dhamelincourt, J. Laureyns, A. Martinez-Alonso and J.M.D. Tascon, *Carbon*, 1994, **32**, 1523 – 1532.
41. L. Bokobza, J.-L. Bruneel and M. Couzi, *Carbon*, 2015, **1**, 77 – 94.
42. A. Kaniyoor and S. Ramaprabhu, *AIP Advances* 2, 032183 (2012); doi: 10.1063/1.4756995.
43. 1. H. Ago, T. Kugler, F. Cacialli, W.R. Salaneck, M.S.F. Shaffer, A.H. Windle and R.H. Friend, *J. Phys. Chem. B*, 1999, **103**, 8116.
44. D. Marton, K.J. Boyd, A.H. Al-Bayati, S.S. Todorov and J.W. Rabalais, *Phys. Rev. Lett*., 1994, **73**, 118.
45. H. Liu, Y. Zhang, R. Li, X. Sun, S. Désilets, H. Abou-Rachid, M. Jaidann and L.-S. Lussier, *Carbon*, 2010, **48**, 1498 – 1507.
46. M. Reyes-Reyes, N. Grobert, R. Kamalakaran, T. Seeger, E. Goldberg, M. Ruhle, Y. Bando, M. Terrones and M. Terrones, *Chem. Phys. Lett*., 2004, **396**, 167 – 173.
47. H.C. Choi, S.Y. Baes, J. Park, K. Seo, C. Kim, B. Kim, H.J. Song, and H.J. Shin, *Appl. Phys. Lett*., 2004, **85**, 5742 – 5744.
48. M. Zhao, Y. Xia, Y. Ma, M. Ying, X. Liu, and L. Mei, *Phys. Rev. B*., 2002, **66**, 155403.
49. J.W. Jang, C.E. Lee, S.C. Lyu, T.J. Lee and C.J. Lee, *Appl. Phys. Lett*., 2004, **84**, 2877 – 2879.
50. P. Ayala, A. Grüneis, T. Gemming, D. Grimm, C. Kramberger, M.H. Rummeli, F.L. Freire, H. Kuzmany, R. Pfeiffer, A. Barreiro, B. Buchner and T. Pichler, *J. Phys. Chem. C*., 2007, **111**, 2879 – 2884.

CHAPTER 6

Heteroatom of chlorine and nitrogen doped carbon nanomaterials using acetonitrile with aromatic and aliphatic chlorinated solvents: Post-doping treatments

---

6.1 Introduction

Properties of the carbon nanotubes (CNTs) can be tailored by their interaction with molecules that can either withdraw of donate electrons. This phenomenon is referred to as doping which is intentional replacement of carbon atoms on the walls of the CNTs by other elements. Tailoring of the properties of the CNTs can also be achieved by their surface functionalization with heteroatoms. Methods of synthesizing nitrogen heteroatom doped CNTs have been developed and were categorized into in-situ and post treatment doping methods. In-situ doping methods involve direct incorporation of nitrogen into the carbon matrix during the CNT synthesis process. The most widely used in-situ techniques include catalytic vapor deposition (CVD), chemical solvothermal, high temperature arc-discharge and laser ablation methods. In the post-treatments methods, CNTs are first synthesized, then annealed at high temperatures together with the nitrogen-containing precursors. Post treatments methods include thermal annealing, wet chemical methods, plasma and arc-discharge approaches. Challenges remain for synthesis of N-doped graphene materials with less defects via an in-situ method. Firstly, the mixed flow of carbon and nitrogen precursors in the gas phase triggers a competition between nitrogen incorporation and the NH*x* group, leading to increased defect densities.[1] Secondly, even though nitrogen doping is increased at low temperatures ~ 600 to 800 °C, defects are also created at low temperatures.[2]

Post-treatments methods have not been used widely because they require, high temperatures (800–1200 °C) and toxic precursors which limits their application. High temperatures required for successful doping of graphene with nitrogen resulted in formation of defects on their structures.[3] High temperature post-treatments of CNTs were also found to favor formation of graphitic nitrogen in the carbon framework with small amounts of defects.[4]

Thermal annealing is the most preferred post-treatment method, because of its high doping efficiency[5] and its ability to recover the sp^2 carbon network.[6] Most work reported on post-doping with N was done on graphene and graphene oxide. Thermal annealing of graphene oxide with a solid source of nitrogen is appealing because the materials can be scaled up without a catalyst.[7] N-doped graphene material with ~ 5 % N doping was synthesized by post-treating graphene oxide with 2-methylimidazole via thermal treatment.[8] N-doped graphene materials which exhibited outstanding catalytic performance were synthesized by post-treatment of graphene oxide with urea at low-temperature in air.[9] Post-treatment of graphene with ammonia resulted in formation of N-doped graphene of which 80 % were graphitic N species with small amounts of defects.[10]

N-doped few-wall CNT with 3–5 walls which possessed excellent electrocatalytic activity towards electrocatalytic oxidation of dopamine, was successfully synthesized by post-treating CNTs with urea via thermal annealing by a solvothermal method.[11] N-doped CNTs were synthesized by post-treatment of oxidized CNTs in NH_3 at 300, 500 and 700 °C. It was found that the type of N-species incorporated into the CNTs depended on the reaction temperature.[12]

High levels of nitrogen, sulphur and boron were produced by post-treating fluorinated carbon nanomaterials (graphene, graphene quantum dots and single-wall CNTs) with a dopant source by thermal annealing.[4] By changing the degree of fluorination, the doping level was tuned over a wide range, which was important for optimizing the performance of doped low-dimensional graphitic materials.[4] Functionalization of acid-treated and annealed graphene oxide with chlorine was achieved by post-treatment of graphene oxide with thionylchloride ($SOCl_2$).[13] Covalently bonded chlorine was suggested to develop at vacancy edges as a result of $SOCl_2$ interaction with hydroxyl groups.[13] Doping of reduced graphene oxide (RGO) with chlorine was achieved by post-treatment of RGO with a mixture of NaClO and H_2SO_4 by a wet chemical method.[14] The Cl-RGO was found to possess high specific capacitance and can be used as an electrode material for high performance supercapacitors.[14] Halogenation of graphene with chlorine, bromine and iodine was achieved by exfoliation of graphene oxide in a halogen atmosphere by thermal annealing.[15]

Doping of CNTs with nitrogen can also yield NCNTs with unusual shapes. Not only is it possible to dope and make NCNTs in a one-step process, but it is also possible to make CNTs that are covered by NCNTs. In this case the NCNTs are produced by post-treatment procedures. For example, CNT/N-CNT interconnects were produced after post-doping CNTs synthesized from C_2H_4 with CH_3CN.[16] The formation of multi-terminal junctions requires the presence of topological defects between the nanotubes.[17] CNTs with substitutional doped junctions such as CNT/NCNT were used in rectifiers,[18-20] photoelectrical switches,[21] logic gates and circuits,[18] etc. Branched CNTs with nitrogen doped/un-doped intratubular junctions have been synthesized by a simple one-step co-pyrolysis of hexamethylenetetramine and benzene over ferrocene as catalyst.[22] Nitrogen-doped bamboo-shaped Y-junction CN_x nanotubes with 7.8 atomic.% nitrogen were synthesized by pyrolysis of monoethanolamine and a ferrocene mixture at 950 °C on a GaAs substrate.[23] He *et al.* showed that the growth of carbon onions was enhanced in a nitrogen environment due to incorporation of nitrogen in the carbon onion.[24]

Chlorine is also known to affect the growth of un-doped CNTs. For example, Nano-onion like carbon structures were obtained from chlorinating TiC at 900 °C, with small amounts of nanotube-like structures formed at the edges of the nano-onions.[25]

This poses a question: will incorporation of chlorine into the N-doped CNTs structure affect their morphology and properties? The preparation of halogen containing NCNTs have been a subject of very few studies. Ombaka et al. investigated the effect of halogens on NCNT growth using a halogenated ferrocenyl catalyst.[26] The authors observed an increase in nitrogen content when a fluorine substituted catalyst was used as compared to a chlorine substituted catalyst.[27] Thermolysis of an acetonitrile:ferrocene mixture, using bromine trifluoride vapor at room temperature, that were grown on a silicon substrate, resulted in formation of a film of F-containing MWNCNTs.[28]

In the previous chapter, we studied the role of chlorine on the morphology of N-doped CNTs grown using a Fe-Co supported on $CaCO_3$ as catalyst by injection of a mixture of acetonitrile and dichlorobenzene. In this study the concentration of both chlorine and nitrogen will be varied to explore their effect on the morphology of the CNMs using a CVD method. Post-treatments of the

N-doped CNTs with dichlorobenzene and of chlorinated CNTs with acetonitrile will also be performed.

6.2 Experimental

6.2.1 Materials and chemicals

$Fe(NO_3)_3 \cdot 9H_2O$ (Sigma Aldrich) ≥ 98 %, $Co(NO_3)_2 \cdot 6H_2O$ (Sigma Aldrich) ≥ 98 %, $CaCO_3$ (Sigma Aldrich) ≥ 99 %, HNO_3 (Sigma Aldrich) ≥ 98 % ACS, 1,2-dichlorobenzene (DCB) (Sigma Aldrich) 99 % Reagent plus, 1,1,2,2-tetrachloroethane (TTCE) (UniLAB SAARChem) 98 % GLC, acetonitrile (CH_3CN) ≥ 99.8 % (Sigma Aldrich) were used. All reagents were commercially available and used without further purification.

6.2.2 Synthesis of chlorinated N-doped CNTs by a bubbling CVD method

The catalyst (1.0 g) was spread in a quartz boat (120 mm × 15 mm) and the boat was placed in the center of a quartz tube. The furnace was then heated to 800 °C at a rate of 10 °C/min under flowing N_2 (50 mL/min). Once the temperature reached 800 °C, the N_2 flow rate was adjusted to 240 mL/min. C_2H_2 was also bubbled through the reactor at a flow rate of 90 mL/min for acetonitrile, dichlorobenzene and their mixtures. For tetrachloroethane and its mixtures with acetonitrile, flow rates were set at 280 mL/min N_2 and 50 mL/min C_2H_2, respectively based on optimized flow rates in chapter 3. Both gases were bubbled through a studied organic solvent, before being introduced into the quartz tube. After 60 min of reaction time, the C_2H_2 flow and bubbling was stopped and the system was left to cool down to room temperature under a continuous flow of N_2 (50 mL/min). The quartz boat was then removed from the reactor and the carbon deposit that formed was weighed.

6.2.3 Post doping of N-MWCNTs with chlorine and of chlorine functionalized MWCNTs with nitrogen

In the first experiment, we preheated the furnace with an empty quartz tube and the temperature was allowed to increase gradually at a rate of 10 °C/min rate until it reached 800 °C. Once the furnace reached a set temperature, a quartz boat containing purified N-doped CNTs was pushed

with an aluminum rod into the quartz tube to the center of the furnace. Dichlorobenzene was then bubbled through using nitrogen as a carrier gas at a flow rate of 240 mL/min for 30 minutes. The furnace was then allowed to cooled down to room temperature before analysis of the product. In another experiment the same procedure was followed but as-synthesized chlorine functionalized CNTs were post-doped with nitrogen by bubbling acetonitrile through the quartz tube using nitrogen as a carrier gas at a flow rate of 240 mL/min for 30 minutes.

6.2.4 Purification of the CNTs

Purification of the CNT materials was performed as described elsewhere.[28,29] The N-doped CNTs, and the chlorinated N-doped CNTs were purified by refluxing them in 55 % HNO_3 in an oil bath at 110 °C for 4 h to remove catalyst residues. The acid-treated CNTs were then washed with distilled water until the washings were neutral and the products were dried in an oven at 120 °C for 12 h. Chlorinated CNTs and the Cl functionalized CNTs post doped with nitrogen were purified by stirring in 30 % HNO_3 at room temperature for 2 h, followed by washing the materials with distilled water until the washings were neutral and finally dried in an oven at 120 °C for 12 h. Nitrogen doped CNTs that were post-doped with chlorine were not purified since we used purified samples as substrates for post-treatments.

6.2.5 Characterization of the CNTs

The morphology and size distribution of the CNTs before and after HNO_3 treatment were analyzed by transmission electron microscopy (TEM) using a FEI TECNAI G^2 SPIRIT. The samples for TEM analysis were prepared by sonication in ethanol and thereafter deposited on a holey carbon-coated TEM Cu grid. The CNTs were also characterized by Raman spectroscopy using a Jobin-Yvon T6400 micro-Raman spectrometer. Excitation was provided by a 532 nm green laser with spectral resolution of 3-5 cm^{-1}. The impurity content of the CNTs was monitored by thermogravimetric analysis (TGA) using a Perkin Elmer TGA 7. The sample was loaded into a platinum pan and heated up to 900 °C at a heating rate of 5 °C/min, in a flowing air and nitrogen stream both at 20 mL/min. The phase composition of the samples was determined by powder X-ray diffraction (PXRD) using a D2 Bruker PXRD with a continuous scan mode using

CoKα radiation. The scan range was 10–90 2θ degree. X-ray photoelectron spectroscopy (XPS) analysis was done using an AXIS Ultra DLD, with Al (monochromatic) anode equipped with a charge neutralizer, supplied by Kratos Analytical.

6.3 Results and discussion

6.3.1 Synthesis of N-doped CNTs: Effect of DCB concentration

6.3.1.1 Structural analysis of the N-doped CNTs: Effect of DCB concentration

Bamboo-compartmented CNTs were produced when acetonitrile was used as a nitrogen source by Tetana et al.[29] Figure 6.1a shows bamboo-shaped MWCNTs produced using acetonitrile as nitrogen source by a pyrolysis CVD method. The outer diameter of the N-MWCNTs varied from 17 to 143 nm with an average of 70 nm (Table 6.1)[29]. Nitrogen incorporation into the nanotubes resulted in an increase in the outer diameter of the MWCNTs. The inner diameter of the MWCNTs also increased when nitrogen was doped into the CNTs (Table 6.1).

Table 6.1 Diameters of purified CNMs generated from pure CH_3CN and pure DCB synthesized using a bubbling CVD method

Hydrocarbon source	Average outer diameter /nm	Number of structures counted (number of samples analyzed)	Carbon structure
CH_3CN	70	>200 (duplicates)	Bamboo CNTs including those with intratubular junctions (50 %), hollow CNTs (45) CNSs (5 %)
DCB	33	>200 (duplicates)	CNTs and CNTs with secondary growth (80 %), CNFs (15 %), carbon nano-onions (5 %)

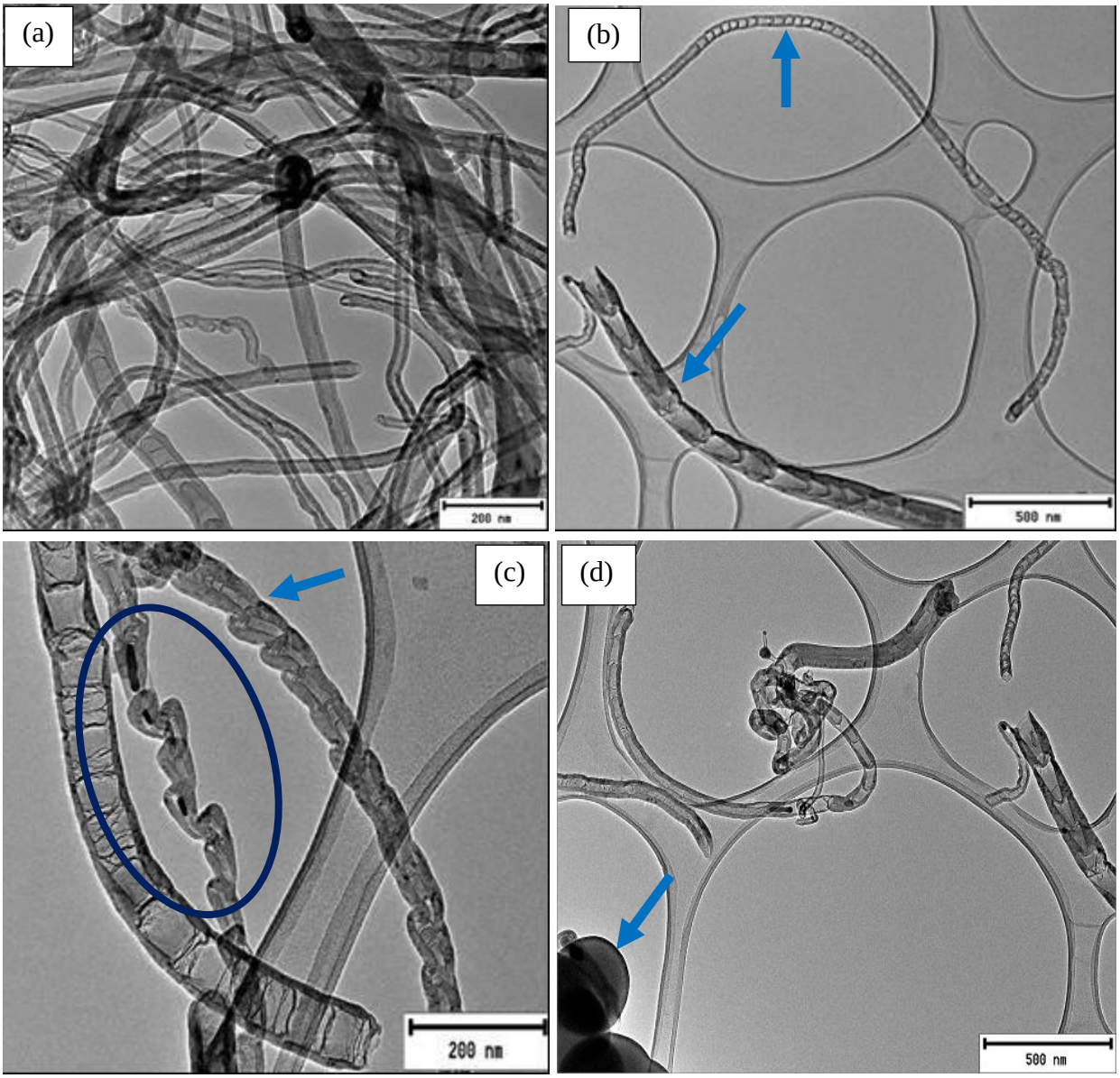

Figure 6.1 TEM images of purified CNMs generated from pure CH_3CN at 800 °C, and 240 mL/min N_2 and 90 mL/min C_2H_2 flow.

In our previous study[28] MWCNTs with secondary carbon nanofibers (CNFs) attached to their outer walls were synthesized using dichlorobenzene as chlorine source (Figure 6.2). The outer diameters of the chlorinated CNTs varied from 22 to 41 nm with an average of 33 nm (Table 6.1).

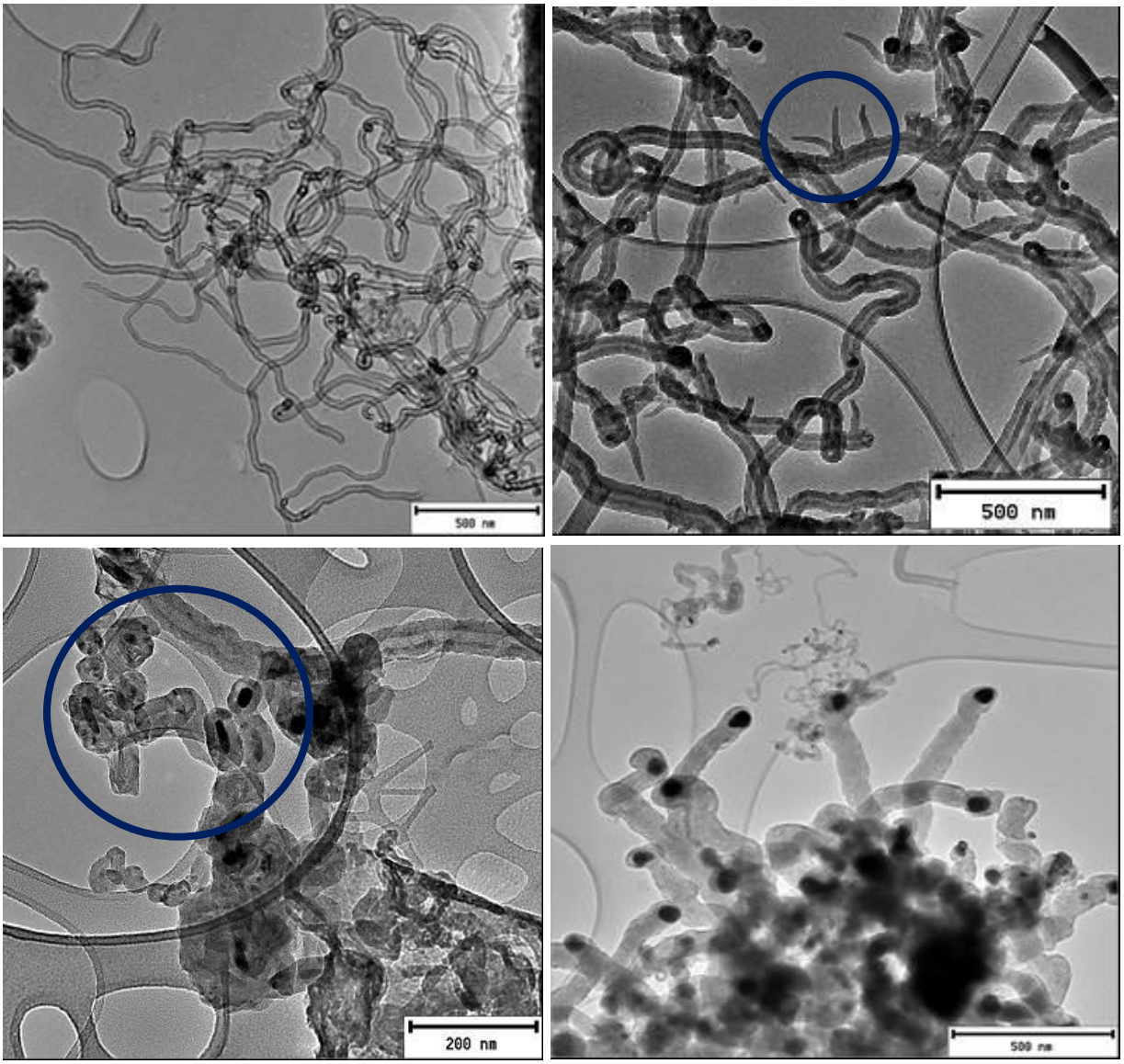

Figure 6.2 TEM images of purified CNMs generated from pure DCB at 700 °C, and 240 mL/min N_2 and 90 mL/min C_2H_2 flow.

The effect of chlorine on the growth of N-doped CNTs was investigated using two DCB concentrations, 33.3 and 66.7 vol.%. Addition of 33.3 vol.% of DCB into a 66.7 vol.% CH_3CN solution, resulted in production of CNMs of variable morphologies (Figure 6.3). Bamboo-compartmented CNTs (white arrow), metal-filled carbon nano-onions (circled part) and CNTs with intratubular junctions (dashed arrow) were obtained (Figure 6.3). Hollow CNTs were also

observed (Figure 6.3). CNTs with intratubular junctions were observed after nitrogen doping by other authors.[22]

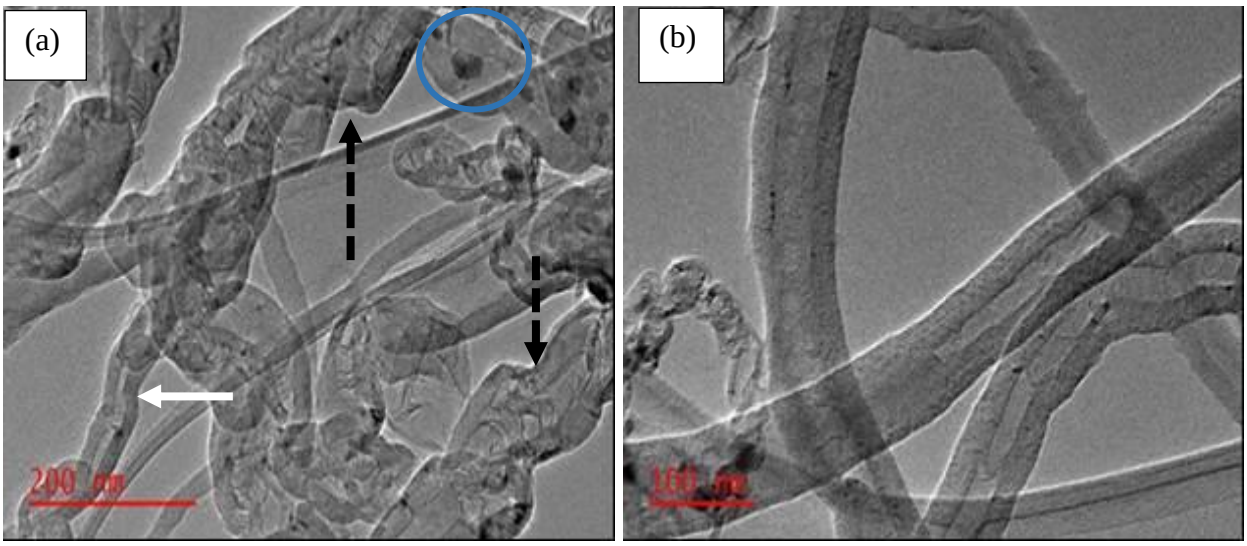

Figure 6.3 TEM images of purified CNMs generated from CH_3CN feed containing 33.3 vol.% DCB by bubbling CVD method.

Entangled CNMs were observed from the SEM images (Figure 6.4). The diameter distribution curve showed that the outer diameters of the CNMs ranged from 75 to 176 nm, with an average of 115 nm (Figure 6.4b, and Table 6.2). The CNMs were very long as we could not see where they begin and were they end, from the high magnification SEM (Figure 6.4c and d).

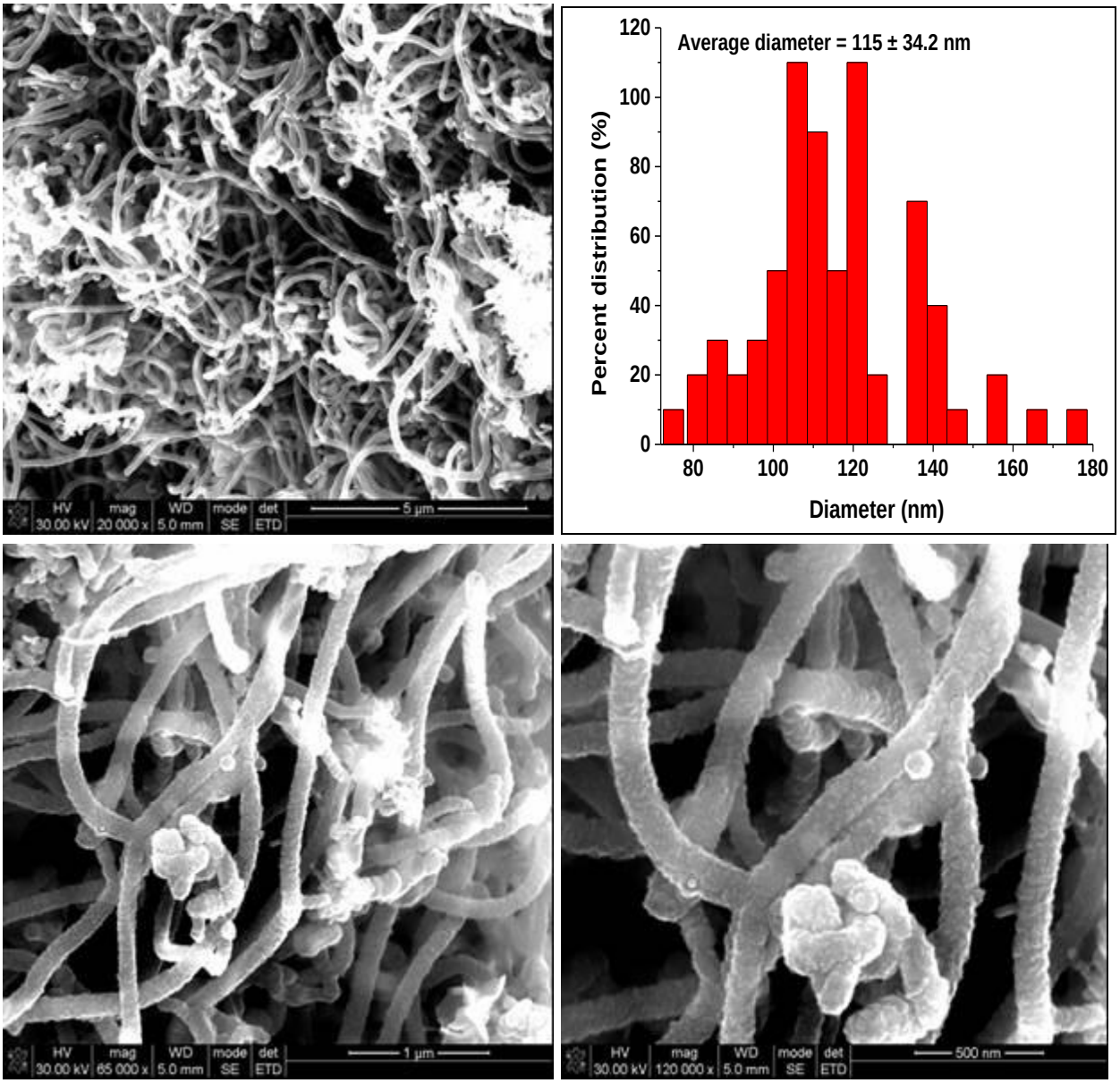

Figure 6.4 SEM images and diameter distributions curves of purified CNMs generated from CH_3CN feed containing 33.3 vol.% DCB by bubbling CVD method.

An increase in the amount of chlorine in the feed to 66.7 vol.% resulted in formation of regular hollow and bamboo-shaped CNTs with open-ends (Figure 6.5). Branched CNTs with N doped/un-doped Y-junctions were also obtained, where the main CNT was hollow and the branch was compartmented or had a bamboo-shape (Figure 6.5d circled part).

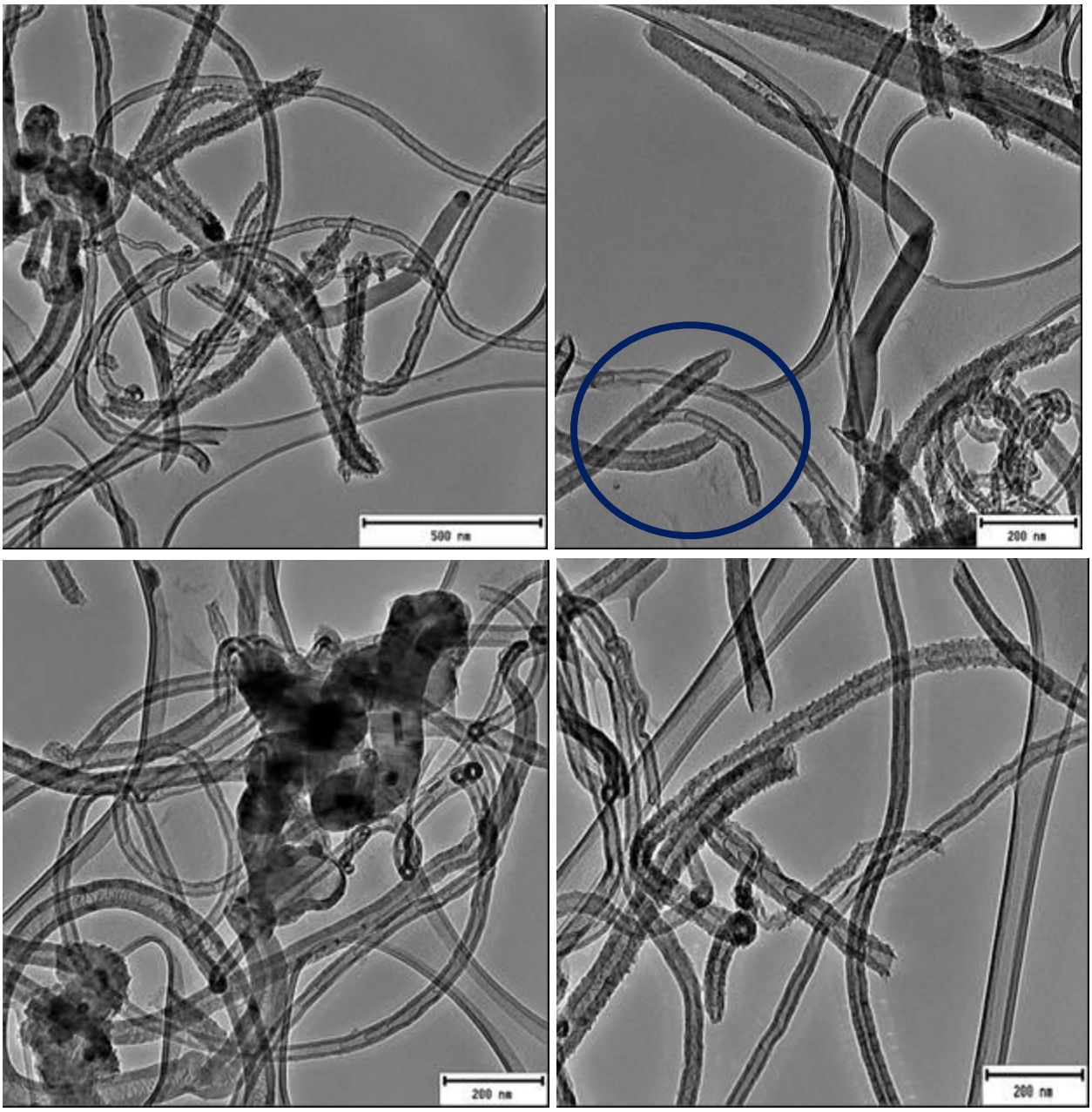

Figure 6.5 TEM images, SEM images and diameter distributions curves of purified CNMs generated from CH_3CN feed containing 66.7 vol.% DCB by bubbling CVD method.

SEM images revealed the presence of entangled CNTs of various sizes (Figure 6.6). Diameter distribution curves showed that the obtained CNTs had outer diameters varying from 30 to 90 nm and an average of 57 nm (Figure 6.6b, and Table 6.2).

From our results we can conclude that an increase in chlorine concentration in the CH_3CN feed resulted in a decrease in the average outer diameter of the CNTs. Inner diameters of the CNTs were also observed to decrease with an increase in the amount of chlorine in the feed (Table 6.2).

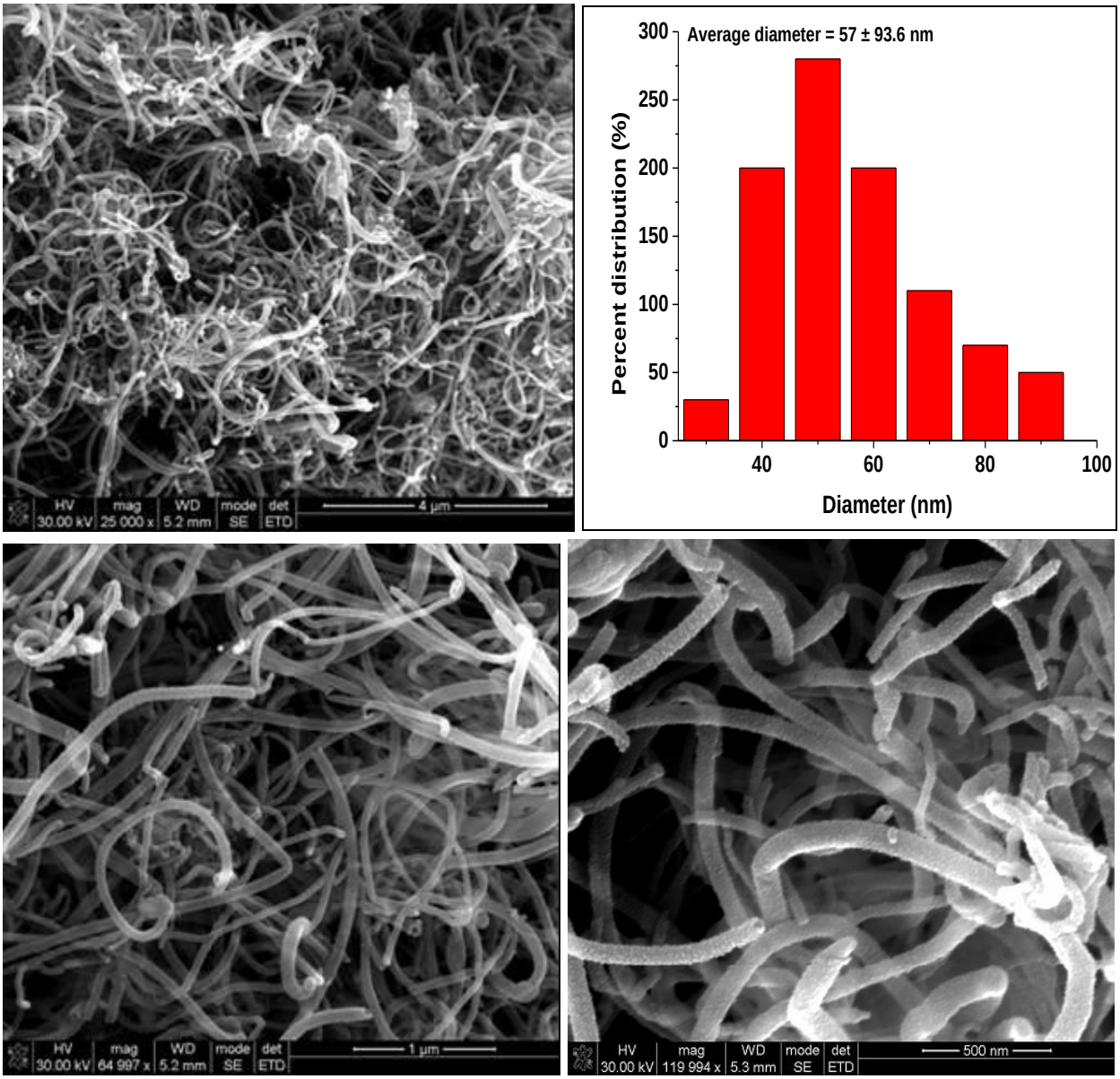

Figure 6.6 SEM images and diameter distributions curves of purified CNMs generated from CH_3CN feed containing 66.7 vol.% DCB by bubbling CVD method.

Table 6.2 Diameters of purified CNMs generated from CH_3CN feeds containing various concentrations of DCB synthesized using a bubbling CVD method

CH_3CN:DCB volume ratio /vol.%	Outer diameter distribution /nm	Average outer diameter /nm	Average inner diameter /nm	**Number of structures counted (number of samples analyzed)**	Volume of reagent used /mL
66.7:33.3	75 – 176	115	22	>500	4
33.3:66.7	30 – 90	57	14	>500	3

6.3.1.2 Thermogravimetric analysis of the N-doped CNTs: Effect of DCB concentration

TGA and DTGA curves of un-purified and purified CNTs generated from pure CH_3CN and DCB are presented in Figure 6.7. Un-purified CNTs generated from CH_3CN showed two weight losses the first at 568 °C due to oxidation of N-doped CNTs and the second at ~ 690 °C due to oxidation of other graphitic carbons like carbon nanospheres observed from the TEM images (Figure 6.7a and b and Table 6.3). Purified CNTs generated from CH_3CN showed one mass loss at ~578 °C due to oxidation of N-doped CNTs.

Un-purified CNTs generated from DCB shows a variety of weight losses, the initial minor weight loss observed around 100 °C was due to evaporation of physisorbed water (Figure 6.7c and d). The second minor weight loss at ~ 450 °C was due to decomposition of amorphous carbon structures. The third major weight loss with an onset temperature of ~ 500 °C was due to oxidation of CNTs, while the fourth minor weight loss at 700 °C was due to oxidation of other graphitic carbon structures (i.e. carbon nanofibers, CNTs with funnel-like open ends, observed from the TEM images) (Figure 6.7c and d and Table 6.3). Purified CNTs generated from DCB showed one broad weight loss at ~ 550 to 700 °C due to an overlap between oxidation of CNTs and other graphitic carbon structures mentioned above (Figure 6.7c and d and Table 6.3). The CNTs generated from DCB possess comparative stability possibly due to functionalization of their surface with chlorine.[30] Incorporation of chlorine also resulted in production of highly graphitic materials, as seen by the absence of an amorphous carbon oxidation peak from DTGA curves obtained after purification. The amount of residual metal was greatly reduced after

purification, which shown that un-purified samples contained a large number of un-reacted catalyst metal particles. Some residual metal particles were observed at the tip of the carbon fibers observed from TEM images obtained from pure DCB.

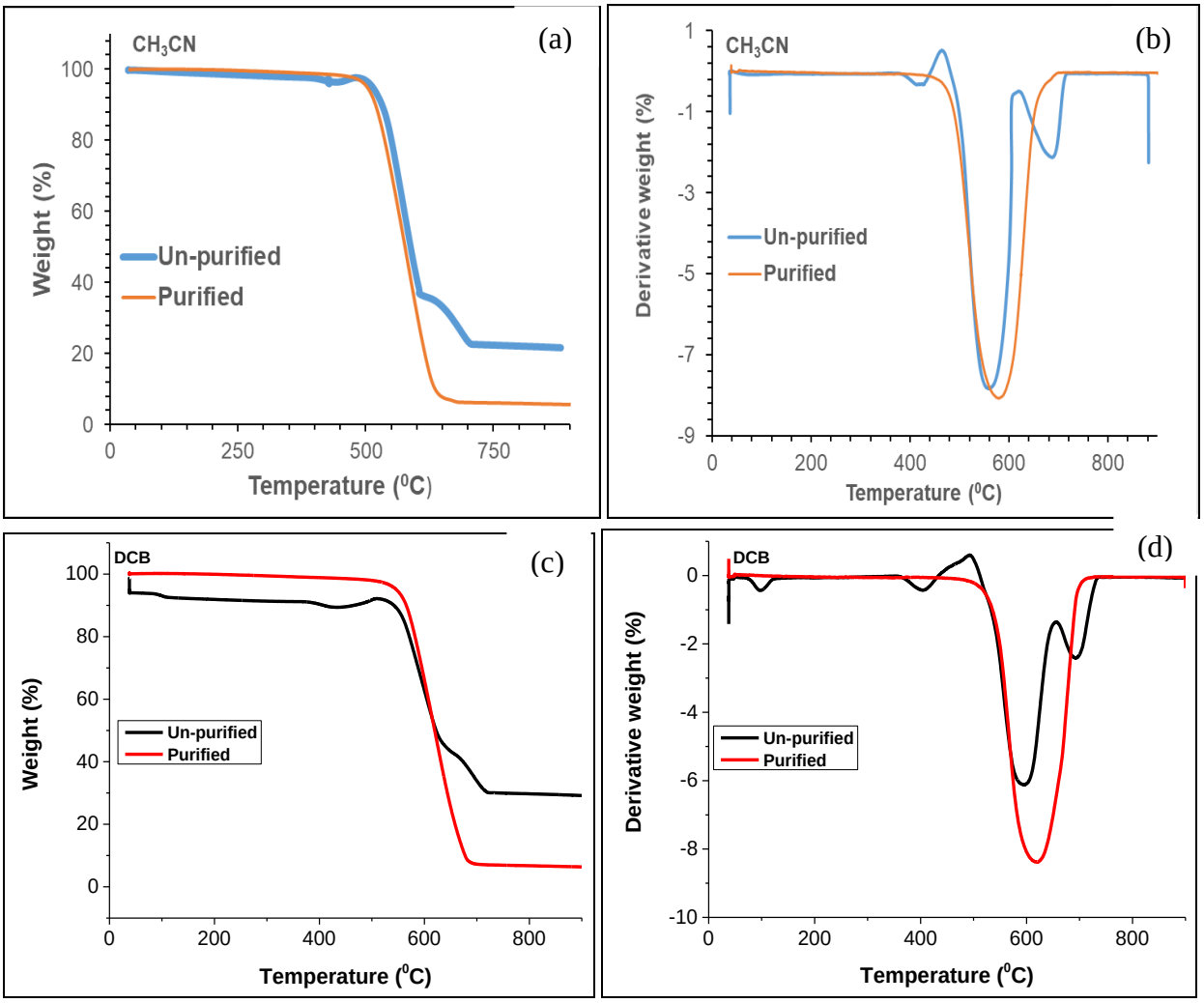

Figure 6.7 TGA and DTGA curves of un-purified and purified CNMs generated from room temperature solutions of pure CH_3CN (a and b) and pure DCB (c and d)

Table 6.3 Decomposition temperatures and residual masses (determined by TGA) of the un-purified and purified (P) chlorinated N-MWCNTs generated by bubbling different ratios of a CH_3CN and DCB.

Hydrocarbon source	Decomposition temperature /°C	Residual mass /%
CH_3CN	568 & 690	21.7
CH_3CN (P)	578	5.6
DCB[28]	597	29.6
DCB[28]	600	6.6

TGA and DTGA curves of un-purified and purified CNTs generated from acetonitrile feeds containing low concentration of DCB (33.3 vol.%) appeared similar. A broad oxidation peak was observed at ~ 550 to 750 °C and ~ 550 to 800 °C for un-purified and purified materials respectively (Figure 6.8 and Table 6.4), assigned to oxidation of chlorinated CNTs and other graphitic carbon materials (carbon nanoonions, hollow CNTs and CNTs with junctions). This oxidation peak had a shoulder peak at ~ 800 °C and above 800 °C for un-purified and purified materials, due to evolution of nitrogen which is known to be released from N-doped carbons.[31] These results agree with the TEM observations where various types of CNTs of various sizes and morphologies were obtained.

Two regions of mass losses were observed from un-purified CNTs generated from acetonitrile solutions containing 66.7 vol.% DCB (Figure 6.8c and d). The first major weight loss was observed at ~ 600 to 650 °C, due to oxidation of chlorine functionalized bamboo N-doped CNTs (Figure 6.8 and Table 6.4). The second minor weight loss at ~ 700 °C was due to oxidation of functionalized hollow CNTs (Figure 6.8 and Table 6.4). DTGA curves of purified CNTs generated from feed solutions containing 66.7 vol.% DCB showed only one broad region of mass loss at 550 to 650 °C, which could be due to overlap between oxidation of chlorine functionalized N-doped and hollow CNTs. TGA data agrees with the TEM observations where bamboo-compartmented and hollow were observed. The results show that the carbon materials of different morphologies can be obtained by varying the amount of chlorine in the feed.

We also analyzed the residual mass present in chlorinated N-doped samples after purification with acid. The residual mass of 7.7 and 0 were obtained for N-CNTs generated from a feed

containing 33.3 and 66.7 vol.% DCB, respectively (Table 6.4). From this results it appears that metal particles were completely removed from solutions that contained high concentrations of DCB rather than those that contained lower concentrations of DCB. This can be attributed to greater encapsulation of metal particles into large diameter CNTs generated from low concentration of DCB, which were difficult to remove by acid treatment.

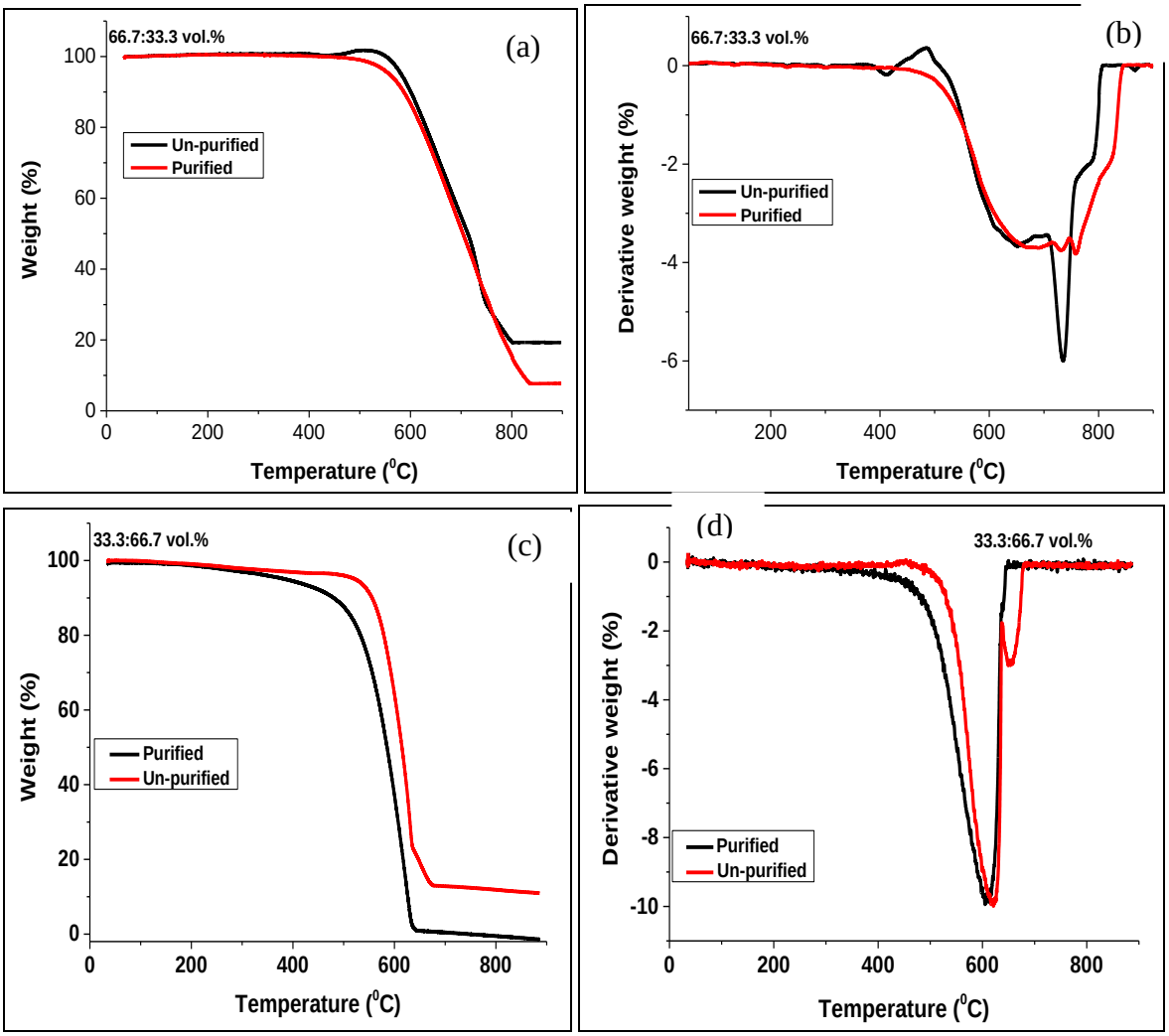

Figure 6.8 TGA and DTGA curves of un-purified and purified CNMs generated from room temperatures solutions of acetonitrile containing various concentrations of DCB.

Table 6.4 Decomposition temperatures and residual masses (determined by TGA) of the un-purified and purified (P) chlorinated N-CNTs generated from solutions containing different CH_3CN:DCB volume ratios.

CH_3CN:DCB volume ratio /%	Decomposition temperature /°C	Residual mass /%
66.7:33.3	651 & 737	19.3
66.7:33.3 (P)	671	7.7
33.3:66.7	610 & 643	11.0
33.3:66.7 (P)	600	0

6.3.1.3 Raman spectroscopy analysis of the N-doped CNTs: Effect of DCB concentration

Raman spectra analysis of the purified CNTs generated from pure CH_3CN and pure DCB are presented in Figure 6.9. A disorder-induced band (D-band) and a graphitic band (G-band) were observed in both Raman spectra. For CNTs generated from pure CH_3CN, a broad D-band was deconvoluted into two bands, a D4-band at 1210 cm^{-1} attributed to C=C stretching vibrations and a D-band at 1339 cm^{-1} attributed to topological defects on the CNT walls due to substitution of carbon with nitrogen. A G-band was also deconvoluted into two peaks, a D2-band at 1513 cm^{-1} assigned to the presence of amorphous carbon structures and a G-band at 1585 cm^{-1} due to sp^2 carbon atoms in a graphitic plane. An I_D/I_G value of 1.2 was obtained, which suggest the materials are highly defected. Large FWHM values of 126 and 71 cm^{-1} for D and G-band respectively also suggest the presence of amorphous carbon structures (Table 6.5).

Raman bands of purified CNTs generated from pure DCB also showed a D-band that was deconvoluted into two peaks, a D4-band at 1236 cm^{-1} and a D-band at 1338 cm^{-1} (Figure 6.9). A G-band was also deconvoluted into two peaks, a D2-band at 1498 cm^{-1} and a G-band at 1587 cm^{-1}. The amorphous carbon D2-band also is very broad and intense as compared to the one obtained from Raman curves generated from CH_3CN, which suggest the formation of sp^3 carbon due to chlorine functionalization.

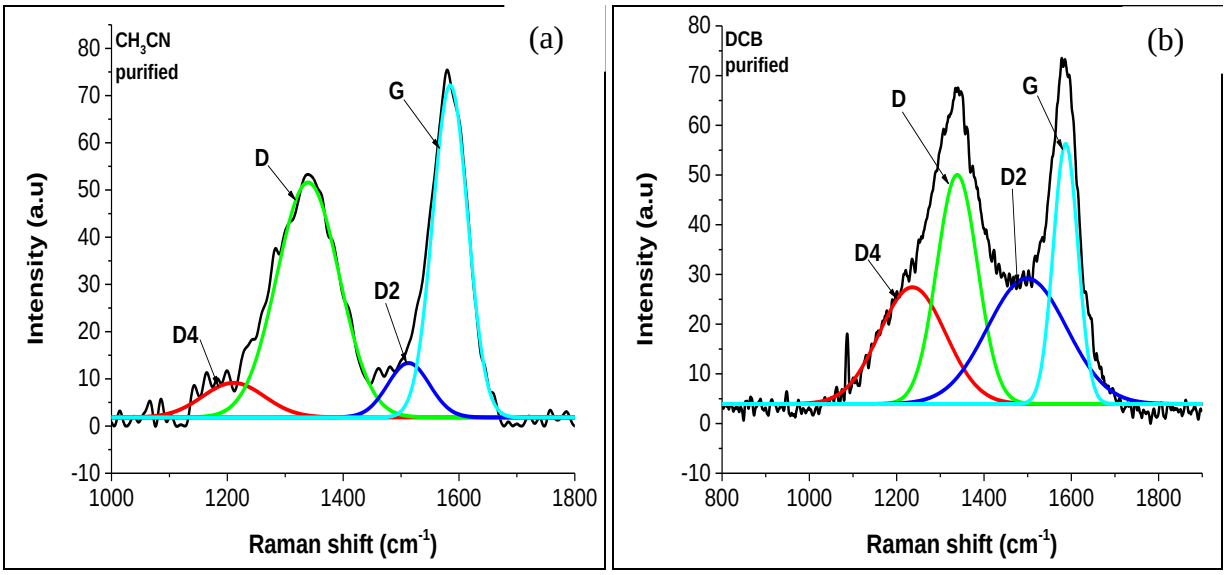

Figure 6.9 Deconvoluted Raman spectra of purified MWCNTs generated from (a) CH_3CN and (b) DCB using a bubbling CVD method.

An I_D/I_G value of 1.0 was obtained, which suggest that the materials are highly defected due to surface functionalization of the CNTs with chlorine. The lower value of I_D/I_G of 1.0 for CNTs generated from DCB as compared to 1.2 for CNTs generated from CH_3CN suggests that the CNTs generated from DCB were less defected. This data agrees with the TGA analysis of the materials. Also from comparison of FWHM values with those obtained from CH_3CN samples, lower FWHM values were obtained from CNTs generated from DCB 109 and 66 cm^{-1} for D and G-band respectively (Table 6.5). This again suggest that the materials generated in DCB were more graphitic than those generated from CH_3CN.

Table 6.5 Raman bands of the purified CNMs generated from pure CH_3CN and pure DCB using injection CVD method at an injection rate of 0.24 mL/min

Heteroatom Source	Band name	Band Position (cm^{-1})	Bond type	FWHM (cm^{-1})	Peak Area	Designation
CH_3CN purified	D4	1210	sp^2–sp^3	126	983	C=C stretching vibrations
	D	1339	sp^2	126	6701	Disordered graphite
	D2	1513	sp^3	85	1042	Amorphous carbon structure
	G	1584	sp^2	71	5312	Graphitic like carbonyl group
DCB purified	D4	1236	sp^2–sp^3	179	4472	C=C stretching vibrations
	D	1338	sp^2	109	5375	Disordered graphite
	D2	1498	sp^3	214	5760	Amorphous carbon structure
	G	1587	sp^2	66	3703	Graphitic like carbonyl group

Raman spectra was also recorded for materials generated from varying the concentration of DCB in the CH_3CN feed. Raman curves of un-purified CNTs generated from solutions containing 33.3 vol.% DCB in the feed presented three bands namely, a D, G and 2D band (Figure 6.10). A D-band was deconvoluted into one band a disorder-induced D-band at 1341 cm^{-1}. A G-band was deconvoluted into two peaks, a minor D2-band at 1551 cm^{-1} assigned to amorphous carbon structures and an intense G-band at 1581 cm^{-1} assigned to sp^2 carbons in a graphitic plane. A 2D band which is an overtone of a D band was also deconvoluted into two peaks a $2D_1$ at 2669 cm^{-1} and a $2D_2$ at 2702 cm^{-1}. This split has been described as a characteristic feature of undisturbed or highly ordered graphitic lattices.[32] The spliting of the 2D band was also assigned to splitting's of the π and π^* electronic states, owing to the interactions between the succesive layer planes.[33] Raman spectra of the purified CNTs showed only three bands that were deconvoluted into one

peak each, a D, G and single 2D band. The G-band was very intense and higher than the D-band which suggests highly graphitic materials were generated after purification.

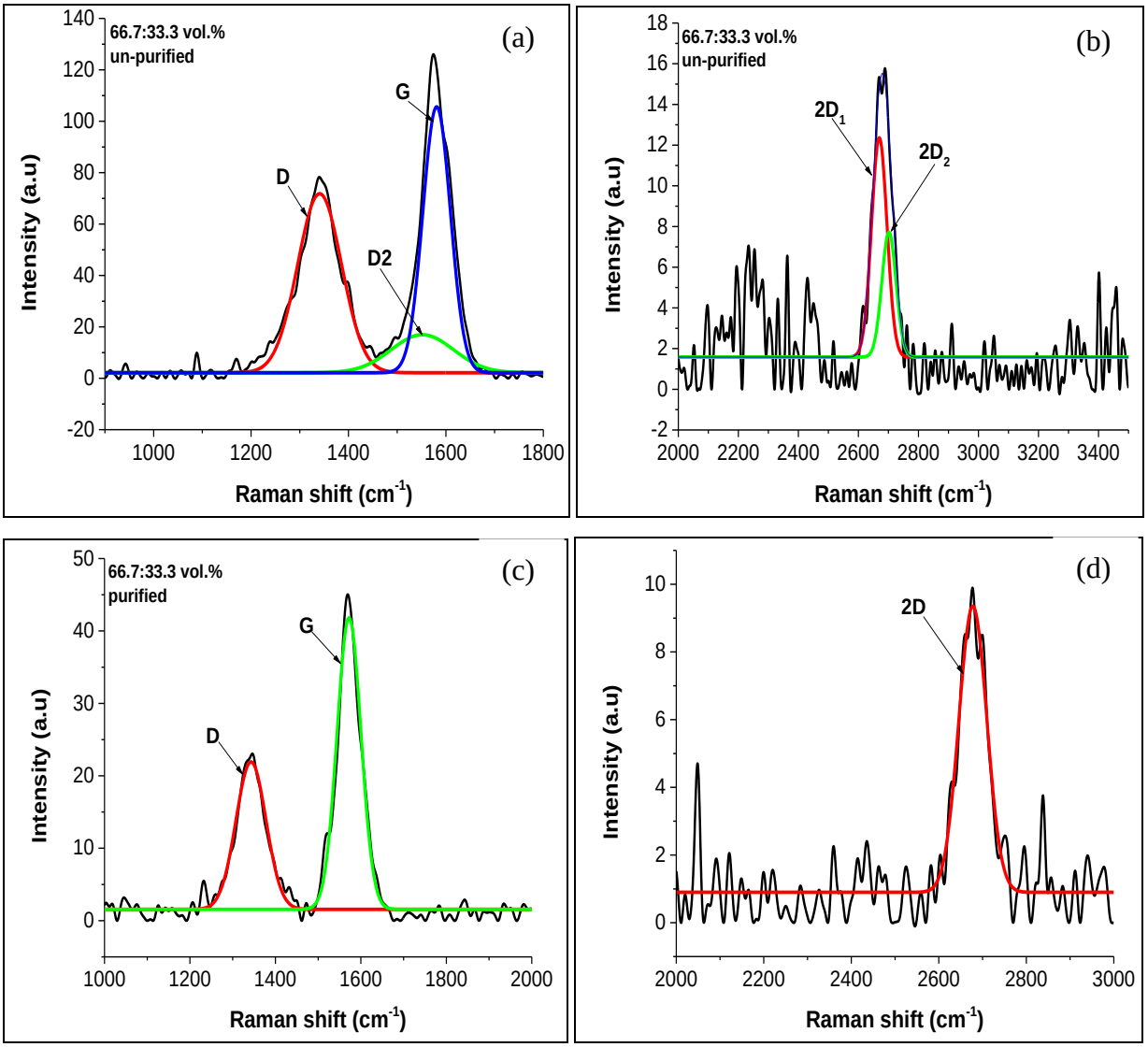

Figure 6.10 Deconvoluted Raman spectra of un-purified (a and b) and purified (c and d) MWCNTs generated from a feed made of 66.7:33.3 vol.% CH_3CN:DCB reagents using a bubbling CVD method.

Analysis of the peak ratios revealed I_D/I_G values of 0.81 and 0.63 which suggest that some amorphous carbon structures were removed by acid-treatment. FWHM value of 66 cm^{-1} for a G-

band were obtained from un-purified and purified samples, which suggest that the graphitic nature of the materials was the same (Table 6.6).

Table 6.6 Raman bands of the un-purified and purified CNMs generated from a 66.7:33.3 vol.% CH_3CN:DCB solution mixture using injection CVD method at an injection rate of 0.24 mL/min

66.7:33.3 vol.% CH_3CN:DCB	**Band name**	**Band Position (cm^{-1})**	**Bond type**	**FWHM (cm^{-1})**	**Peak Area**	**Designation**
Un-purified	D	1341	sp^2	106	7865	Disordered graphite
	D2	1551	sp^3	151	2371	Amorphous carbon structure
	G	1581	sp^2	66	7316	Graphitic like carbonyl group
	$2D_1$	2669		60	694	1^{st} overtone of D1
	$2D_2$	2701		55	364	1^{st} overtone of D1
Purified	D	1343	sp^2	83	1797	Disordered graphite
	G	1572	sp^2	66	2824	Graphitic like carbonyl group
	2D	2678		75	676	1^{st} overtone of D1

Raman spectra of both un-purified and purified CNTs generated from CH_3CN feed solutions containing 66.7 vol.% DCB are presented in Figure 6.11. A D-band was deconvoluted to one peak at 1337 and 1334 cm^{-1} for un-purified and purified CNTs attributed to presence of defects on the CNT walls. A G-band was deconvoluted into two bands, a D2-band attributed to amorphous carbon structures and a G-band attributed to graphitic planes. A G-band was larger than a D-band in purified samples but a D-band was larger than a G-band in un-purified samples, which suggests that purification improved the graphitic nature of the CNTs.

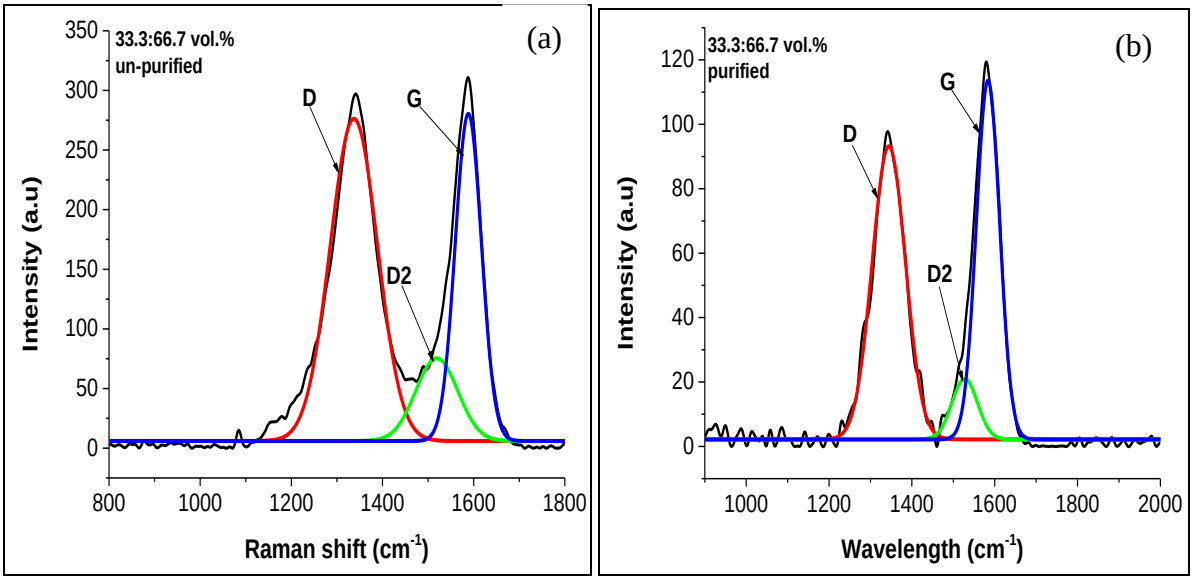

Figure 6.11 Deconvoluted Raman spectra of un-purified (a) and purified (b) MWCNTs generated from a feed made of 33.3:66.7 vol.% CH_3CN:DCB reagents using a bubbling CVD method.

Analysis of the I_D/I_G band showed values of 1.3 and 1.0 for un-purified and purified samples. Comparison with the I_D/I_G value of 0.63 for CNTs generated from feeds containing 33.3 vol.% DCB, suggest that CNTs generated from feeds containing 66.7 vol.% DCB were highly functionalized with chlorine, which resulted in formation of more sp^3 carbon bonds and greater defects in the CNT walls. FWHM value of 66 cm^{-1} was obtained for a G-band of both CNTs generated from feeds containing 33.3 and 66.7 vol.% DCB, which suggest that CNTs generated from both feeds contained similar amounts of amorphous carbon structures (Table 6.7).

Table 6.7 Raman bands of the un-purified and purified CNMs generated from a 66.7:33.3 vol.% CH_3CN:DCB solution mixture using injection CVD method at an injection rate of 0.24 mL/min

33.3:66.7 vol.% CH_3CN:DCB	**Band name**	**Band Position (cm^{-1})**	**Bond type**	**FWHM (cm^{-1})**	**Peak Area**	**Designation**
Un-purified	D	1337	sp^2	122	35189	Disordered graphite
	D2	1519	sp^3	108	8002	Amorphous carbon structure
	G	1588	sp^2	67	19698	Graphitic like carbonyl group
Purified	D	1344	sp^2	94	9149	Disordered graphite
	D2	1527	sp^3	72	1446	Amorphous carbon structure
	G	1572	sp^2	66	2824	Graphitic like carbonyl group

6.3.1.4 XPS analysis of the N-doped CNTs: Effect of DCB concentration

XPS analysis of N-MWCNTs were produced in our group from pyrolysis of acetonitrile.[29] About 1.32 % of total N concentration was found in this study. Peaks corresponding to C 1s, N 1s and O 1s at 284.7, 400 and 532 eV were obtained from the wide scan XPS spectra of the CNTs. The N 1s XPS spectrum was deconvoluted into three peaks, identified as molecular nitrogen (N_{Mo}) intercalated within the wall and inside the CNTs at 405 eV, quaternary nitrogen (N_Q) at 401.4 eV and pyridinic nitrogen (N_P) at 398.7 eV. Molecular nitrogen was dominant in these NCNTs as shown by their peak intensities. About 0.35 % N_Q, 0.21 % N_P and 0.76 % N_{Mo} were obtained. The C 1s peak was deconvoluted into three peaks at 284.7, 287.2 and 286.1 eV attributed to C–C sp^2 hybridized carbon, C–N and O–C=O bonding respectively.[29]

XPS data of chlorinated MWCNTs was reported earlier in our study from pyrolysis of DCB.[28] A C 1s spectrum of the materials was deconvoluted into four peaks with binding energies of 284, 284.8, 285.4, 286.2, and 287 eV attributed to C–C sp^2, C–C sp^3, C–Cl, C–OH and O–C=O respectively (Supplementary Figure S16).

Wide scan XPS spectra of both chlorine containing N-doped CNTs revealed peaks at 200, 284, 400 and 532 eV assigned to Cl 2p, C 1s, N 1s and O 1s, respectively (Supplementary Figure S17). The deconvoluted C 1s peaks of the materials produced from various volume ratios of DCB, was fitted into four components at 283–284 eV for C–C sp^2 and sp^3 carbon bonds, at ~ 286 eV for overlap between C–N and C–Cl groups and ~ 289 eV for O–C=O carboxylic groups (Supplementary Figure S18). The peak at 286 eV assigned to overlap between C–N and C–Cl carbon bonds, increased in intensity from 12.9 % to 20.1 % with an increase in DCB concentration from 33.3 to 66.7 vol.% (Supplementary Figure S18).

The N 1s XPS spectra was deconvoluted into four and five peaks for both studied concentrations of CH_3CN and DCB (Figure 6.12a and c). For chlorinated N-CNTs generated from solutions containing 33.3 vol.% DCB in the feed, the N1s was deconvoluted into five peaks appearing at 397.6 (6.3 %), 398.5 (10.9 %), 399.9 (0.94 %), 400.8 (60.1 %) and 405.7 (21.8 %) eV and were assigned to tetrahedral nitrogen bonded to sp^3–C (probably due to un-decomposed N–H bond), pyridinic N (N_P), pyrrolic N (N_{Pry}), quaternary N (N_Q) and molecular N (N_{Mo}), respectively (Table 6.8 and Figure 6.12a). The atomic percentages suggest that quaternary nitrogen was the most predominant form of nitrogen present at this studied concentration. These results suggest a more homogeneous distribution of nitrogen species in the CNTs. Graphitic N forms by merging N atoms into the defect region of the graphene, resulting in a graphene with less defects.[10] This data is consistent with Raman data where low I_D/I_G value was obtained at this DCB concentration, showing that the CNTs contained less defects.

N 1s XPS spectra of N-CNTs generated from CH_3CN feed solutions containing 66.7 vol.% DCB was deconvoluted into four peaks appearing at 398.2 (2.0 %), 400.2 (31.7 %), 401.9 (4.8 %) and 405.8 (61.6 %) eV attributed to N_P, N_{Pyr}, N_Q and N_{Mo}, respectively (Table 6.8 and Figure 6.12c). An increase in the concentration of DCB resulted in a reduction of the amount of nitrogen incorporated into the CNTs, as shown by a great reduction in the atomic percentage of quaternary nitrogen species (Figure 6.13a). Molecular nitrogen was found to be the dominant nitrogen species at this concentration (Figure 6.13a). An increase in peak intensity of the 400.2 eV peak which was assigned to pyrrolic nitrogen was also observed at this concentration (Figure 6.13a). The pyrrolic nitrogen is a substitutional nitrogen, that is part of a five-membered ring and is sp^3 hybridized. An increase in the contribution of pyrrolic nitrogen causes an increase in the

number of defects and disorders in the CNTs. The dominance of the pyrrolic nitrogen species at high concentrations of DCB was the reason for the observed capped tube ends and bent structures of NCNTs observed from the TEM image. This data is consistent with Raman data where an I_D/I_G peak ratio increased from 0.63 to 1.0 with an increase in DCB concentration from 33.3 to 66.7 vol.%, due to highly disordered CNTs.

Table 6.8 Nitrogen content and type of the N-species incorporated in the chlorinated N-MWCNTs grown at various volume ratios of CH_3CN:DCB solution.

CH_3CN:DCB volume ratio (mole ratio) /%	N–Csp^3 /%	Pyridinic nitrogen (N_P) /%	Pyrrolic nitrogen (N_{Pyr}) /%	Quaternary nitrogen (N_Q) /%	Molecular nitrogen (N_{Mo}) /%
66.7:33.3 (1:0.25)	6.3	10.9	0.94	60.1	21.8
33.3:66.7 (1:1)	–	2.0	31.7	4.8	61.6

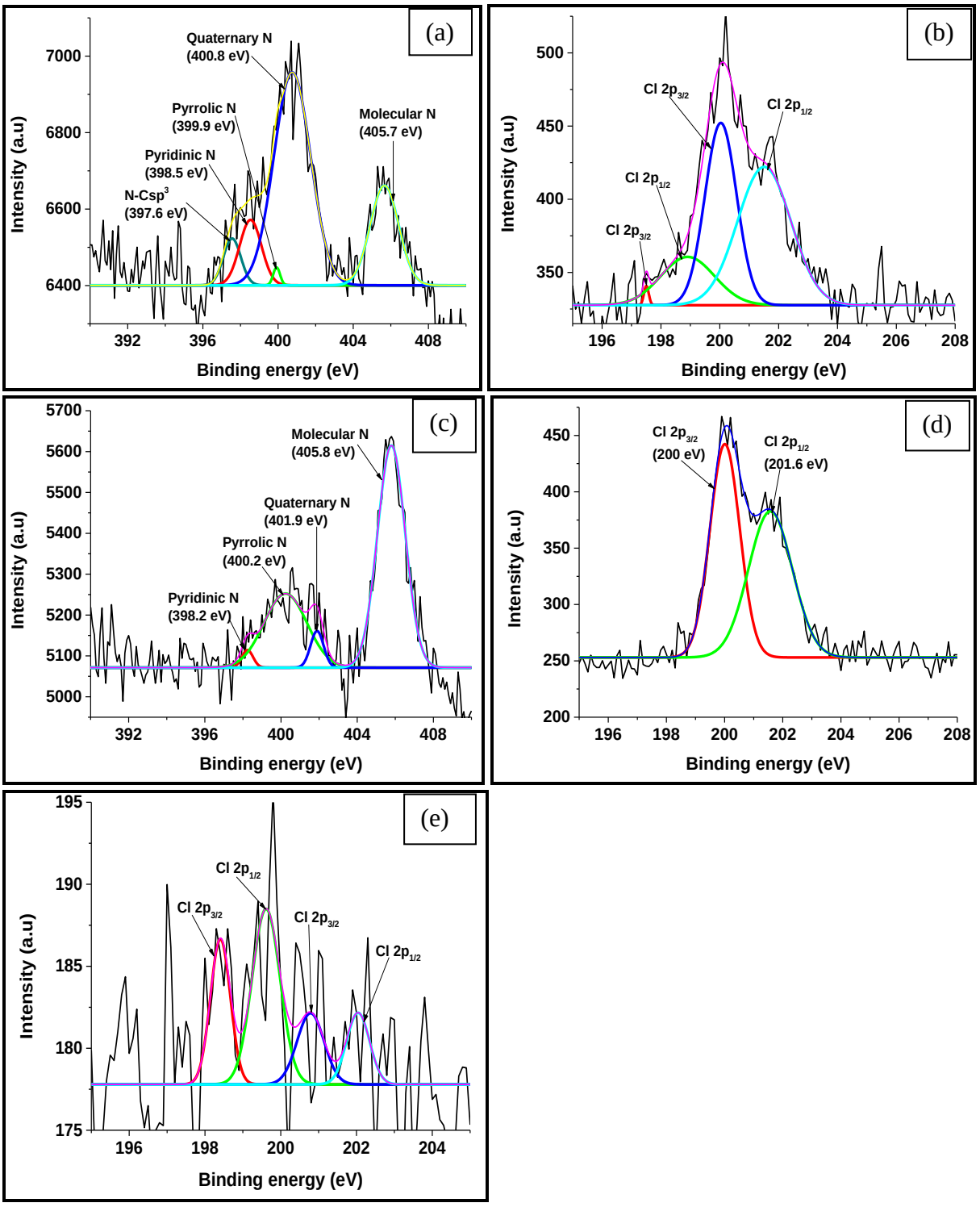

Figure 6.12 N 1s and Cl 2p XPS spectra of purified N-MWCNTs generated from (a and b) 66.7:33.3, (c and d) 33.3:66.7 vol.% of CH_3CN:DCB and (e) Cl 2p XPS spectra of DCB alone synthesized by bubbling CVD method.

The deconvoluted Cl 2p XPS peaks for CNTs generated from DCB and CH_3CN/DCB of various ratios showed two and three distinct peaks at ~198, 200 and 202 eV (Figure 6.12 c,d, and e). For CNTs generated from pure DCB and CH_3CN solutions containing 33.3 vol.% of DCB, two main peaks appearing at ~199 and 200 eV were observed (Figure 6.12b and e). Each of this Cl 2p peaks was split into two peaks, where the first two peaks located at the lower binding energy ~ 199 eV were assigned to the ionic state of Cl and the two peaks located at higher binding energies ~ 200 eV were assigned to covalently bonded Cl. For CNTs generated from 66.7 vol.% DCB, a peak at ~200 eV which was split into two peaks at 200 and 201.6 eV was observed (Figure 6.12d) and attributed to Cl–C=O and covalent C–Cl bonds, respectively. The two Cl 2p peaks appearing at ~ 199 eV for feeds containing pure DCB and 33.3 vol.% DCB in CH_3CN, were assigned to the presence of a chloride ion propably bonded to metals in the catalyst or ionically bonded to the carbon in the CNT. This data is consistent with the TGA analysis where ~7.7 of residual mass was found from CNTs generated from a solution containing 33.3 vol.% DCB and no residues were found from CNTs generated when the concentration of DCB in the feed was increased to 66.7 vol.%. A graph of I_D/I_G peak ratio versus the percentage of covalent Cl $2p_{1/2}$ peak was plotted to see the correlation between Raman and XPS data (Figure 6.13b). I_D/I_G decreased with addition of 33.3 vol.% DCB which shows reduction of defects in the N-MWCNTs by chlorine. Further increase in DCB concentration to 66.7 vol.% resulted in an increase in I_D/I_G but the value but was still less that the one obtained in pure CH_3CN. We suggest that increase in the amount of chlorine in the feed result in increased formation of sp^3 C–Cl bonds, which resulted in increased disorder.

Table 6.9 Binding energy and atomic concentrations of chlorine in the chlorinated NCMTs grown at various volume ratios of CH_3CN:DCB solution.

CH_3CN:DCB volume ratio	Binding energy (eV) and atomic concentration of $Cl\ 2p_{3/2}$/% for ionic Cl	Binding energy (eV) and atomic concentration of $Cl\ 2p_{1/2}$/% for ionic Cl	Binding energy (eV) and atomic concentration of $Cl\ 2p_{3/2}$/% for covalent Cl	Binding energy (eV) and atomic concentration of $Cl\ 2p_{1/2}$/% for covalent Cl
66.7:33.3	197.5 (0.60)	198.9 (16.30	200 .0 (36.4)	201.5 (46.7)
33.3:66.7	–	–	200 (49.8)	201.6 (50.2)
0:100	198.4 (25.5)	199.6 (43.2)	200.8 (17.0)	202.0 (14.4)

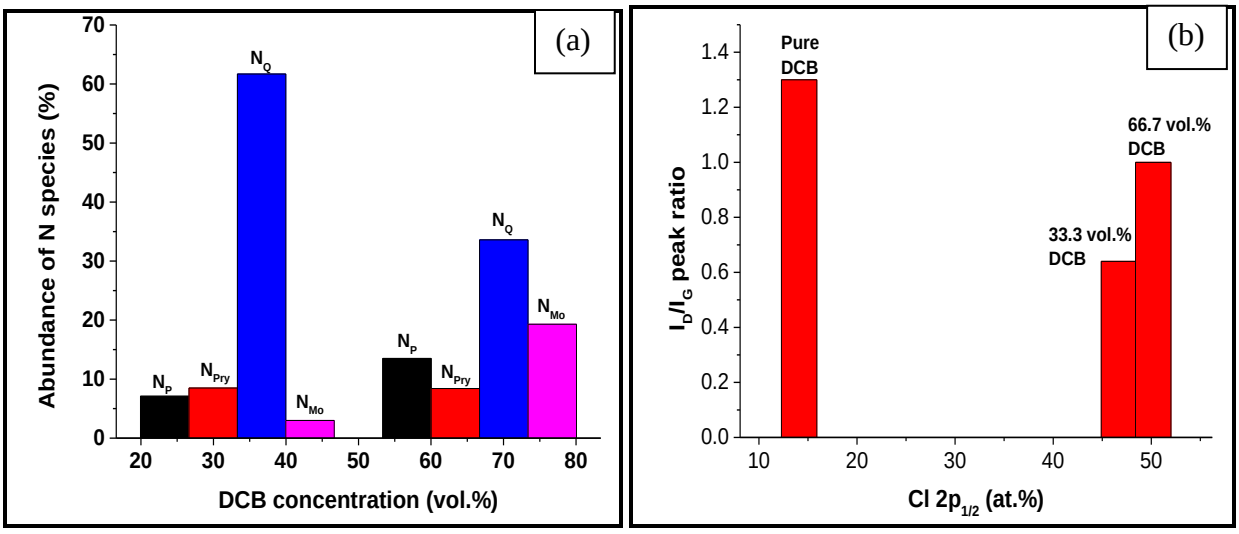

Figure 6.13 XPS data analysis of N-MWCNT and chlorine functionalized N-MWCNTs (a) relative abundance behavior of different types of nitrogen as a function of chlorine content, bars are labelled with the type of nitrogen, (b) Raman peak ratio (I_D/I_G) versus Cl $2p_{1/2}$ (C–Cl covalent bonds) percent, squares on the graph are labelled with the DCB volume percent used.

6.3.2 Post-doping of chlorinated CNTs and N-doped CNTs

In this section we investigated the effect of chlorine on the morphology of N-CNTs by post-doping the N-doped CNTs with chlorine using DCB as a source of chlorine. In the second test we post-doped the chlorine functionalized CNTs with nitrogen using CH_3CN as a source of nitrogen.

6.3.2.1 Structural analysis of post-treated CNTs

TEM images for N-doped CNTs post-doped with chlorine are shown in Figure 6.14 below. Bamboo compartmented CNTs are still observed after post-treatment with chlorine (Figure 6.14 shown by arrow). The distance between the compartments also increased after post-doping with chlorine. TEM images also revealed the formation of intratubular junctions in some of the produced CNTs, where some portions of the inside of the CNTs appear branched (Figure 6.14b shown by arrow). Metal filled carbon onions were also observed from images in Figure 6.14b circled parts, whose growth was possibly initiated by the presence of chlorine. The TEM images are similar to those observed from solutions that contained 33.3 and 66.7 vol.% of DCB in the N/Cl feed mixture. The average outer diameter of the CNTs increased from 70 nm for N-CNTs to 88 nm for N-CNTs post-doped with chlorine (Figure 6.16a). An increase in the inner diameter of the N-CNTs was observed after post-doping with chlorine which suggests increased N-doping. An increase in the internal diameter of N-CNTs and a decrease in wall thickness with increased N-doping was observed by other authors.[34]

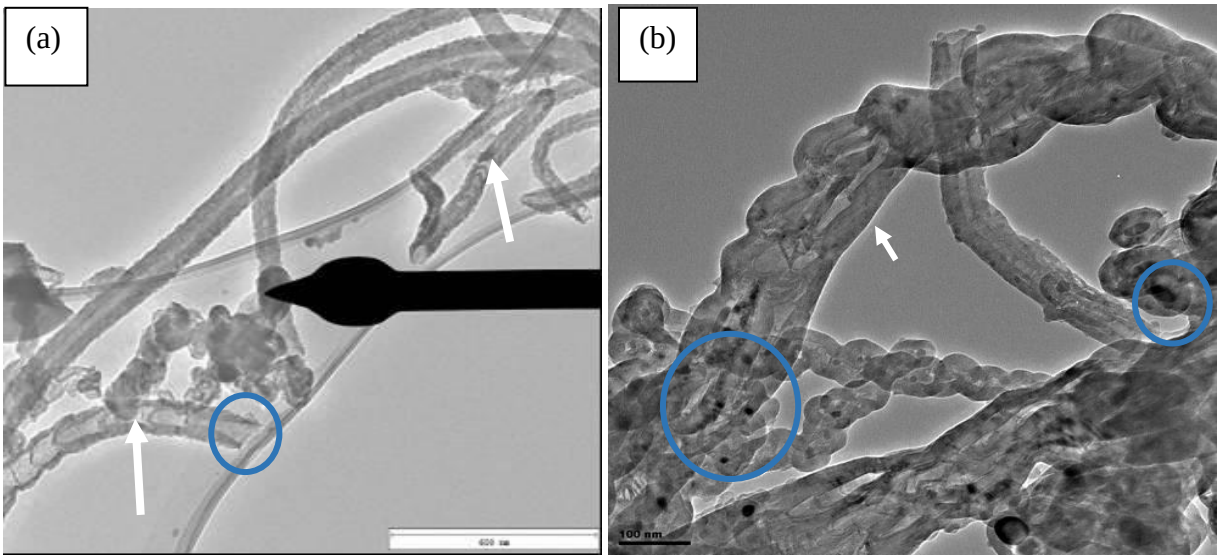

Figure 6.14 TEM images of purified N-CNTs (a and b) generated after post-doping with DCB as chlorine source.

TEM images of CNTs generated using DCB as a chlorine source, post-doped with nitrogen are presented in Figure 6.12. About 50 % of bamboo-shaped CNTs which appeared as stacked cups were generated after post-doping with nitrogen (Figure 6.15a), and the rest of the CNTs were hollow (Figure 6.15b). CNTs with secondary CNF growth were also still present after post-doping with nitrogen (Figure 6.15b insert and circled part). CNTs generated after post-doping with nitrogen were mostly bamboo-compartmented (Figure 6.15a), suggesting that post-doping was an effective method to introduce nitrogen into the CNTs by replacing one of the carbon atoms. Some authors found that in-situ doping of nitrogen atoms into the structure of CNTs during the growth gives much better nitrogen stabilities than the post-treatment method.[35] The average diameter of the chlorine containing CNTs decreased from 33 nm to 28 nm after post-doping with nitrogen (Figure 6.17b).

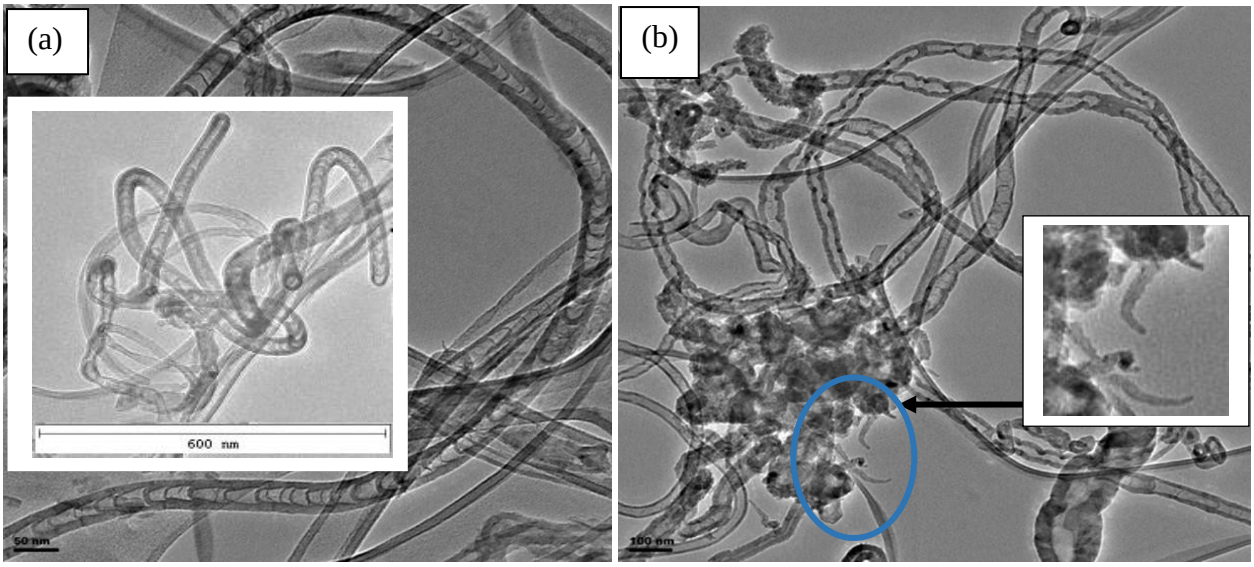

Figure 6.15 TEM images of chlorinated CNTs (a and b) generated after post-doping with CH_3CN nitrogen source.

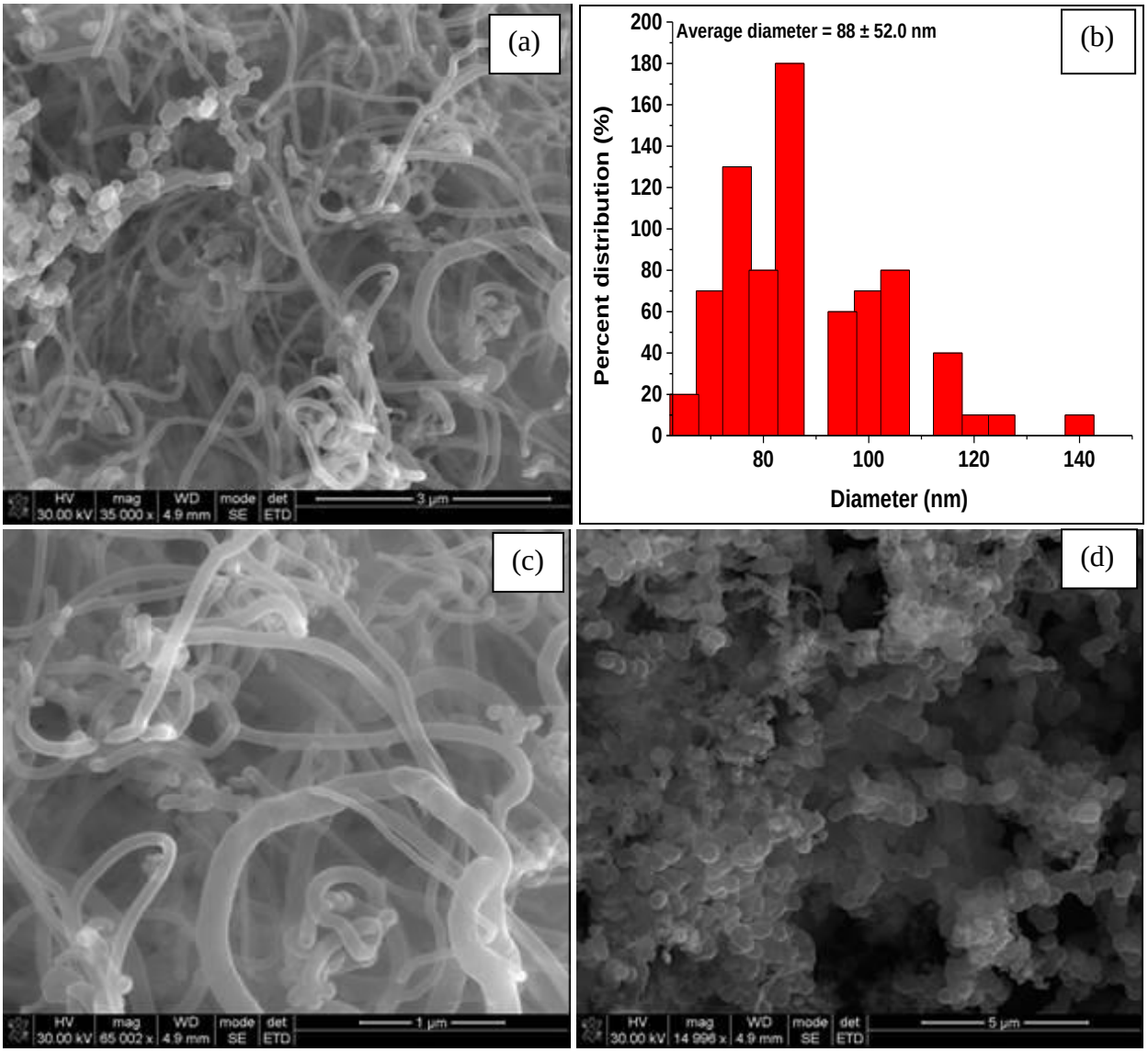

Figure 6.16 SEM images and diameter distribution curve of purified N-CNTs post-doped with chlorine.

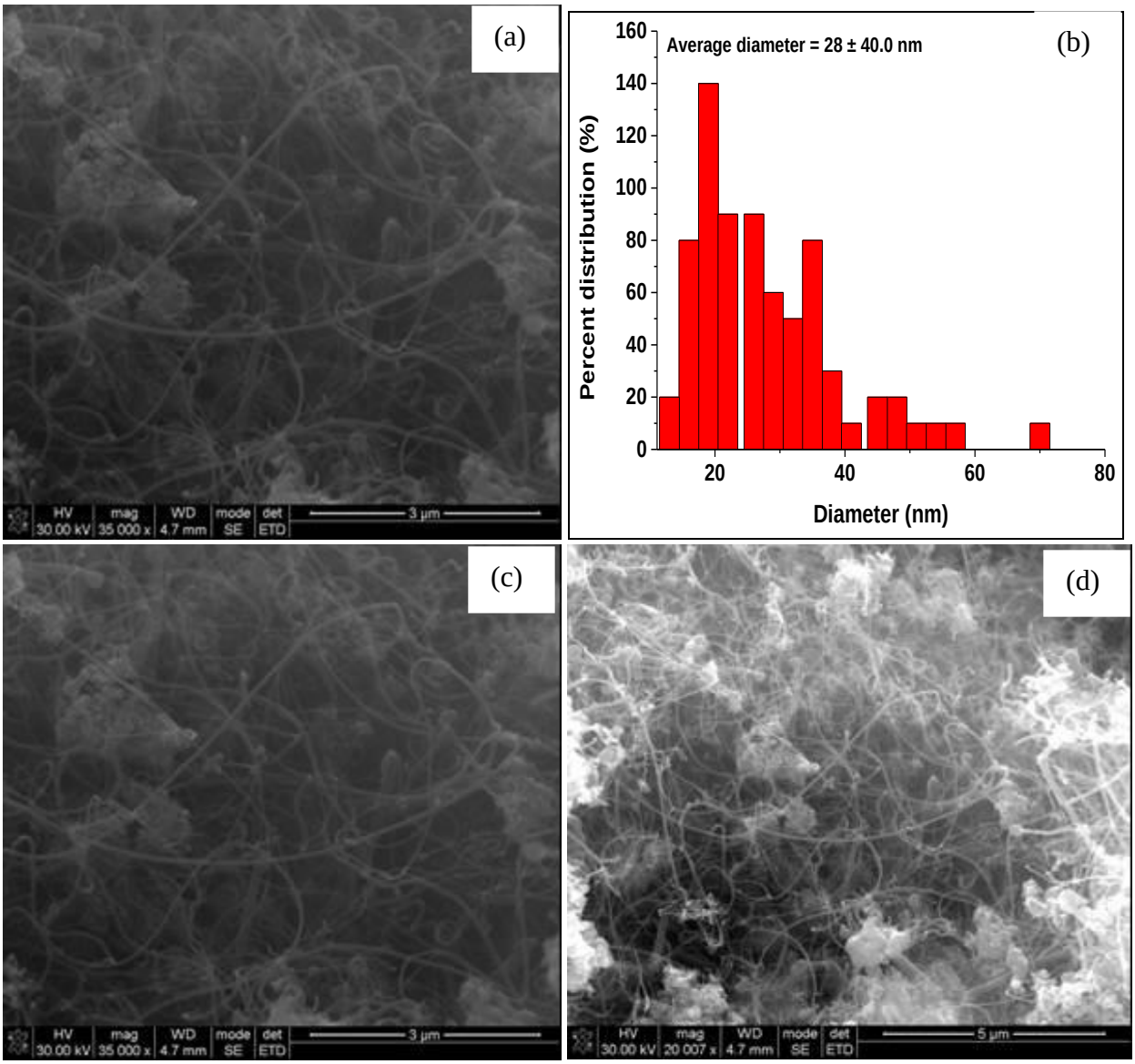

Figure 6.17 SEM images and diameter distribution curves of purified chlorinated CNTs post-doped with nitrogen.

6.3.2.2 Raman spectroscopy analysis of post-treated CNTs

Raman spectra of the N-CNTs post-doped with chlorine showed three bands, the D-, G-and 2D-band (Figure 6.18). The disorder induced D-band was deconvoluted into one peak at 1344 cm^{-1} and the graphitic peak G-band was deconvoluted into two peaks a graphitic carbon G-band at 1573 cm^{-1} and a disordered graphitic plane D'-band at 1613 cm^{-1}. A low intensity 2D band also appeared at 2686 cm^{-1} and a very low intensity defect-induced G^* peak at 2440 cm^{-1}. A 2D peak

was not observed from the N-doped CNTs generated from CH_3CN, which suggest that post-treatment with chlorine resulted in the formation of highly graphitic materials. The I_D/I_G peak area values of 1.2 and 0.65 for NCNTs and NCNTs post-treated with chlorine, which also suggest that the graphitic nature of the CNTs was improved by Cl incorporation. FWHM values of 71 and 40 cm^{-1} for NCNTs and NCNTs post-treated with Cl also suggest that post-incorporation of chlorine resulted in formation of amorphous free NCNTs (Table 6.10). A $I_D/I_{D'}$ value of 5.5 corresponds to formation of vacancy-like defects, a property of removed carbon. Vacancy-like defects with an I_D/I_G value of 5.7 were obtained from CNMs generated from pure CH_3CN by an injection CVD method. This suggest that post-doping with chlorine might have increased the number of nitrogen atoms doped into the CNTs.

Table 6.10 Raman bands of the purified N-doped CNTs generated from pure CH_3CN and after post-treatment with DCB

Carbon nanostructure	**Band name**	**Band Position (cm^{-1})**	**Bond type**	**FWHM (cm^{-1})**	**Peak Area**	**Designation**
Purified N-doped CNTs	D4	1210	sp^2–sp^3	126	983	C=C stretching vibrations
	D3	1339	sp^2	126	6701	Disordered graphite
	D2	1513	sp^3	85	1042	Amorphous carbon structure
	G	1584	sp^2	71	5312	Graphitic like carbonyl group
N-doped CNTs post-treated with DCB	D3	1338	sp^2	77	1793	Disordered graphite
	G	1587	sp^2	50	2347	Graphitic like carbonyl group
	D’	1613	sp^2	31	429	Defects in graphitic plane
	G^*	2440		36	82	1^{st} overtone of D4
	2D	2686		55	300	1^{st} overtone of D1

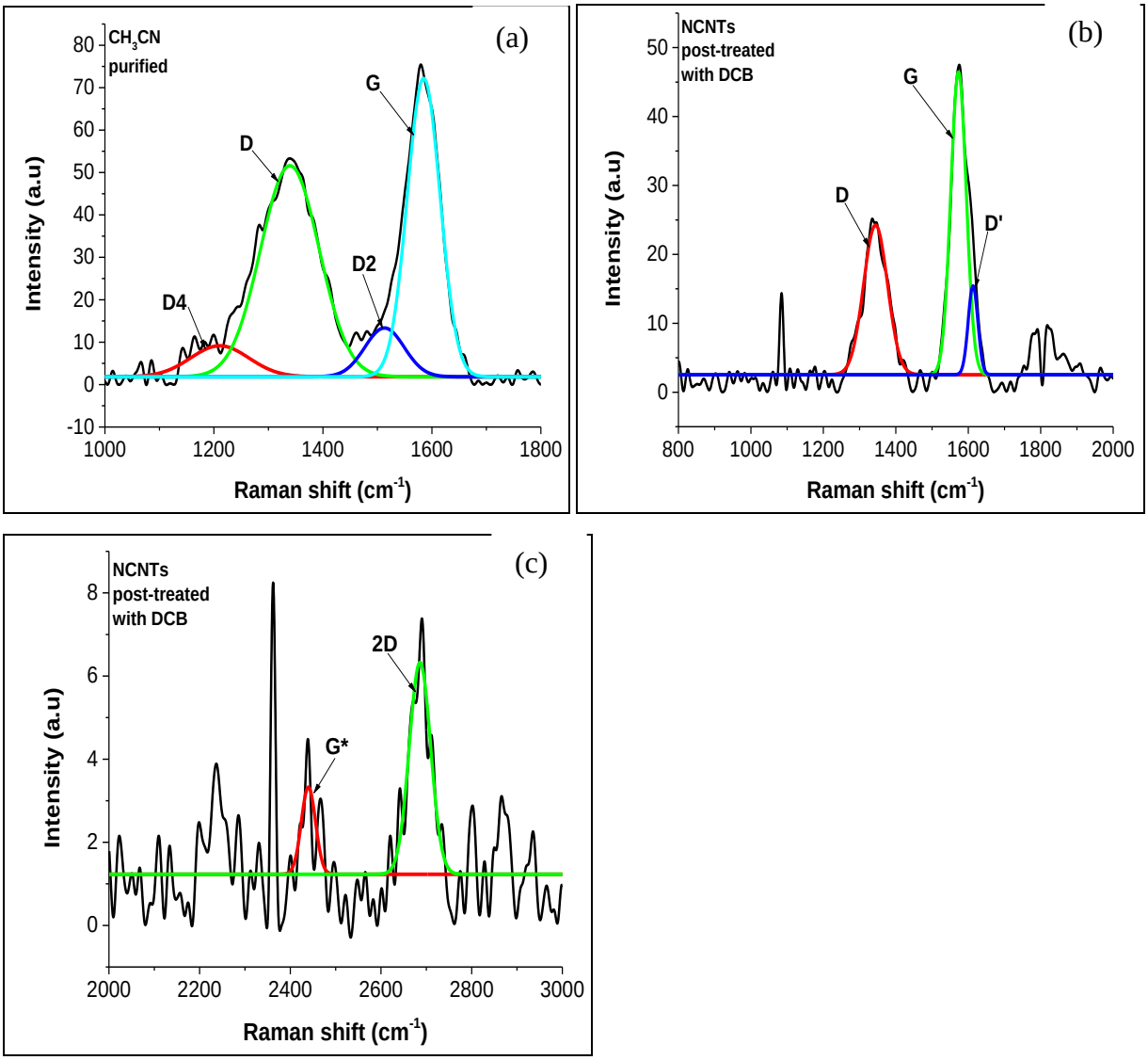

Figure 6.18 Deconvoluted Raman spectra of purified N-doped CNTs generated from (a) CH_3CN, and (b and c) after post-treatment with DCB.

Raman spectra of the chlorinated MWCNTs post-doped with nitrogen showed three bands, the D-, G-and 2D-band (Figure 6.19). The disorder induced D-band was deconvoluted into one peak at 1340 cm^{-1} and the graphitic peak G-band was deconvoluted into one peak at 1576 cm^{-1}. A highly intense 2D band also appeared at 2678 cm^{-1} and a very low intensity defect-induced G^* peak at 2444 cm^{-1}. A 2D band was not observed from the chlorinated CNTs generated from DCB, which suggests that they were introduced during post-doping treatments with nitrogen.

This suggests that post-treatment with nitrogen results with the formation of more graphitic materials. Unfortunately, we did not have access to XPS (hence we could analyze only a limited samples) it would have been informative to see the type of dominating nitrogen species in this samples.

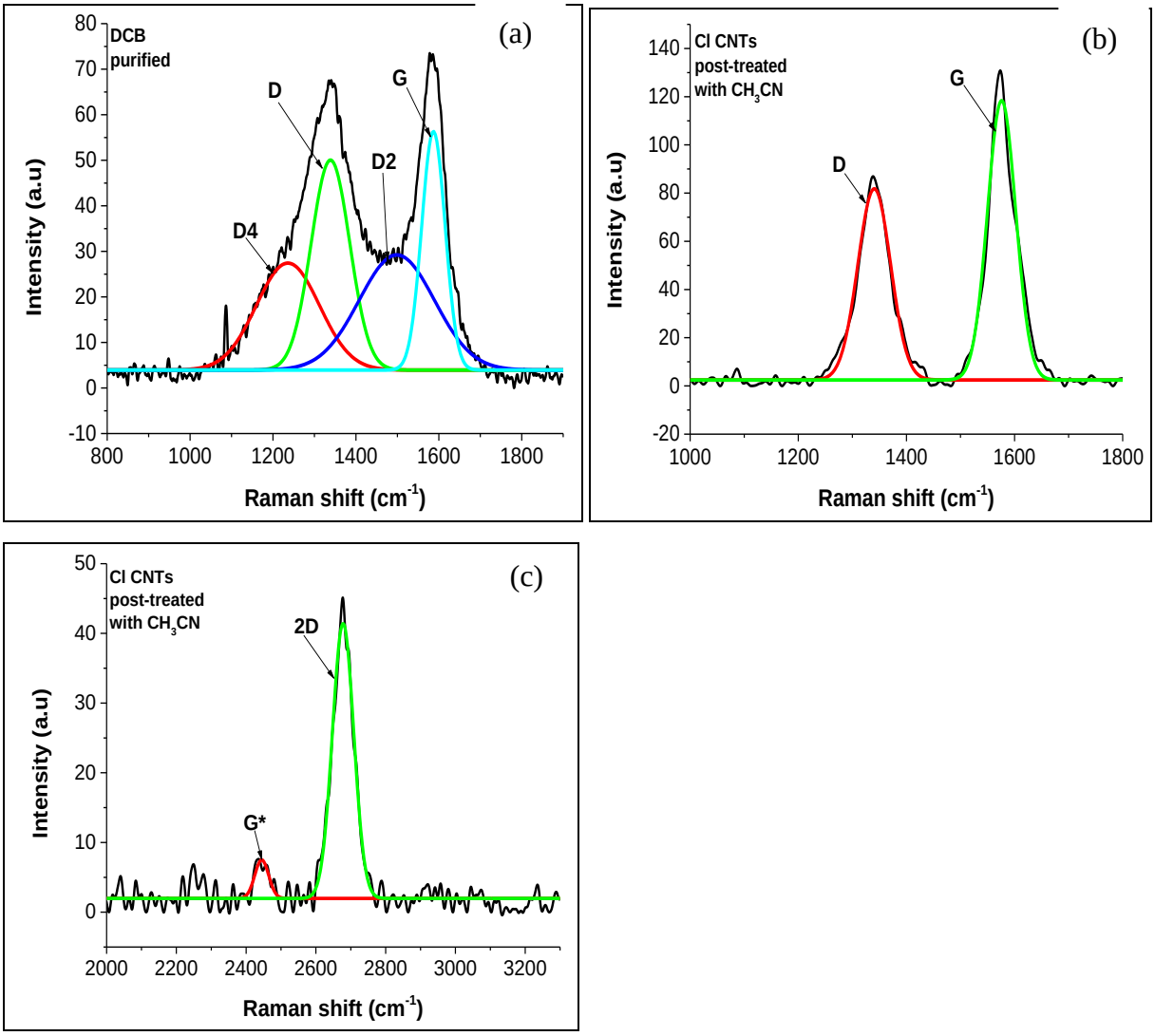

Figure 6.19 Deconvoluted Raman spectra of purified chlorinated CNTs generated from (a) DCB, and (b and c) after post-treatment with CH_3CN.

The I_D/I_G peak area values of 1.0 and 0.8 for chlorinated CNTs and chlorinated CNTs post-treated with nitrogen, also suggest that the graphitic nature of the CNTs was improved by post-doping with nitrogen. FWHM values of 66 and 61 cm^{-1} for chlorinated CNTs and chlorinated CNTs post-treated with N also suggest that post-incorporation of nitrogen resulted in formation of amorphous free CNTs (Table 6.11).

Table 6.11 Raman bands of the purified chlorinated CNTs generated from pure DCB and after post-treatment with CH_3CN

Carbon nanostructure	**Band name**	**Band Position (cm^{-1})**	**Bond type**	**FWHM (cm^{-1})**	**Peak Area**	**Designation**
Purified chlorinated CNTs	D4	1236	sp^2–sp^3	179	4472	C=C stretching vibrations
	D	1338	sp^2	109	5375	Disordered graphite
	D2	1498	sp^3	214	5760	Amorphous carbon structure
	G	1587	sp^2	66	3703	Graphitic like carbonyl group
Purified Chlorinated CNTs post-treated with CH_3CN	D	1340	sp^2	71	6026	Disordered graphite
	G	1576	sp^2	61	7584	Graphitic like carbonyl group
	G^*	2444		46	274	1^{st} overtone of D4
	2D	2678		72	3015	1^{st} overtone of D1

6.3.4 Effect of concentration of TTCE in CH_3CN

Various CH_3CN:TTCE reagent volume ratios namely, 100:0, 0:100, 50:50, 66.7:33.3 and 75:25 vol.% were studied to see their effect on the morphology of the CNMs. Pyrolysis of the mixture of nitrogen and chlorine source was performed at room temperature and at 100 °C.

6.3.3.1 Structural analysis of the N-doped CNMs: Effect of TTCE concentration and synthesis temperature

Synthesis of CNTs using only tetrachloroethane (TTCE) as chlorine source was performed using the method developed previously.[28] Hollow CNTs were generated and metal particles were observed at the tip of some CNTs suggesting a tip-growth mechanism (Figure 6.20a and b shown by arrow). SEM images of purified CNTs generated from room temperature TTCE solutions revealed formation of highly entangled CNTs and clumps particles (Supplementary Figure S19).

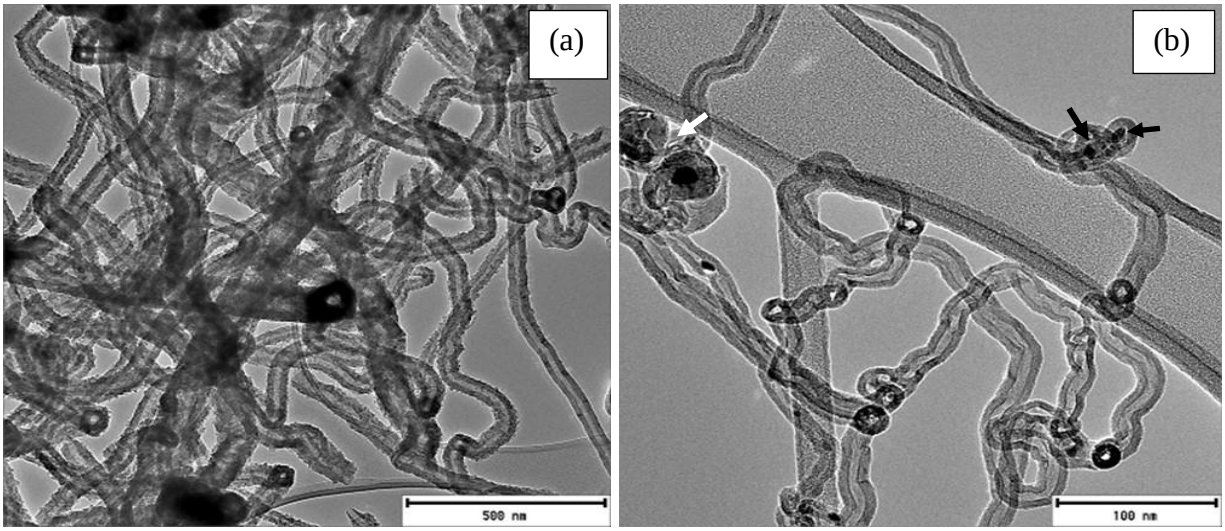

Figure 6.20 TEM images of purified CNMs generated from (a and b) tetrachloroethane (TTCE), (N_2 = 280 mL/min, C_2H_2 = 50 mL/min, T = 700 °C, t = 60 min).

Studies were then performed to investigate the effect of chlorine on the growth of N-doped CNTs using a mixture of room temperature solutions of CH_3CN and TTCE of various volume ratios. TEM images obtained at different volume ratios of the two organic reagents at room temperature are presented in Figure 6.21 to Figure 6.23. In all the studies, carbon nano-onions were formed and metal-nanoparticles were encapsulated in some of the nano-onions. A

measurable quantity of other shaped CNTs with funnel-shaped (or Y-shaped) mouths or open-ends (Figure 6.21b and Figure 6.22b) were also observed. Similar Y-shaped tube ends were observed in this study from CNTs obtained when DCB was used as a chlorine source mixed with CH_3CN using an injection CVD method (Chapter 5). At lower concentrations of DCB (25 and 33.3 vol.%) carbon nano-onions were connected to bamboo-shaped carbon nano-bells which showed increased nitrogen incorporation (Figure 6.21c and Figure 6.22c).

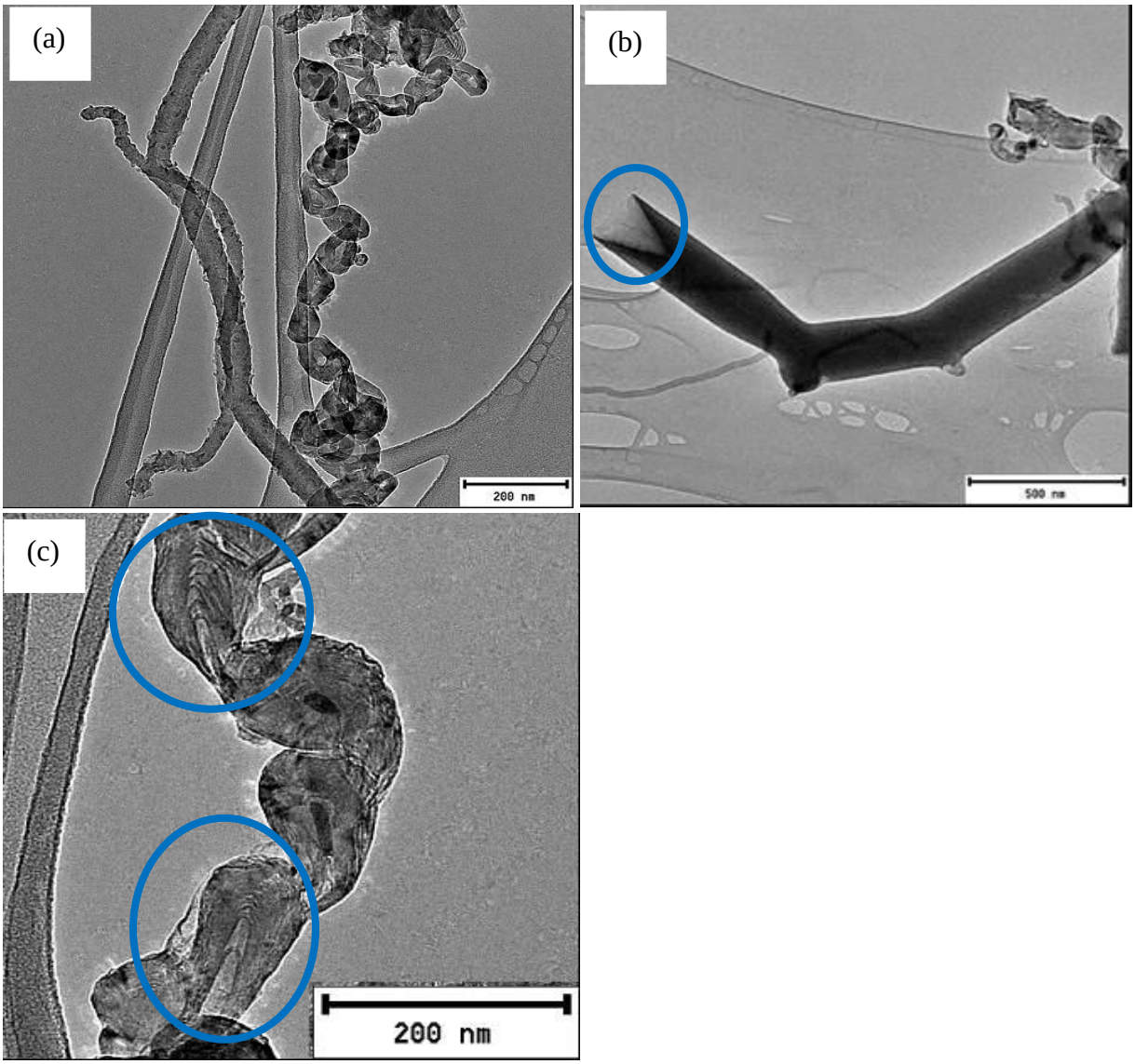

Figure 6.21 TEM images obtained from purified CNMs generated from a 75:25 vol.% CH_3CN:TTCE solution mixture (N_2 = 280 mL/min, C_2H_2 = 50 mL/min, T = 800 °C, t = 60 min).

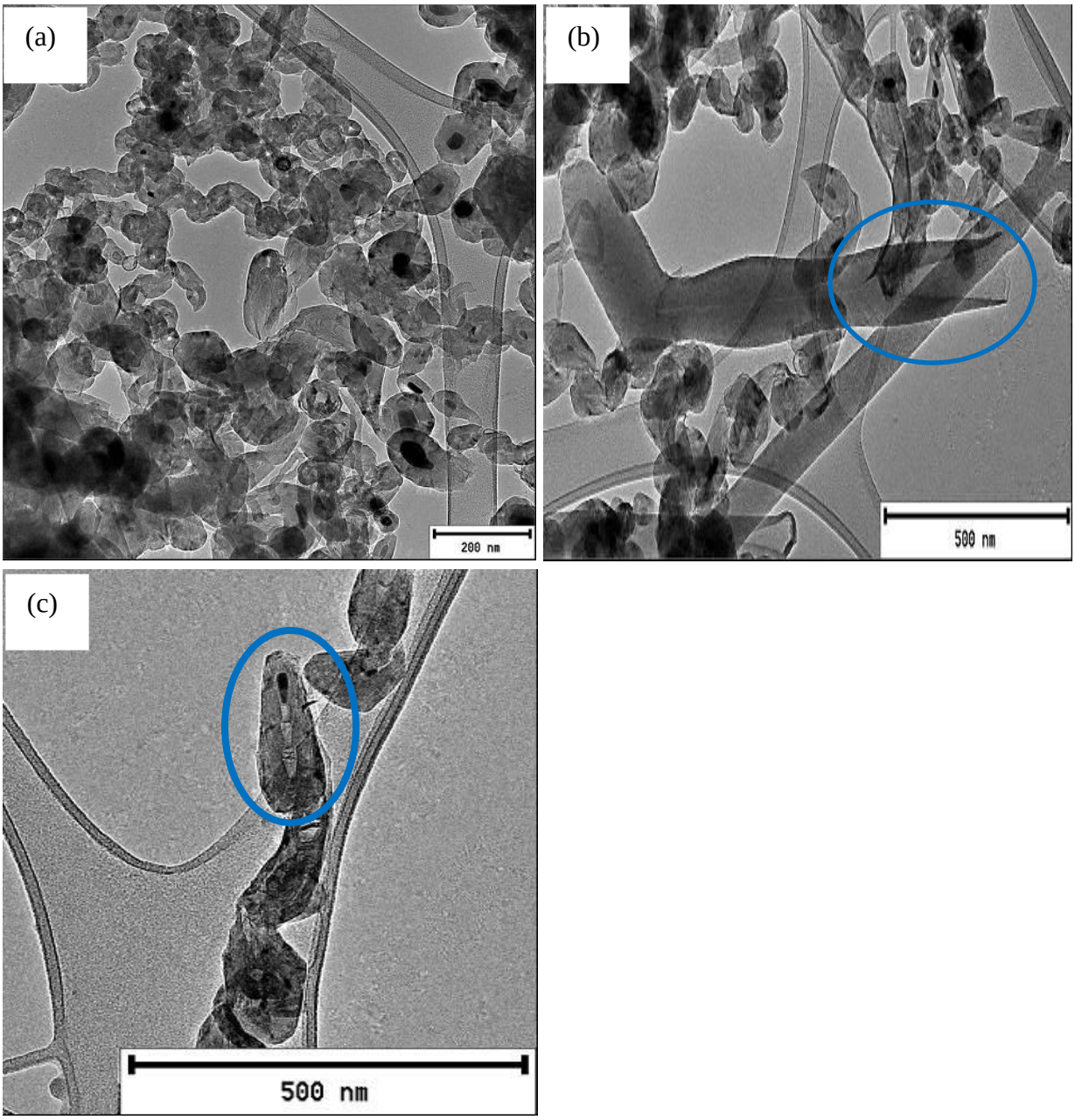

Figure 6.22 TEM images obtained from purified CNMs generated from a 66.7:33.3 vol.% CH_3CN:TTCE solution mixture (N_2 = 280 mL/min, C_2H_2 = 50 mL/min, T = 700 °C, t = 60 min).

Studies were also performed to investigate the effect of chlorine on the growth of N-doped CNTs using a mixture of room temperature solution of CH_3CN and TTCE of various volume ratios. The formation of carbon nano-onions increased with an increase in the concentration of DCB (50 vol.%) in the feed (Figure 6.23). Chlorination of metal carbides was found to enhance formation

of carbon nano-onions.[25] From the XRD studies in our previous work we found that iron carbide was formed as a bi-product[28] of the chlorinated CNTs. Carbon nano-onions were formed in another study when nitrogen was used as a carrier gas unlike when hydrogen was used.[24] The nitrogen concentration in the carbon nano-onions and the carbon nano-onion yield increased with increasing reaction time.[24] Atomic scale electron loss spectroscopy analysis of nano-onions in CN_x thin film[36] and CN_x nanotube[37] showed that the nitrogen concentration increases as the curvature of the graphitic layer increases. The carbon onion could be easily obtained due to presence of nitrogen, which can reduce the strain energy required for the spherical graphitic layer of carbon onion and thus decrease the activation energy for both the nucleation of the graphitic layer on the catalyst surface and the structural evolution of the carbon onion during growth.[24] We conclude that combination of chlorine and nitrogen resulted in the enhanced growth of carbon nano-onions based on the above explanations. SEM images recorded for all studied TTCE concentrations showed that the interconnected carbon nano-bells are dominating structures (Supplementary Figure S20 to S22).

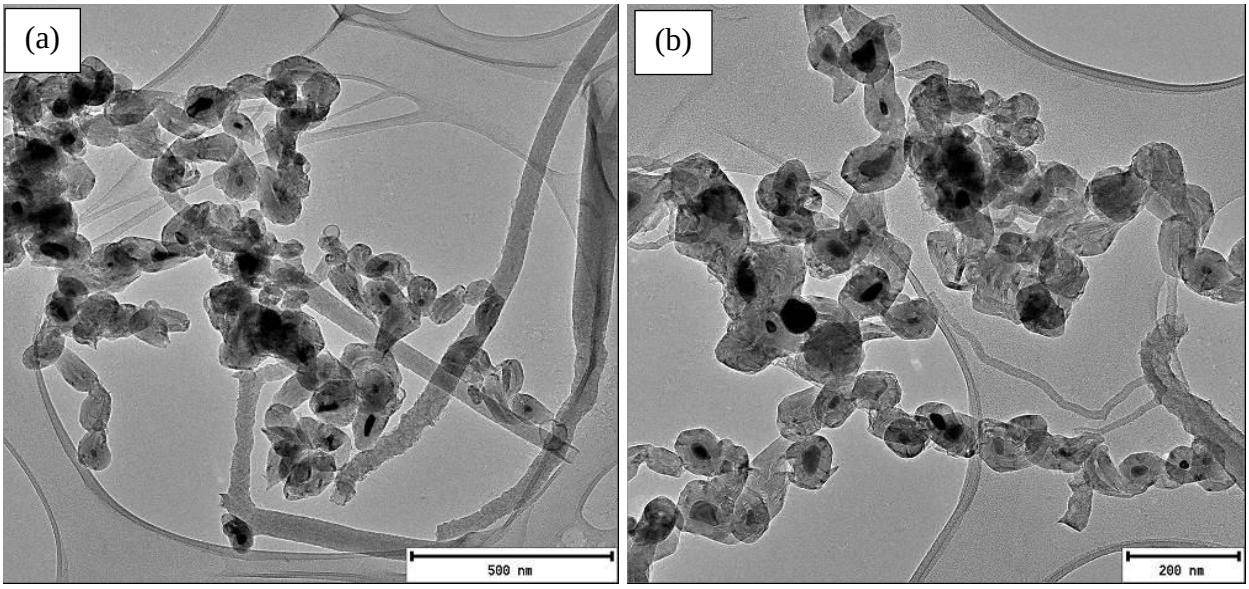

Figure 6.23 TEM images obtained from purified CNMs generated from a 50:50 vol.% CH_3CN:TTCE solution mixture (N_2 = 280 mL/min, C_2H_2 = 50 mL/min, T = 700 °C, t = 60 min).

Studies were also performed to investigate the effect of chlorine on the growth of N-doped CNMs using heated solutions of CH_3CN and TTCE and of their mixtures of various volume ratios. In this study the temperature of acetonitrile was kept at 90 °C, while that of TTCE and CH_3CN/TTCE reagents mixtures were kept at 100 °C to evaluate its effect on the morphology of the CNMs.

Bamboo-shaped CNTs and connected carbon nano-bells were observed from the TEM images generated from heated solutions of CH_3CN (Figure 6.24). The amount of bamboo-compartmented CNTs was increased when we compare to those generated from room temperature CH_3CN. SEM images of CNMs generated from CH_3CN revealed the presence of various carbon structures, carbon nanospheres (CSs), carbon nano-platelets, some coiled structures (which are probably connected carbon nano-bells or carbon nanospheres) (Supplementary Figure S23). Carbon nanospheres which were linked together in a necklace-like fashion were observed in another study from vaporization of CH_3CN at 80 °C.[29] CSs of this nature are usually prepared by pyrolysis of a hydrocarbon by CVD in the absence of a catalyst.[38] The ratio of the produced N-CNTs/carbon nano-bells/CSs was about 60/30/10.

Hollow CNTs (Figure 6.25a to c) and carbon nano-onions (Figure 6.25d) were produced when heated TTCE was used as a source of chlorine. Few carbon nano-onions were observed from room temperature solutions of TTCE and their formation seem to have increased at increased reagent temperature. An increase in temperature of TTCE led to greater vaporization of chlorine which resulted in chlorine interacting with the Fe_3C formed on the catalyst surface, enhancing the formation of carbon nano-onions. SEM images reveal formation of CNMs of various morphologies, CNTs, CNFs, coiled CNTs, some clustered carbon structures (probably carbon platelets or amorphous carbon structures) and a few large open-ended CNTs (Supplementary Figure S24). CNTs seems to be dominating but it was very difficult to determine the ratio of the various carbon structures.

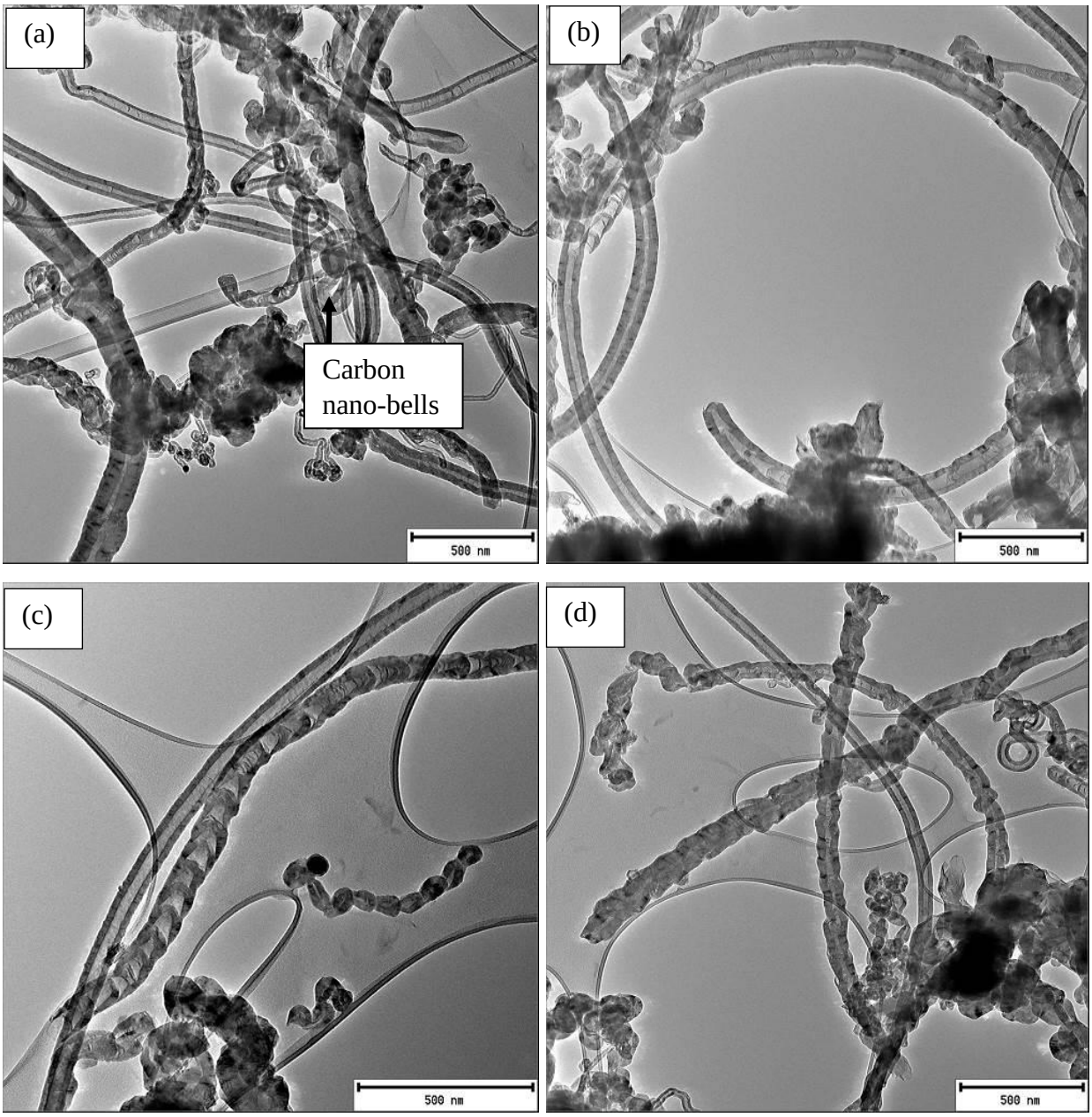

Figure 6.24 TEM images of purified CNMs generated from a heated solution of acetonitrile (90 °C) (N_2 = 240 mL/min, C_2H_2 = 90 mL/min, T = 800 °C, t = 60 min).

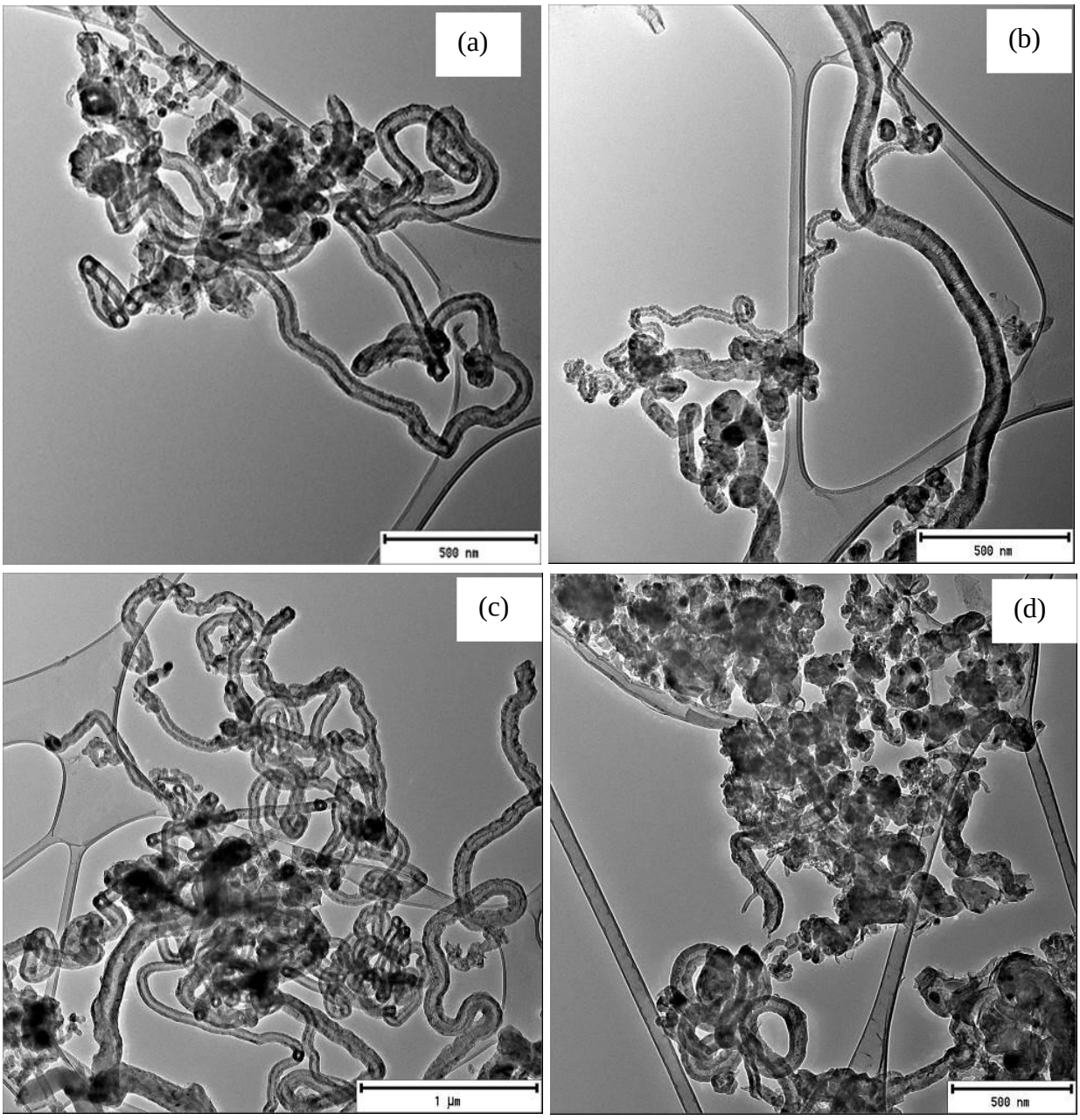

Figure 6.25 TEM images of purified CNMs generated from heated solutions of tetrachloroethane (100 °C) (N_2 = 280 mL/min, C_2H_2 = 50 mL/min, T = 700 °C, t = 60 min).

An effect of temperature was also investigated for systems that contained a mixture of CH_3CN:TTCE with different volume ratios. TEM images obtained from acetonitrile feed solutions that contained low concentration of TTCE (25 vol.%), revealed formation of CNMs of variable morphologies. Coiled and un-coiled bamboo-compartmented CNTs, hollow CNTs, connected carbon nano-bells and nano-onions, bamboo-compartmented carbon nano-bells, carbon nano-bells with metal particle encapsulated inside and a variety of carbon nano-bells connected to each other in a leave branches format (Figure 6.26). We suggest that the presence of chlorine molecules enhanced the formation of carbon nanostructures with intratubular junctions, as it interacted with an iron carbide formed on the surface of the catalyst substrate. It was found in another study that carbide-forming elements like titanium as dopants in the catalyst can also facilitate the synthesis of branched junctions.[17] SEM images (Supplementary Figure S5) and TEM images reveal that the majority of the CNMs were interconnected carbon nano-bells.

Increasing the DCB concentration in the CH_3CN feed to 33.3 vol.%, resulted in the formation of bamboo-compartmented and hollow CNTs (Figure 6.27). Metal particles encapsulated inside some of the CNTs was observed from Figure 6.27b. Some coiled hollow CNTs were also observed from the TEM images. The formation of carbon nano-bells was greatly reduced at this concentration (Figure 6.27c insert). SEM images reveal formation of regular CNTs of similar sizes (Supplementary Figure S26). The ratio of CNTs/carbon nano-bells can be estimated as 80/20.

TEM images obtained from acetonitrile feeds containing 50 vol.% TTCE also revealed formation of mixed CNMs with various morphologies, bamboo-shaped CNTs and interconnected carbon nano-bells (Figure 6.28c), hollow CNTs (Figure 6.28a), and some carbon nano-onions (Figure 6.28d). SEM images also shows mixtures of CNTs, and interconnected carbon nano-bells (Supplementary Figure S27). From the SEM images we estimated the ratio of the CNTs/carbon nano-bells as 20:80. The amount of chlorine in the feed had a great effect on the morphological changes of the N-doped CNMs. A solution containing 66.7:33.3 CH_3CN:TTCE volume ratio selectively produced CNTs, while a 50:50 and 75:25 volume ratio solutions gave mixtures of CNMs. One can find tune the amount of chlorine in the feed to obtain CNMs for their desirable application. SEM images recorded for all studied TTCE concentrations showed that the

interconnected carbon nano-bells are the dominating structures (Supplementary Figure S20 to S22)

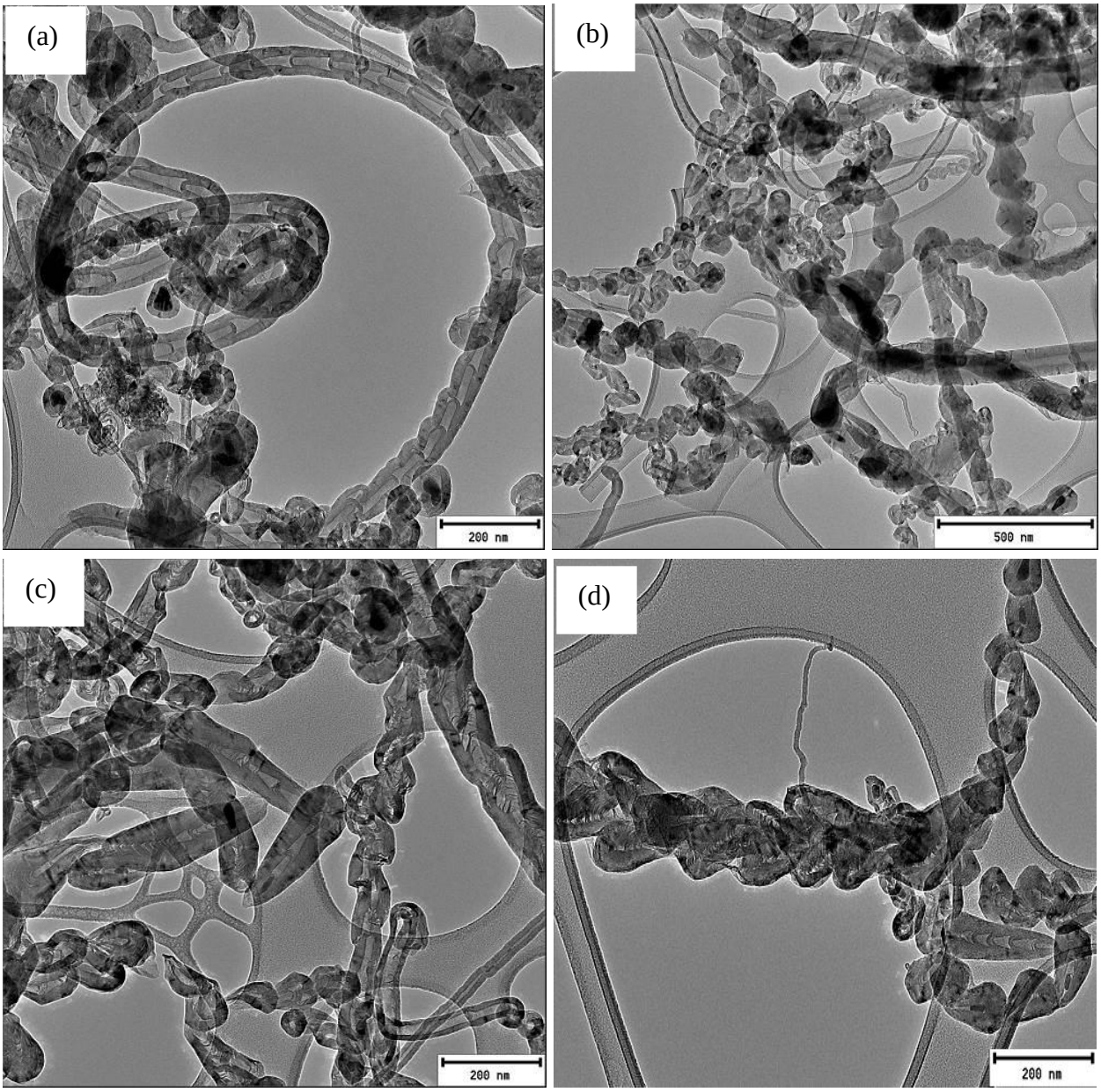

Figure 6.26 TEM images obtained from purified CNMs generated from a 75:25 vol.% CH_3CN:TTCE solution mixture (N_2 = 280 mL/min, C_2H_2 = 50 mL/min, T = 700 °C, t = 60 min).

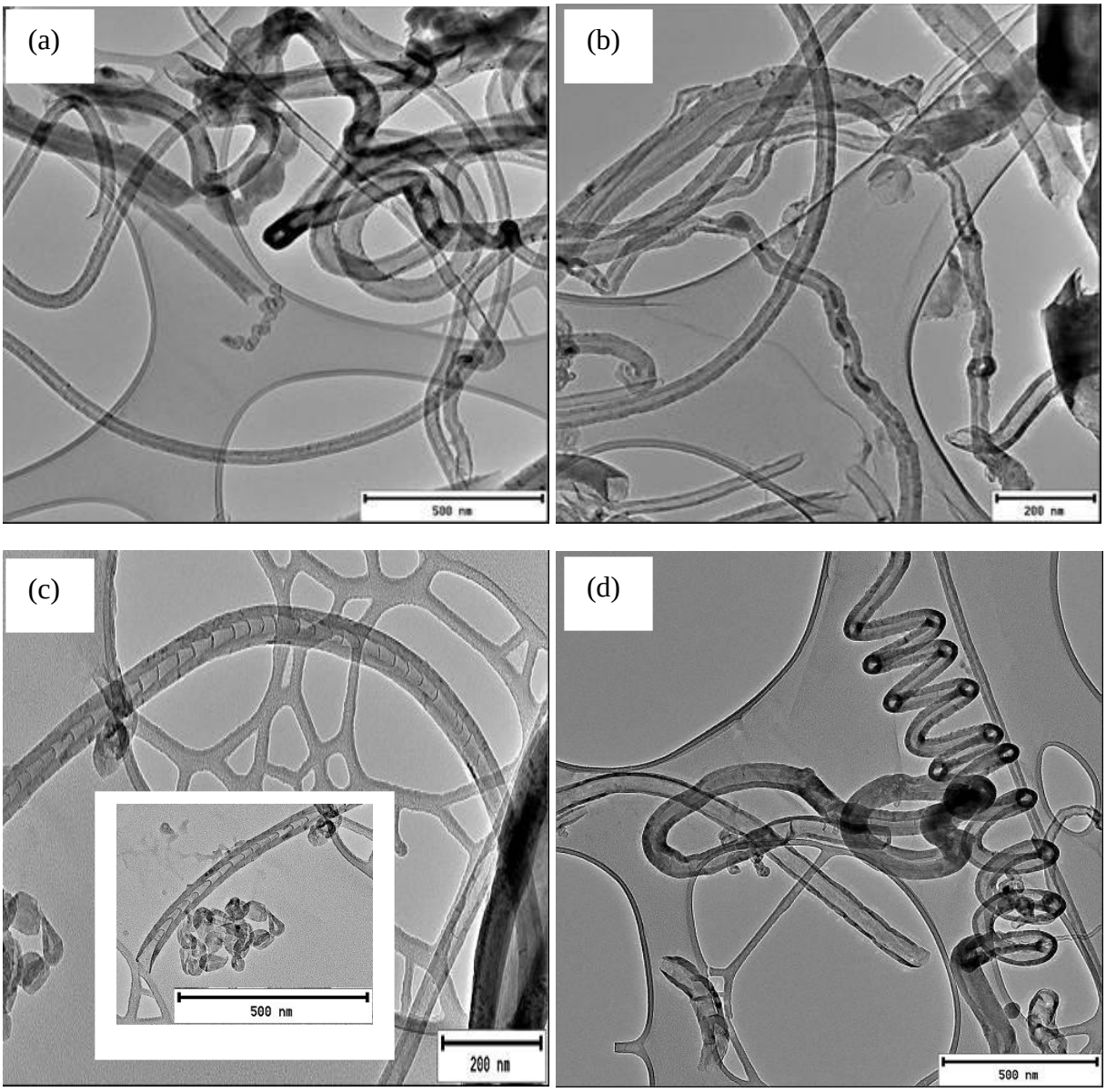

Figure 6.27 TEM images obtained from purified CNMs generated from a 66.7:33.3 vol.% CH_3CN:TTCE solution mixture (N_2 = 280 mL/min, C_2H_2 = 50 mL/min, T = 700 °C, t = 60 min).

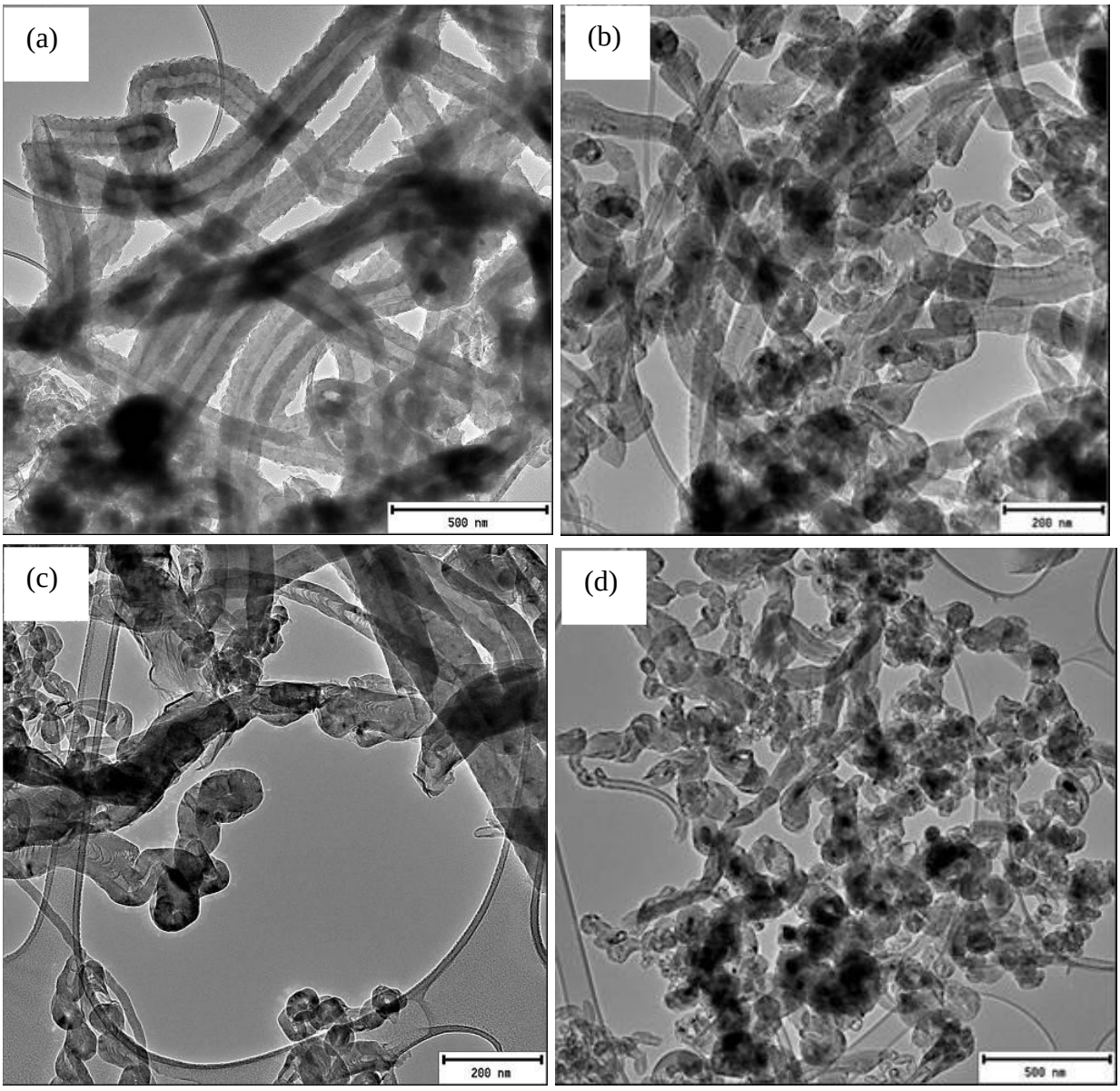

Figure 6.28 TEM images obtained from purified CNMs generated from a 50:50 vol.% CH_3CN:TTCE solution mixture (N_2 = 280 mL/min, C_2H_2 = 50 mL/min, T = 700 °C, t = 60 min).

6.3.3.2 Thermogravimetric analysis of the N-doped CNMs: Effect of TTCE concentration and synthesis temperature

TGA and DTGA curves of un-purified and purified CNTs generated from heated pure CH_3CN (90 °C) and TTCE (100 °C) are presented in Figure 6.29. Un-purified CNTs generated from CH_3CN showed a variety of weight losses, the initial minor weight loss observed around 100 to 300 °C was due to evaporation of physisorbed water at the onset temperature of 100 °C, together with decomposition of chemisorbed water and surface chloride groups at ~ 150 to 300 °C. The second minor weight loss at ~ 450 °C was due to decomposition of amorphous carbon structures. The third major weight loss (~ 55 %) with an onset temperature of ~ 580 °C was due to oxidation of CNTs, while the fourth minor weight loss at 700 °C was due to oxidation of other graphitic carbon structures (i.e. carbon nano-bells, carbon nanospheres, observed from the TEM images). Purified CNTs generated from CH_3CN showed three mass losses. The weight loss due to physisorbed and chemisorbed water together with surface chlorides was not observed after purification. The water could have been removed during drying of the CNTs at high temperature after purification and the surface chlorides could have reacted with the hydrogen from the acid used for treatment. The first minor weight loss was observed at ~350 to 400 °C due to amorphous carbon structures. The second major weight loss was observed at ~ 500 °C and was assigned to oxidation of N-doped CNTs.

Only one major broad weight loss was observed from TGA curves of un-purified and purified CNMs generated from room temperature TTCE solution (Figure 6.29). The weight loss occurred at ~ 580 to 700 °C which could be attributed to oxidation of chlorinated CNMs (Figure 6.29). The broadness of the oxidation peak suggest that various stable carbon nanostructures were oxidized at this temperature range. This data is consistent with the TEM observations where CNTs and carbon-nano-onions were generated, with CNTs dominating. The residual mass of ~ 10 and 15 % was observed from the TGA curves obtained from CH_3CN and TTCE before purification, which was completely removed after purification shown by a residual mass of zero. This shows that purification with acid was effective for removal of any catalyst metal particles that remained on the surface of the CNMs after synthesis.

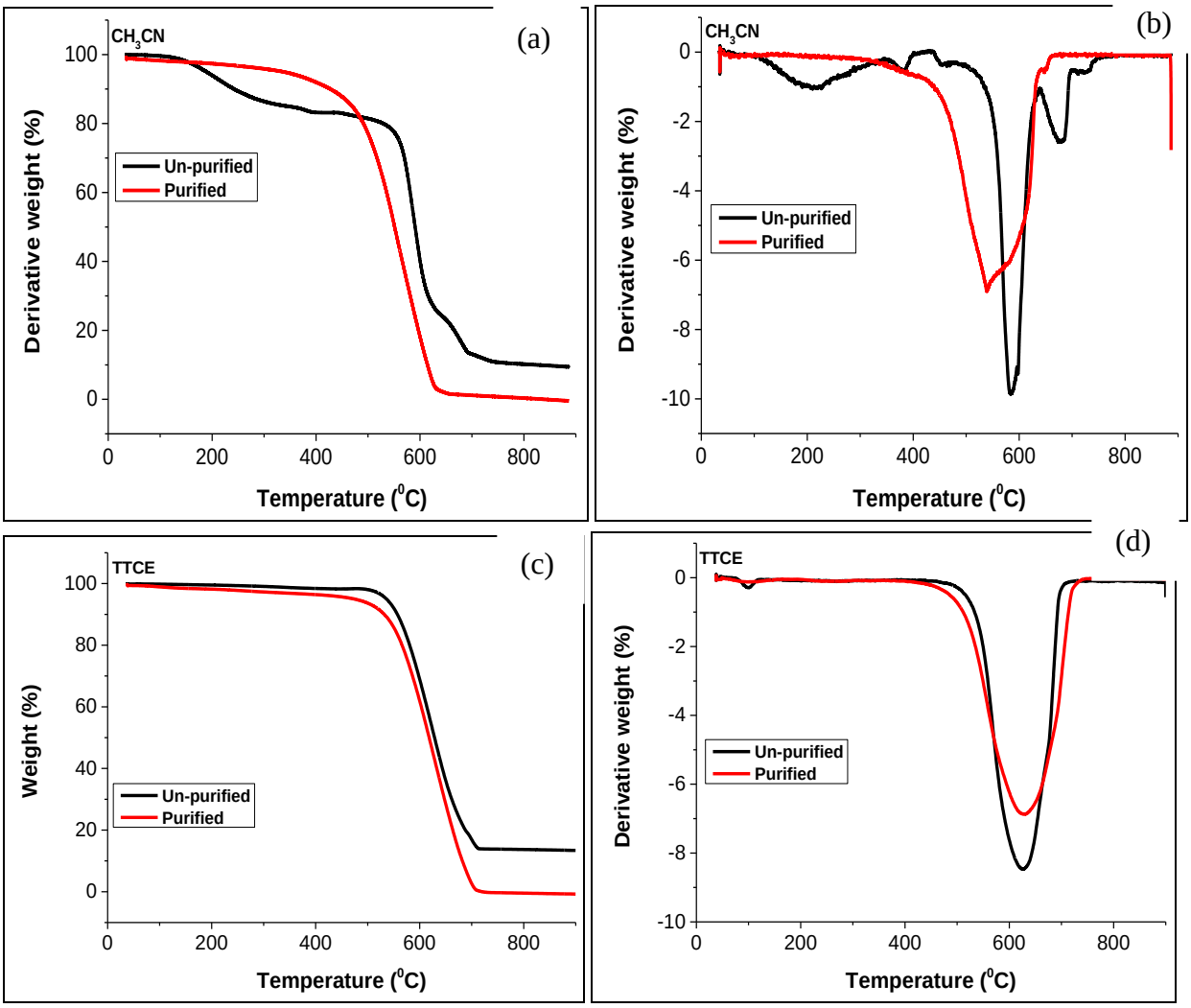

Figure 6.29 TGA and DTGA curves of un-purified and purified CNMs generated from room temperature solutions of pure CH_3CN (a and b) and pure TTCE (c and d)

A two stage oxidation process shown by two regions of weight losses was observed in the TGA and DTGA curves of the unpurified CNMs generated from room temperature CH_3CN feeds containing low concentration of DCB (25 vol.%). The first major weight loss was broad and occurred at ~ 550 to 680 °C, which could be attributed to oxidation of various N-doped CNTs and carbon nano-bells which are chlorine functionalized and un-functionalized (Figure 6.30a and b). The second minor weight loss at ~ 680 to 750 °C could be due to carbon platelets and other metal encapsulated CNMs (Figure 6.30a and b). This data agrees with the TEM observations were carbon nanostructures of various morphologies were observed. The weight losses shifted to higher oxidation temperatures after acid treatment, due to stabilization of the CNMs by

functionalization of the CNMs with oxygen functional groups (Figure 6.30a and b). Another weight loss was observed at higher temperatures > 800 °C from purified CNMs due to evolution of nitrogen. The residual mass was again reduced from ~ 20 % to zero, suggesting that acid treatment was effective in removal of catalyst metal particles that could have been on the surface of the CNMs.

TGA and DTGA curves of CNMs generated from room temperature solutions containing increased concentration of TTCE in the acetonitrile feed to 33.3 vol.% are presented in Figure 6.30c and d. Two weight losses are observed from both the un-purified and purified samples. The first major weight loss was at ~ 550 to 650 °C for un-purified CNMs and was at ~ 530 to 680 for purified CNMs, due to oxidation of chlorinated and un-chlorinated N-doped CNTs. The second weight loss at ~ 650 to 700 °C was due to oxidation of other graphitic materials like carbon nano-bells observed from the TEM images. The residual mass loss was not reduced to zero after acid treatment which suggest that some catalyst particles were still present after acid treatment. Catalyst particles encapsulated into the CNTs were observed from the TEM images.

TGA and DTGA curve of un-purified CNMs generated from a further increase in the amount of TTCE in the CH_3CN feed to 50 vol.% was similar to the one obtained from solutions containing 33.3 vol.% (Figure 6.30e and f). Three weight losses were observed from purified CNMs generated from solutions containing 50 vol.% TTCE concentration (Figure 6.30e and f). They were at about 550, 600 and 700 °C which were assigned to oxidation of un-functionalized CNTs, chlorine functionalized CNTs and other chlorine functionalized carbon structures (carbon nano-bells and carbon nano-onions) observed from the TEM images.

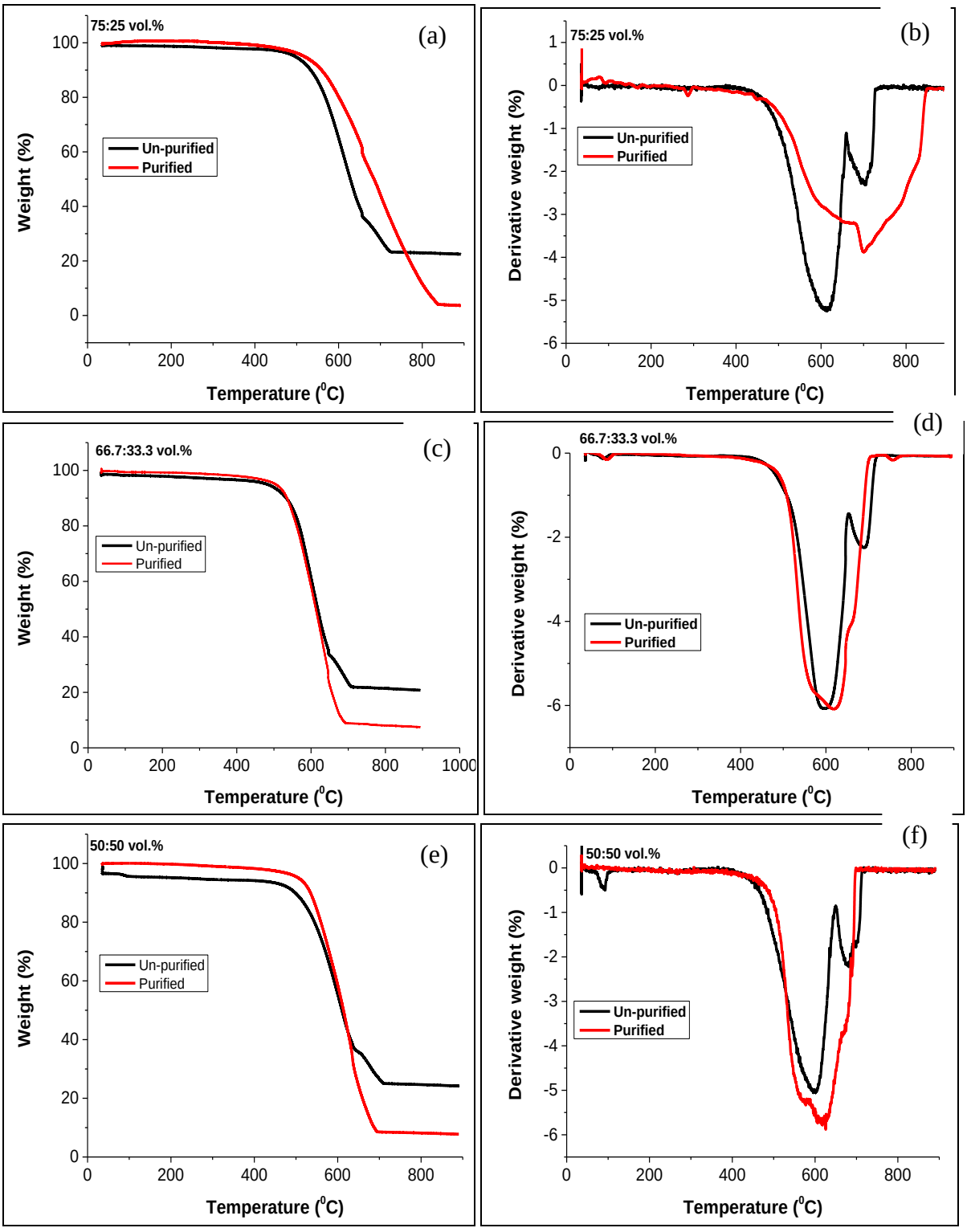

Figure 6.30 TGA and DTGA curves of un-purified and purified CNMs generated from room temperatures solutions of various concentration of TTCE in the acetonitrile feed.

The level of purity of the CNMs generated from hot solutions was also investigated using TGA and DTGA. TGA and DTGA curves of un-purified CNMs generated from heated TTCE all solutions revealed two main oxidation peaks for the oxidation of chlorine functionalized CNTs at ~ 580 °C and other crystalline graphitic particles (carbon-nano-onions, large-sized CNTs with open-ends and carbo platelets) at ~ 700 °C (Figure 6.31a and b). Purified CNMs showed one broad weight loss at ~ 600 °C that had a shoulder peak at ~ 650 °C due to oxidation of chlorine functionalized CNTs and other graphitic materials mentioned above for the un-purified CNMs (Figure 6.31c and d).

Table 6.12 Decomposition temperatures and residual masses (determined by TGA) of the un-purified and purified (P) chlorine functionalized NCNMs generated by bubbling different ratios of CH_3CN and TTCE at room temperature.

Hydrocarbon source	Decomposition temperature/°C	Residual mass/%
CH_3CN	697	7.9
CH_3CN (P)	633	0
TTCE[28]	615	13.5
TTCE (P)[28]	619	0
CH_3CN:TTCE (50:50)	600	24
CH_3CN:TTCE (50:50) (P)	627	7.7
CH_3CN:TTCE (66.6:33.3)	600	21
CH_3CN:TTCE (66.6:33.3) (P)	615	7.5
CH_3CN:TTCE (75:25)	600	22.5
CH_3CN:TTCE (75:25) (P)	630	3.6

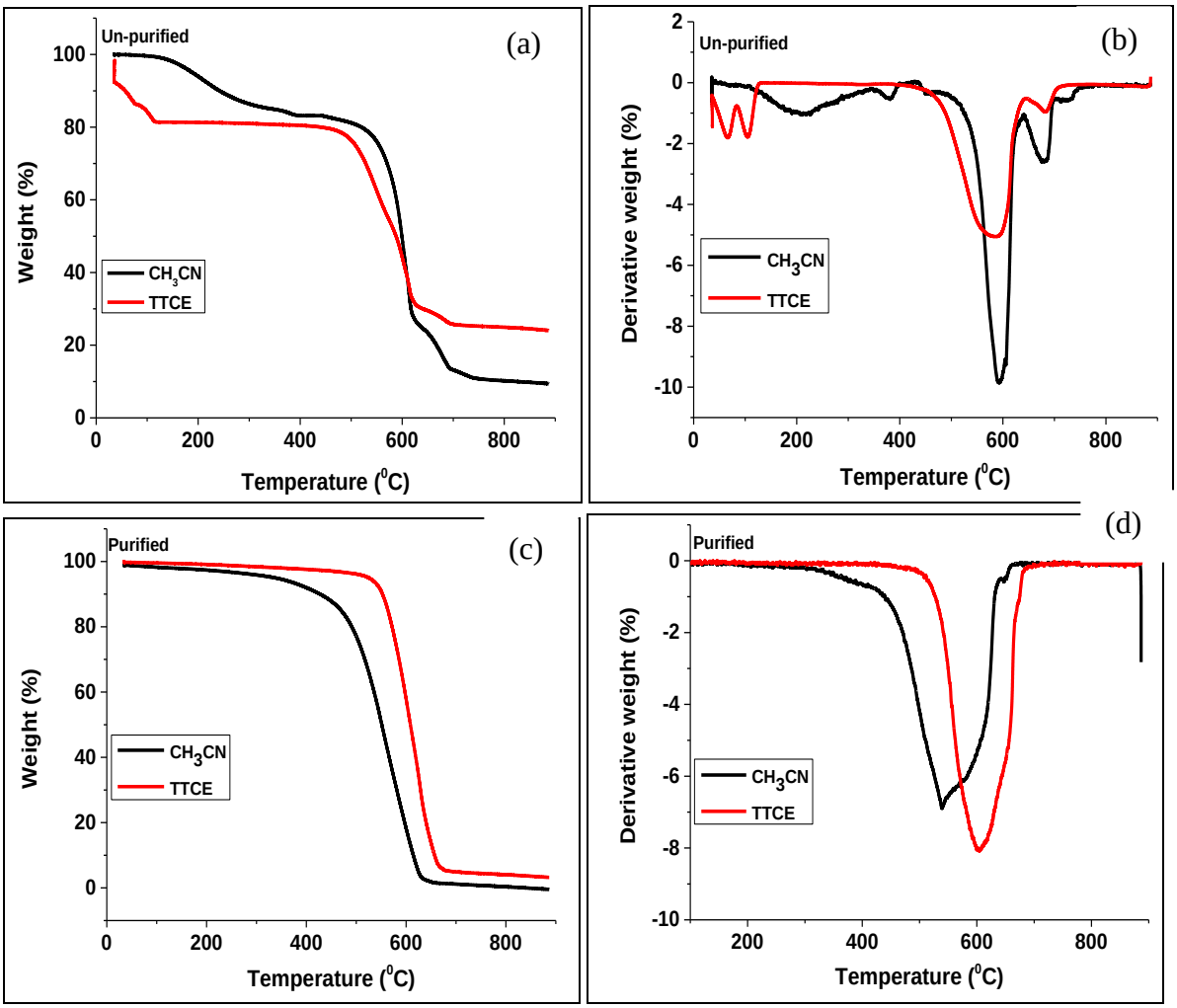

Figure 6.31 TGA and DTGA curves of un-purified (a and b) and purified (c and d) CNMs generated from heated solutions of pure CH_3CN (90 °C) and pure TTCE (100 °C)

TGA and DTGA of CNMs generated from heated solutions of CH_3CN containing 25 vol.% DCB showed two weight losses in the un-purified samples and one weight loss from the purified samples (Figure 6.32a and b. The weight loss at ~ 600 °C observed from both un-purified and purified samples was due to oxidation of chlorine functionalized N-doped CNMs (Figure 6.32a and b). The minor peak at ~ 700 °C observed from un-purified solution is probably due to oxidation of carbon platelets, which were removed by purification. Similar observations were obtained from CNMs generated from feed solutions containing 33.3 and 50 vol.% TTCE concentrations, except that the amorphous carbon peak was also observed at this feed solutions at ~ 450 °C from both un-purified and purified CNMs (Figure 6.32c to f). Residual mass of zero

was obtained from all studied TTCE concentrations, suggesting that the materials were free of any metal catalysts particles on their surface.

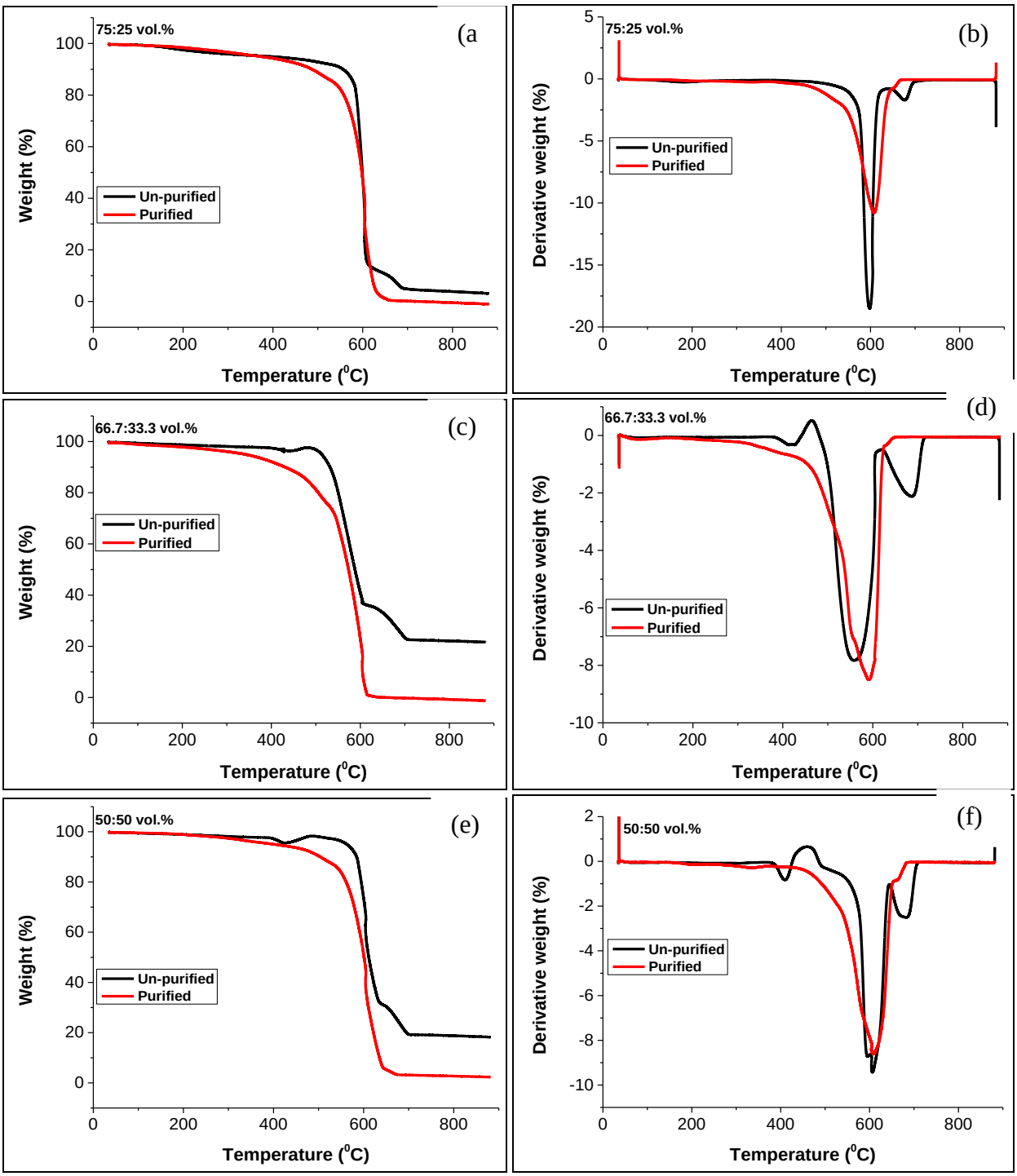

Figure 6.32 TGA and DTGA curves of un-purified and purified CNMs generated from heated (100 °C) solutions of various concentration of TTCE in the acetonitrile feed.

Table 6.13 Decomposition temperatures and residual masses (determined by TGA) of the un-purified and purified (P) chlorine functionalized NCNMs generated by bubbling different ratios of a CH_3CN and TTCE at 100 °C.

Hydrocarbon source	Decomposition temperature/°C	Residual mass/%
CH_3CN	592	9.4
CH_3CN (P)	544	0
TTCE	589	24
TTCE (P)	611	3.2
CH_3CN:TTCE (50:50)	628	18.2
CH_3CN:TTCE (50:50) (P)	627	2.3
CH_3CN:TTCE (66.7:33.3)	568	21.6
CH_3CN:TTCE (66.7:33.3) (P)	592	0
CH_3CN:TTCE (75:25)	611	3.1
CH_3CN:TTCE (75:25) (P)	627	0

6.3.3.3 Powder XRD analysis of the N-doped CNMs: Effect of TTCE concentration and synthesis temperature

XRD patterns of the purified N-CNTs, Cl functionalized CNMs and chlorine functionalized NCNMs samples generated from room temperature solutions and from heated solutions, are presented in Figure 6.33. The XRD data for materials generated from reagents at room temperature, showed a strong intensity peak at $2\theta \sim 26$ ° (Figure 6.14a), assigned to the $C_{(002)}$ reflection of graphite associated with the interlayer spacing of graphene.[39] The full width at half maxima (FWHM) of the C_{002} peak increased with an increase in the TTCE content in the feed (Table 6.14). Broadening of the FWHM of the C_{002} peak can be due to an increase in the amount of nitrogen doped into the CNMs. An increase in nitrogen doping increased the structural strain by increasing the surface defects on the regular graphite layers of the CNTs leading to broadening of the FWHM.[40] The data is consistent with the TGA analysis, where an increase in the amount of TTCE in the feed resulted in the production of less thermally stable materials. The peak appearing at $2\theta \sim 45$ ° which had a shoulder peak was attributed to the C_{100} (shoulder) and C_{101} (main peak at 45 °) plane of CNMs and to some traces of iron carbide (Fe_3C) or iron

metallic catalyst.[39] Two additional peaks were observed at 2θ ~ 32 ° and 37 ° from the diffractogram obtained from a 50:50 and 66.7:33.3 volume ratio solutions and pure TTCE and were assigned to Fe_3C reflections. The peak at 54 ° theta was also observed and was assigned to the presence of iron (II) oxide, FeO. The presence of an Fe_3C peak could imply that Fe_3C was the predominant catalytic phase during CNM growth.[41] The intensity of the Fe_3C peak was the same for chlorine functionalized NCNMs generated from a CH_3CN:TTCE with 50:50 and 66.7:33.3 volume ratios, and disappeared from XRD patterns generated from CNMs generated from a CH_3CN:TTCE of 75:25 volume ratio. A decrease in the Fe_3C peak with low amounts of TTCE was also evidenced from the TGA curves of chlorine functionalized NCNMs, where a decrease in the residual weight was observed from feeds containing 25 vol.% of TTCE (Table 6.14). The Fe_3C peak was also not observed from PXRD patterns of N-CNTs (Figure 6.34a), which is also consistent with the TGA data where no residual weight was observed after purification (Table 6.14). The XRD data correlates with the TEM images where carbon nano-onions were formed from reagent mixtures that contained high concentrations of TTCE (50 and 33.3 vol.%) in the feed. The amount of metal particles encapsulated inside the nano-onions was also observed from solutions that contained appreciable amount of TTCE.

Table 6.14 Powder X-ray structural parameters of chlorine functionalized MWCNTs, N-MWCNTs and chlorine functionalized NCNMs generated using room temperature solutions of TTCE and CH_3CN.

Chlorine/nitrogen source	Position of $C_{(002)}$ peak	FWHM of $C_{(002)}$ peak / °	Intensity of $C_{(002)}$ peak	Intensity of Fe_3C peak	Volume of hydrocarbon source used /mL
TTCE	25.90	2.30	918	–	0
CH_3CN	25.82	2.07	619	–	8
CH_3CN:TTCE (75:25)	25.81	1.50	1502	_	8
CH_3CN:TTCE (66.7:33.3)	25.91	1.75	1220	220	6
CH_3CN:TTCE (50:50)	25.93	1.83	993	220	4

All diffractogram generated from heated reagents also displayed, similar behavior to those generated at room temperature (Figure 6.33b and Table 6.15). In this case the Fe_3C peak was only observed from the diffractogram of CNMs generated from solutions containing high concentrations of TTCE (50 vol.%).

Table 6.15 Powder X-ray structural parameters of chlorine functionalized MWCNTs, N-MWCNTs and chlorinated NCNMs generated using room temperature solutions of TTCE and CH_3CN.

Chlorine/nitrogen source	Position of $C_{(002)}$ peak	FWHM of $C_{(002)}$ peak / °	Intensity of $C_{(002)}$ peak	Intensity of Fe_3C peak	Volume of hydrocarbon source used /mL
TTCE	25.8	2.07	669	–	0
CH_3CN	26.0	1.92	1234	–	45
CH_3CN:TTCE (75:25)	25.8	1.50	1492	_	26
CH_3CN:TTCE (66.7:33.3)	26.2	1.60	2298	–	20
CH_3CN:TTCE (50:50)	25.9	1.70	1270	291	10

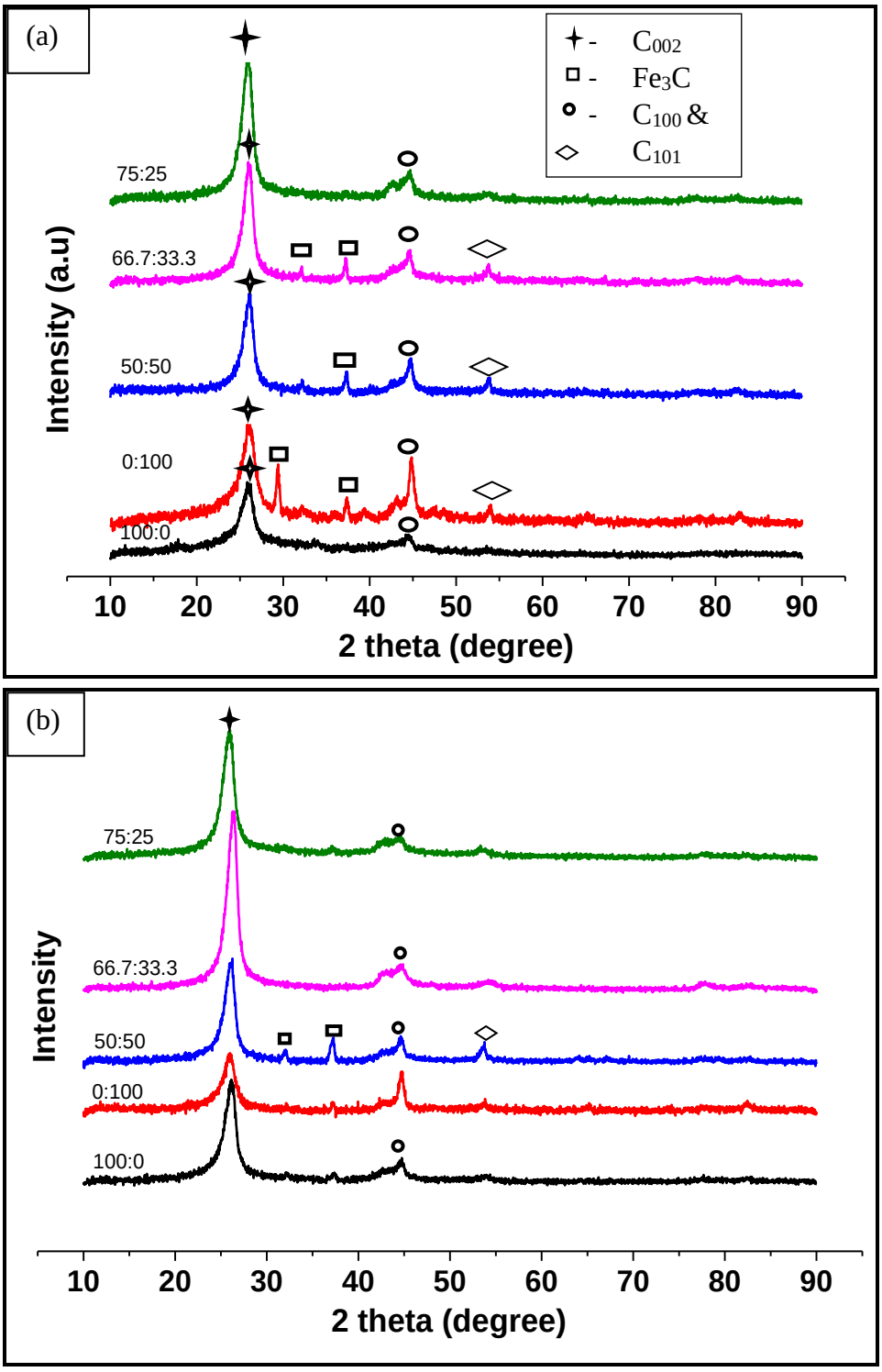

Figure 6.33 P-XRD spectroscopy of purified CNMs generated from varying the volume ratio of (a) room temperature and (b) hot (100 °C) mixture of CH_3CN:TTCE.

6.3.3.4 Raman spectroscopy analysis of the CNMs: Effect of TTCE concentration and synthesis temperature

Raman spectra analysis of the purified CNTs generated from room temperature pure CH_3CN and pure TTCE are presented in Figure 6.34. A disorder-induced band (D-band) and a graphitic band (G-band) were observed from the Raman spectra of CNMs generated from CH_3CN. A broad D-band was deconvoluted into two bands, a D4-band at 1210 cm^{-1} attributed to C=C stretching vibrations and a D-band at 1339 cm^{-1} attributed to topological defects on the CNT walls due to substitution of carbon with nitrogen. A G-band was also deconvoluted into two peaks, a D2-band at 1513 cm^{-1} assigned to the presence of amorphous carbon structures and a G-band at 1585 cm^{-1} due to sp^2 carbon atoms in a graphitic plane. An I_D/I_G value of 1.2 was obtained, which suggest the materials are highly defected. Large FWHM values of 78 cm^{-1} (average of D2 and G-band) also suggest the presence of small amounts of amorphous carbon structures (Table 6.). These amorphous carbon structures were not detected by TGA analysis, which shows that their amounts are very little.

Raman bands of purified CNTs generated from pure TTCE showed a D-band that was deconvoluted into a single peak at 1337 cm^{-1} (Figure 6.34). A G-band was deconvoluted into two peaks, a D2-band at 1469 cm^{-1} and a G-band at 1574 cm^{-1} (Figure 6.34). The amorphous carbon D2-band is very small as compared to the one obtained from Raman curves generated from CH_3CN, which suggest the reduced formation amorphous carbon. A second order 2D band which was highly intense was also observed from CNMs generated from TTCE, which suggest that these materials were highly graphitic. An I_D/I_G value of 0.83 suggest that the materials were highly graphitic in comparison to those obtained from pure CH_3CN. FWHM value of 78 cm^{-1} (average of D2 and G band) also suggest the presence of small amounts of amorphous carbon present (Table 6.16). These amorphous carbon structures were not detected by TGA analysis, which shows that their amounts are very little.

Table 6.16. Raman bands of the purified CNMs generated from room temperature pure CH_3CN and pure TTCE

Heteroatom Source	Band name	Band Position (cm^{-1})	Bond type	FWHM (cm^{-1})	Peak Area	Designation
CH_3CN purified	D4	1210	sp^2–sp^3	126	983	C=C stretching vibrations
	D	1339	sp^2	126	6701	Disordered graphite
	D2	1513	sp^3	85	1042	Amorphous carbon structure
	G	1584	sp^2	71	5312	Graphitic like carbonyl group
TTCE purified	D	1337	sp^2	88	3094	Disordered graphite
	D2	1469	sp^3	89	539	Amorphous carbon structure
	G	1574	sp^2	66	3202	Graphitic like carbonyl group
	2D	2678		108	1652	1^{st} overtone of D1

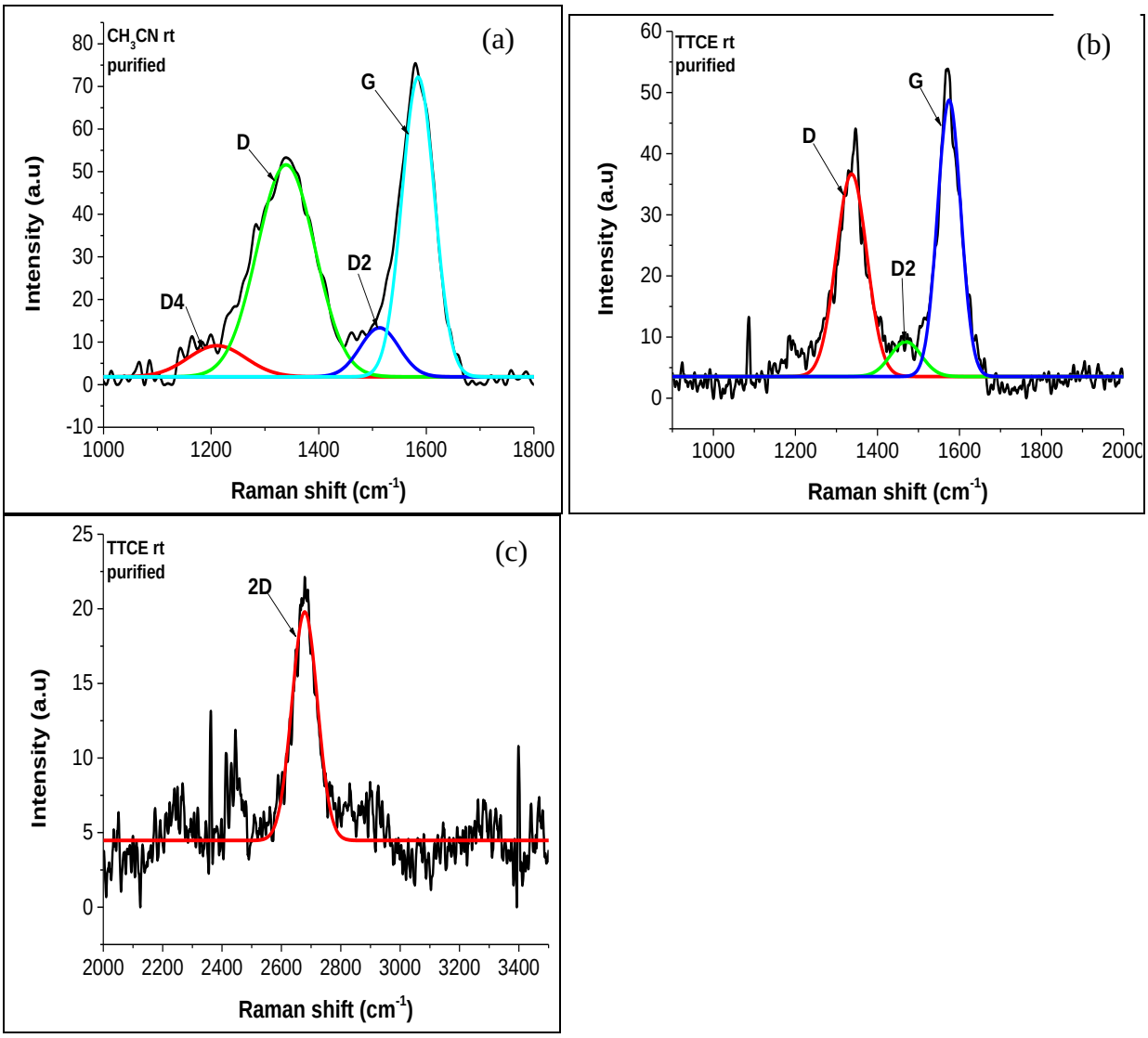

Figure 6.34 Raman spectra of purified CNTs generated from room temperature solutions of (a) pure CH_3CN and (b and c) pure TTCE.

Raman spectra analysis of the purified CNMs generated from room temperature CH_3CN feed solutions containing 25 vol.% TTCE are presented in Figure 6.35. A disorder-induced band (D-band), a graphitic band (G-band) and a second order 2D band were observed in the Raman spectra. A D-band was deconvoluted into one peak at 1349 cm^{-1} attributed to topological defects on the CNT walls due to substitution of carbon with nitrogen. A G-band was deconvoluted into two peaks, a D'-band at 1616 cm^{-1} assigned to the defects in the graphitic plane and a G-band at 1585 cm^{-1} due to a perfect graphitic plane. A very weak defect induced G* band was also observed at 2429 cm^{-1} due to the presence of defects in the CNMs. A 2D band which was split into two bands a $2D_1$ at 2674 cm^{-1} and a $2D_2$ at 2702 cm^{-1}. This split has been described as a characteristic feature of undisturbed or highly ordered graphitic lattices[32] and interaction of succesive layers.[33] An I_D/I_G value of 0.4 was obtained, which suggest that the materials were highly graphitic. Small FWHM values of 40 cm^{-1} (average of D' and G-band) also suggest that the materials were free of amorphous carbon structures (Table 6.17). The Raman data is consistent with the TGA data since amorphous carbon structures were not detected from the TGA curves.

Similar Raman spectra were obtained from CNMs generated from CH_3CN room temperature feed solutions containing 33.3 and 50 vol.% TTCE (Figure 6.35c to f). I_D/I_G values of 0.4 and 0.6 were obtained for solutions containing 33.3 and 50 vol.% TTCE respectively, suggesting that the materials are highly graphitic. Low FWHM values of 43 cm^{-1} also suggest materials with no amorphous carbon as observed from the TGA curves (Table 6.17). An $I_D/I_{D'}$ value of 4.3 was obtained from CNMs generated from feed solutions containing 25 vol.% TTCE due to vacancy-like defects with additional small boundary-like defects. An $I_D/I_{D'}$ value of 3.17 was obtained from CNMs generated from feed solutions containing 33.3 vol.% TTCE corresponding to boundary-like defects and small on-site defects. On-site defects describe out-of-plane atoms bonded to sp^3 hybridized carbon atoms. An $I_D/I_{D'}$ value of 6.3 was obtained from CNMs generated from feed solutions containing 50 vol.% TTCE corresponding to vacancy-like defects.

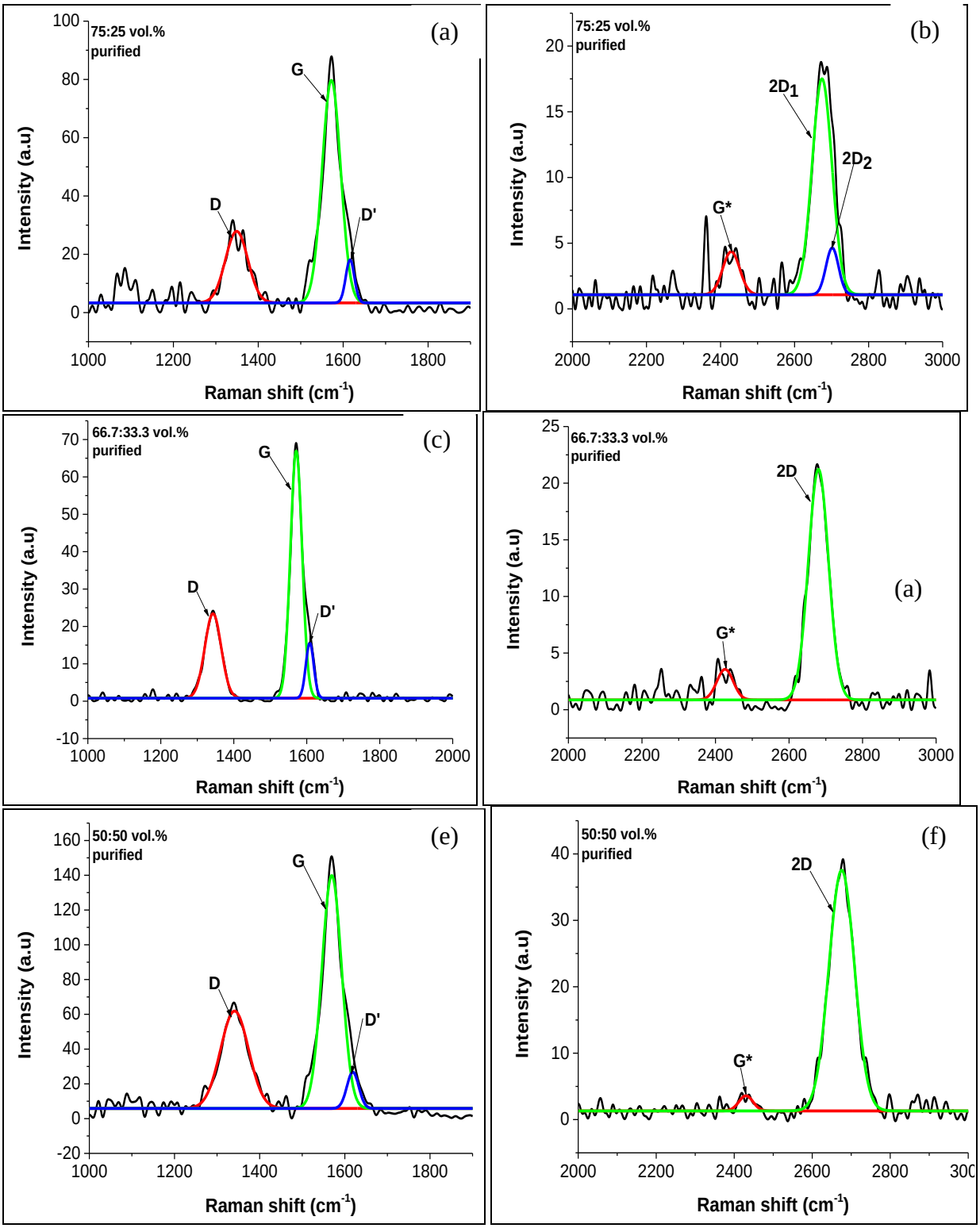

Figure 6.35 Raman spectra analysis of purified CNMs generated from varying the volume ratio of CH_3CN:TTCE solution at room temperature

Table 6.17 Raman bands of the purified chlorinated N-doped CNTs generated from various volume ratios of room temperature CH_3CN and TTCE solution mixtures

CH_3CN:TTCE volume ratio (%)	**Band name**	**Band Position (cm^{-1})**	**Bond type**	**FWHM (cm^{-1})**	**Peak Area**	**Designation**
75:25	D	1349	sp^2	62	1623	Disordered graphite
	G	1572	sp^2	51	4171	Graphitic like carbonyl group
	D’	1616	sp^2	24	376	Defects in graphitic plane
	G*	2429		54	198	1st overtone of D4
	$2D_1$	2674		62	1099	1st overtone of D1
	$2D_2$	2701		40	151	2D overtone
66.7:33.3	D	1343	sp^2	52	1268	Disordered graphite
	G	1571	sp^2	37	2636	Graphitic like carbonyl group
	D’	1608	sp^2	25	400	Defect in graphitic plane
	G*	2425		52	150	1st overtone of D4
	2D	2680		64	1394	1st overtone of D1
50:50	D	1341	sp^2	77	4629	Disordered graphite
	G	1569	sp^2	54	7558	Graphitic like carbonyl group
	D’	1618	sp^2	33	729	Defect in graphitic plane
	G*	2430		42	103	1st overtone of D4
	2D	2675		76	2957	1st overtone of D1

Raman spectra analysis of the purified CNTs generated from heated solutions of pure CH_3CN and pure TTCE are presented in Figure 6.36. A disorder-induced band (D-band), a graphitic band (G-band) and a second order 2D band were observed from Raman spectra generated from both

reagents. For CNTs generated from pure CH_3CN, a D-band was deconvoluted into one band at 1343 cm^{-1} attributed to topological defects on the CNT walls due to substitution of carbon with nitrogen. A G-band was also deconvoluted into two peaks, a D'-band at 1614 cm^{-1} and a G-band at 1573 cm^{-1}. A second order 2D band which was highly intense was also observed at 2698 cm^{-1}. An I_D/I_G value of 0.9 was obtained, which was smaller than that obtained from room temperature solutions, suggest that heating resulted in formation of more graphitic CNMs. Low FWHM values of 40 cm^{-1} compared to 78 cm^{-1} (average of D2 and G-band) generated from room temperature CH_3CN also suggest materials with no amorphous carbon structures (Table 6.18). An $I_D/I_{D'}$ value of 8.9 corresponding to hoping defects produced by the deformation of the carbon bond, was obtained. The data is consistent with the TGA analysis were no amorphous oxidation peak was observed.

Raman bands of purified CNTs generated from heated solution of pure TTCE showed a D-band that was deconvoluted into a single peak at 1336 cm^{-1} (Figure 6.37). A G-band was deconvoluted into two peaks, a D2-band at 1508 cm^{-1} and a G-band at 1589 cm^{-1} (Figure 6.36). The amorphous carbon D2-band is very small which suggest small amounts of amorphous carbon. A weak second order 2D band was also observed, which suggest that these materials were less graphitic as compared to those generated from room temperature TTCE. An I_D/I_G value of 1.7 suggest that the materials were highly defected in comparison to those obtained from room temperature TTCE. Heating of the TTCE probably results in generation of more chlorine vapors which results in generation a large number of functionalized CNMs leading to highly defected materials. FWHM value of 67 cm^{-1} (average of D2 and G band) suggest the presence of small amounts of amorphous carbon (Table 6.18). These amorphous carbon structures were not detected by TGA analysis, which shows that their amounts are very little.

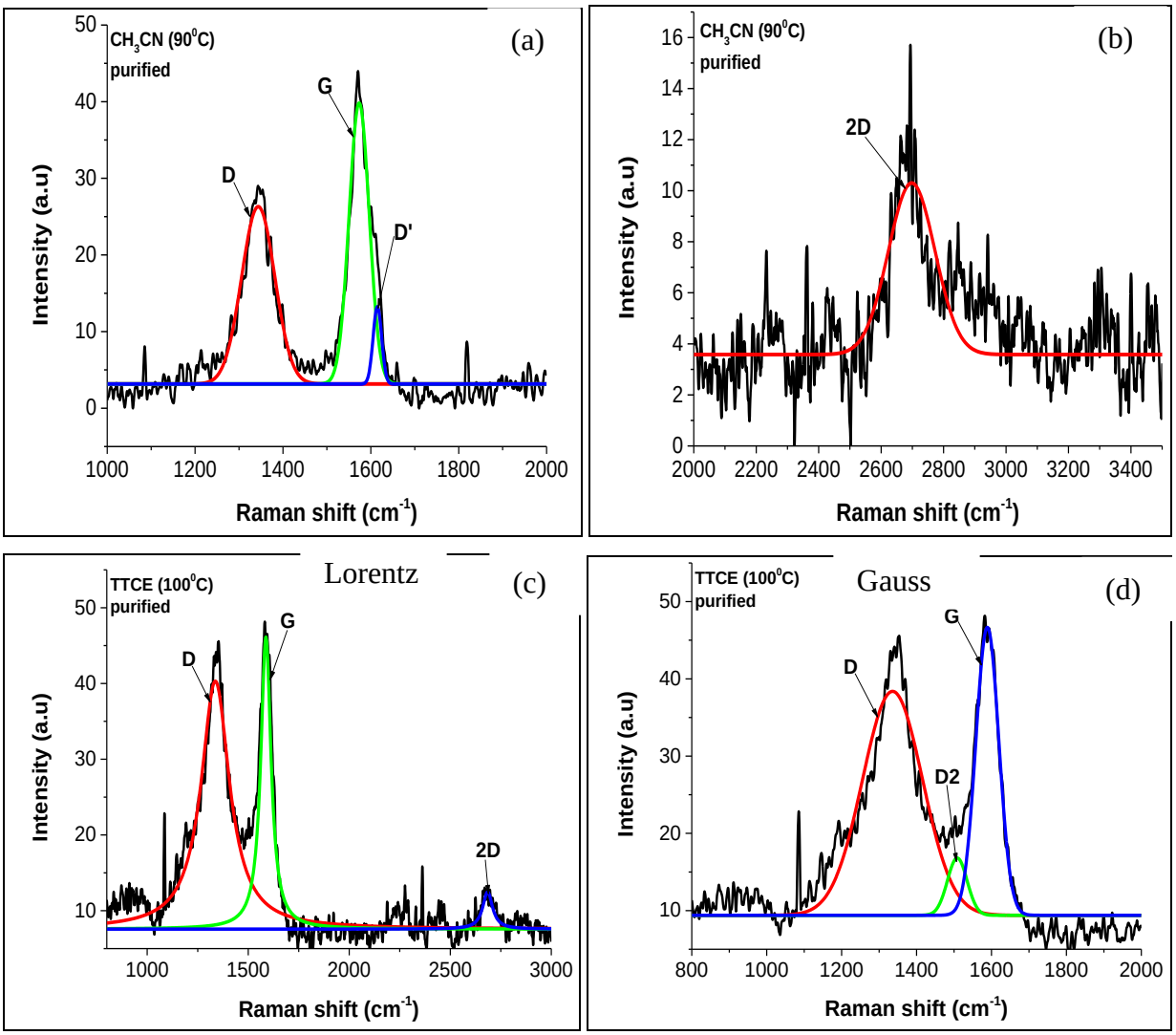

Figure 6.36 Raman spectra of purified CNTs generated from heated solutions of (a) pure CH_3CN (90 °C) and (b) pure TTCE (100 °C).

Table 6.18. Raman bands of the purified CNMs generated from heated solutions of pure CH_3CN and pure TTCE

Heteroatom Source	Band name	Band Position (cm^{-1})	Bond type	FWHM (cm^{-1})	Peak Area	Designation
CH_3CN purified	D	1343	sp^2	89	2190	Disordered graphite
	G	1573	sp^2	54	2098	Graphitic like carbonyl group
	D’	1614	sp^3	23	245	Amorphous carbon structure
	2D	2698		175	1254	1st overtone of D1
TTCE purified	D	1336	sp^2	188	5820	Disordered graphite
	D2	1508	sp^3	62	488	Amorphous carbon structure
	G	1589	sp^2	72	2868	Graphitic like carbonyl group
	2D	2685			451	1st overtone of D1

All Raman spectra curves of the purified CNMs generated from heated solutions of an CH_3CN feed containing 25, 33.3 and 50 vol.% TTCE are presented in Figure 6.37. A disorder-induced band (D-band), a graphitic band (G-band) and a second order 2D band were observed in the Raman spectra. A D-band was deconvoluted into one peak at ~ 1347, 1352 and 1344 cm^{-1} for solutions containing 25, 33.3 and 50 vol.% TTCE respectively, attributed to topological defects on the CNT walls due to substitution of carbon with nitrogen. A G-band was deconvoluted into two peaks, a D2-band at 1482, 1488 and 1472 cm^{-1} assigned to amorphous carbon structures and a G-band at 1577, 1579 and 1575 cm^{-1} due to a perfect graphitic plane for solutions containing 25, 33.3 and 50 vol.% TTCE respectively. An intense 2D band was also observed at 2689, 2695 and 2687 cm^{-1}, suggesting that the materials were highly graphitic. The presence of a D + G band at 2908, 2923 and 2903 cm^{-1}, shows characteristics of disturbed graphitic structures, as a result of functionalization with chlorine. An I_D/I_G value of 0.9, 0.9 and 0.7, for CNMs generated from feeds containing 25, 33.3 and 50 vol.%, suggesting that the materials obtained at low TTCE concentrations had similar graphitic natures. The highly graphitic materials were generated from

feeds containing high concentration of TTCE (50 vol.%). Small FWHM values of 74, 72, and 84 cm^{-1} (average of D' and G-band) suggest that the materials contained some amorphous carbon structures (Table 6.19). The Raman data is consistent with the TGA data since amorphous carbon structures were also detected from the TGA curves.

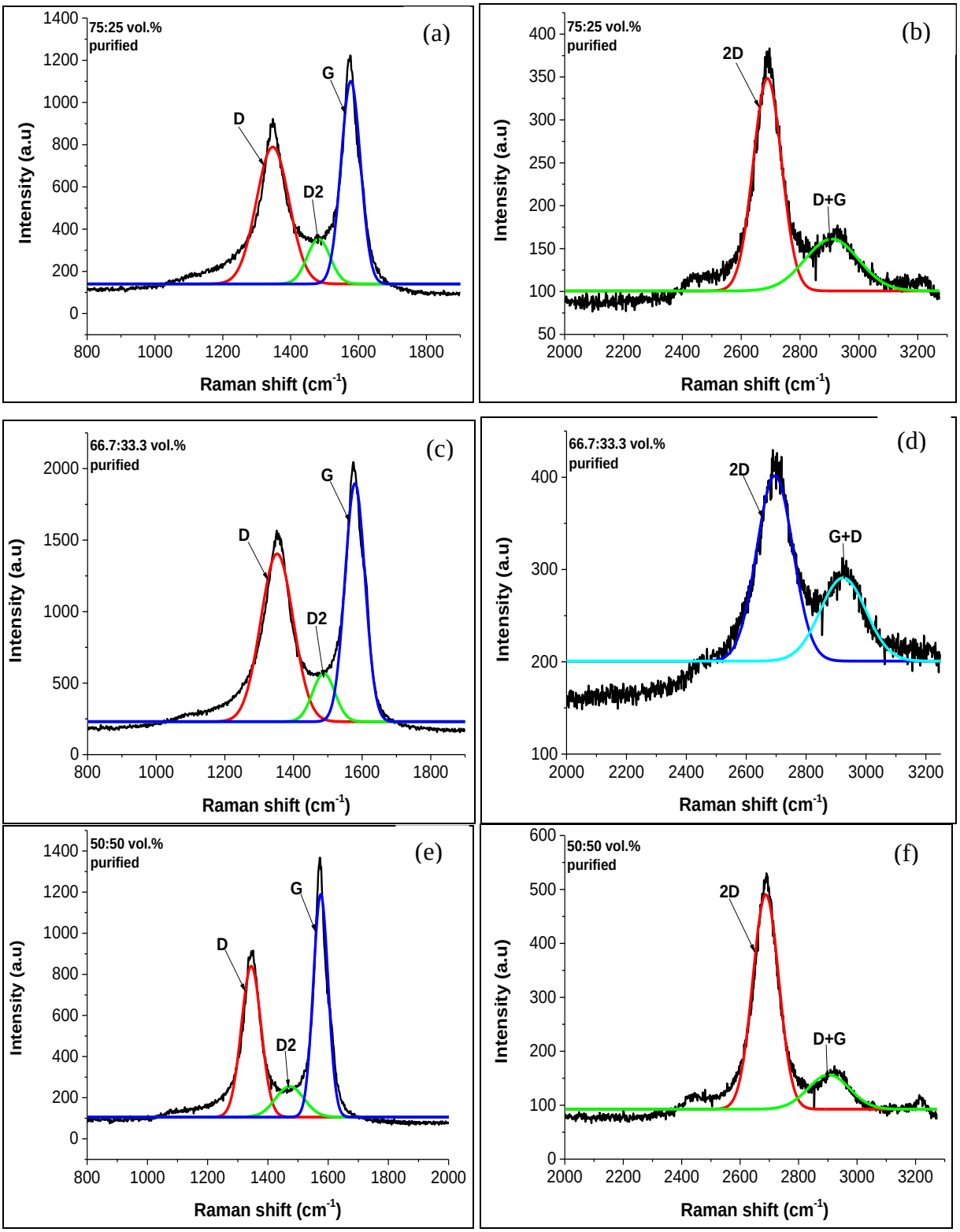

Figure 6.37 Raman spectra of purified CNTs generated from heated solutions of CH_3CN:TTCE (100 °C) of various volume ratios.

Table 6.19 Raman bands of the purified chlorinated N-doped CNTs generated from various volume ratios of heated solutions of CH_3CN containing various TTCE concentrations

CH_3CN:TTCE volume ratio (%)	**Band name**	**Band Position (cm^{-1})**	**Bond type**	**FWHM (cm^{-1})**	**Peak Area**	**Designation**
75:25	D	1347	sp^2	113	78427	Disordered graphite
	D2	1482	sp^3	80	18040	Amorphous carbon structure
	G	1577	sp^2	67	68937	Graphitic like carbonyl group
	2D	2689		114	29998	1st overtone of D1
	D+G	2908		214	13841	2D overtone
66.7:33.3	D	1352	sp^2	111	139335	Disordered graphite
	D2	1488	sp^3	76	27481	Amorphous carbon structure
	G	1579	sp^2	68	121571	Graphitic like carbonyl group
	2D	2695		142	30442	1st overtone of D1
	D+G	2923		180	17287	2D overtone
50:50	D	1344	sp^2	77	60154	Disordered graphite
	D2	1472	sp^3	111	17692	Amorphous carbon structure
	G	1575	sp^2	58	66910	Graphitic like carbonyl group
	2D	2687		105	44496	1st overtone of D1
	D+G	2903		166	11298	2D overtone

6.3.3.5 CN elemental analysis of the N-doped CNMs: Effect of TTCE concentration

CN elemental analysis of the purified chlorine functionalized NCNMs obtained from heated solutions (100 °C) was also performed to quantify the amount of nitrogen in the carbon product (Table 6.20). The percentage of nitrogen inserted into the CNMs was found to increase with a

decrease in the amount of TTCE in the feed from the reagents with ratios of 50:50 to 66.7:33.3 vol.% CH_3CN:TTCE. The 33.3 vol.% TTCE concentration gave the maximum insertion of nitrogen onto the CNMs. These data agree with the Raman spectroscopy analysis recorded for these materials. Solutions containing low concentrations of chlorine resulted in an increase in the amount of nitrogen inserted into the CNMs since their percentage was higher than that of CNMs obtained from using only acetonitrile (Table 6.20). The amount of nitrogen inserted into the CNMs was reduced when high concentrations of chlorine were added into the feed. We conclude that chlorine aided in increasing the percentage of nitrogen into the CNMs but the amount of chlorine needs to be controlled to maximize this effect.

Table 6.20 CN elemental analysis of the purified NCNTs and chlorine functionalized NCNMs

Reagent	**Solvent Temperature/°C**	**Atomic % C**	**Atomic % N**
CH_3CN	100	85.21	1.31
CH_3CN:TTCE (50:50)	100	89.18	1.19
CH_3CN:TTCE (66.7:33.3)	100	93.84	2.21
CH_3CN:TTCE(75:25)	100	89.54	1.45

6.4 Conclusions

The effect of chlorine on the morphology of the N-doped MWCNTs was evaluated using DCB and TTCE as chlorine sources by use of a bubbling CVD method over an Fe-Co/$CaCO_3$ as a catalyst. Mixtures of bamboo compartmented CNTs, CNTs with intratubular junctions, carbon-nano-onions and carbon nano-bells were observed from CH_3CN feed solutions containing low concentrations of DCB. Increasing the concentration of DCB resulted in formation of hollow and bamboo-compartmented CNTs. A large increase in the amount of nitrogen doped into the CNTs was achieved at a high DCB concentrations, evidenced by a decrease in the outer diameters of N-MWCNTs with an increase in the DCB concentration. Highly graphitic materials were produced at low concentrations of DCB (33.3 vol.%) as evidenced by the TGA, Raman and XPS data. N-

MWCNTs that were thermally stable, had a small value of the I_D/I_G peak ratio and had graphitic N species dominating in their N1s XPS spectra were produced when low concentrations of DCB (33.3 vol.%) were used, as compared to N-MWCNTs obtained from pure CH_3CN and high DCB (66.7 vol.%.) concentration. Post-doping of the N-MWCNTs with chlorine and of the chlorinated CNTs with nitrogen resulted in production of highly graphitic materials, as evidenced by the low I_D/I_G peak ratios obtained after post-doping. Carbon nano-onions were observed from NCNMs when TTCE was used as a source of chlorine. The formation of carbon nano-onions increased at a low TTCE concentration, which was attributed to greater incorporation of nitrogen into the CNMs. An increase in the TTCE concentration resulted in the formation of mixtures of carbon nano-onions and bamboo-compartmented carbon nano-bells. NCNMs generated from heated solutions of CH_3CN and TTCE mixtures, resulted in formation of mixtures of CNMs, especially at high concentrations of TTCE. Selectivity was achieved at low concentrations (33.3 and 25 vol.%) of TTCE. Hollow and bamboo-compartmented NCNTs were observed from 33.3 vol.% TTCE feed solutions and bamboo-compartmented carbon nano-bells with intratubular junctions were obtained from 25 vol.% TTCE solutions. NCNMs generated from 25 vol.% TTCE solutions were thermally stable, had little residual catalyst material, had a small narrow FWHM value for the C_{002} peak, and a small I_D/I_G peak ratio values, suggesting that the materials were highly graphitic. Chlorine functionalization of the CNTs with DCB gave selective CNMs as compared to when TTCE was used, where mixtures of CNMs were produced. Aromatic chlorinated organic compounds are better suited for use in studies of the effect of chlorine on the morphology of the CNMs than are aliphatic chlorinated organic compounds. Chlorinated NCNTs that contained smaller amounts of DCB (33.3 vol.%) can be used to enhance the electrical conductivity of NCNMs due to a better wetting with the electrolyte.[42] This appears to be related to quaternary nitrogen being the dominant nitrogen species.

Selective carbon nanomaterials were obtained for chlorinated NCNMs generated using an injection CVD method rather than when using the bubbling CVD method.

References

1. S. Christiansen, E. Fau, and B. Staudtstrasse, *ACS Appl. Mater*. 2017, **9**, 10003–10011.
2. B. Liu, C.-M. Yang, Z. Liu and C.-S. Lai, *Nanomaterials*, 2017, **7**, 302 (1–12).
3. P. Chen, T.Y. Xiao, Y.H. Qian, S.S. Li, and S.H. Yu, *Adv. Mater*. 2013, **25**, 3192–3196.
4. T. Sharifi, G. Hu, X. Jia, and T. Wågberg, *ACS Nano*, 2012, **6**, 8904–8912.
5. Y. Liu, Y. Shen, L. Sun, J. Li, C. Liu, W. Ren, F. Li, L. Gao, J. Chen, F. Liu, Y. Sun, N. Tang, H.-M. Cheng and Y. Du, *Nature Communications,* 2016, **7**, 10921 (1–9).
6. X. Wang, G. Sun, P. Routh, D.-H. Kim, W. Huang and P. Chen, *Chem. Soc. Rev*., 2014, **43**, 7067–7098.
7. Z. Lin, G. Waller, Y. Liu, M. Liu and C.-P. Wong, *Adv. Energy Mater*., 2012, **2**, 884–888.
8. E. Haque, Md. M. Islam, S.N. Faisal, A.K. Roy, S. Ansari, D. Cardillo, K. Konstantinov and E. Haque, *J. Nanotech Mater. Sci*, 2015, **2(1),** 1-5.
9. D. Li, X. Duan, H. Sun, J. Kang, H. Zhang, M.O. Tade, and S. Wang, https://espace.curtin.edu.au/bitstream/handle/20.500.11937/50850/248286.pdf?sequence=2
10. R. Lv, Q. Li, A.R. Botello-Mendez, T. Hayashi, B. Wang, A. Berkdemir, Q. Hao, A.L. Elías, R. Cruz-Silva, H.R. Gutiérrez, Y.A. Kim, H. Muramatsu, J. Zhu, M. Endo, H. Terrones, J.-C. Charlier, M. Pan and M. Terrones, *Sci. Rep.*, 2012, **2**, 586.
11. J. Xu, D. Huang, L. Nie, C. Wang, and Z. Xu, *Int. J. Electrochem. Sci*., 2016, **11**, 944–952.
12. K.F. Ortega, R. Arrigo, B. Frank, R. Schlögl, and A. Trunschke, *Chem. Mater*., 2016, **28**, 6826−6839.
13. V. A. Tur1, A. V. Okotrub, Yu. V. Shubin, B. V. Senkovskiy, and L. G. Bulusheva, *Phys. Status Solidi B*, 2014, **251**, 2613–2619.
14. K. Kakaei, M. Hamidi and S. Husseindoost, *J. Colloid Int. Sci*., 2016, **479**, 121–126.
15. H.L. Poh, P. Šimek, Z. Sofer and M. Pumera, *Chem. Eur. J.* 2013, **19**, 2655–266.
16. G-L. Tian, M-Q. Zhao, Q. Zhang, J-Q. Huang, and F. Wei, *Carbon*, 2012, **50**, 5323-5330.
17. D. Wei and Y. Liu, *Adv. Mater*., 2008, **20**, 2815–2841.
18. P.A. Hu, K. Xiao, Y.Q. Liu, G. Yu, X.B. Wang, L. Fu, G.L. Cui and D.B. Zhu, *Appl. Phys. Lett*., 2004, **84**, 4932.
19. K. Xiao, Y.Q. Liu, P.A. Hu, G. Yu, L. Fu, and D.B. Zhu, *Appl. Phys. Lett*., 2003, **83**, 4824.
20. Y. Chai, X.L. Zhou, P.J. Li, W.J. Zhang, and J.L. Wu, *Nanotechnology*, 2005, **16**, 2134.

21. K. Xiao, Y. Fu, Y.Q. Liu, G. Yu, J. Zhai, L. Jiang, W.P. Hu, Z.G. Shuai, Y. Luo and D.B. Zhu, *Adv. Funct. Mater*, 2007, **17**, 2842.
22. G.K. Goswami, R. Nandan, and K.K. Nanda, *Carbon*, 2013, **56**, 97-102.
23. P. Ghosh, M. Subramanian, R.A. Afre, M. Zamri, T. Soga, T. Jimbo, V. Filip, and M. Tanemura, *Appl. Surf. Sci.*, 2009, **255**, 4611–4615.
24. C. He, N. Zhao, C. Shi, X. Du, J. Li, L. Cui and F. He, *Scr. Mater.*, 2006, **54**, 1739 – 1743.
25. J. Zheng, T.C. Ekström, S.K. Gordeev and M. Jacob, *J. Mater. Chem.*, 2000, **10**, 1039–1041.
26. L.M. Ombaka, P.G. Ndungu, B. Omondi, J.D. McGettrick, M.L. Davies and V.O. Nyamori, *J. Solid State Chem.*, 2016, **235**, 202–211.
27. L.G. Bulusheva, A.V. Okotrub, A.G. Kudashov, N.F. Yudanov, E.M. Pazhetnov, A.I. Boronin, O.G. Abrosimov, and N.A. Rudina, *Russ. J. Inorg. Chem*., 2006, **51**, 613–618.
28. W.K. Maboya, N.J. Coville and S.D. Mhlanga, *S. Afr. J. Chem.*, 2016, **69**, 15–26.
29. Z.N. Tetana, S.D. Mhlanga, G. Bepete, R.W.M. Krause, and N.J. Coville, *S. Afr. J. Chem.*, 2012, **65**, 39–49.
30. C. Yuan, W. Chen and L. Yan, *J. Mater. Chem*., 2012, **22**, 7456–7460.
31. S. Zhang, S. Tsuzuki, K. Ueno, K. Dokko and M. Watanabe, *Angew. Chem. Int. Ed.*, 2015, **54**, 1302–1306.
32. A. Cuesta, P. Dhamelincourt, J. Laureyns, A. Martinez-Alonso and J.M.D. Tascon, *Carbon*, 1994, **32**, 1523–1532.
33. L. Bokobza, J.-L. Bruneel and M. Couzi, *Carbon*, 2015, **1**, 77–94.
34. M.I. Ionescu, Y. Zhang, R. Li, H. Abou-Rachid and X. Sun, *Appl. Surf. Sci*., 2012, **258**, 4563–4568.
35. D. Goldberg, Y. Bando, L, Bourgeois, K. Kurashima, and T. Sato, *Carbon*, 2000, **38**, 2017–2027.
36. Z. Czigany, IF. Brunell, J. Neidhardt, L. Hultman and K. Suenaga, *Appl. Phys. Lett*., 2001, **79**, 2639.
37. W.Q. Han, P. Kohler-Redlich, T. Seeger, F. Ernst, M. Ruhle, N. Grobert, W.K. Hsu, B.H. Chang, Y.Q. Zhu, H.W. Kroto, M. Terrones and H. Terrones, *Appl. Phys. Lett*., 2000, **77**, 1807–1809.
38. A.A. Deshmukh, S.D. Mhlanga, and N.J. Coville, *Mater. Sci. Eng., R*, 2010, **70**, 1–28.

39. A. Hachimi, B. Merzougui, A. Hakeem, T. Laoui, G.M. Swain, Q. Chang, M. Shao, and M.A. Atieh, *J. Nanomater.*, 2015, http://dx.doi.org/10.1155/2015/453725.
40. Y.C, Chiang, W.-H. Lin, and Y.-C. Chang, *Appl. Surf. Sci*., 2011, **257**, 2401–2410.
41. C.T. Wirth, B.C. Bayer, A.D. Gamalski, S. Esconjaurequi, R.S. Weatherup, C. Ducati, C. Baehtz, J. Robertson, and S. Hofmann, *Chem. Mater*., 2012, **24**, 4633–4640.
42. I. Kunadian, S.M. Lipka, C.R. Swartz, D. Qian, and R. Andrews, *J. Electrochem. Soc*., 2009, **156**, K110eK115.

CHAPTER 7

Fabrication of chlorine functionalized MWCNT/polyvinylpyrrolidone composite nanofiber mats by electrospinning for use in oil adsorption studies

---

7.1 Introduction

Materials play a key role in every field of technology with the aim of making our lives more comfortable. As technology advances there is a need to develop new materials with improved properties. In order to create new generation materials, it is necessary to understand the relationship between the existing materials and their structure. By combining appropriate materials, new desired properties can be achieved.[1] Nanocomposites are made by placing a nanomaterial into a matrix, in order to introduce new functionalities into the matrix to harness new properties. A nanocomposite thus consists of a matrix to which nanoparticles (a filler) has been added to improve a particular property of the material. Polymer composites containing fillers such as carbon nanotubes (CNTs) have been studied.[2-13] CNT/polymer nanocomposites are promising materials with excellent mechanical and physical properties, due to the extraordinary properties introduced by the CNTs coupled with easily tailored characteristics of polymers.[14-23] Polymer materials have properties such as low density, good insulation, flexibility and outstanding mechanical properties and they are cheap. CNTs possess high flexibility, low mass density, large aspects ratio, and extremely high tensile moduli and strength. CNT/polymer composites have been applied in various fields, namely in sensors,[24-26] electromagnetic interference shielding,[6,27] electronic packaging,[28] aerospace technology,[29] drug delivery,[30] in filtration,[31-36] as biomaterials for wound dressing,[37] and for tissue engineering.[38] Challenges still arise in the fabrication of CNT/polymer nanocomposites, such as lack of uniform dispersion of CNTs and orientation of nanotubes within the polymer matrix. The challenges arise due to the fact that (a) CNTs tend to aggregate to form tight bundles due to strong van der Waals interactions and their small size which leads to non-uniform dispersion[39,40] and (b) the poor interfacial bonding of the CNTs with the polymer matrix which results in production of non-oriented CNTs within the polymer.[41,42] As a result of these problems, the mechanical and physical properties of the composite material can be considerably lower than expected.

Interaction between CNTs and polymers can be enhanced by functionalization of CNTs. Functionalization can create defects on the side walls,[43,44] which decrease the Young's modulus and strength of CNTs.[45] CNT/polymer composites have been fabricated using solution casting,[46] melt processing,[47] electrospinning[48] and in-situ polymerization[49] with the aim of deagglomerating the CNTs to realize a uniform dispersion inside the polymer matrix. It has been demonstrated that electrospinning is a potential method for aligning and debundling CNTs.[50] Electrospinning is a relatively low cost, fast and versatile method to produce continuous nanofibers mainly from polymer solutions. The resultant fibers have unique properties, namely, high surface area-to-volume ratio, small pore sizes, high porosity and the potential for controlled release of active materials.[51,37] The principle of electrospinning operation involve the use of a high-voltage electrostatic field to draw a jet from a polymer solution. When this jet travels toward the collector electrode, the solvent evaporates and a polymer fiber is formed. Electrospinning is used to produce a conductive polymer by combining additives with a spinnable polymer.[52] Factors that affects the electrospinning process and the nanofiber morphology are the structural properties of the polymer, polymer solution parameters, processing conditions and ambient parameters.[6] Polymer concentration is one of the most significant parameter that affect the morphology of the nanofibers. At very low polymer concentration, the viscosity of the solution is low and not enough polymer entanglements occur for fiber formation, resulting in formation of particles due to instabilities a process called "electrospraying". Electrospinning of low polymer concentration solutions can also result in formation of beaded fibers, due to low viscosity solution which possesses a low viscoelastic force which is not able to match the electrostatic and columbic repulsion forces that stretch the electrospinning jet. This causes the jet to break up.[53] Electrospinning of a low 5 wt.% poly(vinylidene fluoride) (PVDF) solution resulted in formation of droplets. However, using a 10 and 15 wt.% PVDF solution resulted in formation of smooth fibers, with the fiber diameters increasing with an increase in polymer concentration.[54] Highly concentrated solutions have been shown to produce more uniform fibers with fewer beads. The shape of the beads also changed from spherical to spindlelike when a polymer concentration increased.[55] Very high polymer concentrations also produced flattened nanofibers with a ribbon shape, due to solvent evaporation which get reduced with higher solution viscosity, resulting in wet fibers that reach the collector and are flattened by the impact forming ribbon-like structures.[56] A needle-tip to collector distance is another

parameter that greatly affects the shape of the fibers. An increase in nanofiber diameter was observed when a short needle-tip to collector distance ~ 8 cm was used, during electrospinning of TiO_2/PVP nanofibers. A reduction in the nanofiber diameter was obtained by increasing the needle-tip to collector distance to 11 cm.[57] Nanofibers produced from electrospinning polycaprolactone were found to decrease in diameter with an increase in needle-tip to collector distance to ~ 20 cm.[58] As the distance increased the jet became more stretched, thereby reducing the jet diameter. This was attributed to lower electric field found for longer needle-tip to collector distance, which result in breaks in solution flow.[58]

The feasibility of using an electrospinning method to embed CNTs into polymer nanofibers has been demonstrated by various authors. Ajayan et al. were the first to report polymer nanocomposites using CNTs as fillers.[59] There have been numerous reports dedicated to the fabrication of polymer nanocomposites and the study of their mechanical, thermal and electrical properties. A series of polymers have been studied for their ability to suspend individual CNTs, namely polyvinyl alcohol (PVA),[9] polyvinyl pyrrolidone (PVP),[7] poly(ethylene oxide) (PEO),[60] polyacrylonitrile (PAN),[61] polymethyl methacrylate (PMMA),[62] polyurethane,[63] polycaprolactone,[64] polycarbonate,[65] nylon 6,6,[66] polystyrene,[67] to name a few.

PVP was chosen in our study because it is an important synthetic polymer with good complexation and adhesion properties, excellent physiological compatibility, low chemical toxicity and reasonable solubility in water and most organic solvents. Blending of PVP with SWCNTs by electrospinning resulted in formation of nanofibers containing aligned individual SWCNTs.[2] Addition of MWCNTs to PVP to form nanocomposite fibers resulted in an increased charge carrier concentration and polarizability, and reduction of the porosity of the electrospun fiber films.[7] Highly dispersed MWCNTs/PVP composite nanofibers were synthesized by electrospinning and found to be used as an effective, light weight electromagnetic interference shielding material.[6]

The need to provide clean water to communities, in both urban and rural arears is now a huge challenge. Clean water is essential for both human life and for our ecosystem. An increasing growth of population; rapid development of an economy and urbanization; as well as domestic, agricultural, environmental and climate change are great contributors to water pollution. About 3

billion people will be forced to survive under water scarcity by year 2025, as estimated by World Water Council.[68] The increasing pressure on water scarcity issues requires cost-effective water treatment technologies to produce high-quality clean water. [69-71]

Polymeric membranes are currently the most widely used membrane type for water treatment. The polymers have straight pores, higher flexibility, small footprints required for installation and are of relatively low cost compared to their inorganic membrane equivalents.[72] However, use of polymeric membranes is hindered by several challenges for example, low resistance to fouling and a trade-off relationship between permeability and selectivity.[73] Development of cost-effective and energy efficient membranes with good antifouling properties and high permeability and rejection is essential for water treatment. CNT-based composite membranes have been one popular type of separation membrane used for water treatment, since it combines the excellent performances of traditional membrane materials with those of CNTs.[74]

Separation of oil and water is becoming more crucial due to oil spill accidents occurring during transportation, utilization, transfer and storage.[75] Oily wastewaters are produced in many industries such as in the production of crude oil,[76] lubricants,[77] and in the metallurgical,[78] petroleum refinery,[79] food[80] and textile processing[81] industries. This makes it one of the most common pollutant all over the world. Frequent oil spill accidents result in energy loss and waste of resources while posing long-term threats to the ecological environment on which our society depends.[82-84]

Membrane technology has been proved to be one of the best methods for the separation of oil from oil-water mixtures.[85] Membrane separation technology offers higher oil removal efficiency, stable effluent quality and a low energy cost making it one of the most effective ways to separate oil-water mixtures for a wide range of industrial effluents.[86,87] Membrane filtration including microfiltration (MF), ultrafiltration (UF), and nanofiltration (NF) has been applied widely for oil-water treatment with distinct advantages of high quality water produced, low energy consumption and small footprint.[88-90] The difficulty in using these membranes has resulted from the deformable nature of oil droplets, which renders the use of size exclusion separation ineffective for fully removing oil from water.[84] CNTs are hydrophobic and have adequate adsorption site for oil molecules in water. Hence the use of CNTs incorporated into polymers to

make composite materials have been proposed as a way to make effective membranes to treat an oil-in-water emulsion.

Most electrospun fibers used for oil-water separations have superhydrophobic/superoleophilic surface.[85] Due to the hydrophobic properties of the surface, the separation membranes/sponges are unlikely to be contaminated by bacteria.[85] CNT/PVP surface composite were fabricated by electrospinning and found to demonstrate high oil adsorption capabilities.[91] Incorporation of MWCNTs into a PVA barrier layer was found to improve the water flux and showed a high rejection rate during separation of an oil/water emulsion.[92]

7.2 Experimental

A polyvinylpyrrolidone (PVP) powder with molecular weight of 40,000 g/mol, was supplied by Sigma Aldrich. Chlorine functionalized multi-walled carbon nanotubes (MWCNTs) were prepared in this study and purified by stirring in hot (110 °C) HNO_3 for 24 h, washed with distilled water and dried in an oven for 12 h. The dichlorobenzene (DCB) that was used as chlorine source for the synthesis of MWCNTs was supplied by Sigma Aldrich. Dimethylformamide (DMF, Merck), and tetrahydrofuran (THF, Associated Chemical Enterprises (ACE)) were used to disperse the PVP and MWCNT/PVP compounds. Engine oil (Total SAE 40 diesel and gasoline engine oil) was purchased from Builders Warehouse in South Africa. The mineral oil (Shell Spirax S2 ATF D2 power steering and hydraulic oil) was purchased from a Shell garage. Vegetable oil (Sunfoil, triple refined sunflower oil) was purchased from Pick ‘n Pay grocery store.

7.2.1 Preparation of PVP and MWCNT/PVP composite nanofibers by electrospinning

The optimization of the electrospinning parameters for PVP was first established. Solutions with various concentrations of PVP were prepared by dissolving appropriate amounts of PVP in a 1:1 vol/vol (v/v) mixture of DMF and THF using a magnetic stirrer at room temperature for 12 h to form a homogeneous solution. Solutions with 30, 35, 40 and 45 wt.% PVP in DMF/THF were prepared.

A 40 wt.% PVP solution in DMF/THF (1:1) at room temperature was prepared. A homogeneous solution was obtained. Various concentrations of MWCNTs (0.4, 0.5, 0.6 and 0.7 wt.%) were then added to the PVP solution. The MWCNT/PVP solution was stirred using a magnetic stirrer at room temperature for 24 h to obtain a homogeneous suspension of CNTs in the PVP/solvent mixture.

The prepared solutions were added to a 25 mL plastic syringe with a stainless steel needle that was connected to a power supply, which can generate DC voltages in the range of 0 to 30 kV. An electrospinning voltage of 15 kV was applied to the needle and the distance between the needle tip and the drum collector was set at 16 cm. The feed rate of the polymer solutions was set at 1 mL/h and a take-up speed of 6.37 cm/min was selected to collect the electrospun composite nanofibers. A rotating drum covered with an aluminum foil was used as a nanofiber collector. The electrospinning set-up is presented in Figure 7.1.

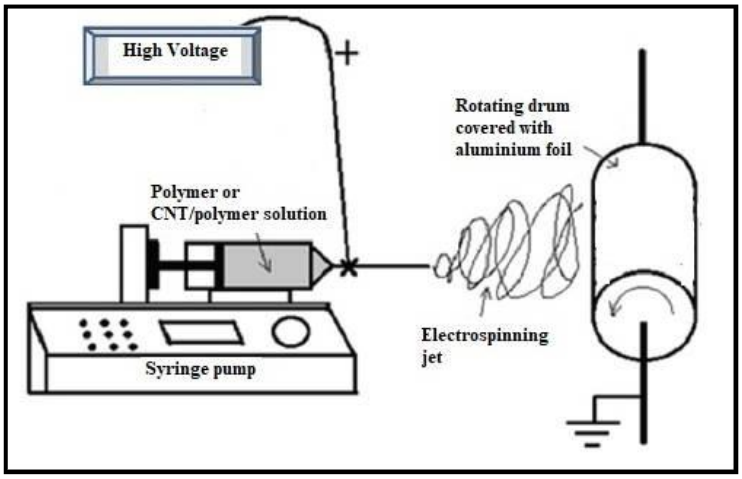

Figure 7.1 Electrospinning set-up used for fabrication of nanofibers.

7.2.2 Adsorption experiments

An MWCNT/PVP composite nanofiber membrane (of 1.5 mm thickness obtained after electrospinning for 16 h) was immersed in a 1 L water bath containing 20 ml of oil. The oil was suspended on top of the water. The electrospun composite membrane was placed on the surface of the water and allowed to move through the oil area. The electrospun membrane was left

immersed in the oil for 1 min. The membrane was then removed from the oil-water solution, held for about 60 s to allow the residual oil that is on the surface to drip away and the membrane was then weighed. In the second experiment, an electrospun membrane was immersed in 20 mL oil bath, for about 10 minutes. The residual oil on the membrane was then allowed to drip off for 60 s and then the membrane was weighed. The sorption capacity of the CNT/PVP electrospun membrane was expressed in grams of the oil absorbed per gram of composite membrane (g/g):

$$Q_t = \frac{m_t - m_0}{m_0} \quad (1)$$

where Q_t (g/g) is the sorption capacity on the CNT/PVP composite at a certain time t(s), m_t (g) is the weight of the CNT/PVP composite after adsorption and m_0 (g) is the initial weight of the CNT/PVP composite. The sorption capacity reached a saturation value Q_e, when Q_t did not change with time.

7.2.3 Characterization of the composite nanofibers

The CNTs, PVP nanofibers and PVP/CNT composite nanofibers mats were characterized by scanning electron microscopy (SEM, FEI Nova NanoLab FIB/SEM), transmission electron microscopy (TEM, FEI TECNAI G^2 SPIRIT), Raman (Jobin-Yvon T6400), X-Ray diffraction (D2 Bruker PXRD with a continuous scan mode using CuKα radiation), and Fourier transform infrared (FTIR) spectroscopy. BET surface areas and pore sizes of the chlorinated MWCNT and MWCNT/PVP composites were obtained through N_2 adsorption using a ASAP 2000 Micrometrics TriStar and Pore Analyzer.

7.3 Results and Discussion

7.3.1. Study of the influence of electrospinning parameters on the morphology of PVP nanofibers

Uniform spinning or ejection of the charged jet requires that the concentration, viscosity, conductivity and surface tension of the polymer solution be optimized. Therefore, prior to electrospinning, parameters that were used to produce CNT/polymer mats were optimized. These parameters included concentration, collector to needle distance, applied voltage and polymer solution feed rate.

The effect of PVP polymer concentration on the morphology of the electrospun nanofibers was investigated using 30, 35, 40 and 45 wt.% PVP concentrations in a 1:1 v/v DMF:THF solvent mixture. SEM images of the electrospun mats are presented in Figure 7.2. The diameter distribution curves at all concentrations are presented in the Supplementary Section Figure S28.

At 30 wt.% PVP, only about 4 cm of a 50 cm Al foil was covered with smooth nanofibers of large diameters ~ 879 nm (Figure 7.2a). At this concentration the solution viscosity was below the limit required for molecular entanglement and fiber formation.[93] At 35 wt.% PVP concentration, the amount of nanofibers formed on the collector increased. Thin nanofibers with outer diameters of ~ 385 nm were obtained but they contained beads (Figure 7.2b). A 35 wt.% solution, generated jets with insufficient viscoelastic forces to fully suppress droplet breakup due to the Rayleigh instability to reduce surface area resulting in beads formation.[94] Uniform smooth nanofibers with diameters of ~ 532 nm were produced when the PVP concentration was increased to 40 wt.% (Figure 7.2c). This is due to the increased solution conductivity which led to more charge density and more elongation forces imposed to the jet under the electric field.[5] A further increase in PVP concentration to 45 wt.% resulted in the formation of nanofibers with very large diameters ~ 2078 nm (Figure 7.2d). Some nanofibers appeared branched and partially fused together, forming fiber doublets. The increase in polymer concentration caused the solvent to dry faster and thus less time was needed for the repulsive columbic force to stretch the fiber, resulting in formation of larger diameter fibers.[95]

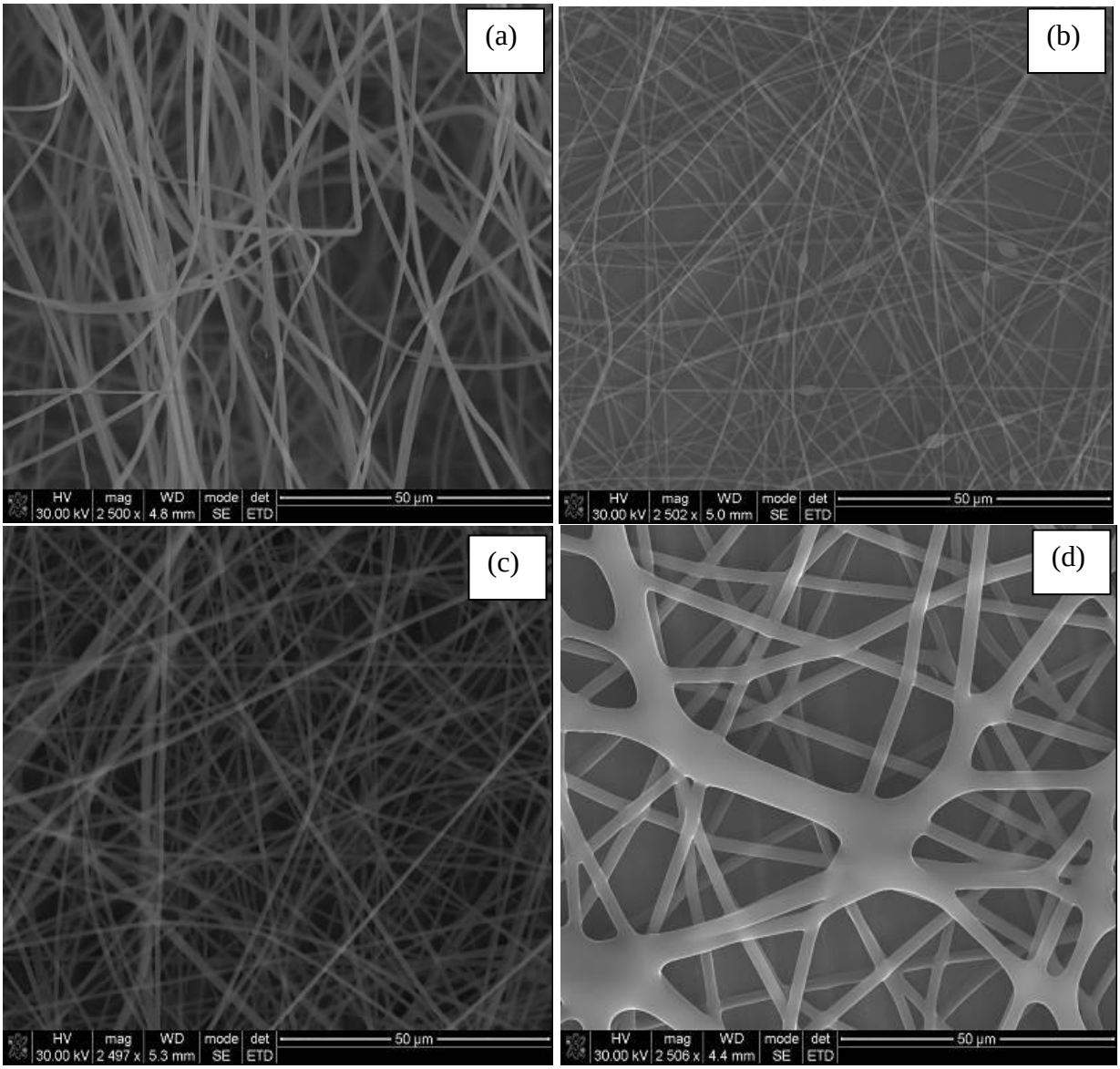

Figure 7.2 SEM images obtained using various concentrations of PVP (a) 30, (b) 35, (c) 40 and (d) 45 wt.%. The fibers were electrospun from a 1:1 v/v DMF/THF solvent mixture (spinning conditions: voltage = 15 kV, distance = 16 cm and feed rate = 1 mL/h).

Electrospinning parameters such as the applied voltage and the distance between the tip of the needle and the collector were also optimized.

The distance between the needle tip and the collector was varied from 8 to 18 cm at an applied voltage of 15 kV and a feed rate of 1 mL/h. SEM images of the obtained nanofibers are presented in Figure 7.3. The average nanofiber diameter was found to be 1030, 992, 723, 523

and 711 nm for spinning distances of 8, 10, 12, 16 and 18 cm, respectively (Supplementary Figure S29). The fiber diameter decreased with an increase in the spinning distance from 1030 to 523 nm but with improved uniformity. This was attributed to complete solvent evaporation, stretching and thinning of the jet which favored the formation of thinner fibers.[96] At 8 cm distance, irregular beaded fibers with large diameters were obtained (Figure 7.3a). Increasing the distance to 10 cm resulted in the formation of smooth, non-beaded uniform fibers (Figure 7.3b). The electrospun mat at a 10 cm distance had holes with no fibers, which showed that at some stage the fiber did not have enough time to solidify before reaching the collector (Figure 7.3b). At a 12 cm distance smooth, curved, large nanofibers with non-uniform diameters were obtained (Figure 7.3c). Curved nanofibers are obtained if the nanofibers cannot be fully stretched under the electrospinning conditions, i.e. under the applied electric force[8]. Increasing the distance to 16 cm resulted in the production of thinner fibers which appeared more regular and uniformly distributed (Figure 7.3d). A further increase in the distance to 18 cm resulted in formation of beaded fibers with large diameters. The 16 cm spinning distance was then chosen as the distance to be used in further optimization studies, since it gave smooth thin fibers without beads.

Nanofibers were then electrospun by varying the applied voltage from 11 to 17 kV at a tip to collector distance of 16 cm and a feed rate of 1mL/h. The diameter distributions are presented in Supplementary Figure S30. At 11 kV, non-uniform branched fibers with very large diameters (1381 nm) were obtained (Figure 7.4a). This was attributed to the voltage not being high enough to produce a stable jet. Applying a voltage of 13 kV, resulted in a reduction in the diameter of the electrospun fibers to 958 nm, but the fibers still appeared non-uniform with some of them curving or bending (Figure 7.4b). Increasing the applied voltage further to 15 kV resulted in production of more uniform, regular, smooth fibers with small diameters ~ 523 nm (Figure 7.4c). A further increase in voltage to 17 kV, resulted in formation of uniform fibers but with large diameters (1184 nm) (Figure 7.4d). This is possibly a result of the stability of the jet due to increased charge density on the surface of the jet, polymer jet velocity and polymer strands elongation forces.[97,98] Hence, a 15 kV applied voltage was chosen as the optimum voltage to study the effect of MWCNT concentration of the morphology of electrospun MWCNT/PVP nanofiber composites.

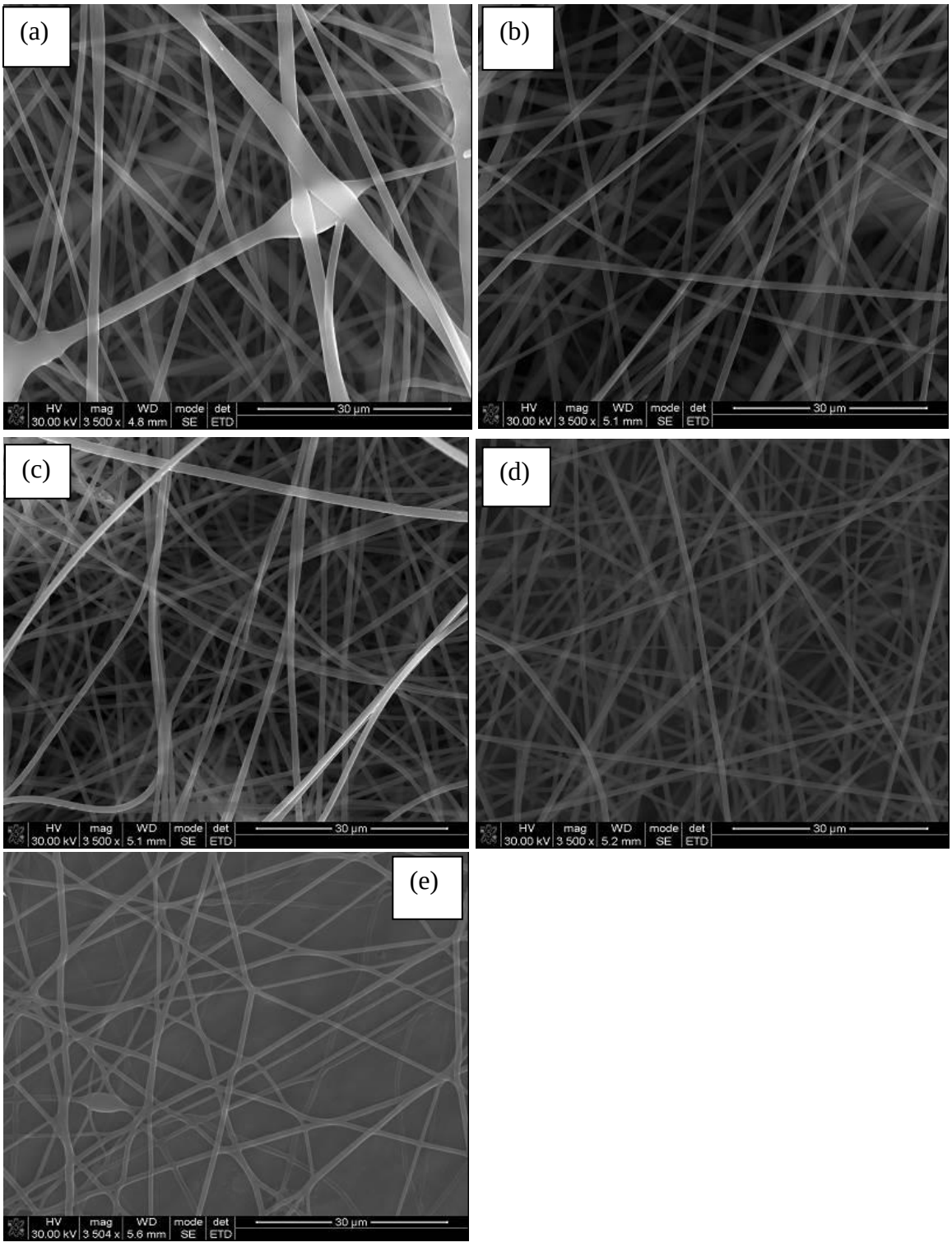

Figure 7.3 SEM images of electrospun nanofibers prepared from 40 wt.% PVP in a mixture of DMF:THF (1:1v/v) applying the voltage of 15 kV at (a) 8, (b) 10, (c) 12, (d) 16 and (e) 18 cm collector distances.

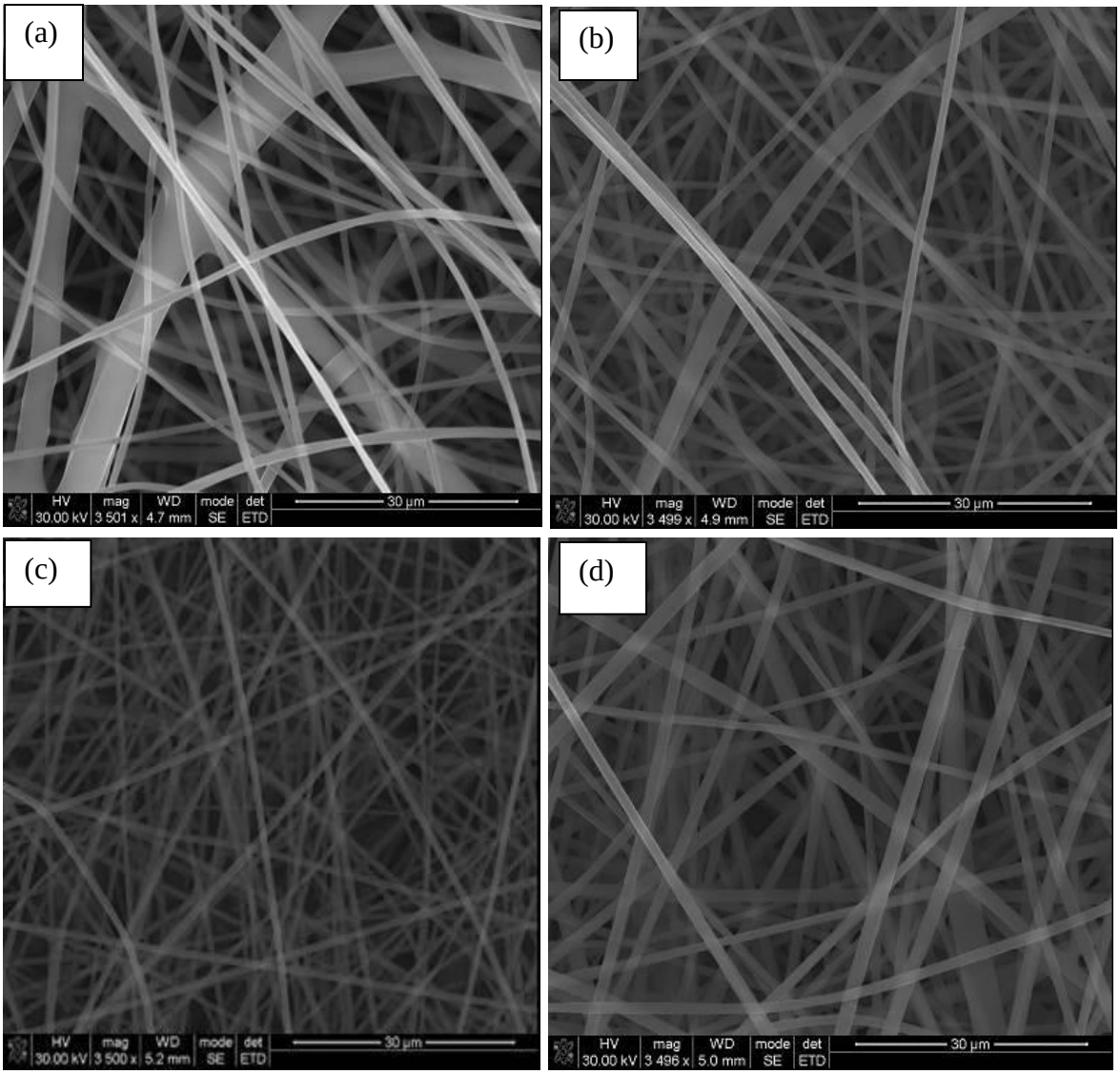

Figure 7.4 SEM images of electrospun nanofibers prepared from 40 wt.% PVP in a mixture of DMF:THF (1:1 v/v) using a 16 cm needle to collector distance at an applied voltage of (a) 11, (b) 13, (c) 15 and (d) 17 kV.

7.3.2 Effect of the MWCNT content on the morphology of the electrospun PVP nanofibers

The concentration of chlorine functionalized MWCNTs was varied from 0.4 to 1 wt.% to obtain the critical viscosity/concentration required to prepare electrospun MWCNTs/PVP solutions. Addition of 0.4 wt.% MWCNTs into the PVP solution resulted in formation of smooth nanofibers of variable diameters with an average diameter of 1828 nm (Figure 7.5a). A PVP solution containing 0.5 wt.% MWCNTs produced nanofibers with highly reduced average

diameters of 402 nm (Figure 7.5b). A further increase in CNT concentration to 0.6 wt.% resulted in formation of curved smooth nanofibers with largely increased average diameter of 2486 nm (Figure 7.5c). A reduction in the average diameter to ~ 1203 nm, was observed again for composites generated from a solution containing 0.7 wt.% of CNTs (Figure 7.5d). CNTs with 1 wt.% concentration could not be dispersed in the solvent mixture, they were insoluble. As a result, we could only electrospin solutions up to 0.7 wt.%. The diameter distribution curves are presented in Supplementary Figure S31. As a result, a 0.5wt.% MWCNT concentration was chosen as an optimum as it gave smooth, uniform thin fibers and was used in further studies.

Electrospinning parameters such as feed rate and voltage were also evaluated for a PVP solution containing 0.5 wt.% CNTs at a spinning distance of 16 cm. At 11 kV beaded curved nanofibers with large diameters (2429 nm) were obtained (Figure 7.6a). Fiber breakage was also observed from the solutions electrospun at an applied voltage of 11 kV (Figure 7.5a circled parts). At a low applied voltage there is a decrease in the concentration of water vapor molecules in the atmosphere (low humidity environments) which result in a decreased amount of electrostatic discharge leading to higher charge density on the jet causing fiber breakage.[94] At 13 kV the size and amount of beads on the nanofibers were greatly reduced due to the increased charge density, but the nanofiber diameter was still large at ~1943 nm. The number of nanofiber breakages were also reduced at 13 kV. At a 15 kV applied voltage smooth, thin, more uniform nanofibers with an average diameter of 402 nm were obtained. Increasing the voltage further to 17 kV resulted in formation of non-uniform branched nanofiber doublets with a very large average diameters of ~ 2293 nm. The formation of branches in jets and fibers occurs with more concentrated and viscous solutions and unusually high electric fields are used.[99] If the excess charge density on the surface of the jet was high undulations are predicted to form on the surface of a cylindrical jet. These undulations grow large enough to become unstable and initiate branches which grow outward from the primary jet.[99] The diameter distribution curves showing the average diameters of the electrospun nanofibers are presented in Supplementary Figure S32.

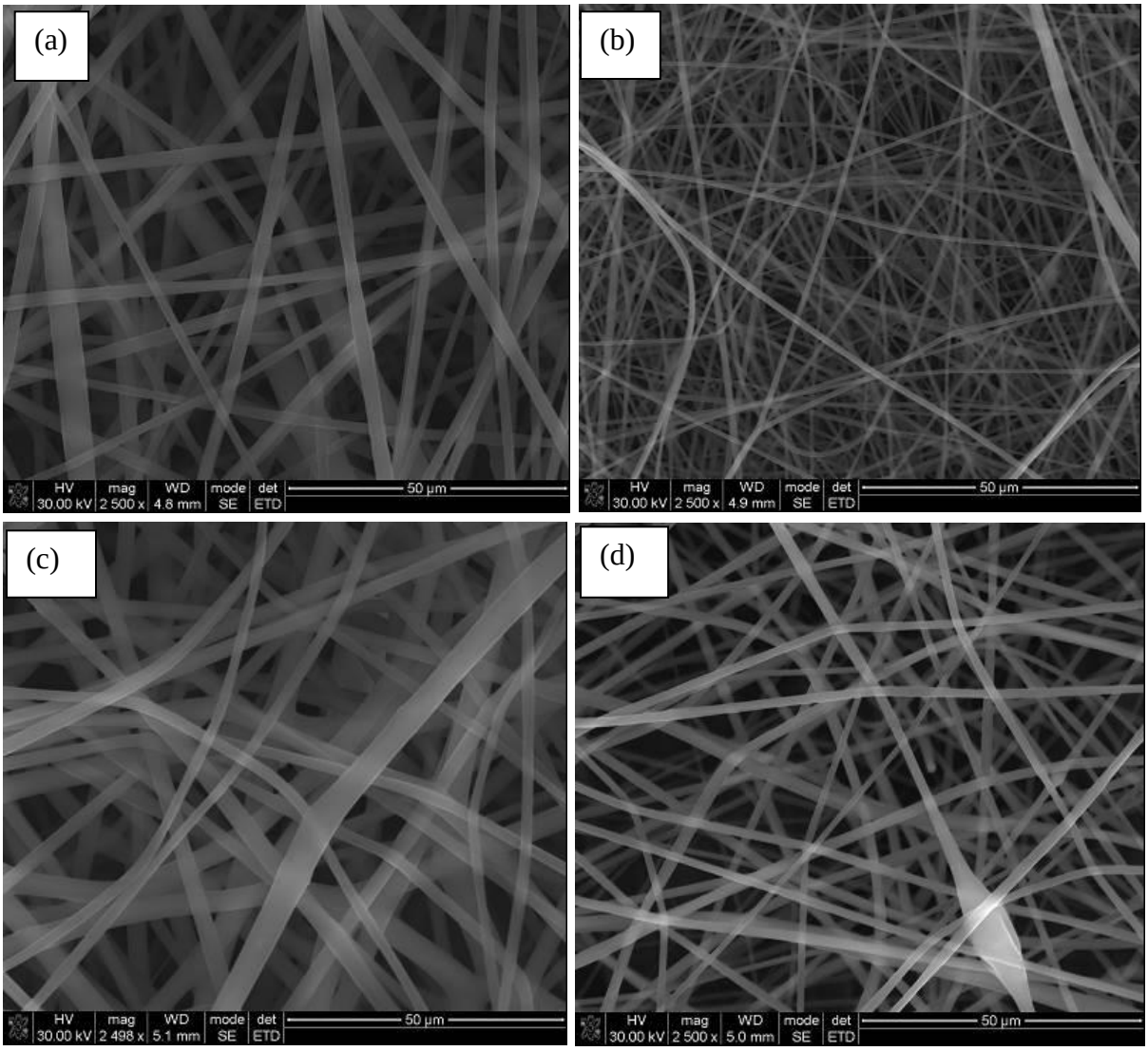

Figure 7.5 SEM images of nanofibers prepared from 40 wt.% PVP containing (a) 0.4 wt.% (b) 0.5 wt.%, (c) 0.6 wt.% and 0.7 wt.% MWCNTs, electrospun from a mixture of DMF:THF (1:1 v/v) at 15 kV, 16 cm and 1 mL/h applied voltage, collector distance and feed rate.

The average diameter of the MWCNTs/PVP nanofibers increased with an increase in the solution feed rate from 402 to 1142 nm for a 1 mL/h to 2 mL/h feed rates, but decreased slightly to 996 nm for a 3mL/h feed rate (Supplementary Figure S33 and Figure 7.7). Zong *et al*. found that low solution feed rates produced fibers with smaller diameters, while relatively large fiber diameters were observed in fibers spun from a higher solution feed rate.[30] They reasoned that since the droplet suspended at the end of the spinneret becomes larger when a higher feed rate is

used, the solution jet can carry the fluid away with faster velocity. Therefore, the electrospun fibers may not be completely dry when they reach the target.[30]

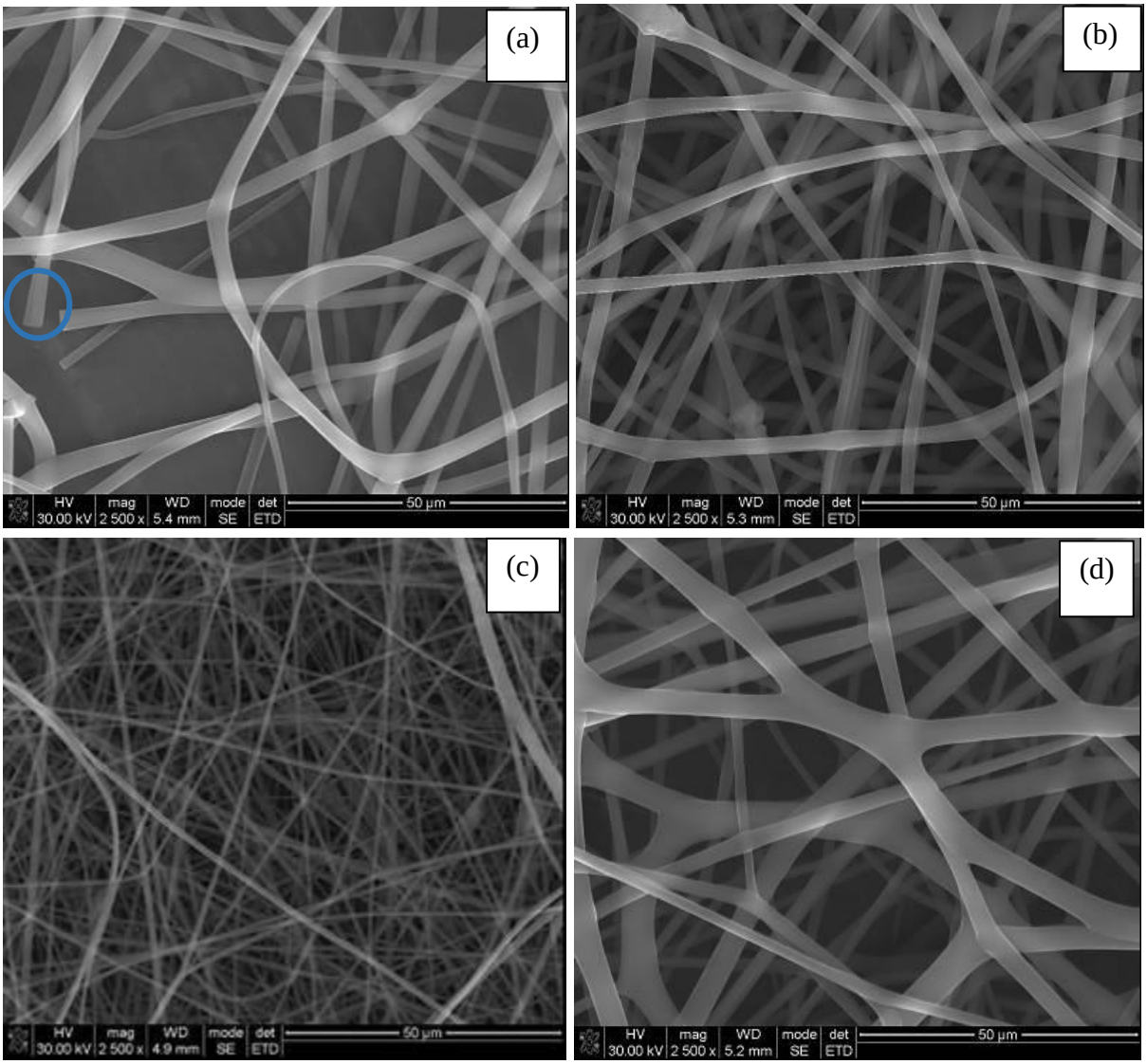

Figure 7.6 SEM images of electrospun nanofibers prepared from 40 wt.% PVP_0.5 wt.% MWCNTs in a mixture of DMF:THF (1:1 v/v) at 16 cm collector distance and an applied voltage of (a) 11, (b) 13, (c) 15 and (d) 17 kV.

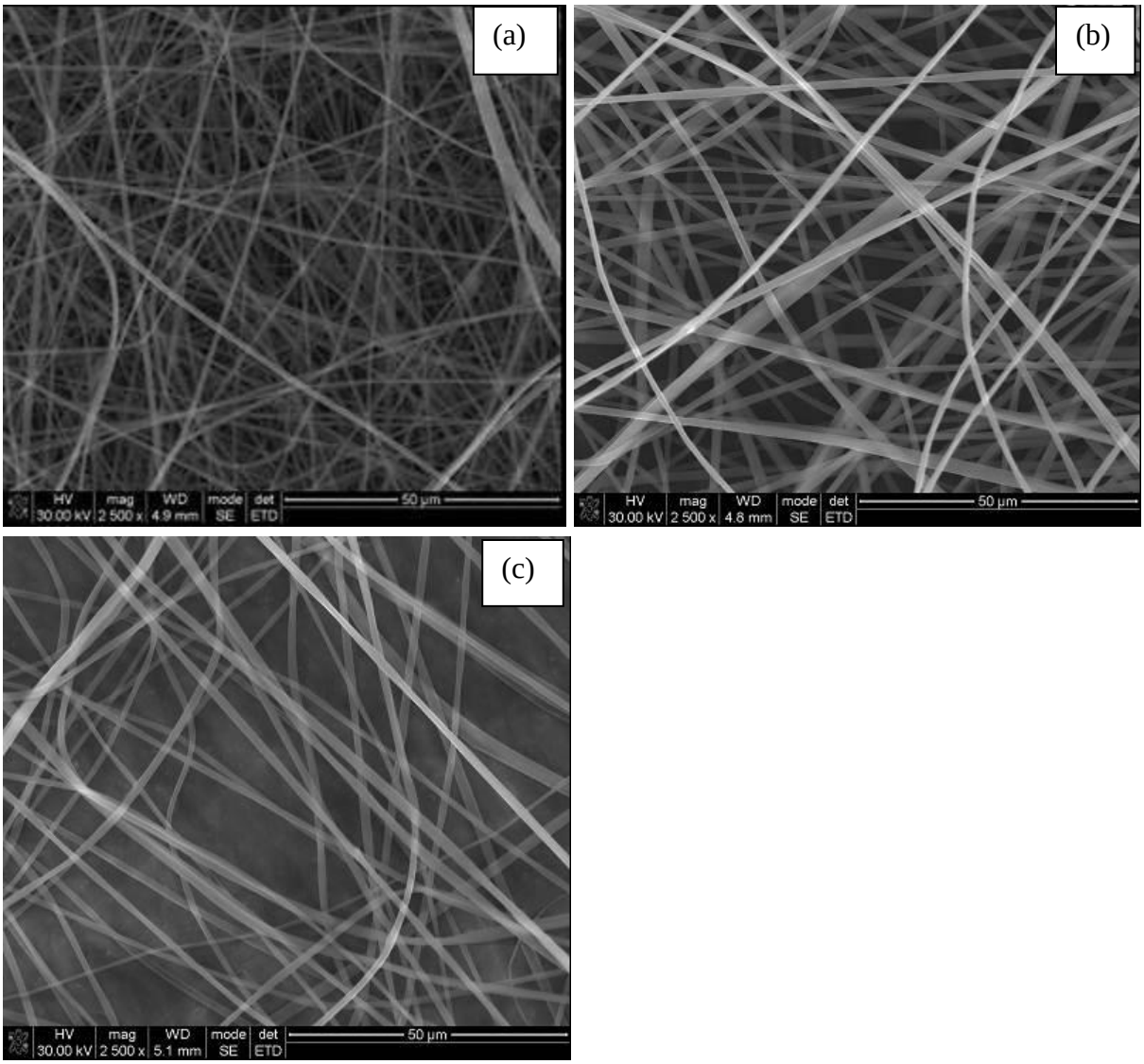

Figure 7.7 SEM images of electrospun nanofibers prepared from 40 wt.% PVP_0.5 wt.% MWCNTs in a mixture of DMF:THF (1:1) at 16 cm and 15 kV, collector distance and applied voltage at various injection flow rates (a) 1, (b) 2, and (c) 3 mL/hr.

7.3.2.1 X-ray diffraction, FTIR spectroscopy and TEM analysis of the materials

The physical states of the MWCNTs in the composite nanofibers was determined from XRD patterns. An XRD pattern of the purified MWCNTs, pure PVP and MWCNT/PVP composite nanofibers are presented in Figure 7.8. Purified MWCNTs exhibit peaks at $2\theta = 26°$, 44.7° and 53.8°, corresponding to graphite 002, 100 and 004 reflections. Additional peaks assigned to Fe_3C were also observed at $2\theta = 32°$, and 37°. PVP nanofibers exhibited only two broad peaks at 11.7°

and 21.2°, in good agreement with the literature.[6] An XRD pattern of a PVP/MWCNT-0.5 wt.% composite nanofibers showed all the peaks that were observed from pure PVP and a small graphitic peak at 2θ = 26° which was also observed in the diffractogram of purified MWCNTs. The absence of other peaks observed from the diffractogram of the purified MWCNTs and the reduction in intensity of the C_{002} peak are correlated with the MWCNT/PVP composite formation. These results are similar to those obtained in the literature for other MWCNT/PVP composite nanofibers.[6]

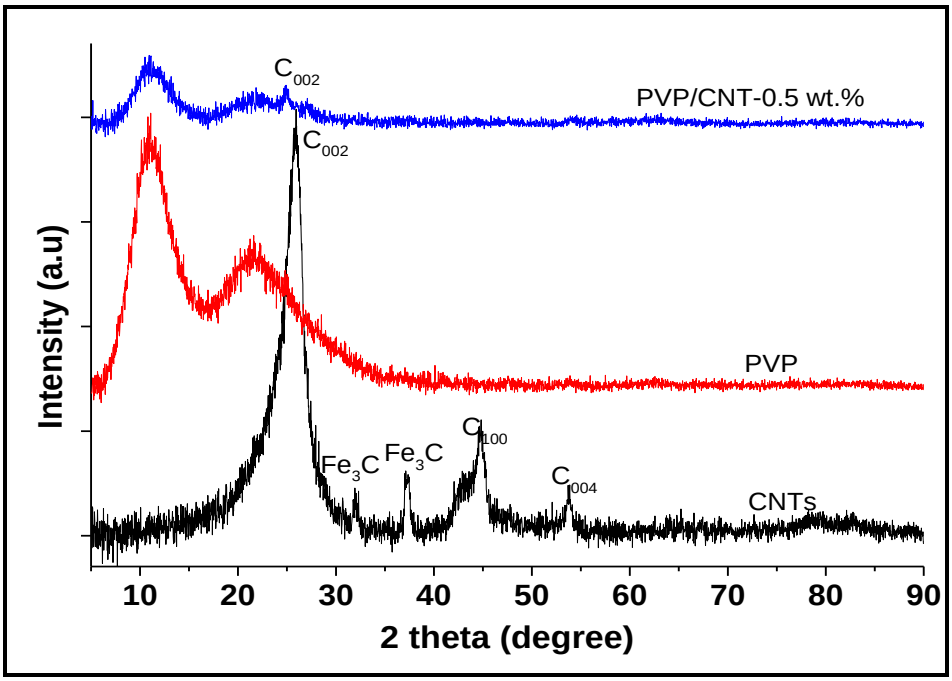

Figure 7.8 XRD patterns of purified MWCNTs, pure PVP and PVP/MWCNT-0.5 wt.% composite nanofibers electrospun from a 1:1 v/v DMF/THF solvent mixture.

FTIR spectra of the purified MWCNTs revealed bands at 1539, 1716, 2328 and 2896 cm^{-1} assigned to C=C stretching in aromatics, presence of C=O group in carboxylic acids, C–OH stretches associated with hydrogen bonding due to oxygen containing groups, and asymmetric C–H stretching modes (Figure 7.9). FTIR spectra analysis of PVP before and after addition of 0.5 wt.% MWCNTs is shown in Figure 7.9. Peaks located at 2918, 1654, 1425 and 1290 cm^{-1} were found in the FTIR spectrum of PVP and can be assigned to C–H, C=O, C=C and C–N

vibrations respectively (Figure 7.9). FTIR spectra of the MWCNT/PVP composite showed additional peaks at 3435, 2891, and 1020 cm^{-1} assigned to an O–H stretch of the hydroxyl group, asymmetric and symmetric C–H and R–OH groups respectively (Figure 7.11c). The shift in the absorption band from 1654 cm^{-1} for PVP to 1651 cm^{-1} for PVP/CNT composite suggests the presence of molecular interactions between CNTs and PVP.[9,100]

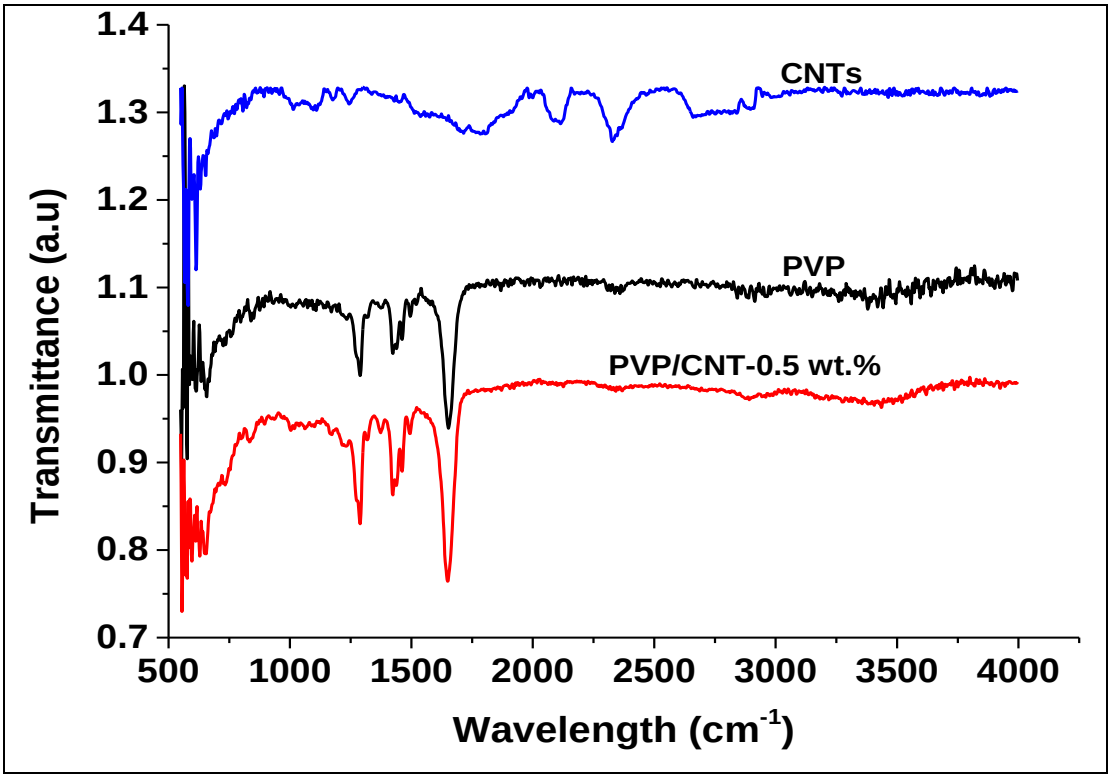

Figure 7.9 FTIR spectra of purified MWCNTs, pure PVP and PVP/MWCNT-0.5 wt.% composite nanofibers electrospun from a 1:1 v/v DMF/THF solvent mixture.

TEM analysis of the composite fibers, prepared by dispersing the nanofibers in ethanol showed only CNTs with an average outer diameters of ~ 48 nm (Figure 7.10). The absence of PVP fibers could be due to the fact that PVP is soluble in ethanol. In order to observe MWCNTs inside the PVP nanofiber one has to directly electrospun the cmposite onto a copper grid and do solid TEM. The analysis will be done later since at the moment we could not access solid TEM.

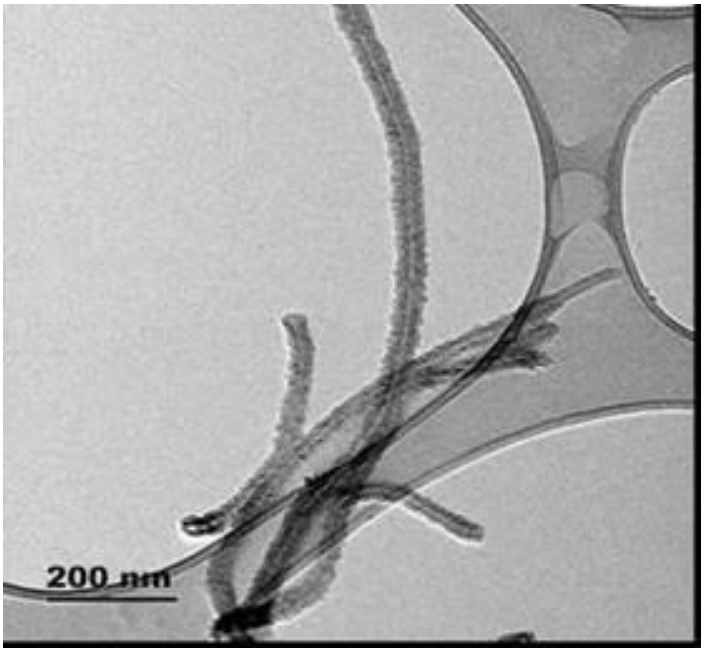

Figure 7.10 TEM image of PVP/MWCNT-0.5 wt.% composite nanofibers electrospun from a 1:1 v/v DMF/THF solvent mixture.

7.3.3 Oil adsorption capacity of the MWCNT/PVP composite nanofibers

The densities and viscosities of the studied oils are presented in Table 7.1. The MWCNT/PVP composite nanofiber membrane used in this study was electrospun for 16 h. The dimensions of the composites were 300 mm long, 247 mm wide and 1.5 mm thick. The BET surface area of the MWCNT/PVP composite was 0.1811 m^2/g while that of acid treated MWCNTs was 59.5 m^2/g. The average pore size of the MWCNT/PVP composite was 275 nm, that of purified MWCNTs was 19.5 nm. The oil adsorption capacity of MWCNT/PVP composite nanofibers was tested using engine, mineral and vegetable oil by either immersing the composite membrane in an oil-water emulsion or in pure oil. For adsorption performed with engine oil-water solutions, MWCNT/PVP composites demonstrated high adsorption capacities of 11 to 16 times their own weight (Figure 7.11). A high adsorption was achieved within 30 s. The MWCNT/PVP composite maintained its shape and size even after 90 minutes of oil adsorption (Figure 7.12).

Adsorption of mineral oil by the composite showed increased adsorption of oil from 12 to 13.49 g/g for a 30 s to 60 s adsorption time (Figure 7.11). The adsorption capacity then decreased from

11 to 4.05 with an increase in adsorption time from 120 s to 1200 s (Figure 7.11). Pictures of the MWCNT/PVP composite after 1 min and 10 min mineral oil adsorption shows that the composite decreased in size and changed shape after 1 min of oil adsorption (Figure 7.12 c and d). The decrease in size of the adsorbent can be attributed to leaching of PVP into water leaving only MWCNTs. The MWCNT/composite mat was not well suspended in an oil-water mixture because of a high density of the mineral oil. The composite was found to be suspended between the oil and water in the mixture, which resulted in PVP leaching into water, since PVP is highly soluble in water. For vegetable oil adsorption, the PVP leached out into solution immediately after the composite was added to an oil-water mixture, CNTs were observed floating on top of the mixture (Figure 7.12e). This was a result of a very high density of vegetable oil which is closer to that of water.

In order to establish the equilibrium time for maximum uptake of oil, pure oil was used and the amount of oil adsorbed on the MWCNT/PVP membrane was studied as a function of contact time. The relationship between the amount of oil adsorbed per gram of adsorbent Q_t as a function of time is plotted in Figure 7.11. The amount of oil adsorbed increased with an increase in the contact time. The rate of oil uptake was rapid at the beginning, and continued until saturation was reached when no more oil adsorption occurred as all the pores have been utilized.

Table 7.1 Physical properties of the oils and organic reagents used in this study.

Oil	**Density (g.mL^{-1})**	**Dynamic viscosity (cP) @ 20 ° C**
Diesel and gasoline engine oil	0.79	345
Mineral oil	0.88	129.8
Vegetable oil	0.94	51.1
DMF	0.95	0.92
Ethyl alcohol	0.79	1.095
Hexane	0.66	0.297

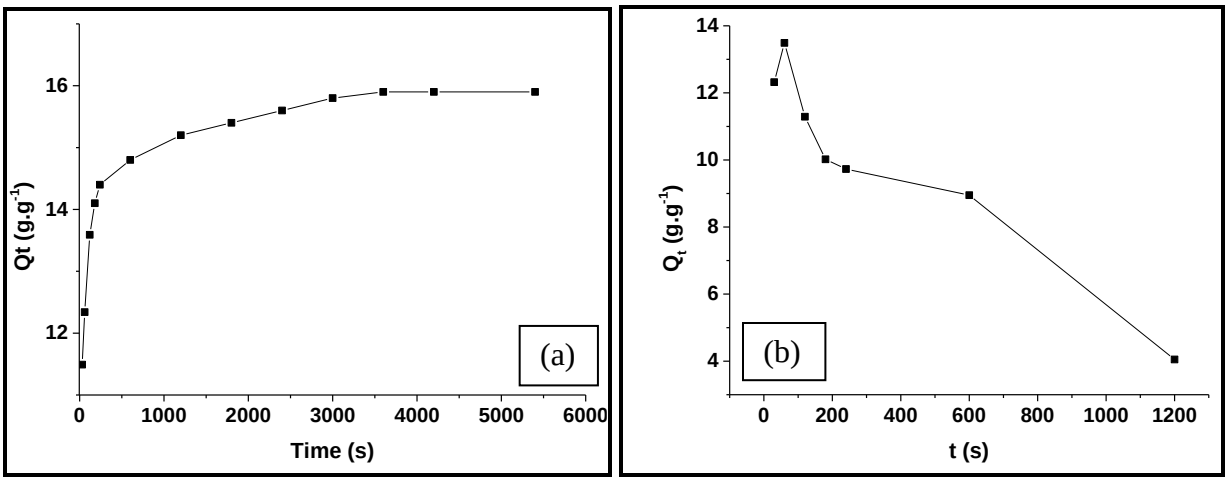

Figure 7.11 Adsorption curves of (a) engine oil, and (b) mineral oil in oil-water mixture oil, using CNT/PVP composite membranes as adsorbents.

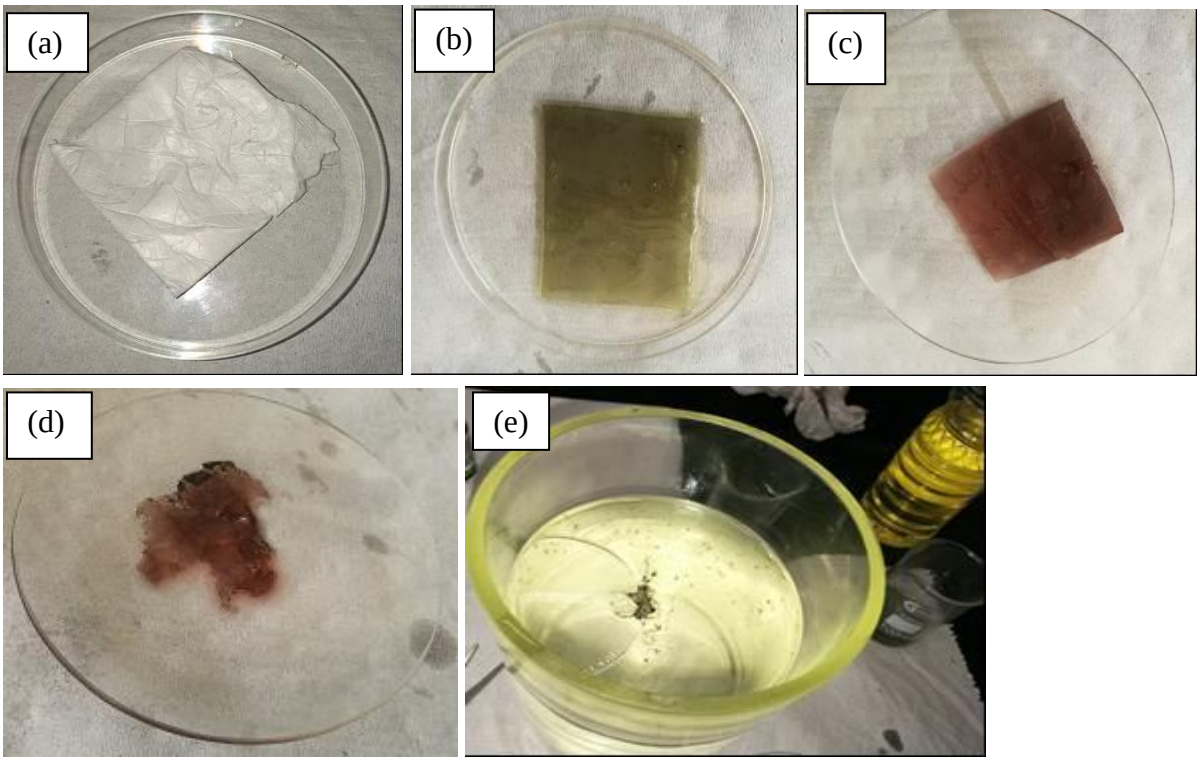

Figure 7.12 Snapshots showing oil adsorption of the CNT/PVP composite in an oil-water mixture (a) before oil adsorption, (b) after 4 min of engine oil adsorption, (c) after 1 min and (d) after 10 min of mineral oil adsorption and (e) after 1 s of dropping the composite in water containing vegetable oil.

For adsorption experiments performed in pure oil, MWCNT/PVP composites demonstrated high adsorption capacities for all studied oils. Adsorption capacities of 15–20, 14–17 and 10–15 times their own weight were observed for engine oil, mineral oil and vegetable oil, respectively (Figure 7.13). The time to reach an equilibrium was greatly reduced for low viscosity oils as they can penetrate much more easily through the web-like structure of the MWCNT/PVP composite nanofibers. The saturated oil adsorption capacity was similar to that of MWCNT/PVP (where CNTs were attached to the outer layer of PVP fiber) composite used in the literature (~ 18 – 20 g/g or 0.9 – 1.1 g/cm^3).[85]

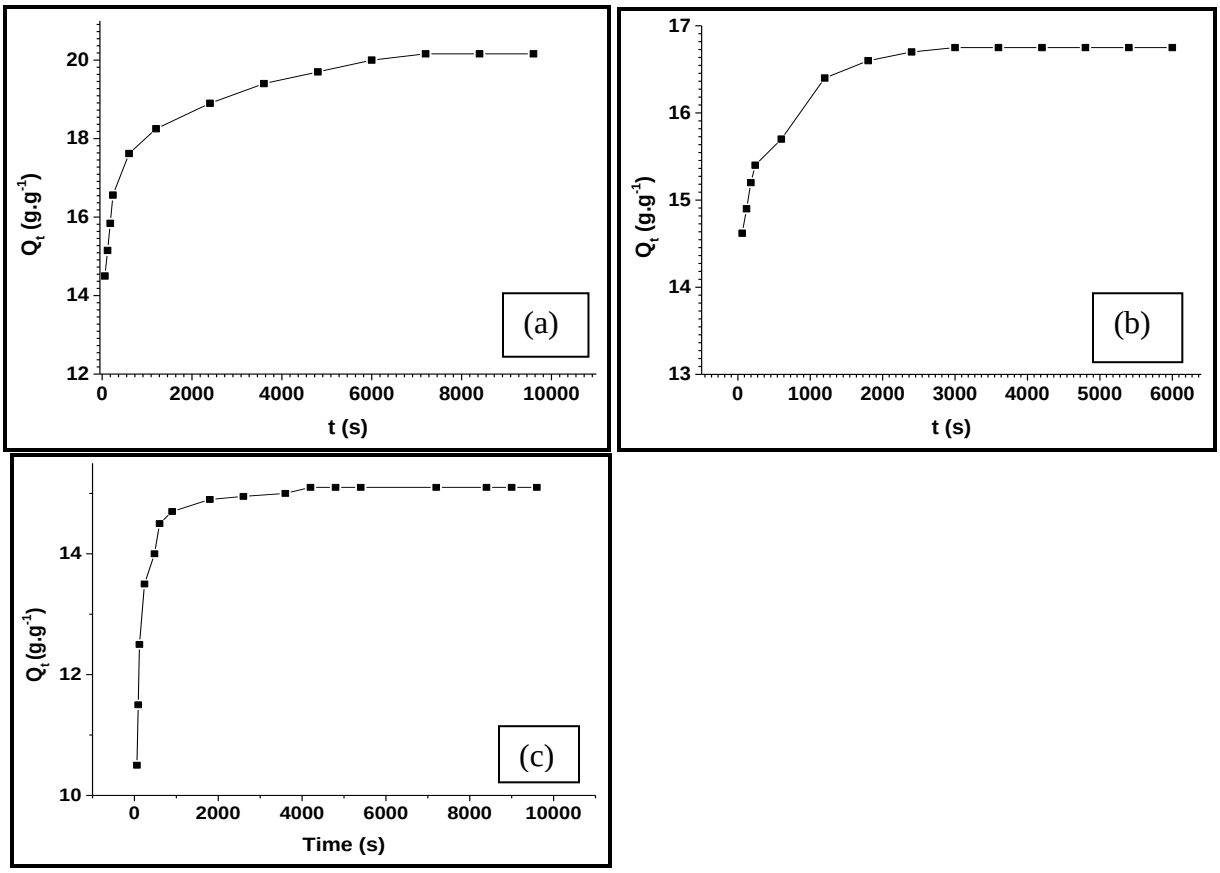

Figure 7.13 Adsorption curves of pure (a) engine oil, (b) mineral oil and (c) vegetable oil using CNT/PVP composite membranes as adsorbents.

The rate of oil adsorption could not be measured using selected organic reagents. For example, the use of low viscosity solutions like ethyl alcohol and DMF resulted in mat disappearance, due to the dissolution of the PVP nanofibers. CNTs remained floating inside the solvents. No dissolution of PVP was observed in a low viscosity, low density hexane, but the mat was greatly wetted and it tore into pieces during pick up. The adsorption capacity of the MWCNT/PVP composite in hexane was only 8.5 times the weight of the composite before adsorption. The adsorption capacity was half the adsorption capacity of the studied oils, which shows that viscosity and density of oils plays a crucial role in their adsorption by the composite nanofiber membranes. Larger Q values were observed for higher density liquids during adsorption of various oils and organic solvents by the CNT sponge.[101]

The sorption kinetics was described using the pseudo-second-order models. This considers the rate-limiting step as the formation of chemisorptive bond involving sharing or exchange of electrons between the adsorbate and the adsorbent.[102]

$$\frac{t}{q_t} = \frac{1}{k_2 q_e^{\,2}} + \frac{1}{q_e}.t \qquad (2)$$

where q_t is the amount of oil removed at time t (g/g), q_e is the adsorption capacity at equilibrium (g/g), t is the contact time (min) and k_2 is the pseudo-second-order rate constant of adsorption. The parameters q_e and k_2 can be estimated from the slope and intercept, respectively of a plot of t/q_t versus t[103,104].

The oil adsorption of surface composites was well fitted by Eq. (2) (Table 7.2). The rate constant and the equilibrium adsorption capacity of different oils were obtained from the intercept and slope of a t/q_t versus t plot (Supplementary Figure S34). The rate constant calculated from the best fit lines (with R = 0.99 in all cases) were 0.0374, 0.154 and 0.1334 $g.g^{-1}.min^{-1}$ for engine, mineral and vegetable oil respectively, for adsorption experiments performed in pure oil (Table 7.2). A rate constant of 0.123 $g.g^{-1}.min^{-1}$ was observed for adsorption of engine oil from oil-water solutions (Table 7.2). The electrospun membrane prepared in this work is highly effective for oil spill cleanups of low density oils that occur in oil-water solutions. The composite membranes are also effective for adsorption of the studied low density oils for land oil spills (as long as the oils are not immersed in water). Nan *et al*. reported rate constants for adsorption of

oil by a MWCNT/PVP composite, of 12.61 s^{-1} (0.757 min^{-1} for engine oil), 1.04 s^{-1} (0.0624 min^{-1} for mineral oil) and 6.52 s^{-1} (0.391 min^{-1} for vegetable oil).[91] The sorption capacities obtained from the slope of the linearized equation (2) were 15.92, 16.67 and 15.13 $g.g^{-1}$ for engine, mineral and vegetable oil (Table 7.4), which are in good agreement with the experimental data obtained in this study.

Table 7.2 Adsorption constant and saturation sorption capacity of MWCNT/PVP composite membrane for various oils

Oil type	**k ($g.g^{-1}.min^{-1}$)**	**R^2**	**Q_t ($g.g^{-1}$)**
Gasoline and diesel oil	0.123 (oil-water mixture) 0.0374 (oil only)	0.999 0.997	15.92 20.19
Mineral oil	0.154 (oil only)	1.00	16.84
Vegetable oil	0.1334 (oil only)	1.00	15.13

7.4 Conclusion

The synthesis of MWCNT/PVP composite nanofibers was successful. Studies showed that the presence of chlorine and secondary CNTs on the surface of the MWCNTs greatly enhanced their interaction with PVP matrix. This was shown by a huge decrease in the 2θ degree peak at 26 ° from XRD patterns and a shift in the absorption band at 1654 cm^{-1} for PVP to 1651 cm^{-1} for MWCNT/PVP composites, suggesting the presence of molecular interactions between PVP and MWCNTs. A CNT concentration of 0.5 wt.% added to the PVP solution was chosen as the optimum to be used in further studies since it gave uniform nanofibers with small diameters. The MWCNT/PVP composite showed high oil adsorption capacities of ~ 15 to 20 $g.g^{-1}$. The adsorption capability of the composite for various oils and organic solvents was found to depend on their viscosity. High viscosity solvents were easily adsorbed, but the rate of adsorption could not be measured for very low viscosity solvents as the MWCNT/PVP composite was dismantled due to dissolution of PVP fibers in the solvents. Best fit linearized plots were obtained for all studied oils and the data was used to obtain the rate constant and the equilibrium adsorption

capacity. A good correlation between the equilibrium adsorption capacity obtained from the linearized equation (2) with the experimental data was obtained.

References

1. G. Mittal, V. Dhand, K.Y. Rhee, S.-J. Park and W.R. Lee, *J. Ind. Eng. Chem*., 2015, **21**, 11–25.
2. J. Gao, A. Yu, M.E. Itkis, E. Bekyarova, B. Zhao, S. Niyogi, and R.C. Haddon, *J. Am. Chem. Soc*, 2004, **126**, 16698–16699.
3. M. Park, H. Kim, J. P. Youngblood, S.W. Han, E. Verplogen and A.J. Hart, *Nanotechnology*, 2011, **22**, 415703 (1–12).
4. S.Y. Ebadi, A. Fakhrali, A.A. Gharehaghaji, S. Mazinani and S.O. Ranaei-Siadat, *Polym. Compos.*, 2016, 3149 – 3159, doi.10.1002/pc.23512.
5. F.A. Chayad, A.R. Jabur and N.M. Jalal, *Karbala Int. J. Modern Sci.*, 2015, **1**, 187–193.
6. K. Nasouri, A.M. Shoushtari, and M.R.M. Mojtahedi, *Polym. Compos.*, 2016, 1–9, doi.10.1002/pc.23774.
7. W.S. Khan, R. Asmatulu, and M.M. Eltabey, *J. Nanomater*., 2013, 1–9, doi.org/10.1155/2013/160931.
8. S-H. Wang, Y. Wan, B. Sun, L-Z. Liu and W. Xu, *Nanoscale Res. Lett.*, 2014, **9**, 522–528.
9. N. Diouri, M. Baitoul and M. Maaza, *J. Nanomater*., 2013, 1–6, doi.org/10.1155/2013/949108.
10. M.Z. Islam, M. Mahboob and R.L. Lowe, *Polym. Compos.*, 2016, 305–314, doi.10.1002/pc.23182.
11. O-K. Park, W. Lee, J.Y. Hwang, N-H. You, Y. Jeong, S.M. Kim and B-C. Ku, *Composites Part A*, 2016, **91**, 22–228.
12. M. Tarfaoui, K. Lafdi and A. El Moumen, *Composites Part B*, 2016, **103**, 113–121.
13. A. Shameli and E. Ameri, *Chem. Eng. J*., 2017, **309**, 381–396.
14. P.-C. Ma, N.A. Siddiqui, G. Marom and J.-K. Kim, *Composite Part A*, 2010, **41**, 1345–1367.
15. P. Saini and V. Choudhary, *J. Nanoparticle Res*., 2013, **15**, 1415 (1–7).
16. Q. Yao, L. Chen, W. Zhang, S. Liufu and X. Chen, *ACS Nano*., 2010, **4**, 2445–2451.
17. C. Yu, Y.S. Kim, D. Kim and J.C. Grunlan, *Nano. Lett*., 2009, **9**, 1283–1283.
18. E. Thostenson, C. Li and T. Chou, *Compos. Sci. Technol*. 2005, **65**, 491–516.

19. P. Saini, V. Choudhary, B.P. Sigh, R.B. Mathur and S.K. Dhawan. *Mater. Chem. Phys*. 2009, **113**, 919–926.

20. K.S.V. Santhanam, R. Sangoi and L. Fuller, *Sensors Actuators B Chem*., 2005, **106**, 766–771.

21. J.A. Rud, L.S. Lovell, J.W. Senn, Q. Qiao and J.T. Mcleskey, *J. Mater. Sci*., 2005, **40**, 1455–1458.

22. Y. Kanai and J.C. Grossman, *Nano. Lett*., 2008, **8**, 908–912.

23. Z. Zhu, G. Wang, M. Sun, X. Li and C. Li, *Electrochim. Acta*, 2011, **56**, 1366–1372.

24. Q. Liu, Y. Li, and M. Yang, *Sensor Actuat. B Chem*., 2012, **161**, 967.

25. L. Dai, *Carbon Nanotechnology: Recent Developments in Chemistry, Physics, Material Science and Device Applications*, Oxford: Elsevier, Amsterdam, 1st Edition, 2006.

26. D. Aussawasathien, J.-H. Dong, and L. Dai, *Synth. Met.*, 2005, **154**, 37–40.

27. D.M. Bigg and D.E. Stutz, *Polym. Compos.*, 1993, **4**, 40–46.

28. E.S.A. Rachid, K. Ariffin, H.M. Akil, and C.C. Kooi, *J. Reinf. Plast. Compos.*, 2008, **27**, 1573–1584.

29. X. Ma, F. Scarpa, H.-X. Peng, G. Allegri, J. Yuan and R. Ciobanu, *Aerosp. Sci. Technol*., 2015, **47**, 367–377.

30. X. Zong, K.S. Kim, D. Fang, S. Ran, B.S. Hsiao and B. Chu, *Polymer*, 2002, **43**, 4403–4412.

31. Z. Tang, C. Qiu, J.R. McCutcheon, K. Yoon, H. Ma, D. Fang, E. Lee, C. Kopp, B.S. Hsiao and B. Chu, *J. Polym. Sci., Part B: Polym. Phys.*, 2009, **47**, 2288–2300.

32. M.O. Daramola, P. Hlanyane, O.O. Sadare, O.O. Oluwasina and S.E. Iyuke, *Membranes*, 2017, **7**, 14 (1–15), doi:10.3390/membranes7010014.

33. L. Wang, X.J. Song, T. Wang, S. Wang, Z. Wang, and C. Gao, *Appl. Surf. Sci*., 2015, **330**, 118–125.

34. Y. Baek, D.K. Seo, J.H. Choi, B. Lee, Y.H. Kim, S.M. Park, J. Jung, S. Lee, and J. Yoon, *Desalin. Water Treat*., 2016, **57**, 28133–28140.

35. S. Maphutha, K. Moothi, M. Meyyapan and S.E. Iyuke, *Sci. Rep*., 2013, **3**, 1509.

36. P. Shah, and C.N. Murthy, *J. Membr. Sci*., 2013, **437**, 90–98.

37. K.H. Hong, *Polym. Eng. Sci*., 2007, **47**, 43.

38. P.R. Supronowicz, P.M. Ajayan, K.R. Ullmann, B.P. Arulanandam, D.W. Metzger and R. Bizios, *J. Biomed. Mater. Res*., 2002, **59**, 499–506.

39. R. Tucknott, and S.N. Yaliraki, *Chem. Phys*., 2002, **281**, 455.

40. Y. Dror, W. Salalha, R.L. Khalfin, Y. Cohen, A.L. Yarin and E. Zussman, *Langmuir*, 2003, **19**, 7012–7020.

41. H. Peng, *J. Am. Chem. Soc*., 2008, **130**, 42–43.

42. E.J. García, A.J. Hart, B.L. Wardle and A.H. Slocum, *Nanotechnology*, 2007, **18**, 165602 (1–11).

43. I. Jang, S.B. Sinnot, D. Danailov and P. Keblinski, *Nano Lett*., 2004, **4**, 109–114.

44. Y. Hu, O.A. Shenderova, Z. Hu, C.W. Padgett and D.W. Brenner, *Rep. Prog. Phys*. 2006, **69**, 1847–1895.

45. G. Withers, J. Souza, Y. Yu, L. Cercone, V. Khabashesku and D. Davis, *J. Compos. Mater*., 2015, 783–793, http://dx.doi.org/10.1177/0021998315581510.

46. Z. Spitalsky, D. Tasis, K. Papagelis and C. Galiotis, *Prog. Polym. Sci.* 2010, **35**, 357–401.

47. P. Verma, P. Saini and V. Choudhary, *Mater. Des*., 2015, **88**, 269–277.

48. Z.M. Huang, Y.Z. Zhang, M. Kotaki and S. Ramakrishna, *Compos. Sci. Technol*., 2003, **63**, 2223–2253.

49. P. Saini. *Fundamentals of Conjugated Polymer Blends, Copolymers and Composites*, John Wiley & Sons, Inc., 1–118, http://doi.wiley.com / 10.1002/ 9781119137160.ch1, 2015.

50. P. Kannan, R.J. Young and S.J. Eichhorn, *Small*, 2008, **4**, 930–933.

51. M. Bourourou, M. Holzinger, F. Bossard, F. Hugenell, A. Maaref and S. Cosnier, *Carbon*, 2015, **87**, 233–238.

52. W. Nuasing, *Electrospinning of Biomolecules*, PhD Thesis, Department of Physics, University of Pais Vasco, Donostia, Spain, 2014.

53. C. Mit-uppatham, M. Nithitanakul, P. Supaphol, Macromol. *Chem. Phys.*, 2004, **205**, 2327–2338.

54. L.M.M. Costa, R.E.S. Bretas, R. Gregorio, *Mater. Sci. Appl*., 2010, **1**, 247–252.

55. X. Zong, K. Kim, D. Fang, S. Ran, B.S. Hsiao and B. Chu, *Polymer*, 2002, **42**, 4403.

56. S Koombhogse, W. Liu and D.H. Reneker, *J. Polym. Sci*., 2001, **39**, 2598.

57. H. Albetran, Y. Dong and I.M. Low, *J. Asian Ceram. Soc*., 2015, **3**, 292–300.

58. S. Sarabi-Mianeji, J. Scott and D.J.Y.S. Page, *Polym. Eng. Sci*., 2015, **55**, 2576–2582.

59. P. Ajayan, O. Stephan, C. Colliex and D. Trauth, *Science*, 1994, **265**, 1212–1214.

60. Y. Dror, W. Salalha, R.L. Khalfin, Y. Cohen, A.L. Yarin and E. Zussman, *Am. Chem. Soc*., 2003, 7012–7020.

61. J.J. Ge, H.Q. Hou, Q. Li, M.J. Graham, A. Greiner, D.H. Reneker, F.W. Harris and S.Z.D. Cheng, *J. Am. Chem. Soc*., 2004, **126**, 15754–15761.

62. H.S. Kim, J.H. Sung, H.J. Choi, I. Chin and H. Jin, *Polym. Prepr.* 2005, **46**, 736.

63. R. Sen, B. Zhao, D. Perea, M.E. Itkis, H. Hu, J. Love, E. Bekyarova, and R.C. Haddon, *Nano Lett.*, 2004, **4**, 459–464.

64. K. Saeed, S.Y. Park, H.J. Lee, J.B. Baek and W.S. Huh, *Polymer*, 2006, **47**, 8019–8025.

65. G.M. Kim, G.H. Michlera and P. Pötschke, *Polymer*, 2005, **46**, 7346–7351.

66. J.S. Jeong, S.Y. Jeon, T.Y. Lee, J.H. Park, J.H. Shin, P.S. Alegaonkar, A.S. Berdinsky and J.B. Yoo, *Diamond Relat. Mater.*, 2006, **15**, 1839–1843.

67. C. Pan, L.Q. Ge and Z.Z. Gu, *Composites Science and Technology*, 2007, **67**, 3271–3277.

68. Urban Urgency, *Water Caucus Summary*, World Water Council (WWC), Marseille, France, 2007.

69. M. Elimelech and W.A. Phillip, *Science*, 2011, **333**, 712–717.

70. M.A. Shannon, P.W. Bohn, M. Elimelech, J.G. Georgiadis, B.J. Marinas and A.M. Mayes, *Nature*, 2008, **452**, 301–310.

71. D. Zhou, L. Zhu, Y. Fu, M. Zhu and I. Xue, *Desalination*, 2015, **376**, 109–116.

72. L.Y. Ng, A.W. Mohammad, C.P. Leo, N. Hilal, *Desalination*, 2013, **308**, 15–33.

73. J. Yin, and B. Deng, *J. Membr. Sci*., 2015, **479**, 256–275.

74. L. Ma, X. Dong, M. Chen, L. Zhu, C. Wang, F. Yang and Y. Dong, *Membranes*, 2017, **7**, 16 (1–21), doi:10.3390/membranes7010016.

75. J. Albaiges, *Int. J. Environ. Anal. Chem*., 2014, **94**, 1–3.

76. Q. Li, C. Kang and C. Zhang, *Process Biochem*, 2005, **40**, 873–877.

77. A.R. Pendashteh, A. Fakhru'l-Razi, S.S. Madaeni, L.C. Abdullah, Z.Z. Abidin and D.R.A. Biak, *Chem. Eng. J.*, 2011, **168**, 140–150.

78. J. Rubio, M.L. Souza and R.W. Smith, *Miner. Eng*., 2002, **15**, 139–155.

79. E. Yuliwati and A.F. Ismail, *Desalination*, 2011, **273**, 226–234.

80. J. Zhong, X. Sun and C. Wang, *Sep. Purif. Technol*., 2003, **32**, 93–98.

81. M.R. Kumar, C.V. Koushik and K. Saravanan, *J. Elixir Chem. Eng., A*, 2013, **54**, 12713–12717.

82. W.M. Graham, R.H. Condon, R.H. Carmichael, I. D'Ambra, H.K. Patterson, L.J. Linn and F.J. Hernandez, *Jr. Environ. Res. Lett*., 2010, **5**, 045301.

83. C.M. Reddy, J.S. Arey, J.S. Seewald, S.P. Sylva, K.L. Lemkau, R.K. Nelson, C.A. Carmichael, C.P. McIntyre, J. Fenwick and G.T. Ventura, *Proc. Natl. Acad. Sci. U.S.A*., 2012, **109**, 20229–20234.

84. M.C. Redmond and D.L. Valentine, *Proc. Natl. Acad. Sci. U.S.A*., 2012, **109**, 20292–20297.

85. W. Ma, Q. Zhang, D. Hua, R. Xiong, J. Zhao, W. Rao, S. Huang, X. Zhan, F. Chen, and C. Huang, *RSC Adv*. 2016, **6**, 12868-12888.

86. Z. Shi, W. Zhang, F. Zhang, X. Liu, D. Wang, J. Jin and L. Jiang, *Adv. Mater*., 2013, **25**, 2422–2427.

87. Z.X. Xue, S.T. Wang, L.Lin, L. Chen, M.J. Liu, L. Feng and L. Jiang, *Adv. Mater*., 2011, **23**, 4270–4273.

88. M. Padaki, R.S. Murali, M.S. Abdullah, N. Misdan, A. Moslehyani, M.A. Kassim, N. Hilal, and A.F. Ismail, *Desalination*, 2015, **357**, 197–207.

89. L. Zhu, M. Chen, Y. Dong, C.Y. Tang, A. Huang and L. Li, *Water Res*., 2016, **90**, 277–285.

90. M. Chen, L. Zhu, Y. Dong, L. Li and J. Liu, *ACS Sustainable Chem. Eng*., 2016, **4**, 2098–2106.

91. D. Nan, J. Wei, F. Guo, G. Fan, F. Xu, L. Li, H. Zhu, K. Wang and D. Wu, *J. Nanosci. Nanotechnol.*, 2014, **14**, 6461–6465.

92. H. You, X. Li, Y. Yang, B. Wang, Z. Li, X. Wang, M. Zhu and B.S. Hsiao, *Sep. Purif. Technol*., 2013, 108, 143–151.

93. M. Ozdemir, E. Celik, and U. Cocen, *Mater. Technol*., 2013, **47**, 735–738.

94. M. Roya, BS. Nezarati, B. Michelle, BS. Eifert, and E. Cosgriff-Hermandez, *Tissue Eng.*, 2013, **19,** 810–818.

95. T. Vongsetskul, T.C.P. Wongsomboom, and R. Rangkupan, *Chiang Mai J. Sci*, 2015, **42**, 436–442.

96. T. Mozoochi, M. Hamadanian, M. Ahmadi and V. Jabbari, *Int. Ind. Chem*., 2012, **3**, 1–8, doi:10.1186/2228-5547-3-2.

97. W. Ding, S. Wei, J. Zhu, X. Chen, D. Rutman and Z. Guo, *Macromol. Mater. Eng*., 2010, **295**, 958–965.

98. J.M. Deitzel, J. Kleinmeyer, H.D. Beck and N.C. Tan, *Polymer*, 2001, **42**, 261–272.

99. D.H. Reneker and A.L. Yarin, *Polymer*, 2008, **49**, 2387-2425.

100. S. Huang, L. Zhou, M.-C. Li, Q. Wu, Y. Kojima and D. Zhou, *Materials*, 2016, **6**, 523 (1-14).

101. Z. Li and C. Wang, *One dimensional nanostructures: Electrospinning Technique and unique nanofibers, Springer*, 2013, doi:10.1007/978-3-642-36427-3_2.

102. M.M. Rahman, S.B. Khan, H.M. Marwani and A.M. Asiri, *PLOS ONE*, 2014, doi:10.1371/journal.pone.0114084, 1-23.

103. Y. Ho, *Water Res*., 2006, **40**, 119-125.

104. M. Faisai, S.B. Khan, M.M. Rahman, A. Jamal, A.M. Asiri, et al., *App. Surf. Sci*., 2012, *258*, 7515-7522.

CHAPTER 8

Summary of Conclusions and recommendations

The synthesis of chlorinated MWCNTs and chlorinated N-MWCNTs was achieved by means of a fixed-bed CVD method using various chlorinated organic solvents as sources of chlorine and acetonitrile as a source of nitrogen over an Fe-Co/$CaCO_3$ catalyst. The morphology of the synthesized carbon materials and composites were confirmed by various characterization techniques such as SEM, TEM, TGA, XRD, BET, XPS, FTIR and Raman spectroscopy.

The number of chlorine atoms substituted on the organic compound had a huge effect on the morphology, yield, diameter, and quality of the MWCNTs produced. XPS analysis confirmed that functionalization of carbon from MWCNTs with chlorine was successful. The average outer diameters and inner diameters of the MWCNTs increased with an increase in the amount of chlorine atoms substituted on the organic compound. CNFs, CNTs, CNTs with secondary growth, and hollow CNTs were produced when DCE, CB, DCB and TCE, TCB and TTCE were used as chlorine sources, respectively. About 10 and 40 % of the CNTs generated from TCE and DCB respectively showed secondary growth on top of the MWCNTs. Raman spectroscopy showed that the materials contained defects, due to the creation of new sp^3 C–Cl bonds. CNTs that had secondary growth were highly disordered. Alkanes gave cleaner CNMs with higher yields than those formed from the aromatic reactants.

Growth of secondary carbon nanostructures on the surface of the primary CNTs was investigated by varying the reaction time and temperature using DCB as a chlorine source. DCB was chosen since from our previous study, it produced an appreciable quantity of CNTs with secondary growth. The graphitic nature, structure, yield of the CNTs and the formation of secondary CNFs on the surface of the main CNTs were affected by the growth time and temperature. Longer synthesis times resulted in formation of highly graphitic CNTs of high purity with no secondary CNF growth and with less defects. The largest number of secondary CNFs were observed at a 90 min reaction time at 700 °C. The average diameters of the CNTs increased with an increase in temperature due to catalyst sintering. Small catalyst particles were formed at lower temperatures

and large catalyst particles were formed at higher temperatures. The presence of secondary CNFs induced defects and disorders in the materials produced as evidenced by the Raman spectral analysis. Growth of the CNTs was greatly reduced at high temperatures. Poisoning of the CNT surface by iron carbides was observed with an increase in reaction temperature due to increased formation of chlorine in the reactor.

Synthesis of chlorine-functionalized nitrogen-doped MWCNTs by injection CVD over a Fe-Co/$CaCO_3$ was successful. DCB was found to be an excellent chlorine source that led to formation of large amounts of CNTs. Chlorine influenced the morphology, length, yield and outer diameter of the N-doped MWCNTs. A limited quantity of rod-shaped MWCNTs were obtained when CH_3CN was used alone as a feed. Horn-, straw- and pencil-shaped N-MWCNTs and CNFs were obtained by varying the amount of DCB in the feed. TGA, Raman and XPS analysis showed that an increase in the amount of DCB in the feed to 66.7 vol.% resulted in formation of CNTs with large defects, due to an increase in the concentration of nitrogen incorporated into the CNT walls. TGA and XPS analysis also confirmed the presence of chloride ions on the surface of the CNTs bound to metal ions. Covalent functionalization of carbon with chlorine was also confirmed by Raman and XPS analysis. Addition of chlorine favored formation of graphitic nitrogen atoms, but the amount of chlorine in the feed has to be controlled. Highly graphitic carbon materials were produced at low (33.3 vol.%) and high (80 vol.%) DCB concentrations. TTCE was found to be a poor chlorine source to make N-doped MWCNTs, and resulted in the production of very little product. The carbon materials produced mostly contained lumps of carbon platelets.

Synthesis of chlorine-functionalized N-doped MWCNTs by a bubbling CVD method was also successful. DCB and TTCE were used as chlorine sources and acetonitrile as a nitrogen source. The morphology of the CNMs depended on the amount of chlorine in the feed. Bamboo-compartmented CNTs and CNTs with intratubular junctions were obtained from solutions containing at a low concentration of DCB (33.3 vol.%). Hollow and bamboo-compartmented CNTs were obtained from solutions containing a high concentration of DCB (66.7 vol.%). A large increase in the amount of nitrogen atoms doped into the CNTs was achieved at low DCB concentration, evidenced by a decrease in the outer diameters of the N-MWCNTs with an increase in DCB concentration. Highly graphitic materials were produced after post-doping of N-

MWCNTs with chlorine and of the chlorinated MWCNTs with nitrogen. Highly graphitic materials were produced at a low concentration of DCB (33.3 vol.%) as evidenced by TGA, Raman and XPS analysis. Thermally stable CNTs with a smaller value of the I_D/I_G peak ratio, which had graphitic N species dominant in the N1s XPS spectra were observed at a low concentration of DCB. Carbon nano-onions were formed when TTCE was used as a source of chlorine. The formation of carbon nano-onions increased at low TTCE concentrations, which was attributed to greater incorporation of nitrogen into the CNMs. Increase in the TTCE concentration resulted in mixtures of carbon nano-onions and bamboo-compartmented carbon nano-bells. NCNMs generated from heated solutions of CH_3CN and TTCE resulted in formation of mixtures of CNMs, especially at high concentrations of TTCE. Selectivity was achieved at low concentrations (33.3 and 25 vol.%) of TTCE. CNTs were produced when DCB was used as a source of chlorine while mixtures of CNMs were produced when TTCE was used. Aromatic chlorinated organic compounds rather than aliphatic chlorinated organic compounds are better suited for use in studies in which the effect of chlorine on the morphology of CNMs is studied.

An MWCNT/PVP composite membrane was successfully synthesized. XRD and FTIR studies showed that the MWCNTs were embedded inside the PVP matrix. The MWCNT/PVP composite membrane is capable of adsorbing oil from land or oil-water mixtures. High adsorption capacities of 15 – 20 g/g were achieved. The adsorption capability of the composite membrane depended on the viscosity of the solvents or oils.

The dependence of the adsorption capability of the MWCNT/PVP composite membrane synthesized in this study on the viscosity of the solvents, limits its use for the adsorption of various solvents and oils. This is mainly attributed to the ability of PVP to dissolve in low viscosity solvents like water.

PVP is indeed a pore former and easily biodegradable, and this warrants its use in these types of applications. It is therefore recommended that PVP must be cross-linked with other chemicals like glutaraldehyde, maleic acid, etc., together with MWCNTs in order to make them water resistant.

Chlorine functionalized CNTs that contains secondary CNFs on their surface can be used as nanoscale templates in various applications, since in this applications materials that form high

density network structures with chemically connected CNTs are required. Chlorinated NCNTs can be applied in electronics to enhance their field emission properties as they are open-ended. The chlorinated NCNTs can also be applied in water treatment as magnets to attract metal pollutants, by first filling them with magnetic metal nanoparticles to render them magnetic.

Appendix A: Supplementary Materials

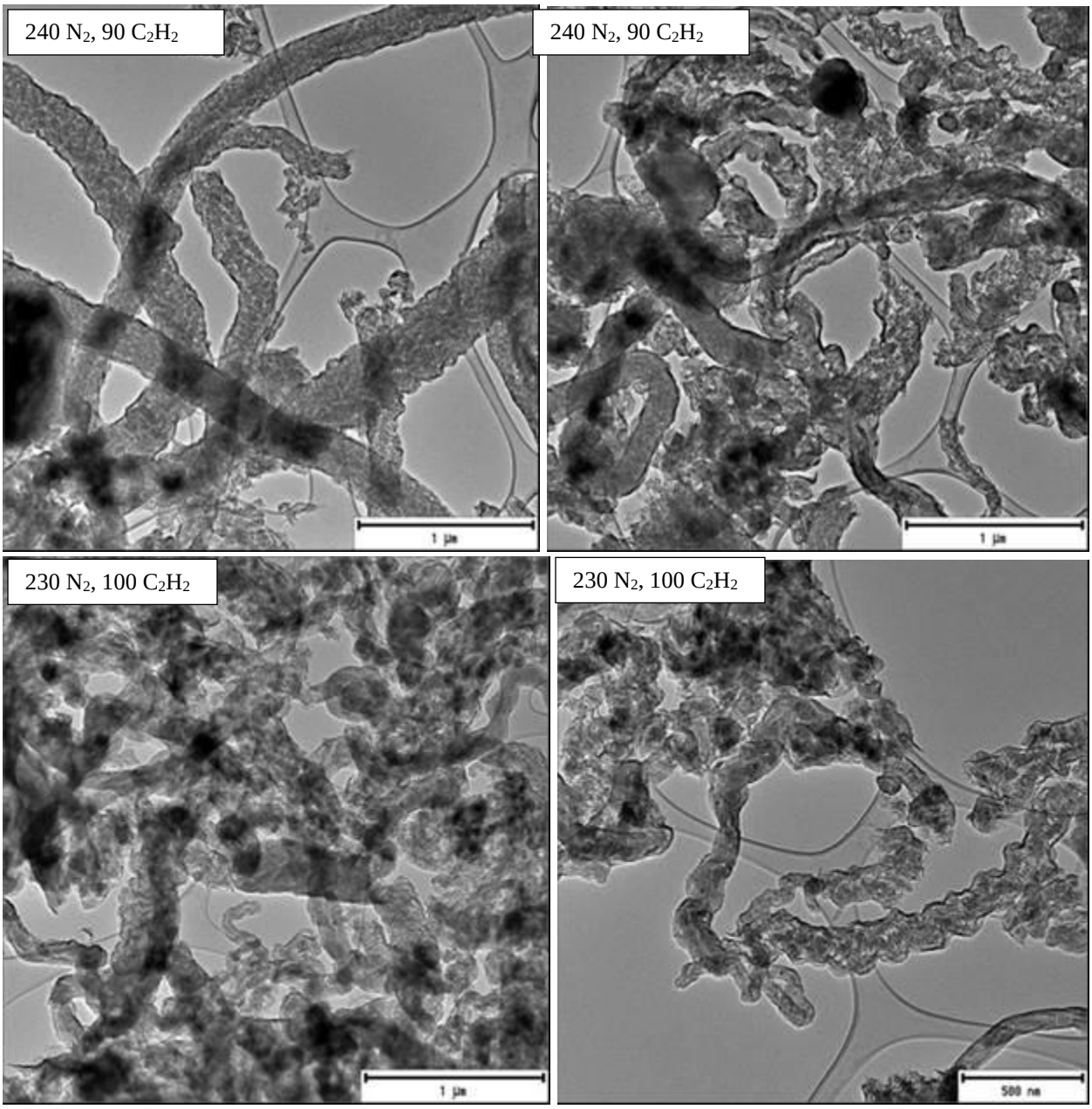

Figure S1 TEM images of CNMs generated from dichloroethane as a chlorine source, varying the flow rate of nitrogen and acetylene.

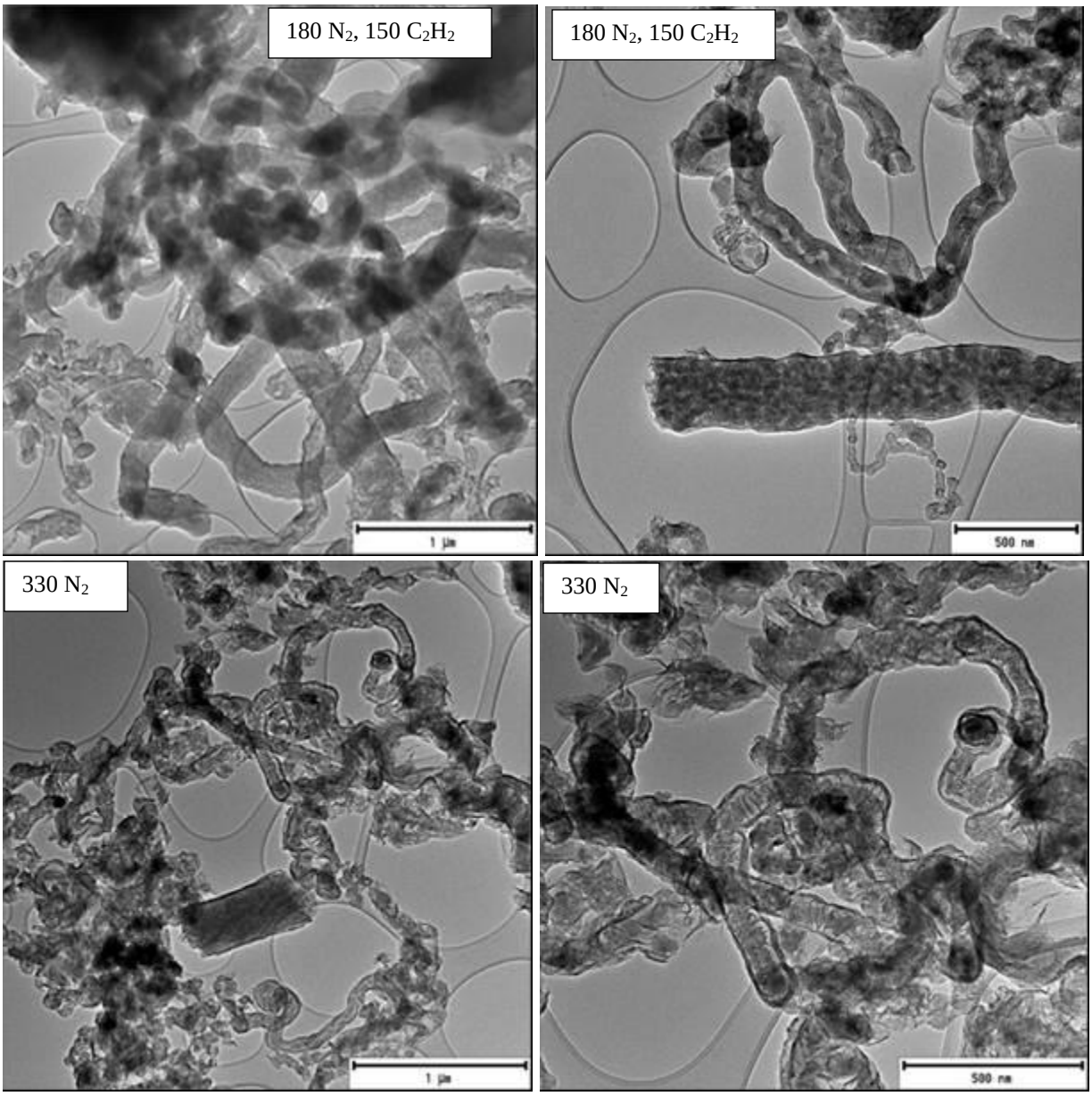

Figure S2 TEM images of CNMs generated from dichloroethane as a chlorine source, varying the flow rate of nitrogen and acetylene.

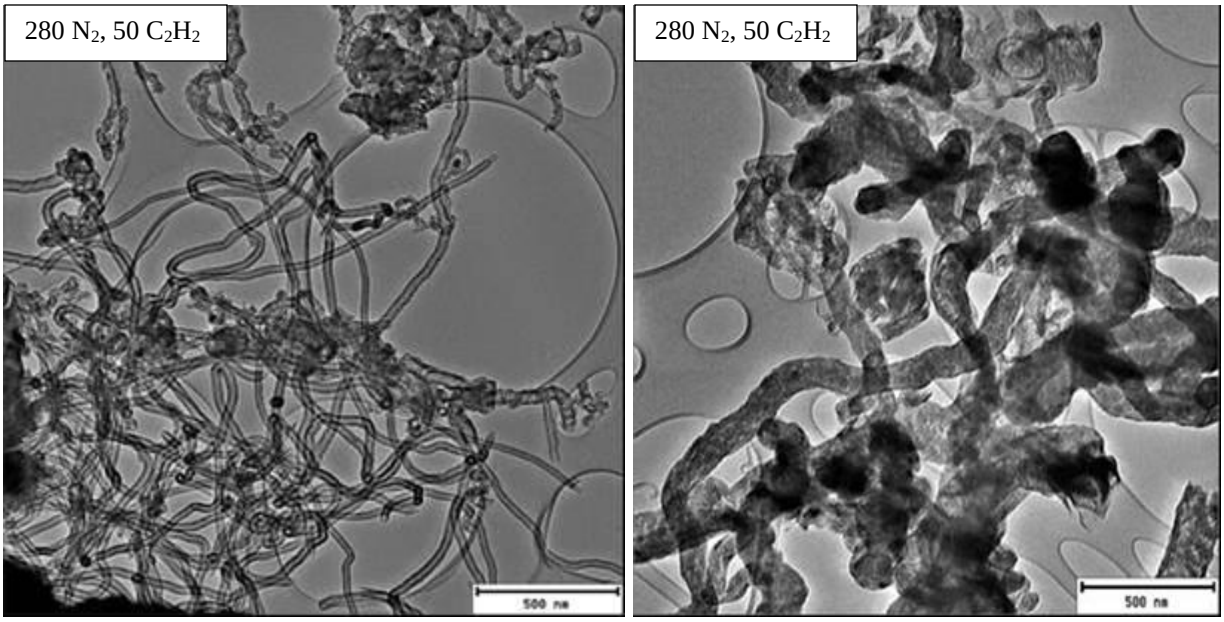

Figure S3 TEM images of CNMs generated from dichloroethane as a chlorine source, varying the flow rate of nitrogen and acetylene.

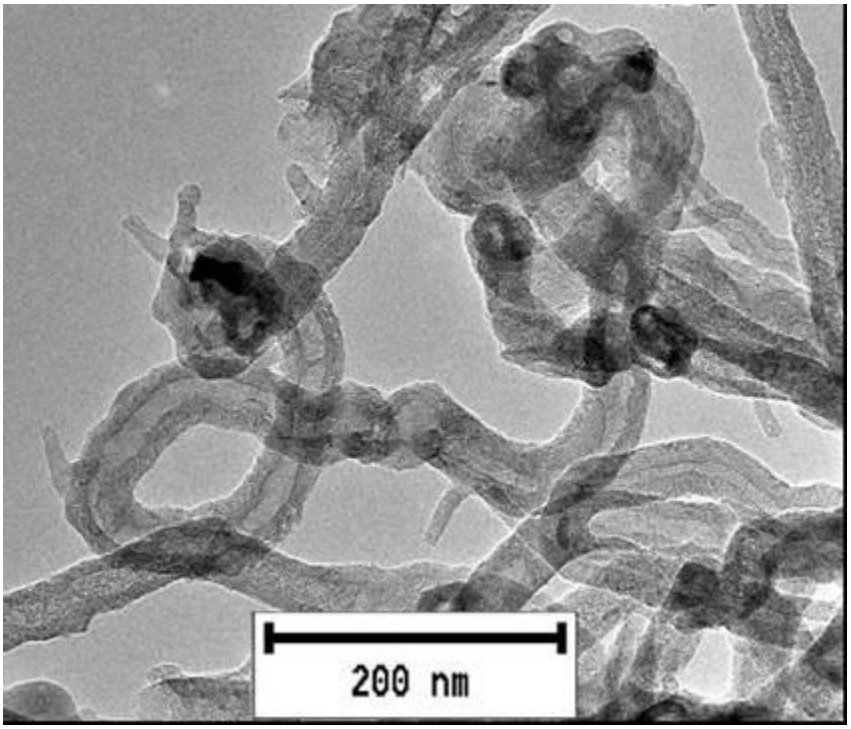

Figure S4 Secondary growth on TEM images of MWCNTs generated using dichlorobenzene (DCB) as chlorine source.

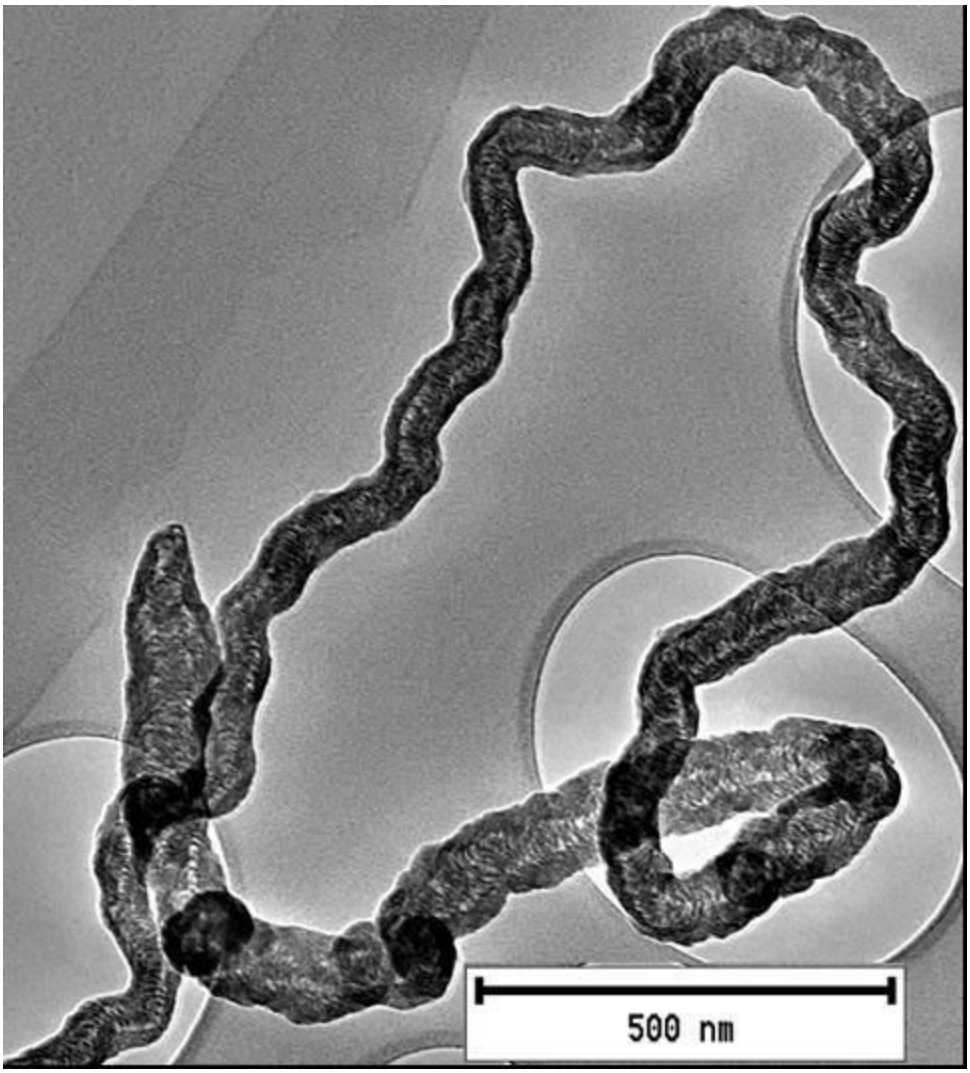

Figure S5 TEM images of segmented CNF generated using dichloroethane (DCE) as chlorine source.

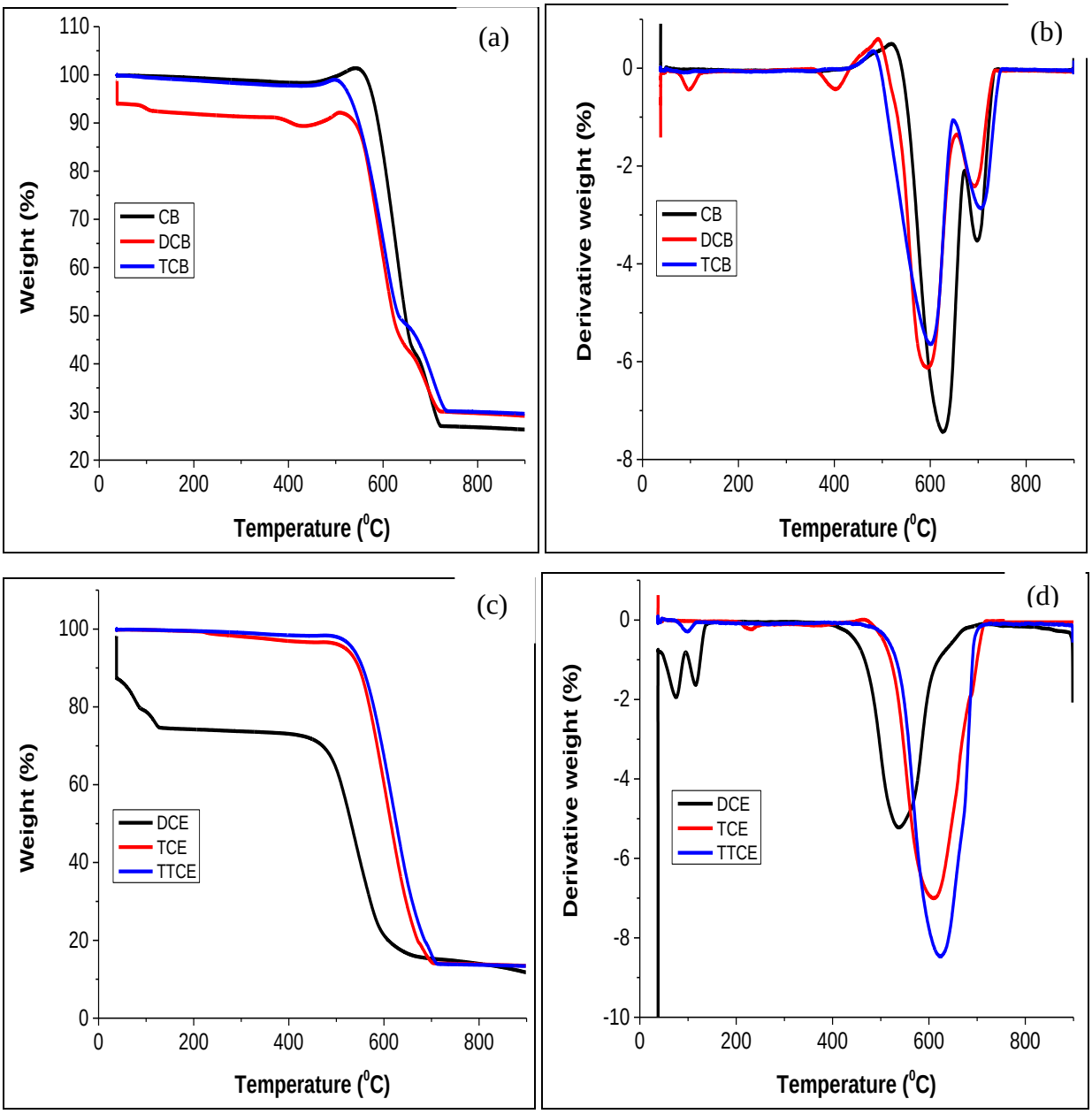

Figure S6 TGA and corresponding derivative profiles of the un-purified MWCNT samples produced using chlorinated benzenes (a and b) and ethanes (c and d) as chlorine sources.

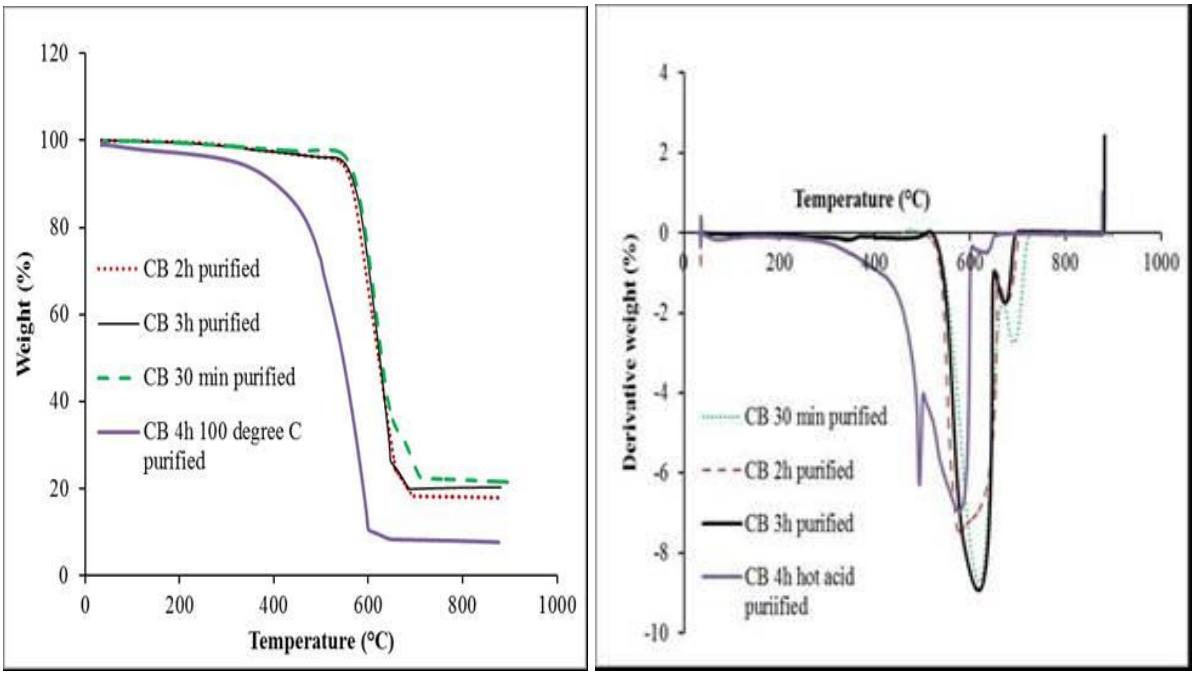

Figure S7 TGA and corresponding derivative profiles of the purified MWCNT samples produced using chlorobenzene (CB) at different acid treatment times.

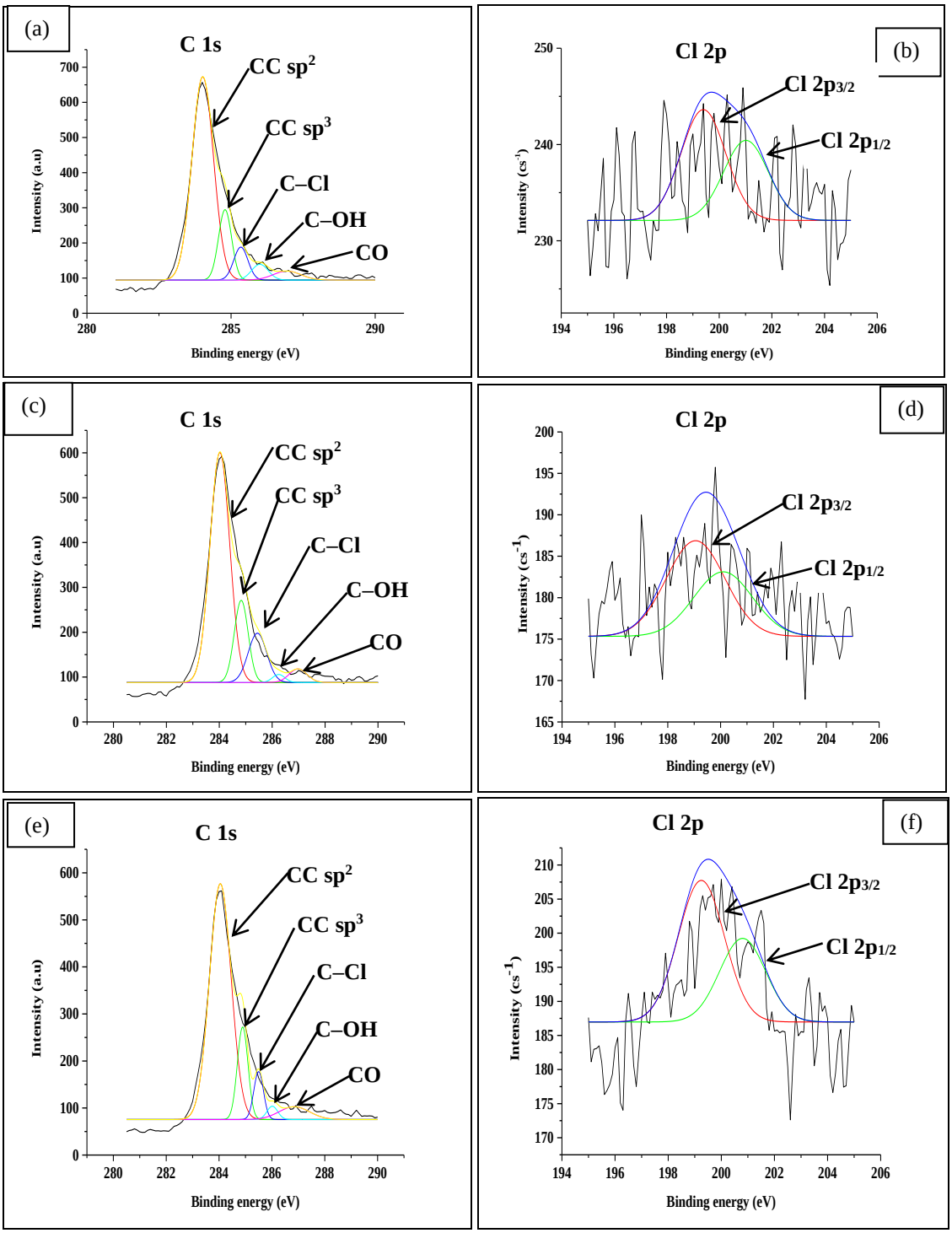

Figure S8 Deconvoluted C 1s and Cl 2p XPS spectra of the purified MWCNT samples produced using chlorobenzene (a and b), dichlorobenzene (c and d) and trichlorobenzene (e and f).

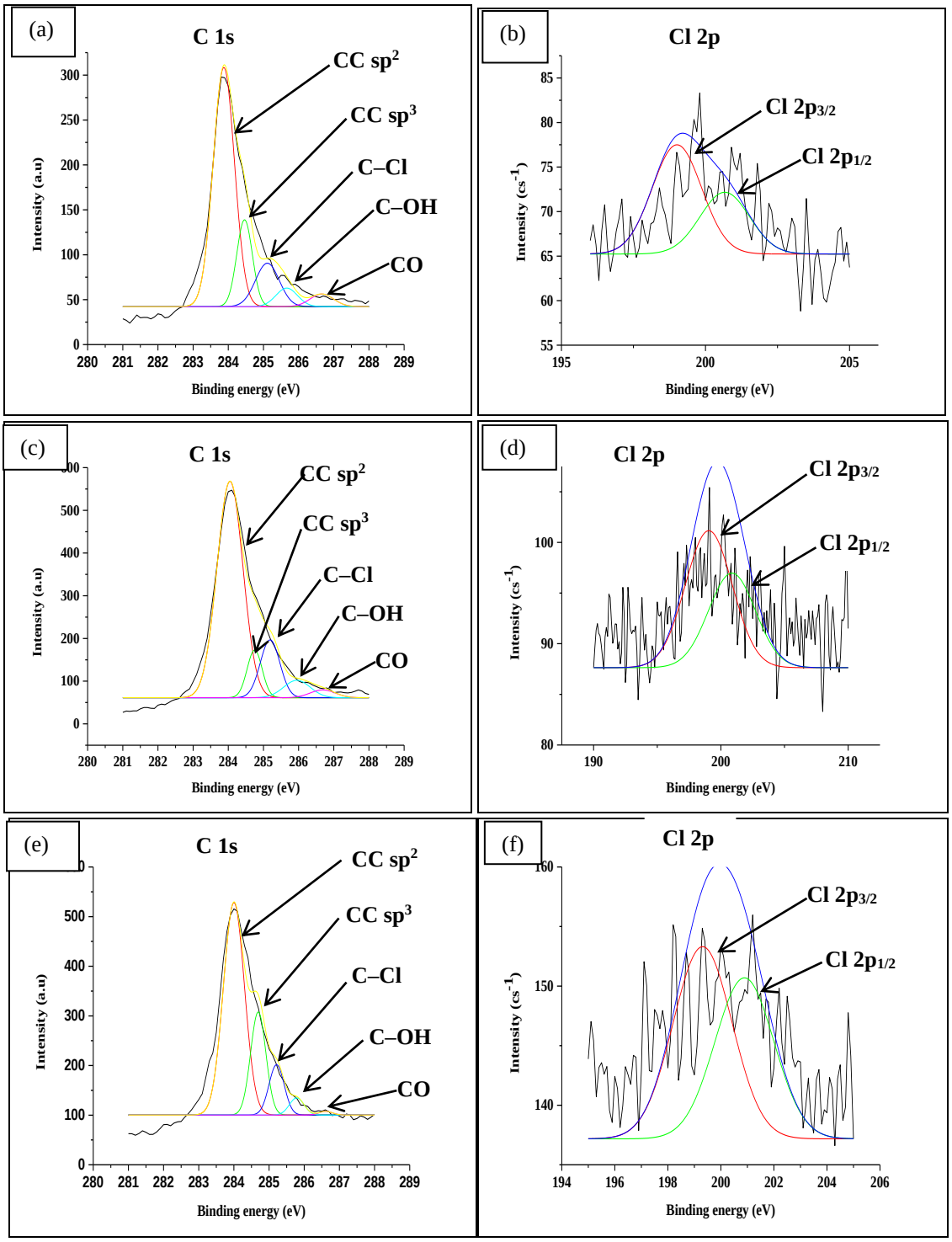

Figure S9 Deconvoluted C 1s and Cl 2p XPS spectra of the purified MWCNT samples produced using dichloroethane (a and b), trichloroethane (c and d) and tetrachloroethane (e and f).

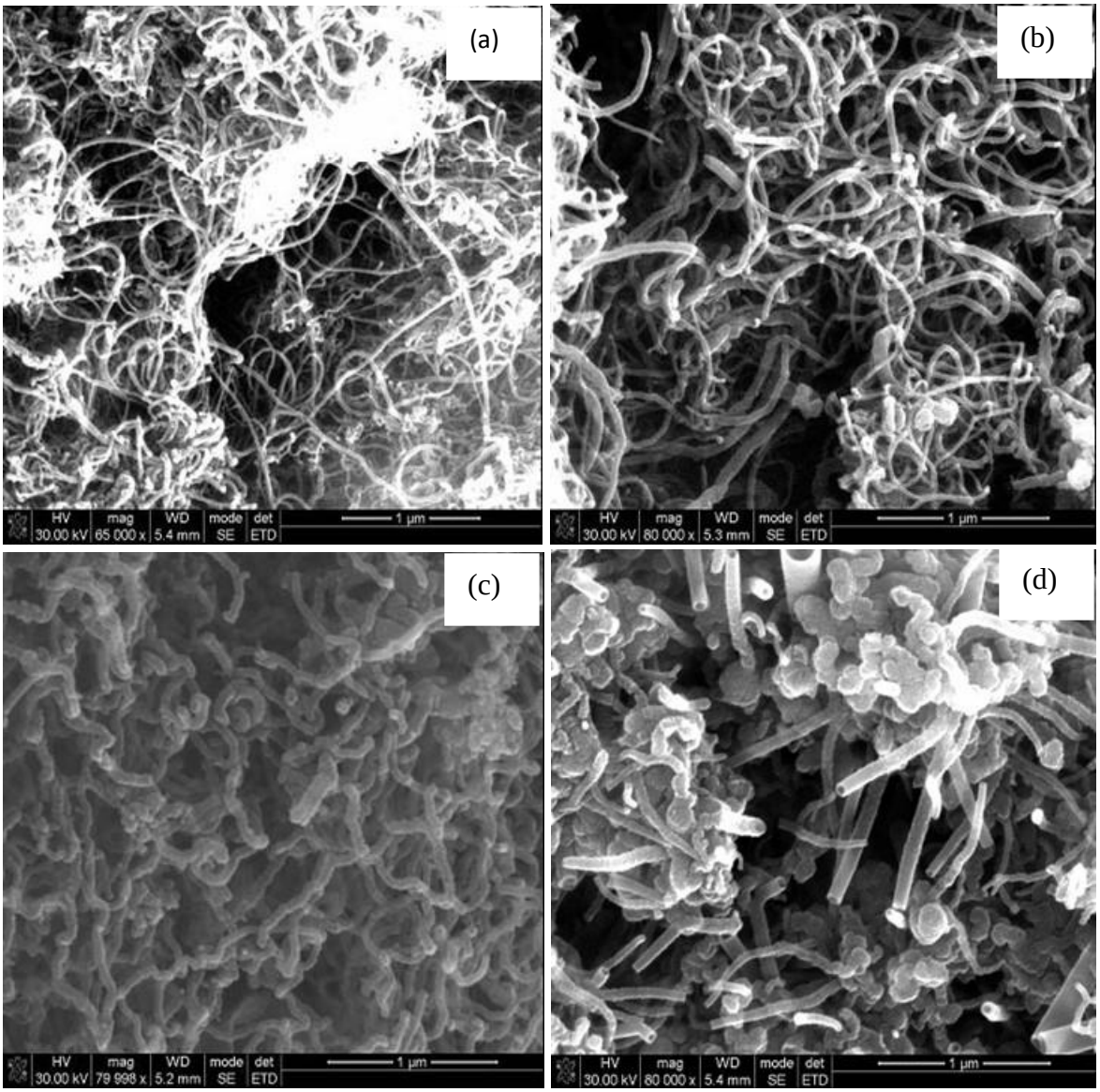

Figure S10 SEM images of purified CNTs generated using DCB at a 90 s reaction time and reaction temperatures of (a) 600 °C, (b) 650 °C, (c) 700 °C and (d) 750 °C.

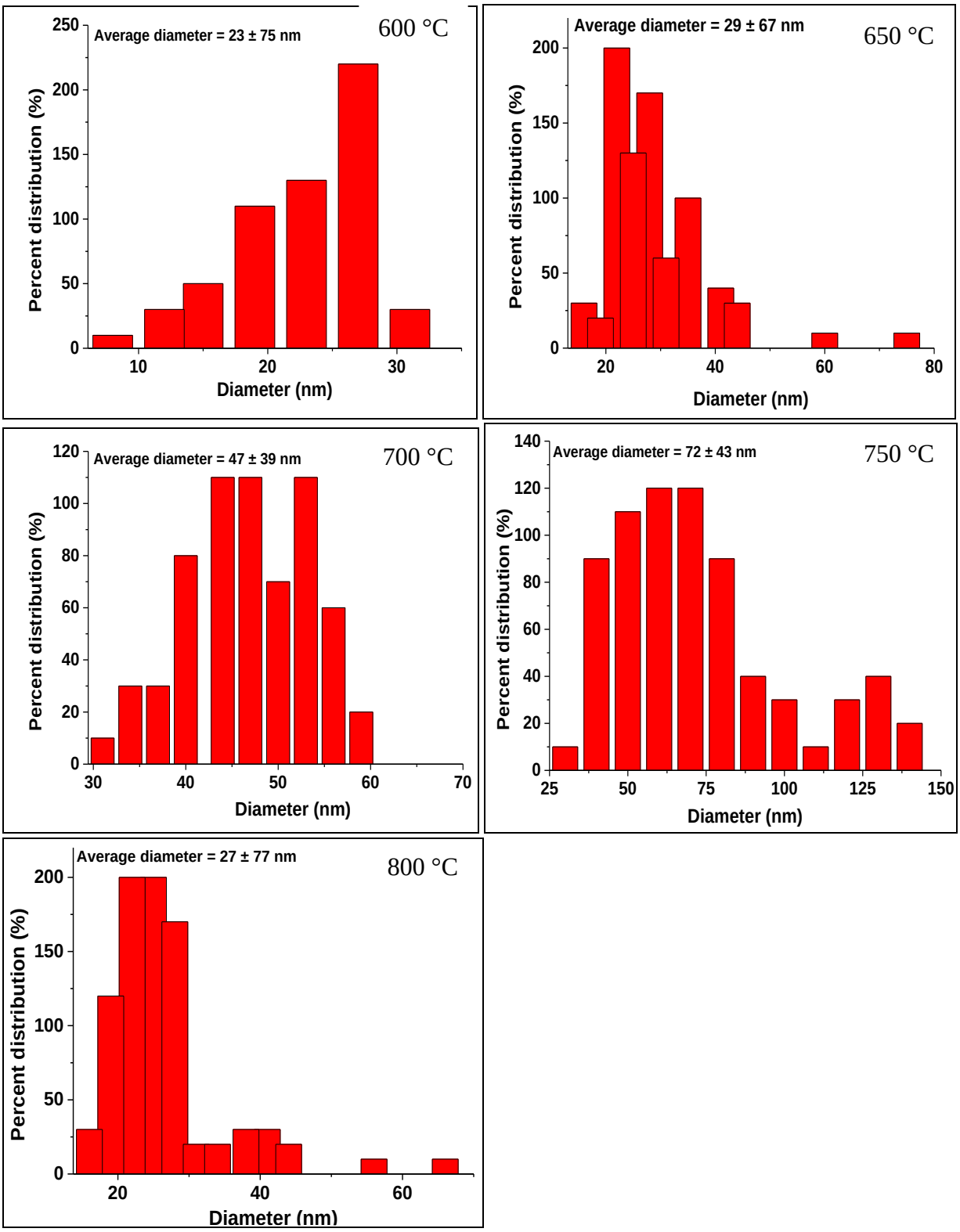

Figure S11 Diameter distribution curves of purified CNTs generated from DCB at various synthesis temperatures for 90 min.

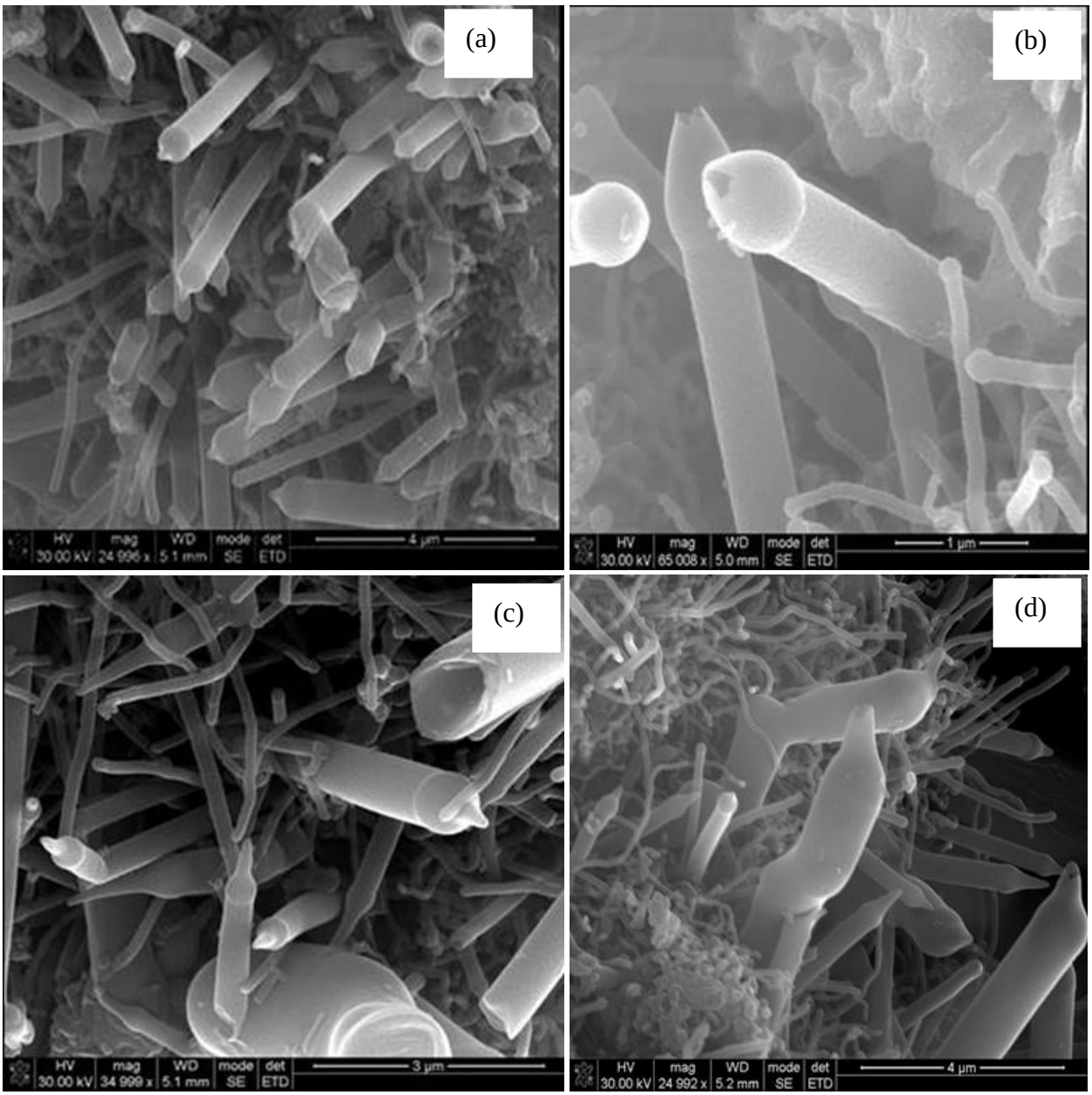

Figure S12 SEM images of purified CNTs generated from a 33:3:66.6 vol.% of CH_3CN:DCB synthesized by a CVD injection method at the following reaction conditions: 0.24 mL/min, 800 °C, 1 h, 240 mL/min N_2, and 90 mL/min C_2H_2.

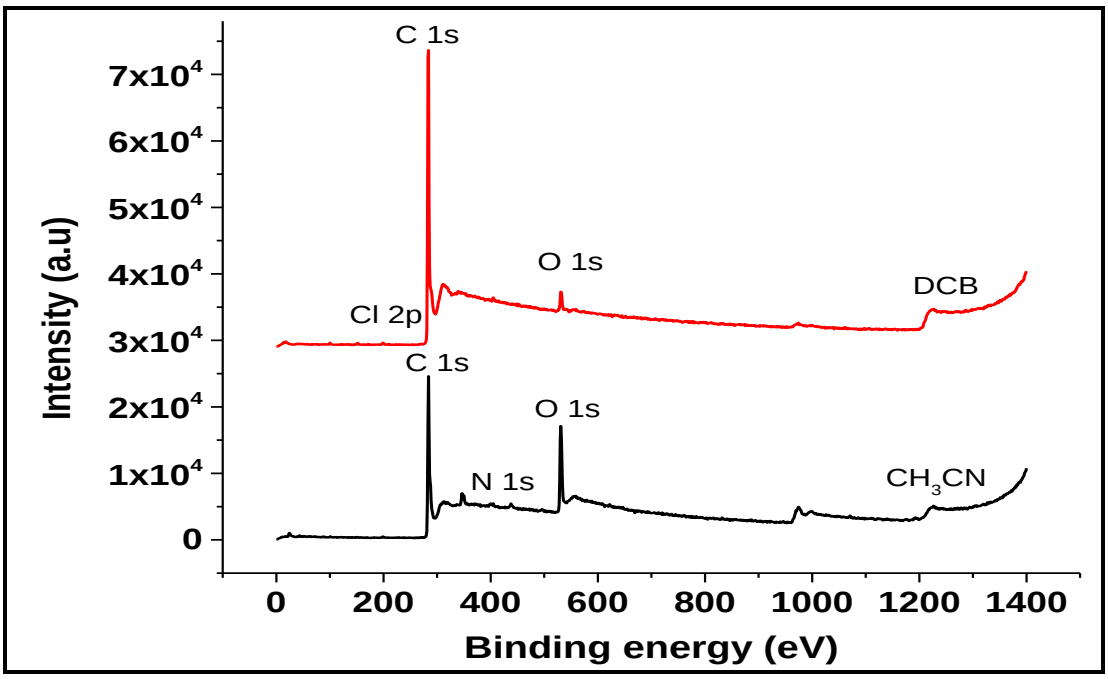

Figure S13 XPS spectra of purified chlorine functionalized and nitrogen doped CNTs generated from DCB and CH_3CN.

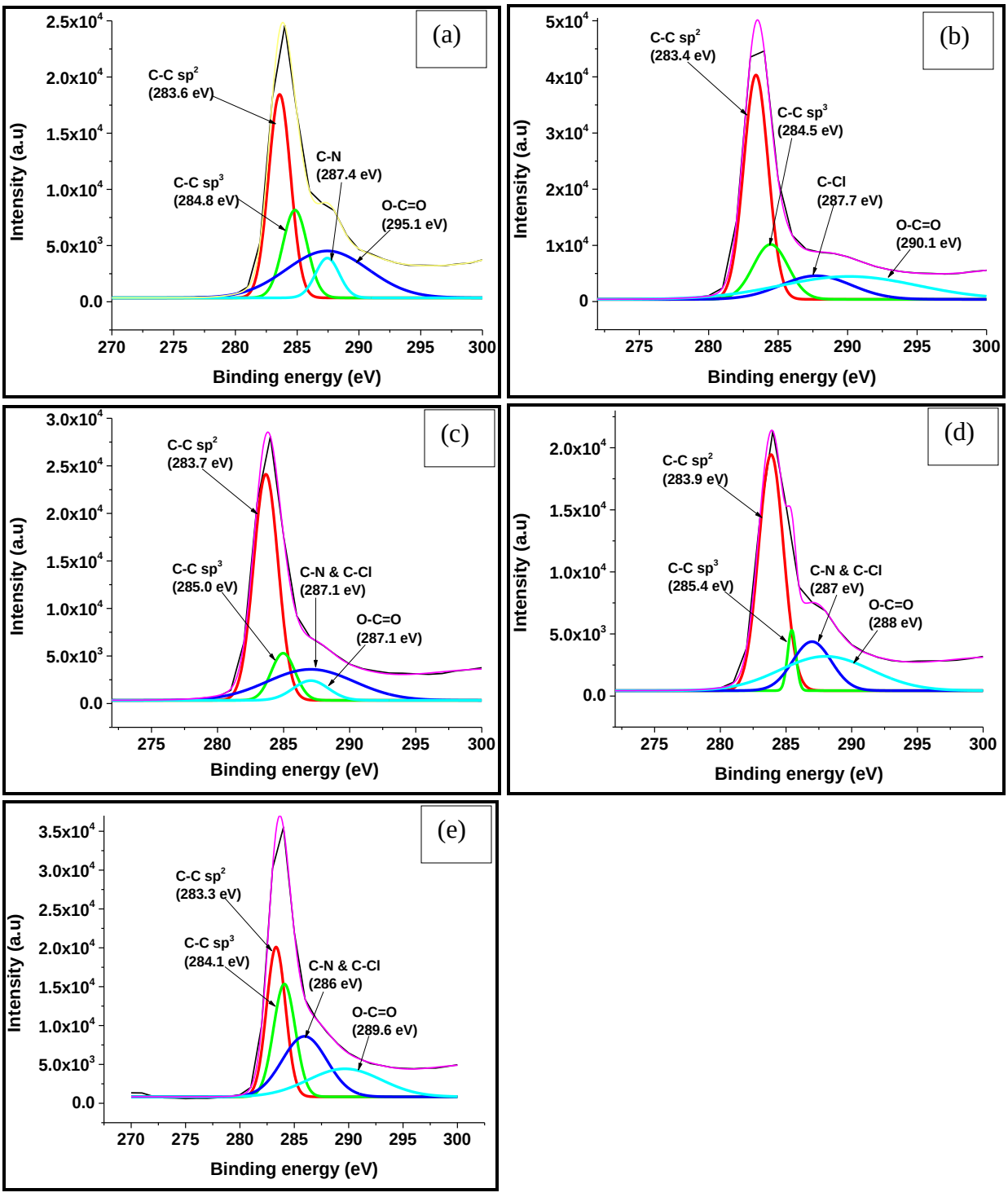

Figure S14 C 1s XPS spectra of purified CNTs generated from (a) pure CH_3CN, (b) pure DCB, and various volume ratios (c) 66.7:33.3 (d) 33.3:66.3 and (e) 20:80 vol.% of CH_3CN:DCB synthesized by CVD injection at 0.24 mL/min.

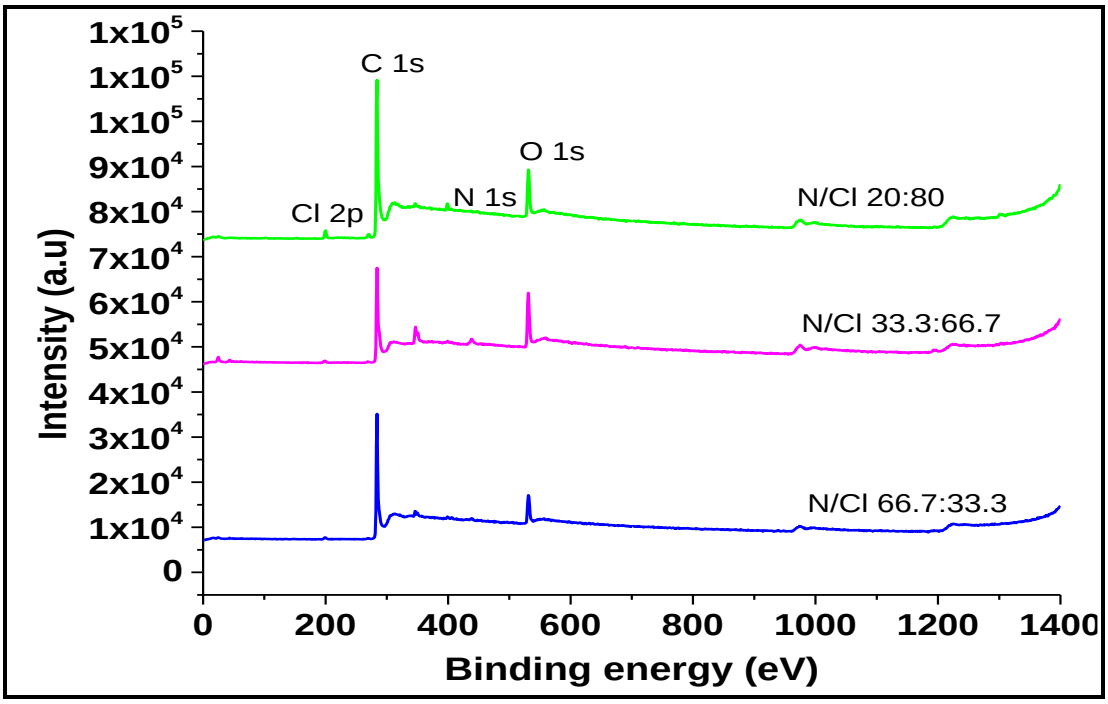

Figure S15 XPS spectra of purified chlorine functionalized nitrogen doped CNTs generated from CH_3CN:DCB solvent mixtures of various volume ratios.

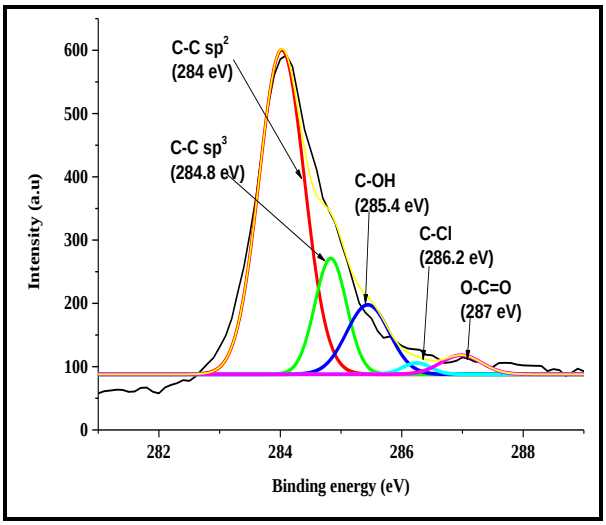

Figure S16 C 1s XPS spectra of chlorinated CNTs generated from DCB by bubbling CVD method.

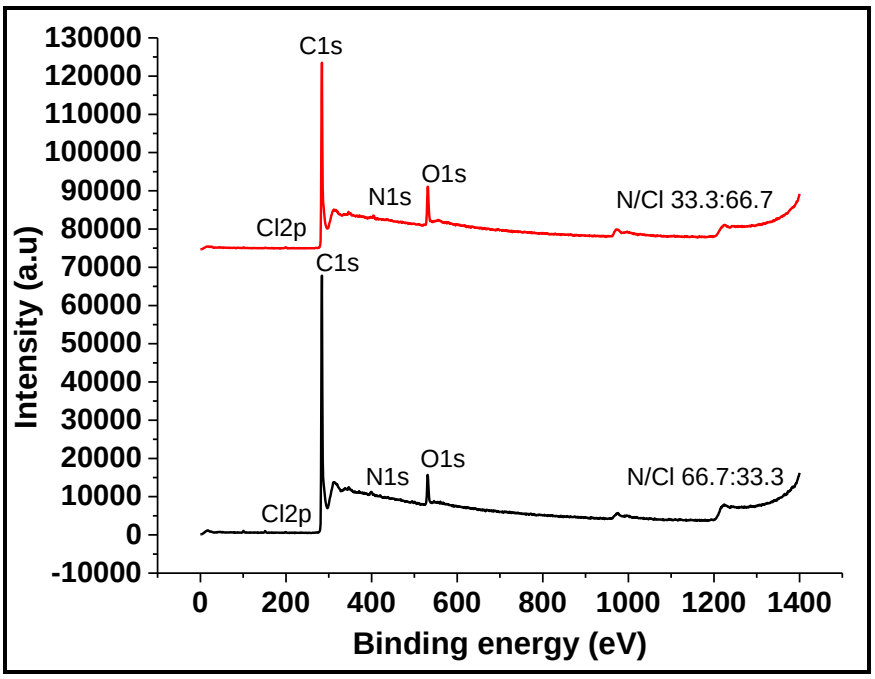

Figure S17 XPS spectra of chlorinated N-doped CNTs generated from various CH_3CN:DCB solvent mixture by bubbling CVD method.

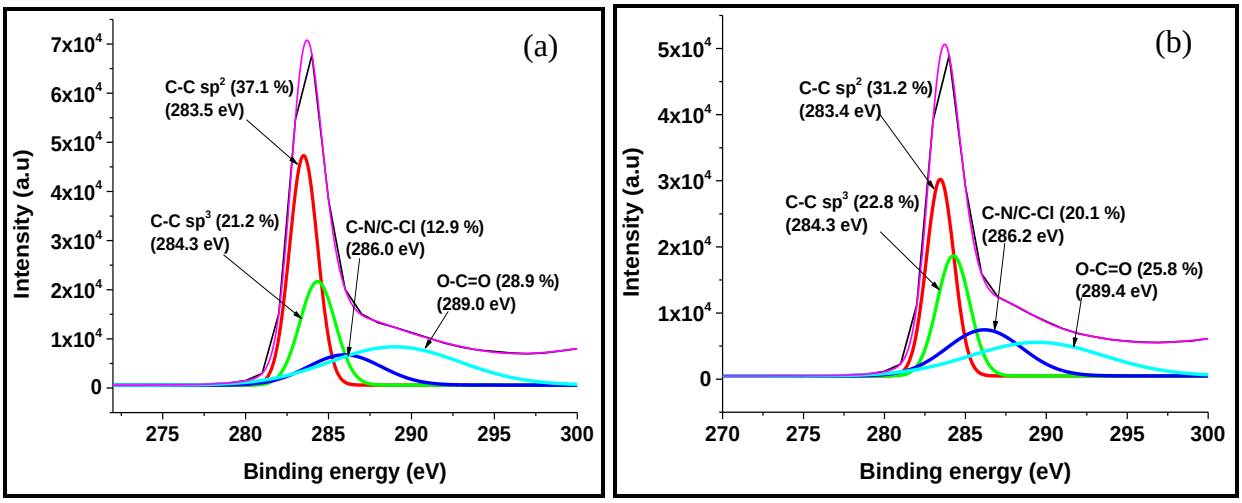

Figure S18 C 1s XPS spectra of chlorinated N-doped CNTs generated from (a) 66.7:33.3 and (b) 33.3:66.7 vol.% CH_3CN:DCB solvent mixture by bubbling CVD method.

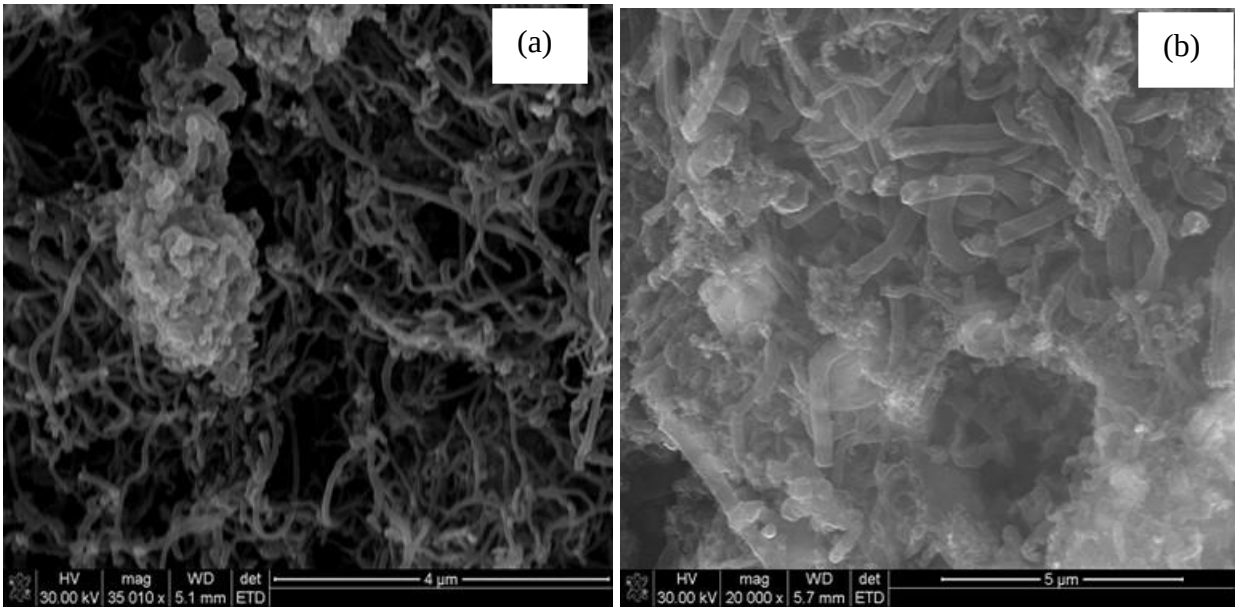

Figure S19 SEM images of CNMs generated from room temperature solutions of TTCE by a bubbling CVD method

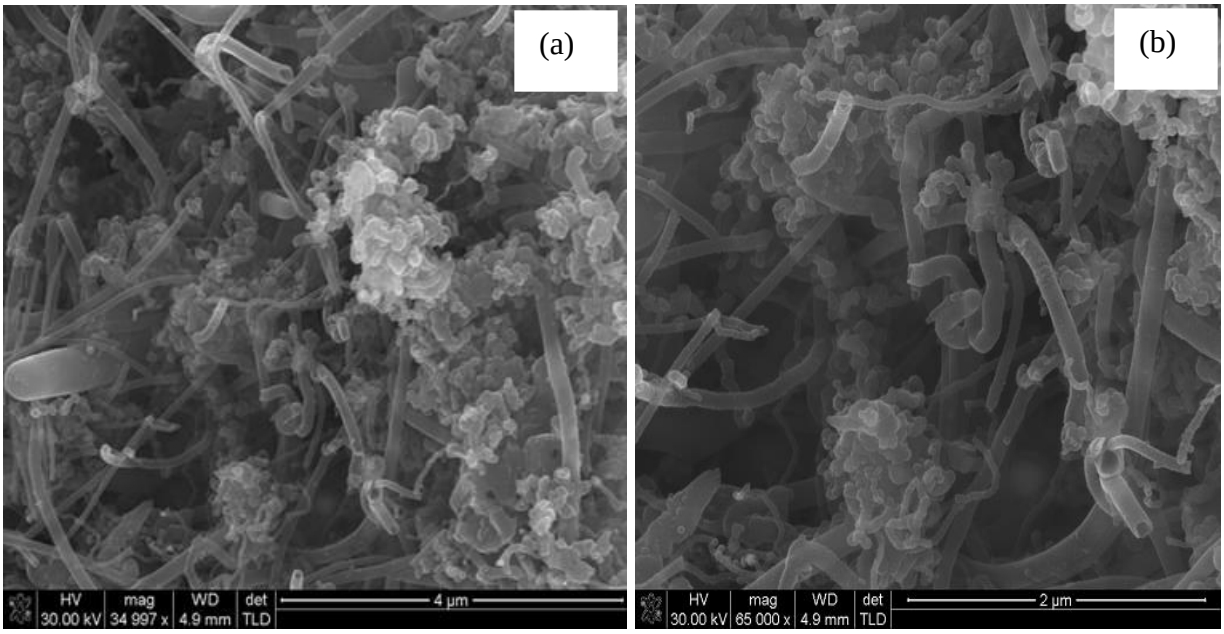

Figure S20 SEM images of CNMs generated from room temperature solution mixtures of CH_3CN:TTCE (75:25 vol.%) by a bubbling CVD method

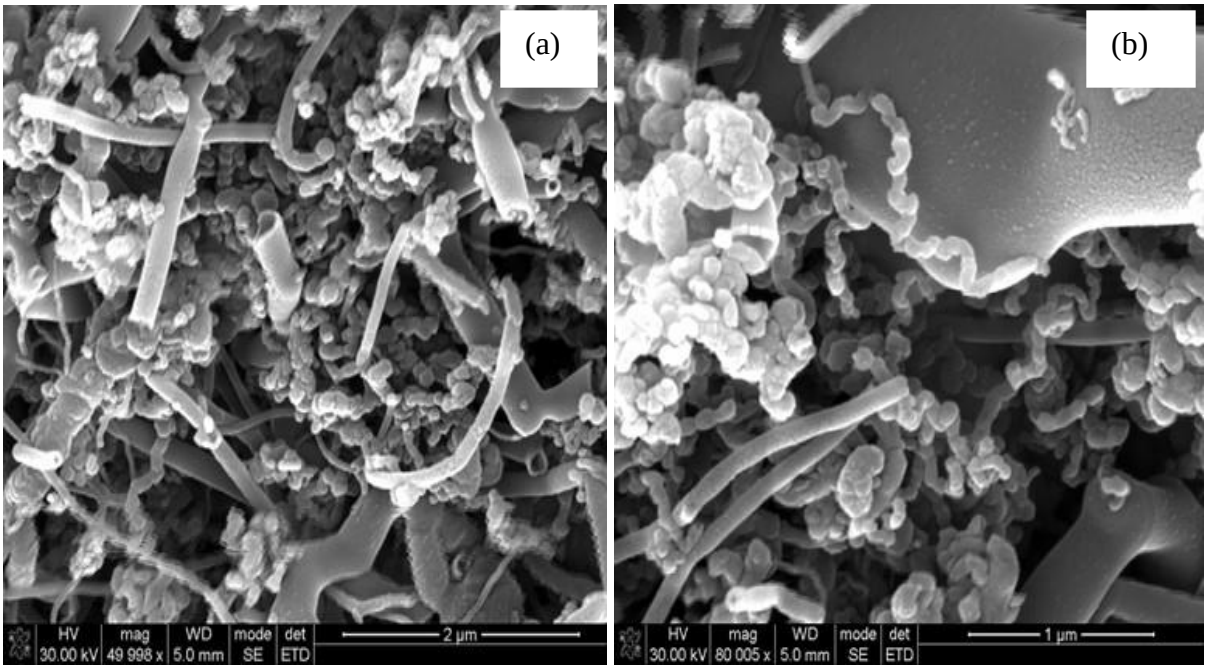

Figure S21 SEM images of CNMs generated from room temperature solution mixtures of CH_3CN:TTCE (66.7:33.3 vol.%) by a bubbling CVD method

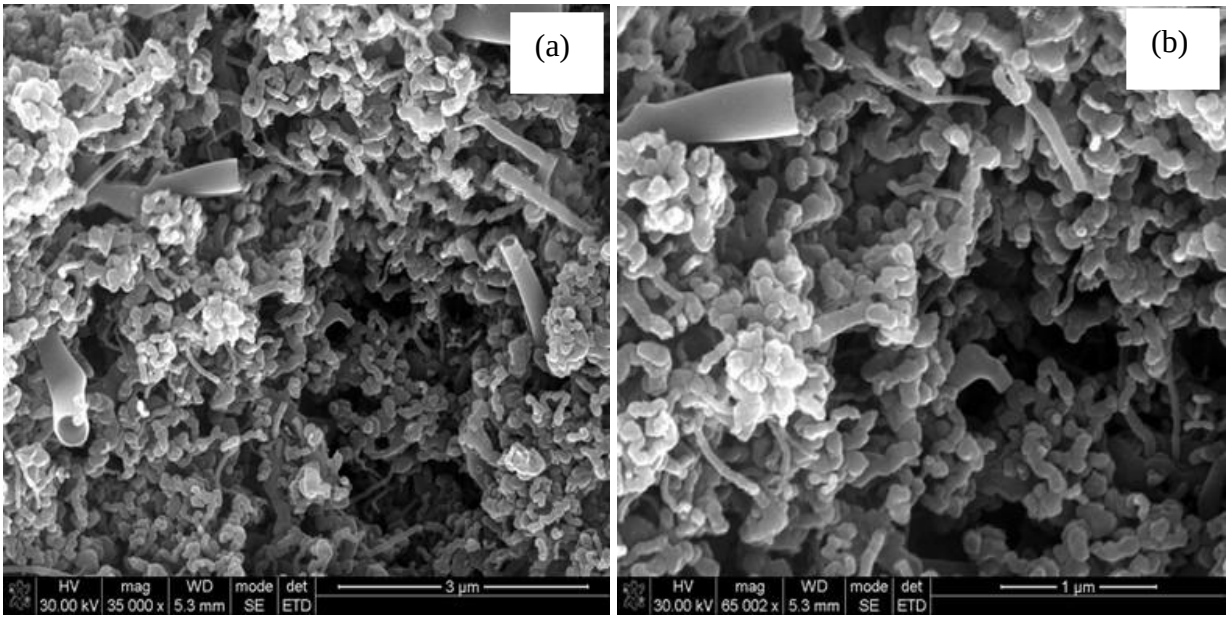

Figure S22 SEM images of CNMs generated from room temperature solution mixtures of CH_3CN:TTCE (66.7:33.3 vol.%) by a bubbling CVD method

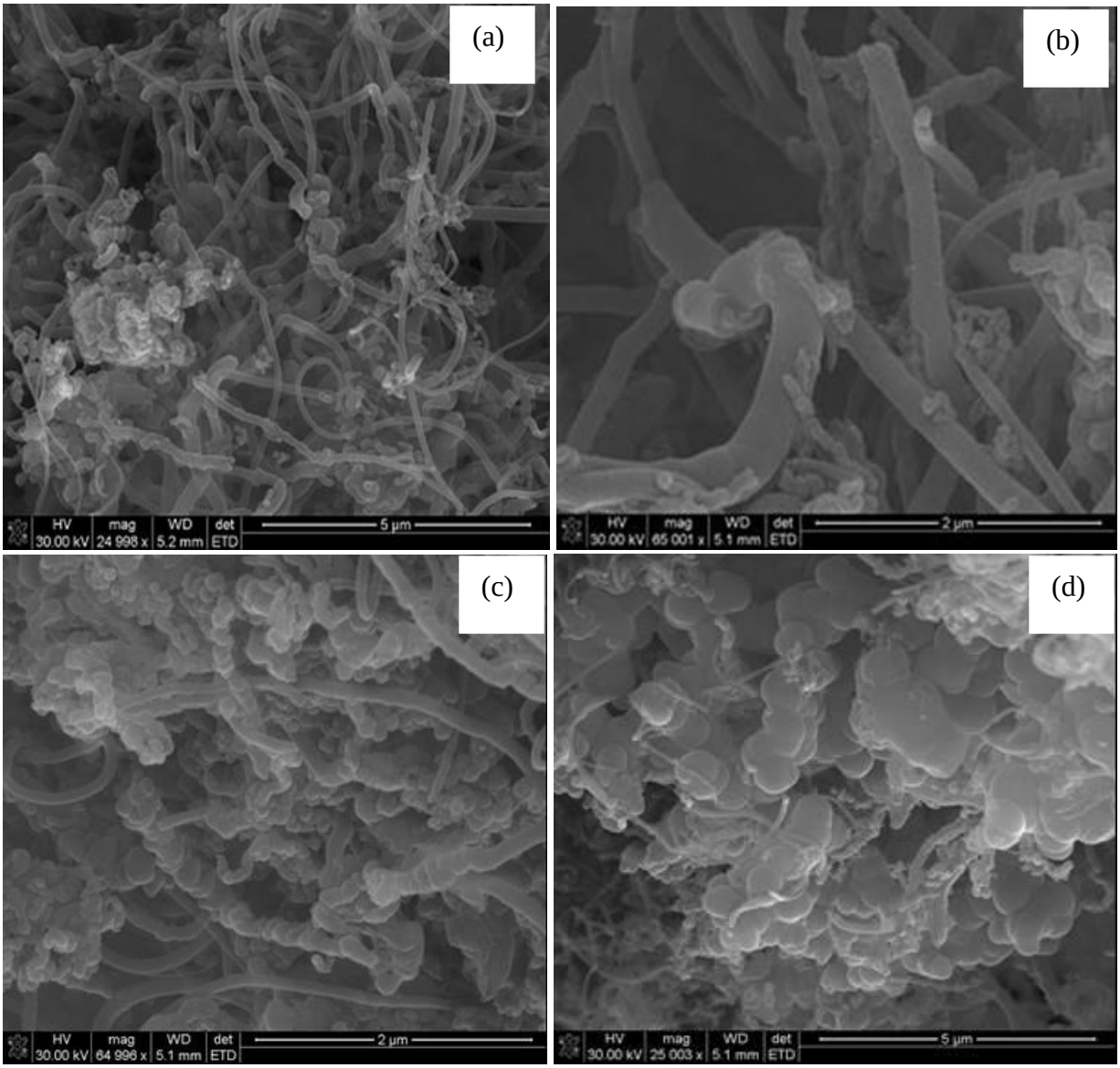

Figure S23 SEM images of N-doped CNMs generated from heated solutions of CH_3CN (90 °C). [N_2 = 240 mL/min, C_2H_2 = 90 mL/min, t = 1h and temperature = 800 °C).

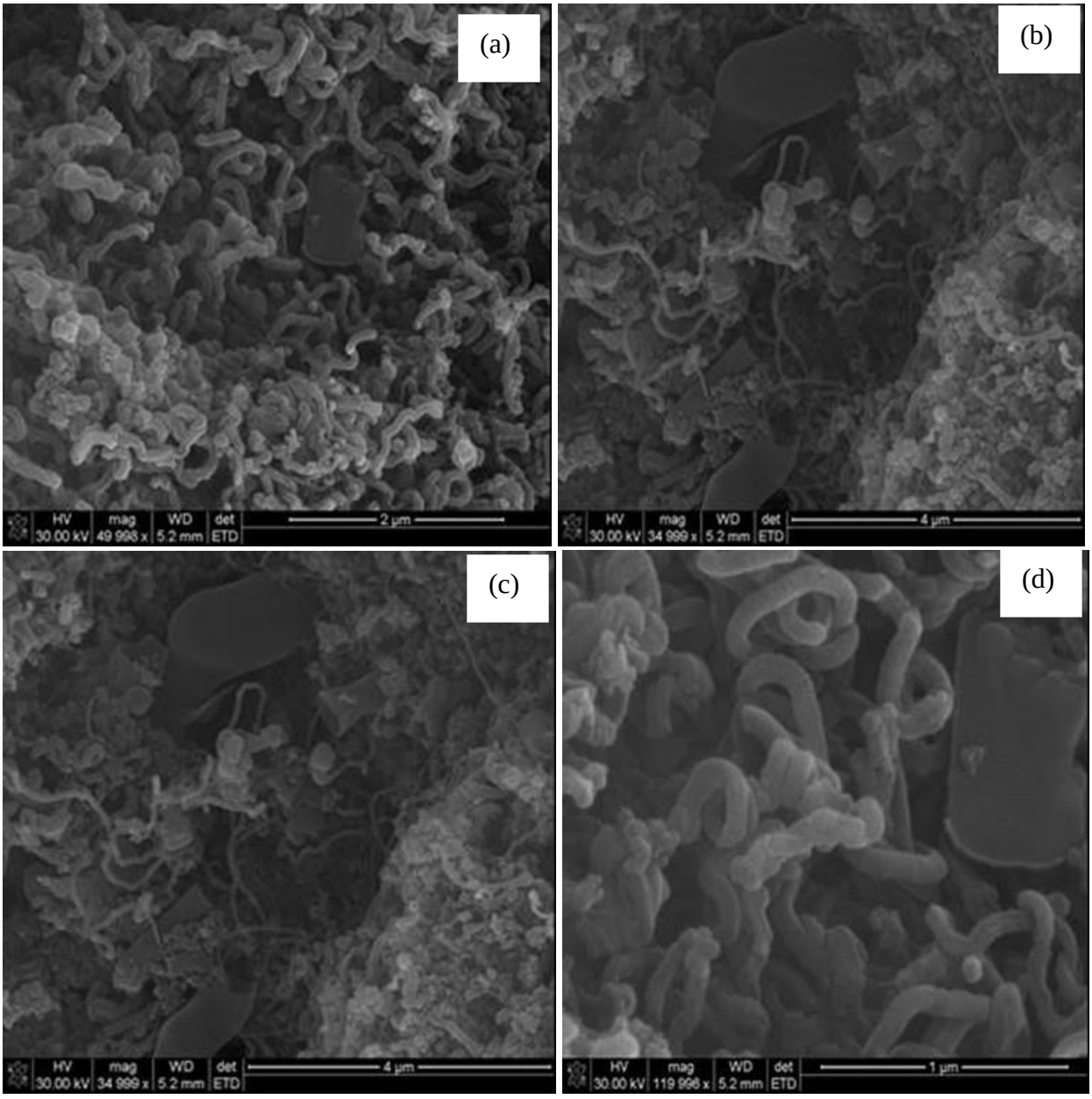

Figure S24 SEM images of chlorinated CNMs generated from heated solution of TTCE (100 °C). [N_2 = 240 mL/min, C_2H_2 = 90 mL/min, t = 1h and temperature = 800 °C)

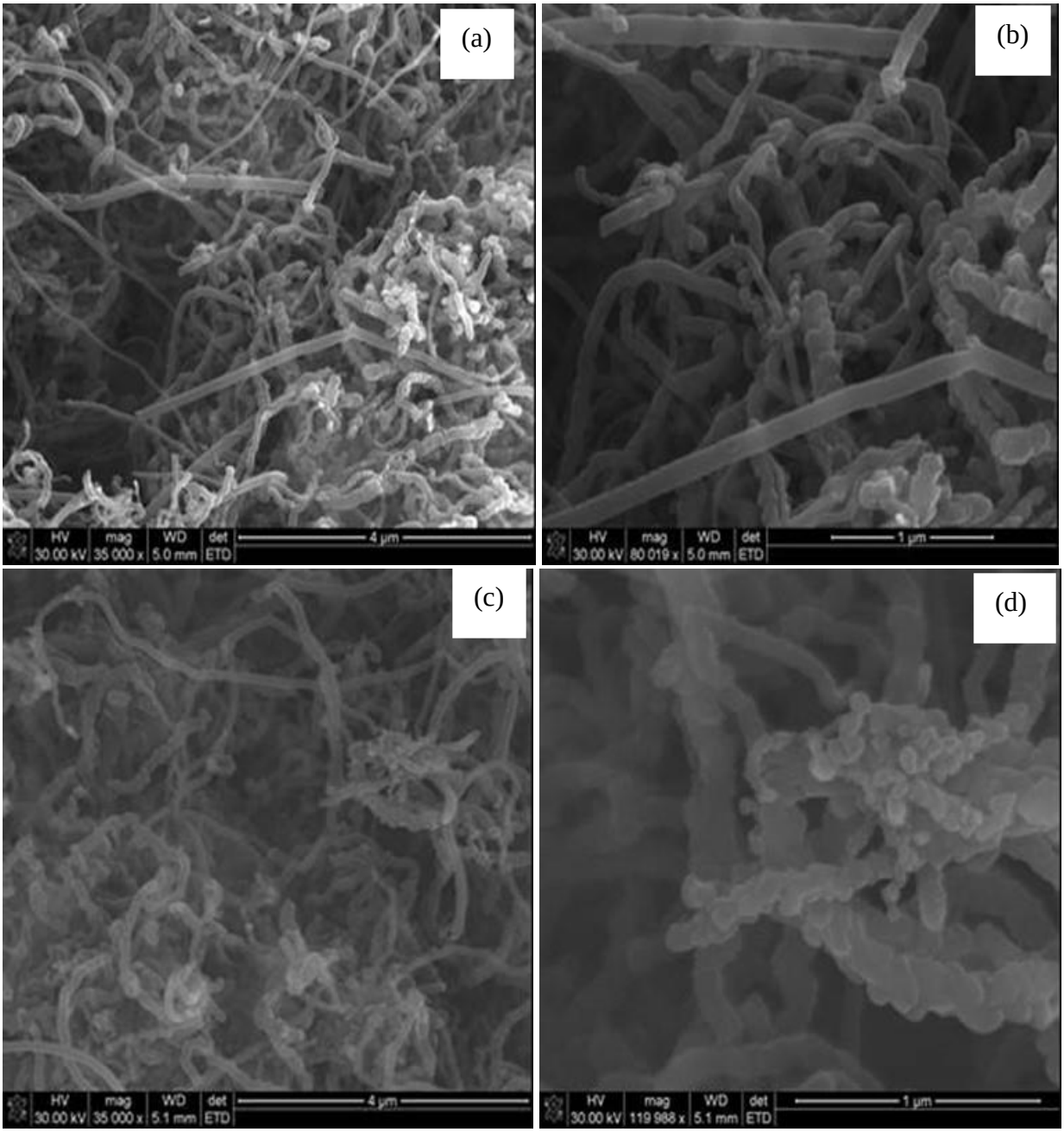

Figure S25 TEM images of purified CNMs generated from a 75:25 volume ratio of heated CH_3CN:TTCE (heated at 100 °C).

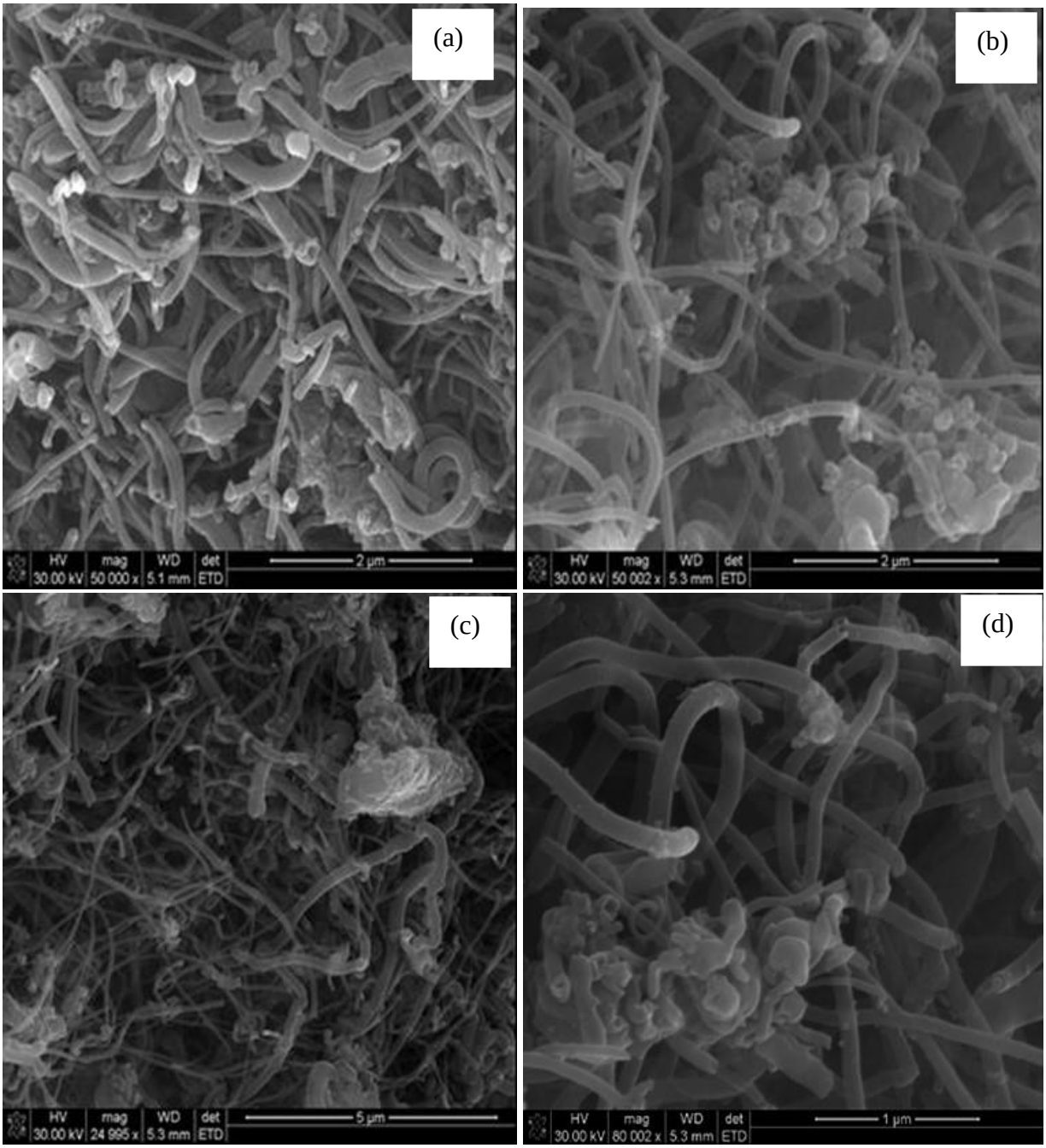

Figure S26 TEM images of purified CNMs generated from a 66.7:33.3 volume ratio of heated CH_3CN:TTCE (heated at 100 °C).

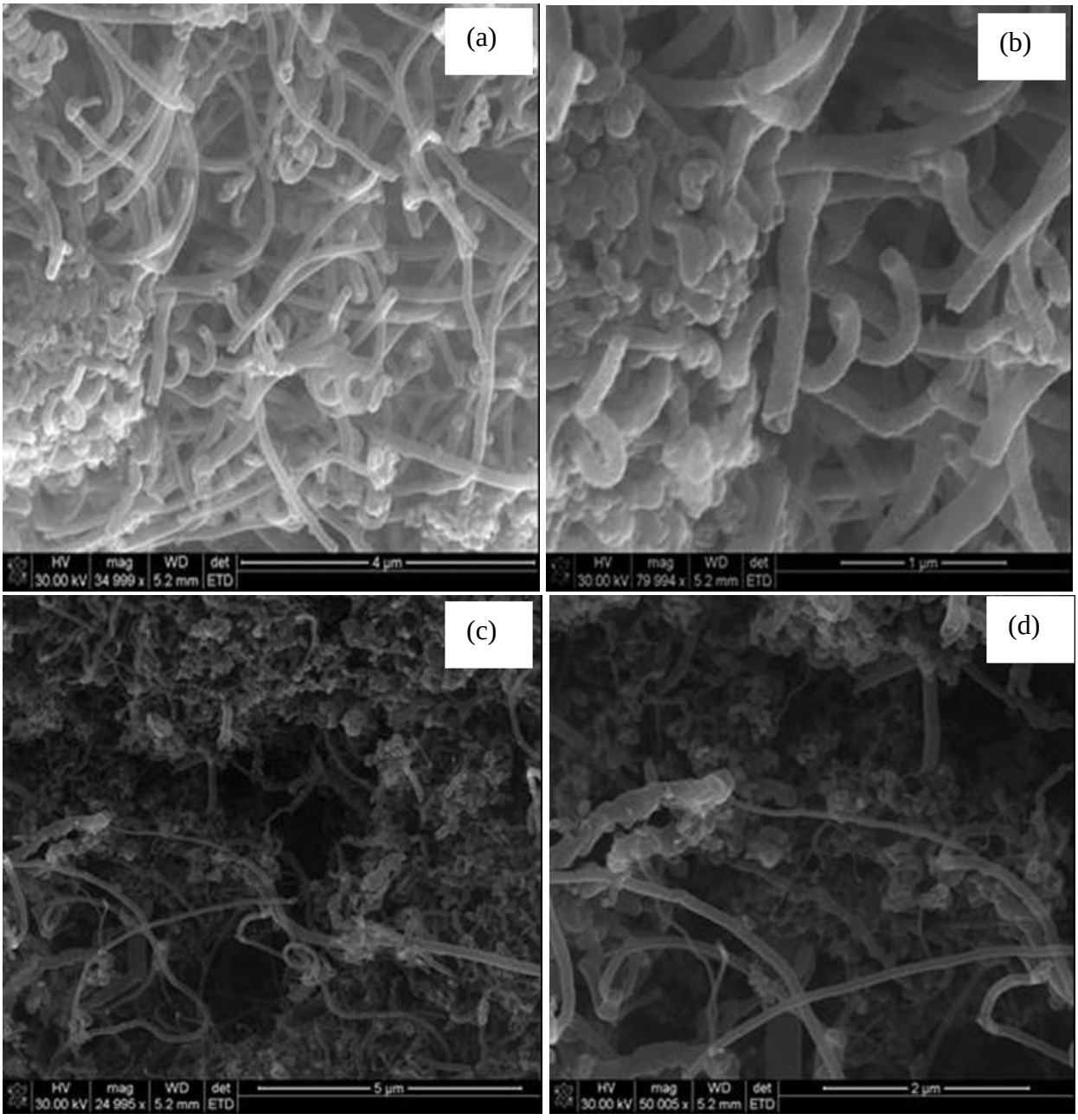

Figure S27 TEM images of purified CNMs generated from a 50:50 volume ratio of heated CH_3CN:TTCE (heated at 100 °C).

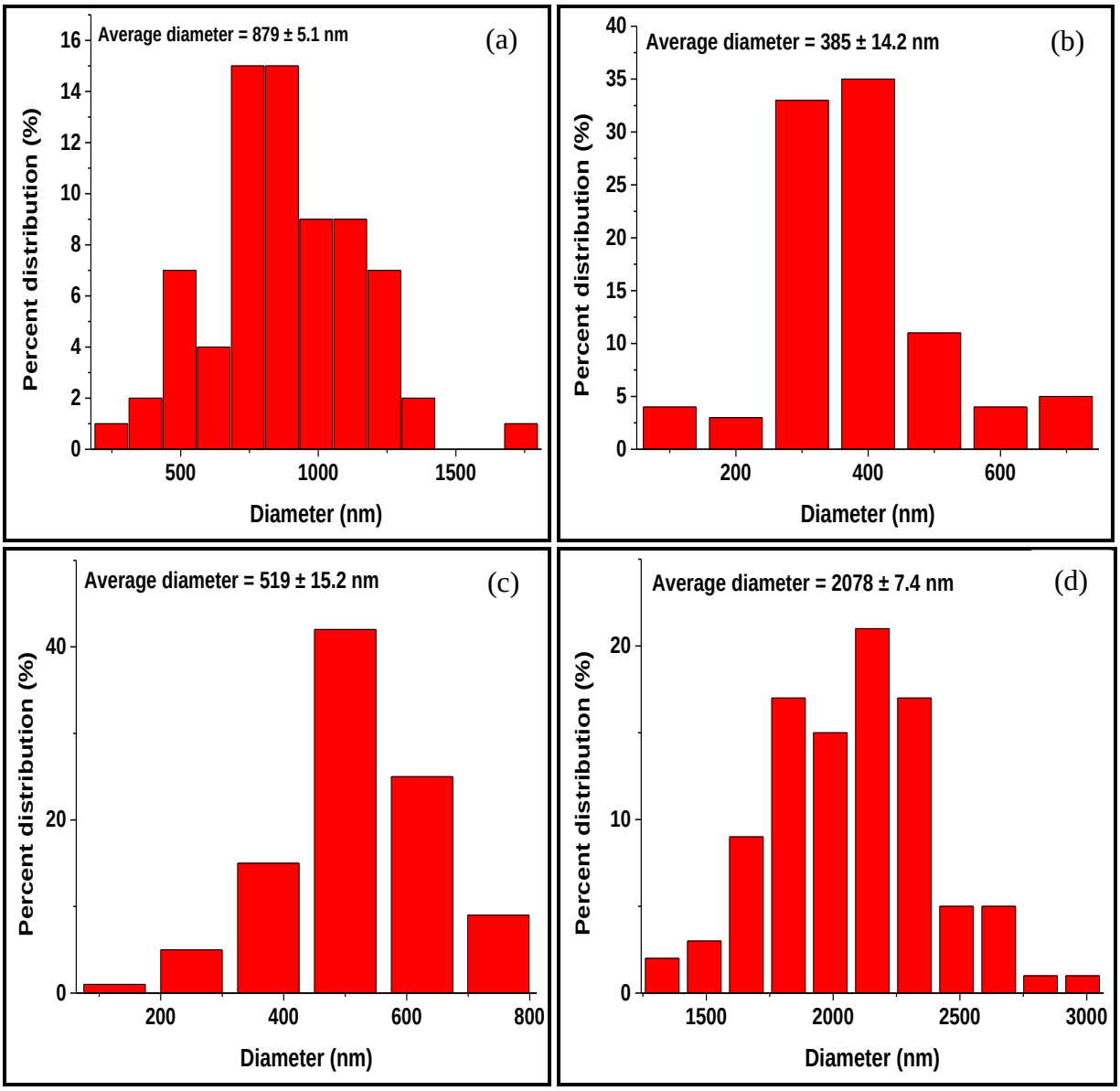

Figure S28 Diameter distribution curves of PVP nanofibers of various concentrations (a) 30 wt.%, (b) 35 wt.%, (c) 40 wt.% and (d) 45 wt.% electrospun from a (1:1 v/v) DMF/THF solvent mixture.

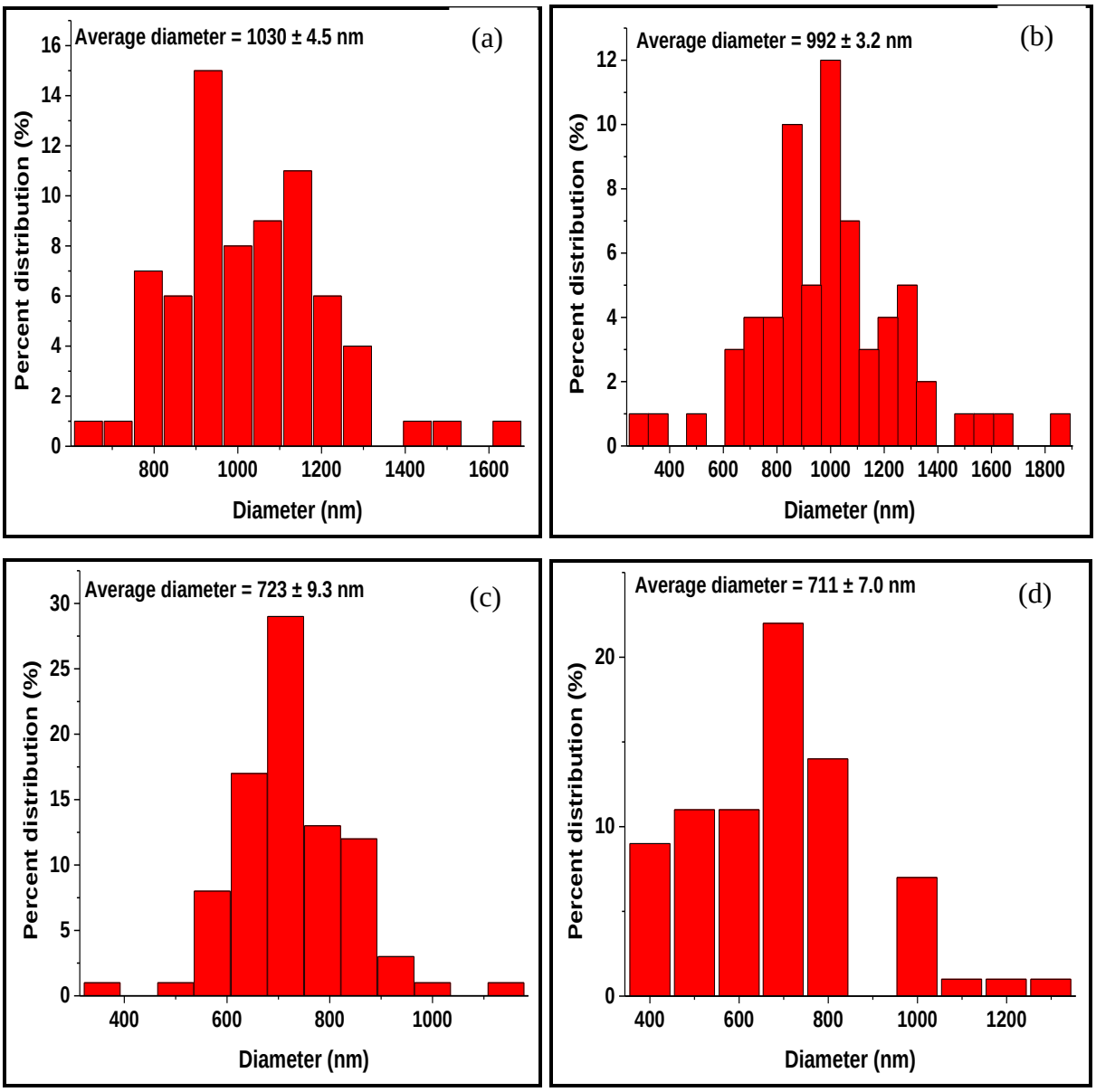

Figure S29 Diameter distribution curves of 40 wt.% PVP nanofibers electrospun at various needle tip to collector distance (a) 8 cm, (b) 10 cm, (c) 12 cm and (d) 18 cm using a (1:1 v/v) DMF/THF solvent mixture.

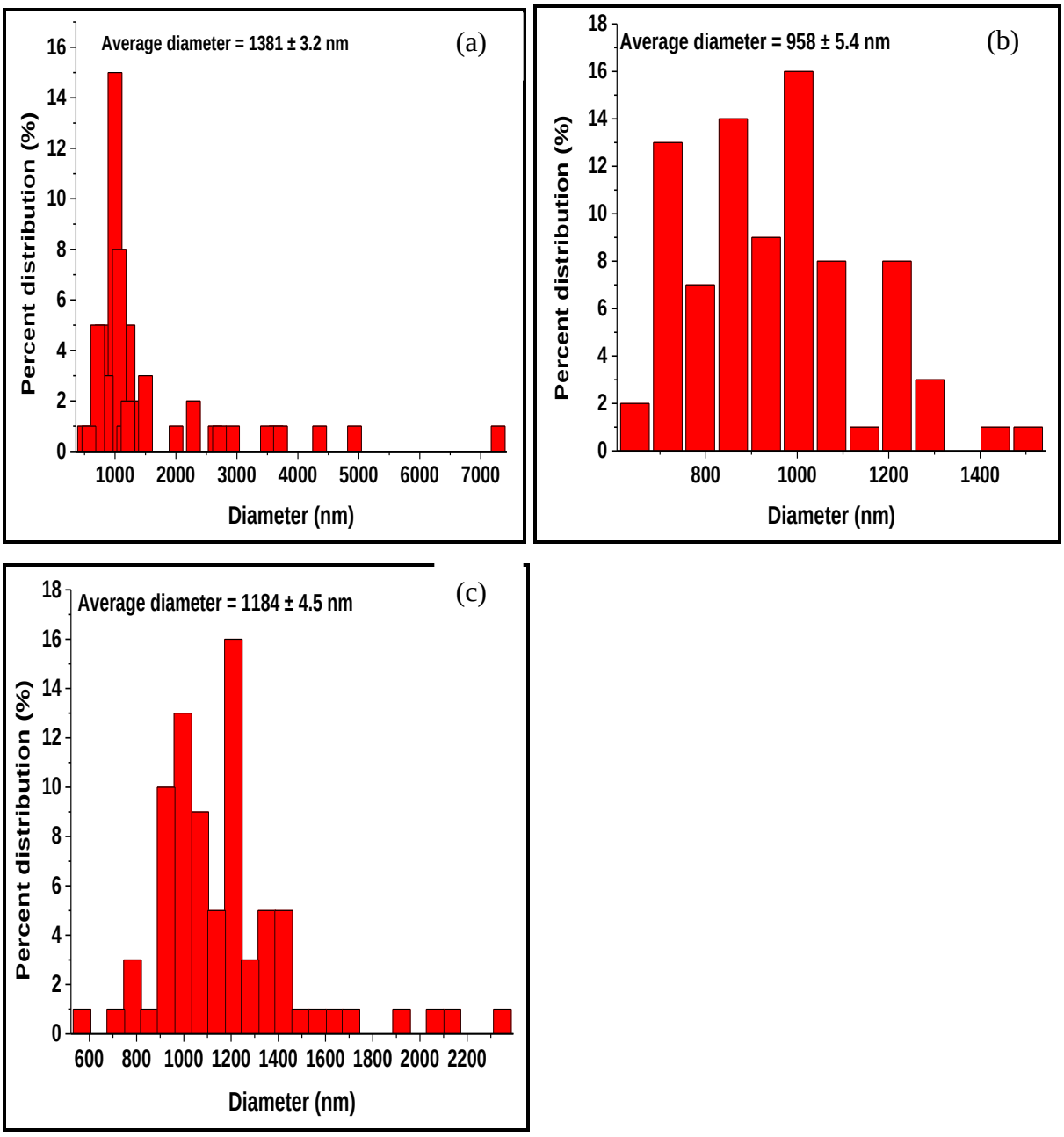

Figure S30 Diameter distribution curves of 40 wt.% PVP nanofibers electrospun by varying the applied voltage (a) 11 kV, (b) 13 kV, and (c) 17 kV using a (1:1 v/v) DMF/THF solvent mixture.

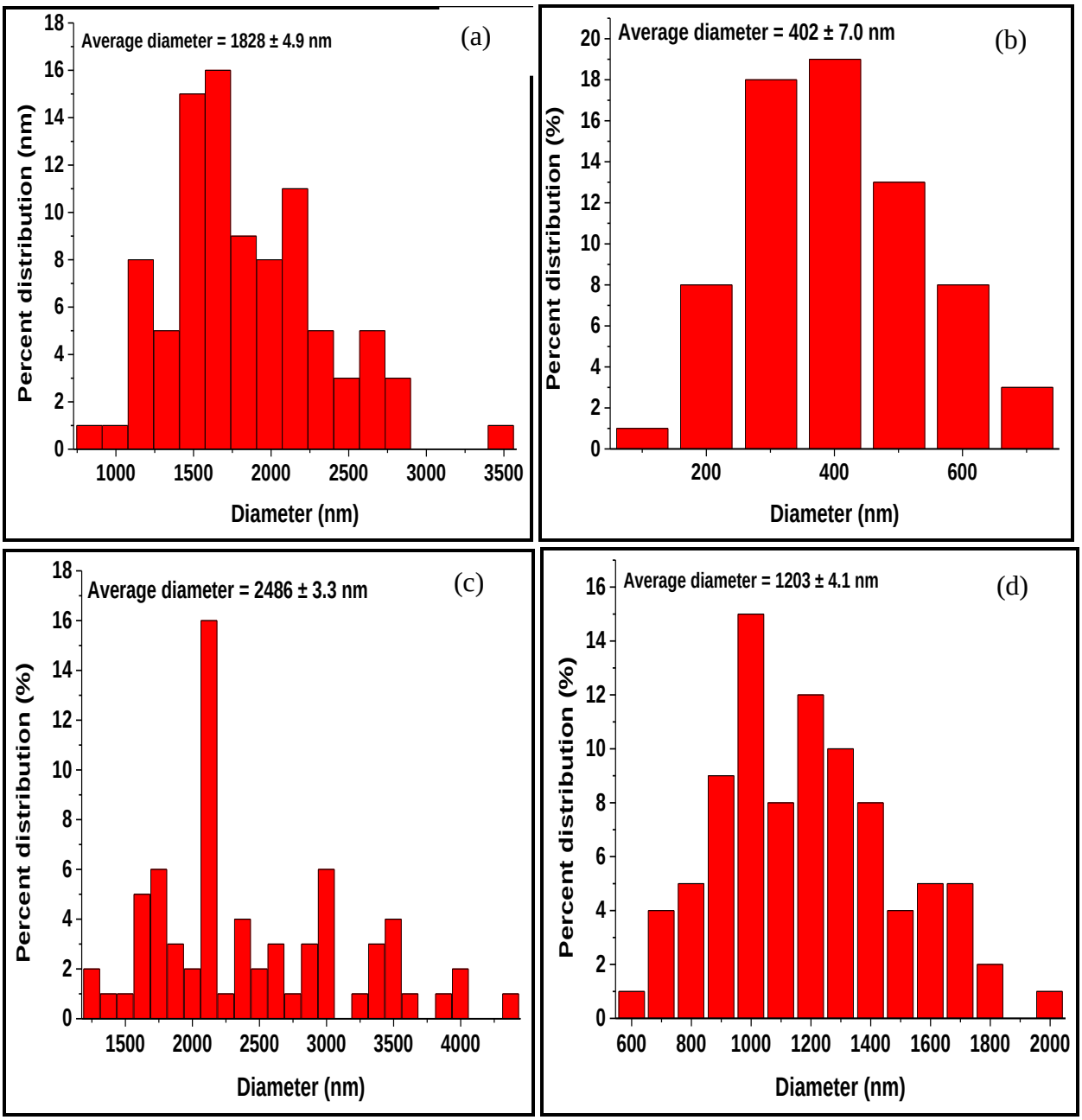

Figure S31 Diameter distribution curves of nanofibers prepared from 40 wt.% PVP containing (a) 0.4 wt.% (b) 0.5 wt.%, (c) 0.6 wt.% and 0.7 wt.% MWCNTs, electrospun from a mixture of DMF/THF (1:1 v/v) at 15 kV, 16 cm and 1 mL/h applied voltage, collector distance and feed rate

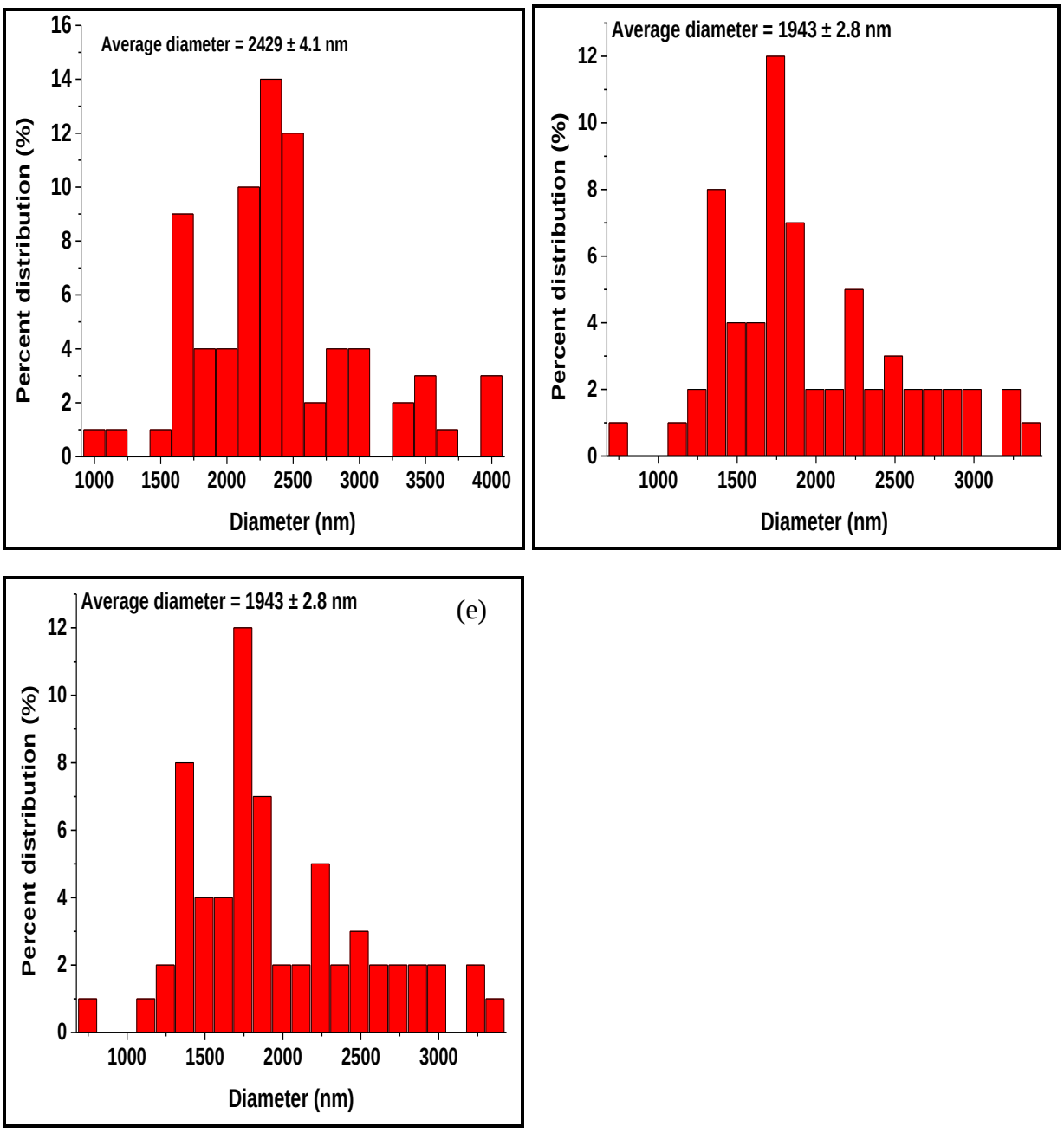

Figure S32 Diameter distribution curve of a PVP/MWCNT-0.5 wt.% composite nanofibers electrospun by varying the applied voltage (a) 11 kV, (b) 13 kV, and (c) 17 kV using a (1:1 v/v) DMF/THF solvent mixture.

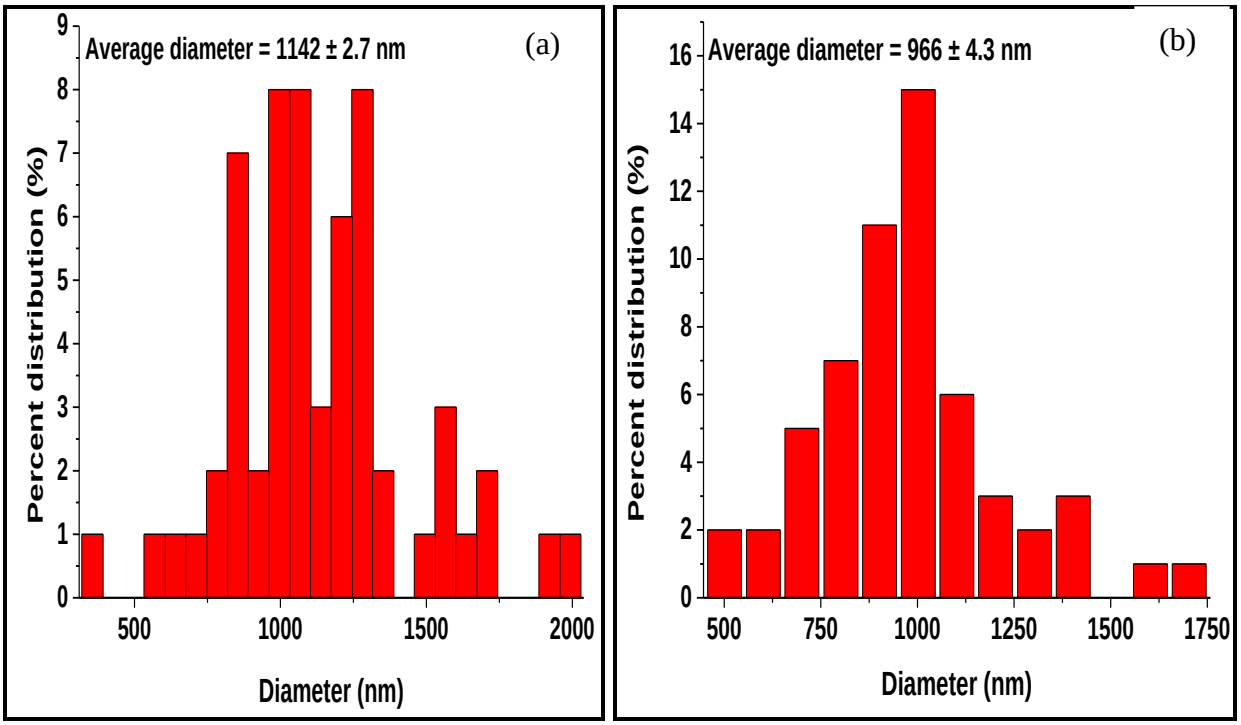

Figure S33 Diameter distribution curve of a PVP/MWCNT-0.5 wt.% composite nanofibers electrospun by varying the feed rate (a) 2 mL/h, and (b) 3 mL/h.

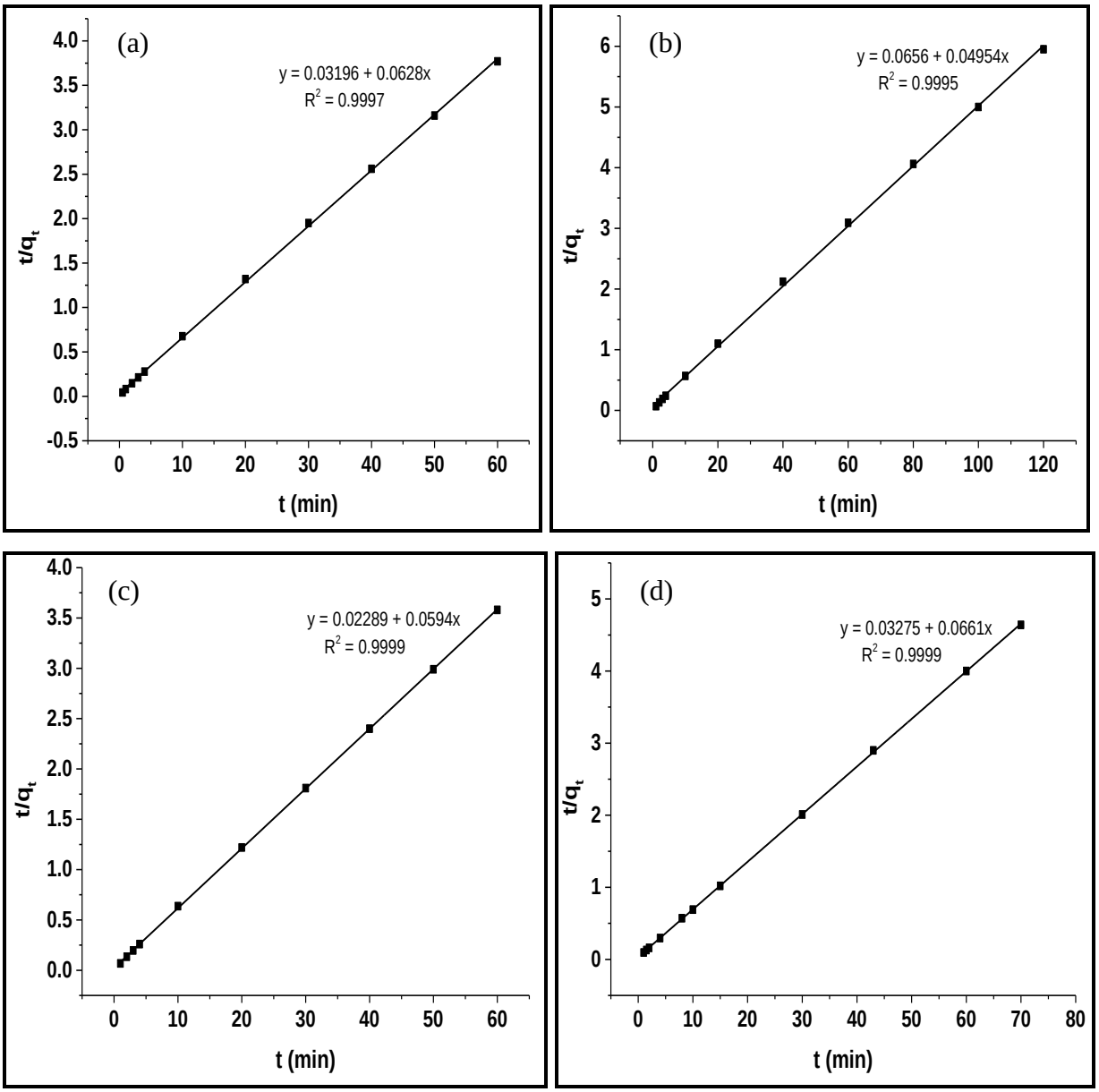

Figure S34 Second-order kinetic model for adsorption of (a) engine oil in oil-water emulsions, (b) pure engine oil, (c) pure mineral oil and (d) pure vegetable oil by MWCNT/PVP composite membrane.